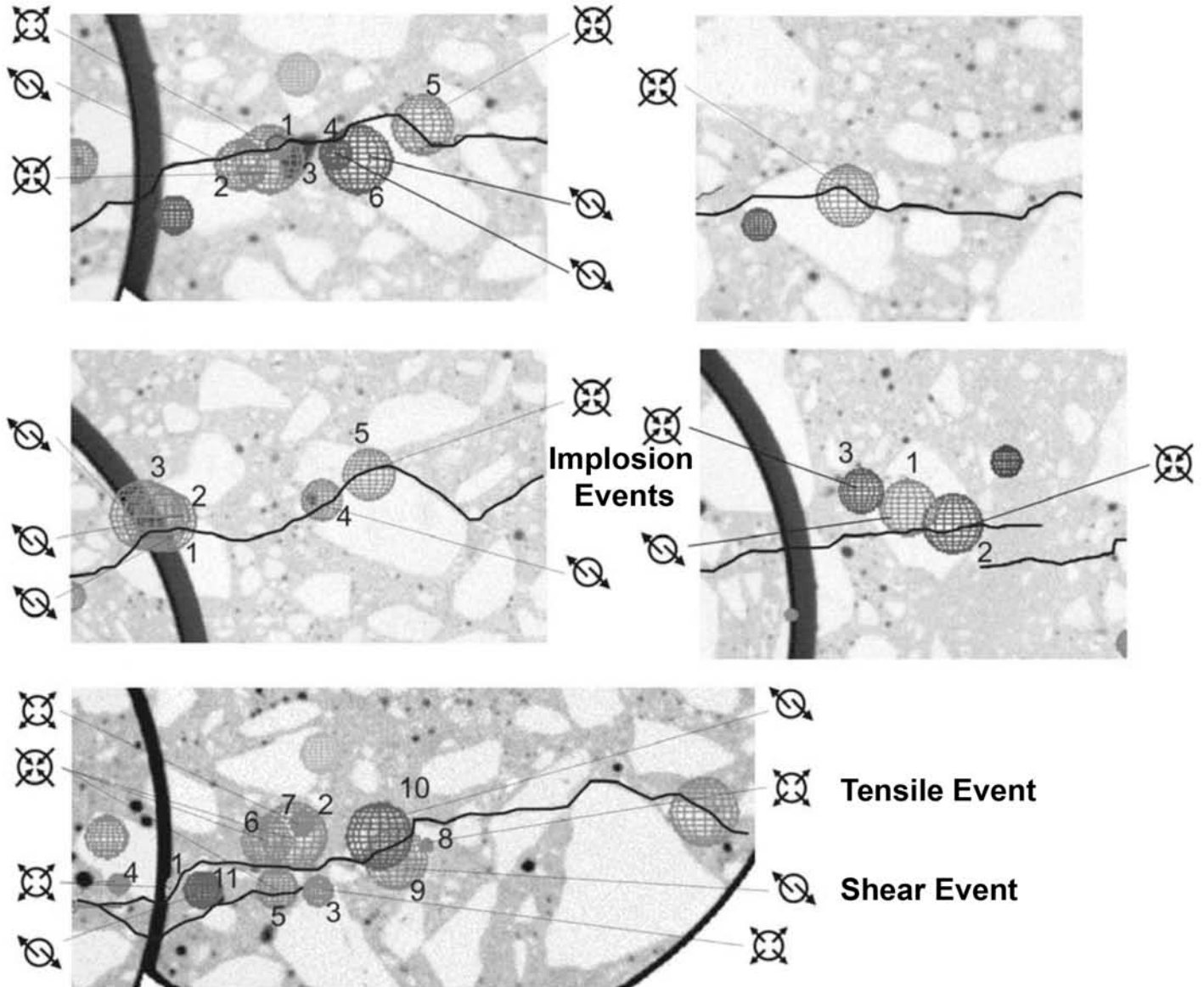


An International
Forum For
The AE Science
and Technology

JOURNAL OF ACOUSTIC EMISSION

Vol.25/January-December 2007



**Three Types of AE Events Located at CT Crack Images
Revealed by University of Toronto Study**

Endorsed by
AEWG
and
EWGAE

Published by
Acoustic Emission Group
Encino, CA USA

JOURNAL OF ACOUSTIC EMISSION

VOLUME 25, 2007

VIEWING AN ARTICLE IN CD-ROM

You need a software that can read a pdf-file, such as Adobe Acrobat Reader®. Install one first before going further. You can download the latest version from www.adobe.com. Use of Adobe Acrobat® (not provided) allows one to utilize the Search function. This gives the power to search for a name or a word in the entire volume and is highly recommended.

PDF Files: Contents are listed below. Individual papers have file names of **25-xxx.pdf**, with xxx as their first page number.

CONTENTS

- 25-001 STRUCTURAL INTEGRITY EVALUATION USING ACOUSTIC EMISSION
KANJI ONO
- 25-021 ACOUSTIC EMISSION TECHNIQUES STANDARDIZED FOR CONCRETE
STRUCTURES
MASAYASU OHTSU, TOSHIRO ISODA and YUICHI TOMODA
- 25-033 ACOUSTIC EMISSION MONITORING OF REINFORCED CONCRETE
FRAME DURING SEISMIC LOADING
A. ANASTASOPOULOS, S. BOUSIAS and T. TOUTOUNTZAKIS
- 25-042 ACOUSTIC EMISSION LEAK TESTING OF PIPES FOR PRESSURIZED
GAS USING ACTIVE FIBER COMPOSITE ELEMENTS AS SENSORS
ANDREAS J. BRUNNER and MICHEL BARBEZAT
- 25-051 ACOUSTIC EMISSION TECHNIQUE APPLIED FOR MONITORING AND
INSPECTION OF CEMENTITIOUS STRUCTURES ENCAPSULATING
ALUMINIUM
L. M. SPASOVA, M. I. OJOVAN and C. R. SCALES
- 25-069 EVALUATION OF REPAIR EFFECT FOR DETERIORATED CONCRETE
PIERS OF INTAKE DAM USING AE ACTIVITY
TOMOKI SHIOTANI and DIMITRIOS G. AGGELIS
- 25-080 ACOUSTIC EMISSION MONITORING OF FLEXURALLY LOADED
ARAMID/EPOXY COMPOSITES BY EMBEDDED PVDF SENSORS
CLAUDIO CANEVA, IGOR MARIA DE ROSA and FABRIZIO SARASINI
- 25-092 ACOUSTIC EMISSION SIGNALS GENERATED BY MONOPOLE (PENCIL-
LEAD BREAK) VERSUS DIPOLE SOURCES: FINITE ELEMENT
MODELING AND EXPERIMENTS
M. A. HAMSTAD

- 25-107 HIGH-TEMPERATURE ACOUSTIC EMISSION SENSING USING ALUMINUM NITRIDE SENSOR
HIROAKI NOMA, TATSUO TABARU, MORITO AKIYAMA, NORIKO MIYOSHI, TOMOHARU HAYANO and HIDEO CHO
- 25-115 DAMPING, NOISE, AND IN-PLANE RESPONSE OF MEMS ACOUSTIC EMISSION SENSORS
AMELIA P. WRIGHT, WEI WU, IRVING J. OPPENHEIM and DAVID W. GREVE
- 25-124 IMMERSION-TYPE QUADRIDIRECTIONAL OPTICAL FIBER AE SENSOR FOR LIQUID-BORNE AE
TAKUMA MATSUO, HIDEO CHO, TAKESHI OGAWA and MIKIO TAKEMOTO
- 25-132 A SIMPLE METHOD TO COMPARE THE SENSITIVITY OF DIFFERENT AE SENSORS FOR TANK FLOOR TESTING
HARTMUT VALLEN, JOCHEN VALLEN and JENS FORKER
- 25-140 DAMAGE IN CARBON FIBRE COMPOSITES: THE DISCRIMINATION OF ACOUSTIC EMISSION SIGNALS USING FREQUENCY
MARK EATON, KAREN HOLFORD, CAROL FEATHERSTON and RHYS PULLIN
- 25-149 CHARACTERISTICS OF ACOUSTIC EMISSIONS FROM DEHYDRATING WOOD RELATED TO SHRINKAGE PROCESSES
SABINE ROSNER
- 25-157 CHARACTERIZATION OF TITANIUM HYDRIDES USING A HYBRID TECHNIQUE OF AE AND FEM DURING INDENTATION TEST
YOSHIHIRO TANIYAMA, HIDEO CHO, MIKIO TAKEMOTO and GEN NAKAYAMA
- 25-166 ANALYSIS OF THE HYDROGEN DEGRADATION OF LOW-ALLOY STEEL BY ACOUSTIC EMISSION
KRYSTIAN PARADOWSKI, WOJCIECH SPYCHALSKI, KRYSTYNA LUBLINSKA and KRZYSZTOF J. KURZYDŁOWSKI
- 25-172 HYDROGEN RELATED BRITTLE CRACKING OF METASTABLE TYPE-304 STAINLESS STEEL
HIDEO CHO and MIKIO TAKEMOTO
- 25-179 ANALYSIS OF ACOUSTIC EMISSION FROM IMPACT AND FRACTURE OF CFRP LAMINATES
KANJI ONO, YOSHIHIRO MIZUTANI AND MIKIO TAKEMOTO
- 25-187 NEURAL NETWORK BURST PRESSURE PREDICTION IN COMPOSITE OVERWRAPPED PRESSURE VESSELS
ERIC v. K. HILL, SETH-ANDREW T. DION, JUSTIN O. KARL, NICHOLAS S. SPIVEY and JAMES L. WALKER II

- 25-194 ACOUSTIC EMISSION SOURCE LOCATION IN A THICK STEEL PLATE
BY LAMB MODES
M. A. HAMSTAD
- 25-215 NOVEL ACOUSTIC EMISSION SOURCE LOCATION
*RHYS PULLIN, MATTHEW BAXTER, MARK EATON, KAREN HOLFORD and
SAM EVANS*
- 25-224 ACOUSTIC EMISSION SOURCE LOCATION ON AN ARBITRARY
SURFACE BY GEODESIC CURVE EVOLUTION
G. PRASANNA, M. R. BHAT and C. R. L. MURTHY
- 25-231 PROBABILITY OF DETECTION FOR ACOUSTIC EMISSION
ADRIAN POLLOCK
- 25-238 PLASTIC-REGION TIGHTENING OF BOLTS CONTROLLED BY
ACOUSTIC EMISSION METHOD
YOSHIHIRO MIZUTANI, TADASHI ONISHI and MASAMI MAYUZUMI
- 25-247 REAL-TIME DENOISING OF AE SIGNALS BY SHORT TIME FOURIER
TRANSFORM AND WAVELET TRANSFORM
KAITA ITO and MANABU ENOKI
- 25-252 MONITORING THE EVOLUTION OF INDIVIDUAL AE SOURCES IN
CYCLICALLY LOADED FRP COMPOSITES *RUNAR UNNTHORSSON,
THOMAS P. RUNARSSON AND MAGNUS T. JONSSON*
- 25-260 ON USING AE-HIT PATTERNS FOR MONITORING CYCLICALLY
LOADED CFRP *RUNAR UNNTHORSSON, THOMAS P. RUNARSSON
and MAGNUS T. JONSSON*
- 25-267 AE MONITORING OF SOIL CORROSION OF BURIED PIPE
HIDEO CHO and MIKIO TAKEMOTO
- 25-276 THIRTY YEARS EXPERIENCE OF INDUSTRIAL APPLICATIONS OF
ACOUSTIC EMISSION TESTING AT TÜV AUSTRIA
PETER TSCHELIESNIG
- 25-286 ACOUSTIC EMISSION TESTING OF SEAM-WELDED HIGH ENERGY PIPING
SYSTEMS IN FOSSIL POWER PLANTS
JOHN M. RODGERS
- 25-294 ACOUSTIC EMISSION AND X-RAY TOMOGRAPHY IMAGING OF SHEAR
FRACTURE FORMATION IN CONCRETE
TATYANA KATSAGA and R. PAUL YOUNG
- 25-308 GLOBAL MONITORING OF CONCRETE BRIDGE USING ACOUSTIC
EMISSION
T. SHIOTANI, D. G. AGGELIS and O. MAKISHIMA

- 25-316 DEMAND ON FLEXURAL TENSION STEEL REINFORCEMENT ANCHORAGE ZONES IN FULL-SCALE BRIDGE BENT CAPS QUANTIFIED BY MEANS OF ACOUSTIC EMISSION
THOMAS SCHUMACHER, CHRISTOPHER HIGGINS, STEVEN GLASER and CHRISTIAN GROSSE
- 25-324 DAMAGE EVALUATION OF POST-TENSIONED CONCRETE VIADUCT BY AE DURING PROOF LOADING *EDOARDO PROVERBIO, GIUSEPPE CAMPANELLA and VINCENZO VENTURI*
- 25-331 EARLY FAULT DETECTION AT GEAR UNITS BY ACOUSTIC EMISSION AND WAVELET ANALYSIS *CHRISTIAN SCHEER, WILFRIED REIMCHE and FRIEDRICH-WILHELM BACH*
- 25-341 APPLICATION OF ACOUSTIC EMISSION IN MONITORING OF FAILURE IN SLIDE BEARINGS
IRENEUSZ BARAN, MAREK NOWAK and WOJCIECH DARSKI
- 25-348 MAPPING OF WHEEL FLANGE RUBBING ON RAIL USING AE: LABORATORY TEST
N. A. THAKKAR, R. L. REUBEN and J. A. STEEL
- 25-355 DAMAGE ASSESSMENT OF GEARBOX OPERATING IN HIGH NOISY ENVIRONMENT USING WAVEFORM STREAMING APPROACH
DIDEM OZEVIN, JASON DONG, VALERY GODINEZ and MARK CARLOS
- 25-364 CLUSTERING ANALYSIS OF AE IN ROCK
N. IVERSON, C-S. KAO and J.F. LABUZ
- 25-373 IMPACT IMAGING METHOD TO MAP DAMAGE IN CONCRETE BRIDGE DECK SLABS
STEPHEN D. BUTT, VIDYADHAR LIMAYE and JOHN P. NEWHOOK

Contents25	Contents of Volume 25 (2007)	I-1 – I-4
AUindex25	Authors Index of Volume 25 /e-mail addresses of authors	I-5 – I-7
AusNotes	Policy/Author's Notes/Meeting Calendar/Subscription Information	I-8 – I-10
In Memoriam	Professor Reginald Hardy, Jr.	I-11
EWGAE27	Note on expanded contributions from Cardiff Conference.	I-12

JAE Index Folder* Cumulative Indices of J. of Acoustic Emission, 1982 - 2007

* indicates the availability in CD-ROM only.

Cover photograph is from 25-294 by *TATYANA KATSAGA and R. PAUL YOUNG*.

Volume 25 (2007) AUTHORS INDEX

DIMITRIOS G. AGGELIS,	25-069, 25-308
MORITO AKIYAMA,	25-107
A. ANASTASOPOULOS,	25-033
FRIEDRICH-WILHELM BACH,	25-331
IRENEUSZ BARAN,	25-341
MICHEL BARBEZAT,	25-042
MATTHEW BAXTER,	25-215
M. R. BHAT,	25-224
S. BOUSIAS,	25-033
ANDREAS J. BRUNNER,	25-042
STEPHEN D. BUTT,	25-373
GIUSEPPE CAMPANELLA,	25-324
CLAUDIO CANEVA,	25-080
MARK CARLOS,	25-355
HIDEO CHO,	25-107, 25-124, 25-157, 25-172, 25-267
WOJCIECH DARSKI,	25-341
IGOR MARIA DE ROSA,	25-080
SETH-ANDREW T. DION,	25-187
JASON DONG,	25-355
MARK EATON,	25-140, 25-215
MANABU ENOKI,	25-247
SAM EVANS,	25-215
CAROL FEATHERSTON,	25-140
JENS FORKER,	25-132
STEVEN GLASER,	25-316
VALERY GODINEZ,	25-355
DAVID W. GREVE,	25-115
CHRISTIAN GROSSE,	25-316
M. A. HAMSTAD,	25-092, 25-194
TOMOHARU HAYANO,	25-107
CHRISTOPHER HIGGINS,	25-316
ERIC v. K. HILL,	25-187
KAREN HOLFORD,	25-140, 25-215
N. IVERSON,	25-364
TOSHIRO ISODA,	25-021
KAITA ITO,	25-247
MAGNUS T. JONSSON,	25-252, 25-260
C-S. KAO,	25-364
JUSTIN O. KARL,	25-187
TATYANA KATSAGA,	25-294
KRZYSZTOF J. KURZYDLOWSKI	25-166

J.F. LABUZ,	25-364
VIDYADHAR LIMAYE,	25-373
KRYSTYNA LUBLINSKA,	25-166
O. MAKISHIMA,	25-308
TAKUMA MATSUO,	25-124
MASAMI MAYUZUMI,	25-238
NORIKO MIYOSHI,	25-107
YOSHIHIRO MIZUTANI	25-179, 25-238
C. R. L. MURTHY,	25-224
GEN NAKAYAMA,	25-157
JOHN P. NEWHOOK	25-373
HIROAKI NOMA,	25-107
MAREK NOWAK,	25-341
TADASHI ONISHI,	25-238
TAKESHI OGAWA,	25-124
MASAYASU OHTSU,	25-021
M. I. OJOVAN,	25-051
KANJI ONO,	25-001, 25-179
IRVING J. OPPENHEIM,	25-115
DIDEM OZEVIN,	25-355
KRYSTIAN PARADOWSKI,	25-166
ADRIAN POLLOCK,	25-231
G. PRASANNA,	25-224
EDOARDO PROVERBIO,	25-324
RHYS PULLIN,	25-140, 25-215
WILFRIED REIMCHE,	25-331
R. L. REUBEN,	25-348
JOHN M. RODGERS,	25-286
IGOR MARIA DE ROSA,	25-080
SABINE ROSNER,	25-149
THOMAS P. RUNARSSON,	25-252, 25-260
FABRIZIO SARASINI,	25-080
C. R. SCALES,	25-051
CHRISTIAN SCHEER,	25-331
THOMAS SCHUMACHER,	25-316
TOMOKI SHIOTANI,	25-069, 25-308
L. M. SPASOVA,	25-051
NICHOLAS S. SPIVEY,	25-187
WOJCIECH SPYCHALSKI,	25-166
J. A. STEEL,	25-348
TATSUO TABARU,	25-107
MIKIO TAKEMOTO,	25-124, 25-157, 25-172, 25-179, 25-267
YOSHIHIRO TANIYAMA,	25-157
N. A. THAKKAR,	25-348

YUICHI TOMODA,	25-021
T. TOUTOUNTZAKIS,	25-033
PETER TSCHELIESNIG,	25-276
RUNAR UNNTHORSSON,	25-252, 25-260
HARTMUT VALLEN,	25-132
JOCHEN VALLEN,	25-132
VINCENZO VENTURI,	25-324
JAMES L. WALKER II,	25-187
AMELIA P. WRIGHT,	25-115
WEI WU,	25-115
R. PAUL YOUNG,	25-294

E-MAIL ADDRESSES OF SELECTED AUTHORS

Athanasios Anastasopoulos <nassos@envirocoustics.gr>, Ireneusz Baran <i.baran@arlab.com.pl>, M R BHAT <mrb@aero.iisc.ernet.in>, Andreas Brunner <Andreas.Brunner@empa.ch>, S. D. Butt <sbutt@engr.mun.ca>, Claudio Caneva <claudio.caneva@ingchim.ing.uniroma1.it>, Hideo CHO <cho@me.aoyama.ac.jp>, Mark Eaton <eatonm@cardiff.ac.uk>, "Marvin A. Hamstad" <mhamstad@du.edu>, Eric Hill <Eric.Hill@erau.edu>, Kaita ITO <ito@rme.mm.t.u-tokyo.ac.jp> Tatyana Katsaga <t.katsaga@utoronto.ca>, Joseph F Labuz <jlabuz@umn.edu>, Takuma Matsuo <matsuo.takuma@gmail.com> Yoshihiro MIZUTANI <yimizutan@mes.titech.ac.jp>, Hiroaki Noma <h-noma@aist.go.jp>, Masayasu Ohtsu <ohtsu@kumamoto-u.ac.jp>, Didem Ozevin <dozevin@pacndt.com>, Krystian Paradowski <kparadowski@inmat.pw.edu.pl> Adrian Pollock <apollock@pacndt.com>, Edoardo Proverbio <proverbi@ingegneria.unime.it> Rhys Pullin <pullinr@cardiff.ac.uk>, Reuben, Robert L <R.L.Reuben@hw.ac.uk> John Rodgers <jr_aec@msn.com> Sabine Rosner <sabine.rosner@boku.ac.at> Christian Scheer <scheer@iw.uni-hannover.de>, Thomas Schumacher <schumact@engr.orst.edu>, Tomoki Shiotani <Shiotani@toshi.kuciv.kyoto-u.ac.jp>, L M Spasova <L.Spasova@sheffield.ac.uk>, Tscheliesnig Peter DI. <tsc@tuv.at>, Rúnar Unnthórsson <runson@hi.is>, Hartmut Vallen <hartmut@vallen.de>, Amelia P Wright <apwright@andrew.cmu.edu>
--

JOURNAL OF ACOUSTIC EMISSION

Editor: Kanji Ono

Associate Editors: A. G. Beattie, T. F. Drouillard, M. Ohtsu and W. H. Prosser

1. Aims and Scope of the Journal

Journal of Acoustic Emission is an international journal designed to be of broad interest and use to both researcher and practitioner of acoustic emission. It will publish original contributions of all aspects of research and significant engineering advances in the sciences and applications of acoustic emission. The journal will also publish reviews, the abstracts of papers presented at meetings, technical notes, communications and summaries of reports. Current news of interest to the acoustic emission communities, announcements of future conferences and working group meetings and new products will also be included.

Journal of Acoustic Emission includes the following classes of subject matters;

A. Research Articles: Manuscripts should represent completed original work embodying the results of extensive investigation. These will be judged for scientific and technical merit.

B. Applications: Articles must present significant advances in the engineering applications of acoustic emission. Material will be subject to reviews for adequate description of procedures, substantial database and objective interpretation.

C. Technical Notes and Communications: These allow publications of short items of current interest, new or improved experimental techniques and procedures, discussion of published articles and relevant applications.

D. AE Program and Data Files: Original program files and data files that can be read by others and analyzed will be distributed in CD-ROM.

Reviews, Tutorial Articles and Special Contributions will address the subjects of general interest. Nontechnical part will cover book reviews, significant personal and technical accomplishments, current news and new products.

2. Endorsement

Acoustic Emission Working Group (AEWG), European Working Group on Acoustic Emission (EWGAE), have endorsed the publication of Journal of Acoustic Emission.

3. Governing Body

The Editor and Associate Editors will implement the editorial policies described above. The Editorial Board will advise the editors on any major change. The Editor, Professor Kanji Ono, has the general responsibility for all the matters. Associate Editors assist the review processes as lead reviewers. The members of the Editorial Board are selected for their knowledge and experience on AE and will advise and assist the editors on the publication

policies and other aspects. The Board presently includes the following members:

A. Anastasopoulos	(Greece)
F.C. Beall	(USA)
J. Bohse	(Germany)
P. Cole	(UK)
L. Golaski	(Poland)
M.A. Hamstad	(USA)
R. Hay	(Canada)
K.M. Holford	(UK)
O.Y. Kwon	(Korea)
J.C. Lenain	(France)
G. Manthei	(Germany)
P. Mazal	(Czech Republic)
C.R.L. Murthy	(India)
A.A. Pollock	(USA)
F. Rauscher	(Austria)
I. Roman	(Israel)
T. Shiotani	(Japan)
P. Tschliesnig	(Austria)
H. Vallen	(Germany)
M. Wevers	(Belgium)
B.R.A. Wood	(Australia)

4. Publication

Journal of Acoustic Emission is published annually in CD-ROM by Acoustic Emission Group, PMB 409, 4924 Balboa Blvd, Encino, CA 91316. It may also be reached at 2121H, Engr. V, University of California, Los Angeles, California 90095-1595 (USA). tel. 310-825-5233. FAX 818-990-1686. e-mail: aegroup7@gmail.com or mailto:ono@ucla.edu

5. Subscription

Subscription should be sent to Acoustic Emission Group. Annual rate for 2008 is US \$111.00 including CD-ROM delivery, by priority mail in the U.S. and by air for Canada and elsewhere. For additional print copy, add \$40. Overseas orders must be paid in US currencies with a check drawn on a US bank. PayPal payment accepted. Inquire for individual (with institutional order) and bookseller discounts. See also page I-8.

6. Advertisement

No advertisement will be accepted, but announcements for books, training courses and future meetings on AE will be included without charge.

Notes for Contributors

1. General

The Journal will publish contributions from all parts of the world and manuscripts for publication should be submitted to the Editor. Send to:

Professor Kanji Ono, Editor - JAE
Rm. 2121H, Engr. V, MSE Dept.
University of California
420 Westwood Plaza,
Los Angeles, California 90095-1595 USA
FAX (1) 818-990-1686
e-mail: ono@ucla.edu

Authors of any AE related publications are encouraged to send a copy to:

Mr. T.F. Drouillard, Associate Editor - JAE
11791 Spruce Canyon Circle
Golden, Colorado 80403 USA

Only papers not previously published will be accepted. Authors must agree to transfer the copyright to the Journal and not to publish elsewhere, the same paper submitted to and accepted by the Journal. A paper is acceptable if it is a revision of a governmental or organizational report, or if it is based on a paper published with limited distribution. Compilation of annotated data files will be accepted for inclusion in CD-ROM distribution, so that others can share in their analysis for research as well as training. ASCII or widely accepted data formats will be required.

The language of the Journal is English. All papers should be written concisely and clearly.

2. Page Charges

No page charge is levied. The contents of CD-ROM will be supplied to the authors free of charge via Internet site.

3. Manuscript for Review

Manuscripts for review need only to be typed legibly; preferably, double-spaced on only one side of the page with wide margins. The title should be brief. An abstract of 100-200 words is needed for articles. Except for short communications, descriptive heading should be used to divide the paper into its component parts. Use the International System of Units (SI).

References to published literature should be quoted in the text citing authors and the year of publication or consecutive numbers. These are to be grouped together

at the end of the paper in alphabetical and chronological order. Journal references should be arranged as below. Titles for journal or book articles are helpful for readers, but may be omitted.

H.L. Dunegan, D.O. Harris and C.A. Tatro (1968), *Eng. Fract. Mech.*, 1, 105-122.

Y. Krampfner, A. Kawamoto, K. Ono and A.T. Green (1975), "Acoustic Emission Characteristics of Cu Alloys under Low-Cycle Fatigue Conditions," NASA CR-134766, University of California, Los Angeles and Acoustic Emission Tech. Corp., Sacramento, April.

A.E. Lord, Jr. (1975), *Physical Acoustics: Principles and Methods*, vol. 11, eds. W. P. Mason and R. N. Thurston, Academic Press, New York, pp. 289-353.

Abbreviations of journal titles should follow those used in the ASM Metals Abstracts. In every case, authors' initials, appropriate volume and page numbers should be included. The title of the cited journal reference is optional.

Illustrations and tables should be planned to fit a single page width (165 mm or 6.5"). For the reviewing processes, these need not be of high quality, but submit glossy prints or equivalent electronic files with the final manuscript. Lines and letters should be legible.

4. Review

All manuscripts will be judged by qualified reviewer(s). Each paper is reviewed by one of the editors and may be sent for review by members of the Editorial Board. The Board member may seek another independent review. In case of disputes, the author may request other reviewers.

5. Electronic Media

This Journal will be primarily distributed electronically by CD-ROM. In order to expedite processing and minimize errors, the authors are requested to submit electronic files of the paper. We can read Macintosh and IBM PC formats. On the INTERNET, you can send an MS Word file and the separate figure files to "aegroup7@gmail.com".

6. Color Illustration

We can process color illustration needed to enhance the technical content of an article. With the new format, authors are encouraged to use them.

MEETING CALENDAR:

EWGAE2008

28th European Conference on Acoustic Emission Testing will be held at Krakow, Poland on Sep. 17-19, 2008. It is organized by Dr. Jerzy Schmidt of Faculty of Mechanical Engineering, Crakow University of Technology, Krakow. Over 75 papers will be presented. Meeting details can be found at: <http://www.ewgae.eu/>

AEWG-51

51st Meeting of AEWG will be held at Fogelman Center, University of Memphis, Memphis, Tennessee, USA, on October 13-15, 2008. Abstracts should be sent to Dr. Gang Qi, (gangqi@memphis.edu) before July 16, 2008. <http://www.aewg.org/>

IAES-19, The 19th International AE Symposium

The IAES-19 will be held at Kyoto on Dec. 8-12, 2008. It is organized by Dr. T. Shiotani of Kyoto University and is sponsored by Japan Society for Non-Destructive Inspection. Abstracts are due Apr. 30, 2008. Details can be found at: <http://www.19iaes-kyoto.com/>

2008 SUBSCRIPTION RATES

Base rate (CD-ROM) for one year	\$111.00
CD-ROM + printed copy, US priority mail:	\$151.00
CD-ROM + printed copy, non-US priority mail:	\$156.00
Print copy only with priority shipping (US)	\$140.00
Print copy only with priority/air shipping (non-US)	\$145.00
For countries without Global Priority Service*,	\$160.00
* incl. Argentina, Greece, Italy, Russia, Ukraine	

Payment must be in U.S. dollars drawn on a U.S. bank. Bank transfer accepted at
California Bank and Trust, San Fernando Valley Office (Account No. 080-03416470)
16130 Ventura Blvd, Encino, CA 91436 USA (Swift code: CALBUS66)

PAYPAL payment is accepted. Inquire via e-mail.

Back issues available; Inquiry and all orders should be sent to (or Fax 1-818-990-1686):

Acoustic Emission Group
PMB 409, 4924 Balboa Blvd. Encino, CA 91316 USA

For inquiry through Internet, use the following address: aegroup7@gmail.com
Editor-Publisher Kanji Ono Tel. (818) 849-9190
Publication Date of This Issue (Volume 25): 25 March 2008.

In Memoriam



H. Reginald Hardy, Jr. (1931 – 2008)

H. Reginald Hardy Jr., Professor Emeritus of Mining Engineering, Department of Energy and Mineral Engineering, Penn State University, 76, of State College, PA, passed away Jan. 22, 2008. Born Aug. 19, 1931, in Ottawa, Canada, Reg was the loyal, loving husband of Margaret M. (Lytle) married in 1954, survived also by his two sons and a granddaughter.

After getting BSc. from McGill University (1953), MSc. from Ottawa University (1962), both in physics, and Ph.D. in engineering mechanics from Virginia Polytechnic Institute in 1965, Reg joined the faculty at Penn State in 1966, following 13 years with Canada Department of Energy, Mines and Resources in Ottawa. During the past 40 years, Dr. Hardy had a passion for his scientific work in application of acoustic emission/microseismic (AE/MS) techniques to the geotechnical field. He conducted a number of major field and laboratory research projects and directed some 40 Ph.D. and Masters students, published numerous research papers in geotechnical and mining journals, four technical monographs, and 11 conference proceedings. Dr. Hardy organized six "Conferences on Acoustic Emission/Microseismic Activity in Geologic Structures and Materials," (1975-1996) and was active on the editorial review committee of the *Journal of Acoustic Emission*. His last major work was his book, *Acoustic Emission Microseismic Activity, Vol. 1: Principles, Techniques and Geotechnical Applications* (2003). He was the recipient of the ASTM Hogentogler and Templin Awards, the AEWG Achievement and Gold Medal Awards for "Pioneering work in the geologic applications of acoustic emission."

He was working to his last day, perhaps on the second volume of his book. Reg will be sincerely missed by his family, friends and colleagues. (<http://www.legacy.com/Link.asp?l=LS000101786354X>)

Kanji Ono

JOURNAL OF ACOUSTIC EMISSION, VOLUME 25, 2007

Expanded Articles from EWGAE2006 Cardiff Conference

The following eight articles were expanded from the papers originally given at EWGAE27. This collection has been organized by the Topical Editors, Professor Karen Holford and Dr. Rhys Pullin, Cardiff University, who also hosted EWGAE27. Their efforts are much appreciated.

- | | |
|--------|---|
| 25-001 | STRUCTURAL INTEGRITY EVALUATION USING ACOUSTIC EMISSION
<i>KANJI ONO</i> |
| 25-021 | ACOUSTIC EMISSION TECHNIQUES STANDARDIZED FOR CONCRETE
STRUCTURES
<i>MASAYASU OHTSU, TOSHIRO ISODA and YUICHI TOMODA</i> |
| 25-033 | ACOUSTIC EMISSION MONITORING OF REINFORCED CONCRETE
FRAME DURING SEISMIC LOADING
<i>A. ANASTASOPOULOS, S. BOUSIAS and T. TOUTOUNTZAKIS</i> |
| 25-042 | ACOUSTIC EMISSION LEAK TESTING OF PIPES FOR PRESSURIZED
GAS USING ACTIVE FIBER COMPOSITE ELEMENTS AS SENSORS
<i>ANDREAS J. BRUNNER and MICHEL BARBEZAT</i> |
| 25-051 | ACOUSTIC EMISSION TECHNIQUE APPLIED FOR MONITORING AND
INSPECTION OF CEMENTITIOUS STRUCTURES ENCAPSULATING
ALUMINIUM
<i>L. M. SPASOVA, M. I. OJOVAN and C. R. SCALES</i> |
| 25-069 | EVALUATION OF REPAIR EFFECT FOR DETERIORATED CONCRETE
PIERS OF INTAKE DAM USING AE ACTIVITY
<i>TOMOKI SHIOTANI and DIMITRIOS G. AGGELIS</i> |
| 25-080 | ACOUSTIC EMISSION MONITORING OF FLEXURALLY LOADED
ARAMID/EPOXY COMPOSITES BY EMBEDDED PVDF SENSORS
<i>CLAUDIO CANEVA, IGOR MARIA DE ROSA and FABRIZIO SARASINI</i> |
| 25-092 | ACOUSTIC EMISSION SIGNALS GENERATED BY MONOPOLE (PENCIL-
LEAD BREAK) VERSUS DIPOLE SOURCES: FINITE ELEMENT
MODELING AND EXPERIMENTS
<i>M. A. HAMSTAD</i> |

Karen Holford and Rhys Pullin

Topical Editors

STRUCTURAL INTEGRITY EVALUATION USING ACOUSTIC EMISSION

KANJI ONO

Department of Materials Science and Engineering
University of California, Los Angeles, California 90095-1595

Abstract

This paper reviews various approaches used in acoustic emission (AE) testing of structures so that further improvements can be realized in this important application of AE technology. Since the late 1950s, many successful AE tests of structures have been completed. Yet, the spread of AE technology is underwhelming. To achieve a wider use of AE, we attempt to organize and reexamine the AE methodology applied to structural integrity monitoring in four steps. 1. AE Sources: Primary sources of brittle fracture, micro- or macro-cracks in contrast to secondary sources of friction or fretting, rust, etc. 2. Evaluation Tools: Kaiser effects, arising from the irreversibility of AE, allow the detection of prior loading level and of damage states. Related indices are also useful. 3. Source Location: This approach identifies the area of integrity loss. 4. Source Characterization: Combined AE parameters give good insight to the flaw types, but many other methods, including signal amplitude, signal frequency, waveform and wave propagation analysis and moment tensor analysis, can be useful. Avenues for better AE technology utilization are suggested. These include: to accumulate basic data on structures with standardized procedures, to devise combinatorial approach between localized damage evaluation and long-range detection and to develop regional or global database under international cooperation. The final goal of determining the structural integrity is attainable only with systematic approach with damage quantification via NDT and with the use of fracture mechanics.

Keywords: Structural Integrity; AE Methodology, AE Sources, Source Characterization

1. Introduction

Acoustic emission (AE) testing of structures began in California in the midst of the space race [1]. From the early years, R&D activity was high; 400+ papers on this topic were compiled for 1970-72 period [2]. By now the methodology has well-established commercial basis in most industrialized countries. Yet, we are far from the goal of providing quantitative answers regarding the integrity and remaining lifetime of structures. Current status of AE testing of structures is reviewed here to advance this important application of AE technology.

The basic AE testing strategy is to detect AE signals globally from the entire structure under test using above-normal loading (or pressure), to identify their locations, to group them (clustering) and to rank the groups comparing the collective AE characteristics with empirical database [3-5]. The key issue is the presence or absence of critical intense sources in the structure. During the past 40+ years, many AE tests of structures have successfully utilized this strategy. Most often, AE has been used as an alternative to internal inspection of tanks and pressure vessels. However, details remained inaccessible in proprietary reports and meaningful assessment has been unavailable. Some recent articles give valuable insight to industrial AE practices [6-8]. The strategy of AE testing relies on the presumed principle that active defects produce AE in asymptotically increasing number with rising load. We also assume larger defects give stronger AE.

Both are probably true, although we lack the definitive evidence. Complications arise because non-defects can also generate AE, often quite vigorously. These sometimes aid in finding crack presence, but are impediment to identifying a critical source. AE's main advantage is the global inspection capability, while flaw sizing is beyond its scope, requiring complementary non-destructive evaluation methods.

Here, we examine the AE methodology in four steps. 1. AE Sources: Primary sources of brittle fracture, micro- or macro-cracks vs. secondary sources of friction or fretting, rust, etc. 2. Evaluation Tools: Kaiser effect, arising from the irreversibility of AE, allows the detection of prior loading level and of damage states. 3. Source Location: Using Zone, 2D- and 3D-source location methods or via embedded waveguides, this approach identifies the area of integrity loss. 4. Source Characterization: Many methods are practiced here, including combined AE parameters, attenuation-corrected signal amplitude, signal frequency, waveform analysis and moment tensor analysis. Finally, possible avenues of improvement are discussed.

2. AE Sources

Primary AE

Primary AE sources of interest in structural testing originate from brittle fracture and other fast cracking fracture [9]. Brittle fracture of structural steels generates AE with low b-values and high amplitude. This type also comes from low-energy tear, intergranular and inclusion fracture, various embrittlement modes (hydrogen, stress corrosion), weld flaws and heat-affected zone failure. Generally, plastic deformation plays a minor role as its continuous-type AE is usually weak and is hard to separate from noise. Ductile (dimple) fracture of typical structural alloys is also weak emitters. Some AE from ductile cracking is often related to nonmetallic inclusions [9].

Concrete is another material class producing brittle cracking [10]. In the strong AE emitting materials, the sign of imminent structural failure comes from rapidly increasing numbers of AE signals from a few concentrated sources. The approach we use in finding if the failure of a structure is about to happen from a rapid increase in AE is embodied in Fig. 1. This is the AE generating behavior of a sound concrete, moisture-cured for 28 days, re-plotted in log-log scale from the data of Suzuki et al. [11]. Stress was normalized to the fracture strength, while AE hits were normalized at 80% stress. This kind of power-law behavior between AE events and stress or stress-intensity factor [$N \propto \sigma^n$ or $N \propto K_I^n$] has been known for many years [12] and was first correlated experimentally to the stress dependence of microcrack formation in steels at low temperatures [13].

In microseismic testing, seismic magnitude has been correlated to crack sizes [14]. Distinction of AE from micro-cracks and macro-cracks is shown as changing b-values and amplitude. For concrete, see Fig. 2 [15]. In this graph, improved b-values (or Ib-values) are used, which are evaluated over the amplitude range of the mean amplitude \pm standard deviation [15]. This eliminates the uncertainty from arbitrarily selecting a linear region in the amplitude distribution curve. Unfortunately, they omitted a factor of 20 used in the definition of decibels, so Ib-values need this factor to make them comparable to traditional b-values. It is hard to identify convincing evidence of cracking processes on large-scale structures from AE alone, but a recent comprehensive study of concrete fracture [16] using computed tomography imaging with AE traced crack development and associated AE behavior; initially, cracks are tensile, changing to shear-type toward final fracture. In composite structures like tanks, vessels and piping, matrix cracks, interlaminar failure and fiber failures are of main interest [17, 18].

The power-law AE behavior was recently given a stochastic basis [19]. Re-plotting the final parts of composite tank AE data, the data was found to obey critical phenomena (CP)-based power laws. Another formulation refers to the fracture (critical) time τ' and cumulative AE “energy” $E \propto [(\tau' - t)/\tau']^{-\gamma}$, with time t and an universal critical exhibitor without dimension, γ [20]. Figure 3 includes such CP curves with γ -values of 0.025 to 1. A theoretical value is 0.27 [20], but obviously the curves fit a power law only locally. Thus, the current CP approach needs refinements in analyzing fracture. Practical benefit from the CP approach is also unclear, but better insight may be expected eventually from CP physics.

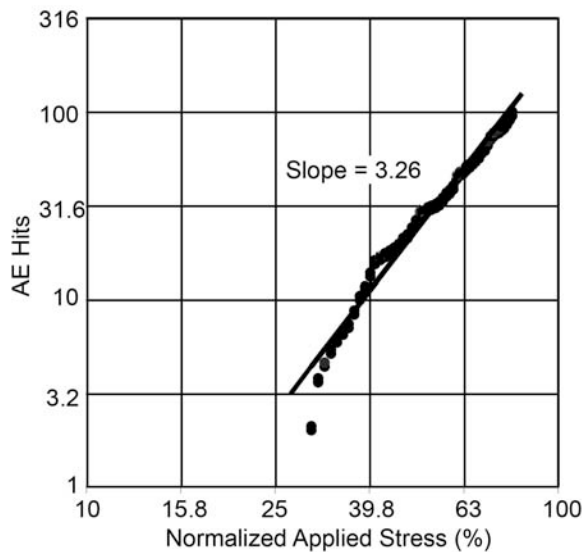


Fig. 1 A log-log plot of AE hits (ref. at 80% stress) vs. stress normalized to the fracture strength. A sound concrete, moisture-cured for 28 days. From the data of Suzuki et al. [11].

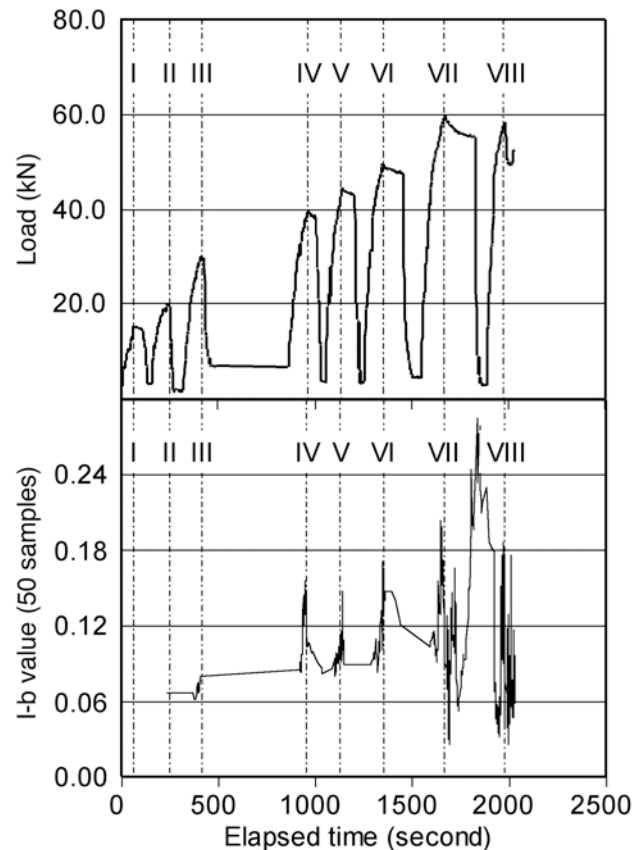


Fig. 2 Loading curves of concrete L-shape with corresponding improved-b (I-b) values. Stage VI nears yielding with an increase in I-b, stages VII and VIII show I-b below 0.05 indicating macro-damages beyond yielding. Shiotani et al. [15].

Secondary AE

Secondary AE sources arising in structural tests can be useful in locating harmful discontinuities, but others interfere with proper AE testing. Structural noise, such as that originated from bearings, can be loud and annoying and its elimination required AE analysis [21]. Structural joints also emit many AE. Friction and fretting of crack faces are widely used to locate otherwise quiet cracks. In concrete structures, the presence of crack networks is common and crack-face friction is a major source of AE. Such AE has different characteristics that can be used to identify them. In Fig. 2, for example, friction-AE during unload at 1750 to 1900 s has high I-b values [15]. Rust in steel cracks acts in similar manner. Rust, oxidation and corrosion products can be active emitters, as demonstrated in [22]. Finding gas and fluid leaks is by itself an impor-

tant goal of AE testing [6, 23]. Weather-induced noise can be a serious obstacle in field tests. A recent study is a good reference on this topic [24].

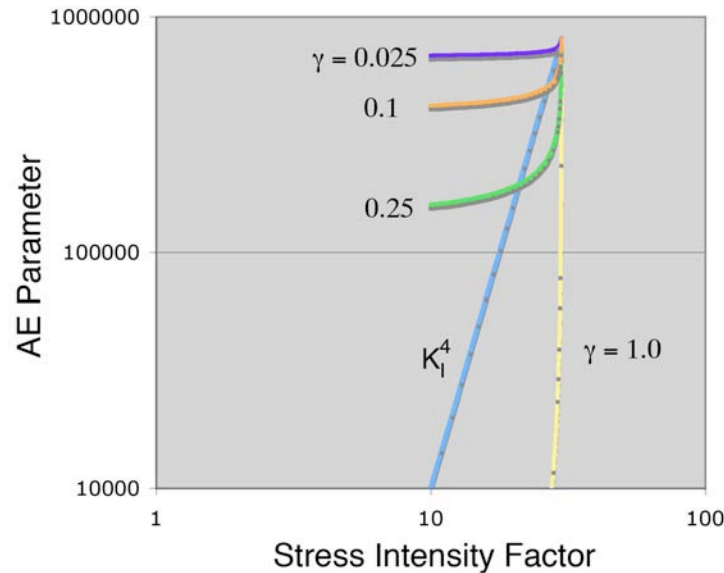


Fig. 3 The power-law AE correlation of $N \propto K_I^n$ for the case of $n = 4$ and the CP formulation of AE “energy” $E \propto [(\tau' - t)/\tau']^\gamma$, with the fracture (critical) time τ' , time t and an universal critical exhibitor without dimension, γ (1, 0.25, 0.1 and 0.025 shown).

Materials Effects

Structural materials affect the attenuation of AE waves and determine the effective range of detection frequency and sensor spacing. In typical metallic alloys, the attenuation is low and primary AE signals at 100 kHz-2 MHz can be routinely utilized. Buttle and Scruby showed the distinction among fatigue cracks, fretting and noise requires MHz-signals, using their special conical sensors extending to 7 MHz [25]. It is often found that secondary AE signals have their main contents below 100 kHz, allowing frequency-based discrimination [26]. In large metallic tanks, pressure vessels and pipes filled with liquids, the usable range is reduced to 30-100 kHz. This comes from the loss of wave energy dissipated into liquid via dispersion and absorption. Heterogeneous concrete, bricks and rocks have high attenuation and the detection frequency is at 10-60 kHz [27]. Even at this range, Shiotani et al. [28] showed the frequency-based discrimination is possible between cracking and fretting signals.

Geological materials have high attenuation and their typically large sizes further limit the usable frequency to sub-kHz range. In the low-frequency range, however, 3-axis sensing becomes practical and this allows detailed evaluation of sources [29]. In geological cases, the large size of propagation media allows the use of body waves. This is in contrast to industrial structures, where guided waves are common and boundaries wield strong effects on the signals reaching sensors. Until the work of Gorman and Prosser [30], the guided waves were long ignored in AE studies, especially in field AE testing, in part due to the difficulties of analyzing them. By now, Lamb (plate) waves have proven the utility in field inspection as well and even cylindrical waves are beginning to be used [31]. Expanded uses of guided-wave analysis should be seriously considered in AE testing.

Wide-frequency signals in low-attenuation materials can provide more detailed waveform information, allowing better source characterization [25]. Reverberation presents a challenge in

sorting out the original signals, especially in smaller shapes. By combining with source location, exact waveform analysis is possible and source parameters can be determined (Suzuki et al. [32]). Such laboratory-scale scheme is difficult to scale up to the industrial level, but increased capability of Lamb-wave simulation should enable this to happen. In structures with high-attenuation materials, limited sound transmission forces the use of lower detection frequency. Low frequency implies wavelength larger than the scale of inhomogeneity, reducing attenuation. While longer transmission becomes possible, low-frequency waveforms carry less information regarding the sources and limit the capability of source characterization. In principle, this can be compensated by increasing the number of sensors, as demonstrated in laboratory studies [14, 16].

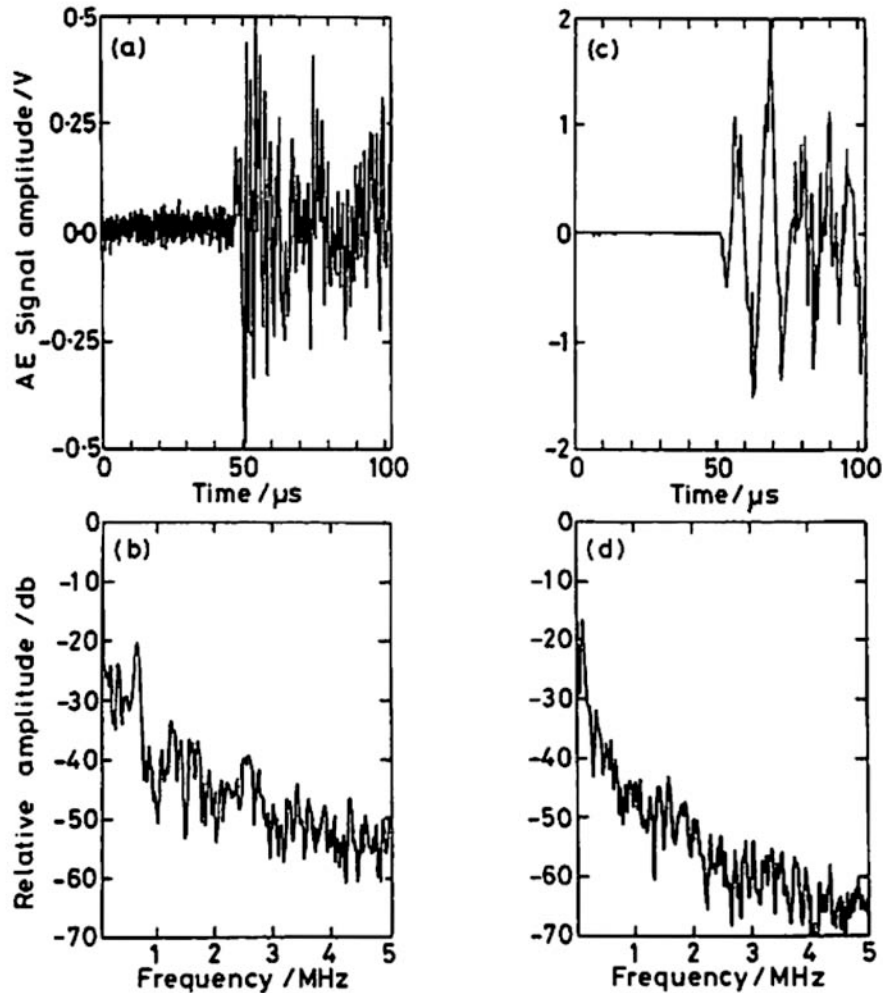


Fig. 4 Two classes of AE signal observed during fatigue of riveted coupon. High frequency AE (attributed to crack advance) (a) AE waveform; (b) Fourier transform. Fretting-AE signal observed periodically; (c) AE waveform; (d) Fourier transform. Buttle and Scruby [25].

3. Evaluation Tools

Kaiser effect enables the detection of the prior loading level and in assessing the state of structural damages. AE emitted below the prior load (Felicity effect) implies the presence of damages, although other measures are needed to verify the damages. In metallic structures, a clear re-start of AE is usually indicated in the absence of flaws. Crack-face cohesion and fretting provide under-preload AE indication of the crack presence, especially under cyclic loading.

Figure 4 shows the comparison of crack advance signal during fatigue cracking of Al sheet and that due to fretting [25]. High-frequency components above 500 kHz signify the cracking signals that generally have low amplitude. The fretting signals are much stronger and stronger low-frequency components. Oxidation and corrosion products amplify this effect.

Successful use of Kaiser effect by Kanagawa and Nakasa in determining the pre-existing stresses in under-sea rocks 30 years ago pioneered this AE application [33]. Large background AE is always present and careful test procedures are required in correct stress determination [34]. See an example of background subtraction in Fig. 5. Refinement of this method continues to present [35].

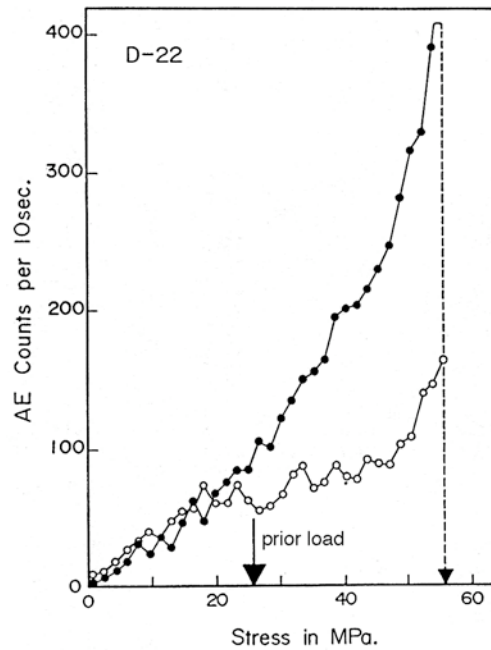


Fig. 5 Rock stress estimation. AE count rates vs. applied stress of first (filled circle) and second (open) reloading. Arrow at 27 MPa indicates the prior load level. Yoshikawa and Mogi [34].

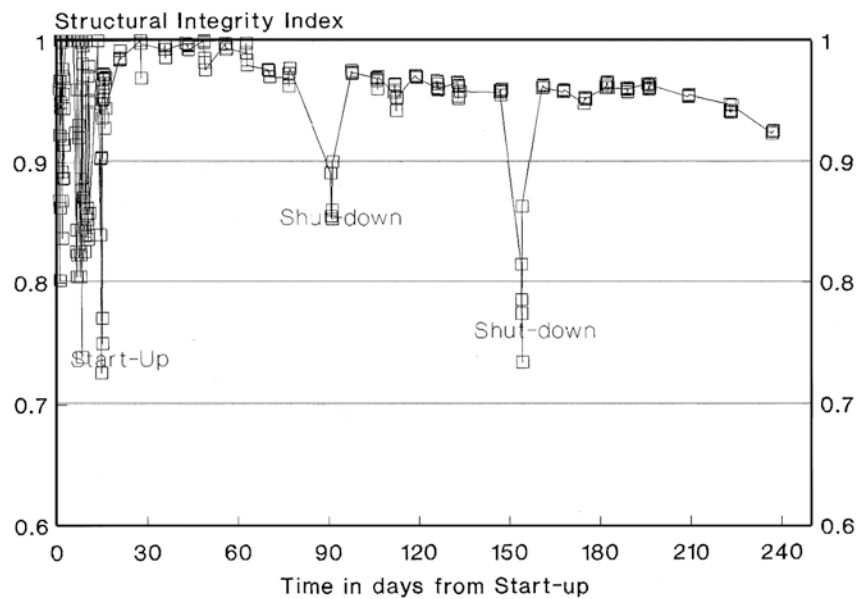


Fig. 6 The structural integrity index from continuous AE monitoring of a defective area during plant operation (Wood et al. [36]).

Wood [36] in Australia has been using Kaiser effect (by defining “structural integrity index” or SII as percent of the prior load where AE starts) in the evaluation of various structures. He reported successful predictions of failure based on expected time to reach the critical value of the structural integrity index (80 for metals, 90 for FRP and geologic/concrete materials and 100 being the sound condition). Figure 6 shows an example, where this area is predicted to fail at 250 days upon reaching SII of 90. Global definition of such an index must take proper account of critical components, and its validity is difficult to confirm. However, this approach is worthy of further consideration in integrity assessment.

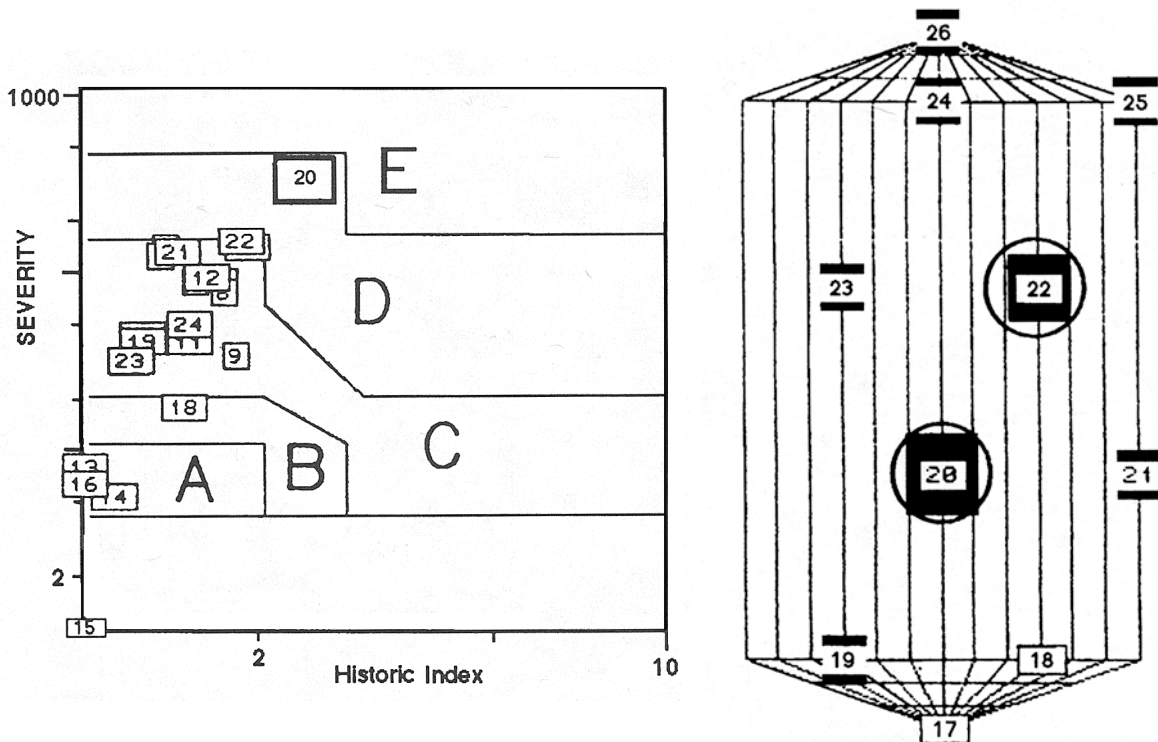


Fig. 7(a) Zone intensity plot of a thermal loading (left) and (b) intensity chart of the first pressurization test (right) of a hydrocracker reactor. Zone 20 and 22 are active. Miller et al. [17].

In AE tests of composites, Felicity effect has played the central role in identifying the damaged states [17, 18].

Felicity ratio is defined as the ratio of the load at AE start in reloading to the prior load.

This parameter was important along with two well-known indices;

Severity Index: a measure of the magnitude of strong emissions or average signal intensity of 50 strongest AE events;

Historic Index: rates of change in AE intensity or characterizing signal intensity of recent (20%) AE events over the average.

The cross plot of Severity Index and Historic Index is called Zone Intensity plot and an example is given in Fig. 7a [17]. This is used to designate from level A (minor emissions) to level E (major defects present). In conjunction with zone location scheme, the test evaluation procedure known as MONPAC[®] identifies the zone intensity of each zone from A to E. When higher level of zone intensity is found in a tested tank, immediate further testing via non-AE methods is recommended. Zone intensity level is characterized for each monitoring zone and is shown on a schematic chart, as in Fig. 7(b). Results shown here are from tests on a hydrocracker reactor and Zones 20 and 22 contain significant damages (levels D and C) [17].

In concrete testing, other parameters have been defined for damage evaluation [11]. For repeating loading tests of concrete, “Load ratio” was defined (as in the case of Felicity ratio):

Load ratio = load at the onset of AE activity under the repeated loading / previous load.

Another term, “Calm ratio” was defined as

Calm ratio = the number of cumulative AE activity during unloading / total AE activity at the previous maximum loading cycle.

In concrete, crack face rubbing generates unload emissions, which are indicators of the presence of cracks in a structure. By cross-plotting these two ratios, three levels of concrete damage (Heavy, Intermediate and Minor) can be identified [11]. This procedure was incorporated in a Japanese industrial standard, NDIS2421. This standard also defined another index, RA ratio, as

RA ratio = rise time of an AE signal / amplitude in V.

This parameter is essentially the inverse of rise-time slope, except the latter typically uses dB-scale so these two are not directly invertible. Ohtsu and coworkers [37] originally developed RA ratio and utilized it in conjunction with average frequency to correlate the tensile vs. shear nature of AE sources. Recently, Takuma et al. [38] used RA ratio for the evaluation of tool wear successfully, so this parameter should be considered in many other applications.

Mizutani and coworkers [39] recently introduced another parameter for evaluating AE observations, i.e., the inverse of Maharanobis distance correlating AE hit rates and b-values. It was applied to detect the onset of plastic deformation of bolts, but may well be applicable to various signal types. Here, Maharanobis distance of AE signals detected is defined as follows [40]:

$$D = \sqrt{\frac{((x - \bar{x})/\sigma)^T \cdot R^{-1} \cdot ((x - \bar{x})/\sigma)}{p}}$$

where $x = [x_{rate}, x_{lb}]$ is a two-dimensional vector consisting of the AE hit rate and the b value of the comparison data and $\bar{x} = [\bar{x}_{rate}, \bar{x}_{lb}]$ is a two-dimensional vector, consisting of the averages of the reference AE parameters.

In the analysis of individual AE waveforms, fast Fourier transform has played a major role over the years. In the past decade, wavelet transform (WT) also contributed to our understanding of AE signals [41-43]. WT allows the visualization of frequency contents as a function of time, especially with the use of AGU-Vallen freeware [43]. An example of WT result is shown in Fig. 8 (right), where a simulated fiber-splitting in a CFRP was generated by a line-focused laser and detected by a Pico sensor [44]. First-arriving So-mode Lamb waves at >300 kHz are followed by slower Ao-mode waves below 250 kHz.

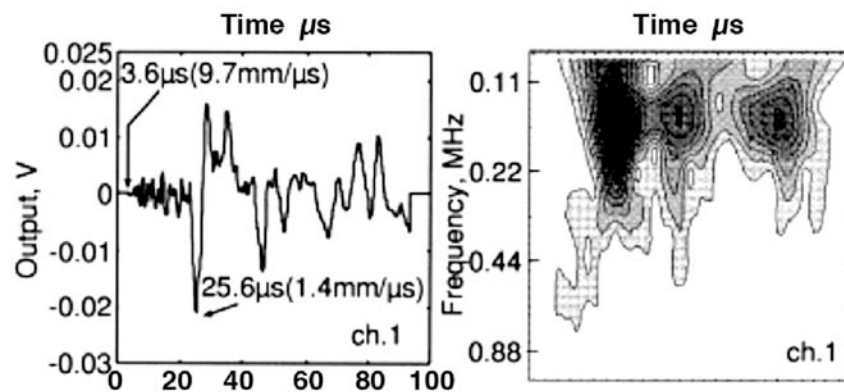


Fig. 8 Laser simulation of matrix cracking on the bottom surface using focused laser beam parallel to the 0° fibers. Mizutani et al. [44].

One needs to appreciate the difficulty of obtaining wideband waveforms of AE signals in general structural testing, where guided-wave propagation is the norm and one may have to deploy waveguides. Still, we should strive for getting more than basic AE parameters. In typical AE sensor selection, high sensitivity has taken precedence over wideband detection capability. Thus, while wave propagation modes have dominant effects on the waveforms received, any information on a source or the propagation path is lost when a narrow-band sensor is used. In order to improve the source characterization capability, we need a comprehensive approach. One should note that some commonly used resonant AE sensors respond at multiple frequency bands. Newer wideband sensors also have increased sensitivity. These can work with higher functionality of modern AE processing equipment and provide us with a better data set for new AE parameters. For example, it is routine now to obtain processed data from multiple frequency bands. Recognizing different modes of guided waves in thin-wall structures is another avenue for vast improvement in interpreting observed AE data. This may lead to the nature of AE sources even under limited frequency band detection.

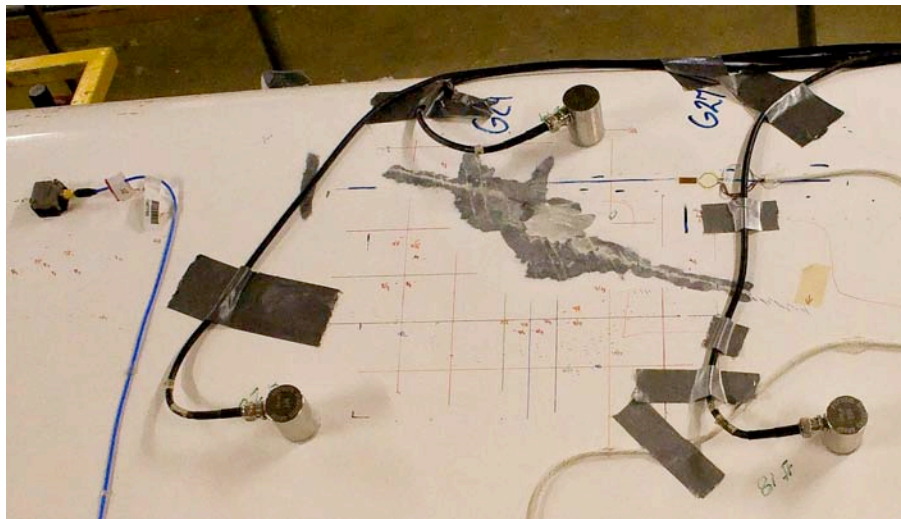
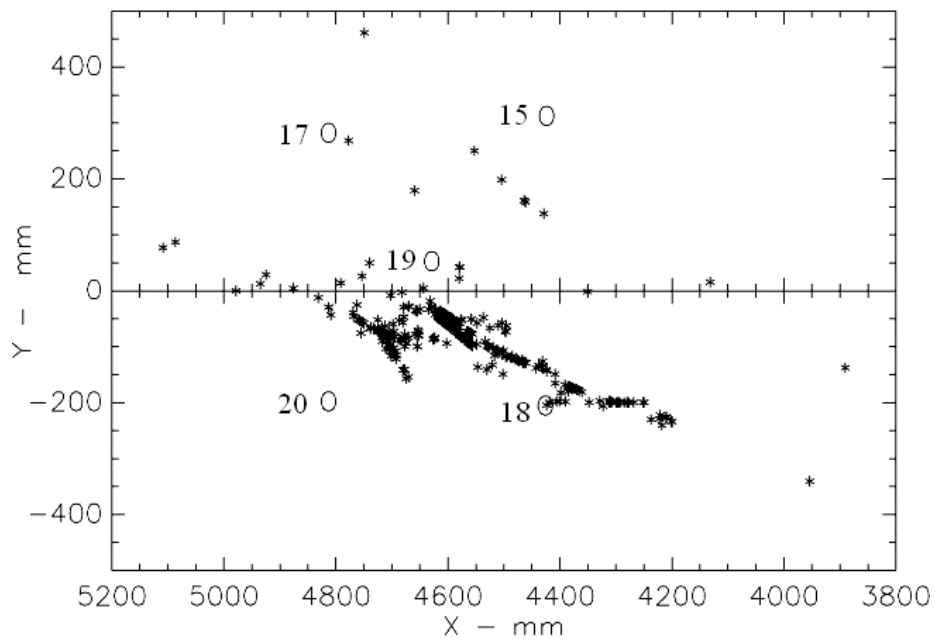


Fig. 9 Total AE event locations seen in the fatigue test of a 9-m-long wind-turbine blade. Photograph shows damages on the blade surface and nearby PAC R6I sensors. Beattie [45].

4. Source Location

Source location identifies the area of integrity loss. At present, most AE equipment incorporates the software for source location and clustering scheme and displays results in various user interfaces. High AE activity at a given area of a structure, or a cluster, implies the possible presence of flaw. The criteria of “high” activity always need careful attention; AE hit counts and rates, amplitude, and energy have initially formed the basis for the grading of clusters. An example of 2D-source location on a cyclically loaded wind-turbine blade is shown in Fig. 9, along with the photograph of damage location with sensors (Beattie [45]). Each AE event source was located in different triangles formed by the three nearest sensors. Damage development is clearly displayed on the source-location map of the fatigue-tested blade after 3.7+ million cycles. An excellent correspondence is displayed between observed damage and source locations.

Source location in AE evolved from the procedures used in seismology. The original electro-mechanical system at Aerojet [1] developed into current PC-based systems. Recently, Ge [46] reviewed available source location algorithms thoroughly with theoretical background. These are applicable to both **2D-source location** and **3D-source location**. A simpler **Zone-location** scheme has been used in structures with high attenuation materials. This method works when the attenuation of AE signals is high and triangulation techniques require too many sensors (and attendant electronics). AE activities at the first-arriving sensor are associated with this sensor location and the “zone” surrounding it. While not as accurate, it identifies the regions of high AE activity. Figure 7b shown earlier is an example of zone location.

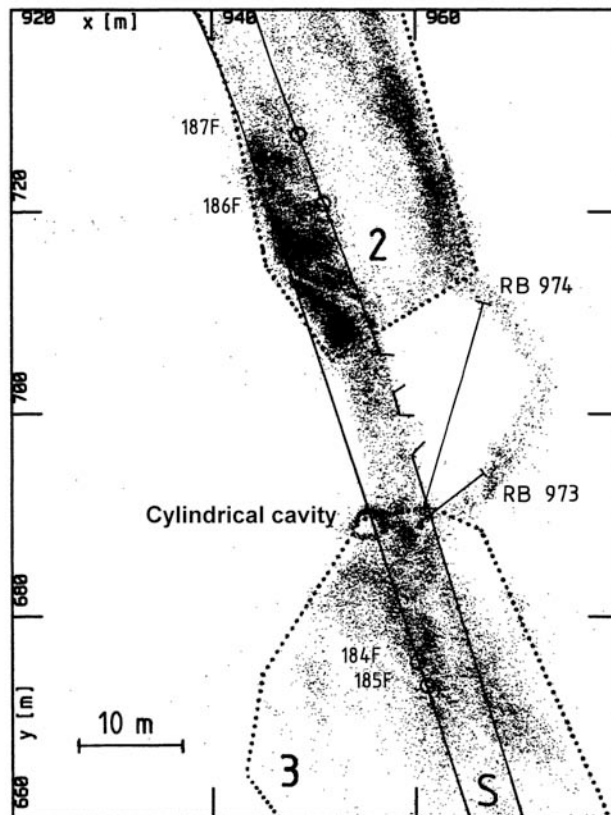


Fig. 10 The AE locations of a 2-m thick depth interval between the floor of the intermediate level and the roof of the lower level (data of one year, 72,902 events). Spies and Eisenblätter [48].

In geotechnical applications, the prediction of rock burst, and coal and gas outburst was historically important from the safety consideration [29, 47]. Increasing AE rates and spatial focusing were carefully evaluated to anticipate impending bursts. The stability of highway and railway slopes has also been much worked AE applications. The stability of excavation of underground cavities and openings is more recently examined, especially in connection with nuclear waste disposal. Microcracking changes the microstructure of the rock so that permeability might increase. Macrofracturing can lead to stability problems. Detected locations of microcracks in a radioactive waste disposal facility are shown in a plan view in Fig. 10 [48]. Geothermal energy extraction is another area AE is actively used for studying and monitoring the distribution of reservoirs, hydraulic fracturing, reservoir volume and hydro-circulation. Similar methods are now being applied to gas and oil production.

In examining the evolution and distribution of AE sources in a cluster, fractal analysis has been used. A fractal dimension of three represents random events occurring in a volume and a fractal dimension of two signifies that the events have localized on a failure plane [49, 50]. An example of decreasing fractal dimension with the progress of fracturing in a rock sample is given in Fig. 11 [50]. Introducing fractal modeling processes, crack distribution is constructed for a real coalmine starting from AE data set and laboratory tests [51].

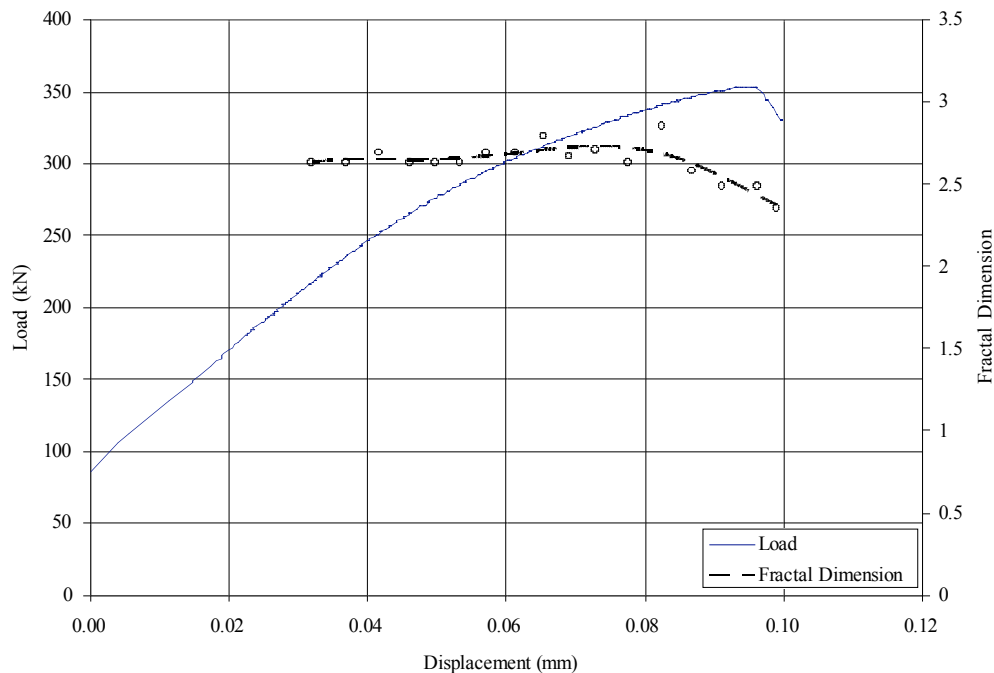


Fig. 11 Load history and fractal dimension for the biaxial test of a rock. Iverson et al. [50].

Source location in an anisotropic or a dispersive propagation medium requires special consideration. Applications of wavelet transform and affine transformation are examples of such effort [52, 53]. The use of wavelet transform defines the arrival times at a given frequency with precision. See Fig. 12 for arrival time determination of L-mode and F-mode cylindrical waves at 190 kHz. The propagation of waves in a large pipeline has been of practical importance for many years, but it should be noted that different wave modes have different attenuation characteristics, as shown in Fig. 13 [54]. Note that fastest moving wave (presumably L(0,1)-mode cylindrical waves) and the second fastest attenuated more than slower moving waves of likely flexural modes. The affine transformation speeds up the source location algorithm in orthotropic plates

by three orders of magnitude [53]. Hamstad and co-workers have conducted extensive finite-element modeling analysis of Lamb wave propagation (see [55] and references included). His most recent study shows among others the value of using pencil-lead break (PLB) sources on edge to represent buried dipole sources and the danger of surface, out-of-plane PLB to assess realistic wave modes.

For very high attenuation media, embedded waveguides provide an effective means of narrowing the zone of AE activity. Waveguides are also used in tests under extreme environment, but often cause severe waveform distortion [56].

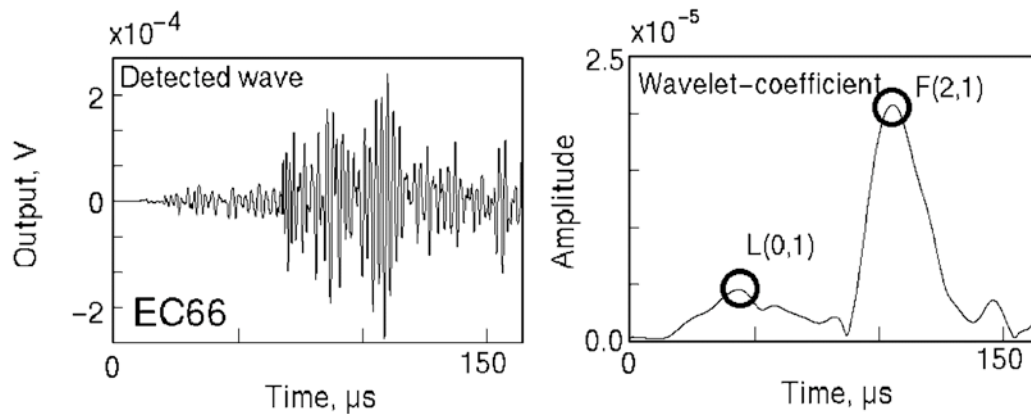


Fig. 12 An AE signal in a brass tube detected at 20 cm from the source (left). Its wavelet coefficient at 190 kHz showing two cylindrical wave modes. Yamada et al. [52].

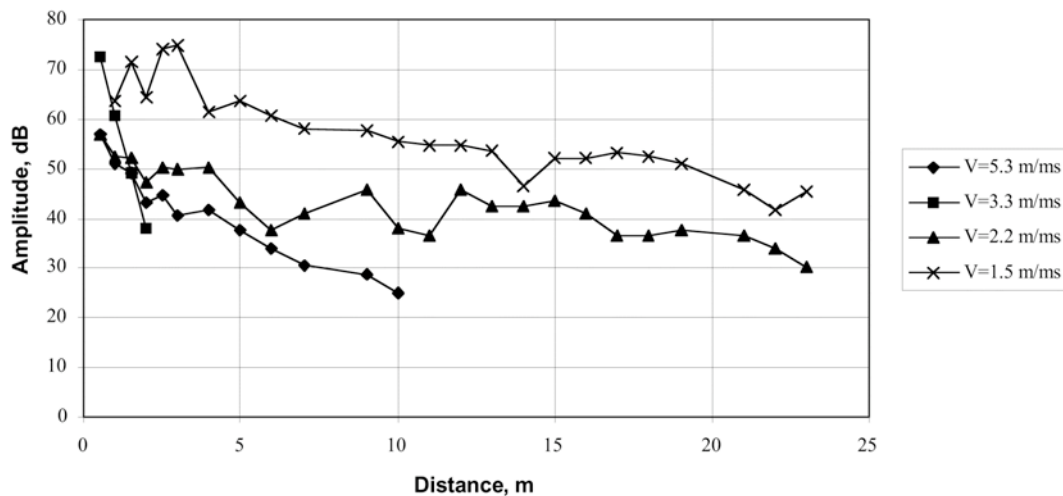


Fig. 13 Wave attenuation in a water-filled buried pipeline. Vahaviolos et al. [54].

5. Source Characterization

Many methods of source characterization are used. The most rigorous one relies on signals from several sensors on a small sample and conducts deconvolution or simulation analysis to obtain the source rise time and magnitude for Mode-I cracks [9]. This applies to idealized cases only and is of little use for large structures. More practical and appropriate approach must be selected. This also means that identification of AE sources relies on complementary knowledge-base on possible failure mechanisms from fracture mechanics and from experience. Typically, materials study accompanies AE examination and empirical deduction leads to AE characterization (although some people are prone to proclaim mechanisms by intuition). The AE analysis

methods include the use of combined AE parameters, signal amplitude and distribution, signal frequency, waveform analysis and moment tensor analysis. However, selected AE parameters (hit rates, amplitude, and their time history, being the typical) are the most common approach used in combination with a source location scheme [3-8]. Various evaluation tools discussed in Section 3 are employed in combination. These have been combined with empirical database of post-test inspection and used in grading tested structures. The highly successful CARP procedures, developed initially for composite vessels, combined AE cluster grading with zone location [5, 17]; cf. Fig. 7. Here, grading utilized severity and historic indices representing cumulative intensity and sudden AE activity jump. A similar (but almost unknown outside Japan) system was actually operational in 1978 [4]. Some have since been packaged into commercial inspection technology products, e.g., MONPAC[®] and TANKPAC[®].

Signal frequency remains controversial as to its effectiveness in source characterization, but it has been used with much success in (high-pass) filtering out background/frictional noise from higher frequency cracking AE signals [26]. This has a firm support from a rigorous experiment (see Fig. 4 and [25]). It is tempting to assign an AE mechanism to its characteristic frequency. It should be pointed out that the direct signal characterization methods have clearly shown that source rise times of a given type of cracking vary by a factor of ten or more so that a single “characteristic frequency” of cracking does not exist [9].

Moment tensor analysis (MTA) is useful in characterizing the nature of AE sources. This identifies the magnitude and orientation of displacement vector of an AE source. From its geological origin, Ohtsu and Ono [57] set forth this method in AE context initially using theoretical simulation. They set a framework for deducing the crack characteristics using only surface AE observations. Ohtsu [58] developed the MTA further, applying to real AE observations in

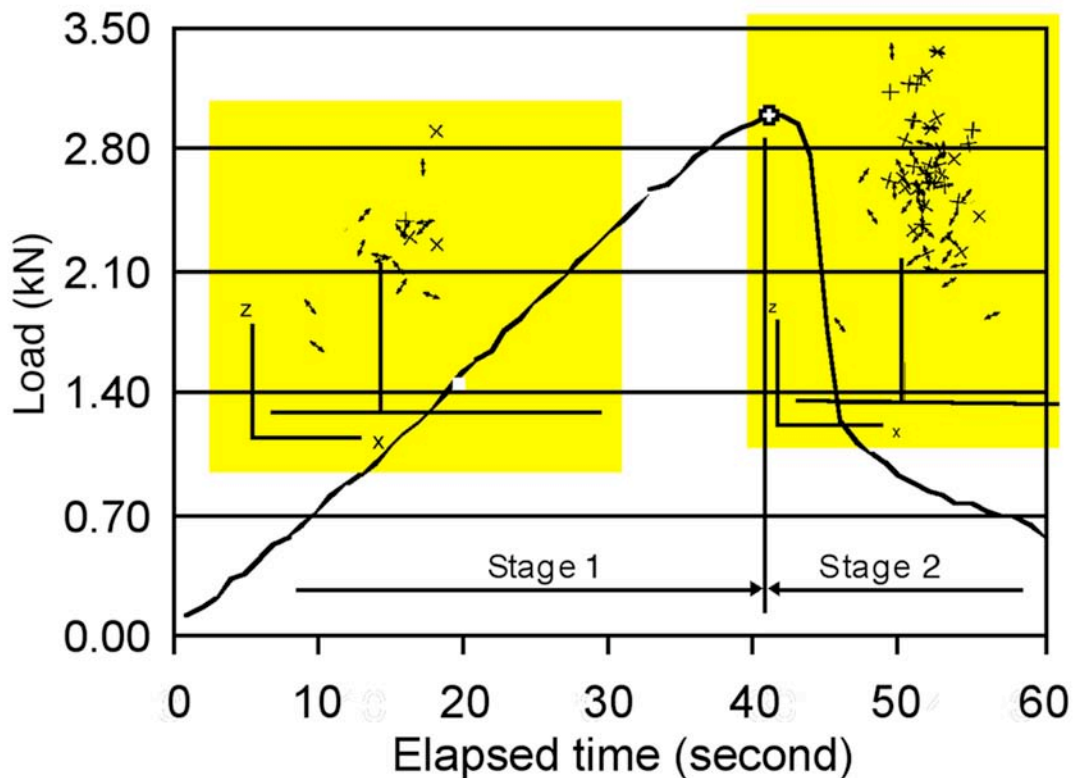


Fig. 14 Loading curve of a center-notched concrete beam, and results of MT analysis within yellow shading. Double arrows are tensile crack and X are shear cracks. Shiotani et al. [59].

concrete structures with great success. MTA software has been available with a major AE system. The MTA provides the classification of AE signals due to tension (crack-opening) and shear modes of fracture. However, this analysis requires the detection of weak, initial P-wave arrivals and sensor spacing cannot be large. It is expected that the MTA of localized sources is the first step of integrating this valuable technique into large-scale structural AE tests.

Practical MT analysis relies on the first arrival P-wave motions with calculated Green's function, resulting in crack types: tensile, shear and mixed. For the case of a center-notched concrete beam, left insert in the loading curve of Fig. 14 shows observed crack types of AE sources around the crack starting from the notch root [58]. This shows crack type is mostly tensile before reaching the maximum load (Stage 1). Beyond the peak in Stage 2, more shear cracks are distributed around the crack tip. The MT analysis method requires 6 sensors receiving clear signals for crack type determination, limiting the sample size and applicable geometry. However, it provides valuable insight to failure processes.

The next stage in AE testing of structures is wider use of pattern recognition analysis (PRA). PRA has long been studied in evaluating AE observations [60], but recent improvements in data-processing speed allow this to be integrated with multi-channel location software [61]. Godinez et al. [62] used a supervised PRA scheme to detect flaw in helicopter tail gearbox in real time. The energy content of different frequency bands was used as the basis for classification features. K-nearest-neighbor and neural-network classifiers are often used in PRA to cluster signals into separate groups based on combinations of "features". Since various schemes of artificial intelligence compare and deduce matching patterns, independent validation is needed to provide appropriate AE context to PRA results. This is especially keen for neural-network results. These are obtained from a "black-box", which was trained by feeding inputs and outputs.

6. Structural Integrity Assessment

Acoustic emission has been used widely in the US since the 1970s as a means of monitoring the structural integrity of large pressurized vessels and structures. This statement describes even the current state reasonably well in that AE has successfully evaluated thousands of structures and alerted conditions of potential failure. Further refining this approach is prudent for AE technology in the near future. Yet, AE is not seriously contributing to "structural integrity assessment" of critical structures. Here, the "assessment" implies far more ambitious goals of predicting remaining lifetime and calculating failure probability. For such goals, the size of flaws has to be estimated, but AE is not a flaw-sizing method.

The procedures for structural integrity assessment require three main groups of input data: 1. material: constitutive (stress-strain) behavior with time and temperature dependence, fracture toughness and fatigue parameters; 2. load: loading regime of primary stresses, residual stresses; 3. geometry: geometry of structure, geometry of flaw. The last item is the most difficult to obtain unless its size is large enough for ultrasonic or radiographic testing or surface-breaking and accessible. Improvement of NDE technology is most urgent in structural integrity assessment. Here, AE can contribute in identifying the positions of active flaws, but flaw (or crack) sizing is probably beyond AE techniques. Digesting the input with various rounds of analysis via finite-element codes, fracture mechanics, material damage and loading schemes, probabilistic lifetime prediction emerges. Thus, unless AE can address AE source characterization issue in structural testing, AE cannot hope for assuming a key role in structural integrity assessment. As suggested earlier, combining global flaw evaluation with localized AE source study is the first step we

should take. Past attempts for structural integrity assessment by AE have been reported, e.g., [63, 64]. However, meaningful progress has been difficult.

Another front is standardization, where many “international” standards appeared instead of consolidation of existing documents. Brunner and Bohse [65] assessed them and concluded that irrespective of the area of AE test procedures, well-documented evaluation criteria must be available for the success of the procedure. From the US-side, ISO seems to have become an irrelevant regional organization. On the other side, ASTM tries to prevail over the whole world. The competitive atmosphere certainly is less than ideal.

In order to fulfill the promises of AE technology, we must continue to accumulate basic data on structures with standardized procedures, to devise combinatorial approach between localized damage evaluation and long-range detection and to develop regional or global database under international cooperation. The needs for more basic data on structures are obvious, but funding for such activity has been low. Mutually beneficial cooperation of laboratory researchers and field practitioners may bring forth a break-through. For example, waveform data may be taken during routine in-service tests and provided for post-analysis by graduate students working for advanced degrees. Seeking the standardization of sensors, procedures, and analysis methods, etc. is likely to stimulate discussion of best possible approach for various test objectives.

Another goal worth pursuing is to devise combinatorial approach between detailed localized evaluation and long-range detection for global flaw location. Waveform data after extended propagation is of lesser value than those collected close to sources. Wavelet and moment tensor analysis methods are best applied near the sources, while CARP procedures and Felicity/Calm ratios can be evaluated on a large scale. It is of critical importance that guided-wave propagation modes are incorporated into any AE analysis of thin-walled structures. A recent work by Takemoto et al. [66] shows the benefit of Lamb-wave analysis in the corrosion detection of large oil tanks. Various simulation and modeling techniques are also beneficial.

Structural tests are expensive and we need wide international cooperation to establish workable and effective standards of AE testing. We should start thinking about developing regional databases for this endeavor that can be expanded to global scale.

7. Concluding Remarks

To raise AE technology into the next level, we must improve it from several fronts. Only then AE can become a serious player in structural integrity assessment. We need to better characterize AE sources; to extract more from AE signals reaching sensors; to devise effective AE parameters; to integrate new analysis methods, such as WT, MTA, and PRA; to include simulation tools in analyses; to accumulate basic data on structures with standardized procedures; to devise combinatorial approach between localized damage evaluation and long-range detection and to develop regional or global database under international cooperation. Using systematic approach along with NDT, fracture mechanics, etc., improved AE can offer more value to industrial users and to contribute substantially to structural integrity assessment.

Bibliography

J. of Acoustic Emission, Vol. 1-{25}*, 1982-{2007}, editor, Kanji Ono, AE Group, Los Angeles and Encino, CA

Progress in Acoustic Emission I – {XIII}, *Proceedings of the International Acoustic Emission Symposium*, 1982 – {2006}, Japan Soc. Nondestructive Inspection, Tokyo.

Acoustic Emission Testing, Nondestructive Testing Handbook, 3rd edition, Vol. 6, American Society for Nondestructive Testing, Columbus, OH, 2005.

Hardy, Jr. H.R., *Acoustic Emission Microseismic Activity, Vol. 1: Principles, Techniques and Geotechnical Applications*, Taylor & Francis, 292 p., 2003.

Acoustic Emission/Microseismic Activity in Geologic Structures and Materials: First to Sixth conference proceedings, edited by H. Reginald Hardy, Jr. and Frederick W. Leighton, Trans Tech Publications; 1977, 1980, 1984, 1989, 1995, 1998.

Scott, I.G., *Basic Acoustic Emission*, Gordon and Breach Science Publishers, New York, 1991.

“Acoustic Emission Inspection”, *Metals Handbook, 9th edition, Volume 17, Nondestructive Testing and Quality Control*, ASM International, Materials Park, OH, pp. 278-294, 1989.

* { } implies continuing publications.

References

1. Green, A.T., *Advanced Materials Research*, **13-14**, 2006, 3-14. See also Green, A.T., Lockman, C.S., and Steele, R.K., *Modern Plastics*, **41**(11), 1964, 137-139, 178, 180.
2. Drouillard, T.F., *Acoustic Emission – A bibliography for 1970-1972, Monitoring Structural Integrity by AE, ASTM-STP-571*, 1974, pp. 241-284.
3. ASNT, *Nondestructive Testing Handbook*, 3rd ed., Vol. 6, *Acoustic Emission Testing*, 2005.
4. Watanabe, T., Hashirizaki, S., and Arita, H., A method of evaluating the harmfulness of flaws in structures using AE techniques, *Proc. 4-th AE Symposium*, 1978, Tokyo, pp. 5-59.
5. Davies, R., AE as a basis for plant integrity monitoring, *Progress in AE, III*, 1986, JSNDI, pp. 9-25.
6. Cole, P.T., and Van de Loo, P.J., Listen to your storage tanks to improve safety and reduce cost, *Acoustic Emission – Beyond the Millennium*, Elsevier, 2000, p. 169.
7. Tschliesnig, P., *Advanced Materials Research*, **13-14**, 2006, 365-376.
8. Allevato, C., *Proc. ICAE-6, Lake Tahoe*, 2007, pp. 229-234.
9. Ono, K., New goals for AE in materials research, *Acoustic Emission – Beyond the Millennium*, Elsevier, 2000, p. 57. See also Ono, K., Current understanding of mechanisms of acoustic emission, *J. of Strain Analysis*, **40**, 2005, 1-15.
10. Yuyama, S., and Ohtsu, M., AE evaluation in concrete, *Acoustic Emission – Beyond the Millennium*, Elsevier, 2000, p. 187. See also Ohtsu, M., *Advanced Materials Research*, **13-14**, 2006, 183-192.

11. Suzuki, T., Ohtsu, M., Aoki, M., and Nakamura R., Damage Identification of a Concrete Water-Channel in Service by Acoustic Emission, *Proc. ICAE-6*, Lake Tahoe, 2007, pp. 46-51.
12. Tetelman, A.S., *Materials Research and Standards*, **11**, 1971, 13-16. Also see: Tetelman, A.S., Acoustic emission and fracture mechanics testing of metals and composites, in *Proc. US-Japan Joint Symposium on Acoustic Emission*, English volume, pp. 1-46, Japan Industrial Plan. Assoc., 1972.
13. Tetelman, A.S. and Chow, R., *Acoustic Emission*, *ASTM-STP-505*, 1972, pp. 30-40.
14. Lei, X., Nishizawa, O., Moura, A. and Satoh, T., Hierarchical fracture process in brittle rocks by means of high-speed monitoring of AE hypocenter, *J. of Acoustic Emission*, **23**, 2005, 102.
15. Shiotani, T., Yuyama, S., Li, Z.W. and Ohtsu, M., Application of AE improved *b*-value to quantitative evaluation of fracture process in concrete materials, *J. of Acoustic Emission*, **19**, 2001, 118-133.
16. Katsaga T., and Young R.P., Acoustic emission and x-ray tomography imaging of shear fracture formation in large reinforced concrete beam, *Proc. ICAE-6*, Lake Tahoe, 2007, pp. 396-401. Also see: *J. of Acoustic Emission*, **25**, 2007, 294-307.
17. Fowler, T.J., Blessing, J.A., Conlisk, P.J., and Swanson, T.L., The MONPAC system, *J. of Acoustic Emission*, **8**, 1989, 1-10. See also Miller R.K., Tobin R.G., Gross D.J. and Tran D.T., A Summary of Experiences with MONPAC™ Testing by the MQS/Dunegan Testing Group, *J. of Acoustic Emission*, **8**, 1989, 25-29.
18. Hamstad, M.A., 30 years of advances and some remaining challenges in the application of AE to composite materials, *Acoustic Emission – Beyond the Millennium*, Elsevier, 2000, p. 77.
19. Johansen, A. and Sornette, D., Critical ruptures, *European Physical J. B*, **18**, 2000, 163-181.
20. Guarino, A., Garcimartin, A., and Ciliberto, S., An experimental test of the critical behaviour of fracture precursors, *European Physical J. B*, **6**, 1998, 13-24.
21. Prine, D., Localization of Noise sources in large structures using AE, *Proc. 26-th European Conf. AE Testing*, Vol. I, DGfZP, 2004, pp. 247-254.
22. Cho, H., Takemoto, M., AE from rust in SCC, *Proc. 26-th European Conf. AE Testing*, Vol. II, DGfZP, 2004, p. 605.
23. Vahaviolos, S.J., Miller, R.K., Watts, D.J., Shemyakin, V.V., and Strizkov, S.A., Detection and location of cracks and leaks in buried pipelines using AE, *J. of Acoustic Emission*, **19**, 2001, 172.
24. Li, Z., Yuyama, S., Yamada, M., Sekine, K., Kitsukawa, K., Maruyama, H., and Konno, S., Investigation on AE signal/noise processing in corrosion damage evaluation of tank bottom, *J. of Acoustic Emission*, **23**, 2005, 233.
25. Buttle, D.J., Scruby, C.B., Characterization of fatigue of aluminum alloys by acoustic emission, Part I –II, *J. of Acoustic Emission*, **9**(4), 1990, 243 and 255.

26. Dunegan, H.L., Modal analysis of acoustic emission signals, *J. of Acoustic Emission*, **15**, 1997, 53-61.
27. Hardy, Jr. H.R., *Acoustic Emission Microseismic Activity, Vol. 1: Principles, Techniques and Geotechnical Applications*, Taylor & Francis, 292 p., 2003.
28. Shiotani, T., Nakanishi, Y., Iwaki, K., Luo, X., Haya, H., Evaluation of reinforcement in damaged railway concrete piers by means of AE, *J. of Acoustic Emission*, **23**, 2005, 233.
29. Niitsuma, H., *Acoustic Emission – Beyond the Millenium*, Elsevier, 2000, pp. 109-125. See also Moriya, H., Niitsuma, H., Baria, R., Measurement of hydraulically activated subsurface fracture system in geothermal reservoir by using AE multiplet-clustering analysis, *J. of Acoustic Emission*, **23**, 2005, 113.
30. Gorman M.R. and Prosser W.H., AE source orientation by plate wave analysis, *J. of Acoustic Emission*, **9**, 1990, 283-288.
31. Uchida F., Nishino H., Takemoto M. and Ono K., Cylinder wave analysis for AE source location and fracture dynamics of stress corrosion cracking of brass tube, *J. of Acoustic Emission*, **19**, 2001, 75-84.
32. Suzuki H., Takemoto M. and Ono K., The fracture dynamics in a dissipative glass-fiber/ epoxy model composite with AE source simulation analysis, *J. of Acoustic Emission*, **14**, 1996, 35-50.
33. Kanagawa T., Nakasa H. “Method of estimating ground pressure”. U.S. Patent No. 4107981 (1978).
34. Yoshikawa S., and Mogi, K., Experimental studies on the effect of stress history on acoustic emission activity: a possibility for estimation of rock stress, *J. of Acoustic Emission*, **8**(4): 1989, 113-123.
35. Lavrov, A., Wevers, M., and Vervoort, A., Acoustic emission during monotonic and cyclic deformation of a brittle limestone, *J. of Acoustic Emission*, **20**, 2002, 292.
36. Wood, B.R.A., Harris, R.W. and Porter, E.L., Structural integrity and remnant life evaluation using acoustic emission techniques, *J. of Acoustic Emission*, **17**, 1999, 121-126.
37. Tsuji N., Uchida M., Okamoto T. and Ohtsu M., Application of acoustic emission technique to evaluation of cracking in concrete structures, in *Progress in Acoustic Emission X*, pp. 189-194, JSNDI, 2000.
38. Takuma M., Shinke N., Nishiura T. and Akamatu K., Acoustic emission evaluation system of tool life for shearing of piano and stainless steel wires, *J. of Acoustic Emission*, **24**, 2006, 52-66.
39. Mizutani, Y., Onishi, T. and Mayuzumi, M., Plastic-region tightening of bolts controlled by acoustic emission method, *Proc. ICAE-6*, Lake Tahoe, 2007, pp. 120-125. Also see: *J. of Acoustic Emission*, **25**, 2007, 239-246.

40. http://en.wikipedia.org/wiki/Mahalanobis_distance.
41. Suzuki, H., Kinjo, T., Hayashi, Y., and Ono, K., with Appendix by Hayashi Y., Wavelet transform of acoustic emission signals, *J. of Acoustic Emission*, **14**, 1996, 69-84.
42. Takemoto, M., Nishino, H. and Ono K., Wavelet transform – Applications to AE signal analysis, *Acoustic Emission – Beyond the Millennium*, Elsevier, 2000, pp. 35-56.
43. AGU-Vallen Wavelet transform software, version R2007.0309, Vallen-Systeme GmbH, Icking, Germany (2007). Available at <http://www.vallen.de/wavelet/index.html>
44. Mizutani, Y., Nagashima, K., Takemoto, M., Ono, K., Fracture mode classification in locally loaded cross-ply CFRP coupons using wavelet transform, *Proc. of AECM-6*, ASNT, Texas, 1998, pp. 114-123; and Fracture mechanism characterization of cross-ply carbon-fiber composites using acoustic emission analysis, *NDT & E International*, **33**(2), 2000, 101-110.
45. Beattie, A.G., Acoustic emission monitoring of a fatigue test of a TX wind turbine blade. (to be published). See also Rumsey M.A., Paquette J., White J., Werlink, R.J., Beattie A.G., Pitchford C.W. and van Dam, J., Experimental results of structural health monitoring of wind turbine blades, *Proc. 46th AIAA Aerospace Sciences Meeting and Exhibit*, Reno, Jan 7-10, 2008. AIAA-2008-1348, Rumsey.
46. Ge, M., Analysis of source location algorithms, Parts I and II, *J. of Acoustic Emission*, **21**, 2003, 14 and 29.
47. Manthei, G., Eisenblätter, J., and Spies, T., Acoustic emission in rock mechanics studies”, *Acoustic Emission – Beyond the Millennium*, 2000, Elsevier, pp. 127-143.
48. Spies, T. and Eisenblätter, J., Acoustic emission monitoring of closely spaced excavations in an underground repository”, *J. of Acoustic Emission*, **19**, 2001, 153-161.
49. Hirata, T., Satoh, T., and Ito, K., *Geophysical Journal International*, **90**, 1987, 369-374.
50. Iverson, N., Kao, C.S. and Labuz, J.L., Clustering analysis of AE in rock, *Proc. ICAE-6*, Lake Tahoe, 2007, pp. 294-299. Also see: *J. of Acoustic Emission*, **25**, 2007, 364-372.
51. Watanabe, Y., Itakura, K.I., Sato, K., Fujii, Y., Balusu, R., Guo, H. and Luo, X., A modeling method on fractal distribution of cracks in rocks using AE monitoring, *J. of Acoustic Emission*, **23**, 2005, 119.
52. Yamada, H., Mizutani, Y., Nishino, H., Takemoto, M. and Ono, K. Lamb-wave source location of impact on anisotropic plates, *J. of Acoustic Emission*, **18**, 2000, 51.
53. Kurokawa, Y., Mizutani, Y. and Mayuzumi, M., Real-time executing source location system applicable to anisotropic thin structures, *J. of Acoustic Emission*, **23**, 2005, 224.

54. Vahaviolos, S.J., Miller, R.K., Watts, D.J., Shemyakin, V.V., and Strizkov, S.A., detection and location of cracks and leaks in buried pipelines using acoustic emission, *J. of Acoustic Emission*, **19**, 2001, 172-183.
55. Hamstad, M.A., Acoustic emission signals generated by monopole (pencil-lead break) versus dipole sources: finite element modeling and experiments, *J. of Acoustic Emission*, **25**, 2007, 92.
56. Ono, K. and Cho, H., Rods and tubes as AE waveguides, *J. of Acoustic Emission*, **22**, 2004, 243-253.
57. Ohtsu M. and Ono K., Crack orientations and moment tensor solutions in acoustic emission, *Progress in Acoustic Emission III*, pp. 771-778, JSNDI, 1986. See also Ohtsu, M. and Ono, K., AE source location and orientation determination of tensile cracks from surface observation, *NDT International*, **21**, 1988, 143-152.
58. Ohtsu, M., Determination of crack orientation by acoustic emission, *Materials Evaluation*, **45**, 1987 1070-1075. See also Ohtsu, M., Moment tensor analysis, *Acoustic Emission – Beyond the Millenium*, Elsevier, 2000, pp. 19-34 and Ohtsu, M., Isoda, T. and Tomoda, Y., Acoustic emission techniques standardized for concrete structures *J. of Acoustic Emission*, **25**, 2007, 21-32.
59. Shiotani, T., Yuyama, S., Li, Z.W. and Ohtsu, M., Application of AE improved *b*-value to quantitative evaluation of fracture process in concrete materials”, *J. of Acoustic Emission*, **19**, 2001, 118-133.
60. Ohtsu, M. and Ono, K., Pattern recognition analysis of magneto-mechanical acoustic emission signals, *J. of Acoustic Emission*, **3**, 1984, 69.
61. Anastasopoulos, A., Pattern recognition techniques for acoustic emission based condition assessment of unfired pressure vessels, *J. of Acoustic Emission*, **23**, 2005, 318.
62. Godinez, V., Shu, F., Anastasopoulos, A., Finlayson, R., and O'Donnell, B., Real time classification of acoustic emission signals for drive system coupling crack detection, *Progress in Acoustic Emission XII*, JSNDI, 2004, pp. 7-14.
63. Runow, P., The use of acoustic emission methods as aids to the structural integrity assessment of nuclear power plants, Defense Technical Information Center, AD D320141, 51 p., 1985.
64. Jeong H.D., Takahashi H., Murakami Y., On-line evaluation procedure for structural integrity by acoustic emission frequency analysis, *Progress in Acoustic Emission IV*, JSDNI, 1986, pp. 428-438.
65. Brunner, A.J. and Bohse, J., Acoustic emission standards and guidelines 2002: a comparative assessment and perspectives, *NDT.net* - **7** (09), September 2002;
<http://www.ndt.net/article/v07n09/21/21.htm>
66. Takemoto, M., Cho, H. and Suzuki, H., Lamb-wave acoustic emission for condition monitoring of tank bottom plates, *J. of Acoustic Emission*, **24**, 2006, 12-21.

ACOUSTIC EMISSION TECHNIQUES STANDARDIZED FOR CONCRETE STRUCTURES

MASAYASU OHTSU, TOSHIRO ISODA and YUICHI TOMODA*

Graduate School of Science & Technology and *Faculty of Engineering, Kumamoto University, Kumamoto, Japan

Abstract

Acoustic emission (AE) techniques have been extensively applied to concrete structures. Results achieved are currently going to be standardized for the inspection and evaluation of infrastructures in service. Test results associated with these standardization activities for concrete structures are discussed. In order to assess the damage levels of the structures, the Japanese Society for Non-Destructive Inspection has established the recommended practice (*NDIS 2421*). Two AE indices of load ratio and calm ratio are defined for qualification of the damages. It is demonstrated that damages qualified are in good agreement with actual damages of reinforced concrete members. AE behavior of concrete under compression could be analyzed, applying the rate process analysis. By evaluating intact moduli of elasticity from AE database, relative damages of concrete cores taken from a road bridge are quantitatively estimated.

The Federation of Construction Materials Industries, Japan, has recently published new standards on estimation of concrete properties by the elastic-wave methods. The standards contain a monitoring method for active cracks in concrete by AE (*JCMS-III B5706*). The classification of cracks is successfully applied to investigate the corrosion process of reinforcing steel-bars in concrete. The moment tensor analysis of AE can identify cracking kinematics of location, crack-type and crack orientation, which has been implemented as SiGMA procedure. Nucleation of micro-cracking due to the expansion of corrosion product is studied. It is found that the mechanisms of corrosion cracking at the meso-scale are really made up of tensile, shear and mixed-mode cracks, while the surface crack and the diagonal cracks of mode I are observed at the macro-scale. These results will form the basis for proposing *RILEM* recommendations.

Keywords: Concrete, damage, corrosion, moment tensor analysis.

1. Introduction

Concrete structures in service deteriorate due to heavy traffic loads, fatigue, aging, chemical reactions and natural disasters. It is now recognized in concrete engineering that concrete structures are no longer considered maintenance-free, and a number of the structures are going to reach their service-life limit. Accordingly, diagnostic inspections on the current state of deteriorated structures have been carried out all over the world. However, the assessment of damage or structural integrity in existing structures is neither an easy task nor fully standardized yet. In this regard, the recommended practice by acoustic emission (AE) is currently published (*NDIS 2421*, 2000), prescribing one criterion to assess the damage of reinforced concrete in service. Here, results applied to bending tests of reinforced concrete beams (Ohtsu et al., 2002) are discussed.

Damage evaluation in concrete by AE activity of a core sample in a compression test is under investigation (Ohtsu and Watanabe, 2001). AE activity is analyzed as the rate process, and the damage parameter is evaluated by applying damage mechanics. Correlating AE rate with the damage parameter, a database has been so successfully created that relative damages of concrete

samples are quantitatively estimated. The procedure is applied to concrete cores taken from a road bridge.

The corrosion of reinforcing steel-bars in concrete can occur due to chloride attack. So far it has been referred to as the most serious deterioration of reinforced concrete. An applicability of AE technique to corrosion monitoring is discussed, applying the code by the Federation of Construction Materials Industries, Japan (*JCMS-III B5706*, 2003).

The moment tensor analysis of AE is available for identifying crack kinematics of location, crack-type and crack orientation (Ohtsu, 2000). The analysis is implemented as SiGMA (Simplified Green's functions for Moment tensor Analysis) procedure. 3-D visualization has been developed by using VRML (Virtual Reality Modeling Language) (Shigeishi and Ohtsu, 2003). Mechanisms of corrosion cracking in concrete at the meso-scale identified by SiGMA are compared with those at the macro-scale.

Currently, another standardizing action is in progress. RILEM TC212-ACD (Technical Committee on Acoustic emission and related NDE for Crack detection and Damage evaluation in concrete) has been established for proposing RILEM recommendations. All results discussed are closely associated with this committee activity.

2. AE Techniques under Standardized Action

(1) Damage Qualification

The concrete structure is structurally stable with high redundancy, as AE activity is low in a sound structure. Since the Kaiser effect is closely associated with structural stability, ratios to qualify the damage are defined in the recommended practice (*NDIS 2421*), as follow;

(a) Ratio of load at the onset of AE activity to previous load:

Load ratio = load at the onset of AE activity in the subsequent loading / the previous load.

(b) Ratio of cumulative AE activity during the unloading to that of the maximum loading cycle:

Calm ratio = the number of cumulative AE activity during the unloading / total AE activity during the whole cycle.

The *load ratio* can become larger than 1.0 in a sound structure. Due to damage accumulation, the ratio decreases to below 1.0, generating AE counts at lower loading levels than before. AE activity during unloading is another indication of structural instability. In the case of the sound structure, AE activity is seldom observed and the *calm ratio* is small. In heavily damaged structures, *load ratio* is below 1.0 and *calm ratio* is large. In the recommendation, the damage is defined as minor, intermediate and heavy as shown in Fig. 1.

(2) AE Rate Process Analysis

AE behavior of a concrete sample under compression is closely associated with nucleation of micro-cracks. These cracks are gradually accumulated until final fracture, as the number of AE counts due to nucleation of these cracks increases. Since the process could be referred to as stochastic, the rate process theory has been introduced (Ohtsu and Watanabe, 2001). The following equation of the rate process is derived to formulate the number of AE events, dN , due to the increment of stress from V to $V + dV$,

$$\frac{dN}{N} = f(V)dV, \quad (1)$$

where N is the total number of AE events and $f(V)$ is the probability function of AE activity at stress level $V(\%)$. Here, a hyperbolic function $f(V)$ is assumed,

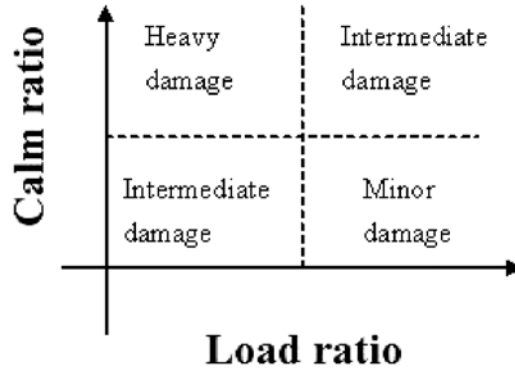


Fig. 1 Damage qualification by the load ratio and calm ratio.

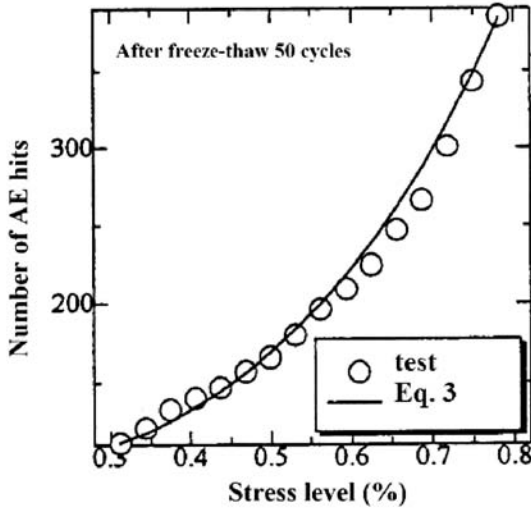


Fig. 2 Result of AE rate process analysis.

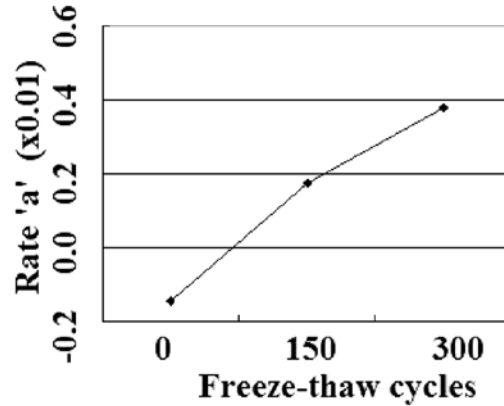


Fig. 3 Relation between rate 'a' and freeze-thaw cycles.

$$f(V) = \frac{a}{V} + b, \quad (2)$$

where a and b are empirical constants. ' a ' is here called the rate, since it reflects AE activity at a given stress level. It is found that the rate could increase due to accumulation of the micro-cracks in concrete. Substituting Eq. 2 into Eq. 1, a relationship between total number of AE events N and stress level V is obtained as,

$$N = CV^a \exp(bV), \quad (3)$$

where C is the integration constant. We have applied Eq. 3 to AE generating behavior of a concrete sample in a compression test. Approximating the probability function by Eq. 2, AE generating behavior is modeled. A relation between total AE counts and compressive stresses in a standard sample (10-cm diameter and 20-cm height) is shown in Fig. 2. The sample was damaged with 50 cycles of freeze-thaw action. It is demonstrated that AE generating behavior observed in the test is in good agreement with the relation approximated by Eq. 3. We focused on the rate ' a ', because the value could reflect the damage degree. During the freezing and thawing of concrete samples, where temperature was varied from 5°C to -15°C for 3 hours, a relation between the rate " a " and the number of cycles was examined. Results are given in Fig. 3. It is clearly observed that the rate ' a ' increases from a negative value to a positive value with the increase in freeze-thaw cycles. Thus, it is confirmed that the rate ' a ' is a sensitive parameter to the damage degree.

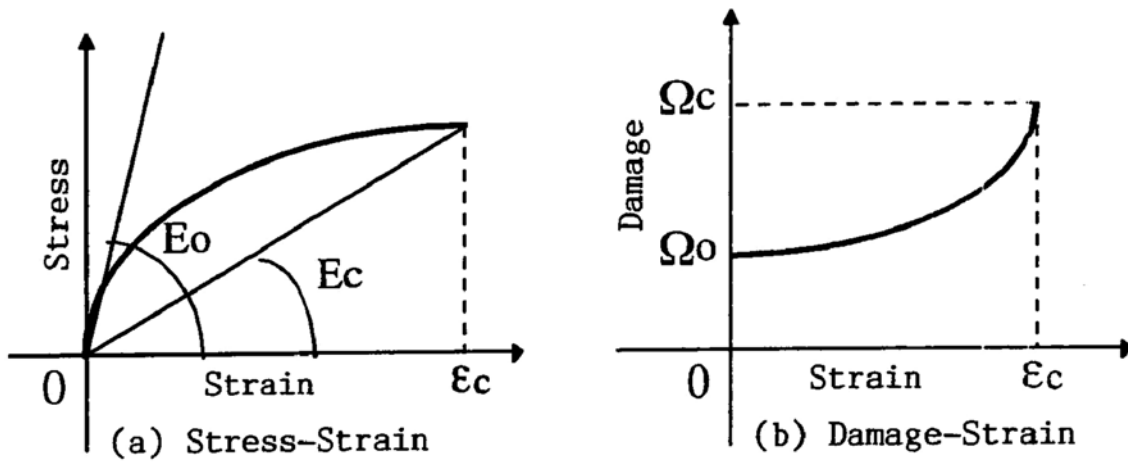


Fig. 4 (a) Stress-strain relation and (b) the corresponding damage-evolution process.

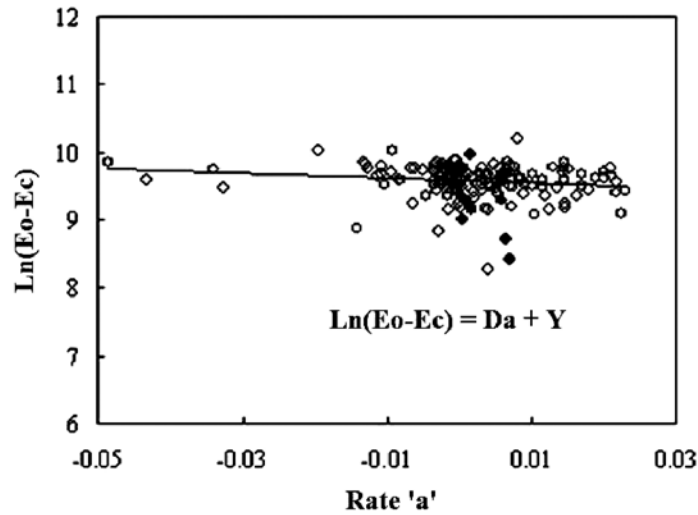


Fig. 5 Database on the damage evolution and the rate 'a'.

A damage parameter Ω in continuum damage mechanics is defined as a relative ratio of the modulus of elasticity,

$$\Omega = 1 - \frac{E}{E^*} \quad (4)$$

where E is the modulus of elasticity of concrete and E^* is the intact modulus of elasticity. In the compression test of a concrete sample, a relation between stress and strain is obtained as shown in Fig. 4(a). The modulus varies from initial modulus E_0 to final modulus E_c . The former is a tangential modulus and the latter is a secant modulus. Then, the initial damage Ω_0 is defined as,

$$\Omega_0 = 1 - \frac{E_0}{E^*}. \quad (5)$$

Corresponding to the stress-strain relation, the damage parameter Ω increases from Ω_0 to Ω_c as shown in Fig. 4(b). In order to estimate the initial damage Ω_0 in Eq. 5, it is essential to obtain the intact modulus E^* . Because the rate 'a' is sensitive to the damage degree, a database on a correlation between the damage evolution during the compression test, $\ln(E_0 - E_c)$, and the rate 'a' has been constructed as shown in Fig. 5. Most of the data are based on results of the freezing and thawing tests of concrete samples. Assuming a linear correlation, it is derived as,

$$\ln(E_0 - E_c) = \ln[E^*(\Omega_c - \Omega_0)] = Da + Y. \quad (6)$$

After adding the data of a tested sample to the database, a new linear correlation of Eq. 6 is determined. Then, it is assumed that $E_0 = E^*$ when $a = 0$. This allows us to estimate the intact modulus E^* of the sample from,

$$E^* = E_c + \exp(Y). \quad (7)$$

Then a relative damage of the sample is estimated as E_0/E^* .

(3) AE Parameter Analysis

AE parameters obtained by a conventional system are AE count, AE hit, AE event, peak amplitude, AE energy, rise time, duration, arrival time differences in AE sensor array and so forth. In order to classify active cracks, AE indices of RA value, and the averaged frequency Fa are defined from parameters as (JCMS-III B5706),

$$RA = \text{the rise time} / \text{the maximum amplitude}. \quad (8)$$

$$Fa = \text{AE ringdown-count} / \text{the duration time}, \quad (9)$$

By means of these two indices, cracks could be classified into tensile and shear cracks as referring to Fig. 6. Tests were conducted in tensile tests and direct-shear tests of concrete samples, by employing three AE sensors of different resonances. It is observed that crack types are reasonably classified. Here, the classification shall be based on the moving average of more than 50 counts.

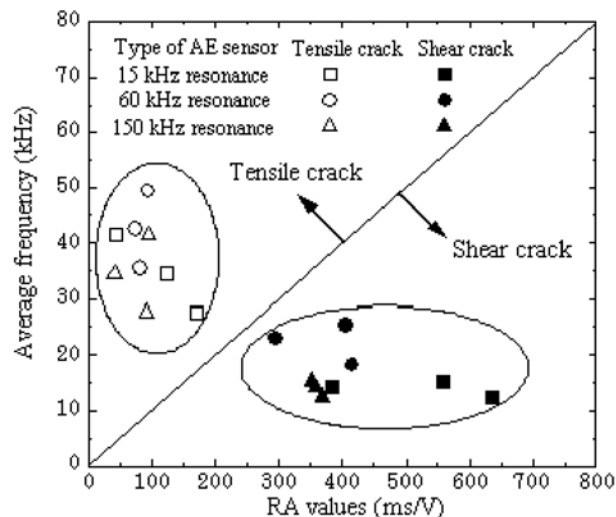


Fig. 6 Relationship between average frequency Fa and RA values for crack classification.

(4) SiGMA Analysis

In order to determine the moment tensor of an AE source, a simplified procedure has been developed. This is suitable for a PC-based processor as it is robust in computation. The procedure is implemented as *SiGMA* (Simplified Green's functions for Moment tensor Analysis) (Ohtsu, 2000). Displaying AE waveform on CRT screen, two parameters of the arrival time and the amplitude of the first motion are determined. In the location procedure, source location is determined from the arrival time differences. Then, distance and its direction vector are determined. From the amplitudes of the first motions at more than 6 channels, the moment tensor is determined. Since the SiGMA code requires only relative values of the moment tensor components, the relative calibration of the sensors is adequate. Then, the classification of a crack is performed by the eigenvalue analysis of the moment tensor. Setting the ratio of the maximum shear contribution as X , three eigenvalues for the shear crack become $X, 0, -X$. Likewise, the

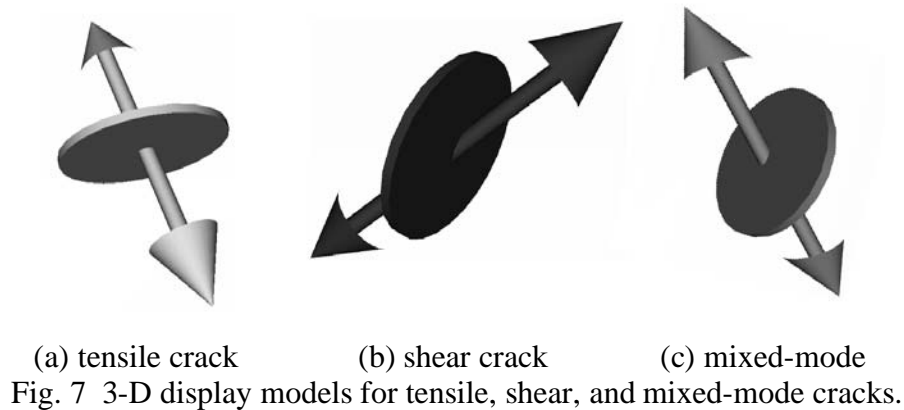
ratio of the maximum deviatoric tensile component is set as Y and the isotropic tensile component as Z . Three eigenvalues are normalized and decomposed;

$$\begin{aligned} \text{Normalization} & & 1.0 &= X + Y + Z, \\ \text{the intermediate eigenvalue/the maximum eigenvalue} & & &= 0 - Y/2 + Z, \\ \text{the minimum eigenvalue/the maximum eigenvalue} & & &= -X - Y/2 + Z, \end{aligned} \quad (10)$$

where X , Y , and Z denote the shear ratio, the deviatoric tensile ratio, and the isotropic tensile ratio, respectively. In the present SiGMA code, AE sources of which the shear ratios are less than 40% are classified into tensile cracks. The sources of $X > 60\%$ are classified into shear cracks. In between 40% and 60%, cracks are referred to as mixed mode. In the eigenvalue analysis, three eigenvectors $\mathbf{e1}$, $\mathbf{e2}$, and $\mathbf{e3}$,

$$\begin{aligned} \mathbf{e1} &= \mathbf{l} + \mathbf{n} \\ \mathbf{e2} &= \mathbf{l} \times \mathbf{n} \\ \mathbf{e3} &= \mathbf{l} - \mathbf{n}, \end{aligned} \quad (11)$$

are also determined. Vectors \mathbf{l} and \mathbf{n} , which are interchangeable, are recovered. In order to visualize these kinematical information of AE source (crack), VRML is introduced (Shigeishi and Ohtsu, 2003). Crack modes of tensile, shear and mixed-mode cracks are given in Fig. 7. Here, an arrow vector indicates a crack motion vector \mathbf{l} , and a circular plate corresponds to a crack surface, which is perpendicular to a crack normal vector \mathbf{n} .



3. Results and Discussion

(1) Qualified Damage in Reinforced Concrete

For damage qualification, reinforced concrete beams of 3.2 m length were tested. Compressive strength of concrete after 28-day moisture curing was 31.1 MPa. These beams were made without lateral reinforcement. Two-point loading spans were varied as 0.65 m and 1 m with 2.84 supporting-span shown in Fig. 8. AE sensor of 150-kHz resonance frequency (PAC: R15) was selected. Frequency range was set from 10 kHz to 1 MHz, and the total amplification was 80 dB. For event-counting, a threshold level was set to 50 dB. The measuring system was a MIS-TRAS-AE system (PAC). After cracks were nucleated, clip gauges were attached to the specimen and the crack-mouth opening displacements (CMOD) were recorded.

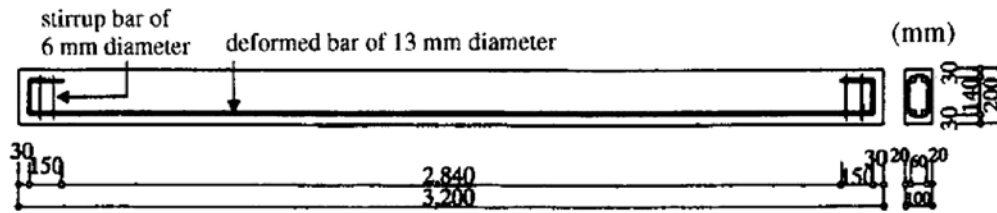


Fig. 8 Sketch of a reinforced concrete beam.

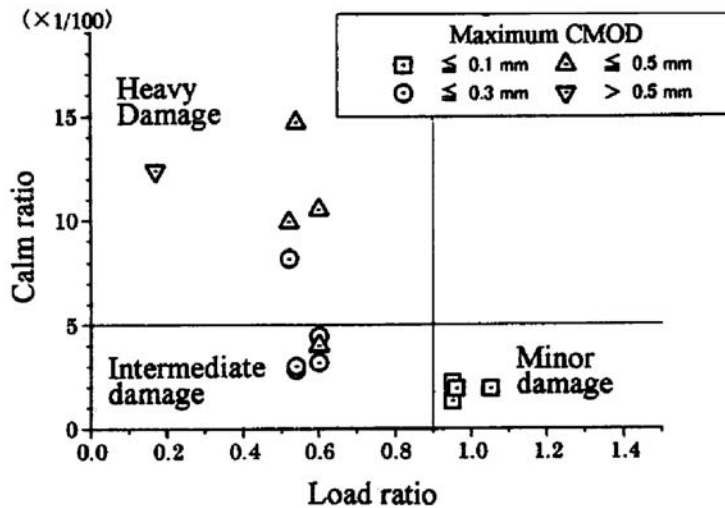


Fig. 9 Qualified damages by the *load ratio* and the *calm ratio*.

For each loading cycle, the *load ratio* and the *calm ratio* were determined. Results are shown in Fig. 9. Based on the maximum CMOD observed in the loaded beams, classification limits are set as 0.9 for the *load ratio* and 0.05 for the *calm ratio*. This is because the serviceability limit of the CMOD in the concrete structure is referred to as less than 0.1 mm in the standard specification and the Kaiser effect was not observed in the case of the CMOD over 0.1 – 0.2 mm (Ohtsu, 1995). Into three zones of the minor, intermediate, and heavy damage, results of the maximum CMODs are classified reasonably well. It demonstrates that the damage levels of reinforced concrete beams can be qualified from the values of the *load ratio* and the *calm ratio* by monitoring AE activity under cyclic loading or traffic loads.

(2) Relative Damage of Concrete in a Road Bridge

Cylindrical samples of 10 cm in diameter were core-drilled from a concrete block (3.0 m×3.0 m×0.68 m), which was taken from an arch fragment of a road bridge shown in Fig. 10(a). The bridge had been in service for more than 50 years, and was recently replaced because of road expansion. After core-drilling, 12 cylindrical samples of 20-cm height were made by sawing and end-polished.

AE measurement in a compression test was conducted as shown in Fig 10(b). Silicone grease was pasted on the top and the bottom of the sample, and a Teflon sheet was inserted to reduce AE counts generated due to friction. MISTRAS-AE system (manufactured by PAC) was employed to count AE hits. AE hits were detected by using an AE sensor (PAC UT-1000 resonance frequency: approx. 1 MHz). The frequency range was from 60 kHz to 1 MHz. For event counting, the dead time was set to 2 ms. It should be noted that AE measurement was conducted

at two channels as well as the measurement of axial strains. AE hits and strains of the two channels were averaged as a function of stress level.

From AE generating behavior, the rate ' a ' was estimated as the probability function $f(V)$ was approximated by Eq. 2, where the least-square method was applied. Then, relative damages E_0/E^* were estimated in all samples. Results are compared with the compressive strengths in Fig. 11. It is observed that relative damages estimated show a similar trend to the compressive strengths. The compressive strength specified is to be over 25 MPa. About a half of the cores seem to satisfy the specification, but the relative damages are lower than 1.0 except core Nos. 4 and 6. This suggests that most concrete cores are slightly damaged as the relative damages are obtained in the range from 0.9 to 0.7. It suggests that the concrete block might have withstood traffic loads as their strengths are over the designed value, but the deterioration has already started as low values of the relative damage. Thus, the damage degree of concrete cores are quantitatively estimated by AE rate process analysis.



Fig. 10 (a) Arch fragment of a road bridge and (b) AE measurement system in compression test.

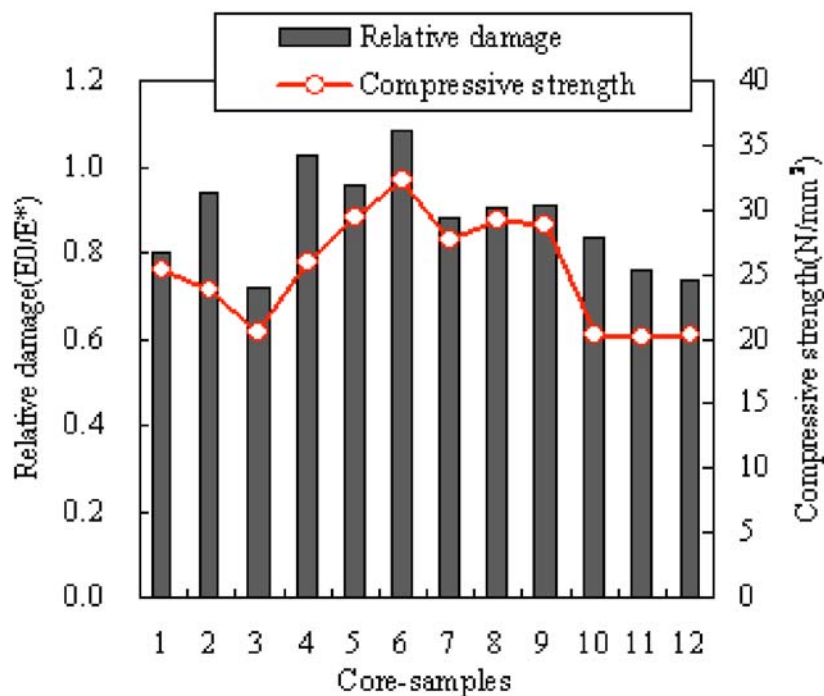


Fig. 11 Relative damages and compressive strengths.

(3) Corrosion Process of Reinforced Concrete

Continuous monitoring of AE events was conducted in an accelerated corrosion test and in a cyclic wet-dry test. A reinforced concrete slab of dimensions 10 cm x 25 cm x 40 cm was cast. The compressive strength at 28 days after moisture-curing in the standard room was 34.6 MPa. The slab specimen was soaked in a tank. A copper plate was placed at the bottom, and then 100 mA electric current was charged between rebars and the copper plate as shown in Fig. 12. To keep electrical conductivity good, the tank was filled with 3% NaCl solution. In a cyclic wet-dry test, the specimen was cyclically soaked into the tank in Fig. 12 without charge for a week, and subsequently taken out of the tank to dry under ambient temperature for another week. In both tests, when the measured potentials became lower than -350 mV (C.S.E.), which is prescribed by *ASTM C876* (1991), the tests were terminated. AE sensors of 50-kHz resonance (RA5) were placed on the top surface of the samples. Amplification was 40 dB in total and the frequency range was set from 10 kHz to 1 MHz. After the tests, core samples were taken, sliced and crashed. Then, chloride contents at depth were measured by the potentiometric titration.

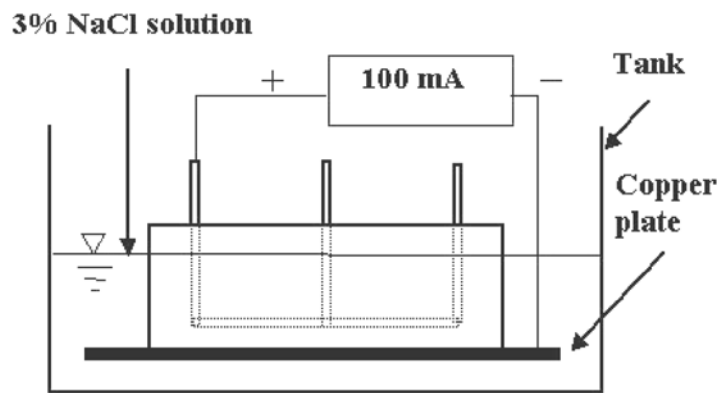


Fig. 12 Set-up for accelerated corrosion test.

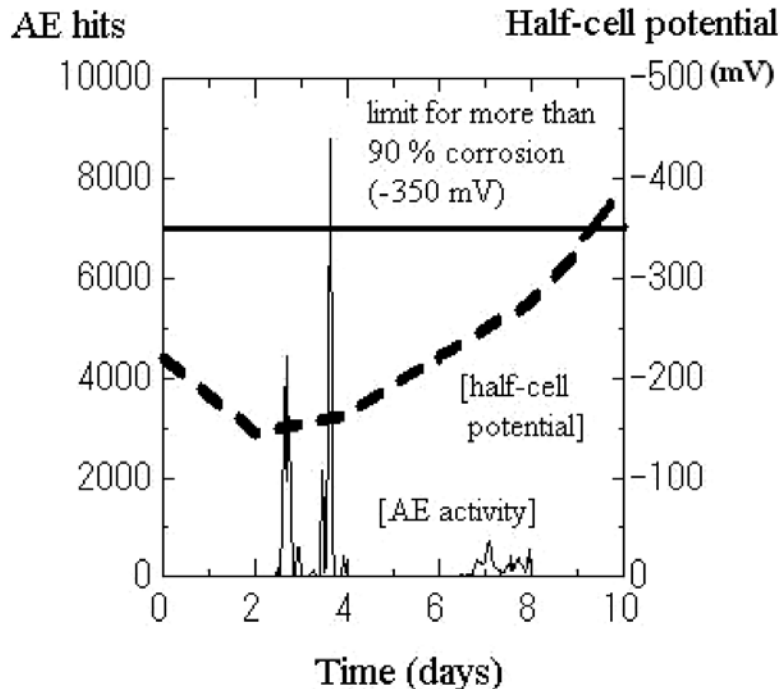


Fig. 13 AE activities and the half-cell potentials in the accelerated corrosion test.

A relation between AE activity and half-cell potentials in the accelerated corrosion test is given in Fig. 13. Two periods of high AE activity (hits) are observed. At the first period, the half-cell potentials start to decrease, where an abrupt increase in AE hits is observed at around three days. The potentials reach lower than -350 mV (C.S. E) after the second period. Because such two periods as the onset of corrosion in reinforcement and the nucleation of cracking in concrete due to the expansion of corrosion products are defined in the standards, the two high AE activities are quite suggestive in the deterioration process due to the corrosion of reinforced concrete.

To classify AE sources (micro-cracks) in the corrosion process, AE parameter analysis was performed. Variations of RA values and the average frequencies in the cyclic wet-dry test are given in Fig. 14. Two stages are reasonably identified from the figure. During the first period of around 40 days elapsed, RA value is high and the average frequency is low. From Fig. 6, this suggests that shear cracks are actively generated. It is considered that shear cracks occur in reinforcement due to the onset of corrosion or rust breakage. During the second period around 100 days elapsed, RA value in Fig. 14 is lower than the first period and the average frequency is high. This implies the occurrence of tensile cracks. The expansion due to corrosion products should result in the nucleation of tensile cracks in concrete. Consequently, it is reasonable to consider that the second high AE activity corresponds to the nucleation of concrete cracking.

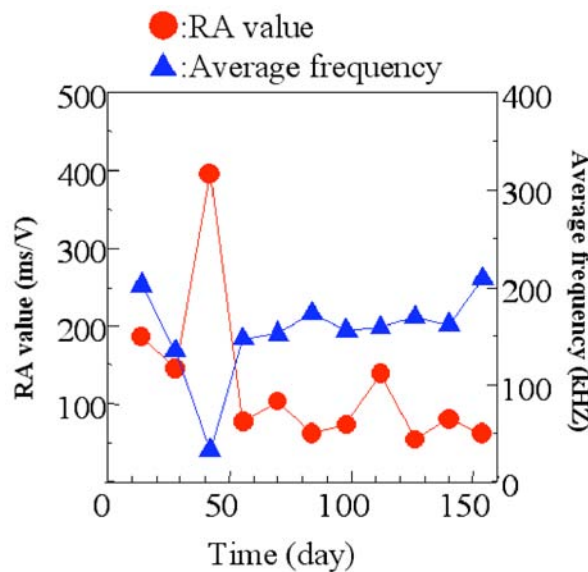


Fig. 14 Variations of AE parameters.

Chloride concentrations at the cover-thickness were also investigated to compare with AE results. It was found that chloride concentrations at reinforcement were higher than 0.3 kg/m^3 after the first period and became higher than 1.2 kg/m^3 after the second. These results are in good agreement with the values prescribed as the lower bound and the upper bound for the corrosion in the specification.

(4) Mechanisms of Corrosion Cracking

A concrete specimen of dimensions $25 \text{ cm} \times 25 \text{ cm} \times 10 \text{ cm}$ with a hole of 3-cm diameter was tested. The hole corresponds to rebar location with 4-cm cover-thickness. The compressive strength of concrete at 28-day standard curing was 37.9 MPa. The velocity of P wave was 4730 m/s and the modulus of elasticity was 29.7 GPa. P-wave velocity was applied to SiGMA

analysis. Corrosion cracking was simulated by casting an expansive agent (dolomite paste) into the hole. After one day, three cracks were macroscopically observed as shown in Fig. 15. These are surface crack and two diagonal cracks. Results of SiGMA analysis are plotted at locations of AE sources with crack types and orientations in the same figure. At the meso-scale, all the types of micro-cracks are observed as AE sources in SiGMA analysis. This implies that micro-cracks are accumulated and macroscopically the cracks are nucleated as the surface crack and the diagonal cracks. In the photo, the crack, which propagated from the hole to the bottom, corresponds to the surface crack. Around this crack, numerous tensile cracks of AE sources are observed, which are almost oriented as vertical to the surface-crack plane. During the test, the surface crack was observed first, and then two diagonal cracks propagated. Around these cracks, AE sources are composed of tensile, mixed-mode and shear cracks. It is noted that the final cracks of the surface crack and the diagonal cracks consist of one crack surface at the macro-scale, but actually many micro-cracks are nucleated around them. This is a typical cracking mechanism in concrete. Mechanisms of corrosion cracking in concrete are of crack-opening failure, but the cracks follow zigzag paths, thus explaining nearly equal contributions of mixed-mode and shear cracks at the meso-scale.

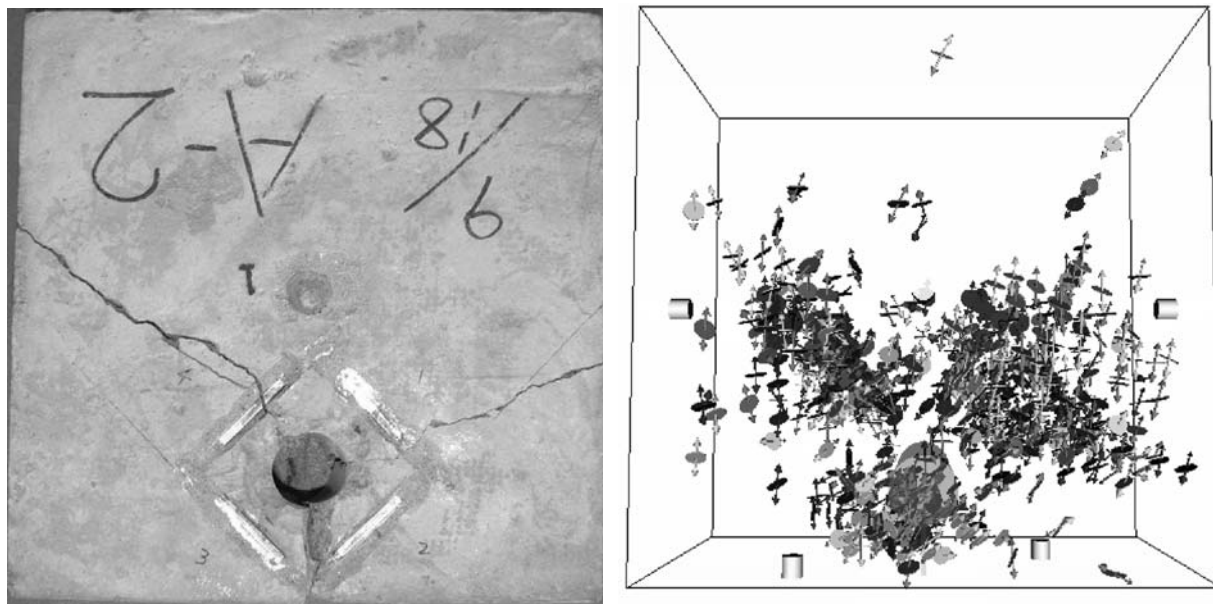


Fig. 15 Observed cracks (left) and visualized results of SiGMA analysis (right).

4. Conclusion

(1) The recommended practice (*NDIS 2421*) is applied to cyclic bending tests of reinforced concrete beams. The applicability of the criterion to qualifying the damage is confirmed. Thus, it is demonstrated that the criterion to assess the damage is useful for inspection of beams in service.

(2) Applying AE rate process analysis to compression tests of concrete cores, it is demonstrated that relative damages estimated are in reasonable agreement with actual damages. The procedure is promising to estimate the damage of concrete quantitatively without knowing initial properties at construction.

(3) It is found that AE monitoring could provide earlier warning of the corrosion than the half-cell potentials. By continuously monitoring AE activity, both the onset of corrosion in reinforcement and the nucleation of cracking in concrete could be identified nondestructively.

This suggests that AE monitoring is practically applicable to in situ monitoring for the corrosion damage in reinforced concrete structures.

(4) Crack propagation due to corrosion of reinforcement in concrete is studied experimentally. Cracking mechanisms are investigated by SiGMA with 3-D VRML display. The surface crack and the diagonal cracks are observed at the macro-scale, while many micro-cracks are identified by SiGMA analysis around them. The results show a promise to apply SiGMA procedure to investigate micro-scale or meso-scale mechanisms of cracking in concrete.

All results discussed are closely associated with standardization actions in the committee, RILEM TC212-ACD, for proposing *RILEM* recommendations.

References

ASTM C876 (1991), Standard Test Method for Half-Cell Potentials of Uncoated Reinforcing Steel in Concrete, ASTM.

JCMS-III B5706 (2003), Monitoring Method for Active Cracks in Concrete by Acoustic Emission, Federation of Construction Materials Industries, Japan.

NDIS 2421 (2000), Recommended Practice for In-Situ Monitoring of Concrete Structures by AE, Japanese Society for Nondestructive Inspection.

Ohtsu, M. (1995), "The History and Development of Acoustic Emission in Concrete Engineering," *Concrete Library of JSCE*, **25**, 121-134.

Ohtsu, M. (2000), "Moment Tensor Analysis and SiGMA Code," *Acoustic Emission-Beyond the Millenium*, Elsevier, Amsterdam, pp. 19-34.

Ohtsu, M. and Watanabe, H. (2001), "Quantitative Damage Estimation of Concrete by Acoustic Emission," *Construction and Building Materials*, **15**(5-6), 217-224.

Ohtsu, M., Uchida, M., Okamoto, T. and Yuyama, S. (2002), "Damage Assessment of Reinforced Concrete Beams qualified by AE," *ACI Structural Journal*, **99**(4), 411-417.

Shigeishi, M. and Ohtsu, M. (2003), "Virtual Reality Presentation of Moment Tensor Analysis by SiGMA", *J. Korean Society for NDT*, **23**(3), 189-199.

ACOUSTIC EMISSION MONITORING OF REINFORCED CONCRETE FRAME DURING SEISMIC LOADING

A. ANASTASOPOULOS, S. BOUSIAS* and T. TOUTOUNTZAKIS

Envirocoustics SA, El. Venizelou 7 & Delfon, 14452 Athens, GREECE;

*Structures Laboratory, Dept. of Civil Eng. Univ. of Patras, 26500, Patras, Greece

Abstract

Acoustic emission (AE) monitoring was performed during pseudo-dynamic testing of an old, two-storey, one-by-one bay reinforced concrete frame structure. The structure represented a 0.7-scale model of a real-size frame structure designed and detailed according to the standards prevailing in Southern Europe in the 60's without engineered earthquake resistance. Real-time monitoring of AE activity versus the complex applied load resulted in semi-quantitative damage characterization as well as comparative evaluation of the damage evolution of the different size columns. Evolution of the AE energy rate per channel, as revealed from zonal location, and the energy rate of linearly located sources enabled the identification of damage areas and the forecast of crack locations before cracks were visible with naked eye. In addition to that, the results of post-processing evaluation allowed for the verification of the witnessed damaged areas and formed the basis for quantitative assessment of damage criticality.

Keywords: Reinforced concrete structures, earthquake damage assessment, pseudo dynamic loading, real-time monitoring.

Introduction

Old, substandard RC buildings designed in the 60's on the basis of vertical loads only are often characterized by irregular distribution of strength and stiffness in-plan. These structural characteristics, usually dictated by architectural requirements, are coupled with those owing to the design according to non-seismic design codes of the 60-70's in Southern Europe (e.g., insufficient detailing of reinforcement, low concrete strength) result in structures with increased vulnerability to earthquakes. An experimental program of a 0.7-scale model of a real-size frame structure designed and detailed as old RC buildings in Greece, without engineered earthquake resistance, was carried out at the Structures Laboratory of the Department of Civil Engineering at the University of Patras, employing the pseudo-dynamic testing method. To represent the actual torsional seismic response of such a structure, pseudo-dynamic testing was performed with four degrees of freedom (DOF): the displacements of the two floors in the direction of the actuators, plus the two floor rotations with respect to the vertical axis. The structure was excited by a 15-sec-long unidirectional input motion that fitted well with the 5%-elastic spectrum of Eurocode 8 modulated after one component of the Herzegnovi record in the 1979 Montenegro earthquake.

Due to their sub-standard design, the columns of the building, both at ground and upper floor, exhibited low strength and ductility capacity and, thus, damage was expected to develop first at their ends, due to the insufficient reinforcement overlapping length there. Acoustic emission was used as an NDT method, to monitor damage development at these vulnerable areas. Due to the complex nature of the applied loading and structural response, techniques previously proposed (Matsuyama et al., 1993, Yuyama et al., 1999) for AE evaluation during controlled stimulus, are not directly applicable. Different source location techniques (zonal, linear and 3-D location) were

applied in order to identify potential high risk areas of increased AE activity during loading. A summary of the experimental procedure and the derived results are reported and discussed herein. Comparison of the differences detected in AE behavior among the different columns as well as between the base and the 1st floor joints is performed and the results are correlated with the applied load. Further processing of the located AE events, enabled the verification of the damage areas observed and the assessment of the building structural integrity.

Experimental Set Up

A nearly full-scale model simulating the structural configuration and seismic response of real-size reinforced concrete structures was constructed and tested. The structure comprised of two floors and one bay per direction, while its four columns formed pairs of unequal resistance and stiffness along the longitudinal (X) direction of the structure. The plan dimensions of the specimen structure were 3.15 x 3.85 m and the floor height was 2.30 m and 2.0 m at ground and top floor, respectively as presented in Fig. 1. To create an asymmetric structure that responds with torsion under translational ground motions, columns of one side were one-half size of those of the other side. All columns were 0.175-m wide while their depth varied from 0.175 m for the pair of columns at one side of the structure, to 0.35 m for the opposite pair. Columns were cast on spread footings anchored on the strong floor of the laboratory and were longitudinally reinforced with four 10-mm-diameter smooth (S220) bars for the columns with the smaller section, and six 10-mm-diameter bars for the larger ones. Transverse reinforcement consisted of 6-mm-diameter smooth (S220) bars placed at 200-mm apart. The beams and the slabs were heavily reinforced so that inelastic response would appear first on columns. A mean concrete strength of 22.8 MPa and 18.05 MPa was obtained on the day of testing at the ground and upper floor, respectively.

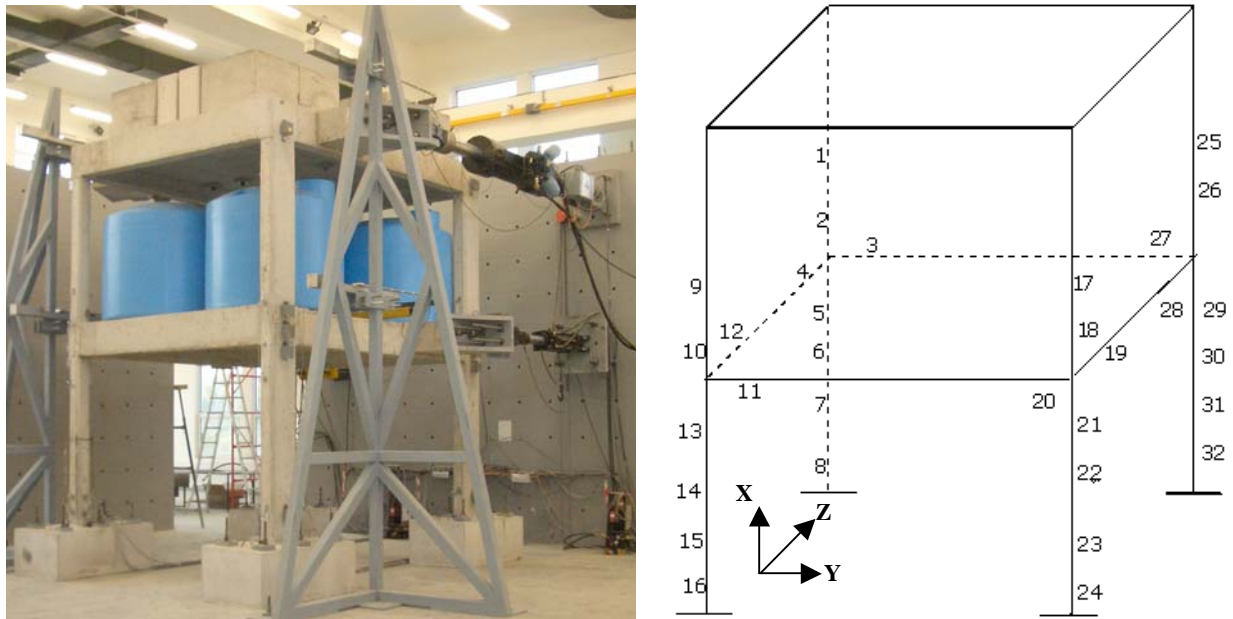


Fig. 1. Specimen layout, left, and AE sensor positions, right, (AE channels. 1-8 placed on column 1, ch. 9-16 on column 2, ch. 17-24 on column 3 and ch. 25-32 on column 4.).

Prior to AE monitoring, the structure was subjected to the selected earthquake record scaled at 0.30 g. During this initial testing phase, the structure exhibited strong torsional response,

which - contrary to current beliefs based on simplistic analytical studies - induced larger displacements on the more flexible side of the building. Columns were subjected to biaxial flexure and exhibited damage concentrated at the base of smaller ground-floor columns, owing to the inadequate force transfer along the small bar overlapping length and slippage of vertical bars within the footing. Beams were over-reinforced – as it was common in this category of structures – and displayed no damage. Some hairline diagonal cracks were observed on the sides of the larger columns, owing to the development of torsional moments in these members, which closed after the test. Some cracks formed also at the beam-column interface due to slippage of the (smooth) column reinforcing bars within the joint. To reinstate the torsional balance, smaller columns (denoted here as columns 1 and 2) were reinforced via a 0.05-m-width concrete jacket cast from the footing to the top of the structure. The structure was excited again with the same seismic record at 0.30 g, while being monitored with AE.

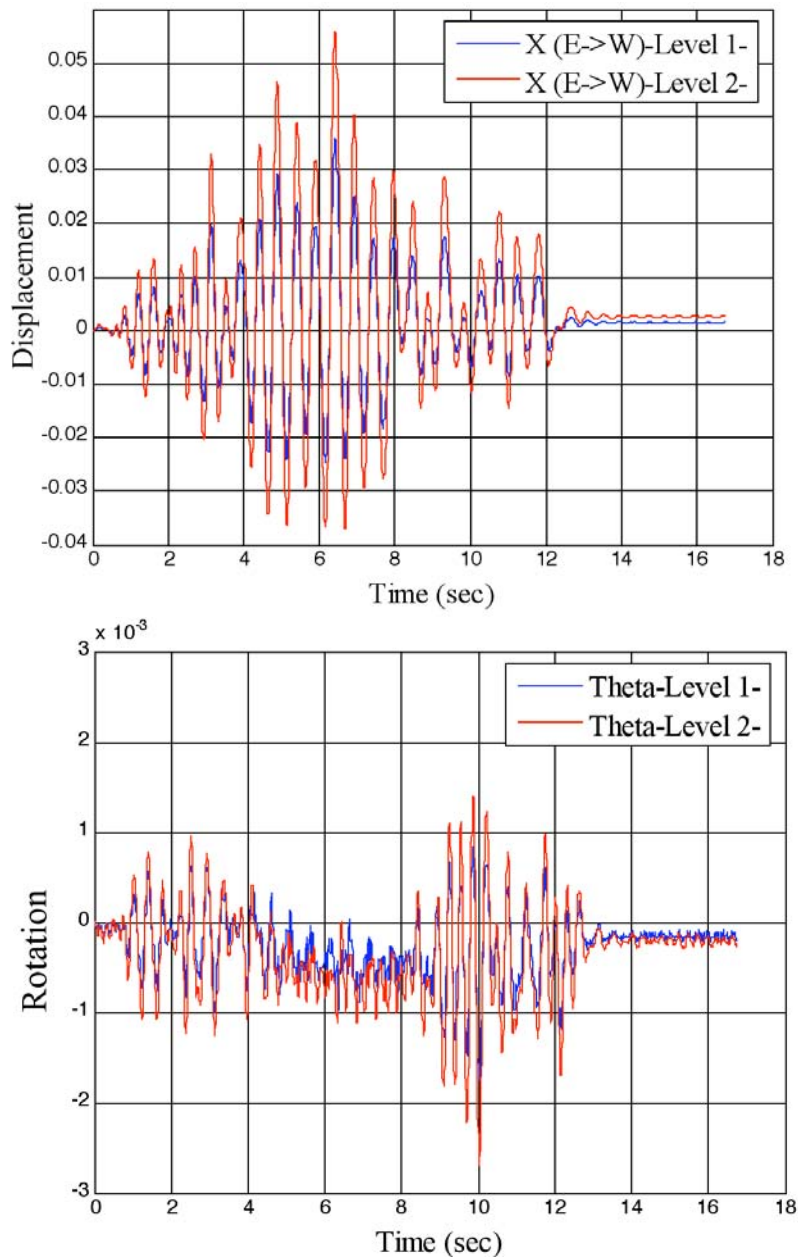


Fig. 2. Retrofitted structure: slab displacement (meters) at the ground and the top floor (top); slab rotation (rads) of the ground and the top floor (bottom).

The observation of the structure during testing and the recorded displacement and rotation data (Fig. 2) reveal that the torsional response almost disappeared and the building displaced along the axis of excitation. The observed damage consisted of cracking in the larger columns and spalling of the concrete cover due to and along the lap-spliced bars at the base of the columns. Cracking also developed at the beam-column joints at the ground and the top floor. During the later stages of the excitation though - and due to the damage inflicted on the larger columns - the torsional response re-appeared, albeit at very low amplitude.

Acoustic emission monitoring was performed using a 40-channel PAC-DiSP (PAC, 2001) system. The sensors used were standard PAC resonant type R15I, 150-kHz resonance with 40-dB integral preamplifier. The position of the AE sensors and the points of applied deformation are shown in Fig. 1. Sensor position was selected in such a way to permit linear location along the column height and linear x-y location at the 1st floor joints. Prior to the test the AE sensors were calibrated and the velocity of the AE signals was calculated in order to achieve the best possible sensor set-up sufficiently covering the areas with expected high AE activity. In addition to that the attenuation of the AE signals was measured, Fig. 3.

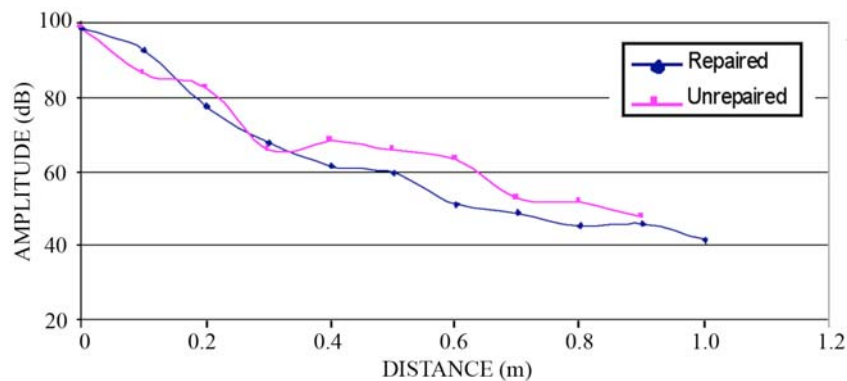


Fig. 3. Attenuation of the AE signal in column 2 and 3.

Acoustic Emission Results

Prior to the actual test a preliminary, trial loading was performed at low load levels. The maximum load of the preliminary test was 2% of the load that the building was eventually loaded. The AE activity that was recorded during the preliminary test was relatively low with low energy levels, as presented in Fig. 4. This preliminary test resulted in useful information concerning the background noise of the system as well as for setting up acquisition parameters for the AE system. In addition to that, the activity recorded in columns 1 and 2, due to the friction between the jackets and the concrete frame, was useful during the analysis phase in discriminating genuine AE signals from friction and defining damage evaluation levels.

The force exerted by each one of the four actuators is presented in Figs. 5 and 6 (four background plots for actuators 1 to 4, respectively) together with AE energy rate from each column. After jacketing the flexible columns, the building response was mainly uniaxial. The complex nature of loading (cyclic loading with varying amplitude and phase shift between actuators) resulted in complicated structural displacements and render infeasible the direct correlation between the applied loading and the AE activity. The majority of the AE activity, around 98%, is emitted from columns 1 and 2. As can be seen from Figs. 5 and 6, the AE activity starts at a deformation level exceeding that which caused the damage during the past loading

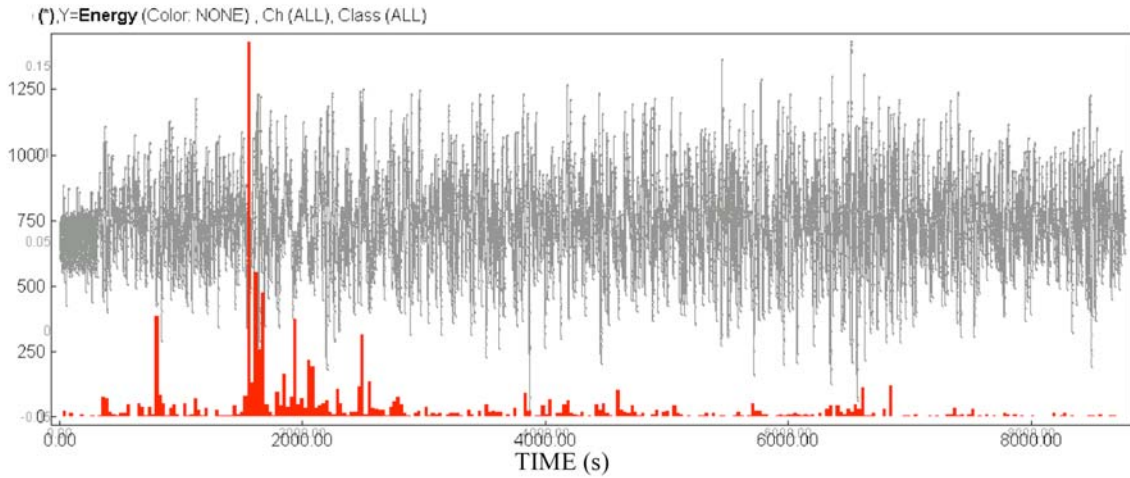


Fig. 4. Applied load (actuator 1) and total energy for the 2% test.

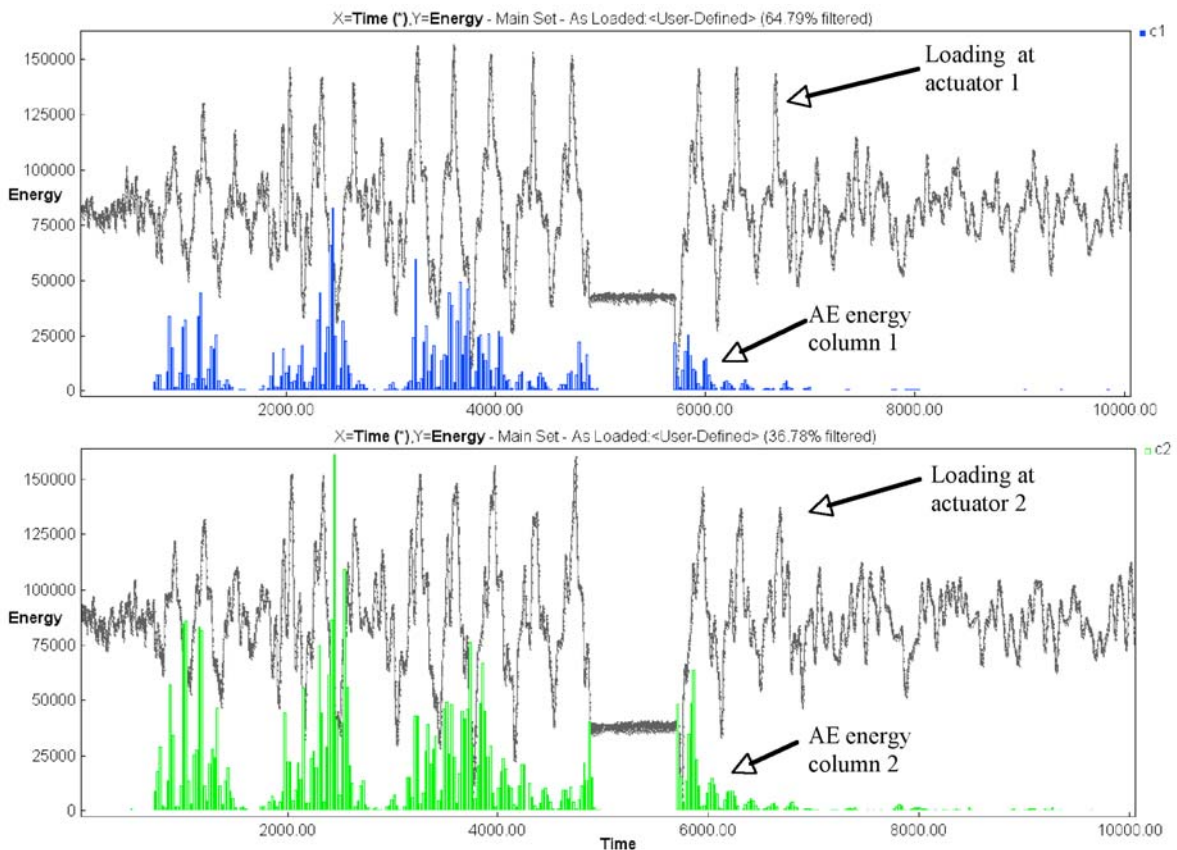


Fig. 5. Applied load at actuators 1 & 2 (background plot) and AE energy from flexible side column 1 (channels 1-8) and for column 2 (channels 9-16), respectively.

(initial test at 0.30 g). Direct comparison between past and present loading, as a means to calculate Felicity effect, is not possible due to the different nature of applied loads as well as the addition of concrete jacket on columns 1 and 2. Moreover, it is worth noting that there is an absence of AE activity during a displacement hold at relative high force level between 5000-5800 sec, implying no creep effects during that period.

Finally, it is worth noting that the energy scale for columns 3 and 4 in Fig. 6 is one order of magnitude lower than that for columns 1 and 2 in Fig. 5.

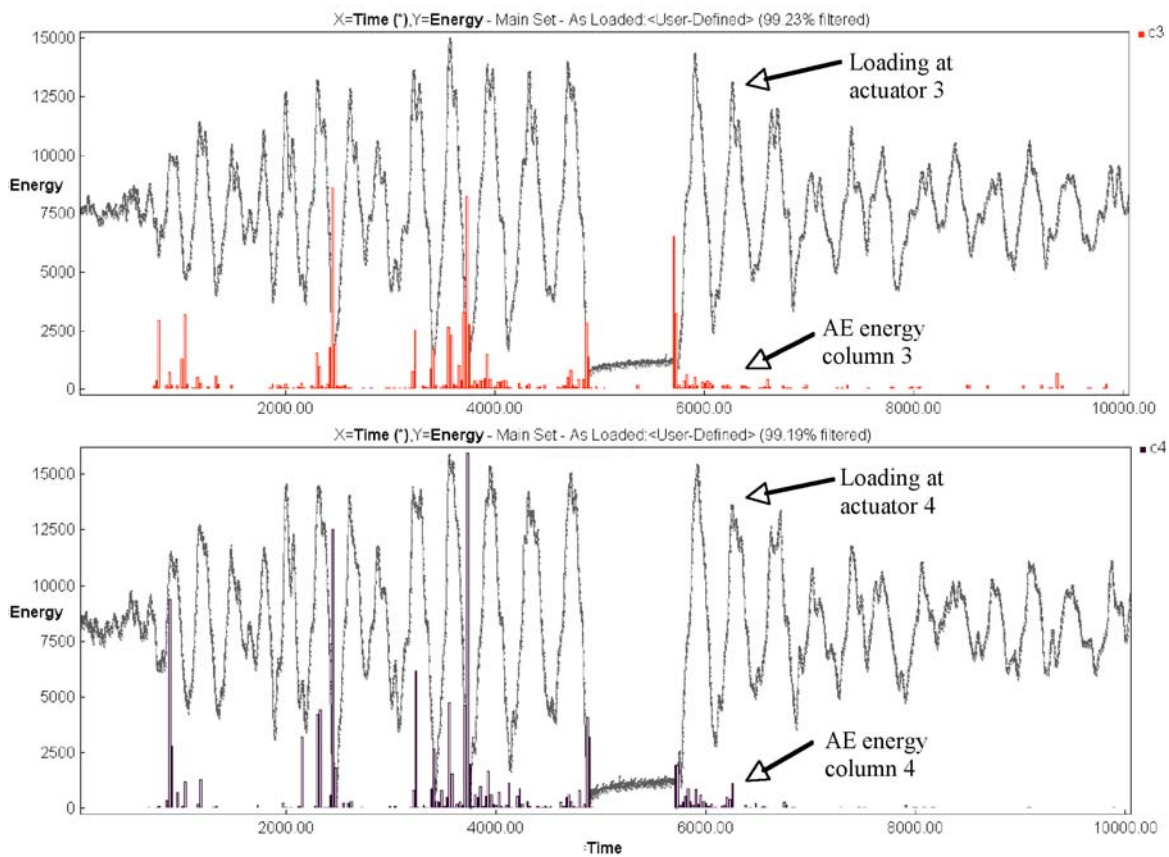


Fig. 6. Applied load at actuators 3 & 4 (background plot) and AE energy from stiff columns 3 (channels 17-24) and 4 (channels 25-32), respectively.

Source Location and Correlation with Visual Inspection

During the entire test high AE data rates were recorded on most channels covering the structure, especially on the channels attached on flexible columns 1 & 2 after they had been externally reinforced by means of concrete jacketing. The use of various AE signal source-location algorithms provided the necessary focus of the analysis to locate the main areas where damage developed and to find areas with high likelihood of failure. A complex source-location strategy was employed with each column being treated as a separate entity to avoid signal time overlap and event mirroring. The basic source location algorithms used to locate damage was the Linear X-Y and Linear 3D modes in Noesis AE Data Analysis software (Envirocoustics SA, 2005). Typical location results for column 1 are presented in Fig. 7. The height of column 1 is represented on the horizontal axis of the plot, starting from sensor #8 (0 m column bottom) up to sensor #1 (3 m, top area of column) and sensors #3 and #4 projected also on the x-axis.

The linear location strategies showed the areas sustaining damage during the test. This damage is attributed to cracks and hairline cracks or crack face friction in the columns and the reinforcing jacket. The two un-strengthened columns (columns 3 and 4) showed little located AE activity compared to the other two columns. Any activity was mainly from the joint at the first floor and more specifically in the area of beam-column-slab joint at the floor slab. Some activity was also recorded from the lower section of the columns. Columns 1 and 2 that had sustained damage during the initial earthquake record of 0.3 g and had been reinforced with concrete jackets produced significantly more AE activity, which corresponded to more clearly visible hairline cracking on the jacket itself. This is attributed to the eventual slippage between the initial

concrete and the jacket. Visual inspection did not yield any information about damage to the inner column. In this case also, the located activity was concentrated to the lower section of the joint and immediately below the joint of the 1st floor. This is clearly shown in Fig. 8 of Column 1, where the concentration of activity is immediately below the node is the most significant of any column in this test.

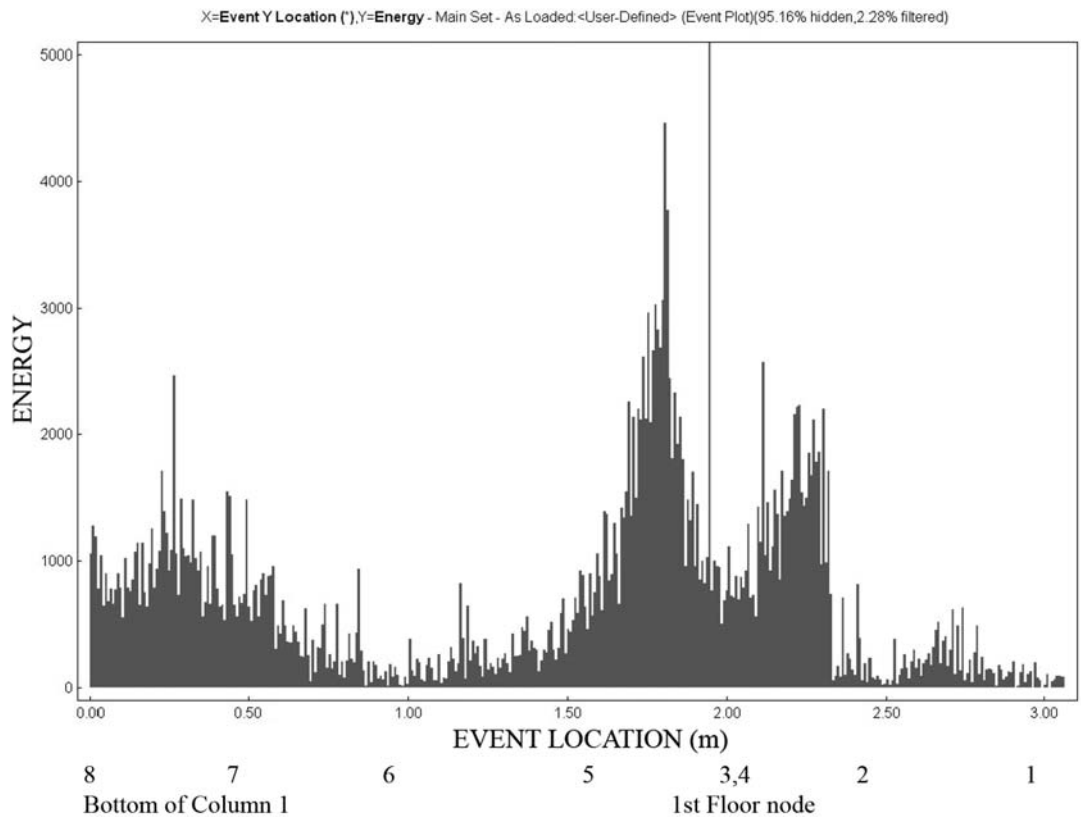


Fig. 7. AE energy for column 1 with respect to sensor location along column height.

This concentration of activity shows the areas that are actually subjected to damage during the test. It is generally estimated that any failure during the re-positioning of the structure to a higher deformation state will occur in these areas first. Visual inspection and correlation of visible cracks with AE located activity was not always possible during the test, since it was found by closer inspection later and the present data analysis that cracking, which was invisible to naked eye produced significant AE. Although no cracks of significant width were observed, either on the retrofitted or the un-retrofitted columns, the amount of AE recorded distinguishes these areas as subject to further damage. The success of AE to individualize, at an early stage, the specific areas, at which medium damage is manifested and most likely enhanced at higher drifts, was demonstrated in subsequent tests to 0.45 g and 0.55 g. These tests (not reported in this work) produced a level of damage sufficient to visually confirm the existence of concrete cracking and reinforcement slippage. Significant damage at the joint at the top of Column 1 mentioned above was observed and in other areas where AE had given early warning. More specifically, increased AE activity recorded from both the node and the base of column 2. Compared with the activity and events identified on column 1, the activity at the node of column 2 was lower while that at the base (channel 16) was higher.

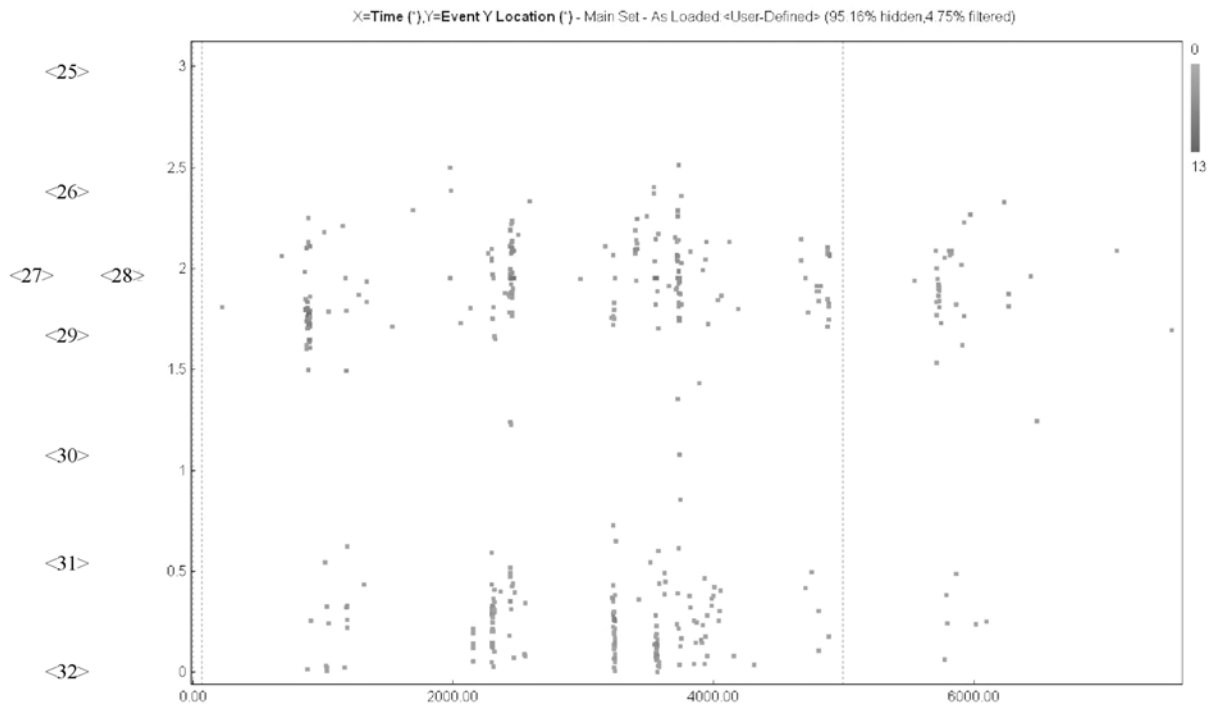


Fig. 8. Event density plot with respect to column height (sensor numbers on the left), x-axis represents time and density represents events concentration (scale 0 to 13 events).

Concerning the activity from the joints of columns 3 and 4, AE events of similar level, indicating the onset of emission, were recorded from both columns. For example, the events located on column 4 versus time are presented in Fig. 8. More specifically the AE activity is displayed for the full height of the column (y-axis, with sensor number) versus time (horizontal axis). For example, at approximately 800 sec, there is some activity located at joint (sensors #27, #28, #29). On the other hand, the base of column 4 (channels #31 and #32) emitted more signals resulting in well-defined sources. Figure 8, in conjunction with Fig. 6, provides important information about the behavior of column 4 and its correspondence to the level of structural deformation and time parameters. The successful correlation of located events, both in time and position, with the hairline cracks observed, is worth noting.

Discussion and Conclusions

A series of full-scale tests on retrofitted or un-reinforced concrete structures were performed, during which acoustic emission was monitored. The retrofitted columns of the building tested showed minor cracking on the reinforced concrete jacket with some damage developing at the base of the ground floor and the joints of the structure. Throughout the test, AE monitoring identified activity at the bottom of ground floor columns and the joints of the ground-floor beam-column intersection, thus, indicating the most damage prone areas. This was evident by the increased overall AE activity in these areas and significant activity concentration.

Results during subsequent loading tests under 0.40 g and 0.45 g seismic events (not reported here) proved that the AE method identified correctly the areas of damage as these were the exact locations where failure occurred (large cracks, concrete spalling and slippage of reinforcement).

Based on conventional analysis, AE data signatures from crack and reinforcement slippage cannot be easily separated. Future work utilizing displacement measurements at the various positions around the structure for correlation with AE activity versus time and position as well as unsupervised pattern recognition for the treatment of AE data, can provide further insight to the damage mechanisms (crack propagation, reinforcement slippage etc) and possibly yield quantitative damage growth assessment in similar structures and repair techniques.

Acknowledgments

The work reported in this paper was funded by the Greek General Secretariat for Research and Technology, through the project ARISTION (ARISTION, 2006) within the framework of the program “Built Environment and Management of Seismic Risk”.

References

Anastasopoulos, A., Bousias, S.N., Tsimogiannis, A., Toutountzakis, T., “Acoustic emission testing of concrete frame during pseudodynamic loading”, *27th European Conference on Acoustic Emission Testing*, Cardiff, Sept. 2006.

DiSP User’s Manual Rev 1 & AEWin User’s Manual Rev. 2, Physical Acoustics Corp, Sept 2001.

Bousias, S. N, Fardis, M.N., Spathis, L.-A. and Kosmopoulos, A. “Pseudodynamic response of torsionally unbalanced 2-story test structure”, *J. of Earthquake Engng Struct. Dyn.* **36**:1065–1087, 2007.

Bousias, S.N., Spathis, A-L, Fardis, M.N., Papanicolaou, C.C., and Triantafillou, T.C. "Pseudodynamic Tests of Non-Seismically Designed RC Structures Retrofitted with Textile-Reinforced Mortar", *8th International Symposium on Fiber Reinforced Polymer Reinforcement for Concrete Structures (FRPRCS-8)*, Patras, July 2007.

Bousias, S.N., Spathis, A-L, and Fardis, M.N. "Experimental Seismic Response of Eccentric RC Structures, before or after CFRP-Rehabilitation", *8th International Symposium on Fiber Reinforced Polymer Reinforcement for Concrete Structures (FRPRCS-8)*, Patras, July 2007.

Matsuyama K., Fujiyama T., Ishibashi A. and Ohtsu M., (1993), “Field Application of Acoustic Emission for the Diagnosis of Structural Deterioration of Concrete”, *J. of Acoustic Emission*, **11**(4), 65-73.

NOESIS Ver. 4.1 (2005) - Reference Manual, Envirocoustics S.A.
www.aristion.gr (2006).

Yuyama S., Okamoto T., Shigeishi M., Ohtsu M. and Kishi T., (1999), “A proposed standard for evaluating structural integrity of reinforced concrete beams by acoustic emission”, *ASTM STP 1353*, pp. 25-40.

ACOUSTIC EMISSION LEAK TESTING OF PIPES FOR PRESSURIZED GAS USING ACTIVE FIBER COMPOSITE ELEMENTS AS SENSORS

ANDREAS J. BRUNNER and MICHEL BARBEZAT

Empa, Swiss Federal Laboratories for Materials Testing and Research,
Laboratory for Mechanical Systems Engineering,
Überlandstrasse 129, CH-8600 Dübendorf, Switzerland

Abstract

In order to explore potential acoustic emission (AE) applications for piezoelectric active-fiber-composite (AFC) sensor elements made from piezoelectric fibers, a model experiment for leak testing on pipe segments has been designed. A pipe segment made of aluminum with a diameter of 50 mm has been operated with compressed air (gaseous medium) for a range of operating pressures (between 400 and 800 kPa). Leaks have been simulated by use of screws with holes of various diameters (between 0.1 to 1.2 mm). One AFC sensor has been mounted directly on the pipe surface, complemented by two conventional AE sensors mounted on waveguides. AE signal parameters and waveforms were recorded at different pressures with and without simulated leaks. The experiments to date show distinct differences in the power spectra obtained from fast Fourier transform of the AE waveforms depending on whether a leak is present or not.

Keywords: Leak testing, pressurized pipe, gaseous media, active-fiber-composite sensors, comparative analysis

1. Introduction

Leak testing can be performed with various non-destructive test methods, among them acoustic emission (AE), on both, pressure vessels [1-4] and pipes or pipelines [5]. Leak testing with AE can be performed to indicate the presence of leaks and/or to locate the leak position, as well [6]. The references indicate that AE leak testing can be performed on pressure vessels made from metal [2, 3] or composites [4], containing either gaseous [2] or liquid media [3].

Based on a model experiment for detecting the presence of a leak in a pipe segment pressurized with fluid (water) and gaseous media (compressed air) using conventional AE sensors [7], the present contribution investigates the feasibility of performing leak testing with piezoelectric active-fiber-composite (AFC) elements instead of AE sensors. AFC are made with commercially available piezoelectric fibers that are embedded in an epoxy matrix and sandwiched between interdigitated electrodes. Originally developed as anisotropic piezoelectric actuators [8], AFC elements can also be used as piezoelectric sensors. The tests are monitored with the same AE sensors as in the previous experiment [7] for comparison. AFC sensors are thin, planar elements and offer an advantage compared with conventional AE sensors since they are conformable to curved surfaces [9]. Mounting AFC sensors on pipes or pressure vessels does hence not require the use of waveguides, simultaneously reducing time required for mounting and attenuation.

2. Experimental

The model pipe system for the laboratory tests was similar to that reported in [7], i.e. using an aluminum pipe segment, but with a length of 60 cm and a diameter of 50 mm, with a wall thickness of 2 mm (Fig. 1). Leaks were simulated by inserting screws with a hole into a bore-hole in the wall of the pipe segment, located at about one quarter length (Fig. 2). The diameters of the holes in the screws comprised about 0.1, 0.2, 0.35, 0.50, 0.80 and 1.2 mm (Fig. 3). The holes were manufactured by conventional drilling, except for diameters of 0.1 and 0.2 mm, which were made by laser drilling. For the screws with hole diameters below 0.5 mm, the nominal diameter extended about 1 mm into the screw, opening into a hole with a larger diameter (1-mm diameter for the 0.1- and 0.2-mm leaks, 2 mm for the other leaks). The pipe segment was then equipped with fittings connected to the supply of the medium (pressurized air). Pressure in the pipe segment was read off a pressure gauge and noted for each test. The flow of the medium was not recorded and the pressure adjusted by the outlet valve mounted between pressure gauge and supply pipe. The pipe segment was put on wooden supports for the tests.



Fig. 1: Overview of the laboratory-scale model system for AE leak monitoring with conventional AE sensors and AFC elements. The inlet valve is on the left, the T-joint on the right connects to the pressure gauge (not shown), the outlet valve is further to the right (not shown).

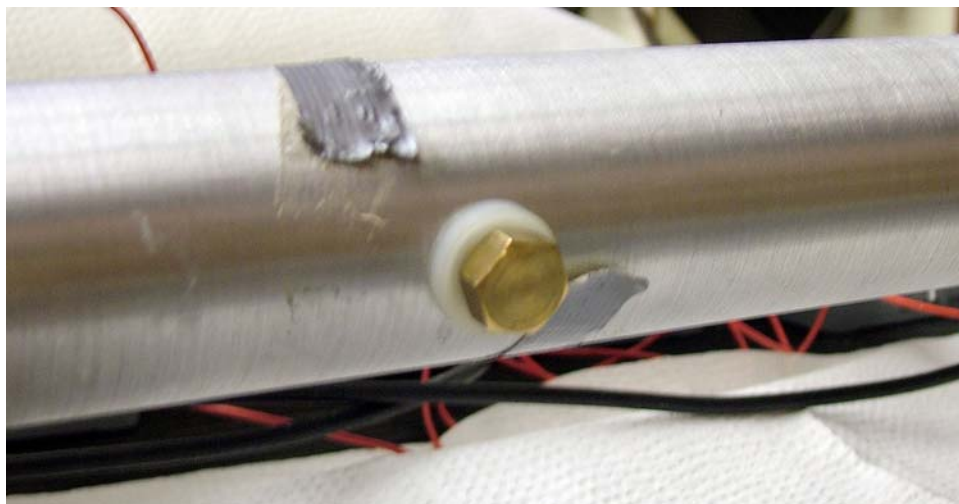


Fig. 2: Simulated leak by inserting a screw with a hole of a specified diameter into a bore-hole at one-quarter length of the aluminum pipe segment; screw-insert without hole for reference shown.

AE data have been recorded with three channels using a system with transient recording capability (type AMS-3 from Vallen Systeme GmbH). One channel was used with the AFC sensor, the others with conventional AE sensors (type SE45-H from Dunegan Engineering Corp). Thresholds were set at $50 \text{ dB}_{\text{AE}}$, preamplifier gain at 34 dB, the rearm time to 3.2 ms, and

frequency band-pass filtering between 30 and 1,000 kHz was used in the preamplifiers and the data acquisition channels. Beside the AE signal parameter set, AE waveforms were recorded (5 MHz sampling rate) with the same threshold. AE data were analyzed with the equipment specific software (VisualAE and VisualTR from Vallen Systeme GmbH). The AFC sensor was mounted directly on the surface of the pipe using a commercial, thermosetting two-component epoxy-based adhesive, while the AE sensors were mounted on waveguides using a silicone-free vacuum grease as coupling agent and duct tape for applying the contact pressure. The AFC sensor was electrically shielded by a self-adhesive aluminum foil, simultaneously connected to its ground wire and the electrical ground of the AE equipment (Fig. 4). The position of the AFC sensor was about one quarter from the outlet end of the pipe segment on the top position (12 o'clock) that of the first AE sensor in the bottom position (6 o'clock) shifted towards the leak by about 6 cm from the center of the AFC. The second AE sensor (9 o'clock) was mounted 180° opposite the bore-hole simulating the leak (3 o'clock) one quarter length from the inlet end of the pipe segment.



Fig. 3: Screws with holes drilled for simulating leaks in the pipe segment model system. Leak diameters of 0.1 mm and 0.2 mm extend over a length of about 1 mm and then open into a diameter of 1 mm, larger leak diameters extend over a length between 2 and 5 mm.

The conventional AE sensors selected for this study and AFC elements do differ somewhat in their spectral sensitivity [9]. In addition, AFC elements show a higher sensitivity along the direction of the piezoelectric fibers than normal to it [10]. There are also indications that AFC elements may have a higher sensitivity to in-plane (shear) waves relative to that for out-of-plane waves than the conventional AE sensors. For the experiment, the AFC element was mounted with the fiber direction parallel to the axis of the pipe segment (compare Fig. 4, center).

Each leak diameter was tested for a range of pressures between about 400 and 800 kPa. The upper pressure was limited by the supply of compressed air available in the laboratory and showed some variation (typically about 20 to 30 kPa). Before recording AE signals and waveforms at a selected pressure corresponding to a setting of the outlet valve, the pressure was allowed to equilibrate for about one to two minutes. Nevertheless, for some tests, pressure variations during data acquisition were observed. This variation, however, was less than the pressure change between different tests. For each setting, data were recorded for about 5 to 10 seconds. Power spectra of selected AE waveforms within the frequency range between 0 and 400 kHz were visually compared for the two types of sensor for a given leak and pressure, as well as for increasing pressure for a given leak diameter and for increasing leak diameter at constant

pressure, respectively. This is analogous to an investigation reported for leaks with other geometry and size [11].

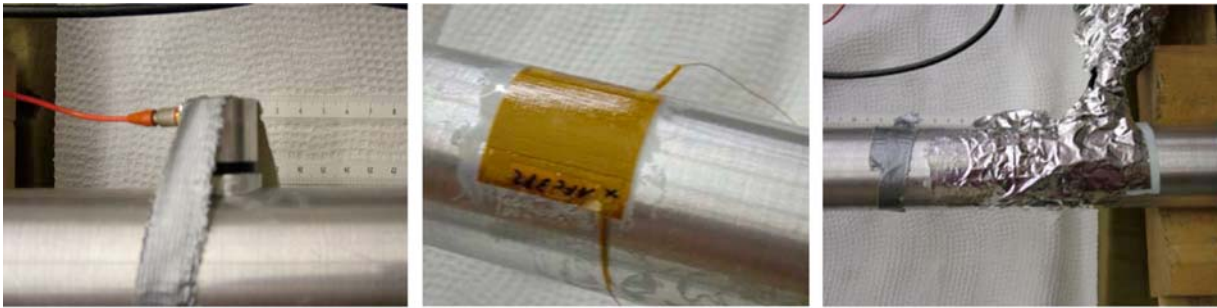


Fig. 4: AE sensor mounting on the pipe segment for leak testing; (left) conventional AE sensor on waveguide with duct tape for applying the contact pressure; (center) AFC element adhesively mounted with a commercial two-component adhesive; (right) AFC element after shielding with an adhesive aluminum foil.

3. Results

Figure 5 shows the power spectra for the pipe without a leak (screw without hole inserted into the bore-hole of the pipe) indicating frequency contributions between about 30 kHz (limit of high-pass filter) and about 150 kHz for both types of sensor, essentially independent of the pressure of the air (varied between about 400 and 800 kPa). As expected, the power spectra for AE sensors and AFC elements are somewhat different for comparable pressure values, and the dominant contributions appear at frequencies around 50 kHz. There are no contributions significantly exceeding the noise level at frequencies above about 160 kHz. For a pressure of 800 kPa both sensors (AE and AFC) show a distinct peak with comparable amplitude just above 150 kHz (note the difference in scale of the graphs for the AE and AFC sensors).

Figure 6 shows power spectra for one leak diameter (0.35 mm) at different pressures between about 400 and 800 kPa. Compared with the spectra shown in Fig. 5, there are clear contributions at frequencies above 150 kHz for all pressures that have been tested. These can be observed for both types of sensor (AE and AFC element). It can be noted that a noticeable contribution to the power spectra above about 160 kHz appears for the chosen leak diameter of 0.35 mm at about 165 kHz. This contribution can be noted in the power spectra of both types of sensors (AE and AFC element). A further contribution appears at a frequency around 275 kHz for the AE sensors and between about 280 and 300 kHz for the AFC element. The latter also shows indications of another contribution at about 375 kHz. Indications of that are also observed for the AE sensor, but are less apparent in the graphs because of the difference in scale. Further, the intensity (amplitude relative to maximum peak in power spectrum) of these contributions is changing with the pressure of the medium (compressed air). Compared with the peak contribution between about 30 and 100 kHz, the peaks at frequencies above 160 kHz are increasing with increasing pressure. This increase is more pronounced for the AE sensor than for the AFC element.

Figure 7 shows power spectra for selected leak diameters at a constant pressure of about 600 kPa. The graphs in Fig. 7 can be complemented with the center part of Fig. 6 showing the power spectra for a leak diameter of 0.35 mm at a pressure of 600 kPa. Compared with the spectra shown in Fig. 5, there are again clear contributions at frequencies above 160 kHz. These can be observed for both types of sensor (AE and AFC element). Contrary to the case of constant leak

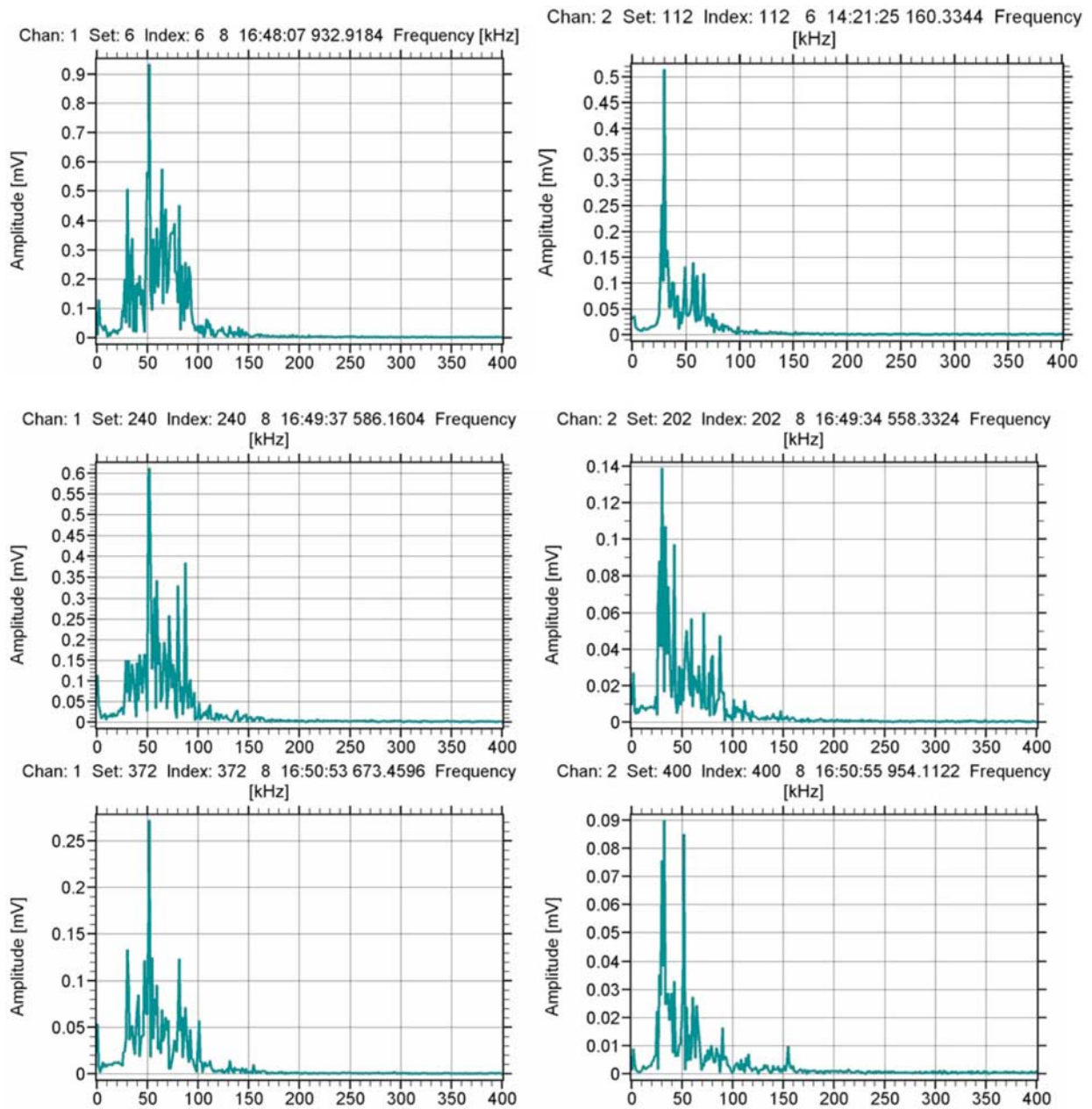


Fig. 5: Power spectra (0 to 400 kHz) from fast Fourier transform of selected AE waveforms recorded with the AE sensor (left) and with the AFC element (right) for the pipe segment pressurized without simulated leak. The pressure is increasing from about 400 kPa (top) to 600 kPa (middle) and 800 kPa (bottom). Note the difference in amplitude for the different sensors and graphs.

diameter tested with different pressures, the frequencies are now changing with leak diameter (if tested at constant pressure of about 600 kPa). For a leak diameter of 0.2 mm, a small, but distinct contribution occurs at about 195 kHz (observed with both sensors), complemented by a weak contribution around about 330 kHz. For the leaks with diameters of 0.35 and 0.5 mm the frequency contributions shift to about 165 and 275 to 280 kHz, respectively, and an additional contribution around 370 kHz appears. For the leak with 0.8 mm the frequency contributions shift again to lower frequencies, namely 130 and 265 kHz. The AE sensor indicates additional

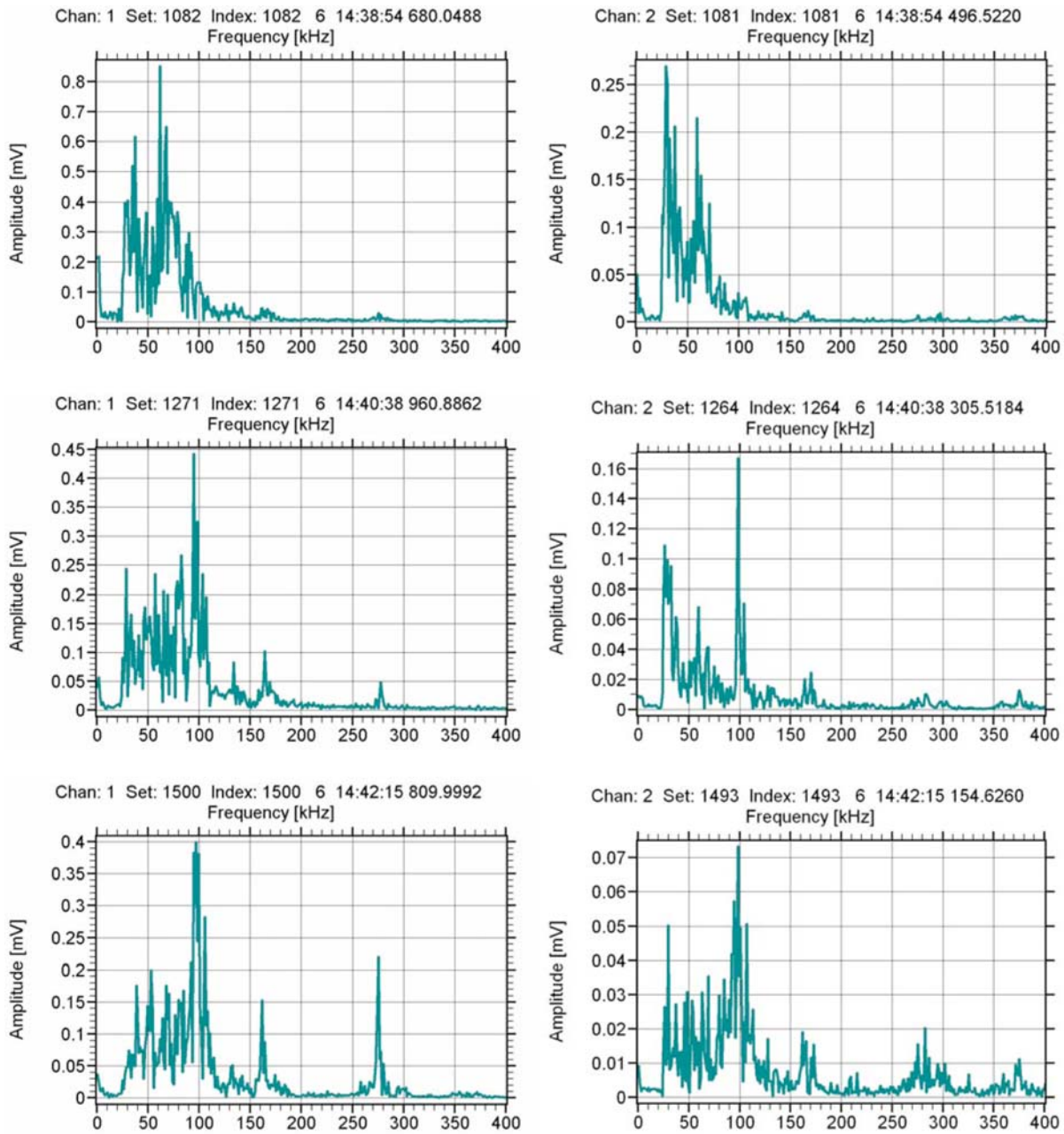


Fig. 6: Power spectra from fast Fourier transform of selected AE waveforms recorded with the AE sensor (left) and with the AFC element (right) for the pipe segment pressurized with a simulated leak (nominal diameter 0.35 mm). The pressure is increasing from about 400 kPa (top) to 600 kPa (middle) and to 800 kPa (bottom).

contributions centered around 265 and 340 to 350 kHz and the AFC sensor around 230 and 270 kHz, respectively.

4. Discussion

Independent of leak diameter (or more general, leak geometry) and operating pressure of the simulated pipe, leaks yielded additional contributions in the power spectra of recorded AE signals at frequencies above about 150 to 160 kHz for both types of AE sensor. Of course, this

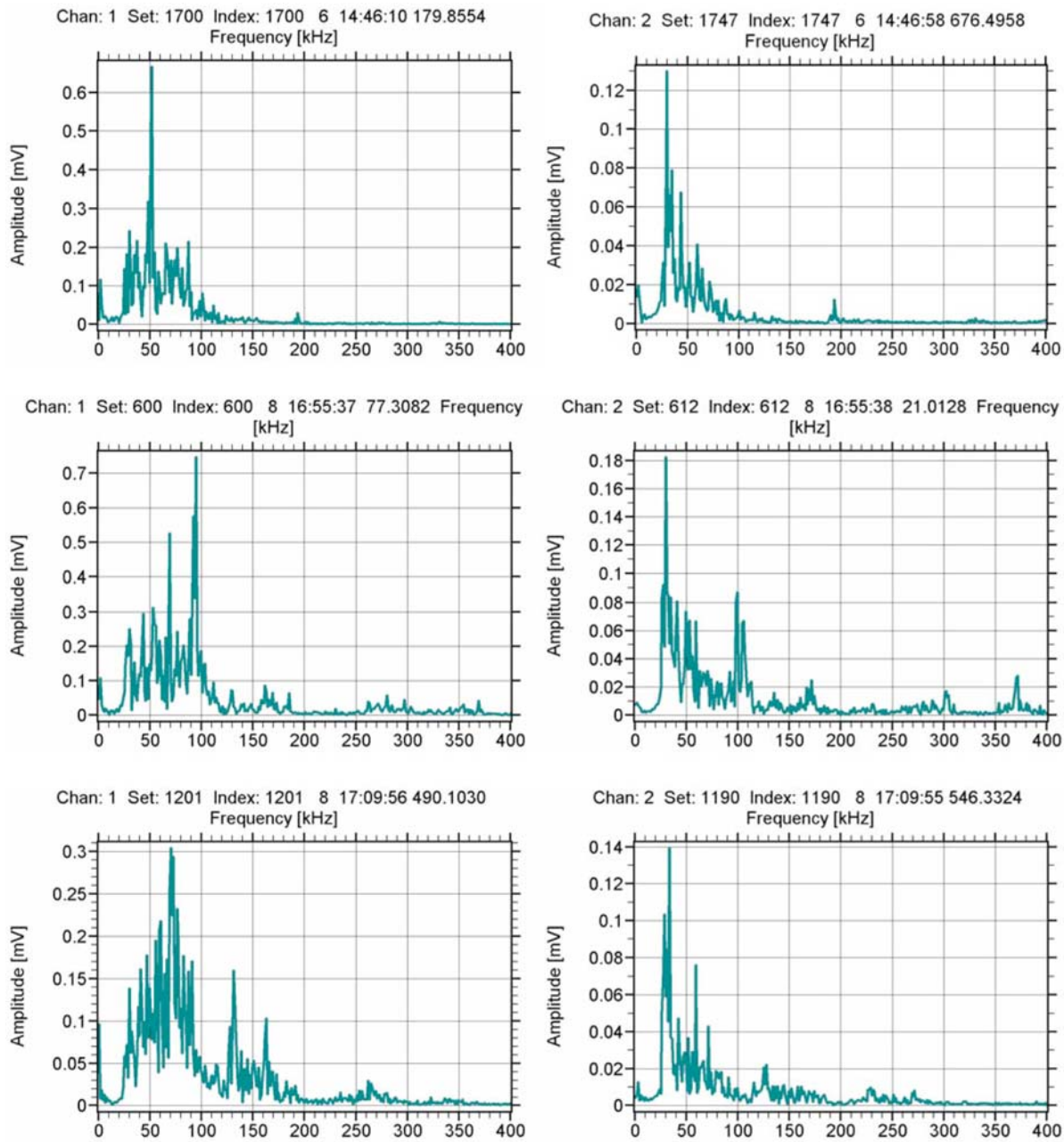


Fig. 7: Power spectra from fast Fourier transform of selected AE waveforms recorded with the AE sensor (left) and with the AFC element (right) for the pipe segment pressurized with a simulated leak at constant pressure of about 600 kPa. The leak diameter is increasing from about 0.2 mm (top) to 0.5 mm (middle) and to 0.8 mm (bottom).

statement holds for the range of leak diameters (0.1 to 1.2 mm) and pressures (about 400 to 800 kPa) that have been investigated to date.

A specific leak diameter (geometry) does seem to yield power spectra contributions at the same frequency, independent of the operating pressure. However, the intensity (amplitude) of the power spectra contributions indicating the leak is increasing with increasing pressure. At an intermediate, but roughly constant pressure (600 kPa) the power spectra contributions do seem to shift to lower frequencies with increasing leak diameter (geometry). These observations imply lower bounds for the size of leaks that can be detected within specific operating conditions. For

small leaks (below 0.1 mm diameter) the indication of the leak may not differ sufficiently from the noise in the power spectrum.

Based on the leak testing performed with gaseous and fluid media using conventional AE sensors on a similar system with the same type of leaks [7], it is expected that AFC elements would also yield indications of leaks, if the pipe were operated with a fluid medium (water) in a similar pressure range. Since the pipe used in the previous experiments [7] was of a different diameter (60 mm instead of 50 mm) and shorter, it is expected that changes in the pipe geometry would not affect the results significantly. Changing to pipes made of a different material has not been explored yet. Pipes made of another metal are expected to yield similar results, while for composite or polymeric pressure pipes, the pronounced frequency-dependent attenuation in the material may affect the sensitivity for leak detection. The dependence of the sensitivity on the distance between leak and sensor has not been investigated (fixed leak and sensor position in the tests reported here). Depending on the pipe material and the distance of the sensor from the leak, attenuation effects may also reduce the sensitivity. Noise interference from operating conditions or environment may further affect the sensitivity for leak detection.

As a last remark, it can be noted that the AFC elements permanently mounted on the pipe can also be used for other types of nondestructive testing or structural health monitoring; for example, electrical impedance measurements [12] by simply connecting the wires to another measurement system.

5. Conclusions

Experiments with a laboratory-scale model system for leak testing of pipes first indicates that piezoelectric active-fiber-composite (AFC) elements yield acoustic emission signatures (power spectra) comparable to those recorded with conventional AE sensors. Conformable AFC elements, however, can be mounted directly on pipes without the use of special waveguides. Simulated leaks yield additional frequency contributions mainly above about 160 kHz, while tests without leaks do not show significant contributions above this limit. Varying leak diameter at constant test pressure shifts the additional frequency contributions to lower frequencies, while varying the test pressure for constant leak diameter changes the intensity of the additional frequency contributions relative to the dominant peaks in the power spectrum at frequencies below 150 kHz. This indicates that there may be a lower limit of the leak diameter (size) that can reliably be detected.

Acknowledgment

The manufacturing of the model pipe system including the simulated leaks, its setup, as well as technical support during operation by Mr. K. Ruf is gratefully acknowledged.

References

[1] M.A. Goodman, R.K. Miller “Acoustic Leak Testing”, in R.K. Miller, E.v.K. Hill, P.O. Moore (Eds.), *Nondestructive Testing Handbook, Vol. 6 Acoustic Emission Testing*, 3rd ed., American Society for Nondestructive Testing, Columbus, 181-226, 2005.

- [2] ASTM Standard Test Method for Examination of Seamless, Gas-Filled, Pressure Vessels Using Acoustic Emission, E1419-02b, American Society for Testing and Materials International, Book of Standards, Vol. 03.03 (annual edition).
- [3] ASTM Standard Test Method for Examination of Liquid Filled Atmospheric and Low Pressure Metal Storage Tanks Using Acoustic Emission, E1930-02, American Society for Testing and Materials International, Book of Standards, Vol. 03.03 (annual edition).
- [4] ASTM Standard Test Method for Acoustic Emission Examination of Pressurized Containers Made of Fiberglass Reinforced Plastic with Balsa Wood Cores, E1888/E1888M-02, American Society for Testing and Materials International, Book of Standards, Vol. 03.03 (annual edition).
- [5] R.K. Miller, A.A. Pollock, D.J. Watts, J.M. Carlyle, A.N. Tafuri, J.J. Yezzi Jr. “A reference standard for the development of acoustic emission pipeline leak detection techniques”, *NDT&E International*, **32**(1), 1-8, 1999.
- [6] ASTM Standard Practice for Leak Detection and Location Using Surface-Mounted Acoustic Emission Sensors, E1211-02, American Society for Testing and Materials, International, Book of Standards Vol. 03.03 (annual edition).
- [7] A.J. Brunner, M. Barbezat “Acoustic Emission Monitoring of Leaks in Pipes for Transport of Liquid and Gaseous Media: A Model Experiment”, *Proceedings 27th European Conference on Acoustic Emission, Advanced Materials Research*, **13-14**, 351-356, 2006.
- [8] A.A. Bent, N.W. Hagood “Piezoelectric fibre composites with interdigitated electrodes”, *Journal of Intelligent Material Systems and Structures*, **8**(11), 903-919, 1997.
- [9] A.J. Brunner, M. Barbezat, P. Flüeler, Ch. Huber: “Composites from piezoelectric fibers as sensors and emitters for acoustic applications”, *Journal of Acoustic Emission*, **22**, 127-137, 2004.
- [10] M. Barbezat, A.J. Brunner, Ch. Huber, P. Flüeler: “Integrated Active Fiber Composite Elements: Characterisation for acoustic emission and acousto-ultrasonics”, *Journal of Intelligent Material Systems and Structures*, **18**(5), 515-525, 2007.
- [11] K. Yoshida, H. Kawano, Y. Akematsu, H. Nishino “Frequency Characteristic of Acoustic Emission Waveforms during Gas Leak”, *Proceedings 26th European Conference on Acoustic Emission Testing*, German Society for Nondestructive Testing, BB 90-CD, 321-327, 2004.
- [12] G. Park, H. Sohn, C.R. Farrar, D.J. Inman “Overview of Piezoelectric Impedance-based Health Monitoring and Path Forward” *The Shock and Vibration Digest*, **35**(6), 451-463, 2003.

ACOUSTIC EMISSION TECHNIQUE APPLIED FOR MONITORING AND INSPECTION OF CEMENTITIOUS STRUCTURES ENCAPSULATING ALUMINIUM

L. M. SPASOVA, M. I. OJOVAN and C. R. SCALES*

Immobilisation Science Laboratory, University of Sheffield, Sir Robert Hadfield Building, Mappin St., Sheffield, S1 3JD, UK; *Nexia Solutions, Sellafield, Cumbria, CA20 1PG, UK

Abstract

The acoustic emission (AE) technique and data analysis have been applied to detect and characterise the corrosion of aluminium and its impact on the mechanical stability of encapsulating cementitious systems. To that purpose laboratory scale samples prepared by ordinary Portland cement (OPC) and blast furnace slag (BFS)/OPC to mass ratio 7:3 with encapsulated aluminium rods were monitored for AE. The cumulative number of signals generated by piezoelectric broadband transducers attached to the samples and recorded by a computer-controlled AE system provided initial indication for the active corrosion process and damage development within the cementitious structures. Additional analysis based on the time domain parameters of the recorded AE signals (in relation to the visual and optical microscopy observations) was used to conclude on the potential AE sources active on micro and macro scale. According to their frequency characteristics the AE signals collected were divided into two main groups. The first group consisted of a large number of signals with two major frequency components distributed respectively below and above 100 kHz. The second group comprised of fewer resonance-like signals with a single frequency component at 34 kHz. Wavelet transformation was subsequently applied for frequency-time analysis. Calculation of the cross-correlation function in time domain was performed to assess the similarity of the acquired AE signals and therefore to conclude on the potential sources activity in time and space. The AE technique was shown as a potential tool for monitoring of the aluminium corrosion development associated with accumulation of structural damage within the encapsulating cementitious structures.

Keywords: Cementation of radioactive wastes, corrosion of aluminium

Introduction

Over a number of years in the UK, cementation of low and intermediate level radioactive waste (LLW and ILW) has been developed and carried out on an industrial scale resulting in the manufacturing of tens of thousands of containers with cemented radioactive wastes, e.g., cementitious monoliths termed wasteforms (Main UK Radioactive Waste Inventory Report, 2005). Composite cement-based formulations with partial replacement of ordinary Portland cement (OPC) by latent hydraulic materials such as blast furnace slag (BFS) or pozzolanic materials such as pulverised fuel ash (PFA) have been extensively used for encapsulation of liquid and solid ILW such as sludges, ion exchange resins and metallic debris (Ojovan and Lee, 2005; Sharp et al., 2003; Streatfield, 2001). The cemented wastes (wasteforms) have been sealed into 500-litre stainless steel containers (Generic Waste Package Specification, 2005; WSP/100, 2005) and placed in interim storage for a minimum of 50 years before final disposal.

The characteristics of the cementitious wasteforms such as setting time, temperature elevation during early stages of hydration, the presence of surface water as well as the mechanical

stability and tensile strength of the final hardened material have been studied for encapsulation of different waste streams (Streatfield, 2001). However, the mechanical behaviour of the cementitious wasteforms in tens and hundreds of years of storage before final disposal can be substantially affected by chemical and electro-chemical interactions between the waste and the immobilising matrix (Streatfield, 2001).

The corrosion of metallic ILW such as aluminium and magnesium-aluminium alloy, termed Magnox, encapsulated in composite cements is a well-known process that can cause damage of the wasteforms due to hydrogen gas generation and deposition of an expansive layer of corrosion products such as aluminium hydroxide and strätlingite or brucite (Setiadi, 2006; Setiadi et al., 2006). The main sources of metallic ILW in the UK are the decanning of the spent nuclear fuel elements and those already accumulated at nuclear sites as legacy radioactive waste aluminium. According to the latest Radioactive Waste Inventory Report (2005) in the UK there are ~8000 tonnes of Magnox and aluminium classified as ILW, and more than 23000 cementitious wasteforms containing radioactive Magnox produced by the encapsulation plants at Sellafield site. Given the scale of these figures the safe storage of the wasteforms with encapsulated metals and assessment of their acceptability for transportation and final disposal is an important issue for the nuclear industry. One of the solutions extensively researched to limit the corrosion of the encapsulated aluminium and Magnox is the application of alternative cement-based formulations such as calcium sulfoaluminate cements, condensed silica fume and sulphate resisting Portland cements (Streatfield, 2001; Zhou et al., 2006). However, non-intrusive methods such as AE applied for continuous monitoring and inspection of the cementitious wasteforms would be of significant benefit.

Advantages of the AE Technique to Monitor Cementitious Structures Immobilising Metallic Radioactive Wastes such as Aluminium

The AE technique has a number of advantages which make it a potentially suitable tool to monitor and inspect structures immobilising nuclear wastes. These are the high sensitivity of the AE technique not only to macro-scale damage but also to micromechanical events providing indication for structure degradation in progress (Ono, 2006; Pollock, 1989). AE testing is easy to implement *in-situ* and examine the overall volume of the structure with a network of sensors. In theory the monitoring can be established for an unlimited interval of time without a need for additional forces to be applied to the structures. Nevertheless, when used as an applied tool the AE technique requires good knowledge of the propagation properties of the medium associated with wave reflection, dispersion or absorption, the type of active sources, e.g., cracks formation and propagation due to compression or tensile loading, fatigue testing, corrosion development, the operational frequency range of the sensors used and the quality of their attachment to the examined structure. Moreover, under conditions of high temperature, aggressive solutions or radioactivity, specially designed sensors or waveguides are needed. All of these factors (determined by the experimental setup) lead to collection of AE signals with diversified parameters and development of relatively complex methods for AE sources location, orientation and differentiation such as moment tensor and wavelet (Grosse et al., 2004; Ohtsu, 2000). However, the AE technique has achieved a high level of capability and industrial approval in various applications with a large database of experimental setups on a wide range of materials, components and structures and procedures for data analysis (Ono, 2006; Pollock, 1989). The major distinct steps in the methodology applied for AE data analysis include (a) variation of the AE signals rate in relation to the alteration of the experimental conditions, e.g., level of loading, (b) change of the AE signal

parameters in time domain and (c) more advanced and computational resources demanding signal processing.

Although used for many years on a large range of materials and structures, the application of the AE technique in the field of nuclear waste management is not fully explored and very limited. Apart from our previous work (Spasova and Ojovan, 2007; Spasova, Ojovan and Scales, 2006a; Spasova and Ojovan, 2006b) only Belov and Aloy (2004) reported on the potential of the AE technique to be applied as a tool for quality control during fabrication of glass and ceramic used for immobilisation of nuclear wastes. Therefore, the AE technique applied for monitoring and inspection of radioactive wastefoms is a new area with a potential for future development and implementation.

AE Technique Applied for Cementitious Structures

AE testing and monitoring of cement-based structures for civil engineering applications has been one of the main driving forces for the development and industrial implementation of the AE technique. For different cement-based materials, the threshold levels used to determine separate phases in the mechanical performance of the cementitious structures under compression or tensile loading have been defined based on strain-stress, load-displacement or load-time curves combined with AE detection and analysis and visual or optical microscopy observations. The physical mechanisms such as microcrack initiation and propagation, formation of a fracture process zone (FPZ), macrocrack nucleation and subsequent growth in relation to the size and shape of the FPZ have been associated with the parameters of the recorded AE signals (Landis and Ballon, 2002; Landis, 1999; Yoon et al., 2003).

A significant contribution to understanding the mechanism of failure of concrete due to the expansive corrosion process of metallic reinforcement has been performed by Uddin et al. (2006). Based on boundary element method (BEM) and SiGMA code (Ohtsu, 2000) using the arrival time and the amplitude of first motion of the recorded AE signal waveforms, the crack type, orientation and location in concrete samples were determined and illustrated in 3D space. According to Uddin et al. (2006) diagonal visible cracks initiated by uniform distributed pressure around the reinforcement due to the expansive corrosion process are most likely to be formed within the concrete structures. In terms of AE, the damage initiation and propagation in the examined concrete samples corresponded to an abrupt increase in the number of the detected AE signals at peak load caused by a number of tensile, shear and mixed-mode cracks (Uddin et al., 2006).

However, when cementitious structures are monitored for AE, it is important to consider that the cement clinker composition, water-to-cement mass ratio, aggregate size and geometry of the prepared samples, the operational range(s) of frequencies of the sensors and their coupling and location can substantially affect the time and frequency domain characteristics of the acquired signals. Moreover, experiments revealed that in the highly damping medium of concrete, mortar and cement paste the ultrasonic pulse attenuation and velocity are frequency dependent (Philipidis and Aggelis, 2005) and the attenuation increases exponentially with increase of the distance from the source (Tarmaratnam and Tan, 1990).

This paper is part of a series of experimental studies (Spasova and Ojovan, 2007; Spasova, Ojovan and Scales, 2006a; Spasova and Ojovan, 2006b) on cement-based samples with encapsulated aluminium aiming to assess the feasibility of the AE technique to be applied for cementi-

tious structures with encapsulated ILW. In the present paper, the established methodology from Spasova and Ojovan (2006b) is used to analyse and compare the collected AE data from a BFS/OPC sample with encapsulated aluminium and those from a reference OPC and to relate the conclusions drawn for the mechanical changes within the structures during the conducted AE monitoring with the findings of the post-test visual and optical microscopy observations.

Experimental Setup

Preparation of the specimens

The AE monitoring was carried out on cement-based samples with encapsulated high-purity (99.999%) aluminium rods. Two types of specimens were prepared. The first type was a pure OPC unit with encapsulated aluminium used as a reference. The second was a composite cement sample with 70 wt% BFS replacement of OPC (BFS/OPC to mass ratio 7:3) used as a lower limit in the composition envelope for nuclear waste encapsulation applied by Sellafield Ltd. The OPC and BFS were supplied respectively by Castle Cement and Redcar Steel Works, UK.

For the preparation of the laboratory scale units the cement powder and water to mass ratio 0.33 were mixed and then poured in 340 mL capacity plastic containers. An aluminium rod with a length ~48 mm and 10 mm diameter (Fig. 1a) was centrally placed in the cement grout before closure of the plastic containers with airtight lids. Cylindrical cementitious samples were formed as shown in Fig. 1b. The specimens were cured at 20°C and 95% relative humidity (RH) in an environmental chamber for more than 180 days. Before the commencement of the AE monitoring 50 mL of distilled water was poured in the plastic containers. The latter was done in order to capture the AE, generated from the cement structures in excess of water. This is a major concern for the safe storage of the cementitious wastefoms in a long period of time (Ojovan and Lee, 2005).

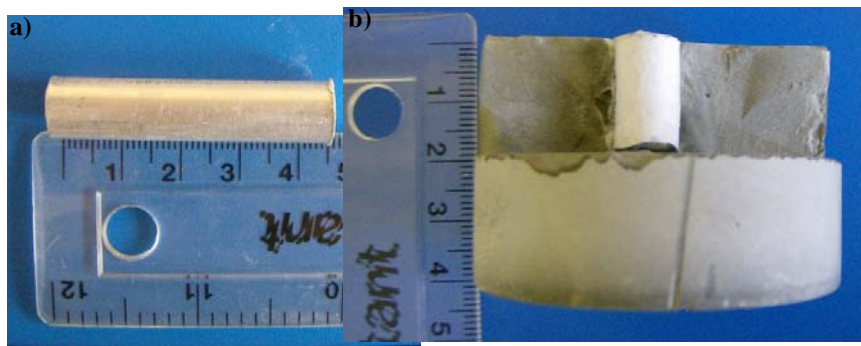


Fig. 1. Aluminium rod as is (a) and after being encapsulated for 90-days in an OPC matrix (b).

AE monitoring and data collection

A schematic diagram of the AE experimental setup used in this study is shown in Fig. 2. A piezoelectric transducer (or sensor) with a diameter of 18 mm and a height of 12 mm in stainless steel casing was attached to the bottom of the plastic container, containing the cement-based sample via a thin layer of grease used as acoustic couplant. Wideband transducers (type WD), calibrated and supplied by Physical Acoustics Corporation (PAC), with broad-band response between 100 and 1000 kHz were used to detect AE from both cement-based samples with encapsulated aluminium. The electrical signals from each of the transducers were amplified by a low-noise preamplifier type 2/4/6/ from PAC set at 40 dB and passed through a bandpass filter operating between 20 kHz and 3 MHz. Each of the analog signals (voltage) then was measured and if

above the threshold level of 40 dB was digitized by an 18-bit analog-to-digital converter (ADC) with 5 MSPS sampling rate.

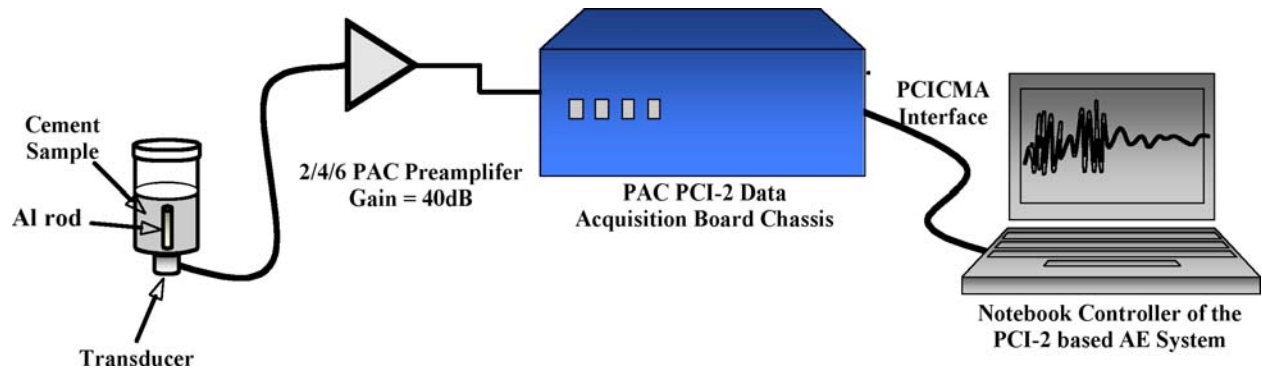


Fig. 2. AE experimental setup for monitoring of the cementitious wasteform samples with encapsulated aluminium.

A hit-driven data acquisition process with a PCI-2 based AE system, calibrated and supplied by PAC, was used. When an acoustic wave was detected by the transducer attached to the sample and its amplitude exceeded the threshold the data streaming was allowed. The data recorded on a conventional PC hard drive in an ASCII file for each detected and measured AE signal (or hit) consisted of a set of parameters such as duration, amplitude, counts, rise time and absolute (ABS) energy. These were used for post-test analysis. The definition of each of those signal parameters in time domain, denoted in Fig. 3, according to ASTM 1316 standard (1989), are given by PAC as follows:

- Duration: the time interval between the first and the last crossing of the threshold level for the AE signal;
- Amplitude: the largest voltage peak in the AE signal waveform given in dB or V. The amplitude for the PCI-2 based AE system covers the range 0-100 dB (0 dB corresponds to 1 μ V at the sensor output and 100 dB to 10 V); The conversion of AE signal amplitude from mV to dB is done using the equation:

$$A_{dB} = 20 \log_{10} \left(\frac{V_{\max}}{V_{\min}} \right) - P \quad (1)$$

where P is preamplifier gain given in dB, V_{\max} and V_{\min} are the amplitude of the AE wave given as positive voltage (in V) and minimum voltage measured by the AE acquisition system (1 μ V for the AE-based system used in this study).

- Counts, N_{counts} : the number of AE signal excursions over the threshold;
- Rise time: the time between the first threshold crossing and the amplitude of the signal measured in μ s;
- Absolute (ABS) energy, E_{ABS} : quantitative measurement of the energy of the AE hit derived as an integral of the squared voltage signal divided by a reference resistance (10 k Ω for the PCI-2 based AE system) over the duration of the AE waveform packet and measured in atto joules (10^{-18} J).

Moreover, the waveform of each AE hit (Fig. 3) was described by 3072 discrete points stored in the PC memory. The pre-trigger time, used to recover the acoustic waveform before the first threshold-level crossing was, set up at 100 μ s. Selective cross-plots such as amplitude versus duration and histograms, plotted by PAC AEWIn software package, provided real-time information for the AE activity from the samples under monitoring.

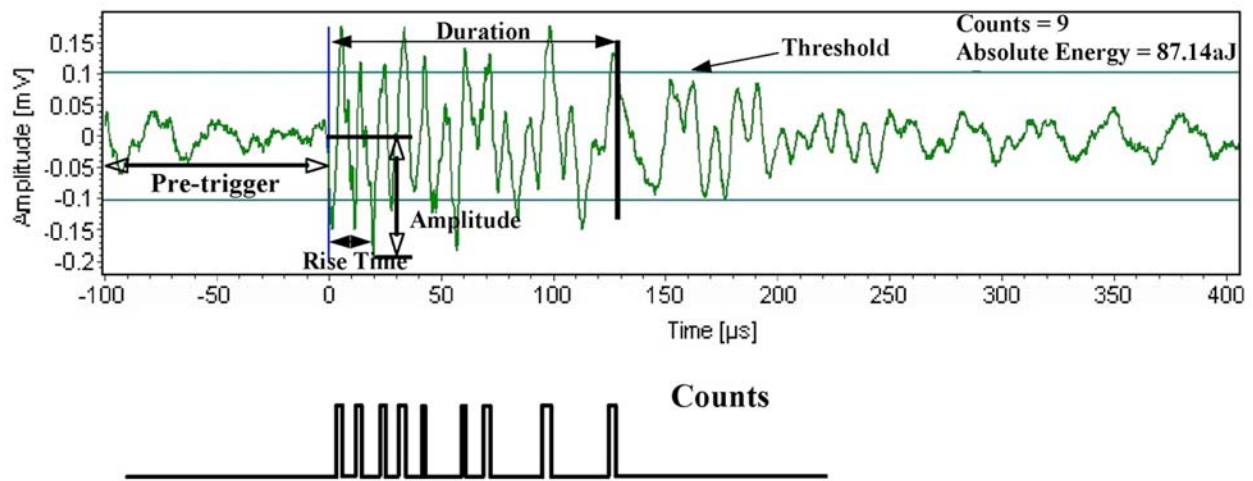


Fig. 3. Schematic of an AE signal and its associated parameters in time domain.

Results and Analysis

Relationship between the AE hit rate and the time domain parameters of the recorded signals from the cementitious samples and their potential sources due to corrosion of the encapsulated aluminium

During the conducted AE monitoring of the cementitious samples with encapsulated aluminium the cumulative AE hit number and associated ABS energy provided initial information (in real time) for micromechanical events within the structures associated with the generation and release of acoustic waves. As it can be seen in Fig. 4 there were several stages in the AE history of the experiments with discriminative rate (high or low) for both the OPC and BFS/OPC samples with encapsulated aluminium, which can be associated with several typical phenomena (Assouli et al., 2005; Landis and Ballon, 2002; Landis, 1999; Yoon et al., 2003; Uddin et al., 2006).

Firstly, the relatively long period of time of 16.5 and 92 hours for the OPC and composite cement specimens respectively was associated with a very low AE activity. The sources of this AE can be related to the process of water infiltration through the cement pores (Assouli et al., 2005) and the porous zone in the aluminium corrosion products layer formed at early stages of cement hydration (Setiadi, 2006; Setiadi et al., 2006). Subsequently as a result of the aluminium corrosion re-initiation, this AE can be generated and released due to the stable growth of the pre-existing microcracks, formed during the setting and curing of the cement samples due to hydro-gas evolution and accumulation of corrosion products (Setiadi, 2006; Setiadi et al., 2006).

After this first stage, a new period characterised by an abrupt increase in the number of the detected signals and their ABS energy was observed likely to indicate nucleation and propagation of critical size crack(s) within the structures corresponding to peak loading (Landis and Ballon, 2002; Landis, 1999; Yoon et al., 2003; Uddin et al., 2006). This period with a duration of only 3.5 hours for the OPC sample but around 50 hours for the composite cement has been followed by a time interval (2b in Fig. 4) where the AE hit rate considerably decreased in comparison with the previous period 2a in Fig. 4. Similar alteration in the AE hit rate were reported to correspond to post-peak loading associated with critical size crack growth in cement-based materials (Uddin et al., 2006; Landis and Ballon, 2002), debonding along the steel reinforcement in concrete (Yoon et al., 2003) or hydrogen gas release as a result of stainless steel corrosion development (Fregonese et al., 2001; Yonezu et al., 2006) associated with the detection of high

energy, i.e., high amplitude and long duration AE signals ultimately leading to decrease of the overall stress level within the structures.

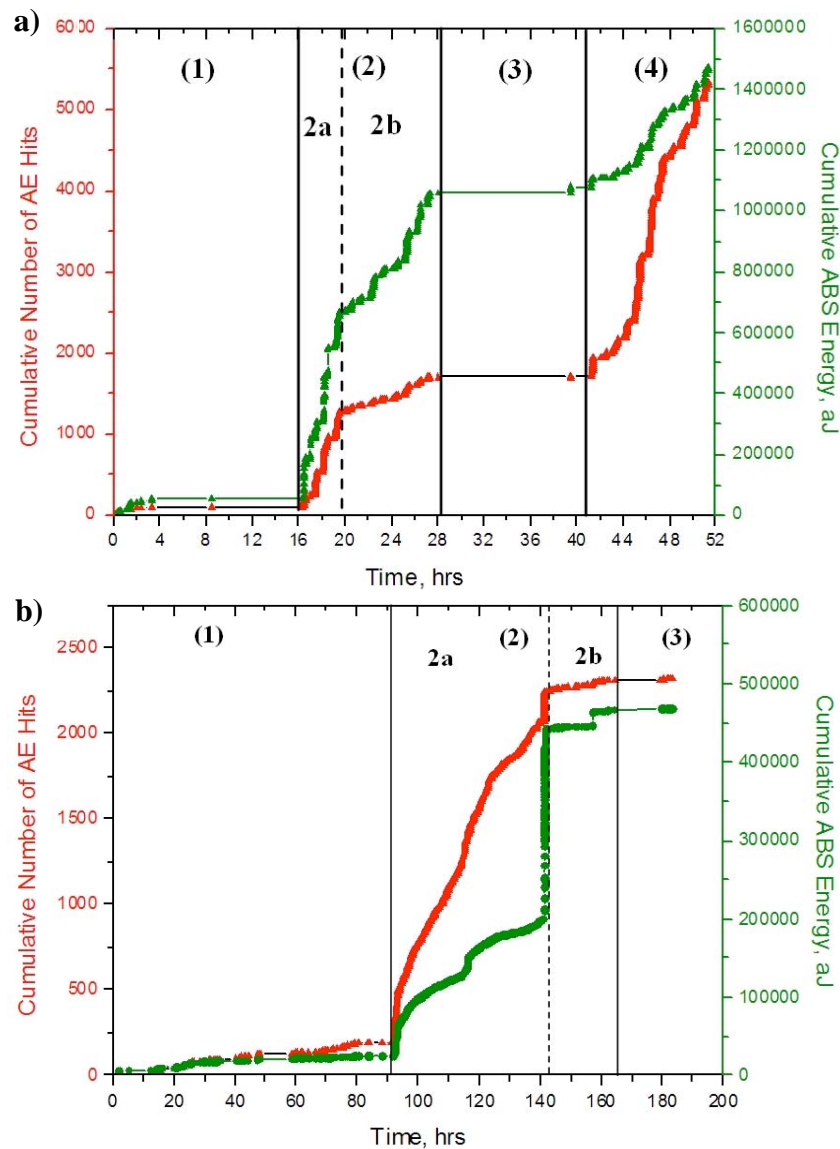


Fig. 4. Cumulative number of AE hits and associated ABS energy during the AE monitoring of (a) the OPC and (b) BFS/OPC samples with encapsulated aluminium.

Then a period of AE “silence” was observed for the OPC specimen followed by a new jump in the number of the detected hits during stage 4 in Fig. 4a. However, a period of AE “silence”, denoted in Fig. 4b as stage 3, was also found in the history of the conducted monitoring of the BFS/OPC sample with encapsulated aluminium.

A visual observation confirmed that visible radial cracks appeared on the surface of the samples, as shown in Figs. 5a and 5c. The latter were found also in the cross-section of the specimens (Figs. 5b and 5d) likely to be formed before the commencement of this AE monitoring for the OPC sample, but not expected to be formed within the BFS/OPC structure at that age of hydration (Setiadi, 2006). The initiation and/or propagation of these cracks were the very first potential source of AE identified during our test.

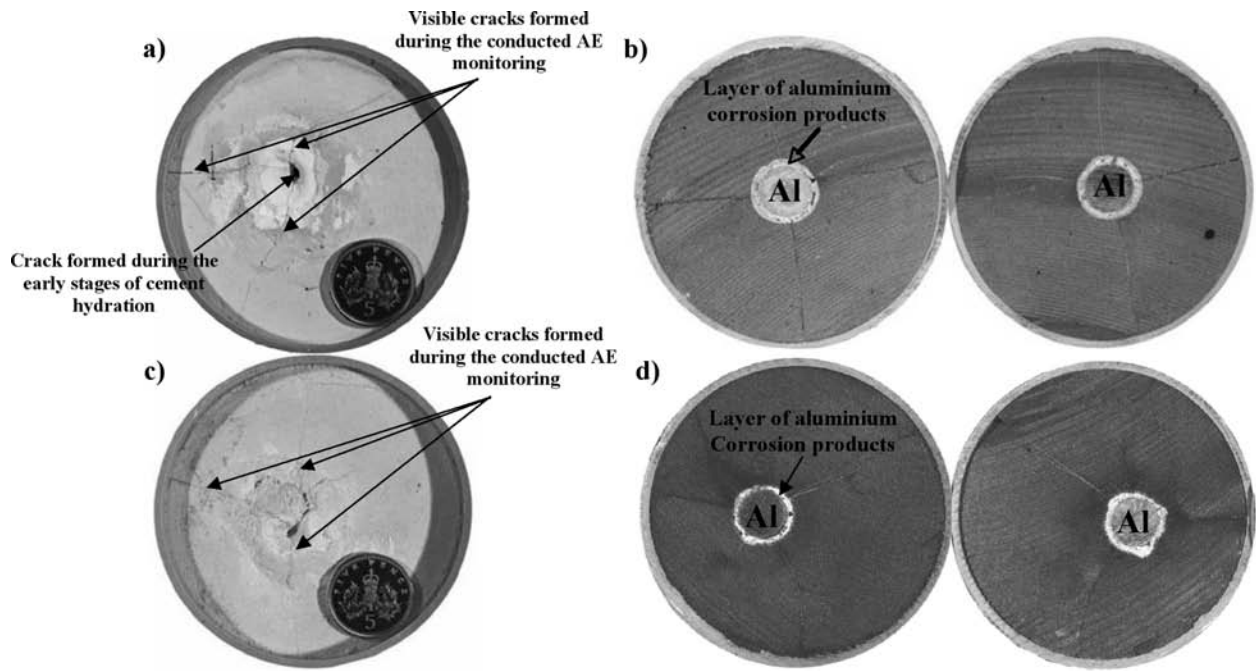


Fig. 5. Visible cracks formed at (a) and (c) surface and (b) and (d) cross-section of the OPC and BFS/OPC samples with encapsulated aluminium respectively.

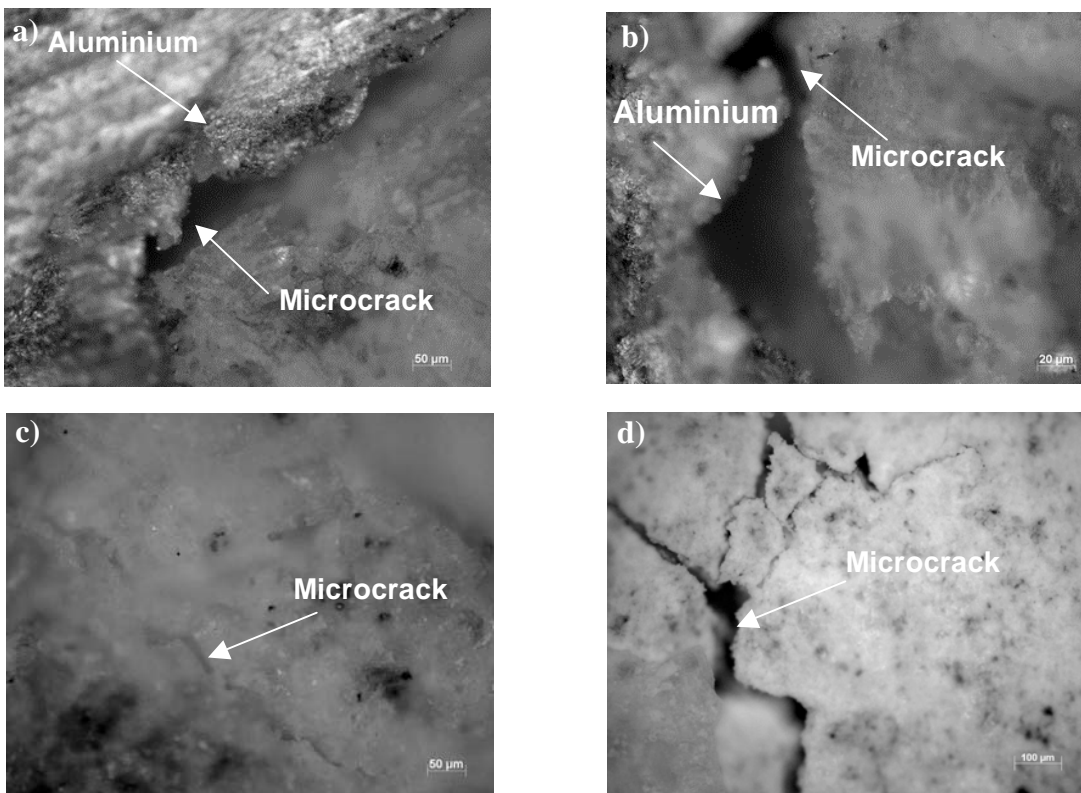


Fig. 6. Micrographs of (a) and (b) splitting cracks between the aluminium rod and the corrosion products layer and (c) and (d) microcracks within the aluminium corrosion products layer identified within the examined OPC and BFS/OPC samples.

An optical microscopy observation of the samples provided additional evidences for the formation of splitting microcracks between the aluminium rod and the corrosion products layer (Figs. 6a and 6b). These can be formed as a result of the increased compressive forces due to the hydrogen gas generation, friction and release. Moreover, the presence of microcracks within the corrosion products layer, as shown in Figs. 6c and 6d, indicated for another type of active AE sources within the cementitious structures.

In an attempt to differentiate collected signals from different sources in the cement-based structures with encapsulated aluminium the analysis was extended from AE hit time distribution, providing information for some kind of structural changes to the parameters of the detected signals. According to Pollock (1989) some of the most commonly used acoustic parameters for characterisation of the AE sources are amplitude, duration, counts and rise time. To the purpose of this study, we applied a selection procedure proposed by Wu et al. (2000) and also adopted elsewhere (Spasova, Ojovan and Scales, 2006a; Spasova and Ojovan, 2006b) to classify detected signals at each of the stages of the conducted monitoring based on their amplitude, duration and counts and associate their appearance with the mechanisms causing damage within the cement-based structures.

Table 1 summarises the results from the application of the selection procedure from Wu et al. (2000) on the parameters of the signals recorded for the BFS/OPC sample with encapsulated aluminium. Similar parameter-based AE study and differentiation of the signals based on their duration, amplitude, counts and average ABS energy ($E_{ABS,av}$), calculated as a ratio between the total number of AE hits (N_{hits}) and total ABS energy (E_{ABS}), for the OPC sample with encapsulated aluminium can be found in Spasova and Ojovan (2006b).

The data in Table 1 show that the AE activity during the stage 1 in Fig. 4b consists of a small number of signals with a relatively short duration (up to 200 μ s) and low amplitude (up to 48 dB) in a good agreement with the data reported for the OPC sample with encapsulated aluminium at stage 1 in Fig. 4a (Spasova, Ojovan and Scales, 2006a; Spasova and Ojovan, 2006b). This type of AE can be associated with distributed microcracking within the aluminium corrosion products layer (Fig. 6d) and the cement structure. The signals with a slightly higher amplitude and longer duration, detected in a most high population at the beginning of the second stage (period 2a in Figs. 4a and 4b) can be attributed to localised microcracking within the cement structure and the onset and/or activation of damage mechanisms such as debonding along the aluminium rod caused by the increase of the compressive forces at the aluminium/corrosion products layer and corrosion products layer/cement interfaces and hydrogen gas evolution. The most energetic signals detected in a high population for the OPC (Spasova and Ojovan, 2006b) and BFS/OPC samples during the second stage can be associated with the extension of the splitting cracks between the aluminium and the corrosion products layer (Figs. 6a and 6b) and the visible radial crack(s) formation within the cement structures (Figs. 5a and 5c). It is important to note that during each of those stages of the conducted monitoring there were signals which cannot be classified using the criteria of the procedure proposed by Wu et al. (2000). These events were less frequent and were characterised by a higher amplitude, average ABS energy ($E_{ABS,av}$) and a longer duration in comparison with the classified dominant populations of recorded signals (Table 1) and indicate for the presence of damage (observed at the end of the test) within the cementitious structures.

Table 1. Parameters of the signals recorded during the AE monitoring of the BFS/OPC sample with encapsulated aluminium.

Time Period	Hits Duration, [μ s]	Amplitude Peak, [dB]	Amplitude Range, [dB]	Max of Counts/Hits	Calculated Average Counts/Hits	N_{hits}	N_{counts}	% of Total N_{hits}	Total E_{ABS} , [aJ]	$E_{ABS,av}$, [aJ]
0 – 92 h (1)	0 - 50	41	40 - 42	1	1.25	92	115	3.95	4120	35.82
	51 - 200	43	40 - 48	4	3.92	88	345	3.78	11100	32.17
	201 - 1993	* Not determined	42 - 54	*10	*19.3	13	251	0.56	68700	5284.6
Total						193	711	8.29	83920	5353.59
92 – 142 h (2a)	0 - 20	41	40 - 46	1	1.14	740	841	31.79	28200	38.1
	21 - 80	42	40 - 46	2	2.07	590	1222	25.34	40900	69.32
	81 - 1000	43	40 - 55	4	4.76	634	3018	27.23	124000	195.98
	1001 - 10136	*Not determined	40 - 64	*Not determined	*91.55	92	8423	3.95	224000	2434.7
Total						2056	13504	88.31	417100	2738.1
142 – 168 h (2b)	0 - 20	41	40 - 45	1	1.13	22	25	0.95	917	41.68
	21 - 601	43	41 - 53	3	*5.6	43	241	1.84	24300	565.11
Total						65	266	2.79	25217	606.79
168 – 183.5 h (3)	0 - 20	40	40 - 42	1	1	8	8	0.34	235	29.37
	21 - 100	42	42 - 44	2	1.83	6	11	0.25	378	63
Total						14	19	0.59	613	92.37

* The criteria for identification of an internal mechanism initiated AE from Wu et al. (2000) are not satisfied

The presented results confirm that the parameter-based approach can provide a good AE description and differentiation of the mechanisms causing damage in the cementitious samples due to the corrosion of encapsulated aluminium. As there is a strong dependence of the measured acoustic parameters on the experimental setup (quality of the sensor coupling, location and orientation) a signal-based analysis was also applied additional results more independent from the experimental setup. To that purpose conventional fast Fourier transformation (FFT) and wavelet transformation (WT) were used.

Frequency characteristics of the main populations of AE signals recorded from the cementitious samples with encapsulated aluminium

The signal-based AE analysis includes advanced mathematical transforms to facilitate the identification of characteristic features of the generated acoustic signals. Conventional FFT (McGille and Cooper, 1984) is typically applied to determine the frequency spectra of the detected acoustic waves. The primary frequency, defined as the most energetic frequency component in the acoustic signal, has been used as a “fingerprint” of different AE sources in concrete structures under loading (Yoon et al., 2003) or corrosion of metals such as stainless steel (Yonezu et al., 2006). However, the FFT is of a fixed resolution at all frequencies and fails to detect small, high frequency events, which usually last for a very short interval of time (tens of μ s). These events can be characterised by WT analysis. WT is a relatively new signal processing technique applied for time-frequency analysis of AE signals. Since AE is not a stationary process, i.e., typically more than one wave mode is present within the signal, WT can be helpful to characterise the processes, causing AE, in the heterogeneous cement-based structures used in this study.

Continuous WT (CWT) is defined as a set of basic functions obtained by compression/dilation or shifting of a “mother wavelet”. CWT of a function $f(t)$ in time t is defined as (Ifeachor and Jervis, 2002):

$$W_{\psi}^f(a,b) = \int_{-\infty}^{+\infty} f(t)\psi_{a,b}^*(t)dt \quad (2)$$

where $\psi_{a,b}(t) = \frac{1}{\sqrt{b}}\psi((t-a)/b)$, and $\psi^*(t)$ is complex conjugate of the mother function $\psi(t)$. The two terms, a and b , are known respectively as translation and scale parameters. The translation, a , defines the shift of the time window through the signal. The scale b in WT is a parameter higher for low frequencies, which correspond to global information of the signal and lower for high frequencies that can provide more details for mechanical events, which usually last very short time. Different mother functions $\psi(t)$ have been studied and applied for analysis of complex signals such as AE transients. In this study Gabor analyzing wavelet was used. Gabor mother wavelet $\psi(t)$ is given as (Suzuki et al., 1996):

$$\psi(t) = \pi^{-1/4} \left(\frac{\omega_p}{\gamma} \right)^{1/2} \exp \left[-\frac{t^2}{2} \left(\frac{\omega_p}{\gamma} \right)^2 + i\omega_p t \right] \quad (3)$$

where ω_p is the centre frequency and γ is a constant calculated as $\gamma = \pi(2/\ln 2)^{1/2} = 5.336$.

The WT of the detected acoustic waves for the cementitious samples was calculated and visualised with AGU-Vallen Wavelet freeware (Vallen, 2005) based on Gabor mother wavelet with key parameters being: maximum frequency 400 kHz, frequency resolution 1 kHz and wavelet size of 600 samples. The results from WT were illustrated in a 3D plot where x -axis corresponds to the time, y -axis to the frequency and z -axis to the calculated coefficients of $\psi(t)$ for given values of a , b and ω_p . Equation (2) written for a continuous function $f(t)$ has been applied for the time series describing the acoustic waves via a built-in algorithm to limit the integration in the interval between 0 and $N\Delta t$, where N is the number of discrete points (3072 for this study), Δt is the sampling interval and limited range of values given for the shift a and the scale b (Hayashi et al., 1999; Suzuki et al., 1996).

Figure 7 illustrates typical acoustic waveforms and their frequency spectrum and 3D plot of WT from the largest population of signals with a duration up to 80 μ s and an amplitude up to 46 dB recorded during stage 2 in Fig. 4 respectively for the OPC (Figs 7a, 7b and 7c) and the BFS/OPC sample with encapsulated aluminium (Figs 7d, 7e and 7f). The plots in Fig. 7 show that the signals detected from both OPC and BFS/OPC structures were characterised by frequency spectrum with a peak at 34 kHz but also energy in the frequency band above 100 kHz. Moreover, the 3D plots of WT (Figs 7c and 7f) confirm the presence of two main frequency modes, below 40 kHz and above 100 kHz, constituting the first 100 μ s of the signals that can be directly related to the initial features of the AE sources. As stated by Grosse et al. (2003) after a few oscillations the signals are dominated by side reflections or geometry, heterogeneity of the materials under study, the intrinsic properties of the sensors such as resonance frequency or quality of the sensor coupling. For the more energetic signals (with a duration above 81 μ s and an amplitude up to 64 dB) also recorded in a high population during stage 2 (Fig. 4) the frequency spectrum was dominated by the low frequency component at 34 kHz (Figs. 8c and 8f). Similar resonance-like signals were attributed to hydrogen gas evolution during monitoring of stainless steel corrosion (Fregonese et al., 2001; Yonezu et al., 2006).

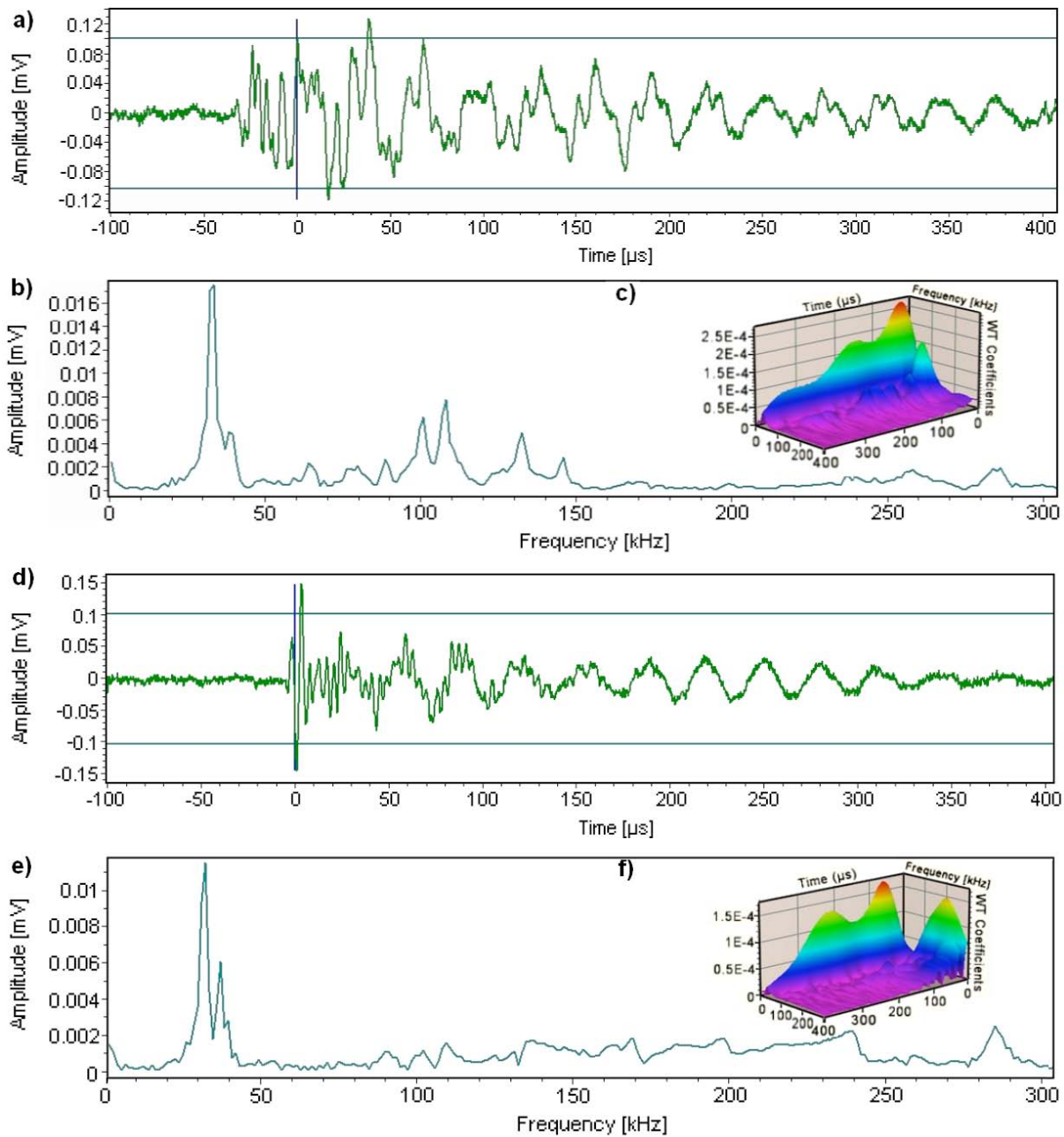


Fig. 7. Typical AE waveforms, their amplitude spectrum by FFT, and 3D plot (inserted) of WT of a short duration (up to 80 μ s) signals detected for the OPC (a, b and c) and BFS/OPC (d, e and f) samples with encapsulated aluminium during stage 2.

Cross-correlation

In order to extend the AE data analysis for characterising and differentiating the potential sources of AE within the cementitious structures the similarity in the recorded signals was assessed using the maximum value of the calculated cross-correlation function. It is known that the shape of the acquired signals in time domain is influenced by the type of the AE source, the propagation path and the intrinsic properties of the sensors used (Kurz et al., 2004; Ono, 2006). Although the frequency response of the AE transducer “masks” the true propagation characteristics of the wave the same type of sensor, applied for monitoring, assures that any changes in the

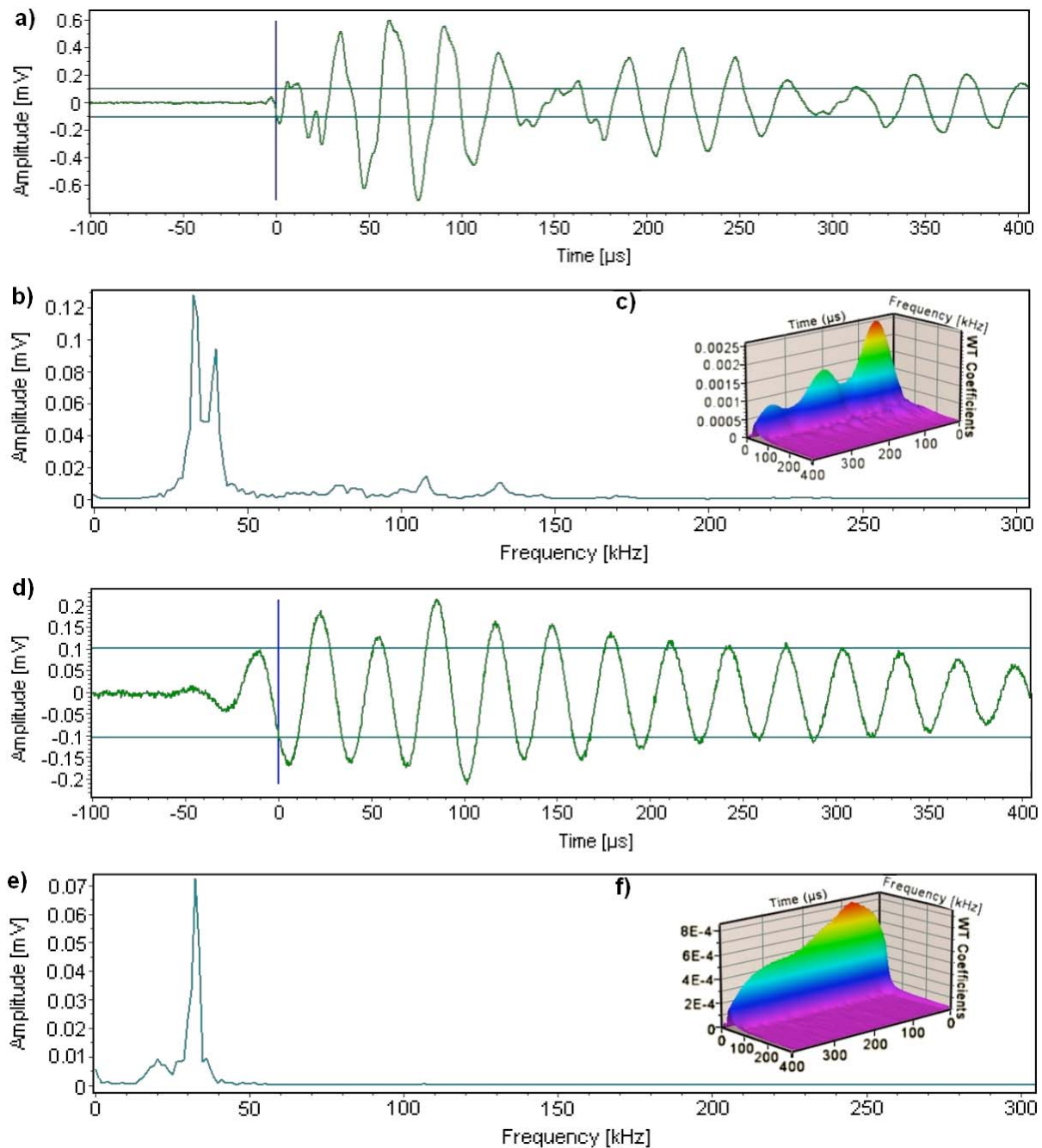


Fig. 8. Typical AE waveforms, their amplitude spectrum by FFT, and 3D plot (inserted) of WT of the more energetic resonance-like signals detected for the OPC (a, b and c) and BFS/OPC (d, e and f) samples with encapsulated aluminium during stage 2.

shape of the recorded signals characterises AE sources with a particular location and activity in time and space. During the conducted AE monitoring of the cementitious samples the sensors were firmly attached to the plastic containers and therefore the shape of the signals detected was influenced by the source-time characteristics, the wave propagation path or the distance and orientation of the source to the sensor.

The cross-correlation is a mathematical operation between two series of samples (or two digitized signals) to produce a third signal called the cross-correlation of the two input signals. Each

Sample $f_{xy}[m]$ of the third signal is calculated from the second input signal $y[n+m]$, shifted by m with respect to the first one $x[n]$, according to the equation:

$$f_{xy}[m] = \sum_{n=0}^{N-|m|-1} x[n]y[n+m] \quad (4)$$

where $m = 1, 2 \dots 2N-1$, and N is the number of samples describing the signal in digital form. The amplitude of each sample in the cross-correlation signal is a measure of how much the second input signal resembles the first one at that location. The value of the cross-correlation is a maximum when the second signal is “aligned” to the first signal.

In this study the cross-correlation function was calculated between each two subsequent in time signals recorded by the sensors attached to the samples, i.e., between the first and the second, second and third and etc. The plots in Fig. 9 show the maximum value of the calculated cross correlation functions for the AE activity for the OPC and BFS/OPC samples using a program written in MatLab.

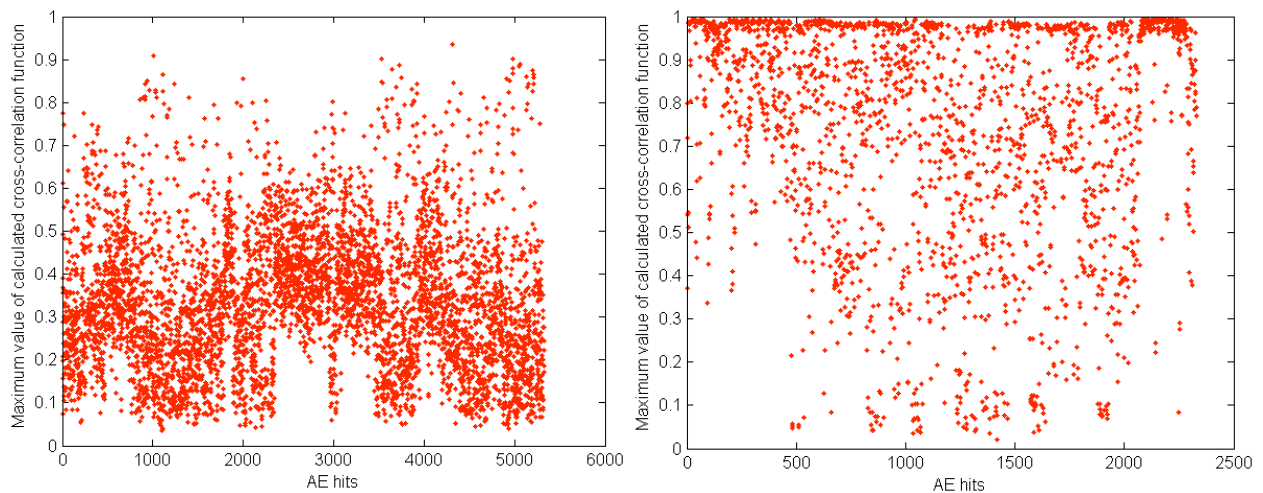


Fig. 9. Maximum value of the cross-correlation function calculated for each two subsequent in time signals recorded by the sensors attached to (a) the OPC and (b) BFS/OPC samples with encapsulated aluminium.

As it can be seen from the plot in Fig. 9a, the signals did not remain identical throughout the test. It can be suggested that they were generated by sources with a different location (toward the sensor) and time activity. The same implies for the signals detected for the BFS/OPC sample with encapsulated aluminium, as evidenced from the plot in Fig. 9b. Nevertheless, significantly larger number of subsequent in time signals recorded for the composite cement specimen were identical (maximum cross-correlation function equal to 1) in comparison with those for the OPC sample. The latter can be used to conclude on more localized (in space and time) AE sources, detected under the established experimental conditions for the BFS/OPC sample with encapsulated aluminium.

Discussion

A large number of signals for the monitored OPC (5340) and BFS/OPC (2328) samples were recorded during clearly defined periods with a very low or almost none AE activity

followed by abrupt jumps in the detected number of hits. This behaviour of the samples (in terms of AE) resembled the response of cement-based structures under loading associated with micro and macro-scale damage (Landis and Ballon, 2002; Landis, 1999; Uddin et al., 2006; Yoon et al., 2003). Moreover, the intervals of AE “silence”, recognised in the history of the conducted AE monitoring, can be related to Kaiser effect (Kaiser, 1953). Thus in the monitored cementitious specimens the stresses induced by further accumulation of corrosion products and hydrogen gas generation caused again AE after a period of time, when the initial loading (suggested by the periods with a high AE hit rate) has been exceeded. The applied conventional parameter-based analysis using the procedure from Wu et al. (2000) for classification of the detected signals according to their duration, amplitude and counts provided the first point to conclude the complex AE nature and activity of a large number of processes (sources) later confirmed by visual and optical microscopy observations.

According to their time domain parameters recorded signals can be divided generally in two main groups. The first group consists of a large number of hits with duration up to 80 μ s and an amplitude up to 46 dB potentially associated with microcracks initiation and propagation. The second group consists of a lesser number of signals with amplitude above 46 dB and duration longer than 80 μ s that can be associated with hydrogen gas evolution due to the aluminium corrosion and critical size crack(s) formation and propagation within the cementitious structures. Moreover, this group of hits was distinguished by resonance-like signals with a primary frequency at 34 kHz whereas the first one was characterised by signals with two frequency modes present: below 40 kHz and above 100 kHz respectively.

It is worth noting that under similar experimental conditions the recorded AE signals for the BFS/OPC sample were significantly less than those recorded for the OPC sample, being nearly half of that for the OPC structure with encapsulated aluminium for more than three times longer period of monitoring. The latter is in a good agreement with the reported by Setiadi (2006) lower rate of aluminum corrosion in BFS/OPC than in pure OPC environment. Additional evidence for the decreased rate of the aluminium corrosion and therefore less damage developed within the BFS/OPC sample prior to this test is also the intensity of the AE generation and release calculated for the same stages 2 in Fig. 4 for the OPC and BFS/OPC samples to be respectively of 335 hits/h and only 41.1 hits/h.

However, the basic parameters and frequency characteristics of the detected signals for both cementitious samples did not reveal any important differences. The maximum of the calculated cross-correlation function between each two subsequent signals recorded by the sensors showed that the potential AE sources in both cementitious structures were with different location (toward the sensor) and time activity throughout the tests.

Conclusions

The AE technique is feasible for monitoring the mechanical performance of cementitious structures with encapsulated metallic wastes such as aluminium. The methodology for analysis performed on the AE hit rate, their parameters and frequency characteristics allows conclusions to be reached on the presence of different AE sources in the cementitious wastefrom samples with encapsulated aluminium using additional visual and optical microscopy observations. An attempt to differentiate damage mechanisms such as distributed and localised microcracking, hydrogen gas evolution and visible cracks formation and extension within the cementitious wastefroms was made based on signals duration, amplitude and frequency components. Although the

AE hit rate and time distribution for the OPC and BFS/OPC samples with encapsulated aluminium were different under similar experimental conditions the recorded signals have been successfully classified using similar parameters and frequency characteristics.

Acknowledgements

This work was possible with the financial support of EPSRC and Nexia Solution Ltd. Authors are grateful for advises to M. Hayes and Dr. A. Setiadi from AMEC, H. Godfrey from Nexia Solutions Ltd, Dr. N. Milestone, Dr. R. Hand and Prof. F.G.F. Gibb from Immobilisation Science Laboratory, University of Sheffield.

References

B. Assouli, F. Simescu, G. Debicki and H. Idrissi (2005), "Detection and identification of concrete cracking during corrosion of reinforced concrete by acoustic emission coupled to the electrochemical techniques", *NDT&E Int.*, **38**, 682-689.

ASTM (1989), "Standard Terminology for Nondestructive Examination", E1316, ASTM International, Volume 03.03, West Conshohocken, Pa.

V. Z. Belov and A. S. Aloy (2004), "Using acoustic emission in quality control of glass and ceramics for radioactive waste immobilisation", *Mat. Res. Soc. Symp. Proc.*, **807**, 163-168.

M. Fregonese, H. Idrissi, H. Mazille, L. Renaud and Y. Cetre (2005), "Initiation and propagation steps in pitting corrosion of austenitic stainless steels: monitoring by acoustic emission", *Corros. Sci.*, **43**, 627-641.

Generic Waste Package Specification (2005), "*Generic Repository Studies Volume 2- Justification*", Nirex report No N/104, June.

C. Grosse, F. Finck, J. H. Kurz and H. W. Reinhardt (2004), "Improvements of AE technique uses wavelet algorithms, coherence functions and automatic data analysis", *Const. Build. Mater.*, **18**, 203-213.

C. Grosse, H. Reinhardt and F. Finck (2003), "Signal-based acoustic emission techniques in civil engineering", *J. Mater. Civil Eng.*, **15**(3), 274-279.

Y. Hayashi, S. Ogawa, H. Cho and M. Takemoto (1999), "Non-contact estimation of thickness and elastic properties of metallic foils by the wavelet transform of laser-generated Lamb wave", *NDT&E Int.*, **22**, 21-27.

E. Ifeachor and B. Jervis (2002), "*Digital signal processing – A practical approach*", 2nd Edition, Wokingham: Addison-Wesley, pp. 141-147.

J. Kaiser (1953), "Erkenntnisse und Folgerungen aus der Messung von Gerauschen bei Zugbeanspruchung von Metallischen Werkstoffen", *Arch. Eisenhüttenwes.*, **24** (1-2), 43-45.

J. Kurz, F. Finck, C. Grosse and H. Reinhardt (2004), "Similarity matrices as a new feature for acoustic emission analysis of concrete", *EWGAE 2004 Proceedings BB 90-CD*, 769-775.

- E. Landis (1999), "Micro-macro fracture relationships and acoustic emission in concrete", *Constr. Build. Mater.*, **13**, 65-72.
- E. Landis and L. Ballon (2002), "Experiments to relate acoustic emission to fracture energy of concrete", *J. Eng. Mater.*, **128**(6), 698-702.
- C. D. McGillem and G. R. Cooper, G. R. (1984), "*Continuous and discrete signal and system analysis*", CBS College Publishing, pp. 174-180.
- M. Ohtsu (2000), "Moment Tensor Analysis and SiGMA Code", *Acoustic Emission – Beyond the Millennium*, Elsevier, Amsterdam, pp. 19-34.
- M. I. Ojovan and W. E. Lee (2005), "*An Introduction to Nuclear Waste Immobilisation*", Elsevier Science Publishers B.V., Amsterdam, pp. 315.
- K. Ono (2006), "AE methodology for the evaluation of structural integrity", *Adv. Mater. Res.* **13-14**, 17-22.
- T. P. Philippidis and D. G. Aggelis (2005), "Experimental study of wave dispersion and attenuation in concrete", *Ultrasonics*, **43**, 584-595.
- A. A. Pollock (1989), "Acoustic emission inspection", Technical Report TR-103-96-12/98. Physical Acoustics Corporation.
- A. Setiadi (2006), "Corrosion of metals in composite cements", PhD thesis, University of Sheffield, UK.
- A. Setiadi, N. B. Milestone, J. Hill and M. Hayes (2006), "Corrosion of aluminium and magnesium in BFS composite cements", *Adv. Appl. Ceram.*, **105**(4), 191-196.
- J. H. Sharp, J. Hill, N. B. Milestone and E. W. Miller (2003), "Cementitious systems for encapsulation of intermediate level waste", in *Proc. of the Ninth International Conference on Radioactive Waste Management and Environmental Remediation*, Oxford, Paper ICEM'03-4554.
- L. M. Spasova and M. I. Ojovan (2007), "Frequency characteristics of acoustic emission signals from cementitious wastefoms with encapsulated Al", *Mat. Res. Soc. Symp. Proc.*, 985, Paper N0985-NN10-03.
- L. M. Spasova, M. I. Ojovan and C. R. Scales (2006a), "Acoustic Emission monitoring of aluminium corrosion in cemented-based wastefoms", *Adv. Mater. Res.*, **13-14**, 223-229.
- L. M. Spasova and M. I. Ojovan (2006b), "Acoustic emission detection of microcrack formation and development in cementitious wastefoms with immobilised Al", *J. Hazard. Mater.*, **138**(3), 423-432.
- R. Streatfield (2001), "A review and update of the BNFL cement formulation development programme for the immobilisation of intermediate level wastes from Magnox power stations", In *Proc. of Waste Management Conference*, Tucson, AZ, Paper 52-02.

H. Suzuki, T. Kinjo, Y. Hayashi, M. Takemoto and K. Ono (1996), Appendix ed. by Y. Hayashi, Wavelet Transform of Acoustic Emission Signals, *J. Acoustic Emission*, 1996, **14**(2), 69-84.

K. Tarmaratnam and B. S. Tan (1990), "Attenuation of ultrasonic pulse in cement mortar", *Cem. Concr. Res.*, **20**, 335-345.

WSP/100: *Introduction to the Nirex Waste Package Specification and Guidance Documentation*, Nirex Ltd. Waste Package Specification and Guidance Documentation 481350, July 2005.

F. A. K. M. Uddin, M. Shigeishi and M. Ohtsu (2006), "Fracture mechanics of corrosion cracking in concrete by acoustic emission", *Meccanica*, **41**, 425-442.

United Kingdom Radioactive Waste Inventory: *Main Report*, DEFRA/RAS/05.002, Nirex Report N/090, October 2005.

J. Vallen (2005), "AGU-Vallen Wavelet software version R2005.1121", Vallen-Systeme GmbH, Munich, Germany, available online at: <http://www.vallen.de/wavelet/index.html>.

K. Wu, B. Chen and W. Yao (2000), "Study of the AE characteristics of fracture process of mortar, concrete and steel-fiber-reinforced concrete beams", *Cem. Concr. Res.*, **30**, 1495-1500.

A. Yonezu, H. Cho and M. Tamoto (2006), "Detection of stress corrosion cracking of type 304 stainless steel using acoustic emission and corrosion potential fluctuation", *Adv. Mater. Res.*, **13-14**, 243-250.

D. J. Yoon, W. J. Weiss and S. P. Shah (2003), "Assessing damage in corroded reinforced concrete using acoustic emission", *J. Eng. Mech.*, **126**(3), 273-283.

Q. Zhou, N. B. Milestone and M. Hayes (2006), "An alternative to Portland Cement for waste encapsulation-The calcium sulfoaluminate cement system", *J. Hazard. Mater.*, **136**, 120-129.

EVALUATION OF REPAIR EFFECT FOR DETERIORATED CONCRETE PIERS OF INTAKE DAM USING AE ACTIVITY

TOMOKI SHIOTANI and DIMITRIOS G. AGGELIS*

Department of Urban Management, Graduate School of Engineering, Kyoto University, C1-2-236, Kyoto-Daigaku-Katsura, Nishikyo, Kyoto 615-8540, Japan; *Research Institute of Technology, Tobishima Corporation, 5472 Kimagase, Noda, Chiba, 270-0222, Japan

Abstract

Deteriorated concrete structures are repaired by means of grouting. In order to evaluate the repair effectiveness, the application of two NDT techniques, namely seismic tomography and acoustic emission is described herein. Using the traveling time of elastic waves, the structural velocity is estimated. AE activity is monitored along with water pressurization of the permeability test. As a result, contrary to the common expectation that the velocity increases after filling with grouting agent, enormous amount of velocity drop was observed after repair, due to the incomplete hydration process of grout material and the resulting property mis-match. On the other hand, AE activity showed dramatic decrease after repair. Furthermore, the results are correlated to the quantity of grouting material injected, showing that this was the source of the velocity behavior, while it became clear that damage indices based on AE activity exhibited well the actual damage of concrete structures.

Keywords: Damage indices, deterioration, concrete structures, tomography, repair effect

Introduction

The present paper reports on the repair evaluation of a water intake diversion facility that was constructed 70 years ago in a cold region of Japan. The concrete piers, which support the rolling gate, the most crucial part of the facility, exhibited deterioration. Referring to the repair record of the facility, both sides of the pier were replaced to the depth of 20 cm with new concrete 20 years ago, since macroscopic surface cracks developed resulting from freezing and thawing. Recently, the surface degradation became critical again; therefore damage investigation was performed by means of core sampling. Two seriously damaged zones were observed: at the boundary between the old and the replaced concrete, and in the deep, internal area of the pier owing to a large amount of voids, pieces of wood and cobblestone. Grouting with injection cement was used for repair and the present paper describes the applicability of NDT to evaluate the repair effectiveness.

Experimental

Repair Technique

The concrete piers described herein are referenced as Pier 1 and Pier 2. Two directions of grouting were used: (i) vertical grouting to fill the internal damaged areas, (ii) horizontal grouting to fill the interface between the old and replaced concrete along both sides. Specifically, a vertical borehole with 50-mm diameter was drilled only for Pier 1, whereas many horizontal boreholes with 20-mm diameter from both bank sides (only to shallow depth ranging from 800 to 1000 mm) were made in both piers. The arrangement of the boreholes can be seen in Fig. 1.

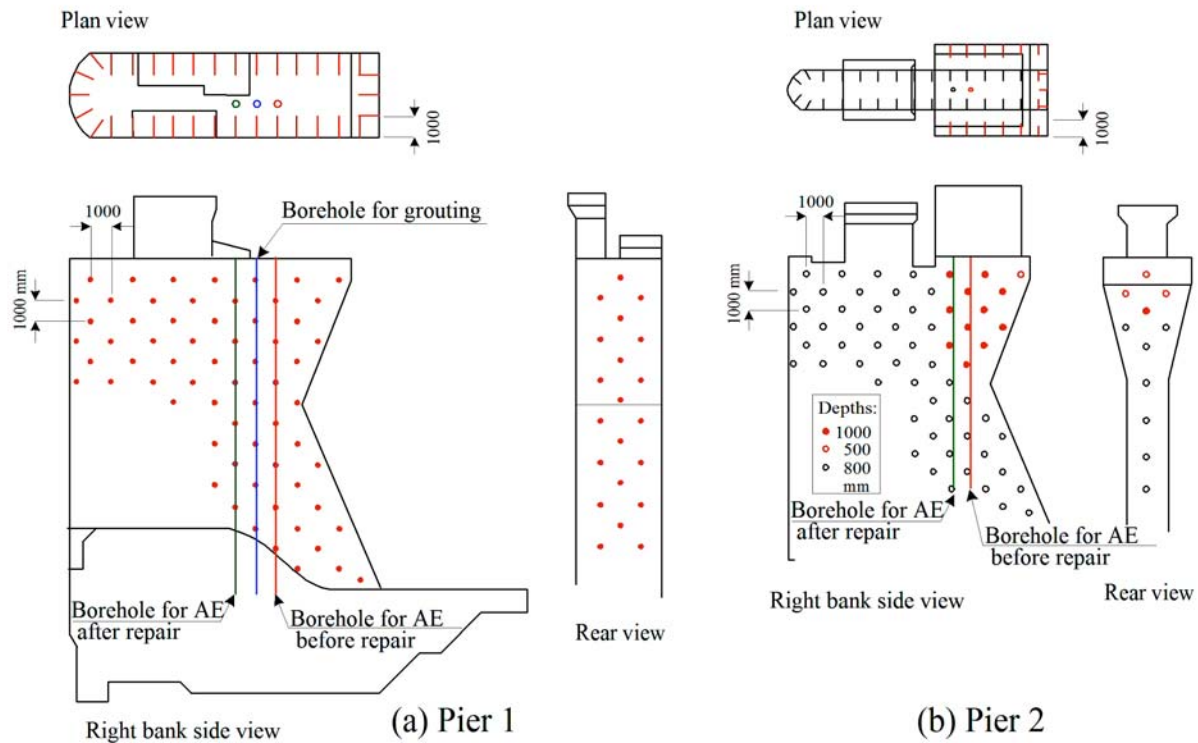


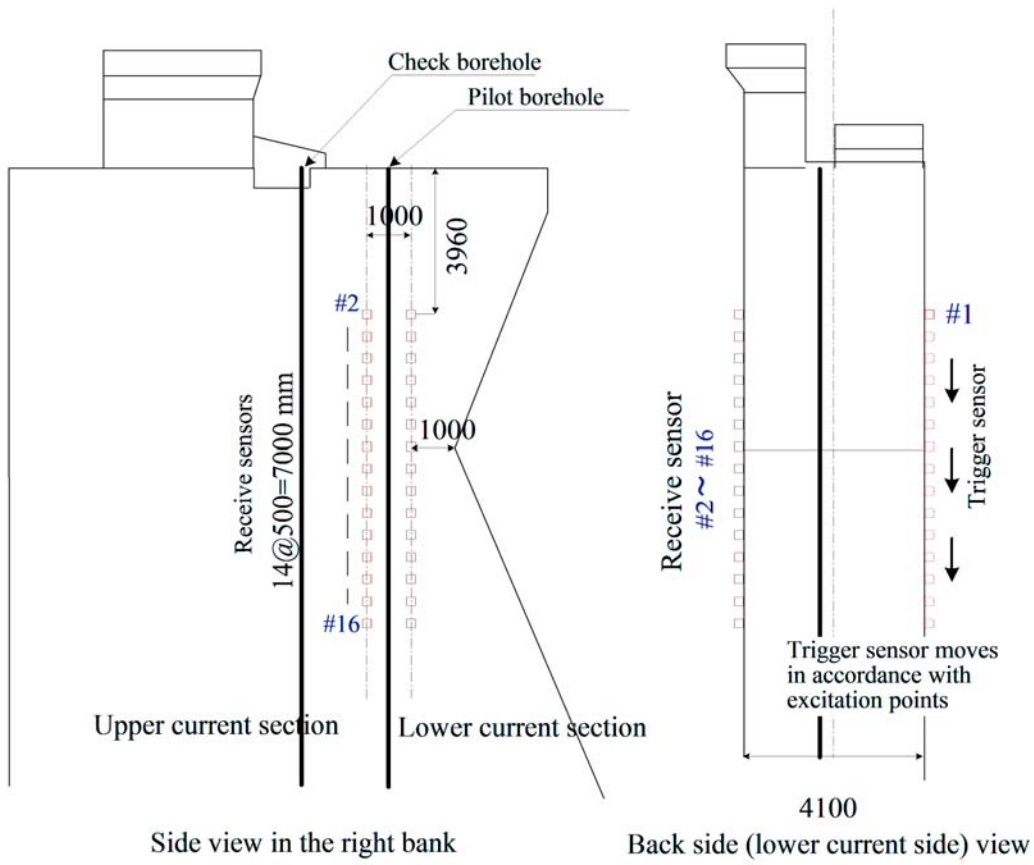
Fig. 1 (a) Grouting maps for Pier 1; (b) Pier 2.

NDT Monitoring

In order to verify the repair effectiveness before and after repair, seismic tomography and acoustic emission (AE) were performed. Through seismic tomography, the velocity structure can be created from P-wave traveling time. The velocity difference between before and after repair leads to the characterization of the repair (Shiotani et al., 2005a). Using AE activity, damage can also be quantified with indices such as RTRI and Calm ratio (Luo et al., 2004), and even in cases when those are difficult to apply, AE peak amplitude distribution can give reasonable evaluation of the damage extent (Shiotani et al., 2005b).

Seismic Tomography

Seismic tomography needs both excitation and detection of elastic waves. They were performed with a hammer drill edged with different curvatures of 10, 20 and 30 mm in radius and piezoelectric accelerometers (SAF51, Fuji Ceramics Corp.). The curvature was altered to examine the relation between resulted velocities and the upper range of excited elastic wave frequency (Sansalone & Street, 1997). The present paper only shows the result of 30 mm in radius (others can be seen in Shiotani and Aggelis, 2006). Figure 2 shows the arrangement of accelerometers in Pier 1 used for tomography. 16 channels of accelerometers were used, one of which acted as a trigger sensor and 15 others as receivers. The receivers are placed in a vertical line, with equal space of 500 mm on one lateral side, while on the opposite side excitation was performed by a hammer drill, with a near-by trigger accelerometer. The hammering was continuously excited for 10 seconds with 30 Hz repetition, resulting in about 300 waveforms. Using the 300 waveforms, stacking was conducted to enhance the signal-to-noise ratio and to facilitate the first-arrival picking. The traveling time was fed to a suitable tomography program (see Kobayashi et al., 2006). Using seismic tomography the velocity structure of the pier was reconstructed in two different cross-sections, namely upper current section and lower current section (see Fig. 2).



Side view in the right bank Back side (lower current side) view
 Fig. 2 Sensor array for tomography in Pier 1.

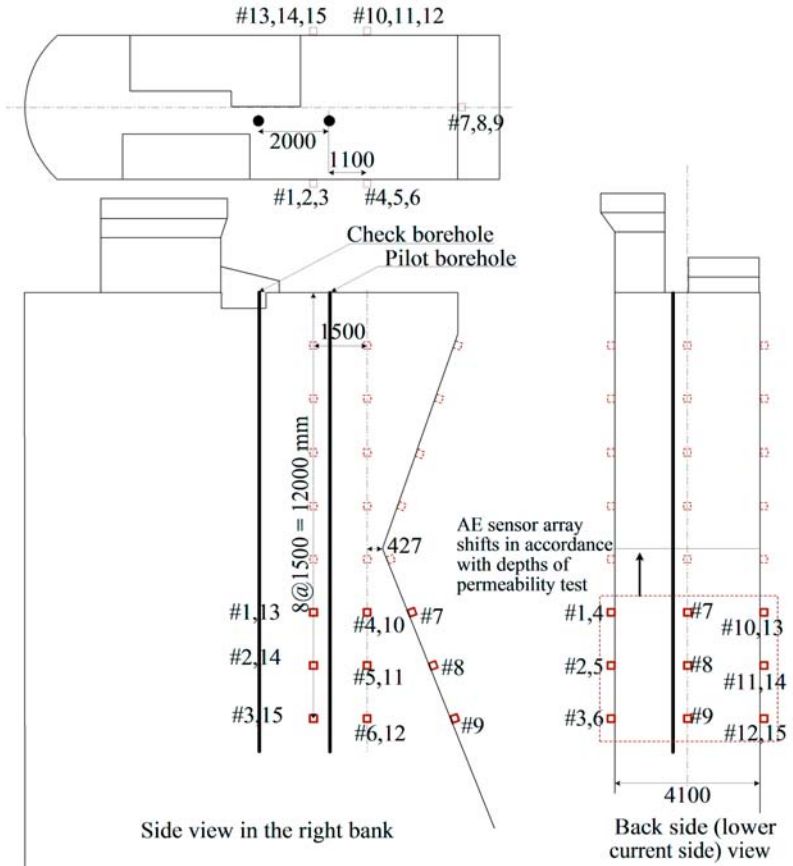


Fig. 3 AE sensor array in Pier 1.

Acoustic Emission

To study if the grouting material filled the cracked or void areas, permeability tests were carried out by means of a water pump. AE monitoring was conducted during the application of water pressure. As shown in Fig. 3, 6 sensors on each side and 3 sensors on the back side were set with 1.5-m spacing, making a total of 15 sensors. The permeability of concrete was monitored in intervals of 1 m in depth, together with AE monitoring. The AE signals detected with AE sensors (R6I, PAC) were amplified 40 dB and the signals over 40 dB were acquired by DISP AE system (PAC) to study their AE parameters as well as waveforms.

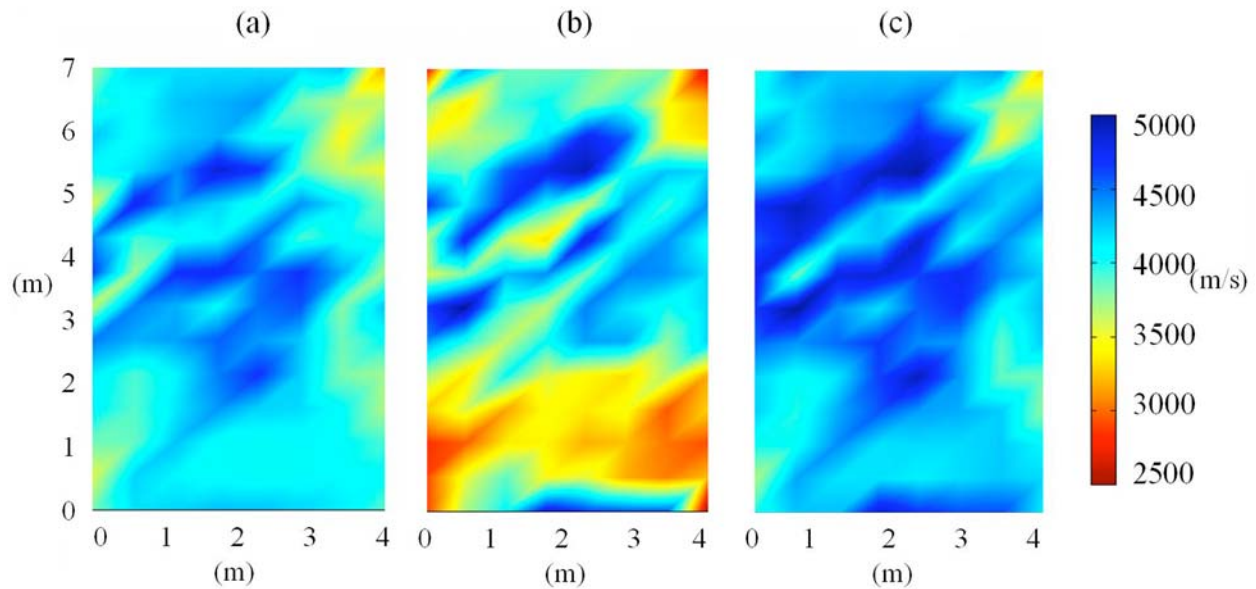


Fig. 4 Tomogram of a dam pier section examined (a) before, (b) after repair, (c) after complete hardening of grout.

Results

Seismic Tomography

In Fig. 4(a) the tomogram of a cross section of Pier 1 before injection of grout is presented. The general condition can be characterized satisfactory since the propagation velocity is generally higher than 3500 m/s, except in some small areas. However, two weeks after repair, the tomogram showed clearly decreased velocity, even as low as 2500 m/s (see Fig. 4(b)). This behavior was not expected since cementitious material replaced the voids. Even if the defects were not completely eliminated, the velocity was not supposed to decrease.

Since grouted concrete is a highly heterogeneous medium, it was deemed essential to investigate stress wave scattering, which is known to produce strong dispersive effects (Tsinopoulos et al., 2000). The model studied was that of an elastic concrete matrix initially containing voids (case before repair), subsequently soft elastic scatterers (shortly after repair) and finally hard elastic scatterers (fully hardened grout pockets). The properties of concrete were derived by cores from the dam, while concerning grout, specimens of the same material were created and tested in laboratory at different ages.

With the knowledge of mechanical properties of the constituent materials, the wavenumber of the composite can be calculated using a suitable dispersion relation (Waterman & Truell, 1961):

$$\left(\frac{k}{k_c}\right)^2 = 1 + \frac{3\varphi}{k_c^2 R^3} f(0) + \frac{9\varphi^2}{4k_c^4 R^6} [f^2(0) - f^2(\pi)] \quad (1)$$

where R is the scatterer radius (in this case void or grout pocket), φ is the particle volume concentration, k_c the wavenumber of the matrix and $f(0)$ and $f(\pi)$ are the forward and backward far-field scattering amplitudes, respectively, showing what part of energy is scattered forward and backward (Ying and Truell, 1956).

The frequency dependent phase velocity $C(\omega)$ and attenuation $\alpha(\omega)$ are calculated from the complex wavenumber of the medium:

$$k(\omega) = \frac{\omega}{C(\omega)} + i\alpha(\omega) \quad (2)$$

where ω stands for radial frequency.

The characteristic size of the voids is not readily known. However, due to the low sonic frequencies excited at the test, wavelengths of typically 0.5 m are employed, which are certainly larger than most cracks present in the material. Therefore, the size of scatterer is not crucial in our investigation. Assuming for example, void size of 40 mm, and void content of 15%, which is typical in literature (Chaix et al., 2006) and frequency 10 kHz, after solution of Eq. (1), the pulse velocity for concrete is calculated at 4300 m/s. If instead of voids, 15% of soft grout of 12 GPa is applied (corresponding to the elasticity of grout at the age of two weeks), the velocity reduces to 3850 m/s. Therefore, the scattering theory suggests that a velocity increase should not be expected immediately, but only after sufficient hardening of grout. This could be further delayed in a cold environment. For the final case of hardened grout of 22 GPa, the velocity increases to 4400 m/s (Aggelis & Shiotani, 2006a, 2006b). Using Eq. (1), since the mechanical properties of the materials have been determined and the velocities measured, the volume fraction of voids is calculated. This is done for each specific tomography cell, corresponding to an area of 0.5 x 0.5 m, for which velocity values have been assigned by tomography. In order to calculate the final velocity structure, which should be anticipated after full hydration of grout, the elasticity of 22 GPa is applied to Eq. (1), along with the corresponding void volume of each cell. Therefore, the final velocity structure is depicted in Fig. 4(c). The average velocity is increased by approximately 100 m/s, something that was not revealed by the monitoring just after the repair. However, using scattering theory, it was possible to explain the behavior and to evaluate the final condition of the structure.

According to the above discussion, the amount of grout is responsible for the initially observed velocity drop. This is confirmed by the correlation of the actual quantity of grout injected at different heights in the structure, with the velocity decrease at the same areas, depicted in Fig. 5. An excellent correlation is observed, since at the positions where a lot of grout was injected (e.g. 120 kg, 9 m from the top), at the same position, a velocity decrease of more than 800 m/s was measured.

Acoustic Emission

The source location algorithm failed to identify AE sources. Thus, the repair effect is discussed with AE hit activity. For Pier 1, Fig. 6a shows accumulated AE hits for each depth for the left bank side (right) and rear side (left). Especially for the left bank side, total AE hits of two allocated sensors at the same height are depicted with horizontal bars. In the chart, the injected quantity of vertical grout is drawn as well. Before repair, AE hit activity was intensively observed particularly below -9.0 m.

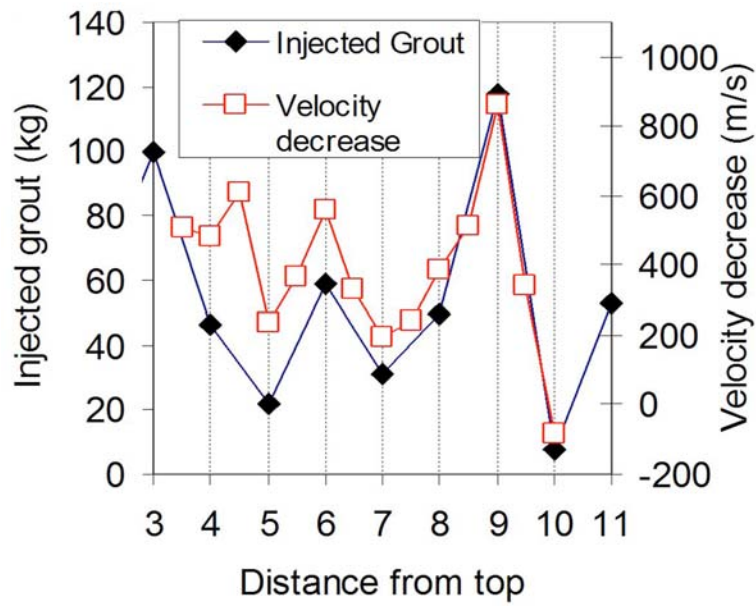


Fig. 5 Amount of grout and velocity decrease for different heights of pier 1.

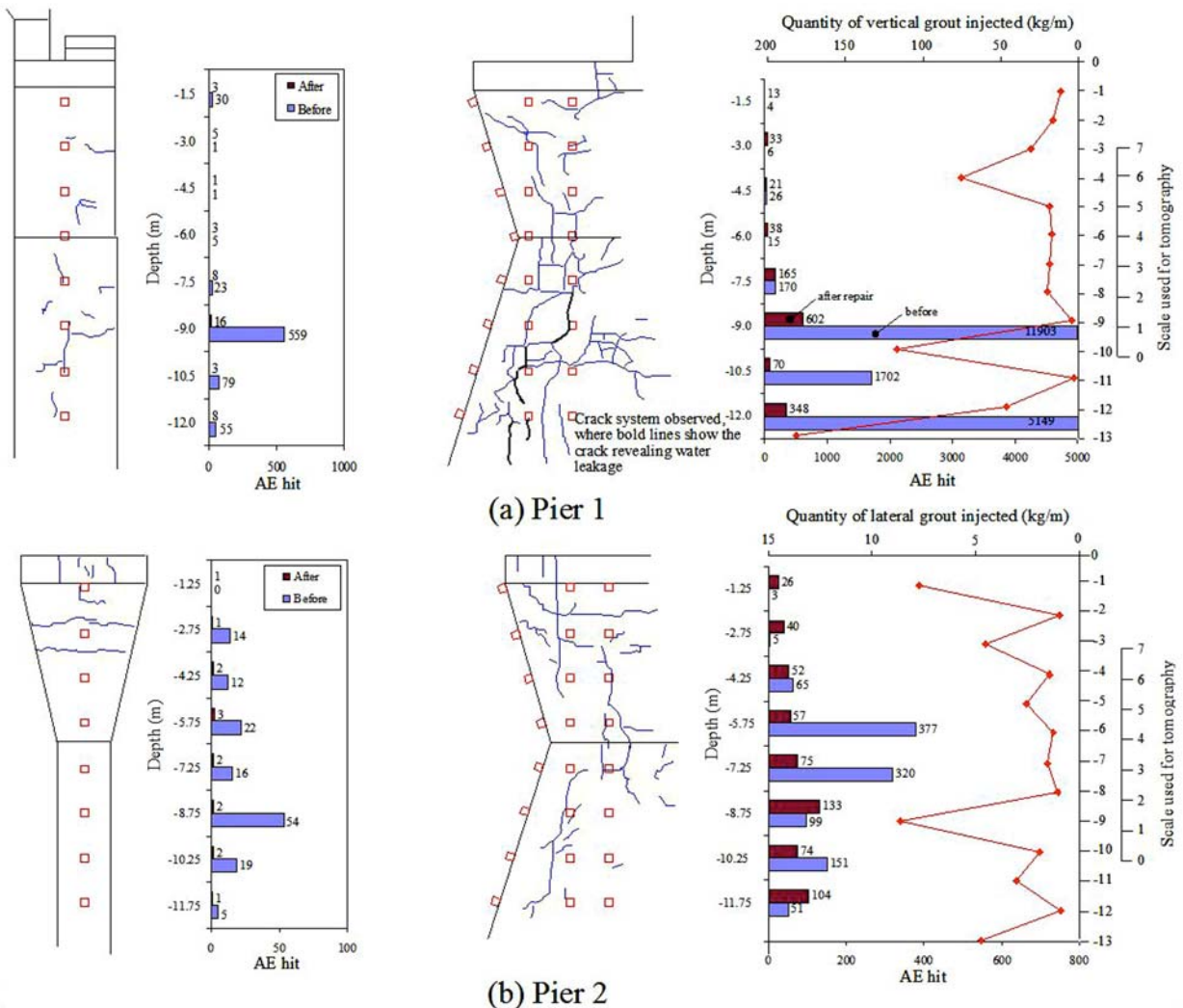


Fig. 6 AE hit activity with crack trace (Right: the left banks side, Left: rear side).

At these depths, a complicated and well-evolved surface crack system was observed, as well as water leakage from some macroscopic cracks among those (see bold lines in the figure), causing a large number of AE hits. A large amount of grout was injected vertically at those depths, implying that the macroscopic cracks were filled with the injection cement. AE activity after repair revealed decrease; i.e., from 5149 to 348 hits at -12 m and from 11903 to 602 hits at -9.0 m. The same trend could be found in the rear view (see the left graph in the figure) as AE hits decreased before and after repair.

The result for Pier 2 is shown in Fig. 6b. Steep changes of AE activity before and after repair were only derived around the middle height of monitoring range where 377 hits before repair decreased to 57 after at -5.75 m and 320 to 75 at -7.25 m (see the right chart in Fig. 6b). No correlation between the AE activity and the quantity of injected horizontal grout was observed.

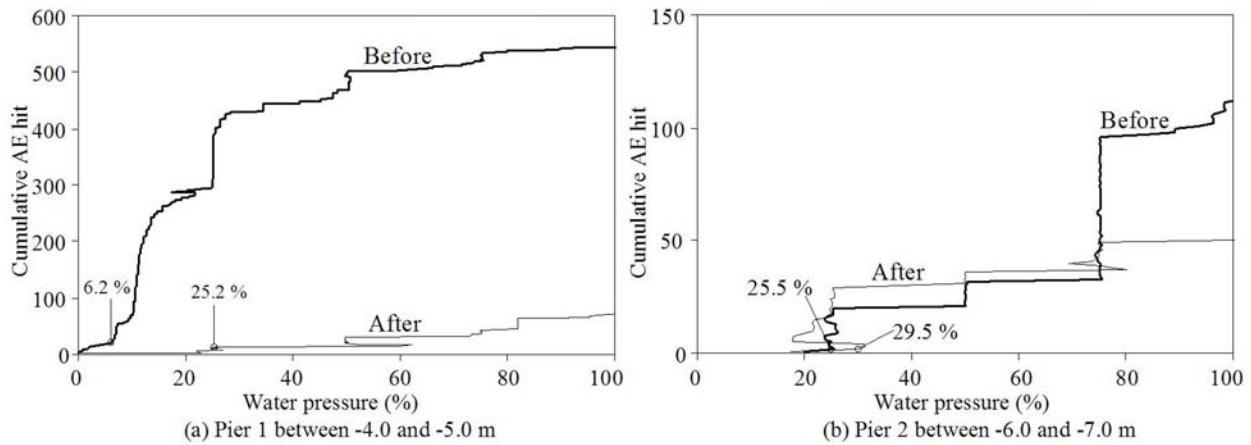


Fig. 7 AE hit activity with water pressurization process.

Hereafter, two damage indices namely Load ratio and Calm ratio are used to discuss the structural integrity. These indices are calculated with respect to a mechanical measurement in the structure. In this case, the water pressure during the permeability test was used. Load ratio was obtained based on the value of water pressure that was accompanied by the first AE burst, divided by the maximum pressure during the experiment. Calm ratio was calculated from AE hits during the unloading (reduction of water pressure) divided by the hits during the whole process of pressurization (JSNDI, 2000). Briefly, a healthier state is indicated by large Load ratios and low values of Calm ratio. Figure 7a shows the cumulative AE hits during the permeability test at -4 to -5 m in depth (cf. at -4.5 m in Fig. 6). For simplicity water pressure is normalized to its maximum value (0.5 MPa) on the horizontal axis, i.e. the Load ratio can be read from the horizontal value showing the onset of AE activity. In the case of Pier 1 before repair, AE started with a slight pressure of 6.2%, while after repair the onset of AE hits shifted to the larger value of 25.2%. In Pier 2, however, no remarkable change was obtained even after repair i.e., 25.5% before, to 29.5% after repair. These results lead to two important conclusions: (i) P1 was damaged but sufficiently reinforced. (ii) P2 was in acceptable damage state even before repair and a slight recovery was obtained afterward.

In Fig. 8a, AE activity of Pier 1 during both processes of water pressurization and its reduction is shown. Since the resulted Calm ratio of 0.11 before, increased to 0.35 after repair, recovery due to repair could not be assumed by the Calm ratio. For Pier 2, improvement after repair could not be obtained from Calm ratio, either (see Fig. 8b). However, the essential reduction of AE activity indicated simultaneous reduction of active sources.

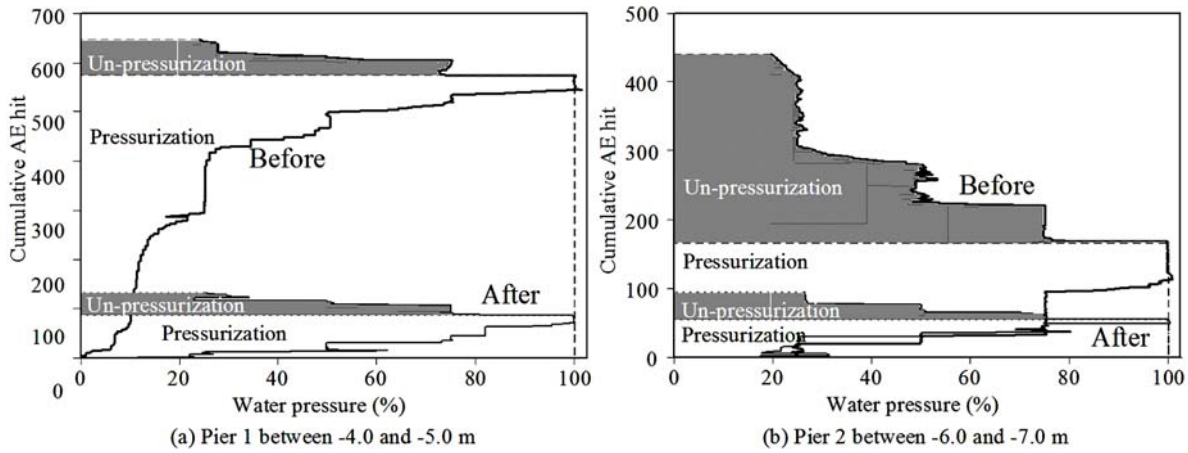


Fig. 8 AE hits activity during both of water pressurization and its reduction processes.

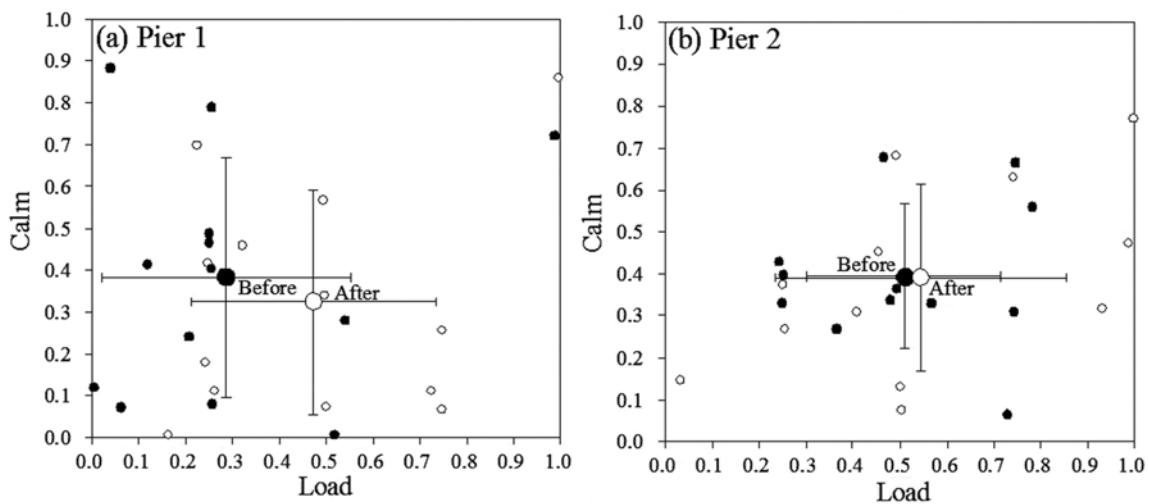


Fig. 9 Calm ratio and Load ratio based on ringdown count.

All derived ratios from both piers are plotted in Fig. 9. The small dots correspond to vertical zones of 1 m and are distributed over the chart; however, from the average of Load ratio a large difference appeared in Pier 1 between before and after, while only a slight difference was obtained in Pier 2. The figure also suggests that Calm ratio seems less sensitive to repair effect than Load ratio.

Discussion

Repair Effect from AE Hit Activity

From the AE activity of Pier 1, a large decrease of AE hits was found in deeper areas, and in those areas considerable quantity of grout was injected; For Pier 2, although the AE hits tended to decrease after repair, the decrease of hits was not as large as in Pier 1, and the quantity of grout did not correlate to the variation of AE activity, either. Here, it should be reminded that grouting in two directions was performed in Pier 1, whereas only in the horizontal direction for Pier 2. Furthermore the vertical grouting employed borehole of larger diameter than that of the horizontal, resulting in increased quantity of injected grout in Pier 1 (see the maximum value in Fig. 6) in comparison with Pier 2. Those all attributed to the difference in AE activity between Pier 1 and Pier 2, suggesting greater repair effect in Pier 1 than in Pier 2.

The number of AE hits after repair should also be discussed. Specifically in Pier 1, a steep change was obtained in the number of AE after repair, which stood at 602 and 348 at -9.0 and -12.0 m, respectively, while Pier 2 showed 133 hits at the maximum. This implies that although recovery rate was estimated to be small for Pier 2, it is healthier than Pier 1. Repair effect/recovery rate, and present health status should thus be considered from different points of view.

Repair Effect from AE Related Damage Indices

The above assumption can also be followed by AE related damage indices. As shown in Fig. 9, a large amount of increase in Load ratio was obtained in Pier 1 while only a slight increase in Pier 2. Thus, the recovery effect due to repair was obviously superior for Pier 1 than for Pier 2. However, from the point of view of soundness, Pier 2 was significantly healthier even from the original state (see the average before repair in Pier 2) and remained so despite the high recovery of Pier 1.

Quantification of Recovery Rate

Using AE related damage indices, current damage status of structures can be evaluated as described above; however, recovery rate, suggesting how much degree the structures were repaired, could not be quantified. Since both Calm ratio and Load ratio are relative values, normalized by an accumulated number of AE activity during the whole loading cycle or by the maximum value of referred parameter like pressure, respectively, these indices do not take into account substantial differences in the obtained number of AE hits before and after repair. As can be found in Fig. 8b and Fig. 9b, the number of AE hits decreased after repair, while the Calm ratio remained the same value even after repair as before. Therefore, we propose the recovery rate considering the numbers of AE hits obtained before and after repair.

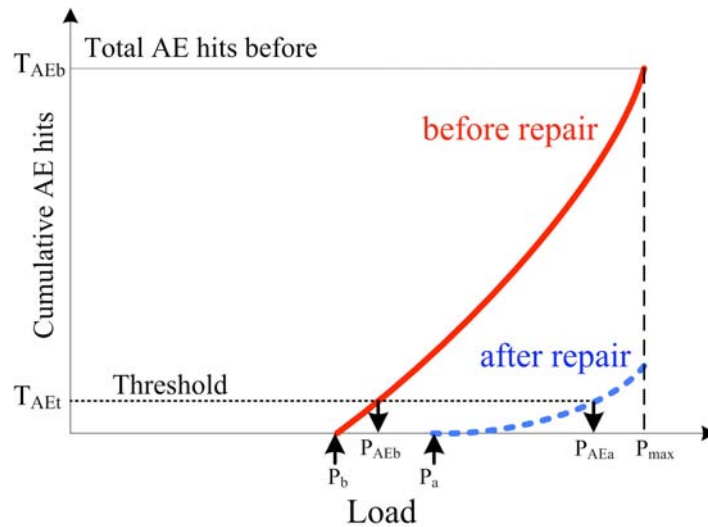


Fig. 10 Conceptual illustration of improved Load (i-Load) ratio.

Specifically for the recovery effect, Load and Calm ratios are modified based on the AE activity observed. The idea is demonstrated in Fig. 10 for the modification of Load ratio. Here, two typical AE hits vs. load curves (before and after repair) are shown. Conventional Load ratios are defined by dividing P_b , or P_a values (before and after repair) with the previous maximum load, P_{max} . Instead, we introduce the threshold value (in percent α) to determine the onset of cumulative AE curve. Suppose total AE hits before repair, T_{AEb} , is 100 and we set α to be 10%. Thus, the threshold hit value or T_{AEt} is 10. This defines P_{AEb} for AE hits vs. load curve before repair.

After the repair, we use the same threshold value as before, i.e., 10 in this case and we obtain P_{AEa} . By dividing P_{AEb} and P_{AEa} with the previous maximum load, P_{max} , we define *improved Load ratios* or “i-Load” ratios. We employ an identical condition for judging the onset of AE curves for before and after repair.

For modification of Calm ratio, we multiply a conventional Calm ratio with the ratio of cumulative AE activity after repair to that before repair. This allows us to factor in the variation of AE hits before and after. This new index is named *improved Calm ratio* or “i-Calm” ratio.

In reference to the AE activity data used in Fig. 9 and setting α as 10%, the i-Load and i-Calm ratios are obtained as shown in Fig. 11. In pier 1, the average coordinate shifted from (0.4, 0.33) before repair to the right bottom on the chart at (0.68, 0.03). This shift clearly indicates a high recovery rate after repair. Recovery can be also found in Pier 2 from (0.4, 0.4) to (0.52, 0.28), but not so dramatic as in Pier 1. As shown in Fig. 9, Calm ratio did not reflect the repaired condition effectively, as almost identical values were obtained before and after. By considering the number of AE hits, we can account for the recovery of the structure due to repair with the use of i-Calm ratio. It is noted that the use of $\alpha = 5\%$ results in the same trend as in 10%, suggesting the proper range of α in this case being 5 to 10%; however, to determine the appropriate value for other structures, further studies are necessary.

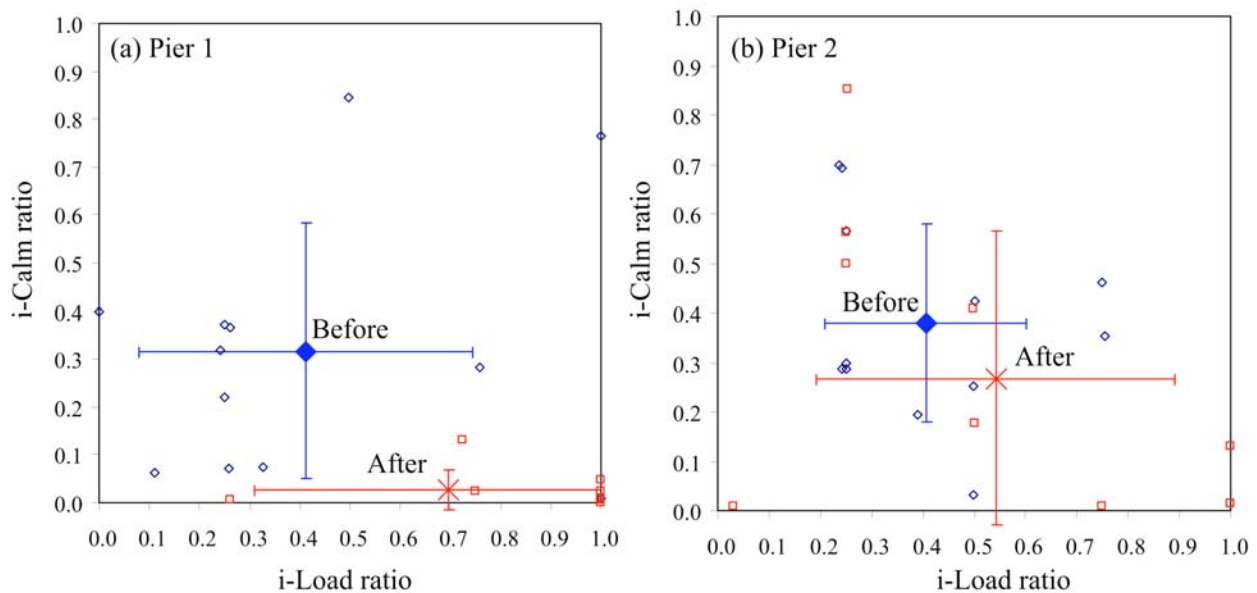


Fig. 11 Improved Calm (i-Calm) ratio and improved Load (i-Load) ratio to assess the recovery rate.

Conclusion

In this paper, two NDT techniques, namely seismic tomography and AE technique, are applied in order to evaluate the improvement after repair in severely deteriorated large concrete piers. Pier 1 was repaired well with a large amount of grout injection in the vertical and lateral direction, while a less volume of grout was filled in Pier 2. Contrary to the general assumption, a substantial velocity decrease was found in Pier 1, owing to the resultant low mechanical properties of the freshly injected grout that is assisted by scattering effect. With hardened grout properties, velocity values are further estimated, resulting in velocity increases. Discrepancies of AE activity before and after repair indicated the repair effectiveness, specifically with employing

damage indices of Calm and Load ratios. Additionally in order to quantify the recovery rate improved Calm and improved Load ratios are newly defined, with the consideration of the number of AE hits, and a lowered AE activity in the structure due to repair.

References

Aggelis, D. G. and Shiotani, T. (2006a), “Wave behavior of concrete structures repaired by cement injection“, submitted.

Aggelis, D. G. and Shiotani, T. (2006b), “Damage Evaluation on Concrete Materials Using Characteristics of Elastic waves”, *Proc. of Structural Faults and Repair 2006*, Edinburgh, 13-15 June, (in CD).

Chaix, J. F., Garnier, V., and Corneloup, G. (2006), “Ultrasonic wave propagation in heterogeneous solid media: Theoretical analysis and experimental validation”, *Ultrasonics*, **44**, 200-210.

Kobayashi, Y., Shiojiri, H. and Shiotani, T. (2006), “Damage Identification Using Seismic Travel Time Tomography on the Basis of Evolutional Wave Velocity Distribution Model”, *Proc. of Structural Faults and Repair 2006*, Edinburgh, 13-15 June, (in CD).

Luo, X., Haya, H., Inaba, T., Shiotani, T., and Nakanishi, Y. (2004), “Damage Evaluation of Railway Structures by Using Train-Induced AE”, *Construction and Building Materials*, **18**(3), 215-223.

M. J. Sansalone, and W. B. Streett (1997), *Impact-Echo, Nondestructive Evaluation of Concrete and Masonry*, Bullbrier Press, Ithaca, N.Y.

Shiotani, T., Nakanishi, Y., Iwaki, K., Luo, X. and Haya, H. (2005a), “Evaluation of Reinforcement in Damaged Railway Concrete Piers by Means of Acoustic Emission”, *Journal of Acoustic Emission*, **23**, 260-271.

Shiotani, T., Luo, X., Haya, H. and Ohtsu, M. (2005b), “Damage Quantification for Concrete Structures by Improved *b*-Value Analysis of AE”, *11th International Conference on Fracture*, CD-ROM.

Shiotani, T. and Aggelis, D. G. (2006), “Damage Quantification of Aging Concrete Structures by Means of NDT”, *Proc. of Structural Faults and Repair 2006*, Edinburgh, 13-15 June, (in CD).

The Japanese Society for Non-Destructive Inspection (2000), “Recommended Practice for In Situ Monitoring of Concrete Structures by Acoustic Emission”, NDIS2421. JSNDI, Japan.

Tsinopoulos, S. V., Verbis, J. T., Polyzos, D. (2000), “An iterative effective medium approximation for wave dispersion and attenuation predictions in particulate composites”, *Adv. Composite Lett.*, **9**, 193–200.

Waterman, P.C., Truell, R. (1961), “Multiple scattering of waves“, *J. Math. Phys.*, **2**, 512–537.

Ying, C.F., Truell, R. (1956), “Scattering of a plane longitudinal wave by a spherical obstacle in an isotropically elastic solid“, *J. Appl. Phys.* **27**, 1086–1097.

ACOUSTIC EMISSION MONITORING OF FLEXURALLY LOADED ARAMID/EPOXY COMPOSITES BY EMBEDDED PVDF SENSORS

CLAUDIO CANEVA, IGOR MARIA DE ROSA and FABRIZIO SARASINI

Department of Chemical and Materials Engineering, University of Rome,
“La Sapienza”, Via Eudossiana 18, 00184 Rome, Italy

Abstract

Cost-effective and reliable damage detection is crucial for the use of composite materials due to the relatively large number of failure mechanisms they can experience in service. Of the methods available, acoustic emission (AE) is considered as one of the most effective for on-line and in situ evaluation of structural health of composites. Thus, AE generated during three-point bending of aramid-reinforced epoxy composites was monitored by embedded and surface-mounted polyvinylidene-fluoride (PVDF) thin-film sensors instead of traditional piezoceramic ones. The parametric analysis of the AE signals detected and scanning electron microscopy observations enabled to verify the suitability of these sensors to be embedded as well as to characterize the failure mechanisms of the specimens tested. This work confirms the use of AE as an advanced, cost-effective, sensitive technique for detecting and locating potential damage mechanisms in composite materials.

Keywords: PVDF sensors, aramid-epoxy composites, three-point bending, structural health monitoring.

Introduction

Woven fabric reinforced composites are among the most important and widely used forms of textile structural composites due to their cost-effectiveness, high processability and enhanced out of plane mechanical properties. The increased use of such composites in the industry, from aerospace to construction, has required suitable and reliable testing procedures. Of primary importance in developing such procedures is the detection of damage initiation, progression and failure modes during loading of composites in real time. A host of nondestructive test methods have been developed to detect defects and damage in composite materials but AE monitoring is the primary technique used for the identification of different types of failure in composites for in service monitoring because it is a passive method, which only requires a network of receivers (Hamstad and Sendekyj, 1993). In this regard, AE monitoring has some unique advantages over other NDT techniques: can detect the dynamic processes associated with the degradation of structural integrity, it is nondirectional and can be used in situ to monitor a structure while it remains in service. This feature makes AE a suitable sensing technique for structural health monitoring (SHM) (Speckmann and Henrich, 2004). Other unique capabilities include: high sensitivity, location of damage regions and sensitivity to any process that generates stress waves.

The solution analyzed in this work involved the use of polyvinylidene fluoride as sensor's material and the AE as sensing technique. In particular, to fulfill the task concerning the in situ damage detection, the AE sensors have been embedded in the composite laminates during their manufacturing stage.

PVDF is a semicrystalline polymer, which owes its strong piezoelectricity to the strength of the electric dipole (between carbon and fluorine atoms) and to the large number of dipoles per unit volume, but most importantly because it crystallizes in a polar crystal phase characterized by a cooperative dipole alignment (Davis, 1987). PVDF differs in many respects from traditional piezoceramic materials. Ceramic transducers are in general brittle, stiff, easily damaged from mechanical shock or vibration and are difficult to machine in complex shapes. In contrast, polymeric transducers can be easily tailored to different shapes, are tough, flexible when machined into thin films thus not affecting the mechanical motion of the structures they are mounted on. Nevertheless, polymeric transducers can undergo mechanical relaxation phenomena and are prone to thermal depolarization and electromagnetic interference. At present, some of the most important applications of PVDF can be considered to involve pyroelectric, electromechanical and electroacoustic transduction (Sessler, 1981; Marcus, 1982; Bar-Cohen et al., 1996; Riande and Diaz-Calleja, 2004; Measurement Specialties, 2006).

Several papers are available in literature dealing with the use of PVDF as AE sensor (Stiffler and Henneke, 1983; Narisawa and Oba, 1984, 1985; Hamstad, 1995; Or et al., 2000; Kim et al., 2005; Park et al., 2005; Bar et al., 2004, 2005) even though as surface mounted AE sensors.

The aim of this work is to verify the suitability of PVDF sensors to be embedded and their influence on the flexural behavior and integrity of the resulting composite laminates. Furthermore, the AE monitoring of composites during loading and the characterization of AE signals acquired were addressed to identify the failure mechanisms involved.

Materials

The specimens tested in this work were obtained from square aramid/epoxy panels (250 x 250 mm) made using RA175H4 fabric and a SP106 resin, both from SP Systems. The areal weight of the fabric, a 4-harness satin weave containing Kevlar49 fibers, was 170 g/m^2 . The samples were manufactured by hand lay-up in a closed mould using ten layers of fabric. This manufacturing technique made the embedment of PVDF sensors easier. In fact, during the layer stacking process, PVDF sensors were arranged in the middle of the stacking sequence of the laminate. The thickness of the cured laminates was $3 \pm 0.2 \text{ mm}$ and the fiber volume fraction was 0.38 ± 0.02 (as calculated from the perform weight per unit area). From the panels, rectangular specimens having a length of $200 \pm 5 \text{ mm}$ and a width of $30 \pm 0.5 \text{ mm}$ were removed and subjected to three-point bending tests. Two different types of specimens were produced: the first type (labeled as type A) had no embedded sensors (served as reference material) whilst the second one (labeled as type B) had two embedded sensors.

PVDF sensors used in this work were the DT1-052K manufactured by Measurement Specialties Inc. These sensors are rectangular element piezo-film with silver ink screen printed electrodes and are supplied with a thin urethane coating over the active sensor area; the lead attachment legs are free of this coating (Measurement Specialties, 2006). In Table 1 are reported some typical properties of the piezo-film and the geometrical dimensions of the sensors used in this work (Measurement Specialties, 2006). The PVDF sensors for type A specimens were surface mounted using a double-side tape. A reliable interconnection to piezo-film was made through the use of a conductive silver epoxy resin manufactured by ITW Chemtronics (CW 2400), which provided not only excellent electrical conductivity but also high-strength bonding.

Table 1. Typical properties of piezo film and dimensions of PVDF sensors used.

Symbol	Parameter	PVDF	Units
d_{31}	Piezo Strain Constant	23	10^{-12} (m/m)/(V/m)
d_{33}	Piezo Strain Constant	-33	10^{-12} (m/m)/(V/m)
g_{31}	Piezo Stress Constant	216	10^{-3} (V/m)/(N/m ²)
g_{33}	Piezo Stress Constant	-330	10^{-3} (V/m)/(N/m ²)
k_{31}	Electromechanical Coupling Factor	12%	
k_t	Electromechanical Coupling Factor	14%	
Y	Young's Modulus	2-4	10^9 N/m ²
ρ	Pyroelectric coefficient	30	10^{-6} C/m ² K
ϵ	Permittivity	106-113	10^{-12} F/m
ϵ/ϵ_0	Relative Permittivity	12-13	
ρ_m	Mass Density	1.78	10^3 kg/m ³
T	Temperature Range	-40 to 80...100	°C
PVDF Sensor DT1-052K	Length (mm)	Width (mm)	Thickness (μm)
	41	16	70

Methods

Before performing flexural tests, the wave velocity of AE signals in the laminates was measured in order to make possible the localization of AE events during the tests. The procedure used is described elsewhere (Caneva et al., 2007). The value obtained was 4600 m/s, which should be considered as an approximate value due to the highly anisotropic nature of composite materials. Its accuracy was checked by means of calibration tests through the Hsu-Nielsen source method (Caneva et al., 2007) providing satisfactory results.

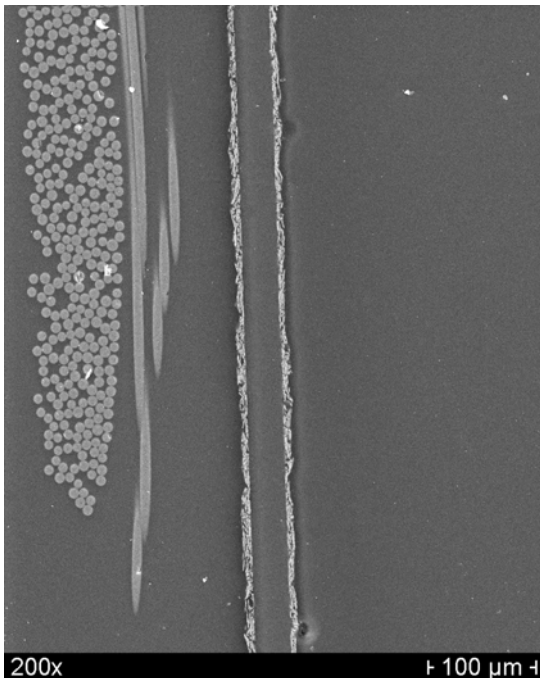


Fig. 1. SEM micrograph showing the PVDF sensor embedded in aramid reinforced epoxy.

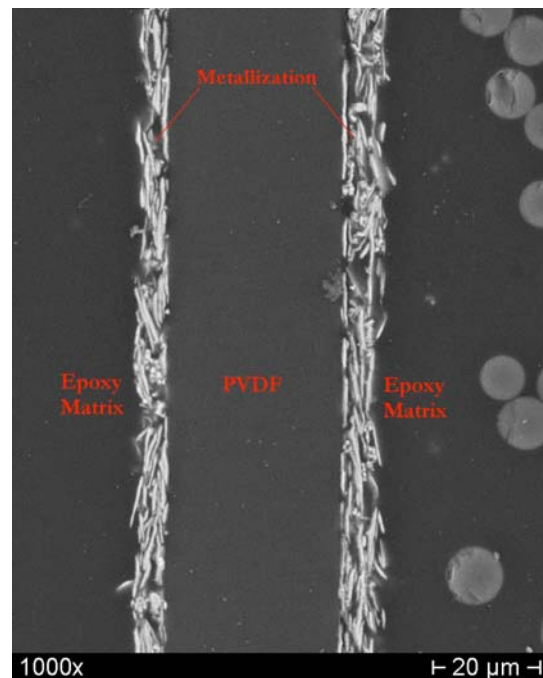


Fig. 2. SEM micrograph showing details of the sensor/matrix interface of an aramid reinforced laminate

After these preliminary tests, the specimens were subjected to three-point bending tests in accordance with ASTM D-790 (three-point loading). These tests were performed in an Instron 5584 at a constant crosshead speed of 2.5 mm/min with a span-to-thickness ratio of 20:1. The strain at the mid-span was determined by means of strain gauges. In order to embed PVDF sensors, width and length ratios were selected to limit edge and large inclusion effects. The PVDF sensors were located within the span length with a center-to-center distance of about 60 mm. The position of sensors was selected in order to have them close to the stressed area during bending with the aim of enabling the detection of AE signals as well as verifying their influence on the mechanical response of the composite laminates. Ten specimens were tested for each composite system (types *A* and *B*). The tests were monitored by two PVDF sensors and the signals were acquired by an AMSY-5 AE system manufactured by Vallen Systeme GmbH. The AE acquisition settings were as follows: threshold = 40 dB (ref. 0 dB = 1 μ V), rearm time = 0.4 ms, duration discrimination time = 0.2 ms and total gain = 34 dB. Attenuation of AE waves was measured using the Hsu-Nielsen source procedure. It was small enough to prevent from doing any correction of the measured amplitudes owing to the small distance between the sensors. In linear location calculations, the position of the sensor is assumed coincident with the center of the sensor itself. Only AE signals localized between the sensors have been considered in the off-line parametric analysis.

The failure modes and microstructures in the composites were investigated with scanning electron microscopy (SEM).

Results and Discussion

A major concern during the laminate cure cycle was with the health of the embedded sensors. The maximum temperature of 75°C during fabrication of laminates was very close to the Curie transition temperature for PVDF sensors, which could result in depoling associated with a sharp decrease of piezoelectric properties. In addition, residual stresses at the matrix/sensor interface could affect the ability of the sensor to detect AE events. To investigate these aspects, SEM analysis was performed on composite laminates. The results of this investigation are summarized in the following micrographs (Figs. 1-3), which refer to the cross section of the specimens. The cross sections were graphite coated before SEM observations.

As for embedded PVDF sensors, as it can be seen in Figs. 1-3, the interface between the sensor and the surrounding matrix represents a region of continuity between the different materials and does not seem to be present any kind of remarkable damage able to affect in a negative way the piezoelectric behavior of the sensor itself. In fact, especially from Fig. 3, there are no defects such as microcracks due to different thermal expansion coefficients of the metal and the polymer at the interface and the metallization adheres well to the matrix, thus enhancing the ability of the matrix to transfer the AE signals to the sensor. These observations confirm the ability and the easiness of PVDF sensors to be embedded.

Even though the future of smart structure technology seems promising, its application to engineering systems cannot be accomplished until its integrity issues are fully understood. As sensors are integrated into complex structures, questions arise on the mechanical behavior and integrity of the structure. Therefore, the first step in the development of a reliable damage detection system based on AE technique has to be an investigation of the mechanical properties of the resulting structures.

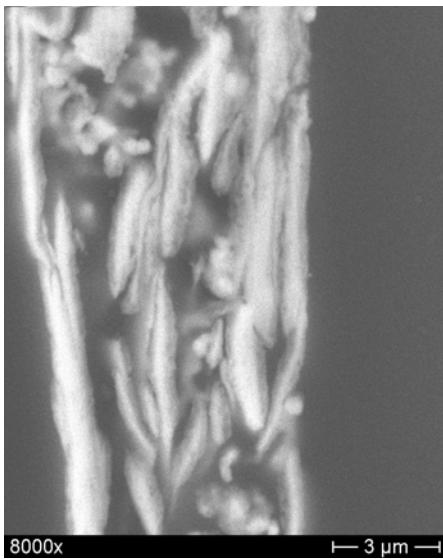


Fig. 3. SEM micrograph showing details of the PVDF sensor metallization.

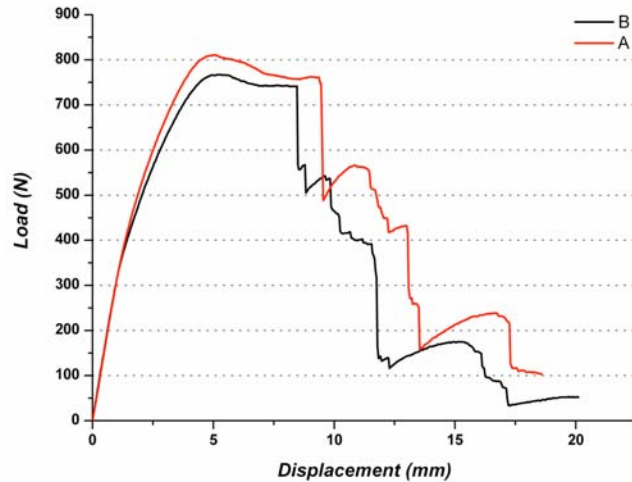


Fig. 4. Typical longitudinal flexural load-displacement curves for specimen types *A* and *B*.

A comparison between typical flexural load-displacement curves of *A* and *B* specimens is shown in Fig. 4. As it can be noticed, the behavior of specimens with and without embedded PVDF sensors is almost identical. The failure of aramid-reinforced epoxy composites in three-point bending can occur by either one of two modes being failure by longitudinal fracture of fibers in the tensile side or by shear delamination. The transition between these failure modes is controlled by the fiber volume fraction (Davidovitz et al., 1984). The curve of the fiber fracture mode is characterized by a yielding stage and a longer ultimate deflection whilst the curve for delamination mode is characterized by a main delamination event followed by a number of secondary delamination. Furthermore, the span length was long enough so that the specimen does not fail in shear and short enough to neglect the effects of large deformations. The composite specimens tested exhibited curves characterized by a yielding stage and a long ultimate deflection, during which the composites failed gradually, thus indicating an increased energy absorption and a good damage tolerance. The flexure curve is strongly non-linear and this behavior is consistent with the non-linear compressive behavior of composites reinforced with aramid fibers (Zweben, 1978; Mittelman and Roman, 1990).

In this case, it can be seen that the failure of both sides, namely tension and compression, may occur during flexural loading. This is due to the fact that Kevlar fibers are characterized by poor transverse and shear properties thus providing a composite, which shows poor strength in compression. This aspect can be enhanced by fiber crimps, which tend to lower the composite compressive strength since they make easier the appearance of kinking. This is not properly the case because in satin-woven fabrics, the crimp ratio is generally smaller if compared, for instance, with plain-woven fabrics. Nevertheless, some kink bands appeared in the specimens tested, as it will be explained later but the catastrophic failure was localized in the outer ply on the tensile side. The interface plays an important role in the behavior of these composites. For aramid/epoxy composites, the interface is thought to be a particularly weak link (Penn and Liao, 1984).

As regards the effect of PVDF sensors on the mechanical properties of composites, the two specimen types exhibited a similar three-point bending strength and flexural modulus (within 3 % of each other in both cases). Therefore, from the results it can be inferred that the embedment

of PVDF sensors does not seem to have any remarkable influence on the damage evolution during three-point bending (Figs. 5-6) in spite of the test conditions' severity, since the sensor embedded takes up most of the specimen's cross section.

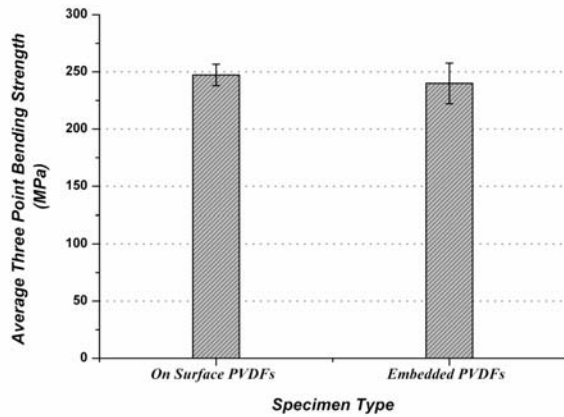


Fig. 5. Average three-point bending strength for specimen types *A* and *B*.

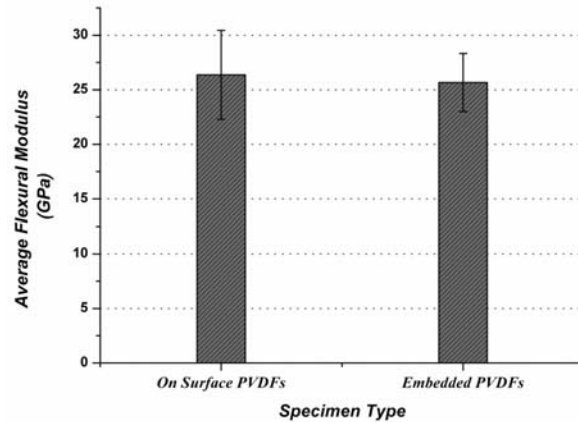


Fig. 6. Average three-point bending modulus for specimen types *A* and *B*.

Final failure of composites is considered to be due to the accumulation of different failure modes such as matrix cracking, debonding and fiber breakage. The peak-amplitude distribution (PAD) of AE signals can be successfully used to characterize the different damage mechanisms in composite materials since it depends strongly on the material as well as on the deformation mechanism present thus providing insight into how the structure behaves under a given loading condition. In this work, AE events generated during three-point bending were recorded until final fracture occurred. Figure 7 shows typical amplitude distribution plot for specimens *A*. The same

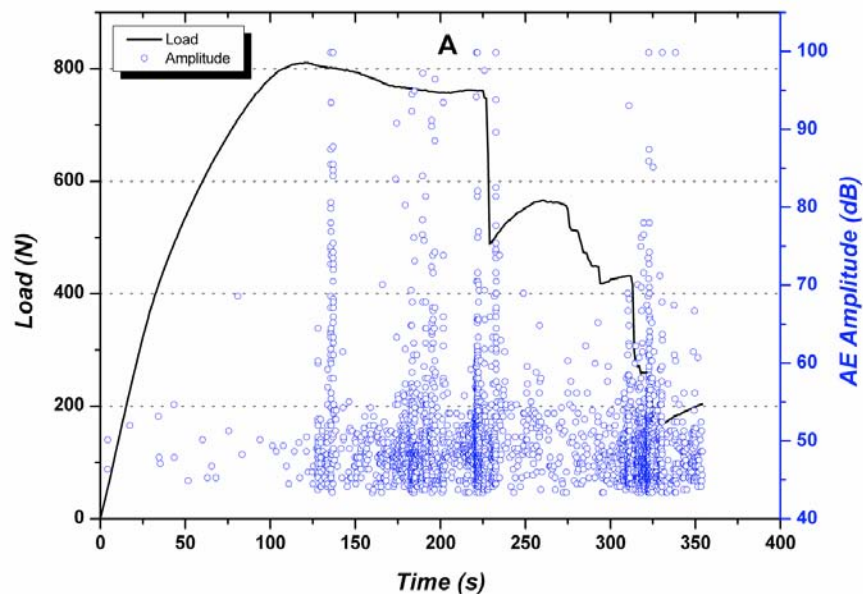


Fig. 7. Load and amplitude distribution for *A* specimen.

curve for specimens *B* is shown in Fig. 8. As it can be noticed, typical load-displacement curves and AE activity patterns for both types are almost identical. In order to better understand the failure of these composites and to verify whether or not embedded PVDF sensors are able to follow on line the structural changes occurring, the cumulative event distributions have been

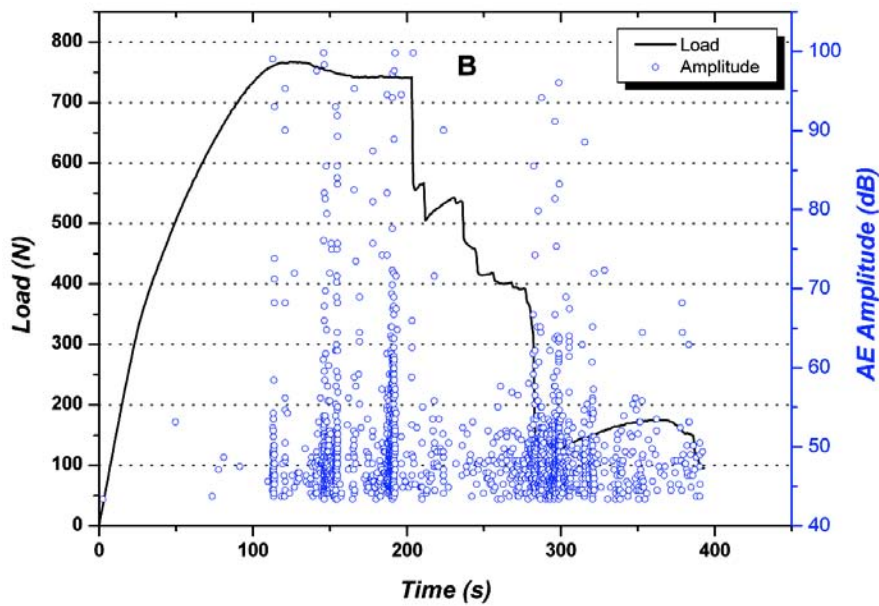


Fig. 8. Load and amplitude distribution for *B* specimen.

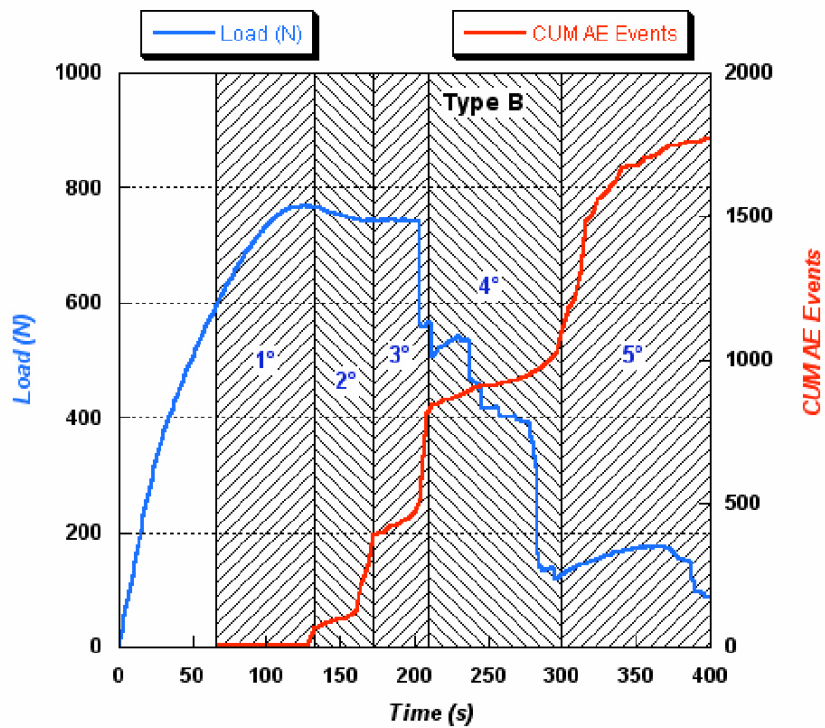


Fig. 9. Typical load and cumulative AE events versus time for specimen *B*.

divided in different intervals because, during the flexural tests, the testing machine was periodically stopped and the specimens examined by SEM so as to correlate the different PADs detected to the actual damage modes and progression (Fig. 9). The PADs corresponding to the different intervals labelled 1°-5° in Fig. 9 are shown in Fig. 10. During the first part of the loading (intervals 1 and 2), the PAD shows that events are generally situated in the range of 43-50 dB, which in literature is, in this condition, well documented as related to matrix microcracking and matrix-matrix friction. They also show some events around 55-63 dB characterizing the interface de-adhesion. This behavior can be explained referring to the low strength of the aramid/epoxy inter-

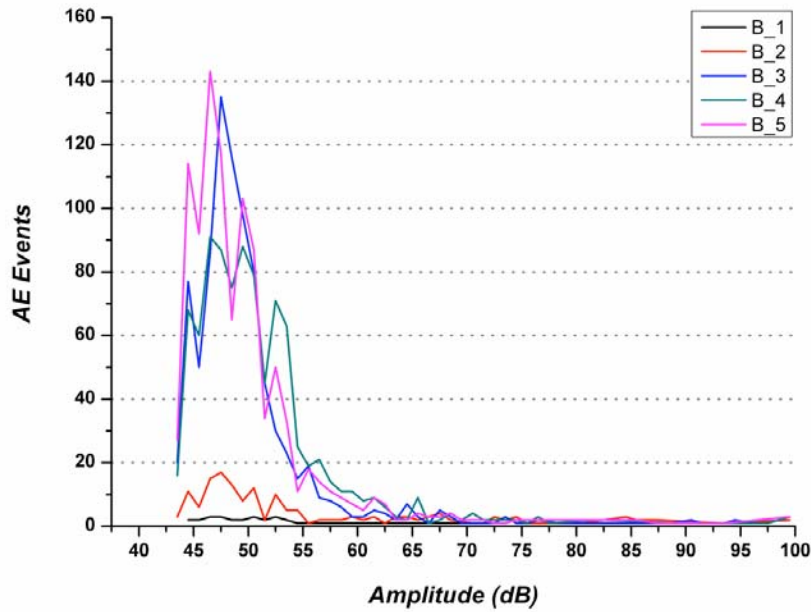


Fig. 10. Evolution of a typical PAD during flexural loading for specimen *B*.

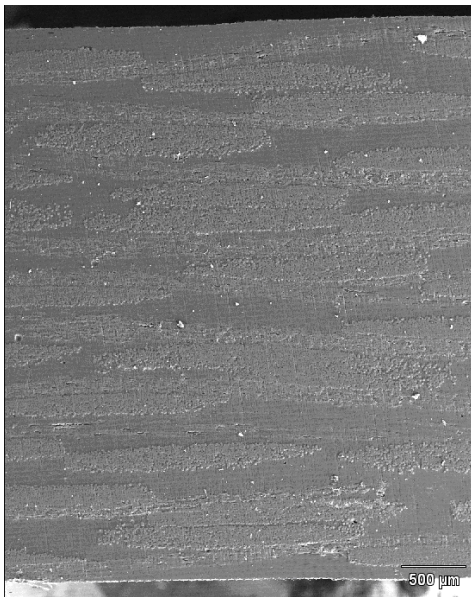


Fig. 11. SEM micrograph showing the cross section of a *B* specimen in the as-manufactured stage.

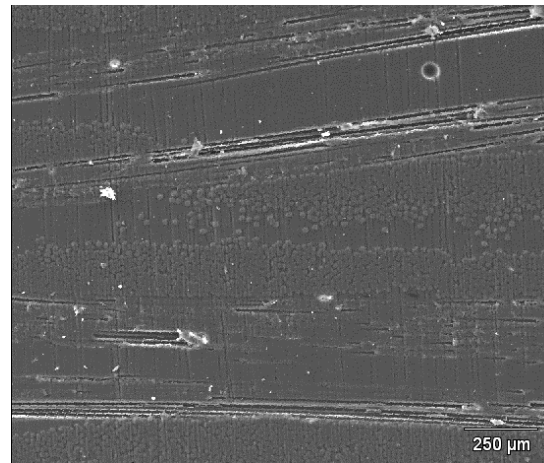


Fig. 12. SEM micrograph from flexural tests showing longitudinal cross section at the mid span at the end of interval 2.

face, while fiber failure seems to be negligible in this stage (no significant events characterized by high amplitude values). These sensors seem to be insensitive to interfacial debonding due to fiber straightening, which is supposed to happen at the onset of loading. In fact, during the very first part of the loading, few signals or even no signals were detected. This behavior seems to contradict the experimental evidence that in composite materials AE is noted from the beginning of loading. This implies that a damage-producing mechanism should be already active at low stress levels. Since both matrix and fibers are not active at such low stress levels, it is reasonable to assume that some damage develops at the interface between fiber and matrix. Two different mechanisms can account for the occurrence of this kind of damage. The first is related to a fiber straightening process, during which the strains produced are higher than the failure strain of the

matrix, thus resulting in interfacial debonding. The second is due to residual stresses at the interface developed during the manufacturing stage of the composites as a result of different coefficients of thermal expansion. The SEM observations agree with what is suggested by the PAD, as it can be seen in Fig. 12, where de-adhesion in the warp fiber bundle and small matrix cracks can be seen. In order to make a comparison, Fig. 11 shows a SEM micrograph of a composite in the as-manufactured stage.

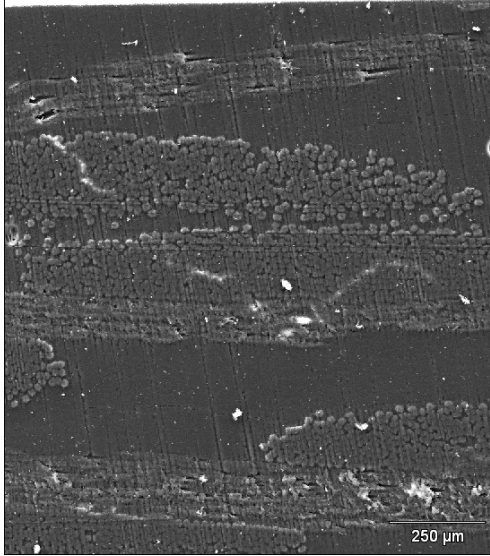


Fig. 13. SEM micrograph from flexural tests showing longitudinal cross section at the mid span at the end of interval 3.

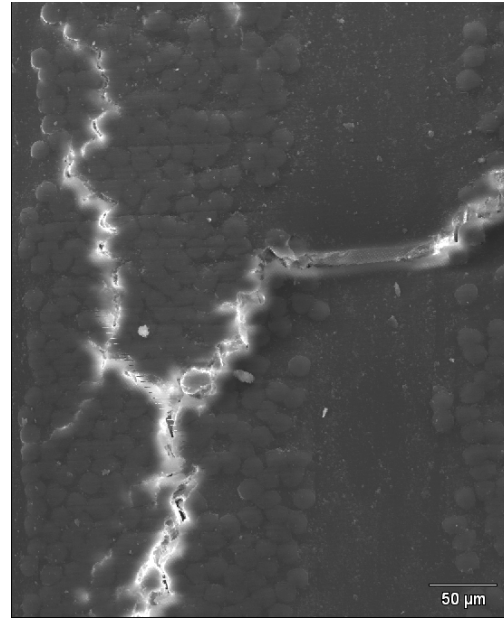


Fig. 14. SEM micrograph showing cracks in the weft fiber bundle.

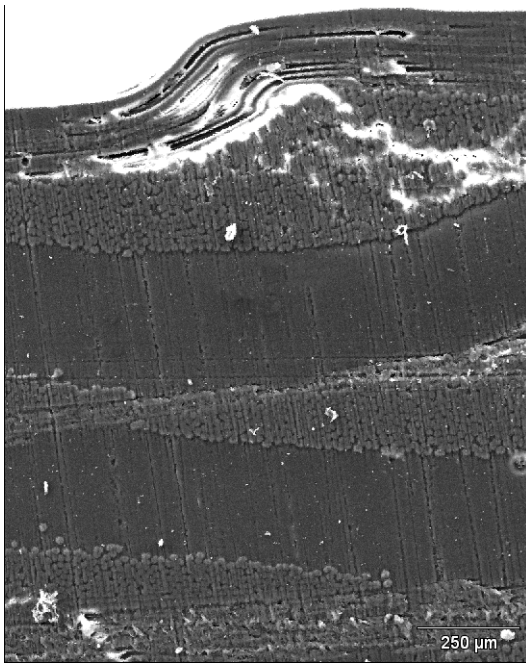


Fig. 15. SEM micrograph showing some fiber kinking.

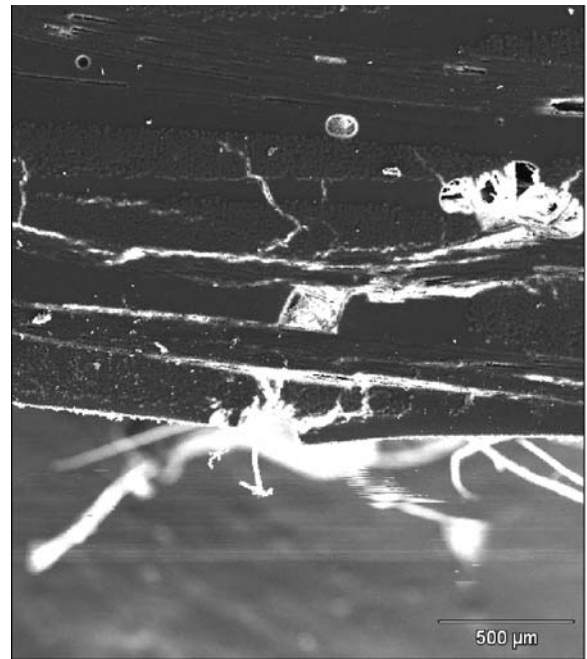


Fig. 16. SEM micrograph from flexural tests showing longitudinal cross section at the mid span after final failure occurred.

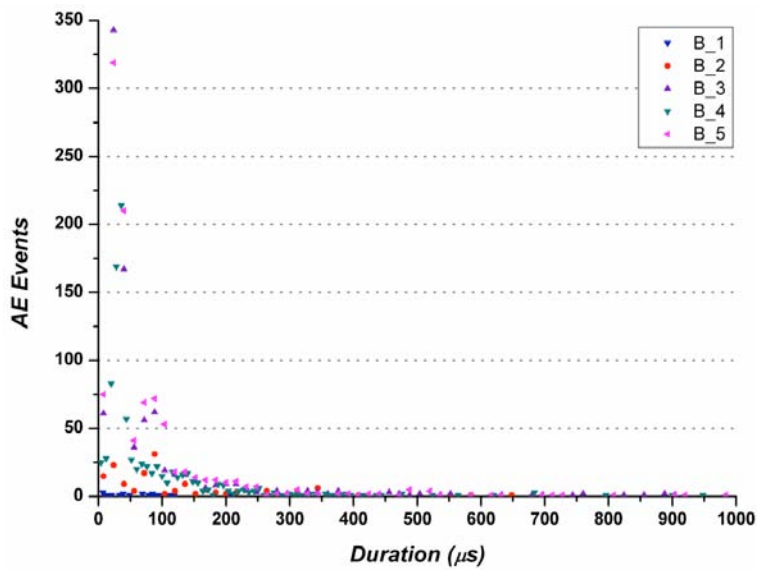


Fig. 17. Evolution of a typical duration distribution plot for a *B* specimen.

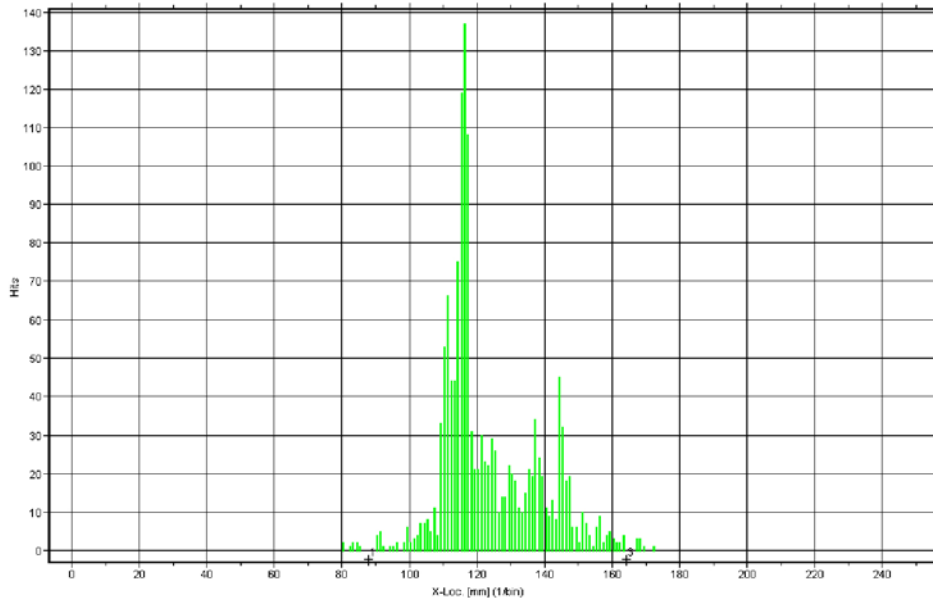


Fig. 18. Linear localization plot from flexural testing of *B* specimen.

The stage that leads to the first drop in the load, is characterized by a large number of events situated in the amplitude range 40-65 dB, characterizing the growth of transverse cracks in weft fiber bundle and some delaminations (see Figs. 13 and 14), and events with high amplitudes (80-90 dB), which belong to fiber fracture located mainly in the outer ply on the tensile side. Fiber fracture occurs late during the loading due to the small scatter of aramid fiber strength. This behavior is strongly dependent on the type of the weaving structure used. In this stage, the tensile failure is the dominant failure mode even though micro-damage and fiber kinking were observed on the compression side of the specimens (Fig. 15).

As loading continues, the corresponding failure is characterized by the growth and accumulation of the micro-damages discussed above, as PAD and SEM observations confirm. Figure 16 shows the longitudinal cross section at the mid-span after final failure occurred. It is evident the accumulation of the several damage mechanisms discussed so far. These results are also con-

firmed by the duration distribution of the AE events, as can be seen in Fig. 17, which shows the evolution of the duration distribution for a *B* specimen (the intervals being the same as Fig. 9). As loading continues, most of the signals are located at 0-200 μ s, which are values typical of matrix cracking while longer durations begin to be significant during the third interval and up to final fracture (delamination and debonding), where the occurrence of even longer durations should be attributed to fiber ruptures.

The embedded PVDF sensors were also able to localize the AE events (see Fig. 18). Due to the type of loading, most of the signals are located at the center of the specimen even if the AE signals seem to be more spread around the point of the maximum applied load, probably due to the enhanced toughness of Kevlar fibers.

Conclusions

Results from this work indicate that the embedment of PVDF sensors in aramid/epoxy laminates affects negligibly the mechanical response of reference materials. In fact, the two specimen types (*A* and *B*) exhibited very similar three point bending strength and flexural modulus (within 3% of each other in both cases). The mechanical characterization was preceded by SEM analysis, which enabled to confirm both the possibility of successfully embedding PVDF sensors in composite laminates and the sensor's ability to withstand the composite curing temperature without experiencing significant degradations (especially depoling). The mechanical tests were monitored on-line through the use of AE. A parametric off-line analysis of the signals detected showed that different failure mechanisms have different characteristics, which can be properly studied and identified using the AE responses. Through these investigations it can be concluded that PVDF film sensors can be effectively used as acoustic emission sensors for a SHM system. However, a more in-depth investigation of AE through the use of techniques such as statistical pattern recognition is necessary. These results are nonetheless promising in view of the development of a reliable, low cost, effective and in situ damage monitoring system.

References

- H.N. Bar, M.R. Bhat, and C.R.L. Murthy (2004), *Composite Structures*, **65**, 231-237.
- H.N. Bar, M.R. Bhat, and C.R.L. Murthy (2005), *J. of Nondestructive Evaluation*, **24**, 121-134.
- Y. Bar-Cohen, T. Xue and Shyh-Shiuh Lih (1996), *NDTnet*, **1**, No.09.
- C. Caneva, I.M. De Rosa, F. Sarasini (2007), *Strain*, accepted for publication.
- M. Davidovitz, A. Mittelman, I. Roman, G. Marom (1984), *J. of Materials Science*, **19**, 377-384.
- G.T. Davis (1987), *Adv. Dent. Res.*, **1**, 45-49.
- M.A. Hamstad, G.P. Sendeckyj (1993), *J. of Acoustic Emission*, **11**, 33-41.
- M.A. Hamstad (1995), *Proc. of the 5th International Symposium on Acoustic Emission from Composite Materials*, pp. 111-119.

- I-G. Kim, H-Y. Lee and J-W. Kim (2005), *J. of Intelligent Material Systems and Structures*, **16**, 1007-1013.
- M.A. Marcus (1982), *Ferroelectrics*, **40**, 29-41.
- Measurement Specialties, Inc. (2006), "Piezo Film Sensors, technical manual," www.meas-spec.com.
- A. Mittelman and I. Roman (1990), *Composites*, **21**, 63-69.
- I. Narisawa, H. Oba (1984), *J. of Materials Science*, **19**, 1777-1786.
- I. Narisawa, H. Oba (1985), *J. of Materials Science*, **20**, 4527-4531.
- S.W. Or, H.L.W. Chan, C.L Choy (2000), *Sensors and Actuators*, **80**, 237-241.
- J-M. Park, J-W. Kong, D-S. Kim, D-J. Yoon (2005), *Composites Science and Technology*, **65**, 241-256.
- L.S. Penn and T.K. Liao (1984), *Comp. Technol. Rev.*, **6**, 134-136.
- E. Riande, R. Diaz-Calleja (2004), *"Electrical properties of polymers,"* CRC Press.
- G.M. Sessler (1981), *J. Acoust. Soc. Am.*, **70**, 1596-1608.
- H. Speckmann, R. Henrich (2004), *Proc. World Conference on NDT*, Montreal, Canada.
- R. Stiffler and E.G. Henneke II (1983), *Materials Evaluation*, **41**, 956-960.
- C. Zweben (1978), *J. of Composite Materials*, **12**, 422-430.

ACOUSTIC EMISSION SIGNALS GENERATED BY MONOPOLE (PENCIL-LEAD BREAK) VERSUS DIPOLE SOURCES: FINITE ELEMENT MODELING AND EXPERIMENTS

M. A. HAMSTAD

Department of Mechanical and Materials Engineering, University of Denver
Denver, CO 80111, USA

Abstract

Acoustic emission (AE) practitioners routinely use surface pencil-lead breaks (monopoles) to observe expected AE signal characteristics. In contrast, stress-generated AE sources are almost universally composed of dipoles. Thus, understanding the primary differences between the signals generated by these two different source classes is of key importance. This research had the goal of analyzing and contrasting the AE signals generated by monopole and dipole sources. A finite-element-modeled (FEM) database of AE signals provided an ideal means to study these two source types. The AE signals represented the top-surface out-of-plane displacement versus time from point sources inside an aluminum plate of 4.7-mm thickness. In addition, monopole sources both on the plate top surface and the edge surface were included in the database. The AE signals were obtained from both in-plane and out-of-plane monopole and dipole sources. Results were analyzed with both a bandpass filter of 100 to 300 kHz and a 40-kHz high-pass filter. The wide-plate specimen domain effectively eliminated edge reflections from interfering with the direct signal arrivals. To supplement and compare with the FEM results, experiments with pencil-lead breaks were carried out on the top surface and the edge of a large aluminum alloy plate of 3.1-mm thickness.

Keywords: Pencil-lead break, AE monopoles, AE dipoles, finite-element modeling, Lamb waves.

Introduction

A standard tool used in experimental acoustic emission (AE) studies is a pencil-lead break (Hsu-Neilsen source). The resulting signals detected at AE sensors have been characterized as similar to the real AE generated during stressing of the sample. Due to the similarity, the pencil-lead break is often used for various purposes prior to testing a sample. These purposes include: (a) wave propagation studies, including AE signal attenuation with propagation distance, (b) AE signal characterization, including the frequencies and the intensity of the different modes in the signal, (c) selection of sensors and frequency bandpasses, (d) verification of sensor coupling and normal operation of sensors and system electronics, (e) determination of typical signal propagation velocities, including “demonstration” of source location capabilities, and (f) assessment of typical signal durations. The purpose of the research presented here was to characterize both the similarities and the significant differences between pencil-lead breaks and real AE signals both by finite element modeling and experimental pencil-lead breaks. In particular, the characterization examined the relative intensity of the Lamb modes excited as well as the frequencies within the modes that carry significant energy as a function of the source type and the source orientation relative to a plate.

Pencil-lead breaks are monopoles and real AE signals are nearly all dipoles. Since the monopole pencil-lead break is normally applied to the outside of a test sample and the dipole AE sources originate from source points buried inside the sample, it is not clear how a purely experimental study might be carried out on metal samples. For the purposes of this study, the technique of finite-element modeling (FEM) of the operation of AE sources and the subsequent propagation of the waves is a way to overcome some of the difficulties of experiments alone. The FEM approach allows placement of monopoles (to simulate pencil-lead breaks) and dipoles (to simulate real AE sources) at exactly the same positions inside a test object, and it also provides a means to place monopoles on the outside surface as well. Thus, all the necessary comparisons can be made. To enhance the comparisons, the results presented here include not only the out-of-plane displacement signals, but also wavelet transform (WT) results that clearly allow Lamb modes to be identified. The WT results also show the frequencies that are excited with intensity in the modes. Finally, the study included some experiments with actual pencil-lead breaks monitored with a wideband sensor. These results were then compared to the associated FEM results.

Finite Element Modeled AE Signal Database

A small part of an existing near-field and far-field AE signal database for a 4.7-mm thick aluminum plate was used in the research reported here. This database has been described in previous publications (Hamstad et al., 2002a; 2002b; Downs et al., 2003; Hamstad et al., 2003). The validation of this FEM technique is found in a previous publications (Gary and Hamstad, 1994; Hamstad et al., 1996; Hamstad et al., 1999). The entire FEM signals were numerically processed with a 40-kHz (four-pole Butterworth) high-pass filter or a similar 100-to-300-kHz filter followed by resampling from the original time step of 44.6 ns per point to 0.1 μ s per point. These AE signals were examined out to 150 μ s after the source initiation time. This procedure avoids the plate edge reflections, which appear well after the direct signals in the large plate domain. The sources in the continuous mesh domain were either monopoles (single-cell body forces) or dipoles (self-equilibrating forces of two oppositely directed monopoles with one cell between them) using the “equivalent body force” concept for displacement discontinuities (Burrige and Knopoff, 1964). The forces were applied with a “cosine bell” temporal time dependence $T(t)$ given by:

$$T(t) = \begin{cases} 0 & \text{for } t < 0, \\ (0.5 - 0.5 \cos[\pi t / \tau]) & \text{for } 0 \leq t \leq \tau, \text{ and} \\ 1 & \text{for } t > \tau, \end{cases} \quad (1)$$

where $\tau = 1.5 \mu$ s was the source rise time. The three-dimensional cell size was 0.313 mm. The AE signals from a single node provided the out-of-plane top-surface displacement corresponding to a perfect point-contact sensor located in the zero-degree propagation direction (in-plane, x-axis direction, aligned with the in-plane source force direction) at a distance of 180 mm from the source epicenter. To directly compare the results from the two source types, they were located inside the plate at either of two different depths (0.783 or 2.037 mm) below the top surface of the plate. Two depths were chosen due to previous results (Hamstad et al., 2002b) demonstrating that in a thin plate as the source depth of a dipole moves from near the surface to near the mid-plane, the dominate AE signal mode changes from the fundamental anti-symmetrical mode, A_0 , to the fundamental symmetric mode, S_0 . Since pencil-lead breaks are normally done on an external surface, monopole sources (applied over an exterior cell face) activated on the plate top surface and the plate edge were also used. These results were used to characterize any differences between AE signals from buried monopoles compared to surface monopoles.

Wavelet Transform Information

Wavelet transform (WT) results were used to enhance the identification of the AE signal Lamb modes and to indicate highly excited frequency regions within the modes. The WT results were obtained using the AGU-Vallen Wavelet freeware (Vallen, 2005) with the key parameter settings being: maximum frequency = 700 kHz or 1000 kHz (for the experiments to account for the smaller plate thickness); frequency resolution = 3 kHz and wavelet size = 600 samples. The Wavelet Time Range Setting for the number of samples (i.e., points) was 1500 to 2048 allowing the full-direct-arrival signal to be transformed. In the color WT figures, the red color indicates the highest intensity region of the WT coefficients. In a black-and-white print out of the color results, the darkest region inside a lighter region indicates the high intensity region.

Contrasts of a Near-Surface Out-of-Plane Monopole with Dipoles

In order to most directly illustrate the similarities and contrasts between monopoles and dipoles, the point sources were typically centered at the same location in the plate when such a location was relevant. Since pencil-lead breaks normally are applied to the plate surface and/or the plate surface edges, two sections later in this paper demonstrate that the differences between monopoles buried inside the plate and those applied to the surface and/or edge can be ignored for the purposes of the results presented here. Hence, the terms pencil-lead breaks and monopoles are used interchangeably in this work. To distinguish the FEM based pencil-lead breaks from the experimental ones (near the end of this paper), references to the FEM-based pencil-lead breaks will have quotes (“PLB”) while the experimental pencil-lead breaks will not (PLB).

Figures 1 and 2 show the out-of-plane displacement signals (or AE signals) for (a) an out-of-plane monopole, (b) an in-plane dipole and (c) an out-of-plane dipole, all located 0.783 mm below the plate top surface (Note part (d) will be discussed later). Figure 1 provides the signals for a 100-to-300-kHz bandpass, and Fig. 2 has the same results for a 40-kHz high-pass filter. In each of these figures, the first region of the signal is the initial portion of the symmetrical extensional mode followed by a higher amplitude anti-symmetrical flexural mode. It is clear from all the signals shown that the signal durations do not change significantly with source type. In contrast, both of these figures demonstrate that the AE signal generated by an out-of-plane monopole is strongly dominated by the flexural, A_0 , mode as compared to the symmetric, S_0 , mode, while, the signals from dipole sources are not nearly as strongly dominated by the flexural mode. To clarify these modal comments, Figs. 3 (100 to 300 kHz) and 4 (40-kHz high-pass) show the WT results for each displacement signal with the superimposed “modified” group velocity curves of the two fundamental modes. The “modification” was the conversion of the group velocities to time by use of the 180-mm propagation distance. The reader should note in Figs. 3 and 4 that a higher frequency portion of the S_0 mode overlaps in time the A_0 mode.

The dominance of the flexural mode in the signals from the monopole source versus that from the dipole sources can be approximately quantified by calculating the ratio formed from the maximum amplitude of the flexural region of the signal divided by the maximum amplitude of the part of extensional signal present before the first arrival of the flexural mode. For the 100-to-300-kHz signals, the ratios respectively for the out-of-plane monopole, in-plane dipole and out-of-plane dipole are about 31, 12 and 10 dB. For the 40-kHz high-pass signals the same ratios are about 37, 14 and 12 dB. It should be noted for the 40-kHz high-pass dipole signals that the peak amplitude in the flexural part of the signal is really a superposition of the A_0 mode and a smaller higher frequency part (mostly centered about 522 kHz) of the S_0 mode as is clearly shown in

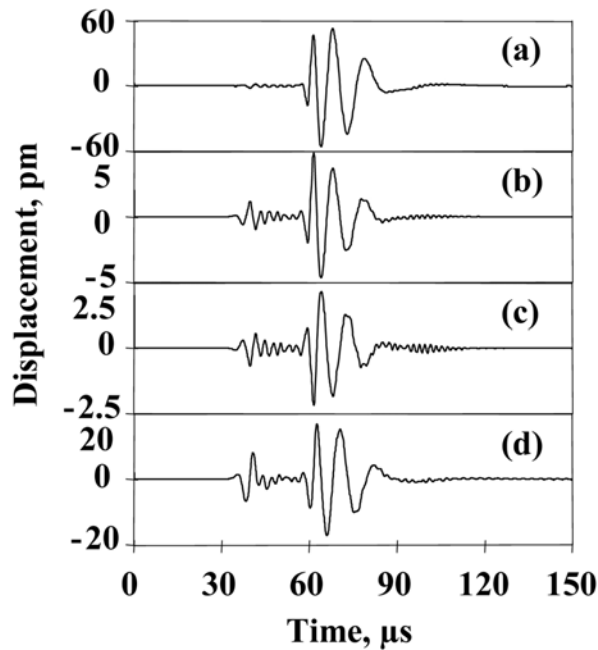


Fig. 1 Displacement vs. time, sources at 0.783 mm below the top surface and 100 to 300 kHz; (a) out-of-plane monopole, (b) in-plane dipole, (c) out-of-plane dipole and (d) in-plane monopole.

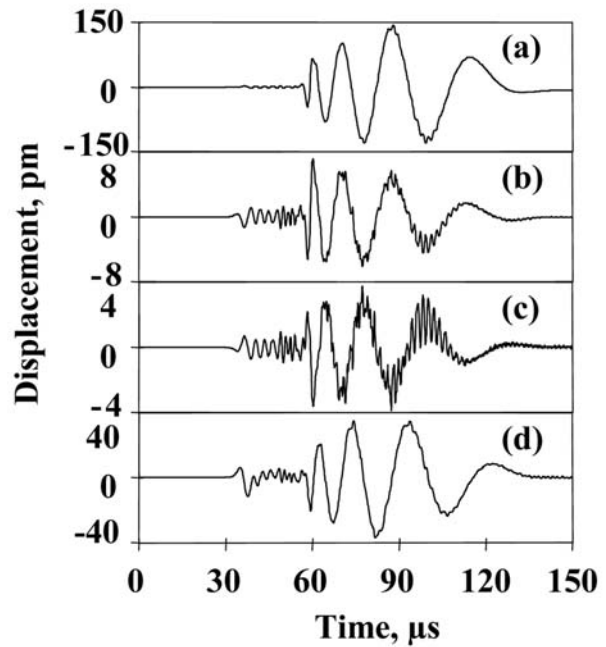


Fig. 2 Displacement vs. time, sources at 0.783 mm below the top surface and 40-kHz high-pass; (a) out-of-plane monopole, (b) in-plane dipole, (c) out-of-plane dipole and (d) in-plane monopole.

parts (b) and particularly (c) of Fig. 2 and in the corresponding WT results shown in Fig. 4. The ratios show for either frequency range the dominance of the flexural mode in the out-of-plane monopole generated signal is about an order of magnitude stronger than for the dipole-based signals.

Contrasts and similarities between signals from a *near-surface* (0.783 mm) out-of-plane monopole and those from buried dipoles close to the midplane at a depth of 2.037 mm below the plate top surface are shown respectively in Figs. 5 (100 to 300 kHz) and 6 (40-kHz high-pass) in parts (a), (b) and (c) (Note part (d) will be discussed later). As was done above, the analysis that follows compares signals from the dipoles with those from an out-of-plane monopole (part (a)) located near the plate surface (referred to as an out-of-plane surface “PLB”, to keep this fact in the readers mind), since most experimental works apply out-of-plane PLBs on the plate surface. As before, the signal durations are very similar for the dipoles and the out-of-plane “PLB”. The 100-to-300-kHz bandpass results (Fig. 5 (a) to (c)) show an even larger difference between the “PLB” signal and the dipole signals than was present when the dipoles were near the plate top surface. With dipoles near the plate midplane, the same peak amplitude ratios for the in-plane dipole and the out-of-plane dipole are respectively about -3 and -4 dB. We note again that for the dipoles, the extensional mode contributes to flexural region amplitude, and thus the ratios are not a perfect measure. Never-the-less these ratio values are in sharp contrast to the previously calculated ratio for the near-surface out-of-plane “PLB” source of 31 dB. This extremely strong modal-dominance difference is also seen in the corresponding WT results when part (a) of Fig. 7 is compared with parts (b) and (c). In these figures, it is clear that both fundamental Lamb modes are present in the dipole-generated signal results, while only the flexural mode has significant intensity in the “PLB” case. To summarize, these results show that the 100-to-300-kHz AE signals from the near-midplane dipoles are dominated by the extensional mode, in particular the

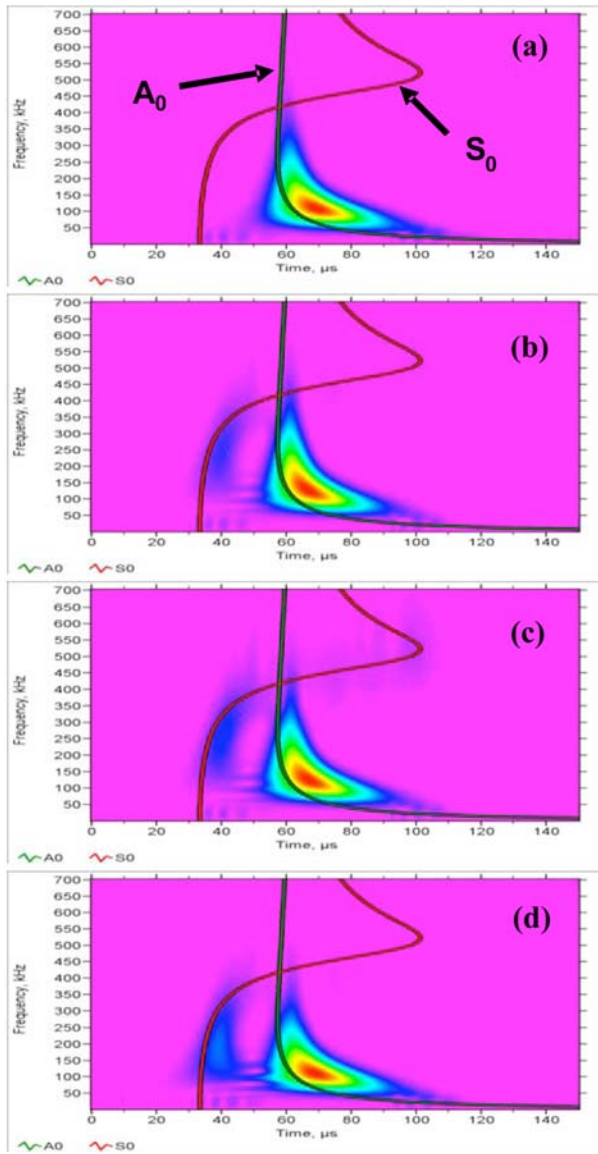


Fig. 3 Wavelet transforms corresponding to Fig. 1, vertical scale 0 to 0.7 MHz, horizontal scale 0 to 150 μ s, sources at 0.783 mm below the top surface and 100 to 300 kHz; (a) out-of-plane monopole, (b) in-plane dipole, (c) out-of-plane dipole and (d) in-plane monopole.

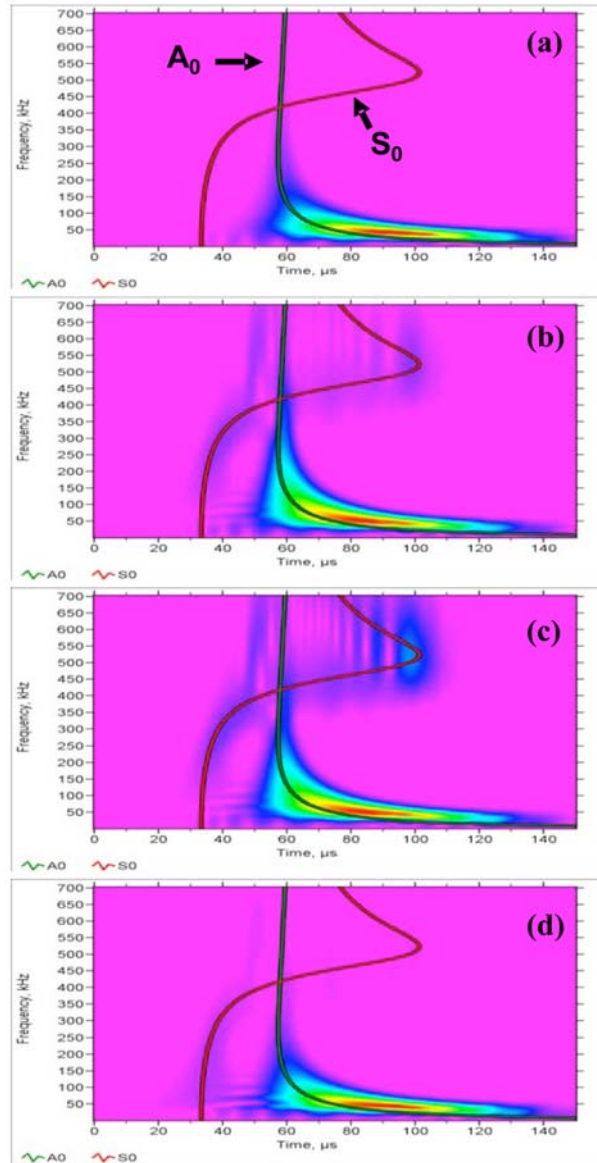


Fig. 4 Wavelet transforms corresponding to Fig. 2, vertical scale 0 to 0.7 MHz, horizontal scale 0 to 150 μ s, sources at 0.783 mm below the top surface and 40-kHz high-pass; (a) out-of-plane monopole, (b) in-plane dipole, (c) out-of-plane dipole and (d) in-plane monopole.

initial arrival of the extensional mode signal. Thus these AE type signals are very different in their dominant modes (and associated frequencies) and their relative modal intensities from the out-of-plane near top surface “PLB” signal. Even though it is not experimentally possible to carry out an out-of-plane buried PLB near the midplane of an aluminum plate, a FEM run was made for this monopole source at the 2.037 mm depth. Figure 8 shows that the signal from an out-of-plane “PLB” at a depth of 2.037 mm was nearly identical with the near surface out-of-plane “PLB” at the 0.783 mm depth.

The 40-kHz high-pass AE signals (Fig. 6) from the dipoles located near the midplane have peak amplitude ratios respectively for the in-plane and out-of-plane cases of about 9 and 13 dB.

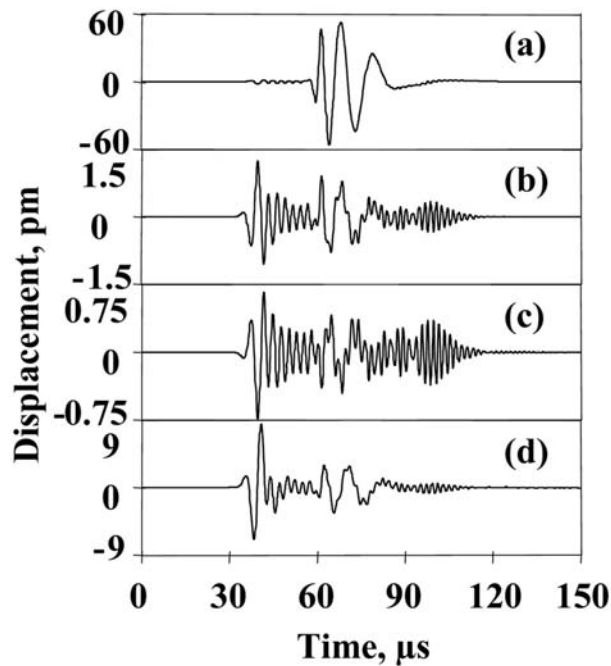


Fig. 5 Displacement vs. time, sources at 2.037 mm below the top surface and 100 to 300 kHz; (a) out-of-plane monopole (0.783 mm), (b) in-plane dipole, (c) out-of-plane dipole and (d) in-plane monopole.

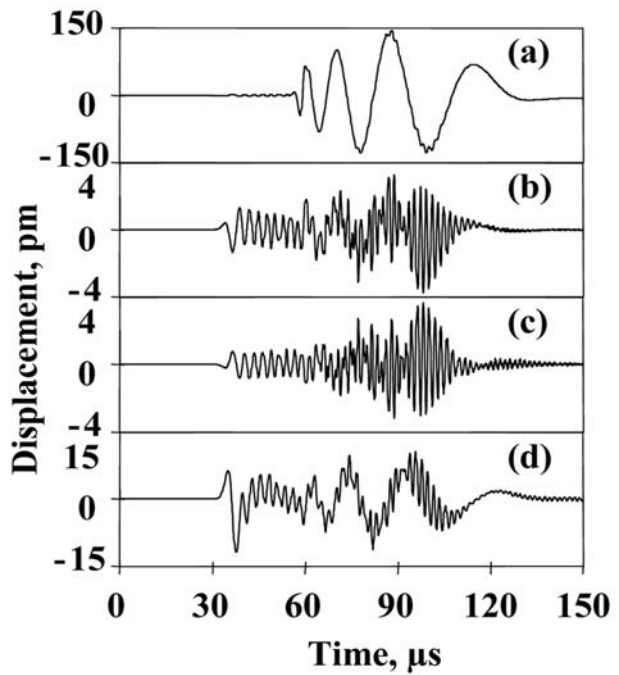


Fig. 6 Displacement vs. time, sources at 2.037 mm below the top surface and 40-kHz high-pass; (a) out-of-plane monopole (0.783 mm), (b) in-plane dipole, (c) out-of-plane dipole and (d) in-plane monopole.

Thus it appears that the flexural mode dominates, but the dominance is not as strong as the flexural mode dominance of 37-dB ratio for the monopole source near the plate top surface. Again even though the AE signal peaks for these two dipoles are in the region often associated with the flexural mode, the peak signal amplitudes are dominated by a slower group velocity and higher frequency part of the extensional mode. This extensional mode higher frequency dominance, centered about 522 kHz, is clearly seen in the displacement signals of Fig. 6(b) and (c) and in the corresponding parts of the WT results in Fig. 9 (in particular, 9(c)). So as was the case before, the ratios are not a perfect measure. But, in summary, the analysis again shows that only the signal durations are similar. In contrast, the dipoles are very different in both the relative intensities of the modes and the relative strength of the dominant frequencies in the signals as compared to the out-of-plane top surface “PLB” results.

Contrasts of an In-Plane Monopole and Buried Dipoles

Since in-plane PLBs can be made on the edge surface of a plate, this section examines comparisons between signals from in-plane monopoles and dipoles each at the two source depths (Note PLBs can be done at multiple depths below the plate top surface on an edge). In part (d) of Figs. 1-7 and 9, the AE signals or WTs of the signals from an in-plane monopole were included. As is clear from the AE signal from the in-plane monopole in Fig. 1(d) (100-to-300-kHz band-pass), its AE signal is much more similar with respect to relative modal intensities to the two dipole-based signals at the same 0.783 mm depth than the out-of-plane monopole generated signal in part (a) of Fig.1. The ratios of the peak amplitude of the flexural region to that of the extensional region are 6.5, 12 and 10 dB respectively for the in-plane monopole, in-plane dipole and out-of-plane dipole. These dipole ratios are much closer to the in-plane monopole than was the case for the out-of-plane “PLB”. The WT results (100 to 300 kHz) for these three cases, in Fig. 3

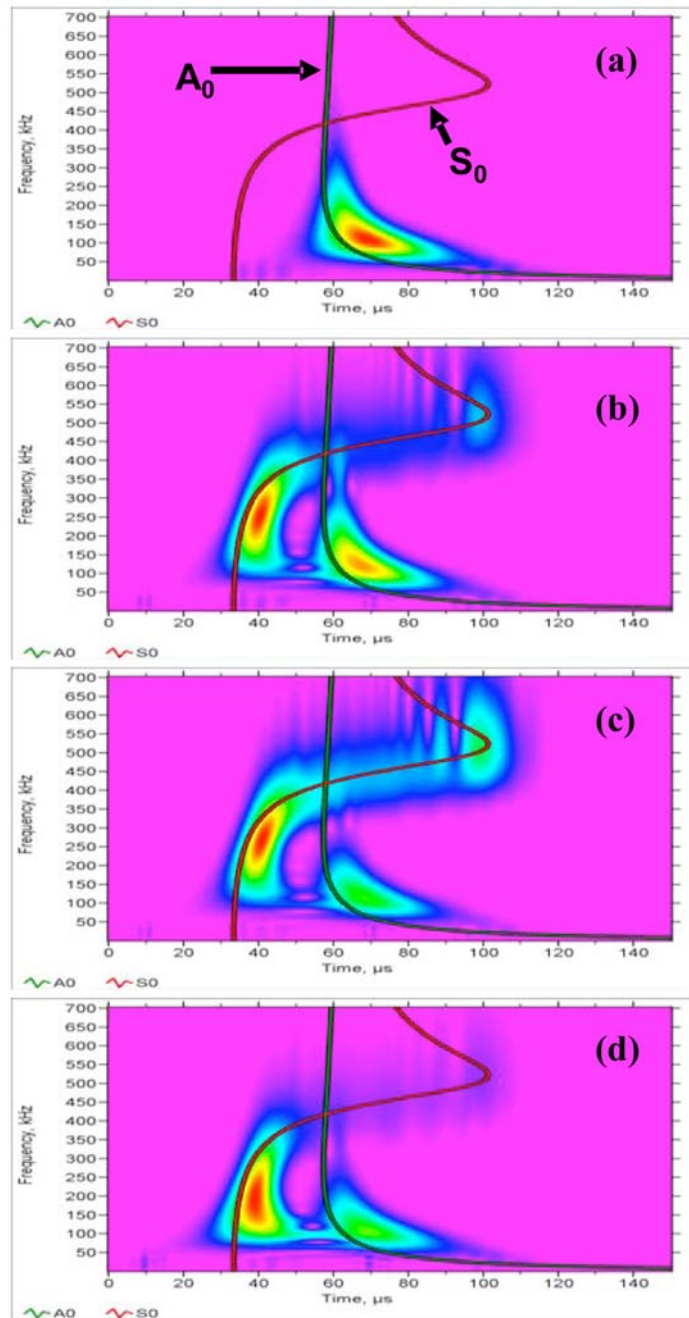


Fig. 7 Wavelet transforms corresponding to Fig. 5, vertical scale 0 to 0.7 MHz, horizontal scale 0 to 150 μ s, sources at 2.037 mm below the top surface and 100 to 300 kHz; (a) out-of-plane monopole (0.783 mm), (b) in-plane dipole, (c) out-of-plane dipole and (d) in-plane monopole.

(b) through (d), also show more similarity in the relative intensity of the two fundamental modes (and frequency regions excited) between the dipole sources and the in-plane monopole sources. This increased similarity can be seen in that the initial part of the extensional mode is apparent in the WT (blue or darker region) for all three cases, whereas for the out-of-plane monopole (Fig. 3 (a)), the initial part of the S_0 mode in the WT is not apparent compared to the highly dominate A_0 mode.

For the 40-kHz high-pass signals from the sources at the 0.783 mm depth, analysis of Figs. 2 (b) through (d) shows that the signal from the in-plane monopole at this depth does have a more

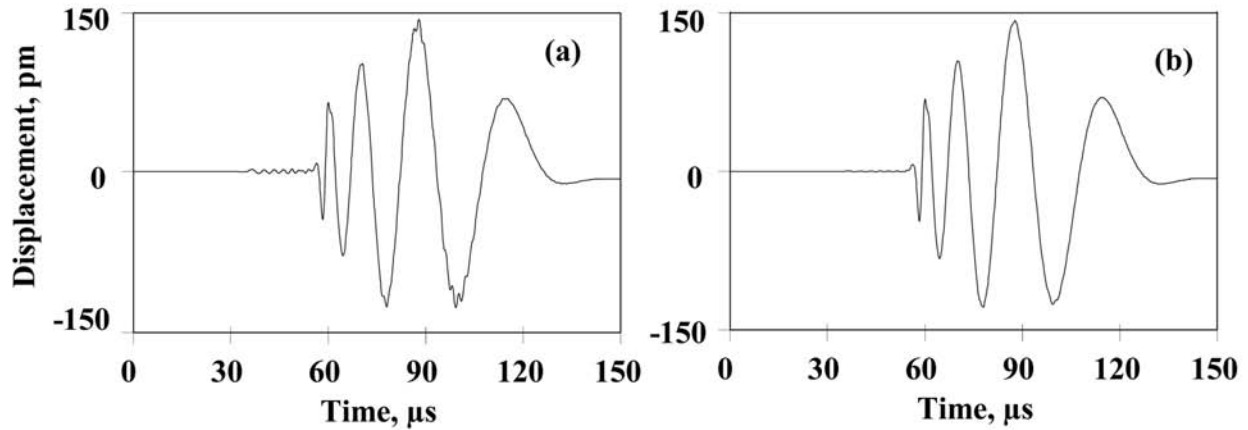


Fig. 8 Displacement versus time for 40-kHz high pass signal after propagation of 180 mm, out-of-plane monopoles at (a) 0.783 mm and (b) 2.037 mm below the top surface.

favorable ratio between the intensities of the two modal regions than the signal from the out-of-plane monopole (a). For these wideband signals the corresponding peak amplitude ratios are 10, 14 and 12 dB respectively for the in-plane monopole, in-plane dipole and the out-of-plane dipole. Now the monopole signal modal intensity ratio is very close to the dipole signal ratios. But as is clear from the corresponding WT results in Fig. 4, the in-plane monopole signal (d) does not fully represent the higher frequency and later arrival parts of the S_0 mode of the dipoles (see (b) and (c)). Also, it should be noted in Fig. 2 that the higher frequency and slower part of the extensional mode for the two dipole sources is clearly more intense than the in-plane monopole (see superimposed higher frequency near the end of the flexural mode in the dipole AE signals (b) and (c)). This fact is particularly true for the out-of-plane dipole source, where the flexural region signal has significant energy in both the flexural mode and the extensional mode.

When both the in-plane monopole and the dipoles are centered near the plate midplane at 2.037 mm below the plate top surface, Figs. 5 (AE displacement signals) and 7 (corresponding WTs) show for the 100-to-300-kHz bandpass that the in-plane “PLB” is again considerably more similar in relative modal intensity to the dipoles at the same depth than the near-surface out-of-plane “PLB”. For this frequency range, the corresponding peak amplitude ratios are about -8, -3 and -4 dB, respectively, for the in-plane monopole, in-plane dipole and the out-of-plane dipole. The only missing region in the in-plane monopole signal is that for the high-frequency part of the extensional mode. This later observation can be clearly seen in the WT shown in Fig. 7 part (c) versus part (d) for the out-of-plane dipole and in-plane monopole, respectively. Note that this high-frequency region is apparent for the out-of-plane dipole in spite of the filter.

At the 2.037-mm depth, the 40-kHz high-pass results are shown in parts (b) through (d) of Figs. 6 (AE) and 9 (corresponding WTs). The ratios, which correspond to those pointed out above for the 100-to-300-kHz bandpass, are -0.5, 9 and 13 dB. Thus, with this frequency range, the ratio of the two modal amplitudes for the in-plane monopole is not as close to that of the dipoles as it was for the bandpass data, but it is much closer than the ratio for the out-of-plane monopole (near the top surface). It is also again clear (at this source depth) in the flexural region of the dipole-based signals that the high-frequency part of the extensional mode dominates, while for the in-plane “PLB” signal this higher-frequency region is present but not dominant. Instead, the initial arrival of the “PLB” S_0 mode weakly dominates compared to that portion for the dipoles, and the latter part of the monopole-generated signal is more dominant compared to the dipole-generated signals. In summary, Fig. 9 (d) for the in-plane monopole source shows all the

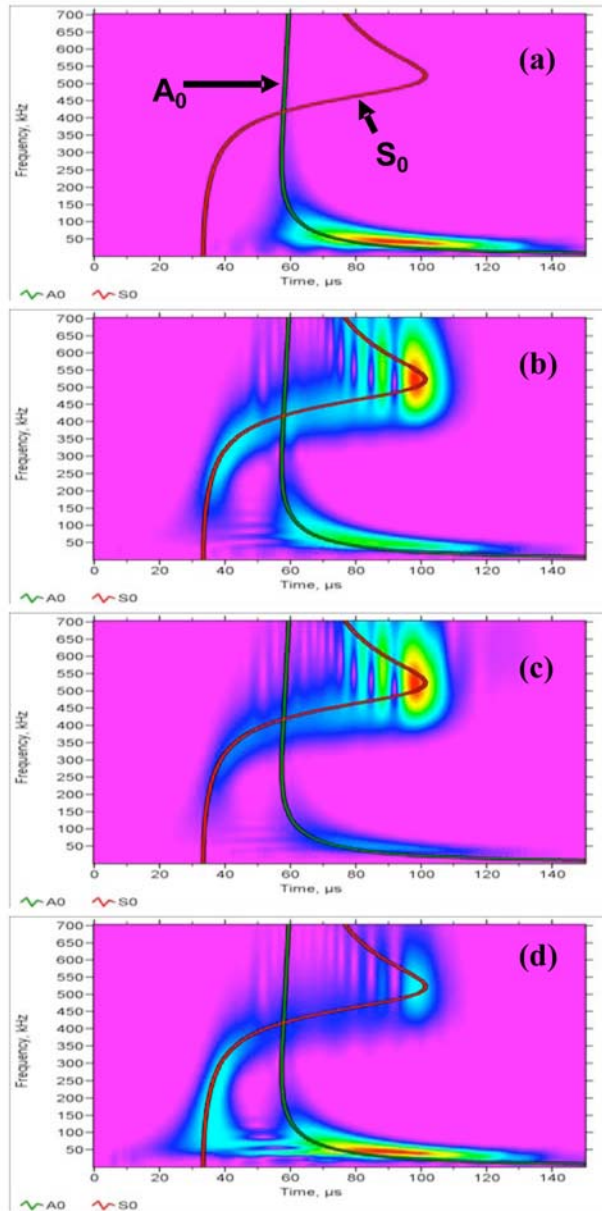


Fig. 9 Wavelet transforms corresponding to Fig. 6. Vertical scale 0 to 0.7 MHz, horizontal scale 0 to 150 μ s, sources at 2.037 mm below the top surface and 40-kHz high-pass. (a) out-of-plane monopole (0.783 mm), (b) in-plane dipole, (c) out-of-plane dipole and (d) in-plane monopole.

modal regions that appear in the dipole source cases. The intensity of the in-plane monopole signal varies in some regions of the modes relative to that of the dipole signals. But, the in-plane “PLB” corresponds much more closely to the dipole generated signals than those from the out-of-plane “PLB”.

Differences between Surface and Below-Surface Out-of-Plane Monopoles

To establish the relevance of the previous sections to PLBs, we next show that there are minimal differences between the signals from an out-of-plane monopole source on the plate top surface and the same source located a small distance below the top surface of the plate. Figure 10 shows the comparison of the out-of-plane displacement signals at a propagation distance of 180 mm for the out-of-plane top surface monopole (a) versus one located at 0.783 mm below the

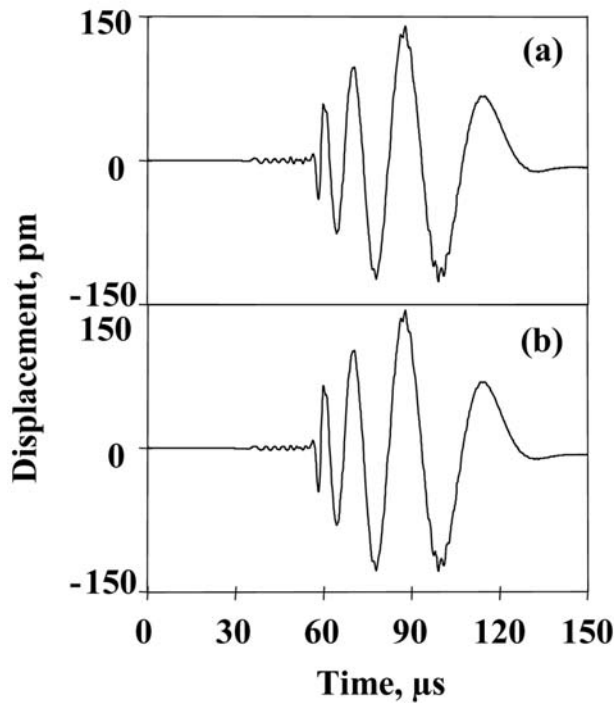


Fig. 10 Displacement vs. time. Source out-of-plane monopole, 40-kHz high-pass; (a) source located on top surface of plate, (b) located at a depth of 0.783 mm below the top surface.

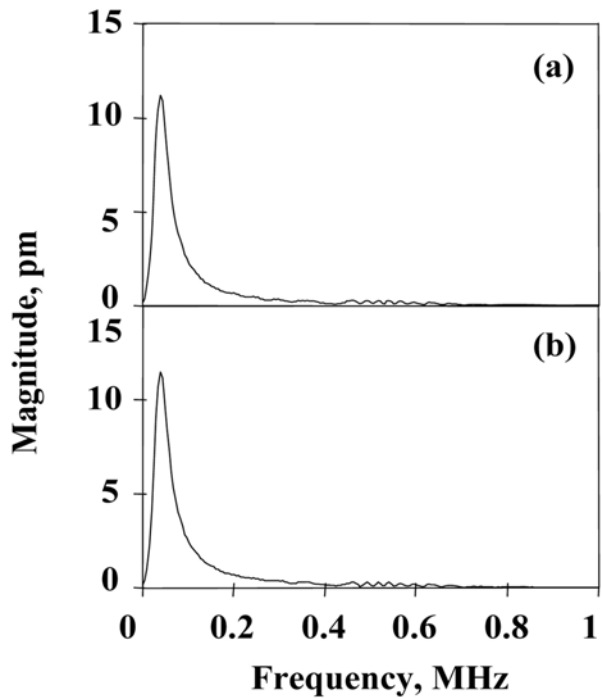


Fig. 11 Spectral magnitude of corresponding signals in Fig. 10; (a) source located on top surface of plate, (b) located at a depth of 0.783 mm below the top surface.

surface (b). These results for 40-kHz high-pass filter data are nearly identical for each source position. The spectra for these signals were also calculated and are nearly identical as illustrated in Fig. 11. Thus, the earlier assertion that using the buried out-of-plane monopole at 0.783 mm to be representative of a PLB on the top surface was valid.

Differences between Edge Surface and Buried In-Plane Monopoles

For the in-plane monopole, Fig. 12 shows that the surface edge source location gives essentially the same modal distribution of signal energy as the same source buried and located transversely near the middle of the large plate. In this comparison, we have chosen to show the similarity by use of the WT of the 40-kHz high-pass displacement signals for the edge surface versus the buried source. Figure 12 shows the results for a source depth of 0.783 mm below the top surface, and Fig. 13 shows the same type of presentation of the results for the two in-plane monopoles at a depth of 2.037 mm. In these figures the maximum color scale of the WT result was set at 70 % instead of the WT program default of 100 % to better illustrate the distribution of signal energy. It is clear in Figs. 12 and 13 that at the 180-mm propagation distance, the same regions of the same modes are present with slightly different intensity for both source positions. Thus again it was valid to use buried in-plane monopoles to represent edge surface PLBs. But for the in-plane monopole case, the reader should note that there are *significant changes in the modal distribution of energy as the depth along the edge of the in-plane monopole or PLB changes* (compare Fig. 12(a) with Fig. 13(a)).

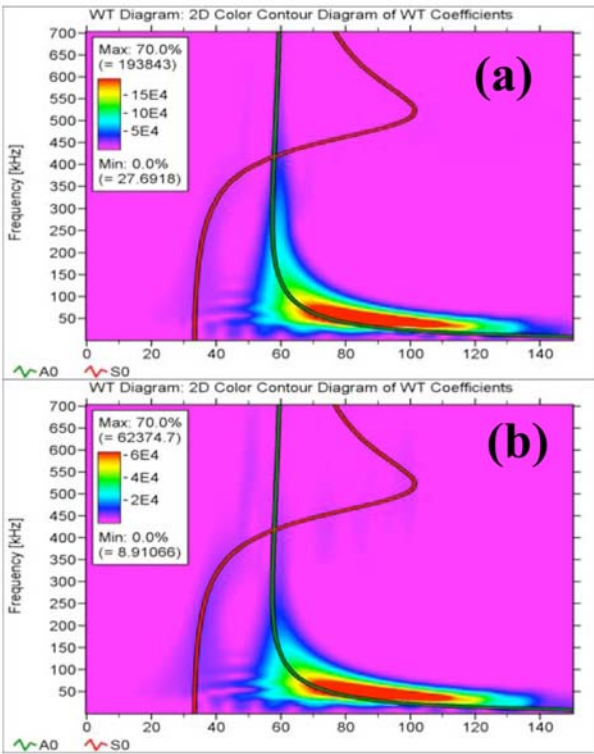


Fig. 12 Wavelet transform, source at depth of 0.783 mm below top surface.

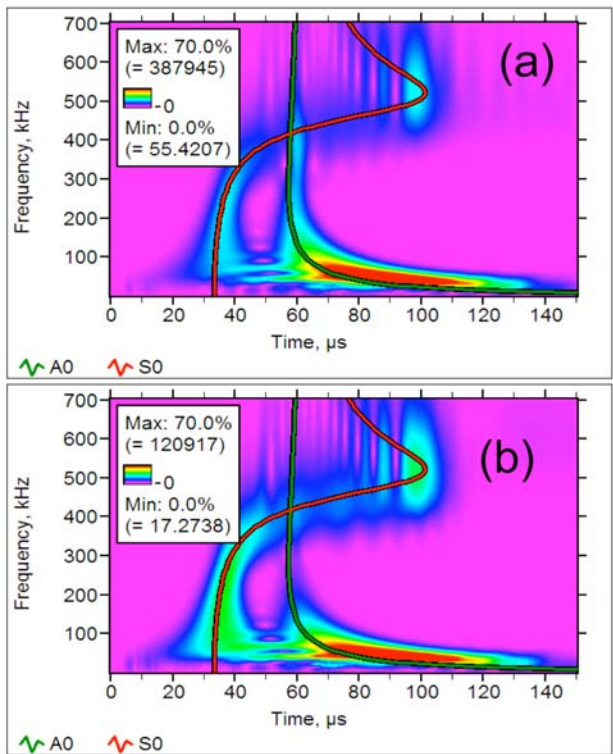


Fig. 13 Wavelet transform, source at depth of 2.037 mm below top surface.

For both figures above, source in-plane monopole, 40-kHz high-pass, vertical scale 0 to 0.7 MHz with horizontal scale 0 to 150 μ s; (a) source located on edge surface of plate, and (b) located near center of the plate (buried).

Experiments with Pencil-Lead Breaks

A large aluminum-alloy plate was used for pencil-lead breaks (PLBs) to obtain experimental results that relate to the preceding FEM results. The dimensions of the plate were 1520 mm by 1220 mm by 3.1 mm. The large transverse plate dimensions precluded reflections from the plate edges arriving at the AE sensor during the duration of the direct-path signal for the 254-mm propagation distance used in the experiments. The sensor used in these experiments had a conical sensitive element with a 1.5-mm aperture. This sensor is nearly flat with frequency (sensitive to out-of-plane displacements of the surface it is mounted on) from about 40 kHz to 1 MHz. It was developed at NIST Boulder, CO, USA (Hamstad and Fortunko, 1995; Hamstad, 1997). It has a low-noise, internal field-effect transistor, and it has a signal-to-noise ratio that is considerably better than typical commercial wideband sensors calibrated by the NIST Gaithersburg developed technique (Hamstad, 1997). The sensor was coupled to the top surface of the plate with vacuum grease, and it was spring loaded with a force of about 5 N against the plate. In these experiments a 50-kHz high-pass passive filter was used prior to recording the signals with a 12-bit digital scope at a sampling rate of 0.1 μ s per point. Pencil-lead breaks were done near the center of the plate's top surface and midway along one of the long edges of the plate. The in-plane edge PLBs were done near the plate mid-plane and near the top of the edge. The 2H lead had a diameter of 0.3 mm, and it was broken with a length of about 2 mm.

Figure 14 shows typical results for the signals from the PLBs at the three different positions: (a) top surface out-of-plane, (b) edge surface, in-plane near the top of the edge and (c) edge

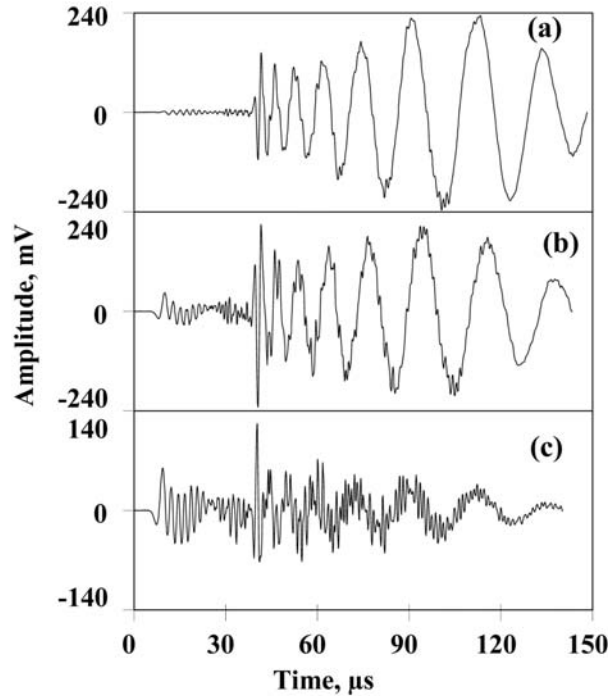


Fig. 14 Signal amplitude versus time for 0.3-mm pencil-lead breaks with 50-kHz high-pass filter after 254-mm propagation distance from the source position; (a) out-of-plane PLB, (b) near top of edge in-plane PLB and (c) edge in-plane near mid-plane PLB.

surface, in-plane near the mid-plane. In the same sequence of PLB locations, Fig. 15 shows WT results of these signals for the three different lead break positions. Qualitative comparisons of the experimental Figs. 13(a) and 14(a) with the FEM results (40-kHz high-pass) in Figs. 2(a) and 4(a) demonstrate that there is a strong dominance of the flexural mode for both top surface out-of-plane PLBs and near top surface out-of-plane monopoles.

When the PLB source was near the top surface on the plate edge, a qualitative comparison of the PLB results in Figs. 14(b) and 15(b) with the FEM (40-kHz high-pass) in-plane monopole (near the top surface) results in Figs. 2(d) and 4(d) again show that the edge in-plane PLB and the in-plane monopole signals are similar. Namely, with this position and orientation of the monopole sources, the amplitude of the extensional mode is now considerably closer to the amplitude of the flexural mode than was the case with the out-of-plane sources.

When the PLB source was near the mid-plane on the plate edge, a qualitative comparison of the PLB results in Figs. 14(c) and 15(c) with the FEM (40-kHz high-pass) in-plane monopole results in Figs. 6(d) and 9(d) again show for the two different sources similar signals result. Namely, with this position and orientation of the monopole sources, the amplitude of the extensional mode is now even closer to the amplitude of the flexural mode than was the case with the out-of-plane monopole sources and the in-plane monopole sources near the top edge. Thus, in both edge source positions (in-plane orientations), even with the differences in the plate thicknesses of the FEM data and the PLB data, the modal emphasis of the signals with an in-plane PLB source or monopole are qualitatively much more similar to dipole-type AE sources. Hence, with in-plane PLB or monopole sources, there are not the extreme differences in the relative amplitudes of the two fundamental modes as are present in the out-of-plane PLBs and out-of-plane monopoles.

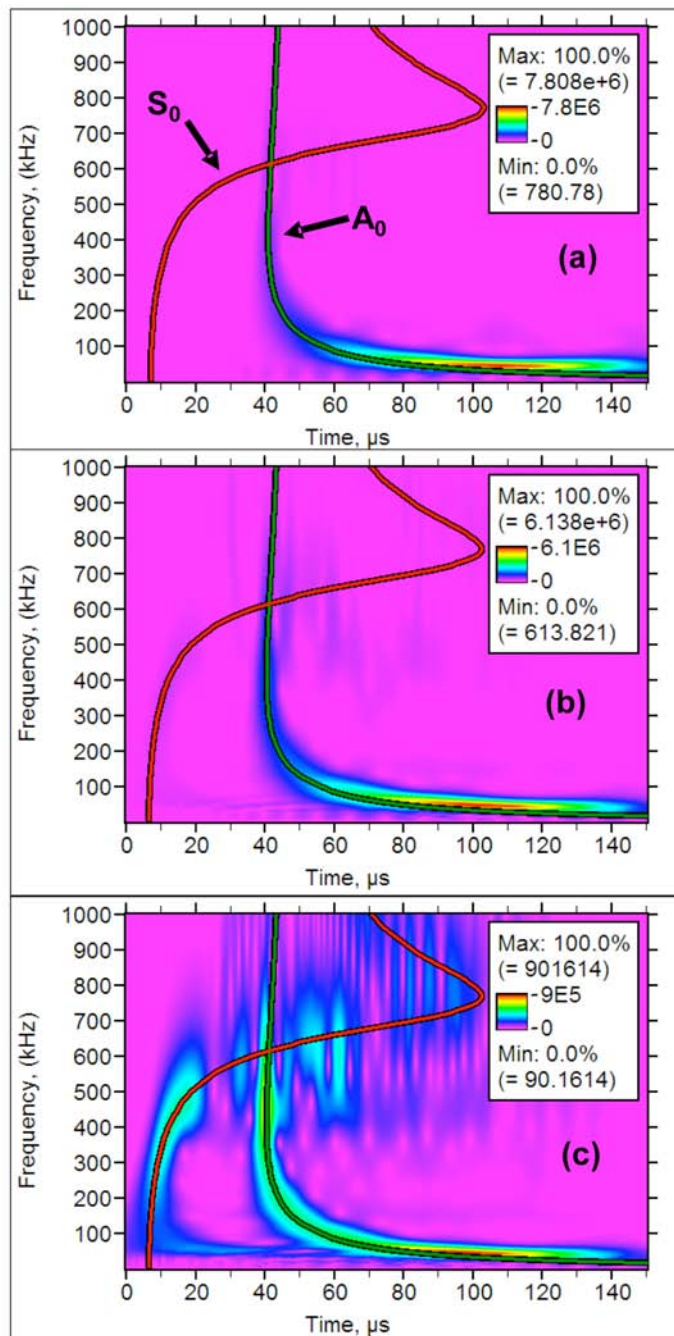


Fig. 15 Wavelet transforms with superimposed group velocities corresponding to Fig. 14; (a) out-of-plane PLB, (b) near top of edge in-plane PLB and (c) edge in-plane near mid-plane PLB.

To make the comparisons of the FEM (monopole and dipole) and PLB results more quantitative but not perfect due to changes in plate thickness, overlapping of modes (as pointed out earlier), the experimental sensor not being perfect, propagation distance differences and a small difference in the high-pass frequency of the experimental work, Table 1 was created using the 40-kHz high-pass data (modeled data) and 50-kHz high-pass (experimental data). This table shows the ratios (as was done earlier in the paper) of the flexural mode region peak amplitude divided by the peak amplitude of the extensional mode region. Clearly, in this more quantitative comparison, the trend is the same as was described above in the qualitative comparison.

To better relate these PLB and FEM monopole results to real dipole AE sources additional rows (shown in bold type) in Table 1 show the same ratios for FEM dipoles (40-kHz high-pass data) at the same positions as the monopoles. These results clearly show that the distribution of peak amplitudes of the two fundamental modes for in-plane and out-of-plane dipoles is much better simulated by in-plane edge PLBs at the two depths.

Table 1 Ratios of peak amplitudes of flexural mode region to extensional mode region.

Monopole source type	Ratio of flexural to extensional mode amplitude, dB
Out-of-plane top surface PLB	28
Out-of-plane near top surface monopole (FEM)	37
Out-of-plane dipole near top surface (FEM)	12
In-plane edge PLB near top of edge	13
In-plane monopole near top surface (FEM)	10
In-plane dipole near top surface (FEM)	14
In-plane edge PLB near mid-plane of edge	1.6
In-plane monopole near mid-plane (FEM)	-0.5
In-plane dipole near mid-plane (FEM)	9

Implications on the Use of Experimental PLBs to Simulate Real AE Sources

Based on the study done in this paper (AE signals, WTs and ratios of modal regions), the use of in-plane edge PLBs seems to be a much better choice to simulate the modal intensities of real AE signals that might be expected in thin plate or shell-type structures. This choice of PLB locations and orientations results in the simulated AE exciting both modes (and the associated frequencies) rather than just the flexural mode. The PLB testing need not be done on the real structure. Instead, it could be done on a plate or shell of the same thickness and material as the real structure. Also, the edge PLBs should include breaks with the lead position both nearer the top or bottom plate surface *and* near the mid-plane of the plate. From practical experience, this author has found that some visual magnification of the pencil-lead contact region helps to locate the lead at the desired depth.

Conclusions

- Surface “PLBs” sources on either the top surface or edge surface of a 4.7-mm thick plate are respectively well represented by interior buried out-of-plane monopole or in-plane monopole sources.
- In-plane PLB sources on a plate edge provide displacement signals with relative modal (A_0 and S_0) intensity distributions much closer to those from buried dipoles at the same depths than do surface out-of-plane PLBs.
- In-plane edge PLBs should be done both near the top or bottom edge surface *and* near the mid-plane to excite all the modal intensities (with most of their associated frequencies) of real dipole sources over this range of depths.
- Out-of-plane PLBs on a plate surface and modeled out-of-plane monopoles do not provide displacement signals with relative modal (A_0 and S_0) intensity distributions at all similar to those from buried dipoles.

Acknowledgements

The development of the finite element code by Dr. John Gary (NIST retired) and the finite element computer runs by Ms. Abbie O’Gallagher, NIST Boulder, are appreciated.

References

- Burridge, R. and Knopoff, L. (1964) “Body force equivalents for seismic dislocations,” *Bulletin Seismic Society of America*, **54**, 1875-1914.
- Downs, K. S. Hamstad, M. A. and O’Gallagher, A. (2003) “Wavelet transform signal processing to distinguish different acoustic emission sources,” *J. of Acoustic Emission*, **21**, 52-69.
- Gary, John and Hamstad, Marvin (1994) “On the far-field structure of waves generated by a pencil-break on a thin plate,” *J. of Acoustic Emission*, **12**, (3-4), 157-170.
- Hamstad, M. A., Gary, J. and O’Gallagher, A. (1996) “Far-field acoustic emission wave by three-dimensional finite element modeling of pencil-lead breaks on a thick plate,” *J. of Acoustic Emission*, **14**, (2) 103-114.
- Hamstad, M. A. and Fortunko, C.M. (1995) "Development of practical wideband high fidelity acoustic emission sensors," *Nondestructive Evaluation of Aging Bridges and Highways*, Steve Chase, Editor, Proc. SPIE 2456, pp. 281-288.
- Hamstad, M. A. (1997) "Improved signal-to-noise wideband acoustic/ultrasonic contact displacement sensors for wood and polymers," *Wood and Fiber Science*, **29**. (3), 239-248.
- Hamstad, M. A., O’Gallagher, A. and Gary, J. (1999) "Modeling of buried acoustic emission monopole and dipole sources with a finite element technique," *J. of Acoustic Emission*, **17**, (3-4), 97-110.
- Hamstad, M. A., O’Gallagher, A. and Gary, J. (2002a) “Examination of the application of a wavelet transform to acoustic emission signals: part 1 source identification,” *J. of Acoustic Emission*, **20**, 39-61.
- Hamstad, M. A., O’Gallagher, A. and Gary, J. (2002b) “Examination of the application of a wavelet transform to acoustic emission signals: part 2 source location,” *J. of Acoustic Emission*, **20**, 62-81.
- Hamstad, M. A., Downs, K. S. and O’Gallagher, A. (2003) “Practical aspects of acoustic emission source location by a wavelet transform,” *J. of Acoustic Emission*, **21**, 70-94 and A1-A7.
- Vallen, J. (2005) “AGU-Vallen Wavelet transform software version R2005.1121,” Vallen-Systeme GmbH, München, Germany. Available at <http://www.vallen.de/wavelet/index.html>.

HIGH-TEMPERATURE ACOUSTIC EMISSION SENSING USING ALUMINUM NITRIDE SENSOR

HIROAKI NOMA, TATSUO TABARU, MORITO AKIYAMA, NORIKO MIYOSHI,
TOMO HARU HAYANO* and HIDEO CHO*

Measurement Solution Research Center, National Institute of Advanced Industrial Science and
Technology (AIST), 807-1 Shuku, Tosu, Saga 841-0052, Japan;

* Faculty of Science and Engineering, Aoyama Gakuin University,
5-10-1, Fuchinobe, Sagamihara, Kanagawa, 229-8558, Japan

Abstract

We developed a heat-resistant acoustic emission (AE) sensor using AlN thin films and detected AE signals from molten-salt attack of Type-304 stainless steel pipe. Aluminum nitride (AlN) is a promising AE sensor element for high-temperature environment, such as gas turbines and other plants because AlN maintains its piezoelectricity up to 1200°C. Highly *c*-axis-oriented AlN thin-film sensor elements were prepared on silicon single crystals by rf magnetron sputtering. The AE sensor sensitivity increased with d_{33} and thickness of AlN elements and the heat-resistant AE sensors were developed using AlN elements with high d_{33} values and thickness of 9 μm. The sensor showed a constant sensitivity across a frequency range of 100 kHz to 1 MHz at ambient temperature. The sensor characteristics were evaluated at elevated temperatures up to 700°C. It was confirmed that the AE sensor works well up to 700°C and does not deteriorate. The AE sensor detected AE signals from frequent cracking of oxide scales produced by molten-salt attack (85% V₂O₅ + Na₂SO₄) at 700°C during cooling of the pipe.

Keywords: AE sensor, high temperature, aluminum nitride, molten-salt attack

Introduction

Plant monitoring systems are on high demand due to a series of recent accidents of power stations and chemical plants in Japan. Thus, there is the need to monitor high-temperature members in large structures. The AE method offers advantages such as observing the progress of plastic deformation and microscopic fracture in real time, locating a flaw using several AE sensors, and diagnosis capability without shutdowns. The AE method is used in a wide range of fields, including the inspection of manufactured products, monitoring the safety of structures and detecting natural disasters such as landslides [1]. The most common detection material for application in AE sensors is lead-zirconate titanate (PZT). Its Curie point, the temperature above which a piezoelectric material loses its piezoelectricity, is approximately 300°C. When an AE sensor with a PZT element is applied in high-temperature environment, a waveguide and/or a cooling device are essential and so it is difficult to measure AE correctly. Therefore, the development of a heat-resistant AE sensor that can be used above 300°C is strongly desired.

Aluminum nitride (AlN) is a piezoelectric material, which has a piezoelectric strain constant d_{33} of 5.6 pm/V [2] and an ability to maintain piezoelectricity up to 1200°C [3]. AlN is a promising material as the active element of a heat-resistant AE sensor without a cooling device. However, the polarization of AlN cannot be controlled after preparation and sintered AlN poly-

crystals exhibit no piezoelectricity. This had been a major hindrance to the commercialization of AlN piezoelectric devices. After trying several methods, we finally succeeded in making highly oriented AlN thin films by rf magnetron sputtering [4].

In our previous studies [5-7], we developed both ordinary AE sensors and heat-resistant AE sensors using the AlN elements. The sensor characteristics were evaluated at ambient temperature and at elevated temperatures. To evaluate of d_{33} and thickness of AlN elements on sensor sensitivity, AlN elements with d_{33} from 2 to 7 pm/V and thickness from 3 to 9 μm were prepared. It is confirmed that the AE sensor sensitivity increased with d_{33} and thickness of AlN elements [7]. The sensitivity of the heat-resistant AE sensor was also improved by a design of the sensor structure. The sensor characteristics were evaluated at elevated temperatures from 200 to 600°C. It was confirmed that the AE sensor works well at 600°C and does not deteriorate.

In this study, we developed a heat-resistant AlN AE sensor using AlN element of 9- μm thickness and Inconel-600 housing. The sensor characteristics were evaluated at elevated temperatures up to 700°C. Finally, using this AlN AE sensor, we succeeded in detecting AE signals from frequent cracking of the oxide scale produced by the molten salt attack (85% $\text{V}_2\text{O}_5 + \text{Na}_2\text{SO}_4$) at 700°C during cooling of the pipe.

Experimental Procedures and Results

Preparation of AlN Thin Films

AlN thin-film sensor elements were prepared on silicon single-crystal substrates (thickness: 0.625 mm) by rf magnetron sputtering. The sputtering conditions for the AlN thin film are reported in a previous study [4]. The thickness of AlN thin film was controlled by the sputtering time. The full width at half-maximum (FWHM) of the X-ray rocking curves of the film deposited under the optimized sputtering conditions was 2° and the film was highly oriented along the c -axis. A platinum (Pt) thin film used as the upper electrode was also prepared by rf magnetron sputtering. The crystal structure and orientation of the film were investigated by X-ray diffraction (XRD) analysis.

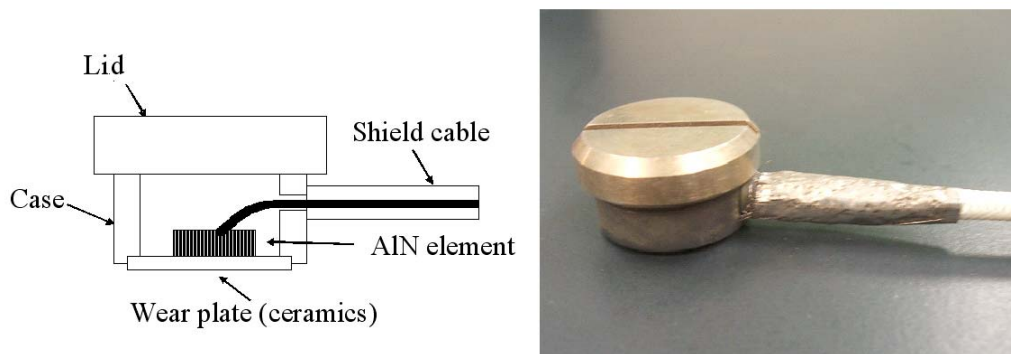


Fig. 1 Diagram and photo of a heat-resistant AlN AE sensor.

Development of Heat-resistant AlN AE Sensors

Disk-like AlN elements with 6-mm diameter were cut out from Si wafer for AE sensors. The d_{33} value of each AlN element was measured using d_{33} PiezoMeter System (Piezotest). The heat-resistant AlN AE sensors were developed using AlN element with high d_{33} values and

thickness of 9 μm . The AlN elements were selected and directly fixed to the wear plate (alumina) by Ag paste just like an ordinary AE sensor. The diagram and the photo of the heat-resistant AlN AE sensor are shown in Fig. 1. The metal housing was made of Inconel 600, which has high thermal and corrosion resistances. A heat-resistant coaxial cable was developed for connecting the sensor to a preamplifier.

Evaluation of Characteristics of AlN AE Sensor

To measure the frequency responses of the AlN AE sensor, a commercial PZT AE sensor, AE-900S-WB (NF Corporation), was used to generate quasi-AE waves. This AE sensor is a wide-band model and possesses a constant sensitivity in the range of 100 kHz to 1 MHz (± 10 dB). A preamplifier (9913, NF Corporation) with a 40-dB gain in the frequency range of 100 Hz to 20 MHz was used for the AlN AE sensor. The AlN AE sensor was fixed to the PZT sensor using an acoustic coupler, Gelsonic (Nihon Kohden Corporation). Single-cycle sine wave (V_{p-p} : 20 V) was applied to the PZT sensor and the output from the AlN AE sensor was measured and expressed in dB (the ratio of the output to the input 20 V). The frequency of the sine wave was varied from 100 kHz to 1 MHz by 10 kHz intervals.

The frequency responses are shown in Fig. 2. It showed a constant sensitivity across the range of 100 kHz to 1 MHz (± 5 dB) like the PZT commercial AE sensor. While the PZT commercial AE sensor has a damper for constant wideband sensitivity, the AlN AE sensor shows a constant sensitivity without such a damper. The thickness of AlN element is 9 μm so that the resonance frequency must be much higher than 1 MHz. That is the reason why the AlN AE sensor shows a constant sensitivity, which is an advantageous feature of this heat-resistant AlN AE sensor.

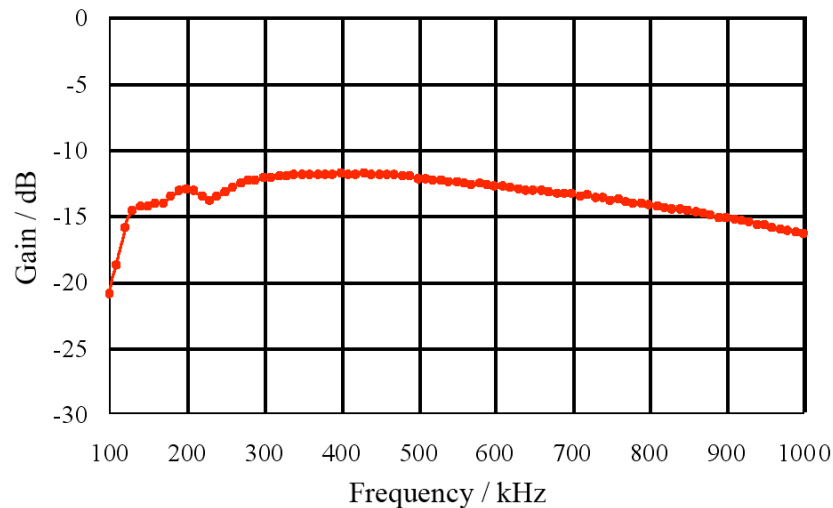


Fig. 2 Frequency responses of AlN AE sensor.

Evaluation of AlN AE Sensor at High-temperatures

Figure 3 shows a diagram of the experimental setup for AE sensor responses at elevated temperatures. A stainless steel rod (diameter: 20 mm, length 400 mm) was used as an AE waveguide, which transmitted elastic waves from the PZT sensor outside an electric furnace. The waveguide was cooled by water outside the furnace and the temperature of PZT sensor was maintained under 60°C. The responses of the AlN AE sensor were measured at ambient temperature, 200, 300, 400, 500, 600 and 700°C after keeping the AlN AE sensor at each temperature for more

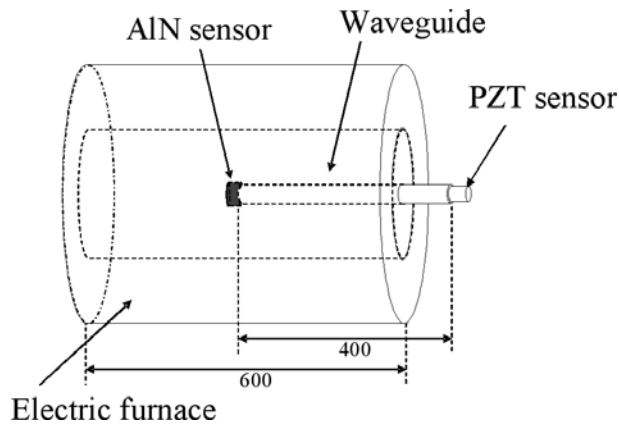


Fig. 3 Experimental setup for AE sensor responses at elevated temperatures.

than 30 min. A tone-burst of 10 sine waves was generated and the output of AlN AE sensor was observed. A preamplifier was used for the AlN AE sensor.

The AlN AE sensor was coupled using an anti-seize paste (PBC® aka polybutylcuprysil, <http://www.kspaul.de/TDB-engl/MP-PBC-engl.pdf>). This is semi-synthetic grease with metallic powders and inorganic thickener. After high temperature exposure, it became powdery, but still functioned as a couplant during cooling. The sensor was mechanically held with a ceramic spring.

Figure 4 shows a generated envelope of a tone-burst wave with 10-cycle sine waves of 200 kHz, and the response signals of the AlN AE sensor at 300, 500 and 700°C. It is confirmed that the sensitivity of the AlN AE sensor is maintained from ambient temperature up to 700°C.

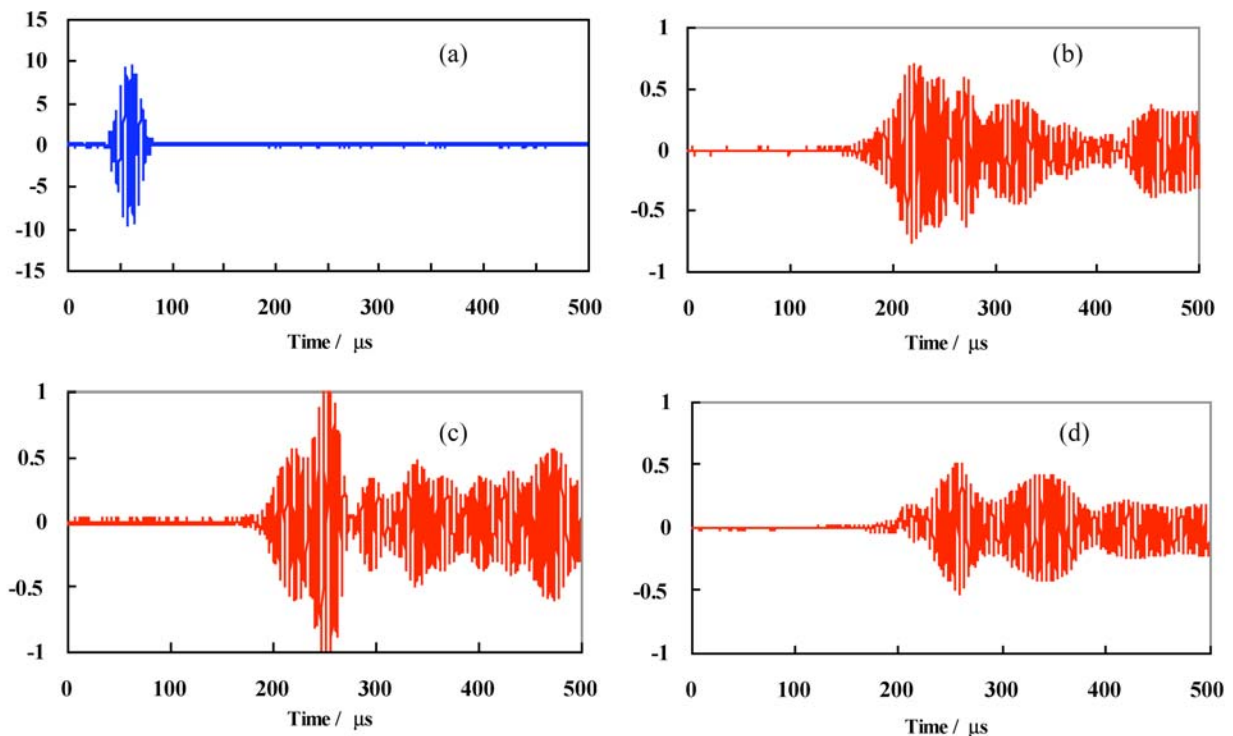


Fig. 4 Generated tone-burst wave (a) with 10 sine waves of 200 kHz and the response signals of AlN AE sensor at (b) 300°, (c) 500° and (d) 700°C.

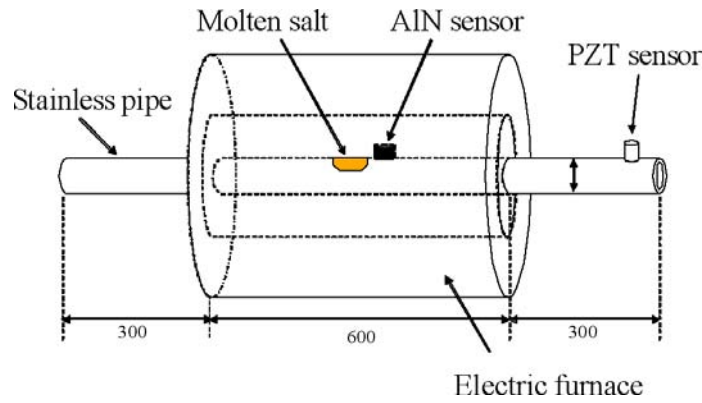


Fig. 5 Experimental setup for AE monitoring of molten salt attack.

AE Monitoring of Molten Salt Attack by AlN AE Sensor

Accelerated oxidation of heat-resistant alloys by molten salt is well known as the most dangerous damage, and often called as catastrophic oxidation. We measured AE signals by molten-salt attack (85 mol% $V_2O_5 + Na_2SO_4$) by using the AlN AE sensor. We used a similar experimental setup reported previously [8]. Figure 5 shows an experimental setup for molten-salt attack and AE monitoring method of a hot stainless steel pipe (type-304) of 34-mm diameter, 3.0-mm thickness and 1200-mm length. The PZT sensor (AE-900S-WB) was also mounted as a reference on the pipe end, where the temperature was lower than 40°C. Preamplifiers (2/4/6, PAC) with 40-dB gain were used for the AlN AE and PZT sensor. We used an AE monitoring system (PAC, DSP PCI-2). We placed 0.1 g of a mixed salt (85 mol% $V_2O_5 + Na_2SO_4$) on the upper portion of the pipe at the center of the furnace and then heated the pipe.

Figure 6 shows cumulative AE hits of the AlN sensor and temperature of the pipe in the furnace. The pipe was heated to 700°C and kept for 3 hours, then the power of the furnace was turned off and the pipe was allowed to cool. The threshold for AE hits of the AlN AE sensor was set at 10 mV. We detected few AE hits during heating and holding, but monitored frequent AE hits during cooling. The similar AE during cooling was observed in a previous study using optical fiber sensors [8]. Therefore, the AE hits must be caused by frequent cracking of the oxide

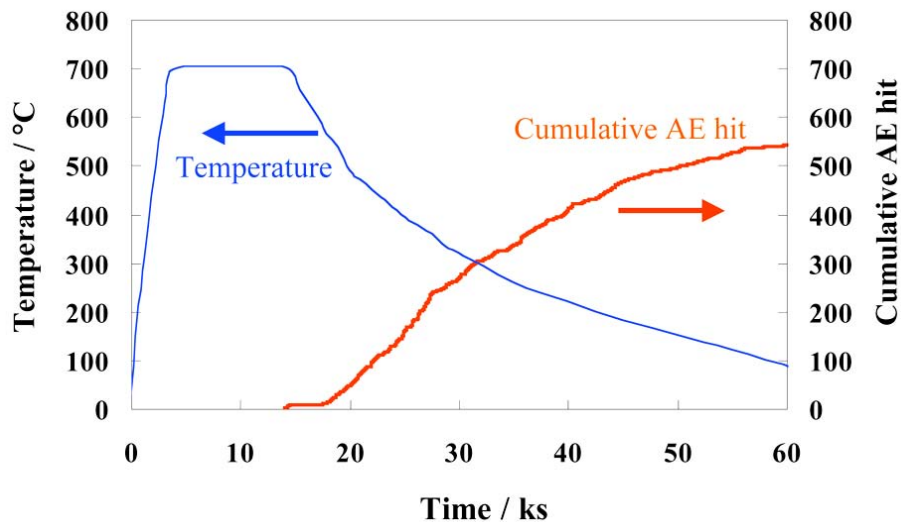


Fig. 6 Cumulative AE counts detected by the AlN AE sensor with temperature after molten-salt attack.

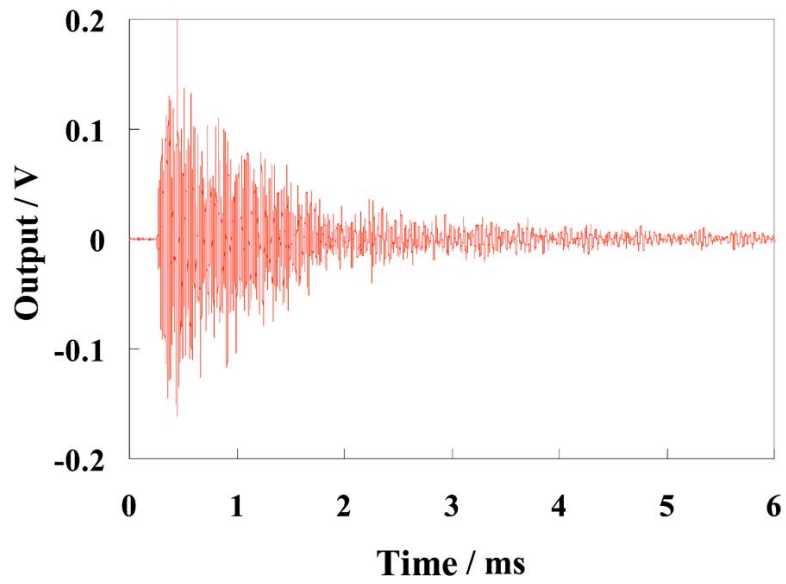


Fig. 7 Waveform of AE detected by AIN AE sensor.

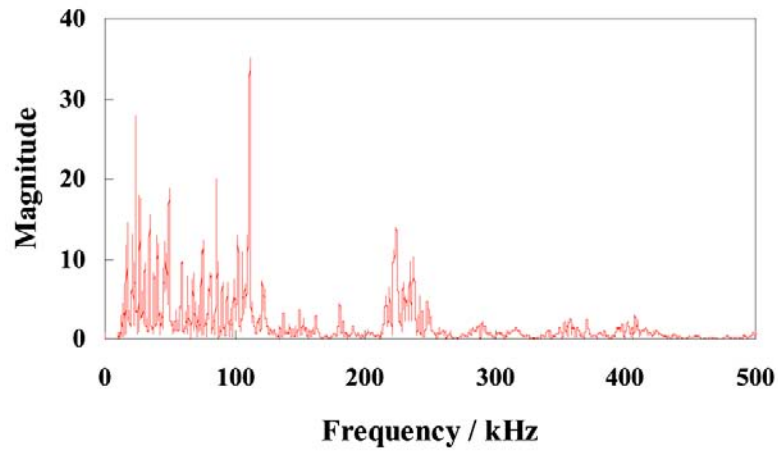


Fig. 8 FFT of waveform in Fig. 7.

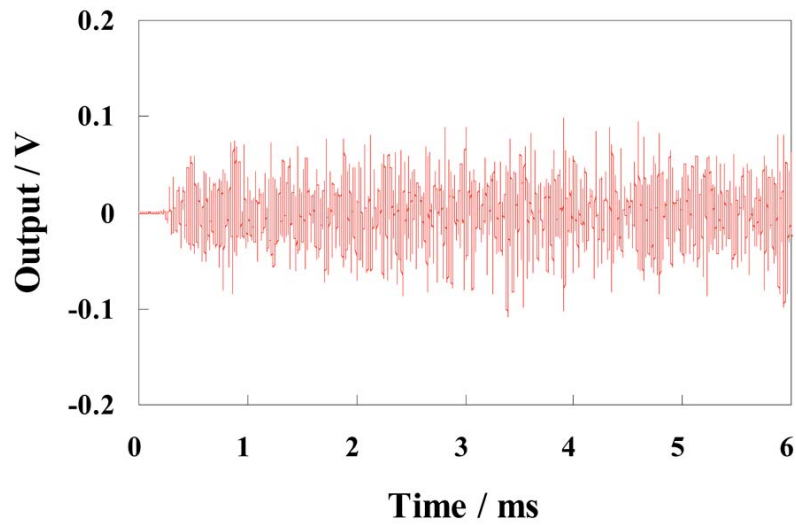


Fig. 9 Same signal as Fig. 7 by PZT sensor.

scales (and possibly salt cracks at lower temperatures) produced by the molten-salt attack during cooling of the pipe. A typical AE waveform is shown in Fig. 7. The power spectra of the AE (Fig. 8) showed many peaks below 100 kHz and a few peaks around 110, 240 and 360 kHz. The latter two appear to be due to F(1,2) and F(2,2) cylindrical waves from the cracking sources propagating on the pipe [9]. When the same signal (Fig. 7) was detected by the PZT sensor outside the furnace, the dispersion of cylindrical waves stretched the signal by several times, as shown in Fig. 9.

We have not tested for the durability on this AlN AE sensor, but it worked at 700°C for at least several hours for these experiments. The high-temperature couplant remained effective. It is confirmed that the AlN AE sensor detected AE signals from the fracture of the oxide scales produced by the molten-salt attack at 700°C during cooling of the pipe.

Summary

We developed a heat-resistant AE sensor using AlN thin films and detected AE signals from molten-salt attack of Type 304 stainless steel pipe. Aluminum nitride (AlN) is a promising acoustic emission (AE) sensor element for high-temperature environments such as gas turbines and other plants because AlN maintains its piezoelectricity up to 1200°C. Highly *c*-axis-oriented AlN thin-film sensor elements were prepared on silicon single crystals by rf magnetron sputtering. The heat-resistant AE sensors were developed using AlN elements with high d_{33} values and thickness of 9 μm . The sensor showed a constant sensitivity across a wide band of frequencies in the range of 100 kHz to 1 MHz at an ambient temperature. The sensor characteristics were evaluated at elevated temperatures up to 700°C. It was confirmed that the AE sensor works well up to 700°C and does not deteriorate for at least several hours. The AE sensor detected AE signals from frequent fractures of the oxide scales produced by the molten salt attack (85% $\text{V}_2\text{O}_5 + \text{Na}_2\text{SO}_4$) at 700°C during the cooling of the pipe.

Acknowledgment

A part of this study was supported by Industrial Technology Research Grant Program in 2004 from New Energy and Industrial Technology Development Organization (NEDO) of Japan.

References

1. A. Chichibu, K. Jo, M. Nakamura, T. Goto and M. Kamata, *Proc. 9th International Acoustic Emission Symposium*, Kobe, Japan, 1988, pp. 92-97.
2. I.L. Guy, S. Muensit and E.M. Goldys, *Applied Physics Letters*, **75**, 1999, 4133-4135.
3. R.C. Turner, P.A. Fuierer, R.E. Newnham and T.R. ShROUT, *Applied Acoustics*, 1994, **41**, 299-324.
4. M. Akiyama, C. N. Xu, K. Nonaka and T. Watanabe, *Thin Solid Films*, **315**, 1998, 62-65.
5. H. Noma, K. Kishi, N. Ueno, M. Akiyama and S. Takahashi, *The Society of Instrument and Control Engineers (SICE) 21st Sensing Forum*, 2004, pp. 51-54

6. E. Ushijima, H. Noma, K. Kishi, N. Ueno and M. Akiyama, *The 3rd U.S.-Japan Symposium on Advancing Applications and Capabilities in NDE*, Hawaii, 2005, pp. 139-142.
7. H. Noma, E. Ushijima, Y. Ooishi, M. Akiyama, N. Miyoshi, K. Kishi, T. Tabaru, I. Ohshima, A. Kakami and T. Kamohara, *Proc. 27th European Conference on Acoustic Emission Testing (EWGAE 2006)*, Cardiff, 2006, pp. 111-116.
8. T. Hayano, T. Matsuo, H. Cho and M. Takemoto, *Progress in Acoustic Emission XIII*, 2006, JSNDI, pp. 205-211.
9. H. Nishino, K. Yoshida, H. Cho and M. Takemoto, *J. Acoust. Soc. Jpn.*, **63**, 2007, 13-20.

DAMPING, NOISE, AND IN-PLANE RESPONSE OF MEMS ACOUSTIC EMISSION SENSORS

AMELIA P. WRIGHT, WEI WU*, IRVING J. OPPENHEIM and DAVID W. GREVE*

Dept. of Civil & Environmental Engineering, *Dept. of Electrical and Computer Engineering,
Carnegie Mellon University, Pittsburgh, PA 15213

Abstract

Resonant sensors for acoustic emission detection have been designed and fabricated as MEMS capacitive transducers with resonant frequencies between 100 and 500 kHz. We report four recent advances in our understanding of their mechanics and in the implications of those advances for improved sensitivity. One advance involves a successful laboratory method to seal and evacuate the MEMS device within its ceramic package, thereby operating in a coarse vacuum and reducing or eliminating squeeze film and radiation damping effects; we present characterization measurements showing an approximate fourfold increase in quality factor Q . A second advance is a summary of our theoretical analysis of noise sources for a resonant, capacitive MEMS transducer; we report that Brownian noise associated with the impact of air molecules is the major source. A third advance is the use of a grillage of beams, rather than a perforated plate, as the moving plate in the spring-mass system; we present characterization measurements showing a significant reduction in damping and therefore a higher Q . The fourth advance is a finger-type mechanism to sense in-plane motion; we show characterization measurements confirming the resonant behavior of that device and showing that the in-plane device has a much higher Q than comparable out-of-plane devices.

Keywords: Damping; in-plane motion; MEMS; sensor innovation.

Introduction

Our research group has developed a series of MEMS devices to function as resonant transducers sensitive to out-of-plane motion. Their mechanics and their use as acoustic emission sensors are most completely described in a paper by Ozevin *et al.* [1]. The transducers are fabricated in the PolyMUMPS surface micromachining process as spring-mass systems to form capacitors in which the moving plate is an elastic structure in polysilicon with a thickness of 2 μm . We typically place on each chip a suite of transducers at different frequencies in the range up to 500 kHz, placing four transducers on a 5 \times 5 mm chip or a larger number of transducers on a 10 \times 10 mm chip.

Figure 1a shows a completed four-channel AE sensor system [2, 3]. It consists of a MEMS chip, nominally 5 \times 5 mm, containing four independent transducers with resonant frequencies in the range between 126 and 500 kHz. The chip is mounted in a Spectrum Semiconductor Materials CPG06856 pin-grid array ceramic package, 26 \times 26 mm, chosen because it provides a smooth bottom surface for coupling to structural plates. The ceramic package engages a bottom PC board and Sullins 2.0 mm connectors engage a bottom PC board containing four amplifier circuits, as shown in Fig. 1a, each with a nominal gain of 100 V/V (40 dB). The whole system (apart from the cable connector) is contained in a volume of 35 \times 35 \times 30 mm.

Vacuum Sealing of a Perforated Plate Transducer

Among various mechanisms limiting the sensitivity of such transducers, the damping effect of air is very significant. Damping occurs both from acoustic radiation into the air and from squeeze-film damping as air is forced through the gap between the moving plate and stationary plate. The effectiveness of a resonant transducer is related to its sharpness of resonance, or (equivalently) to its dynamic magnification, and is commonly calculated as the quality factor Q . Operation in coarse vacuum would reduce the damping effects and increase Q , and we report a practical laboratory method for sealing and evacuating the chip in its ceramic package.

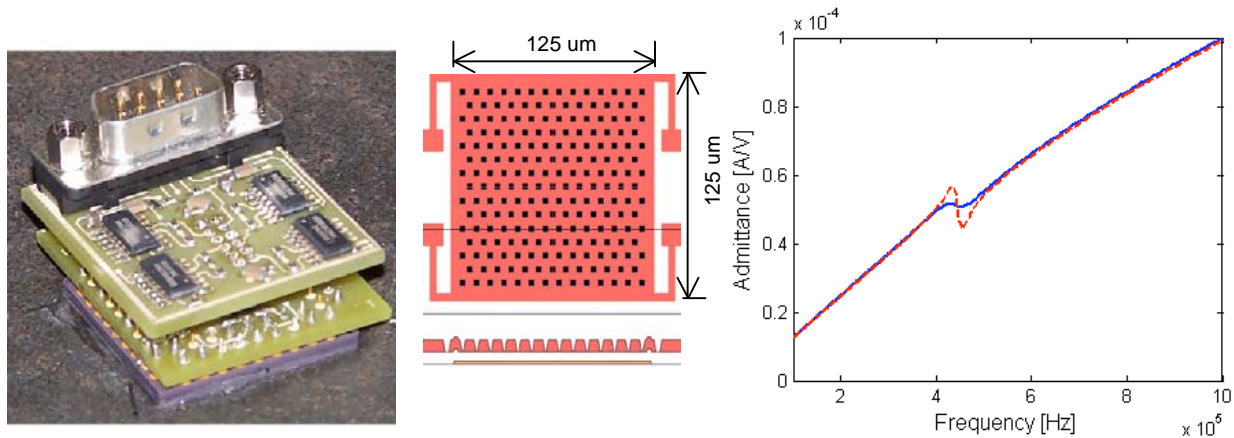


Fig. 1a. Four-channel AE sensor system in $35 \times 35 \times 30$ mm volume.

1b. CAD layout and section of one unit.

1c. Admittance at resonance, $f = 443$ kHz, $Q = 5.5$ (atmospheric), $Q = 19.7$ (evacuated).

Figure 1b is the CAD layout and section of a single unit, showing a perforated square plate ($125 \mu\text{m}$ on a side, with $3.5\text{-}\mu\text{m}$ square etch holes on a triangular grid with $8 \mu\text{m}$ between holes) suspended by four flexural springs, with a gap of $1.25 \mu\text{m}$ between the plate and the underlying stationary electrode. FEM simulation was used in selecting the flexural spring length to achieve target design frequencies between 126 and 500 kHz. Each transducer consists of 144 units (a 12×12 array) to obtain a target design capacitance near 13 pF. Figure 1c shows the admittance plot for the transducer with nominal design frequency of 500 kHz, and resonance is observed near 443 kHz. The admittance plot shows the sharpness of resonance before and after the process of sealing and evacuation. The broader resonance in Figure 1c is the admittance plot at atmospheric pressure, corresponding to a Q of 5.5.

For the different transducers (different resonant frequencies) the admittance measurements at atmospheric pressure showed Q factors ranging from 1.4 to 5.5, and the measured Q generally increased with transducer frequency, as predicted [1]. In an attempt to make the transducers more sensitive, we next developed a laboratory method to seal and evacuate the device within its package. The CPG06856 ceramic package product has a matching lid, plated with nickel and gold. In our method, a hole is drilled in the solder seal lid, the perimeter of the lid is soldered to the CPG06856 package, and a small amount of solder is dropped around the hole. The package is then moved to a vacuum chamber, within which a soldering iron can translate on a vertical axis. After the chamber is evacuated, the soldering iron is energized and the solder around the hole is melted, sealing the hole in the lid. After the solder cools, the package is removed from the vacuum chamber. This method has proven reliable and the resulting seal appears to be durable.

The sharper resonance in Fig. 1c is an admittance plot repeated 28 days after sealing, showing no loss of vacuum, and corresponding to a Q of 19.7. The increase observed in Q , approximately fourfold, is helpful in increasing the expected sensitivity of the transducer. However, it immediately raises the question, what factor is limiting the Q ? The observed Q is substantially lower than that typically observed in polysilicon resonators; for example, other researchers have built resonators in the PolyMUMPS process with a measured Q value between 300 and 550 [4]. It is likely that the observed Q is limited by imperfect coherence in the response of the 144 units that comprise the transducer. The 12×12 array occupies an area less than 2-mm square, which is small compared to the ultrasonic wavelength in steel at the frequencies (below 500 kHz) of our transducers, and therefore it is reasonable to expect that an arriving mechanical excitation will uniformly drive the units in the array. It is more likely that the 144 units do not have identical resonant frequencies. For example, the stiffness of the anchors, assumed to be rigid, will differ from the perimeter of the array to the interior, creating one source for slight deviations in the resonant frequencies. Another likely source of variation in resonant frequencies is variation in the spring constant due to the manufacturing variation in the polysilicon beam width. The effect of imperfect coherence would be a “spreading” of the aggregated peak, which appears as a broader peak in admittance measurements.

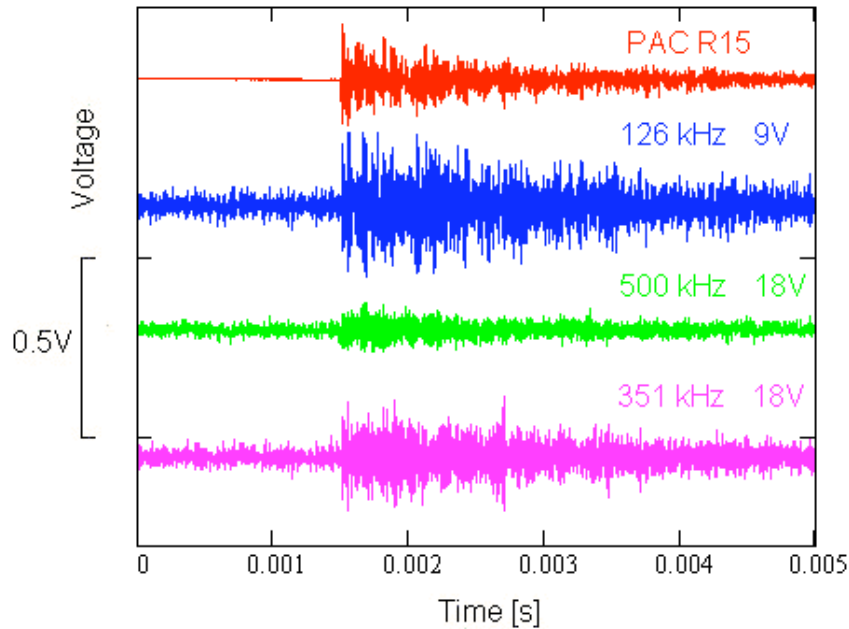


Fig. 2. Pencil lead break response, comparing three MEMS sensors to PAC R15 sensor.

We applied pencil lead breaks on a large steel plate, 9.5 mm thick, with the MEMS system (Figure 1a) and a PAC R15 sensor mounted symmetrically 20 mm from that source. Figure 2 shows the response of three sensor channels on the MEMS device, after onboard amplification, and the raw response of the PAC R15 sensor; for each MEMS channel we indicate in Figure 2 its design frequency and its bias voltage. Signal strength from the sensor channels on the MEMS device is comparable to that from the PAC R15 sensor, although the SNR is not as favorable.

Noise Analysis

We recently developed a theoretical analysis of noise sources in the electromechanical behavior of a resonant, capacitive-type transducer. We examine both Johnson noise from thermal agitation of electrons and Brownian noise from impact excitation of the moving plate by air

molecules. The RMS noise current of Johnson noise is independent of frequency (white noise) and is given by [5]

$$i_{RMS} = G\sqrt{4k_B T \Delta f / R},$$

where G is the amplifier gain, k_B is the Boltzmann constant, T is the absolute temperature, R is the resistance at the amplifier input, and Δf is the bandwidth. We determine that Brownian noise, for example as calculated by Gabrielson [6], is the other mechanism of interest. The spectral density of the squared magnitude of the force [N^2/Hz] caused by air molecules striking a suspended plate with resonant frequency ω_0 is independent of frequency and is given by [6]

$$\langle |F_B(\omega)|^2 \rangle = 4k_B T m \omega_0 / Q,$$

where m the mass of the diaphragm and $\omega_0 Q$ is the mechanical damping coefficient. The equation of motion for the displacement $x(t)$ of the diaphragm is

$$\ddot{x} + \frac{\omega_0}{Q} \dot{x} + \omega_0^2 x = \frac{F_B(t)}{m},$$

where $F_B(t)$ is the Brownian force. Taking the Fourier transform and solving for the velocity spectral density, $V(\omega) = j\omega X(\omega)$, gives

$$V(\omega) = \frac{F_B(\omega) / m}{j\omega + \frac{\omega_0}{Q} + \frac{\omega_0^2}{j\omega}}$$

from which we find for the ensemble average

$$\langle |V(\omega)|^2 \rangle = \frac{\langle |F_B(\omega) / m|^2 \rangle}{\left(\omega - \frac{\omega_0^2}{\omega} \right)^2 + \left(\frac{\omega_0}{Q} \right)^2}.$$

The current in the external circuit is related to velocity spectral density through

$$i(t) = \frac{d(CV_{DC})}{dt} = V_{DC} \frac{dC}{dt} = \frac{V_{DC} C_0}{g} v(t)$$

where V_{DC} is the applied DC bias, g the gap between plates, A the plate area, and $C_0 = \epsilon_0 A / g$ is the capacitance between the plates. Consequently, in the frequency domain

$$\langle |I(\omega)|^2 \rangle = (V_{DC} C_0 / g)^2 \langle |V(\omega)|^2 \rangle$$

and integrating over the amplifier bandwidth we have for the RMS noise current

$$i_{RMS}^2 = \frac{1}{2\pi} \left(\frac{V_{DC} C_0}{g} \right)^2 \int_0^{\omega_H} \frac{4k_B T \omega_0 / (mQ)}{\left(\omega - \frac{\omega_0^2}{\omega} \right)^2 + \left(\frac{\omega_0}{Q} \right)^2} d\omega.$$

The argument of the integral captures the dynamic response of the resonator to air molecule impact, and therefore shows a dependence upon the quality factor Q , together with the influence of amplifier bandwidth. However, if the amplifier bandwidth ω_H encloses the resonant peak, during contour integration (not shown) the upper limit of the integral can be extended to infinity. In this case, the result,

$$i_{RMS}^2 = \left(\frac{V_{DC} C_0}{g} \right)^2 \frac{k_B T}{m},$$

is almost independent of Q . Physically, increasing the resonator Q increases the velocity resulting from a particular collision. However the width of the resonance decreases with Q , resulting in an RMS noise level that is independent of Q . The noise thus consists of a frequency-independent component due to Johnson noise and a peaked component due to Brownian noise.

Table 1 shows the predicted noise voltage at the output of the amplifier for an amplifier gain of 100 V/V and in input resistor of 160 k Ω . The predicted RMS noise voltage is independent of Q . (Our devices have the same area and gap, and the only other parameter leading to a different noise prediction would be the DC bias voltage, which was 9 V for all transducers). Also shown is the measured RMS noise voltage for three transducers with an amplifier of bandwidth 800 kHz. The measured and predicted noise voltages confirm the deduction from the noise analysis, that the RMS noise voltage is independent of Q . This suggests that the performance of the transducer is limited by the combination of Brownian and Johnson noise, rather than amplifier noise and interference.

Table 1. Predicted and measured RMS noise at output of amplifier.

Frequency Measured [kHz]	Q Measured	Brownian Noise Predicted [mV]	Johnson Noise Predicted [mV]	Noise Measured [mV]
126	1.4	12	5	14
351	4.8	12	5	22
500	5.5	12	5	19

Grillage Transducer for Out-of-Plane Motions

We report on a new transducer mechanism, fabricated in 2007, an out-of-plane sensor with a design frequency of 250 kHz. The design features a moving plate constructed as a grillage rather than as a perforated plate with periodically spaced etch holes. We show characterization measurements suggesting two advantages to the grillage geometry. Capacitance measurements and FEM simulations show the grillage to approximate a whole plate in its electrical behavior, and admittance measurements show the grillage to have higher Q (lower damping) than a comparable perforated plate.

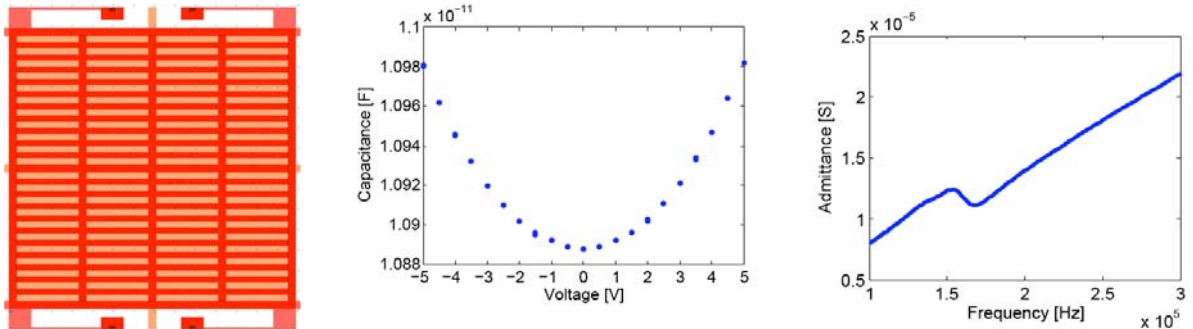


Fig. 3a. CAD layout of grillage unit for out-of-plane sensing.

3b. C - V plot, $C_0 = 10.9$ pF.

3c. Admittance at resonance, $f = 160$ kHz, $Q = 6.7$.

Figure 3a is the CAD layout of a single unit, showing a grillage (outside dimensions $138 \times 140 \mu\text{m}$) supported by four flexural springs; the beams forming the grillage are $3 \mu\text{m}$ in width, with a clear spacing of $3 \mu\text{m}$ between beams, and a gap of $1.25 \mu\text{m}$ between the grillage and the underlying stationary electrode. FEM simulation was used in selecting the flexural spring length to achieve the target design frequency of 250 kHz. The transducer consists of 72 units (a 9×8 array) to obtain a target design capacitance, C_0 , of 5.8 pF, calculated based upon the net area of the grillage. Figure 3b shows the C - V plot, referring to the capacitance as a function of applied DC voltage. A capacitive spring-mass system should show an increase in capacitance with applied DC voltage, because the electrostatic attraction force will deflect the system, reduce the gap, and thereby increase the capacitance. The C - V plot confirms the expected behavior of the transducer, but it indicates a C_0 near 10.9 pF. Subsequent FEM simulations show that the capacitance closely approximates that of the gross area of a whole plate rather than the net area of a grillage; in other words, the “cutouts” between grillage beams do not diminish the capacitance. Figure 3c shows the admittance plot in the vicinity of resonance, which is observed to occur near 160 kHz. (The difference between predicted and observed frequency is attributed to support flexibility and to fabrication deviations in the spring width.) Figure 3c depicts the sharpness of resonance, from which a Q near 6.7 is extracted. A comparable perforated plate transducer (as depicted in Fig. 1b) with a resonant frequency of 182 kHz displayed a Q near 2.0, so the grillage geometry represents substantial improvement. (Considering squeeze-film and radiation damping in air, by theory, Q will increase with frequency, and comparisons must be taken between transducers at comparable resonant frequencies.) Compared to a perforated plate, we predicted that the grillage geometry would decrease damping by permitting freer venting of the air beneath the grillage, reducing squeeze-film damping; we interpret these results as evidence qualitatively confirming that prediction.

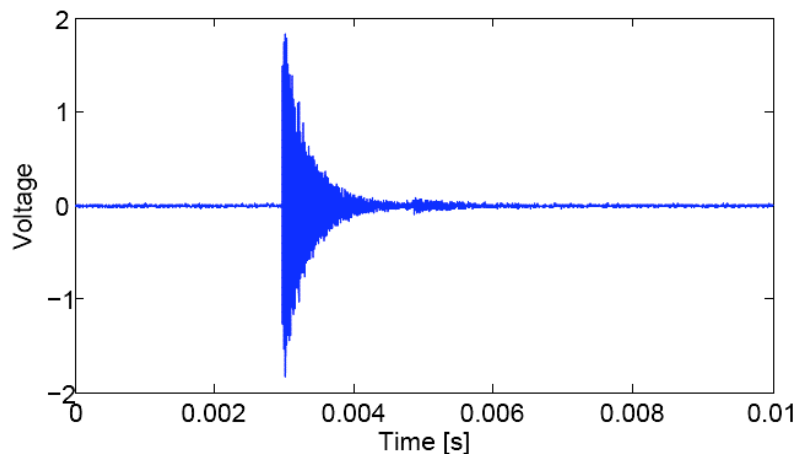


Fig. 4: Pencil lead break response of out-of-plane sensor.

Figure 4 shows the characteristic response of the out-of-plane sensor to a pencil-lead break applied directly to the ceramic package, which is consistent in appearance with the higher Q demonstrated by the device.

Finger Transducer for In-Plane Motions

Finally, we report on another new 2007 transducer, designed to sense in-plane motion. It is a finger-type (comb-type) capacitive transducer with a design frequency of 250 kHz. The predicted Q is much higher (predicted damping is much lower) than for out-of-plane sensors,

because in-plane motion mostly produces a direct shearing of air in the gap, rather than a squeeze-film or radiation actuation of the air. At the same time, squeeze-film damping in the out-of-plane direction is used beneficially to isolate the desired in-plane mechanical response from the unwanted out-of-plane response.

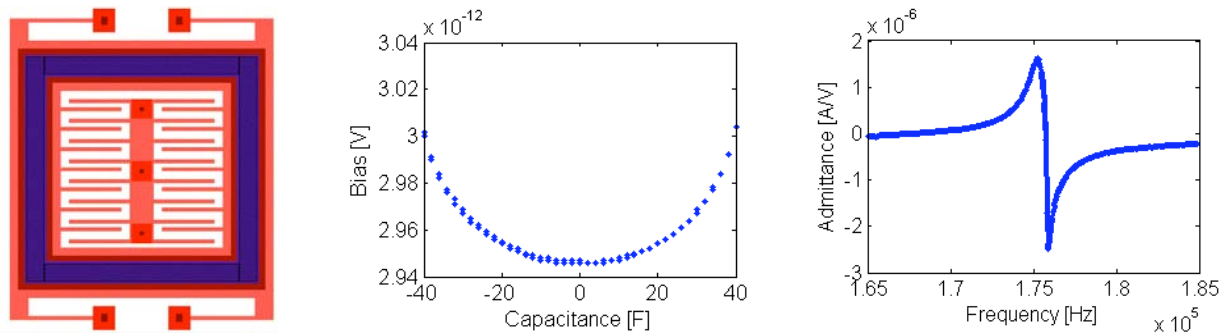


Fig. 5a. CAD layout of finger-type transducer to sense in-plane motion in the y-direction. 5b. C - V plot, $C_0 = 2.95$ pF. 5c. Admittance at resonance, $f = 176$ kHz, $Q = 197$.

Figure 5a is the CAD layout of a single unit ($128 \times 132 \mu\text{m}$) showing a stationary central spine with projecting fingers, which form capacitors in relation to fingers that project from a frame supported by four flexural springs and oriented to sense motion in the y-direction; the pitch between fingers is unsymmetrical in order to effect a change in capacitance during motion. Again, FEM simulation was used in selecting the flexural spring length to achieve the target design frequency of 250 kHz, and to calculate the predicted capacitance C_0 , which is significantly and beneficially influenced by the effects of fringe capacitance. The transducer consists of 532 units (a 19×28 array) to obtain a target design capacitance, C_0 , of 3.1 pF. Figure 5b shows the C - V plot, confirming the expected behavior of the transducer with a measured C_0 near 2.95 pF. Figure 5c shows the admittance plot in the vicinity of resonance, which is observed to occur near 176 kHz, and the sharp resonance corresponds to a Q near 197. The characterization measurements confirm the design characteristics outlined above, and suggest that the transducer may provide a practical approach to sensing in-plane particle displacements. In principle, the transducer can be fabricated on one MEMS chip together with a similar transducer orthogonal to it, along with a third transducer sensitive to out-of-plane motion, creating a sensor system responding to the three-dimensional components of particle motion.

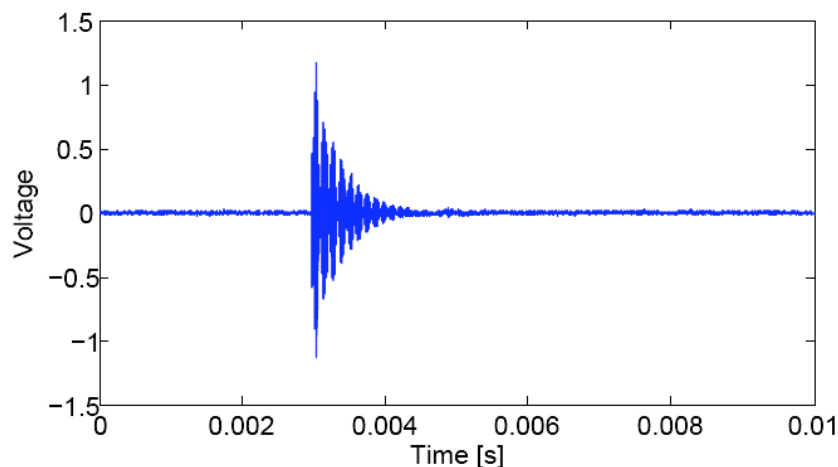


Fig. 6: Pencil-lead break response of in-plane sensor.

Figure 6 shows the response of the in-plane sensor to a pencil-lead break applied directly to the ceramic package. The beat frequency, near 8 kHz, is consistent with a slight difference in frequency between interior and exterior units in the 19×28 sensor array; that frequency difference can be explained by a small difference in their spring lengths, possibly influenced by difference in anchor rigidity. The beat effect is visible only because the in-plane device is a high- Q resonator.

Summary

We have described four recent advances in our understanding of the mechanics of capacitive MEMS transducers resonant in the range between 100 and 500 kHz. We seek to improve the sensitivity of these transducers as acoustic emission sensors, and the advances provide insights for those improvements. Among other factors, damping and noise limit transducer sensitivity, and all four advances guide us to better sensitivity. We have shown an effective laboratory approach for sealing and evacuating a device, thereby reducing the squeeze film and radiation damping effects of air. Characterization experiments show an approximate fourfold increase in quality factor Q , and response of the sensor in pencil lead break testing, after onboard amplification, is compared to the response of a commercial transducer. We have also summarized our recent theoretical analysis of noise, identifying the effective floor to result from Brownian motion and the impact of air molecules with the resonator, confirmed by our measurements. We have reported a significant reduction in squeeze-film damping, in air, when using a grillage of beams as the moving plate rather than a perforated plate with periodically spaced etch holes. Finally, we have reported our first characterization measurements of a new transducer designed to sense in-plane motion. Those results confirm its design characteristics, and show it to be minimally damped (in air) because the in-plane motion mostly produces a shearing of an air volume rather than a squeeze film or radiation excitation of the air volume.

Acknowledgements

This work is supported by the National Science Foundation, Grant CMS-0329880 entitled SENSORS: Collaborative Research: MEMS for Multi-Mode Civil Infrastructure Sensing, and by the Pennsylvania Infrastructure Technology Alliance. We gratefully acknowledge contributions of our research collaborators at Lehigh University, Professor S. P. Pessiki and Dr. D. Ozevin, who is now a Research Scientist with Physical Acoustics Corporation. The opinions, findings, conclusions, and recommendations expressed in this material are those of the current authors and do not necessarily reflect the views of the sponsors or of our collaborators.

References

1. D. Ozevin, D. W. Greve, I. J. Oppenheim, and S. P. Pessiki, Resonant capacitive MEMS acoustic emission transducer, *Smart Mater. Struct.*, **15**, 2006, 1863-1871.
2. D. W. Greve, I. J. Oppenheim, and W. Wu, Modes and Damping in Cmut Transducers for Acoustic Emission, *IEEE Ultrasonics Conf.*, 2006.
3. D. W. Greve, I. J. Oppenheim, W. Wu, and A. P. Wright, Development of a MEMS Acoustic Emission Sensor System, *SPIE Smart Structures/NDE Joint Conf.*, 2007.

4. B. Bahreyni, C. Shafai, Fabrication of Piezoresistive Sensors in Standard MEMS Foundry Processes, *IEEE Sensors Conf.*, 2005.
5. S. D. Senturia, *Microsystem Design*, Springer, 2001, 438.
6. T. B. Gabrielson, Mechanical-thermal noise in micromachined acoustic and vibration sensors, *IEEE Trans. Electron. Devices*, **40**, 903–909.

IMMERSION-TYPE QUADRIDIRECTIONAL OPTICAL FIBER AE SENSOR FOR LIQUID-BORNE AE[†]

TAKUMA MATSUO[†], HIDEO CHO, TAKESHI OGAWA
and MIKIO TAKEMOTO

Department of Mechanical Engineering, Aoyama Gakuin University,
5-10-1, Fuchinobe, Sagamihara, Kanagawa 229-8558, Japan

Abstract

Immersion-type AE sensor is needed for corrosion monitoring of underground fuel tanks. We have developed a multi-directional optical fiber AE sensor to monitor the longitudinal AE signal through liquid (liquid-borne AE). The developed AE system is an optical-fiber-based Mach-Zender-type laser interferometer using a weak laser and is intrinsically safe. Multi-sensing function was facilitated by winding an optical fiber on four small-size short hollow pipes with different diameters, which were installed on the inside walls of a box of 22.5-mm square and 230-mm height. Each sensor element was screwed on a different sidewall. The four fiber sensors were cascaded in series on a single fiber and monitored the liquid-borne AE signals from quadridirection simultaneously via frequency discrimination. As the each fiber-wound sensor element monitors at the resonant frequency of the pipe, we can estimate the direction of AE signals using their frequency spectra and wavelet transform. The functionality of the sensor was demonstrated by 50-day monitoring of liquid-borne AE signals from rust fractures on four corroded carbon-steel sidewalls of a water tank. The immersion-type quadridirectional sensor successfully monitored liquid-borne AE signals from the four corroded plates.

Keywords: Optical fiber AE sensor, intrinsically safe sensor, immersion-type sensor, quadridirectional sensor, rust fracture, parabolic law

Introduction

Integrity loss of underground fuel tanks by localized soil corrosion is becoming serious problems in Japan. Fire and Disaster Management Agency (FDMA) reports leak accidents of 344 tanks in 2001. Localized corrosion was the cause of leaks in 30% of the tanks [1].

AE technique is expected to be a useful tool for monitoring corrosion damages of the tank, however we cannot use the conventional AE system using the piezo-sensors, since the system is not intrinsically safe.

We are developing an optical fiber laser interferometer to monitor AE signals [2]. This system is composed a homodyne Mach-Zender-type laser interferometer with a phase compensation feedback circuit. The sensor of this system uses a telecommunication single-mode optical fiber. This system is intrinsically safe, immune from corrosion and electromagnetic noise. It was previously used to monitor liquid borne P-waves by immersing the sensing fiber into the liquid [3]. We have improved this sensor so it can monitor the corrosion zone or the direction of the P-waves over a long time. Here, a single sensing fiber was spirally wound on four pipes, and detected AE signals quadridirectionally.

[†] A Student Award winner at the 50th Acoustic Emission Working Group Meeting, November 2007.

We first introduce our new quadridirectional AE sensor and next AE monitoring from four plates with rust (corroded steel plate samples) for 50 days. We discuss relationship between the AE activity and corrosion of the steel with rust.

Immersion-Type Optical Fiber Sensor

A sensing box developed is shown in Fig. 1. The box was designed for underground gasoline tanks and contains four AE sensors. Box size is 22.5-mm square and 230-mm height. The top and bottom plug-plates were thick enough so that four aluminum sidewalls were screwed on with special polymer sheet as gasket. This structure can prevent the vibration interference of neighboring walls and gasoline leakage into the box. A hollow long pipe of 16-mm diameter was screwed into the top plug-plate. This pipe is used to insert the sensing box in the tank through a 32-mm diameter nozzle, and to connect the optical fiber to the monitoring system.

Sensing fiber was wound on four cap-shaped aluminum cylinders of 20-mm height (called sensor elements) each with a different diameter (8, 10, 15 or 19 mm). These elements were screwed on the sidewalls with a polymer sheet. The sensing fiber was wound on the holders multiple times. This structure improves the sensor sensitivity significantly. Four sensors were connected by a single fiber in series and connected to the monitoring system via fiber connectors. The four sensors detect the wall vibration excited by liquid-borne P-waves. Here the different resonance frequencies of four sensors are utilized to identify the direction of the P-waves. We call the sensor with 15-mm diameter element as “D15 sensor” and the entire system as ITQS (Immersion-Type Quadririrectional System), hereafter.

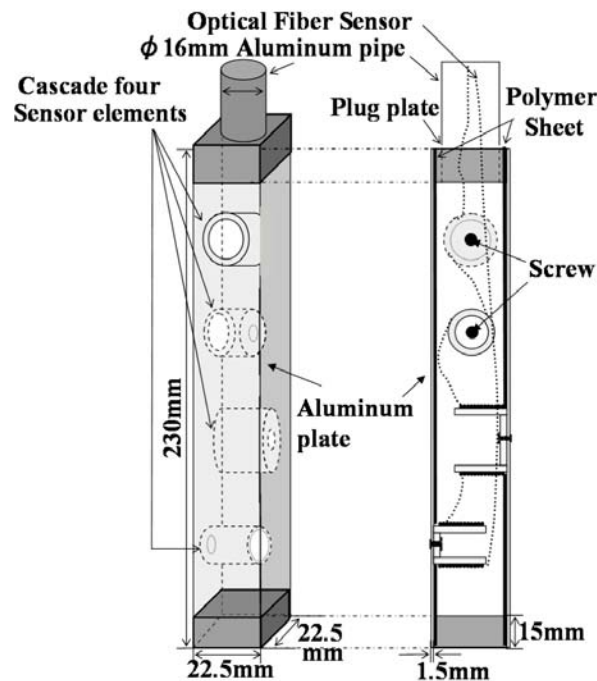


Fig. 1 Immersion-type quadririrectional AE sensor using optical fiber.

Directionality of ITQS was studied using a rectangular water container of 1220 x 700 x 250 mm. Water-borne P-wave was produced using a PZT transmitter (DE, S140B) immersed in water at 1000 mm from the ITQS. We fixed the transmitter and rotated the position of the ITQS counter-clock-wise. Here $\theta = 0^\circ$ designates that the normal of the sidewall with the D19 sensor orients to the transmitter; D10 faces the transmitter at 90° , D15 at 180° and D8 at 270° .

Figure 2 show examples of the waveforms and power spectra at $\theta=0^\circ$, 90° , 180° and 270° . These are waveforms detected by the sensor, whose sidewall faces the transmitter. Resonance frequencies of the sensors were separated with frequency separation of more than 15 kHz.

We next studied relationship between angle θ and wave amplitude. Figure 3 shows examples for the P-waves from 30° , 45° and 60° . These angles are between the D19 sensor and D10 sensor. We observed two or three wave packets. Power spectra show two higher peaks at around 42 and 95 kHz. Using the normalized amplitude profiles of two peaks of Fig. 4, we can estimate the directivity of the P-wave sensing as $\pm 30^\circ$.

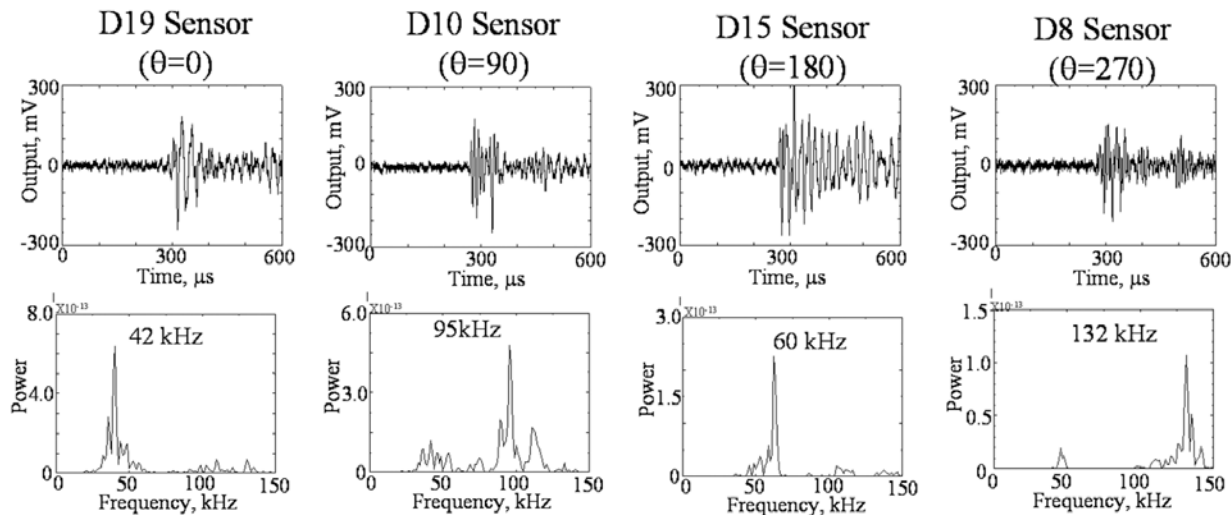


Fig. 2 Waveforms and frequency spectra of AE signals at $\theta = 0^\circ$, 90° , 180° and 270° .

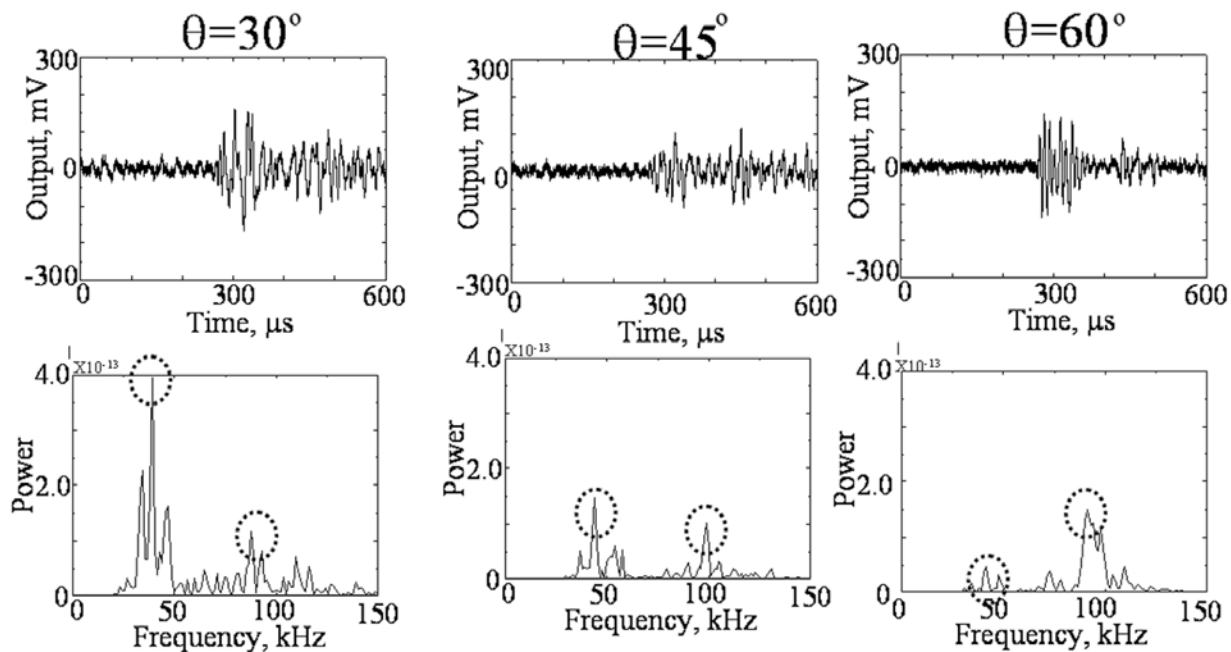


Fig. 3 Waveforms and frequency spectra of AE signals detected by ITQS at $\theta = 30^\circ$, 45° and 60° .

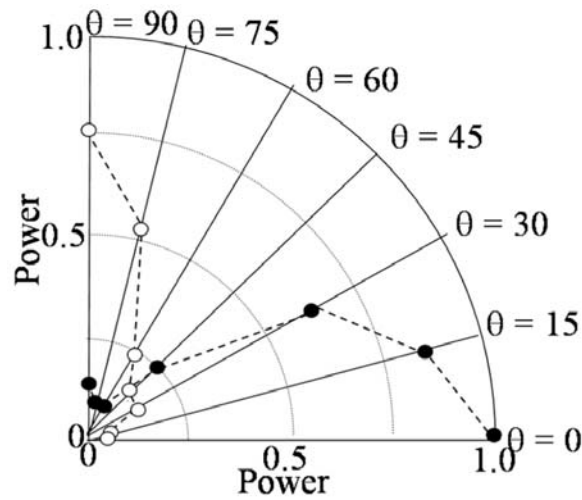


Fig. 4 Amplitude profile as a function of rotating angle of ITQS.

Monitoring of Water Borne P-wave From Rust Fracture

Experimental Setup

We monitored AE signals from rust fracture using the ITQS for 50 days. Experimental setup is shown in Fig. 5. We inserted four steel plates in the four side walls of a rectangular water container, 630 x 450 x 440 mm. Four steel plates with natural rust produced by atmospheric corrosion were taken from a tank yard in a sea coast area. As these samples have rusts on one side, the samples were placed on the sidewalls using silicone rubber sealant such that the rusted surfaces face outward. Sample size, area of rust, rust thickness and corrosion method are shown in Table 1. Rust area is different among the samples, but we used them in as-received condition, since the rust tended to separate during cutting.

These samples were further corroded in a room without air conditioning using different methods in Table 1. Sample A with the thickest rust was exposed to both thermal cycles (heating to 23°C and natural cooling to room temperature) and mist spraying of 5% NaCl solution to the rust. By coating silicone grease, other parts were not corroded. Sample B was mist sprayed with 5% NaCl solution without thermal cycles. Sample C was exposed to the thermal cycles. Thermal cycling and mist spray were not given to sample D. Here, the thermal cycles were given by turning on-off of an infrared lamp at 6-hours intervals. The mist was sprayed for 60 minutes (total spray amount 66 ml for sample A, 24 ml for sample B) at 8-hour intervals. Sample A was exposed to the severest corrosion environment and sample D to the least. These combinations were selected to simulate the corrosion condition, which each sample was supposed to be exposed.

Table 1 Specimen size, area of rust and corrosion test method.

Sample	Size (mm)	Area of rust (cm ²)	Thickness of rust (mm)	Corrosion element
A	380 ^W x370 ^H x10 ^T	247	0.30	Mist spray(5% NaCl)+ Thermal Cycle
B	100 ^W x240 ^H x4 ^T	240	0.18	Mist spray(5% NaCl)
C	80 ^W x290 ^H x6 ^T	232	0.06	Thermal Cycle
D	80 ^W x280 ^H x6 ^T	224	0.04	Room atmosphere

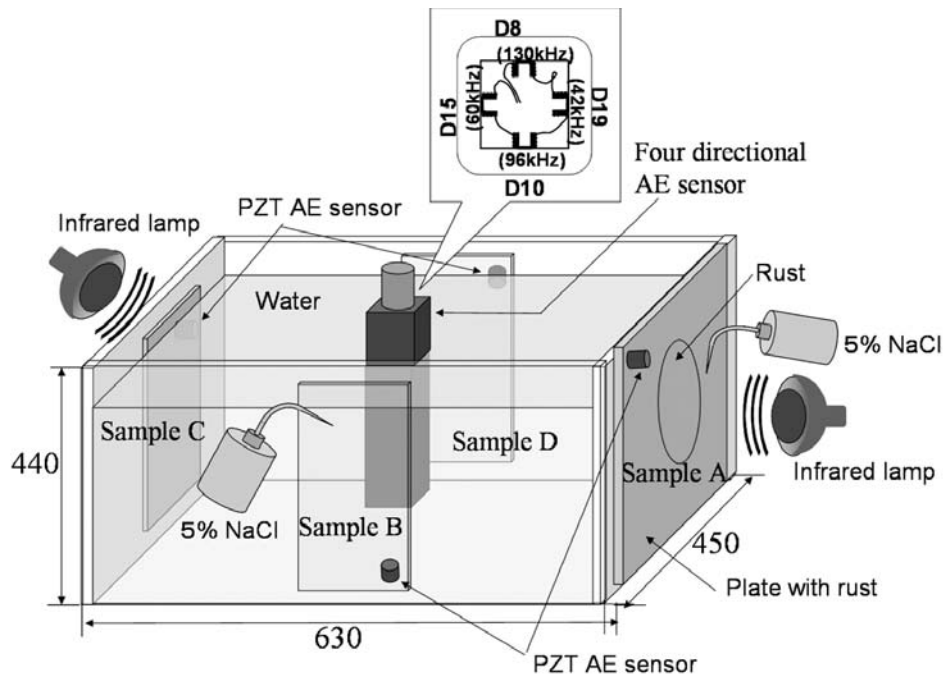


Fig. 5 Experimental setup for monitoring AE from rust fracture of corroded four plates.

The container was filled with water. A trace of corrosion inhibitor was added to prevent wet corrosion of the inner surfaces of the samples. The boxed AE sensor was immersed with its bottom at 200-mm height. Experimental setup is shown in Fig. 5. We also mounted PZT-type AE sensors (PAC, Type PICO) on sanded parts of the samples to examine the timing and amplitude of water-borne P-waves and Lamb waves. Outputs of the PZT sensors were amplified 40 dB, while those of the ITQS were not amplified but used a 20-150 kHz bandpass-filter. AE monitoring was started on February 27, 2007 and continued to April 19 for 51 days. We simultaneously measured room temperature and temperatures of samples A and B.

AE activities

The left of Fig. 6 shows change of room temperature and cumulative AE events counts of the ITQS. Here one cycle of the temperature corresponds to one day, and the cumulative event counts mean all events from four samples, since the four sensors were connected on a single fiber in series. We had two cold days on March 25 and April 9. We observed four fairly large step-wise increases, as marked by four ellipses. Step-wise increases of number 2 and 3 coincide with large temperature changes, but two others (1 and 4) were at higher temperatures. It is noteworthy that less AE signals were emitted for about ten days from 38 to 47th days.

We believe that the rust fracture will be accelerated by temperature changes of the member. Thus, we studied relations between the temperature change of the samples A and B and event counts, since AE signals were supposed to be mostly generated by these samples. As shown in the right of Fig. 6, we observed a fairly good relation between the plate temperature and event counts. Stepwise increases of AE events tend to occur when the plate temperature is at high or low. Stepwise increases of No. 1, 3 and 4 occurred at higher temperatures and that of No. 2 at a low temperature. However, very few AE signals were emitted at 3.7 Ms (42nd day) in spite of low temperature. This appears to be due to capricious nature of living rust, which often makes corrosion monitoring of tanks difficult. It is also noted that the corrosion rate cannot be estimated from AE data monitored for one or two hours.

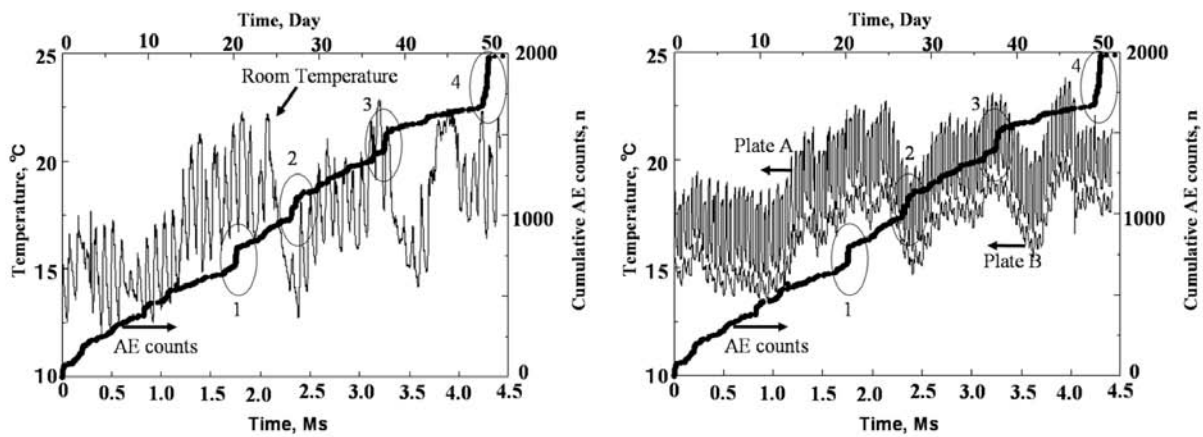


Fig. 6 Change of room temperature (left) and plate A, B (right) and cumulative AE counts by optical fiber AE system.

Direction of the P-wave

We next estimated the direction of the P-wave. Figure 7 shows typical examples of AE signals. Event I was classified as the AE from the sample A due to its strong frequency component at 45 kHz (D19 sensor). It counted 936 events. In the same manner, event II was from the sample B (by D10 sensor). We observe two or three wave packets in events III (D15 sensor) and IV (D8 sensor). Two peaks at 40 kHz and 60 kHz of event III suggest simultaneous emission from the sample C and A, respectively. Two packets of the event IV suggest two AE signals from the sample D due to frequency component at around 130 kHz.

The left of Fig. 8 shows changes of classified events with time. Sample A with large thick rust produced many AE signals when exposed to severe corrosion, but sample D, exposed to mild environment, less AE signals. These are expected result, and nothing new. However, it is noted that the event count of sample C, exposed to the thermal cycles, is large.

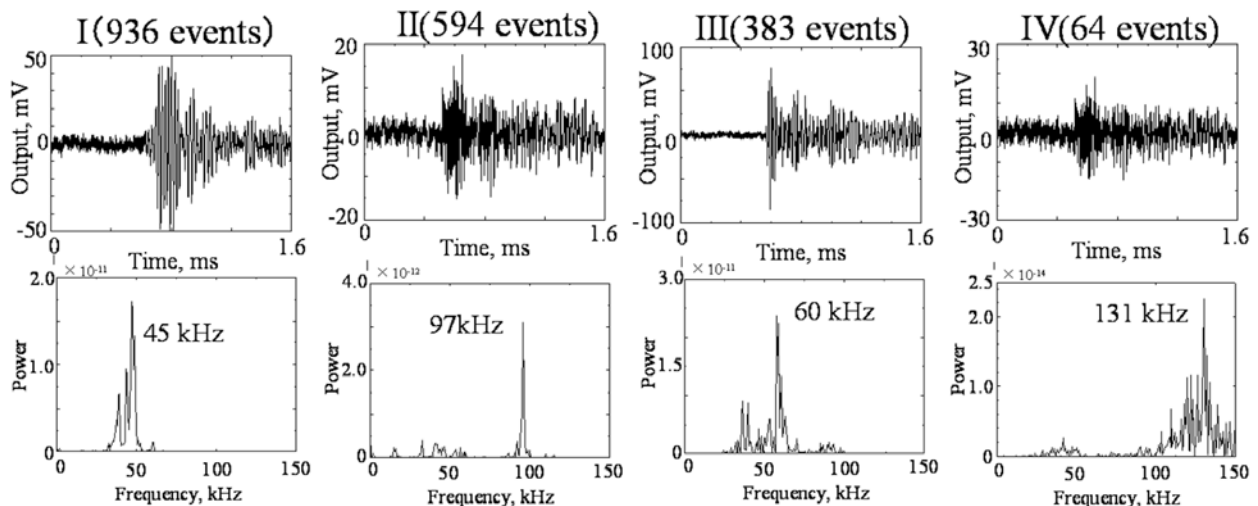


Fig. 7 Waveforms and their frequency spectra detected by four optical fiber sensors.

We next compared the event counts per unit rust area. The right of Fig. 8 shows change of classified event counts per 100 cm^2 from the samples A, B, C and D. There are some interesting findings. These are:

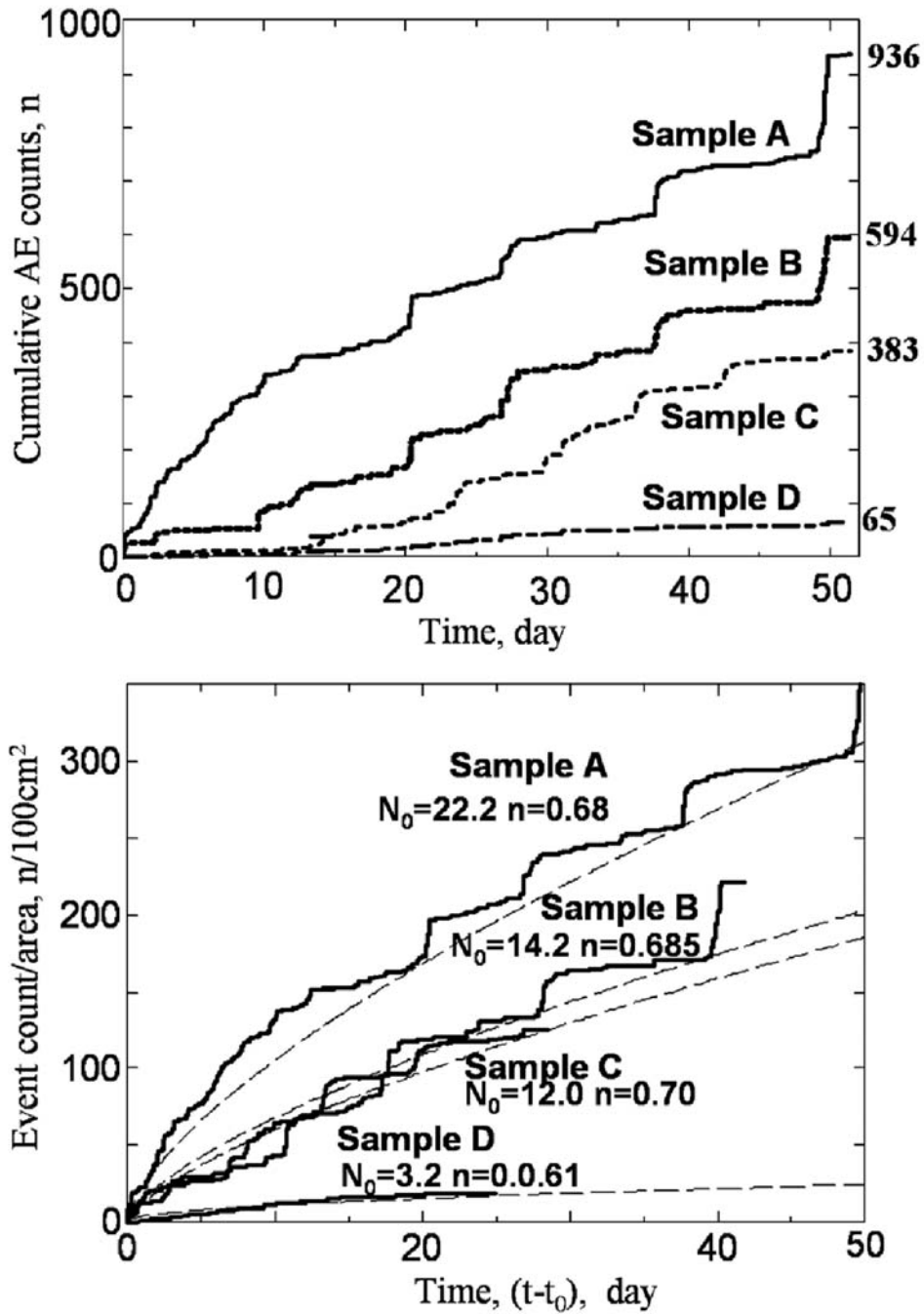


Fig. 8 Cumulative AE counts (top) and changes of classified event counts per 100 cm² from four samples (bottom).

- 1) Cumulative event counts, N , increase with time, t , according to the parabolic law, i.e., $N=N_0(t-t_0)^n$, where $n<1$. This law is common to high temperature oxidation of metals covered by protective oxide films. Small N_0 and n indicate a protective film. Steps in a parabolic oxidation curve indicate the rapid oxidation due to partial breakdown of the film. These correspond to the stepwise increase of AE signals due to fractures of the rust.
- 2) Incubation time, t_0 , becomes longer for the samples exposed to mild corrosion environment.

- 3) There are slight time lags in the timing of steps for samples A, B and C, suggesting that the AE activity changes depending on the rust history and corrosion environment. Step height of samples A and B with thicker rust are larger than that of sample C.
- 4) In spite of non-corrosive environment, sample C shows higher emission rate.

Next we determined two parameters: N_o and n by curve fitting of the time-shifted data. Here the parameters were decided so that the parabolic curves pass through the bottom of the steps, as shown in the right of Fig. 8. Due to the limited data for only 50 days, correct determination was impossible, but tentative values were estimated. The parameter N_o increases in the order of samples $D \rightarrow C \rightarrow B \rightarrow A$, indicating corrosiveness and rust nature. The parameter n presents the role of rust on the corrosion rate. Here, it is noted that the rust plays two roles. One is protection of the base metal as a diffusion barrier of water and oxygen. Another is acceleration effect of corrosion by lowering the acidity of impregnated water. The latter is enhanced by chloride ions. It is noted the sample A, with thicker rust and exposed to severe corrosion environment, shows $n = 0.68$, and almost the same values for the samples B (0.685) and C (0.7). This suggests the rust on sample A is playing a protection role.

Conclusion

We developed a quadridirectional AE system and monitored liquid-borne AE signals from four corroded plates which were exposed to different corrosion environment.

- 1) Immersion-type quadridirectional sensor was developed. Direction of AE can be identified by the frequency characteristics of four sensor elements with the directivity of $\pm 30^\circ$.
- 2) The sensor monitored the water-borne P-wave from rust fracture.
- 3) We observed good relations between AE activity and rusted plate temperature. Stepwise increases of AE events tend to occur when the plate temperature is at higher or lower.
- 4) AE events increased with time according to a parabolic law: $N = N_o(t - t_o)^n$, suggesting protective nature of the rust.

References

1. *Corrosion Center News*, 29, Japan Society of Corrosion Engineering, 2004.
2. H. Cho, R. Arai and M. Takemoto, *J. Acoustic Emission*, **23**, 2005, 72-80.
3. T. Matsuo, H. Cho and M. Takemoto, *Progress in Acoustic Emission XIII*, IAES-18, 2006, 311-318.

A SIMPLE METHOD TO COMPARE THE SENSITIVITY OF DIFFERENT AE SENSORS FOR TANK FLOOR TESTING

HARTMUT VALLEN, JOCHEN VALLEN and JENS FORKER

Vallen-Systeme GmbH, 82057 Icking, Germany

Abstract

AE testing of atmospheric storage tanks filled with liquid becomes more and more accepted. Sensors are attached to the tank wall and shall differentiate smallest amplitudes in the 25-45 kHz frequency range from the background noise. Different sensor models are offered for this application. Are these comparable regarding sensitivity and signal-to-noise ratio? This paper describes a reproducible method to compare such sensors. For continuous as well as for pulse excitation, a suitable setup and obtained results are described. Measuring the noise spectra helps to explain the influence of the frequency filtering on the signal-to-noise ratio.

Introduction

This paper addresses the needs of AE testers of atmospheric storage tanks of various sizes, who want to compare the sensitivity of different sensor models or sensors of same model using a simple method. The most important standards for AE sensor calibration are ISO 12713 (primary calibration) [1] and ISO 12714 (secondary calibration) [2]. Both standards are designed for calibration laboratories. They require a large and heavy calibration block. AE testers usually do not have access to such a calibration block. Additionally, ISO 12714 is recommended for the frequency range 100 kHz – 1 MHz, whereas tank testing is usually done in the frequency range 25-45 kHz. Hence, these standards are of no help for the AE tester. Other standards like EN 13477 [3] and ASTM E976 [4] are general and do not consider the fact that plate waves propagate in different modes.

To detect smallest AE signals, the sensor should have the largest possible signal-to-noise ratio (SNR). This means that for a certain excitation the sensor shall provide the largest possible signal voltage superposed with the smallest possible inherent noise.

For a sensitivity comparison one has to proceed as follows:

1. Excite both sensors in identical manner (frequency sweep) and strongly enough so that the noise can be neglected against the signal from the excitation. The output signal shall be $U_A(f)$.
2. Measure the inherent noise of the sensors (no excitation!). This is the output voltage U_R .
3. The SNR at given excitation is then: $SNR(f) = U_A(f)/U_R$. It might be of interest to calculate a SNR for peak values and one for RMS values.
4. The frequency response as well as the noise measurement shall be made with the same frequency filters as used for the tank test.
5. The sensor with the higher SNR can distinguish smaller excitations from the background noise. Hence, this is the more sensitive sensor.

Setup

For the comparison the following setup was used:

Function Generator (FG)

The function generator creates a sine wave voltage with adjustable frequency and amplitude or a pulse with selectable duration and amplitude, respectively. In our test we used model 33220A (Agilent).

Sensor Excitation

For a comparison, the sensors under test (SUT) need to be excited acoustically in exactly the same way. As emitter an ultrasonic transducer model V101 (Panametrics) was coupled face to face to one SUT using light machine oil as coupling agent. The emitter was driven by a frequency-swept sine wave and the AE signal amplitude from SUT was measured.

This method provides well reproducible results and is well suited for routine sensor verification. But the following objections could be raised:

- a) AE tank-floor testing analyzes burst AE and not continuous (sine wave) AE. A comparison should also consider burst excitation.
- b) Different SUT models could have different feedback on the V101 emitter and thereby tamper the comparison result.

Considering these objections, a second comparison was made using a pulse excitation via an aluminum rod of 610-mm length and 19-mm diameter with polished ends. Both excitation methods led to almost the same results for the frequency range 25-45 kHz.

Compared Sensor Models

We compared a Vallen VS30-SIC-46dB sensor (S/N 120) with another sensor, hereafter called XXX. Both sensors have an integral preamplifier requiring 28V DC supply voltage on the signal wire and 20.6 mm diameter. The following lists the differences.

Model	Length	Face	Connector
VS30-SIC-46dB	52.8mm	isolated ceramic plate	BNC at case
XXX	38.8mm	non-isolated metal plate	BNC with 1 m cable

Measurement Chain with Various Filters

For measurements we used Vallen AMSY-5 AE system with dual-channel AE processor ASIP-2, a 25-45 kHz band-pass for the first test, and a 25-100 kHz band-pass for a second test. These band-pass filters consist of digital high- and low-pass filters each with 48 dB/octave steepness. Figure 1 shows the response curves of the band-pass at 1 V_{PP} continuous sine wave at ASIP-2 input. Frequency sweep and RMS measurement were controlled by Vallen Sensor Tester software.

Sensor Frequency Response

To obtain Figs. 2 and 3, the FG output (50 mV_{PP}, terminated externally with 50Ω) was connected to the V101, face-to-face with SUT. The red curves were taken with 25-45 kHz filter and the blue curves with 25-100 kHz filter in ASIP-2. For the determination of the inherent noise of the SUT, we removed the acoustic excitation by disconnecting the V101 from the FG. We amplified the sensor output with an auxiliary amplifier by 40 dB, which allowed one to ignore the noise added by subsequent measurement stages. In this way the horizontal lines in orange (25-45 kHz) and green (25-100 kHz) were recorded.

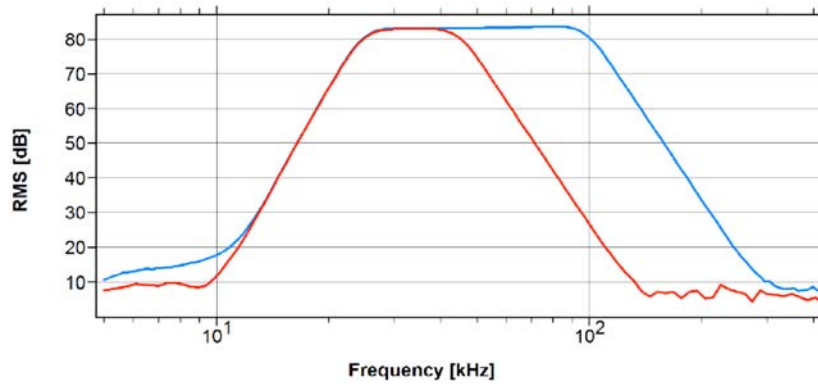


Fig. 1 Frequency response of the used filters.

During this noise measurement, we ensured that no acoustic noise sources like fans, human voices, or others could cause a distortion within the frequency range under evaluation. Both SUT were treated in exactly the same way.

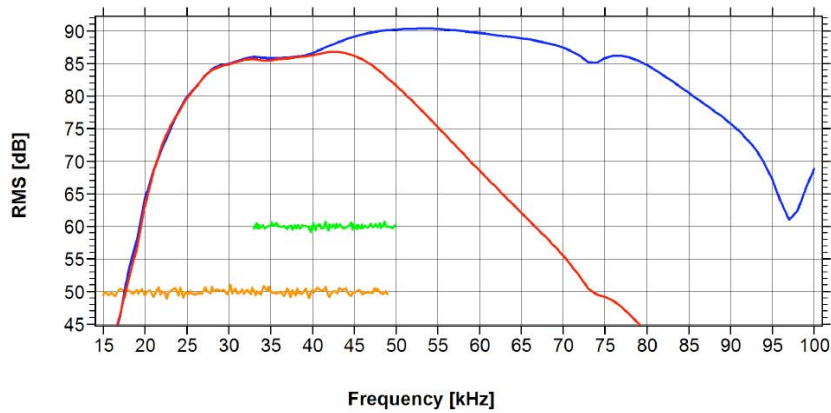


Fig. 2 Frequency response and noise of VS30-SIC-46 dB. 25-45 kHz: red and orange lines; 25-100 kHz: blue and green lines.

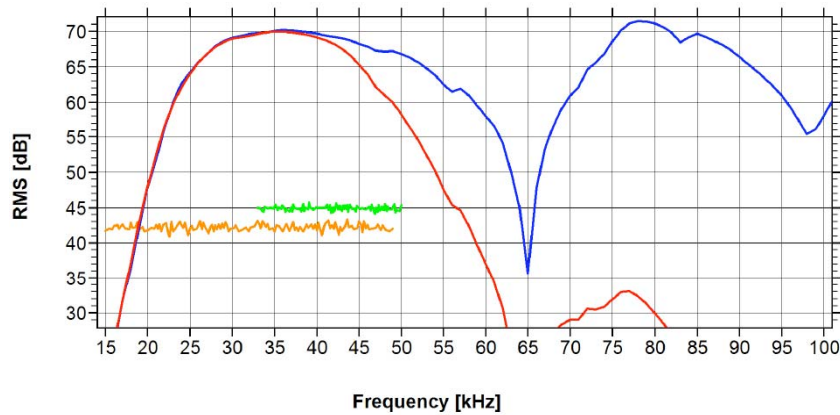


Fig. 3 Frequency response and noise of XXX. Line colors same as in Fig. 2.

The results are summarized in Table 1. They were deduced from the 4 lines of Figs. 2 and 3, whereby the noise has been corrected by the 40 dB post-amplification. As can be seen from noise and maximum amplitude, the gain of the integral preamplifier of XXX is lower than that of the VS30-SIC-46dB, but the deciding factor is the SNR as this is independent of the gain. Results for continuous excitation and 25-45 kHz filter: VS30-SIC-46dB provides 17 dB more signal amplitude and 9.5 dB better SNR.

Table 1 Results for continuous sensor excitation.

Sensor:	VS30-SIC-46dB		XXX	
Filter [kHz]:	25-45	25-100	25-45	25-100
Maximum amplitude (RMS):	87 dB	90.5 dB	70 dB	72 dB
line color:	red	blue	red	blue
Frequency at max. ampl.:	35 kHz	53 kHz	35 kHz	78 kHz
RMS noise:	10 dB	20 dB	2.5 dB	5 dB
line color:	orange	green	orange	green
Signal-to-noise ratio SNR:	77 dB	70.5 dB	67.5 dB	67 dB
Difference wrt. XXX at 25 - 45 kHz:	9.5 dB	3 dB	0 dB	-0.5 dB

Using Burst Excitation

For XXX the exciting pulse amplitude was $5 V_P$. For VS30-SIC-46dB the amplitude was reduced to $1 V_P$ because $5 V_P$ led to saturation due to the larger gain. Figure 4 shows the response of the VS30-SIC-46dB with $1 V_P$ excitation amplitude at V101, and Fig. 5 shows the response of XXX with $5 V_P$ at V101, both with 25-45 kHz filter. For the FFT, a 190- μ s long Hamming window was used. Table 2 lists the maximum amplitude in the time domain (line 2), converted to dB (line 3), the maximum amplitude in the frequency domain (line 4). To compensate for the $5 V_P$ excitation of XXX, its line-2 value is divided by 5 ($600/5 = 120$ mV) and line 4 is reduced by 14 dB ($97-14 = 83$ dB). Table 2 also lists the noise in mV_P (line 5) and converted to dB (line 6). The noise values were recorded separately, in reference to the SUT output (before 40-dB amplification) and are maximum values (peaks), which occurred in a frequency of $1/s$ or less. The resulting signal-noise-ratios are listed in line 7 (time domain) and line 8 (frequency domain). Scaling in Figs. 4-7 refers to the input voltage at the AE signal processor (ASIP-2).

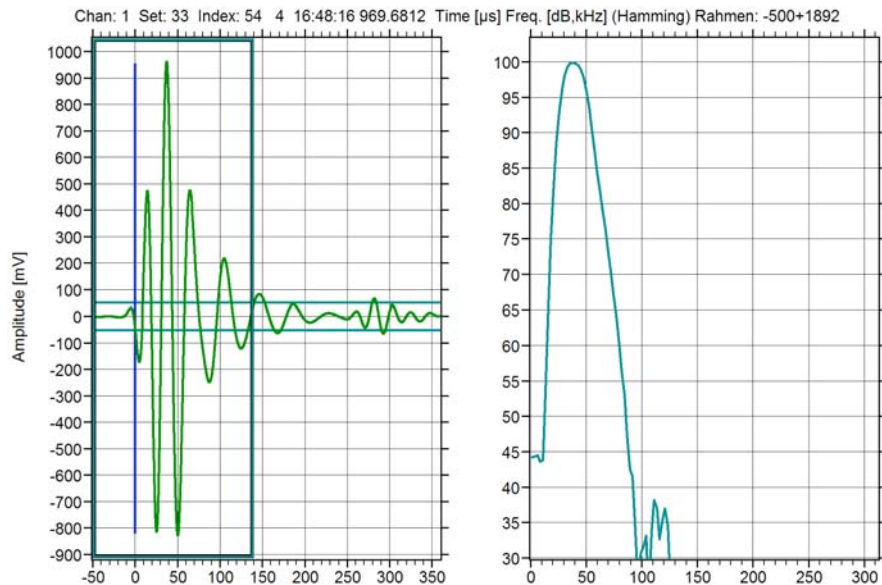


Fig. 4 Pulse response VS30-SIC-46dB, filter: 25-45 kHz, excitation $1 V_P \times 1 \mu$ s. max. 940 mV in time domain or 100 dB in FFT. Noise: $0.58 mV_P$.

Figures 6 and 7 were taken with band-pass of 25-300 kHz. Figure 6 shows at approximately 30μ s the arrival of the s_1 mode, which travels with ~ 4000 m/s at 250 kHz according to Fig. 8. Considerable differences between the two sensor models are seen: VS30-SIC-46dB exhibits a

resonance at ~60 kHz, where XXX exhibits resonances at 40 and 80 kHz and an anti-resonance at 60 kHz. Due to the obscure influence of the s_1 mode, a direct comparison of Figs. 6 and 7 is not recommended.

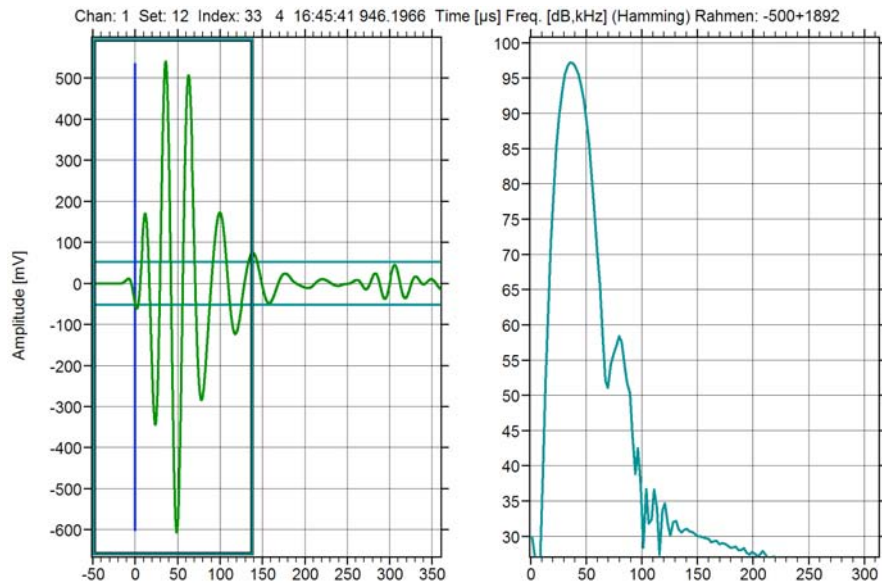


Fig. 5 Pulse response XXX, filter: 25-45 kHz, excitation $5 V_P \times 1 \mu s$. max. 600 mV in time domain, 97 dB in FFT. Noise: $0.20 mV_P$.

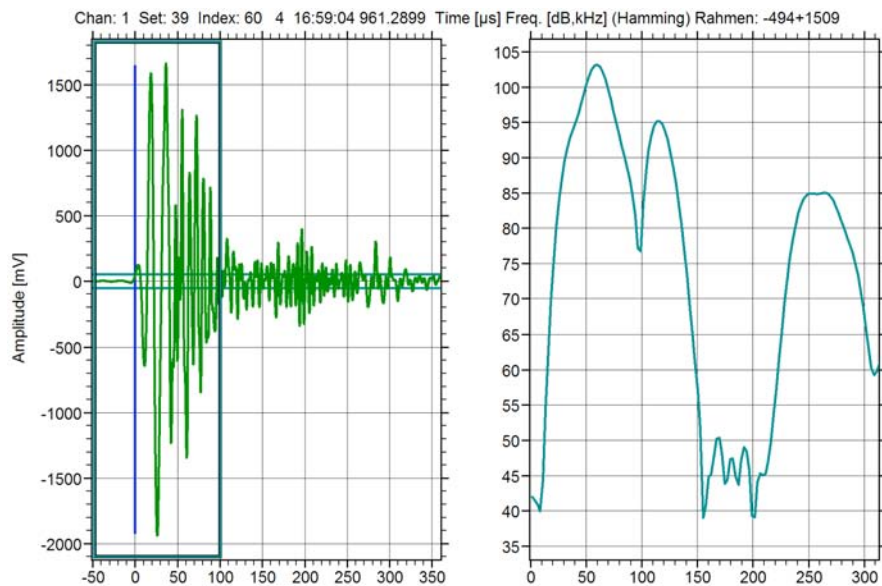


Fig. 6 Pulse response VS30-SIC-46dB, filter: 25-300 kHz, excitation $1 V_P \times 1 \mu s$. max. 1900 mV/103 dB at 60 kHz. Noise: $2.18 mV_P$. Arrival of s_1 mode at $t = 30 \mu s$.

Result for burst excitation with 25-45 kHz filter: Table 2, line 3 indicates that VS30 delivers 17.8 dB more amplitude and line 8 shows 8.6 dB more SNR in time domain and 7.8 dB more in frequency domain. This result is very similar to continuous excitation.

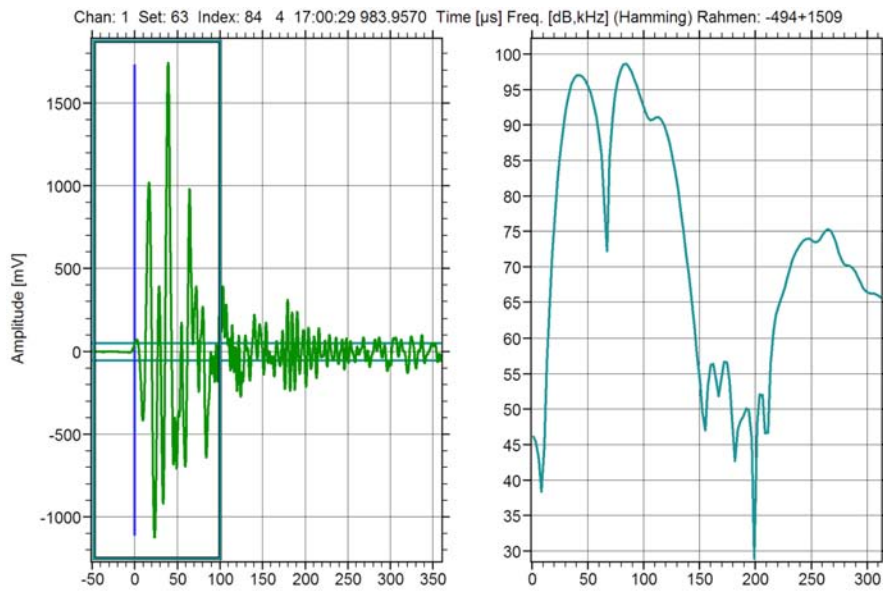


Fig. 7 pulse response XXX, filter : 25-300 kHz, excitation $5 V_P \times 1 \mu s$.
Max. 1750 mV/98 dB at 80 kHz. Noise: $0.33 mV_P$.

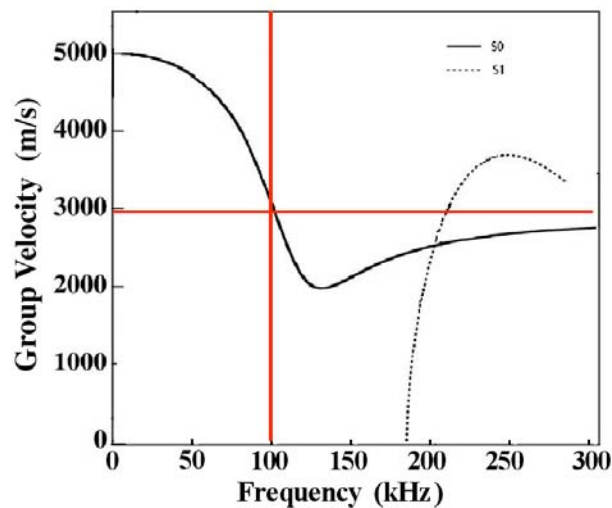


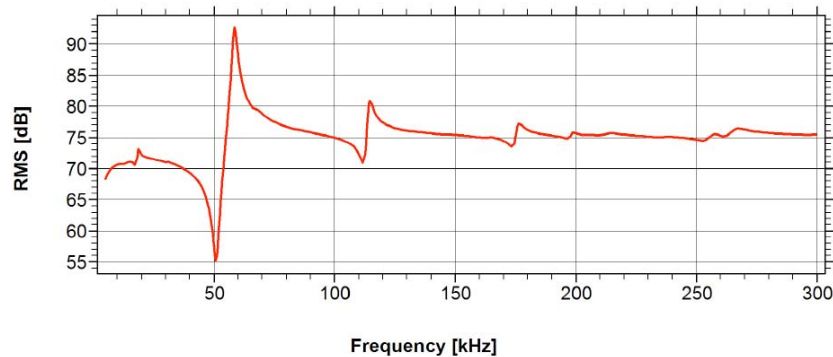
Fig. 8 Dispersion curves for 19 mm aluminum rod, according to [5].

Table 2 Burst excitation results with 25-45 kHz filter.

Line	Sensor:	VS30-SIC -46dB	XXX
<i>Measurements</i>			
2	max. Amplitude [mV_P]:	940	600/5V
3	max. Amplitude [dB]:	119.4	101.6
4	max. Amp (FFT) [dB]:	100	97-14
5	max. Noise [mV_P]:	0.58	0.2
6	max. Noise [dB]:	55.2	46
<i>Results:</i>			
7	SNR (mV_P) (3-6) in [dB]:	64.2	55.6
8	SNR (FFT) (4-6) in [dB]:	44.8	37.0

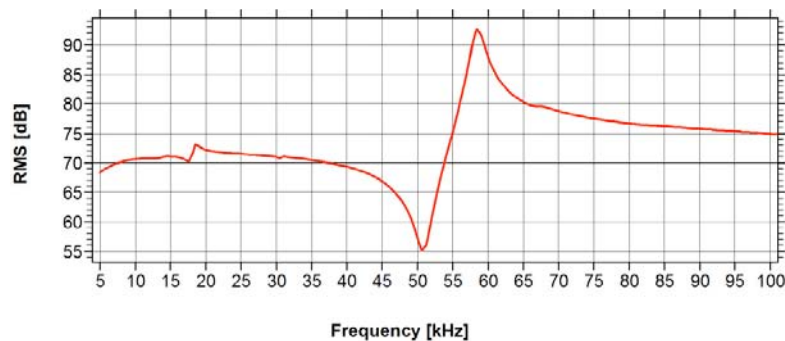
Noise Spectra, Impedance and “Natural Frequency”

The frequency, at which a sensor shows a sudden *jump* in its impedance, is called *natural frequency* [6]. For obtaining an impedance curve (Figs. 9 and 10), a passive sensor must be used. A sine wave of 100 mV_{PP} from a function generator in series with 10 pF was fed in parallel to a sensor VS30-V (same piezo-element as VS30-SIC-46dB) connected to a preamplifier AEP4 (40 dB). Figure 9 shows the lowest impedance at 51 kHz, and the highest at 58 kHz. Peculiar with this frequency is, that the amplitude measured with sensor connected (Fig. 9: 94 dB) is higher than measured with the sensor disconnected (89 dB)! The impedance combination of both, sensor and preamplifier, generate a sharp resonance peak.



FG 100mV --> 10pF --> Sensor -->20cm --> preamp. 40dB --> ASIPP (dummy filter)

Fig. 9 Impedance jumps of VS30-V (no integrated preamplifier).



FG 100mVpp --> 10pF --> Sensor -->20cm --> preamp. 40dB --> ASIPP (dummy filter)

Fig. 10 Zoom of Fig. 9 around the natural frequency (58 kHz).

This peak can also be seen in the noise spectrum (Fig. 11) of a sensor with integrated preamplifier. This dominating peak in the noise spectrum is the reason for the increase of inherent noise when using the 25-100 kHz band-pass filter instead of 25-45 kHz. In both Figs. 9 and 11, further peaks at 112 kHz, 175 kHz and 270 kHz can be identified. XXX has its dominating peak in the noise spectrum below 25 kHz (Fig. 12). This explains why the noise of the XXX does not substantially increase with a 25-100 kHz band-pass filter.

The determination of a reproducible noise spectrum requires averaging the FFT over many measurements as the individual spectra of noise records scatter considerably. For Figs. 11 and 12, we averaged 1000 noise records using the Vallen FFT-Averager. The absolute scaling of Figs. 11 and 12 must not be compared. These figures shall just illustrate the different ‘natural frequencies’ and the effect of filter bandwidth on the noise of the filtered signal.

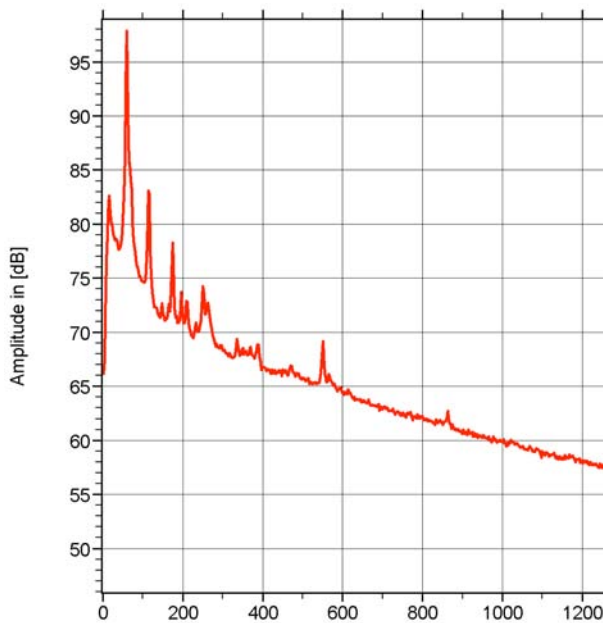


Fig. 11: Noise spectrum VS30-SIC-46dB (average of 1000 FFTs).

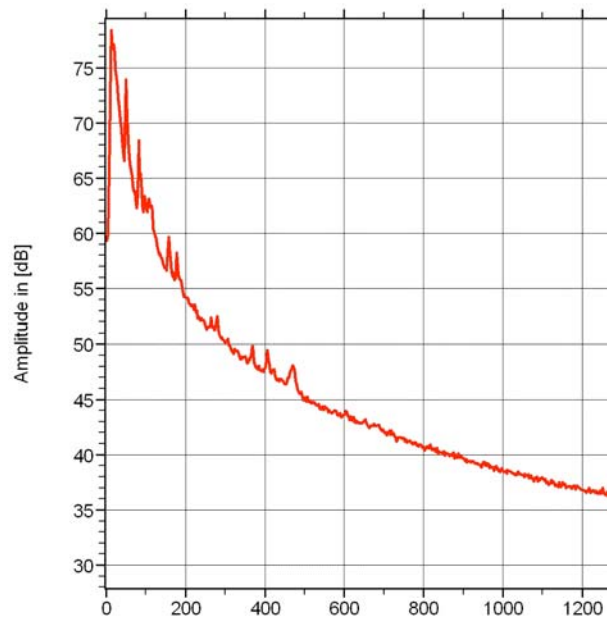


Fig. 12: Noise spectrum XXX (average of 1000 FFTs).

Conclusion

This report describes two setups to compare the sensitivity of different sensor models. One is with face-to-face coupling and continuous excitation, and the other with burst excitation via an aluminum rod. In both cases, the excitation is perpendicular to the sensitive area. When looking at the SNR (signal-to-noise ratio), the inherent noise and the noise spectra have to be considered. Two sensor models have been compared. The result depends strongly on the used frequency range. For 25-45 kHz and identical excitation, one sensor model provides 17 dB more signal and about 9 dB better SNR than the other. For tank floor testing, the frequency range of 25-45 kHz is suited best. The more sensitive sensor model shows a natural frequency of 60 kHz. This causes a peak in the noise spectrum, which is excluded effectively by the 25-45 kHz band-pass filter.

References

- [1] *Non-destructive testing – Acoustic emission inspection – Primary calibration of transducers*, ISO 12713, ISO/TC135, 1998.
- [2] *Non-destructive testing – Acoustic emission inspection – Secondary calibration of acoustic emission sensors*, ISO 12714, ISO/TC135, 1999.
- [3] *Non-destructive testing – Acoustic emission – Equipment characterisation- Part 2: Verification of operating characteristics*, EN13477-2, CEN/TC138, 2001.
- [4] *Standard Guide for Determining the Reproducibility of Acoustic Emission Sensor Response*, ASTM E976 ASTM/E07.04, 2001.
- [5] J.L. Rose, *Ultrasonic Waves in Solid Media*, Cambridge University Press, ISBN 0 521 54889 6, 2004, p. 149+.
- [6] G. Gautschi, *Piezoelectric Sensorics*, Springer Verlag, ISBN 3-540-42259-5, 2002, p. 195+.

DAMAGE IN CARBON FIBRE COMPOSITES: THE DISCRIMINATION OF ACOUSTIC EMISSION SIGNALS USING FREQUENCY

MARK EATON, KAREN HOLFORD, CAROL FEATHERSTON and RHYS PULLIN

Cardiff School of Engineering, Cardiff University, Cardiff, CF24 3AA, UK

Abstract

This work considers the use of frequency content as a discriminating factor for acoustic emission (AE) signals from damage mechanisms in carbon fibre composite materials. Using a broadband conical transducer as an artificial source, investigations were made into the effects of source frequency (relaxation time), specimen geometry and sensor response on the frequency content of the recorded signals. It was shown that source frequency had an effect on the frequency content of the recorded signals, however, the specimen geometry and sensor response were shown to have a more significant effect. Additionally, AE signals were recorded from real damage mechanisms in tensile and beam buckling coupon specimens. The peak frequency content was used to examine signals resulting from the different damage modes identified. It was shown that some level of discrimination could be achieved and observations were in general agreement with previous research studies. However it was shown that great care is required when using peak frequency content as a discriminating factor because geometry and sensor response can have a distorting effect on the results.

Keywords: AE, Composites, Signal Discrimination, Frequency.

Introduction

Due to the widespread use of composite materials in the automotive and aerospace industries, in particular their use in safety critical structures, there is an increasing need to ensure their continued safe operation throughout long service lives. Acoustic emission (AE) can be used for in-service structural health monitoring of composite structures and offers great potential for the location and characterisation of damage. Many different damage mechanisms, such as delamination and matrix cracking, can occur in composite materials which may not be detected visually but can dramatically reduce the ultimate failure load of a component. The prediction of damage type and its onset is difficult due to the possible variations in component lay-ups and manufacturing processes. As such it is very desirable to be able to detect and discriminate between AE signals from different damage mechanisms in composite materials.

A variation of source relaxation time has been shown for different damage mechanisms in glass fibre / epoxy [1] and it is commonly believed that this will result in AE signals with different frequency content. A number of researchers have attempted to utilise frequency content as a discriminating factor for AE signals [2-4]. The results are in good agreement, with all researchers finding matrix failures such as matrix cracking and delamination producing signals with low frequency content ($\sim < 150\text{kHz}$) and fibre failures producing signals with high frequency content ($\sim > 300\text{kHz}$).

Due to their laminate nature, composite material components are commonly manufactured as thin walled structures and as such are approximately plate like. To perform meaningful analysis it is necessary to consider the effects of propagation in a plate on recorded AE signals. When AE

waves propagate in a plate like structure they couple at the surfaces to produce two basic plate-wave modes (also known as Lamb waves). These are the ‘symmetric mode’ (s_0) in which the principal displacement is in the plane of the plate, parallel to propagation direction and the ‘asymmetric mode’ (a_0), in which the principal displacement is perpendicular to the plane of the plate and the direction of propagation [5].

Experimental Procedure

An investigation into the effects of specimen geometry and sensor response on frequency content was conducted on a 1500 mm x 500 mm x 2.16 mm carbon fibre/epoxy plate manufactured from Advanced Composites Group (ACG) MTM28-1/HS uni-directional (UD) pre-preg with a $(0,90)_{4S}$ lay-up. An artificial source of AE was used to generate test signals. This consisted of an in-house manufactured broadband conical transducer provided by the National Physical Laboratory, UK. Two Physical Acoustics Corp. (PAC) S9208 broadband sensors were used for the detection of all signals. The detection sensors were arranged along the 0° material direction at the centre of the plate such that one sensor was adjacent to the conical transducer and the other was at a distance of 200 mm. The conical transducer was coupled once only at the start of the test to avoid any repeatability of coupling issues. The detection sensors were coupled with ultrasound gel and mounted with magnetic clamps. A sensitivity test was conducted using a Hsu-Nielsen source each time a sensor was mounted, to ensure adequate coupling was achieved. A PAC Wavegen-1410 board provided a 160-V single-cycle square-wave with frequency varying from 100-900 kHz at 100 kHz intervals, to drive the conical source transducer. The test was repeated with the sensors in opposite positions. Both tests were repeated using two PAC WD wideband sensors for detection. Signals were recorded throughout all tests using a PAC PCI-2 system at 10 MSPS.

An investigation into the frequency content of signals from various failure modes was conducted using six tensile specimens measuring 240 mm x 30 mm x 1.08 mm and manufactured from ACG’s HTM45/HS UD pre-preg with $(0)_8$ and $(0,90)_{2S}$ lay-ups. To suppress grip noise and minimise slippage, aluminium end tabs were bonded to the specimens reducing the unsupported length to 150 mm. The specimens were instrumented with a single PAC WDi sensor mounted at the centre using electrical tape with brown grease as a couplant and loaded to failure under displacement control at a rate of $0.125 \text{ mm.min}^{-1}$.

An investigation into failure modes during buckling was conducted using six beam buckling specimens manufactured from HTM45/HS UD pre-preg with measurements of 200 mm x 30 mm x 2.16 mm and lay-ups of $(\pm 45)_{4S}$ and $(0,90)_{4S}$. The specimens were subject to an in-plane compressive load along their length. This is facilitated by a loading cage that provides built-in supports at each end, reducing the unsupported length to 170 mm, and ensuring the supports remain aligned throughout the test. The specimens were loaded to failure at 0.5 mm.min^{-1} and 1 mm.min^{-1} for the $(0,90)_{4S}$ and $(\pm 45)_{4S}$ lay-ups, respectively. Two PAC WD sensors were mounted using electric tape with brown grease as a couplant at $\frac{1}{4}$ and $\frac{3}{4}$ of the unsupported length to correspond with the two points of inflection in the deformed mode shape.

Results and Discussion

(i) Effect of specimen geometry and sensor response

The waveforms and FFTs of the signals recorded by two S9208s adjacent to the conical source transducer are shown in Fig. 1a and b for driving pulses of 100 kHz, 500 kHz and 900

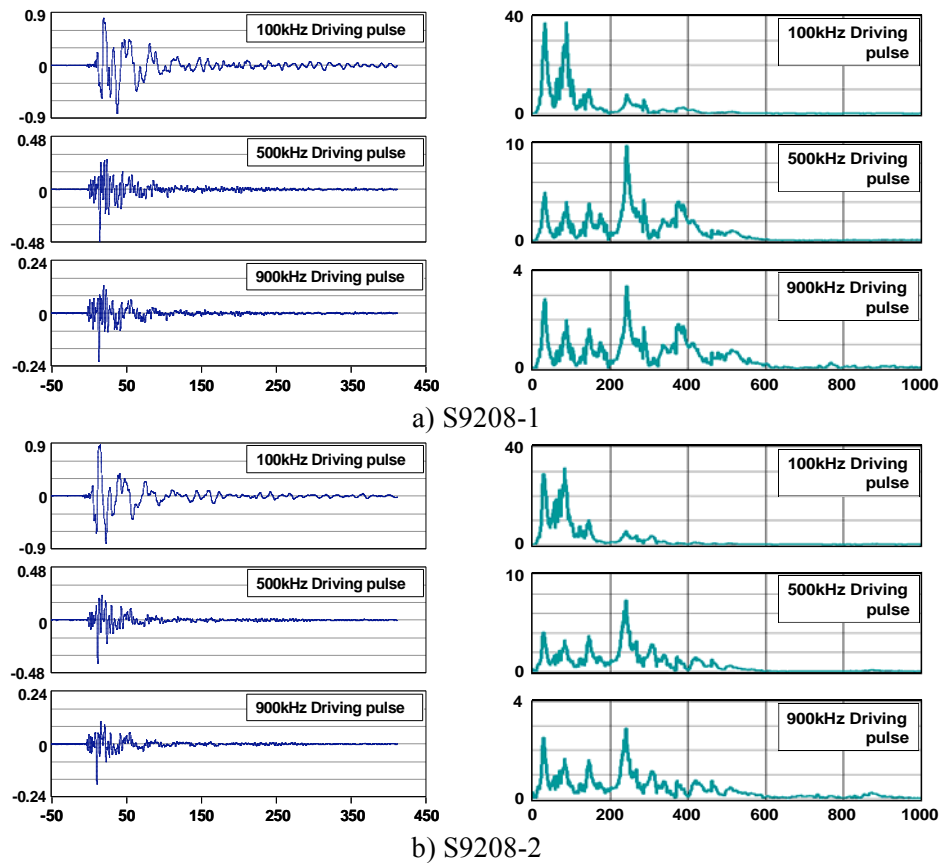


Fig. 1 Waveforms and their FFTs recorded by S9208s adjacent to the source, presented in V versus μs and mV versus kHz respectively

kHz. The response of both sensors to a 100-kHz driving pulse shows that most of the energy in the signal is contained below 100 kHz. As the frequency of the driving pulse increases, so the frequency content of the recorded signal expands to higher frequencies. The response to a 500-kHz artificial source shows that the frequency content of the signals has increased, with most of the energy contained below 400 kHz and very little energy seen above 600 kHz. However, as the frequency of the driving pulse is increased above 500 kHz, there is little increase in the frequency content of the signal, which can be seen in the response to a 900 kHz source where, again, most of the energy is contained below 400 kHz and very little is seen above 600 kHz.

When the sensors are moved away from the conical source transducer, the response becomes very different. Figure 2a and b show the recorded signals and their FFTs for both the S9208 sensors mounted at a distance of 200 mm from the conical transducer, with driving pulse frequencies of 100 kHz, 500 kHz and 900 kHz. Both the s_0 and a_0 plate-wave modes are observed in all the waveforms recorded at 200 mm. The response of the S9208 sensors to a 100-kHz driving pulse show an a_0 mode that is much larger than the s_0 mode. This is reflected in the FFTs by most of the energy being contained below 100 kHz, due to the lower frequency of the a_0 mode. The half-cycle times for the peak of the a_0 modes equate to frequencies of approximately 52 kHz and 55 kHz for S9208-1 and 2, respectively. The 500-kHz and 900-kHz driving pulses generate a response with s_0 and a_0 modes of similar amplitudes, and this is reflected by the observation of higher frequency peaks in their FFTs between 200 kHz and 500 kHz. The two regions of frequency content can be attributed to the fundamental plate-wave modes a_0 and s_0 . This is ratified by the half-cycle times of the peak cycles of the s_0 and a_0 modes from S9208-1 for a 500-kHz

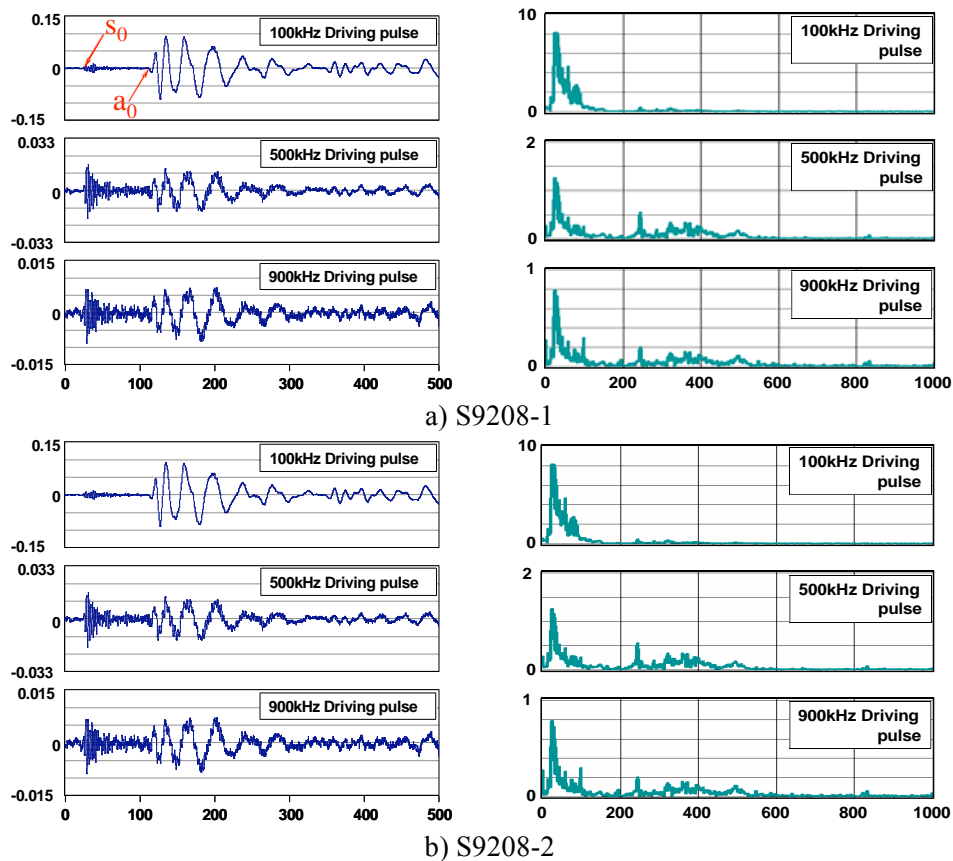


Fig. 2 Waveforms and their FFTs recorded by S9208s 200 mm from the source, presented in V versus μ s and mV versus kHz, respectively.

source, which have corresponding frequencies of 374 kHz and 39 kHz, respectively, suggesting that geometry has a considerable effect on the frequency content of a signal.

The response of two WD sensors mounted adjacent to the conical source transducer is presented in Fig. 3a and b for driving pulse frequencies of 100 kHz, 500 kHz and 900 kHz, respectively. The response of the two WD sensors to a 100-kHz driving pulse contain most of the energy below 150 kHz, which is similar to the response of the S9208 sensors to the same source. As observed in the response of the S9208, the frequency content of the recorded signal expands to higher frequencies as the driving pulse frequency is increased. For a 500-kHz driving pulse, the majority of the signal energy is contained below 600 kHz. For a driving pulse of 900 kHz, there is still very little energy contained above 600 kHz. The increase in higher frequency content observed is thought to be an attribute of the sensor because it is not observed for the broadband S9208 sensors and indeed the WD is known to have a peak in sensitivity at approximately 525 kHz. The observation of most interest from this test is the difference in response between the two WD sensors to the same source. It can be seen in Fig. 3 that the two WD sensors have a considerably different response to a 500-kHz driving pulse. The signal recorded by WD-1 has more low frequency content than that of WD-2 and its peak is approximately 100 kHz, whereas WD-2 has more higher frequency content with significant content observed at approximately 475 kHz and 550 kHz. This demonstrates how the response of a sensor can affect the frequency content of a recorded signal and how the response can vary, even within sensors of the same model.

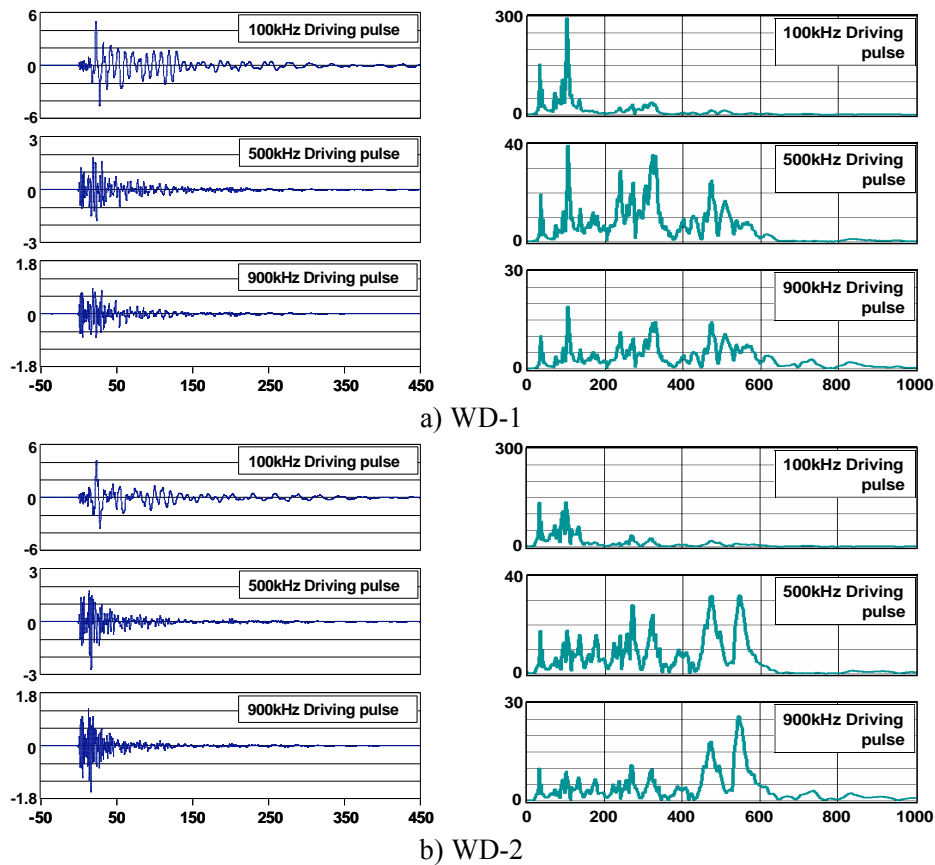


Fig. 3 Waveforms and their FFTs recorded by WDs adjacent to the source, presented in V versus μ s and mV versus kHz, respectively.

The waveforms and their FFTs, recorded by the two WD sensors mounted at a distance of 200 mm from the conical source transducer are shown in Fig. 4a and b for source driving pulses of 100 kHz, 500 kHz and 900 kHz. It can be seen that the level of attenuation observed with the WD sensors is considerably less than that for the S9208 sensors, because the broadband frequency response results in reduced sensitivity. Both the fundamental plate-wave modes are observed in a signal recorded from a 100-kHz driving pulse but as the frequency of the driving pulse increases the a_0 mode rapidly diminishes and for a 500-kHz driving pulse is no longer observed. The FFTs of these waveforms have three distinctive peaks occurring at approximately 100 kHz, 275 kHz and 550 kHz. The amplitudes of these peaks are seen to vary with driving pulse frequency. As expected, more energy is contained at lower frequencies for a low frequency driving pulse and more energy is contained at higher frequencies for a higher frequency driving pulse. The lower and middle frequency peaks are again attributed to the a_0 and s_0 modes in accordance with the S9208 results. It can also be seen that as the a_0 mode loses amplitude with increasing driving-pulse frequency, a corresponding reduction in the amplitude of the low frequency peak in the FFTs is observed. The higher frequency peak centred about 550 kHz is again considered to be an artefact of the sensor response. Additionally, it appears that the frequency content at this level is very different for the two WD sensors, suggesting that the frequency response of the two sensors is different. A difference in sensor response such as this could lead to confusion when considering frequency as a discriminating factor. For example the two FFTs seen in Fig. 4a and b for a 500-kHz driving pulse both have a peak frequency of approximately 275 kHz. WD-1 has a very dominant peak at 275 kHz, whereas WD-2 has a peak at 275 kHz, whose amplitude is only slightly larger than that of the peak at 550 kHz. It is clear that a small variation in the source could quite easily lead to a dramatically different result from

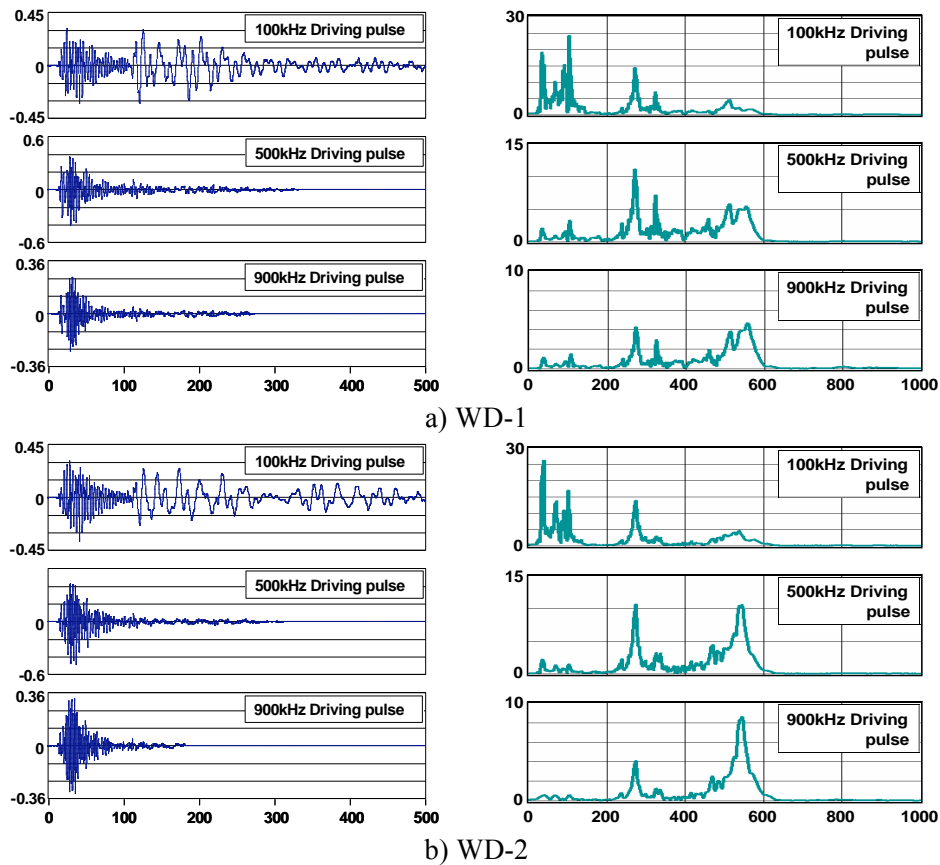


Fig. 4 Waveforms and their FFTs recorded by WDs 200 mm from the source, presented in V versus μ s and mV versus kHz, respectively.

sensor WD-2 to a similar source frequency. It is interesting to note that other researchers [2-4] all observed frequencies in low, medium and high frequency bands using PAC WD sensors that correspond to the three frequency peaks of 100 kHz, 275 kHz and 550 kHz observed here.

(ii) Effect of failure mode type

Figure 5a and b present the failures observed in two tensile specimens having lay-ups of $(0,90)_{2S}$ and $(0)_8$, respectively. In Fig. 5a, $((0,90)_{2S}$ lay-up), large amounts of matrix damage were observed in the form of matrix cracking and fibre-matrix debonding. In Fig. 5b, $((0)_8$ lay-up), the predominant failure mechanism observed was fibre failure, and it should be noted that the longitudinal splitting observed occurred at the point of final failure and was not observed beforehand. Figure 5c and d present the frequency analysis of the AE signals recorded during the tensile testing of the two specimens shown in Fig. 5a and b. The hits for each test are separated using their peak frequency, recorded by AEWin, into three frequency bands of 0-150 kHz, 150-400 kHz and >400 kHz. The hits within each band are then plotted cumulatively against time of test. The low frequency band for the $(0,90)_{2S}$ specimen is clearly dominant and this corresponds to the large amounts of matrix damage observed in Fig. 5a. The $(0)_8$ specimen was observed to have much less matrix damage and more fibre failure. Consequently, the frequency analysis shows the higher frequency band to be dominant for this type of specimen. Previous research in this area [2-4] has also related matrix damage to signals with low frequency content and fibre failure to signals with high frequency content. This demonstrates that some level of discrimination can be achieved between signals resulting from different types of failure mechanism. As yet the cause of activity in the 150-400-kHz band has not been addressed. The previous work presented by others [2-4] has suggested that frequencies in this range may be attributed to fibre pull-out. The

physical identification of fibre pull-out is very difficult, so it is not possible to confirm or refute this. It is worth noting, however, that the results presented in the first part of this paper showed that the s_0 mode generated a peak within this range. Therefore, it is not unreasonable to consider that activity in this band maybe a result of the specimen geometry and/or the sensor response. Additionally, the frequency content of a signal may be further complicated by different source mechanisms occurring simultaneously; for example, a fibre break is likely to be accompanied by some fibre pull-out or movement.

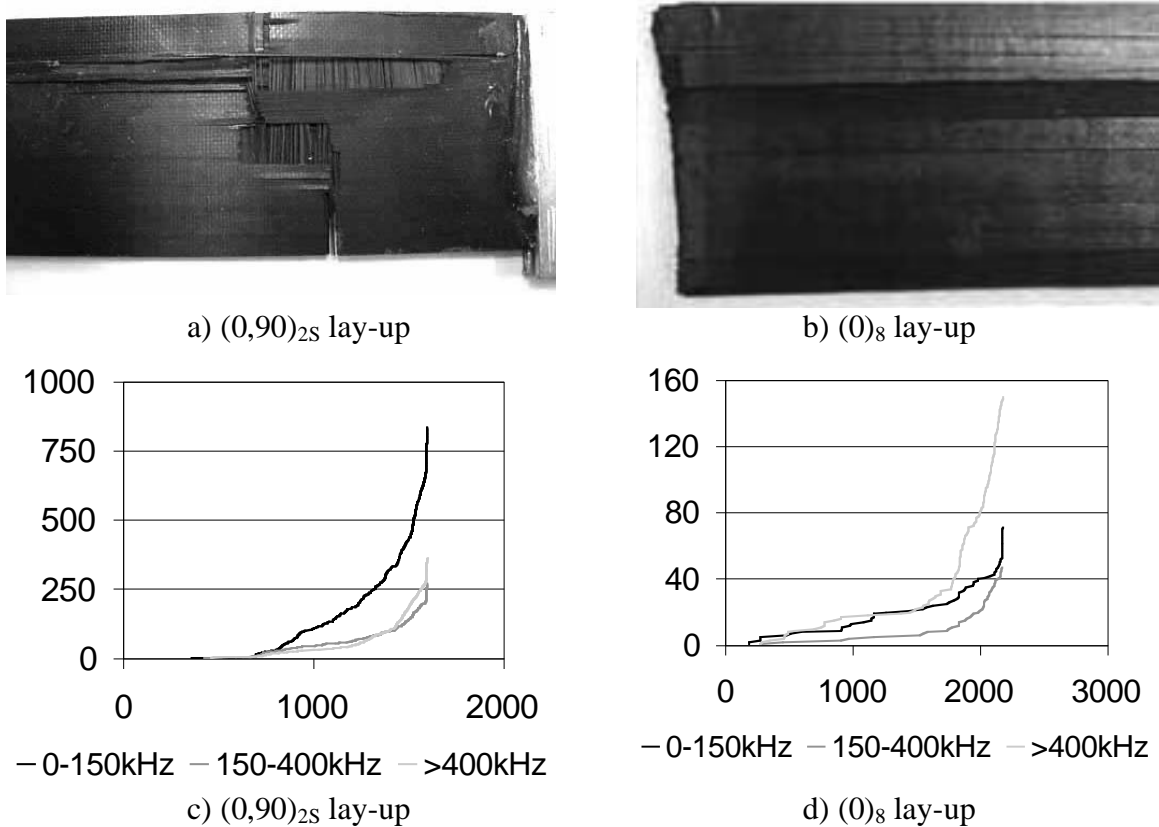


Fig. 5 Frequency analysis of tensile specimens, presented in cumulative hits versus time of test (s).

(iii) Effect of buckling failure

The frequency analysis for two representative beam-buckling specimens is presented in Fig. 6a and b, and the analysis is conducted individually per channel. The damage observed in both specimens was predominantly matrix failure in the form of surface-ply delamination and matrix cracking, which is represented by the presence of a large number of low frequency hits on both channels for both specimens. However, the activity in the middle and high frequency bands was completely different on channels 1 and 2 for both specimens. For channel 1 of specimen 1 (Fig. 6a) the most activity is seen in the middle band and the least activity is seen in the higher band, whereas for channel 2 of specimen 1 (Fig. 6a) the most activity is seen in the high frequency band and the least activity is seen in the middle frequency band. Indeed, the rate of hits recorded on channel 1 between 150-400 kHz is very similar to that of hits recorded above 400 kHz on channel 2 and vice versa. The same effect is observed for specimen 2 (Fig. 6b), where the levels of activity in the middle and high frequency bands are opposite for each channel. The two WD sensors used for these tests are the same two sensors used in the first part of this work to assess

the sensor response to different frequency sources. The variation in results observed between different sensors for the same test is a result of the increased sensitivity of WD-2 in the higher frequency region. Figure 4 shows how the different sensors can produce a different response to the same source. In particular, the 500-kHz source shows that for the same source the peak frequency might lie in either the 150-400-kHz band or the >400-kHz band depending on the sensor. This highlights the effect that sensor response can have on the frequency content of a signal and the potential confusion it can cause.

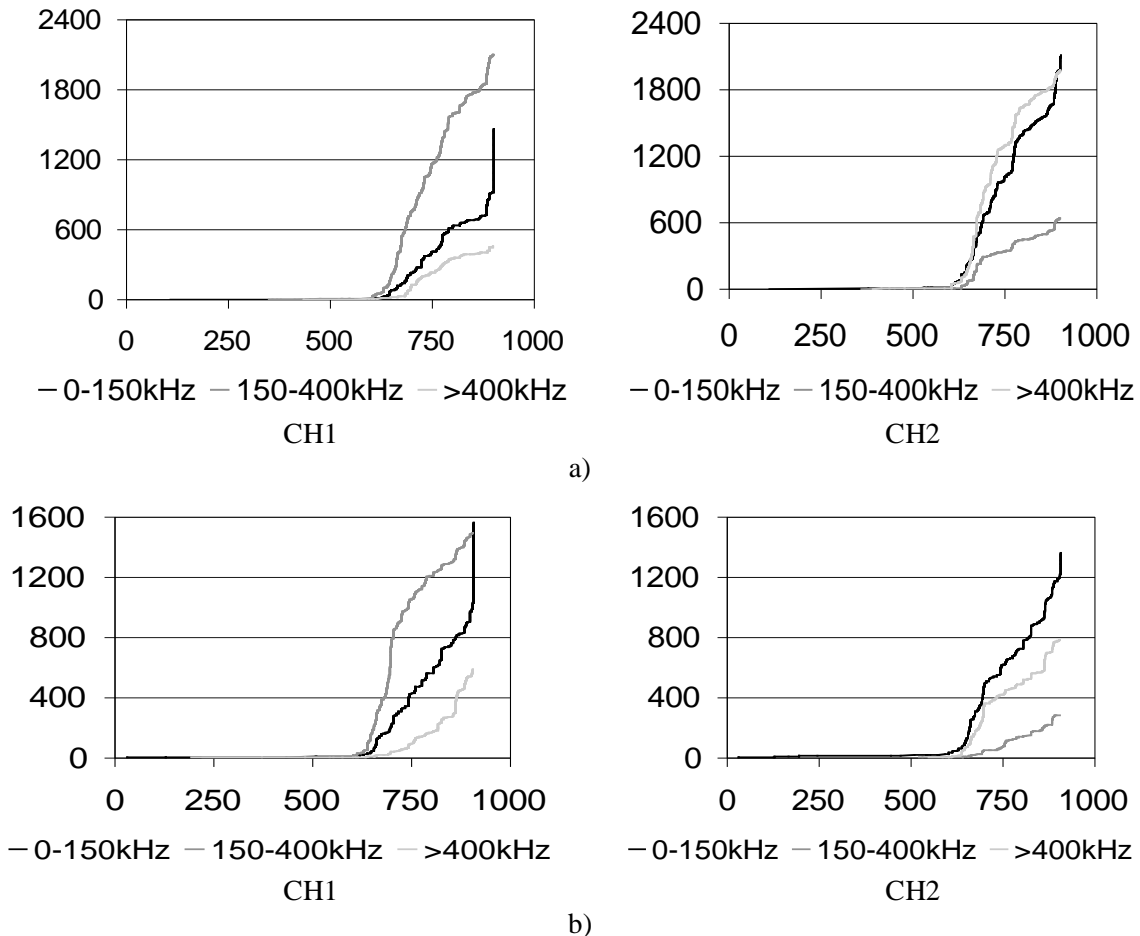


Fig. 6 Frequency analysis of beam buckling specimens, presented in cumulative hits versus time of test (s) per channel.

Conclusions

Differing source mechanisms or more specifically the differing relaxation time of source mechanisms does have an effect on the frequency content of the resulting AE signals. It has been shown that peak-frequency content of an AE signal can be used to provide some level of discrimination between signals resulting from different source mechanisms. However, it has also been demonstrated how the overriding effects of specimen geometry and sensor response can produce misleading results. As such, this technique should be approached with great care and a thorough understanding of the wave propagation and sensor response for a specific case is essential to achieving meaningful results.

Acknowledgements

The authors would like to thank Dr Pete Theobald from the National Physical Laboratory (NPL) for the loan of the conical transducer.

References

1. H. Suzuki, M. Takemoto, K. Ono, *J. Acoustic Emission*, **14**, 1996, pp. 35-50.
2. J. Bohse, *Composites Science and Technology*, **60**, 2000, pp. 1213-1226.
3. C. R. Ramirez-Jimenez, N. Papadakis, N. Reynolds, T. H. Gan, P. Purnell, M. Pharaoh, *Composites Science and Technology*, **64**, 2004, pp. 1819-1827.
4. P. J. de Groot, P. A. M. Wijnen, R. B. F. Janssen, *Composites Science and Technology*, **55**, 1995, pp. 405-412.
5. H. J. Rindorf, *Bruel and Kjaer Technical Review*, **2**, 1981, pp. 3-44

CHARACTERISTICS OF ACOUSTIC EMISSIONS FROM DEHYDRATING WOOD RELATED TO SHRINKAGE PROCESSES

SABINE ROSNER

Institute of Botany, Department of Integrative Biology; University of Natural Resources and Applied Life Sciences, Vienna (BOKU); Gregor Mendel Str. 33, 1180 Vienna, Austria

Abstract

Cavitation events in water-conducting elements of wood and dehydration cracks caused by wood-shrinkage processes induce acoustic emissions (AEs) in the high-frequency range. The aim of this study was to relate spectral features of AEs from dehydrating Norway spruce (*Picea abies* (L.) Karst.) trunkwood to shrinkage processes. Wood shrinkage in the radial direction was assessed by load cells. Resonant 150 kHz, 60 kHz and broadband transducers (operating range 50-200 kHz, 35-100 kHz and 100-1000 kHz, respectively) were used to detect AEs at the same time on standard size samples (5 or 10 cm (length) x 6 mm (radial) x 6 mm (tangential)). Two different shrinkage processes were detected, where the first shrinkage period was termed "tension shrinkage". Shrinkage caused by high tensions is a phenomenon observed also in field measurements and is practically used for drought stress measurements of living trees. The final shrinkage process started at relative water contents around the "fiber saturation point", where most of the cell lumina contain no water, but walls are fully saturated with liquid. The onset of the rapid rise in tension shrinkage coincided with the decrease of the first rapid rise of the total AE rate ($r = 0.99$). The valley between the last two AE peaks was located at the onset of the final shrinkage process. Characteristics for AEs during the tension shrinkage period were higher proportions of AEs with very high amplitudes (> 60 dB) and lower frequency components. Therefore, the highest relative AE energies (pVs) were measured during this stage. AEs during the final shrinkage period showed lower amplitudes, lower energy values and higher frequency components.

Keywords: Lumber drying, wood shrinkage, peak amplitude, frequency, AE transducers

Introduction

Norway spruce wood consists of 90% of small water conducting elements with a diameter of about 10-40 μm and a length of 1-4 mm (tracheids). Water in tracheids exists in three states; first, as "free" liquid water, second, as water vapor and within the tracheids, and third, as chemically "bound" water in the cell wall matrix [1]. „Free" water in the tracheids of the sapwood is transported under tension, requiring high mechanical strength of the cell walls in order to avoid implosion, and hydraulic safety against breakage of the water column (cavitation). During periods of drought stress decreases in the stem diameter of living trees can be observed [2-3]. These shrinkage processes are supposed to induce internal checking in living trees [4]. Stem diameter changes are caused by hydrostatic tension forces resulting in a decrease in diameter of the conducting elements, which still contain "free" water. The breakage of the water column is induced when the tension stress increases above a certain threshold. Once cavitating, the conduit does not conduct water any longer and the hydraulic conductivity of the plant is reduced, leading to impairment of water supply of the crown [5]. Cavitations induce AEs with the highest amplitudes in the range of 100-300 kHz, which are used to detect periods of drought stress non-destructively [2].

AE testing is also an established method for optimizing lumber drying conditions, where the analysis of the amplitude or energy distribution of AE signals has been successfully used to pinpoint wood checking [6-7]. Most of these tests are not performed on fully saturated wood, where still all conducting elements contain “free” water, but on “green” wood at varying moisture contents. When cell lumina contain no water, but cell walls are fully saturated with liquid (“fiber saturation point”), further dehydration leads to a shrinkage process, which can induce drying checks. Drying checks develop because the fiber saturation point is reached far earlier in the shell than in the core of a specimen and because wood is an anisotropic material concerning shrinkage (radial = in direction of the annual rings: tangential = 1 : 1.5) [7-8]. Nevertheless, combined shrinkage and AE tests are rare in AE literature on wood [9] and plant physiologists stop observations of stem diameter changes and AE rates long before most of the tracheids reach the fiber saturation point [2]. The aim of this study was to relate AEs of dehydrating Norway spruce (*Picea abies* (L.) Karst.) sapwood to radial wood shrinkage processes from the totally saturated “green” state till the cessation of all shrinkage processes.

AE Testing Procedure and Data Analysis

AEs were monitored with the μ DiSP™ Digital AE system from Physical Acoustics Corporation (PAC, Princeton Jct, NJ, USA). Preamplifiers (40 dB) were used in connection with 150-kHz R15 resonant transducers, 60-kHz R6 and WD broadband transducers (operating frequency range 50-200 kHz, 35-100 kHz and 100-1000 kHz, respectively). AEs were recorded with a detection threshold of 35 dB (0 dB = 1 μ V input). The detection threshold was chosen as the peak amplitude of signals produced by waving the AE transducer in air, plus 15 dB. Extraction of features such as the number of counts, the peak amplitude (dB), the AE duration (μ s), the relative AE energy (pVs) and the average frequency (kHz) of each AE signal was carried out with AE Win® software (PAC). AE energy (also referred to as “PAC-Energy”) is defined as the area of the rectified voltage signal over the duration of the AE signal.

AE transducers were positioned on the tangential face of fully saturated Norway spruce standard beams (cambial age = 20 - 25) using an acrylic resin clamp [9]. Preparation of fully saturated sapwood beams (0.6 cm tangential, 0.6 cm radial, and 5.0 cm or 10.0 cm longitudinal) is described in [10]. Silicone paste (Wacker, Burghausen, Germany) served as a coupling agent. The samples were positioned on an acrylic resin sample holder fixed upon a compression spring. Coupling pressure during the dehydration process was recorded with a DMS load cell (Type 8416-5500, range 0 - 500 N; amplification with an inline amplifier for DMS, Type 9235; Burster, Gernsbach, Germany) between the AE transducer and the screw of the acrylic resin clamp. The coupling pressure was set to 30 N. The acrylic resin clamp was then kept so deep in water that the wood sample was totally covered till the applied pressure reached a constant value. After quickly removing superficial water from the clamp and the wood, recording of AEs and coupling pressure was started. AE testing was done at ambient temperatures (25°C, 30% r.h.) until coupling pressure reached a constant value, which was the case after about 20 h. The coupling pressure decrease during dehydration induced by shrinkage (about 3 N in total) was related to the total radial shrinkage (digital gauge, accuracy 1 μ m). AE data filtering and presentation was done with Vallen VisualAE™ software (Vallen Systeme GmbH, Munich, Germany).

Values are given as mean values \pm standard error. Differences between mean values were tested for significance with One-Way ANOVA and subsequent Scheffe-test or by *t*-test. Associations between two variables were examined using linear regression analysis.

Results and Discussion

Shrinkage processes and total AE-rate

Two different radial shrinkage processes were observed (Figs. 1-3). First, a shrinkage period at moderate water losses, which was termed “tension shrinkage” (TS), and second, the final shrinkage (FS) period, leading to $3.86 \pm 0.11\%$ ($n = 71$) shrinkage. The onset of the rapid rise in tension shrinkage coincided with the decrease of the rapid rise of the total AE rate ($r = 0.99$, $n = 22$). Tension shrinkage is caused by a decrease in diameter of tracheids, which still contain “free” water. Hydrostatic tension forces acting perpendicular to the cell walls try to draw the walls inwards. When the stress becomes too high cavitation occurs [8]. Accordingly, tension shrinkage was to some extent a reversible process, because the tension was released after cavitation. After this relaxation period, the final shrinkage process started when most of the cell lumina contained no free water, but cell walls were still fully saturated with liquid. The beginning of the final shrinkage process coincided with a rapid rise in the AE rate. Towards the end of AE detection, two peaks in the AE rate could be found in most of the samples. The first peak occurred after $72.76 \pm 0.72\%$ ($n = 42$), the second after $85.38 \pm 0.45\%$ ($n = 42$) of the AE detection time, which was defined as the time between the start of AE testing and when the last AEs were detected. No AEs were detected after no more than 25 % of the total radial shrinkage had taken place (Figs. 1-3). Whereas WD transducers detected a quite similar total AE number in 5 and 10 cm samples, R6 and R15 transducers detected significant higher numbers of AEs in 10 cm samples (Table 1).

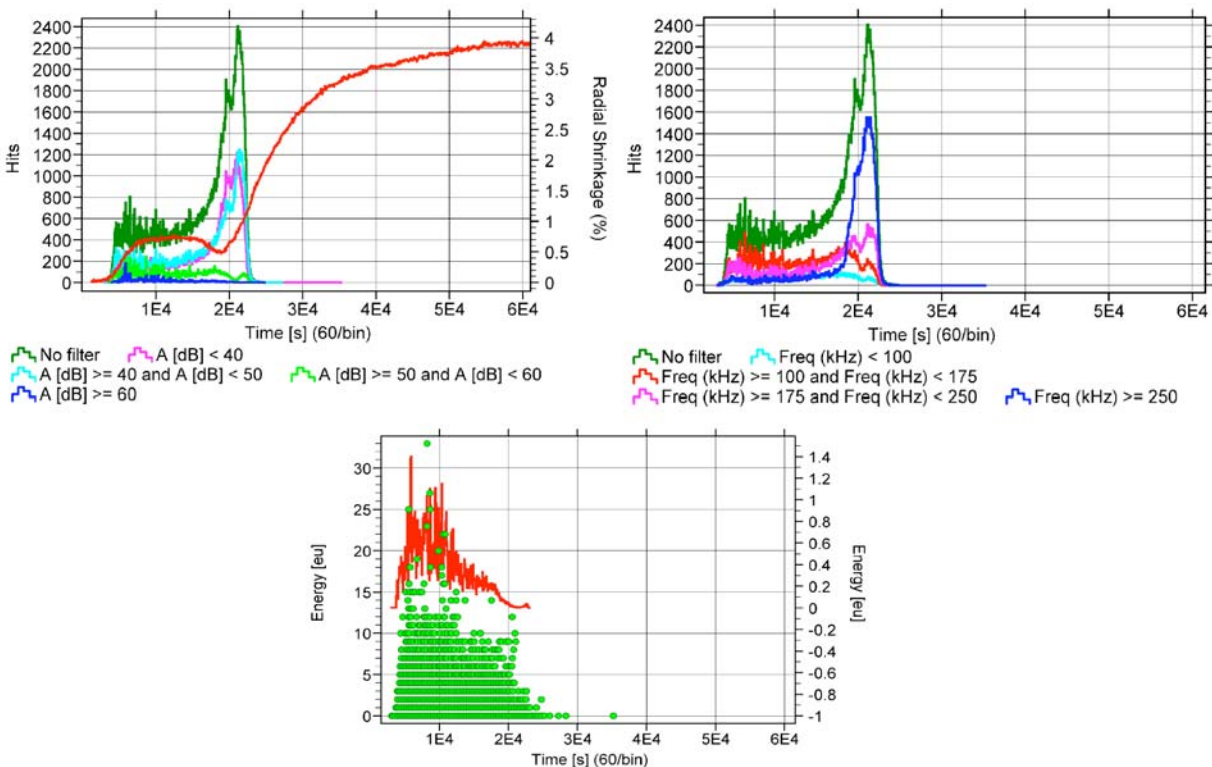


Fig. 1 AE activity (rate/min) and radial wood shrinkage during dehydration detected by WD transducer and load cell, respectively. AE rates were clustered in peak amplitude steps (left side) and average frequency steps (right side). Mean AE energy (1 eu = 1 pVs) was calculated for 1 sec steps (below, red line, right y-axis).

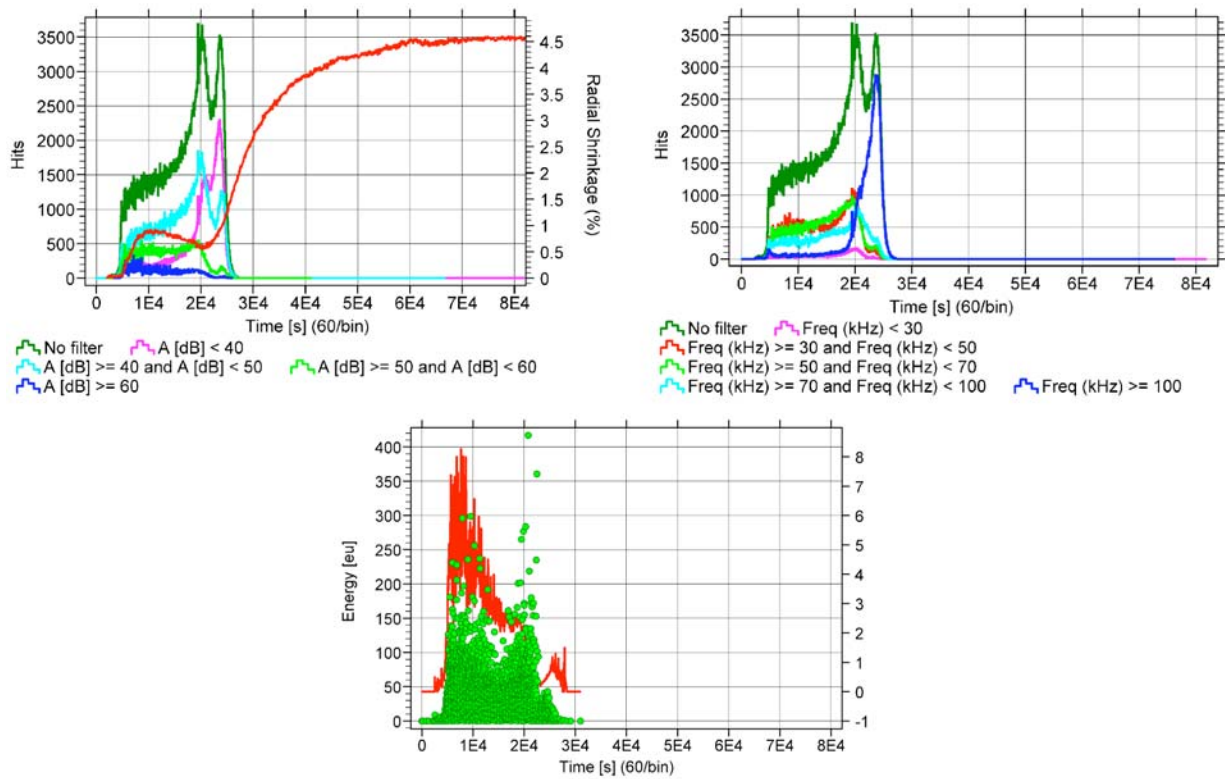


Fig. 2 AE activity (rate/min) and radial wood shrinkage during dehydration detected by R6 transducer and load cell, respectively. AE-rates were clustered in peak amplitude steps (left side) and average frequency steps (right side). Mean AE energy (1 eu = 1 pVs) was calculated for 1 sec steps (below, red line, right y-axis).

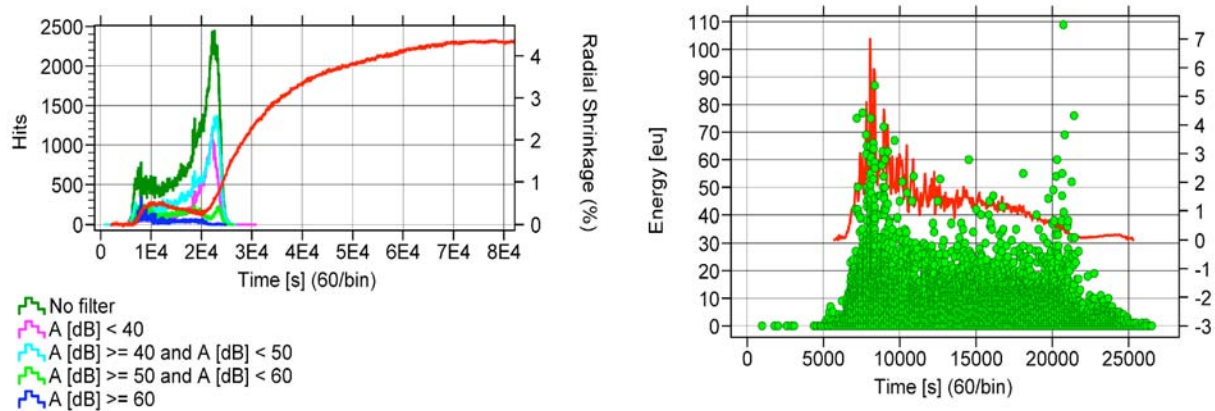


Fig. 3 AE activity (rate/min) and radial wood shrinkage during dehydration detected by R15 transducer and load cell, respectively. AE-rates were clustered in peak amplitude steps (left side). Mean AE energy (1 eu = 1 pVs) was calculated for 1 sec steps (right side, red line, right y-axis).

AE characteristics during shrinkage processes

Highest mean peak amplitudes and energies were measured during the tension shrinkage period at moderate water losses (Figs. 1-3). The relative time occurrence of the maximum mean peak amplitudes/min showed no significant differences between the transducer types (WD, R6, R15). Highest mean amplitude values were reached after $27.77 \pm 0.90\%$ of the AE detection time ($n = 42$). The cumulated AE energy rate can be used to characterize the hydraulic vulnerability of

sapwood. Norway spruce wood consists of 90% of tracheids, which vary in diameter. It is supposed that mean high energy AEs represent cavitations of more vulnerable, larger tracheids, because more elastic energy is stored in larger conduits under tension [10]. Tension shrinkage processes can be observed in living trees and are used to pinpoint periods of drought stress in the field [2, 3]. In accordance, the maximum AE rate of signals >60 dB and the maximum AE energy rate/min were detected in the middle of the tension shrinkage period (R6, R15, $r = 0.88$, $n = 14$). At the time of maximum AE rates of signals >60 dB, lower AE rates/min were measured by WD transducers than by R6 or R15 transducers ($P < 0.05$, Fig. 4). The lower number of AEs recorded by WD transducers might be explained both by the lower sensitivity of WD than R6 and R15 transducers and the frequency operating range (100-1000 kHz). In highly attenuating materials, such as wood, the usable upper frequency level is supposed to be 100-200 kHz [6].

Table 1 Frequency characteristics of AEs measured by transducer types WD, R6 and R15 at different shrinkage stages of wood samples varying in length (L). Frequency factors were calculated from AE rates/min clustered by average frequency steps. Stage TS gives results for the middle of the tension shrinkage period, when the maximum AE energy/min was detected, FS1 for the first AE peak at the onset of the final shrinkage period, and FS2 for the second AE peak during the final shrinkage period. Different letters indicate significant differences ($P < 0.001$) in the Frequency Factors between 5-cm and 10-cm samples.

	L (cm)	AEs total	Frequency Factor	n	Stage TS Mean (SE)	Stage FS1 Mean (SE)	Stage FS2 Mean (SE)
WD	5	350909.5 (23420.8) ^a	< 175 kHz / > 175 kHz	7	1.73 (0.21) ^a	0.95 (0.08) ^a	0.20 (0.02) ^a
WD	10	410353.5 (37057.6) ^a	< 175 kHz / > 175 kHz	7	1.44 (0.06) ^a	0.97 (0.08) ^a	0.17 (0.02) ^a
R6	5	393935.3 (29590.1) ^a	< 50 kHz / > 50 kHz	7	1.43 (0.16) ^a	0.31 (0.06) ^a	0.05 (0.01) ^a
R6	10	620891.8 (26459.2) ^b	< 50 kHz / > 50 kHz	7	0.77 (0.05) ^b	0.47 (0.04) ^a	0.04 (0.02) ^a
R15	5	370243.3 (18305.9) ^a	< 155 kHz / > 155 kHz	7	2.83 (0.19) ^a	2.92 (0.41) ^a	0.99 (0.15) ^a
R15	10	575638.7 (28961.2) ^b	< 155 kHz / > 155 kHz	7	2.51 (0.12) ^a	3.89 (0.35) ^a	1.07 (0.11) ^a

Analysis of average frequencies showed that the number of signals <175 kHz was 1.4 - 1.7 times higher than those of signals >175 kHz when the mean AE energy rate/min reached maximum values (Table 1). At the same time the R6 transducer recorded 1.4 times the number of AEs <50 kHz than of AEs >50 kHz in 5-cm samples, but only 0.8 times the number in 10-cm samples (R6, Table 1). The rate/min of signals <50 kHz, related to the corresponding total AE rate/min, reached maximum values during the tension shrinkage period (R6, $58.57 \pm 2.61\%$ (5 cm), $43.36 \pm 1.52\%$ (10 cm), $P < 0.001$). Sample length-dependent differences were also present in the maximum mean energy/min values. In 10-cm samples, much lower maximum energies/min were detected than in 5-cm samples. Maximum mean energies/min during the tension shrinkage period were positively related to the relative amount of signals <50 kHz (related to the total AE rate at the same time, Fig. 5).

AEs within the frequency range from 30 to 50 kHz reached highest absolute rates shortly before the final shrinkage process started (Fig. 2). The relative rates (related to the corresponding total AE rate) of AEs <50 kHz were, however, lower than during the tension shrinkage period, when maximum mean energies/min were measured (R6, $22.56 \pm 3.52\%$ (5 cm), $31.82 \pm 1.84\%$ (10 cm), $P < 0.05$). The number of signals with average frequencies <50 kHz was less than half

the number of signals >50 kHz at the next to the last AE rate/min peak (R6, Table 1). Shortly before the final shrinkage took place, WD transducers detected a quite similar number of signals <175 kHz and >175 kHz (WD, Table 1). The AE rate/min measured by WD transducers was significantly lower than measured by R15 or by R6 transducers ($P < 0.001$, Fig. 4).

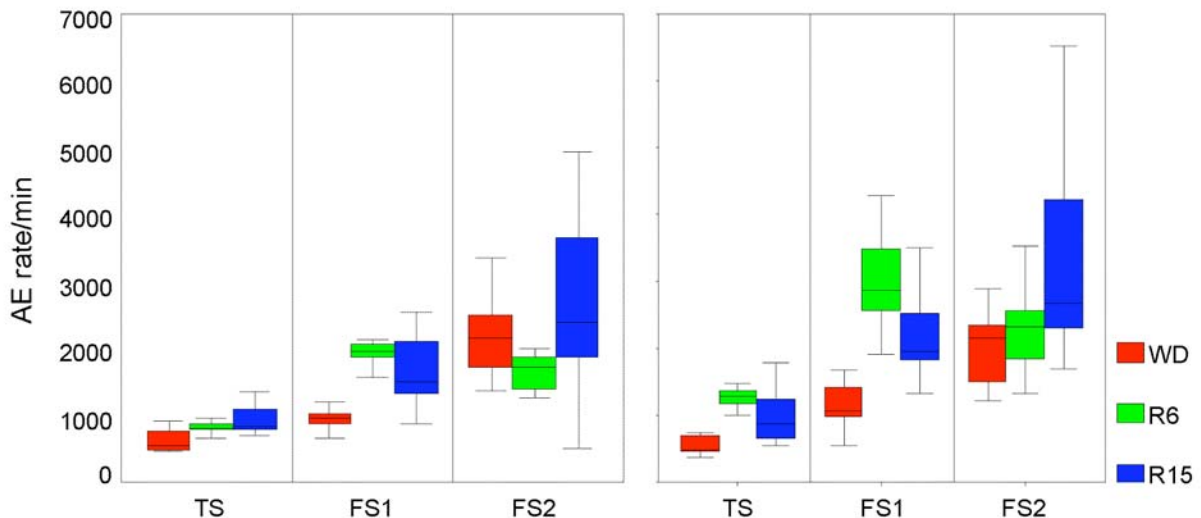


Fig. 4 Box- and whiskers plots of the AE rate/min at different shrinkage stages detected by different transducer types (WD, R6, R15) for 5-cm sample length (left side) and 10-cm sample length (right side). Stage TS gives results for the middle of the tension shrinkage period, when the maximum AE energy/min was detected, FS1 for the first AE peak, located around the fiber saturation point, at the onset of the final shrinkage period, and FS2 for the second AE peak during the final shrinkage period.

The final shrinkage process was characterized by a very high proportion of signals with high average frequencies (>250 kHz (WD), >100 kHz (R6)), low amplitudes and energies (Figs. 1-3). These signals may come from cavitation events in tracheids, which contribute less to axial water transport than to other wood functions such as radial water transport, mechanical support and storage of water, or from cavitations in ray tracheids [10]. At the last AE peak, the number of signals <175 kHz was less than 25 % the number of AEs >175 kHz (WD, Table 1). R6 transducers measured a much more lower number of AEs with average frequencies <50 kHz in relation to signals >50 kHz (Table 1). The relative amount of signals <50 kHz made up only $5.05 \pm 1.00\%$ (5 cm) and $4.25 \pm 0.80\%$ (10 cm) of the total AE rate. R15 transducer detected a lower relative amount of signals <155 kHz than during the tension shrinkage period or at the onset of the final shrinkage period (R15, Table 1). The AE rate/min measured by WD, R6 and R15 transducers showed no significant differences (Fig. 4).

The bulk of AEs during lumber drying resembles cavitation events of water conducting elements [7]. Extremely high energy AEs, which were detected during the tension shrinkage period as well as at the onset of the final shrinkage process may have been induced by mechanical failure [11]. References [12, 13] could distinguish two phases during Norway spruce lumber drying by analyzing AE burst rates. The first peak in the AE rate was interpreted as checking caused by surface tension stress, and the second peak (at high water loss) as checking caused by tensile stresses inside the samples. Reference [8] supposed that sapwood within-ring internal checking is caused by water tension and not by differential shrinkage, because checking occurred long before

most of the cells reached the fiber saturation point. Internal checks caused by high tensions may also occur in low density earlywood of living trees during periods of summer drought, and are a severe problem of short rotation forests [4].

The method presented might help to understand the mechanisms that cause internal checking in living trees. Knowledge about the relationship between shrinkage processes, AE rates and AE features, such as the average frequency, the peak amplitude and energy (especially single high energy events), could be also helpful for analyzing checking processes during lumber drying stages. It is recommended to use standardized sample sizes, because sample length had a significant impact on frequency and energy composition. Both WD and R6 transducers were suitable to characterize the different stages of shrinkage by analyzing the average frequency composition of the AEs. R6 transducers reacted, however, very sensitively to background noise.

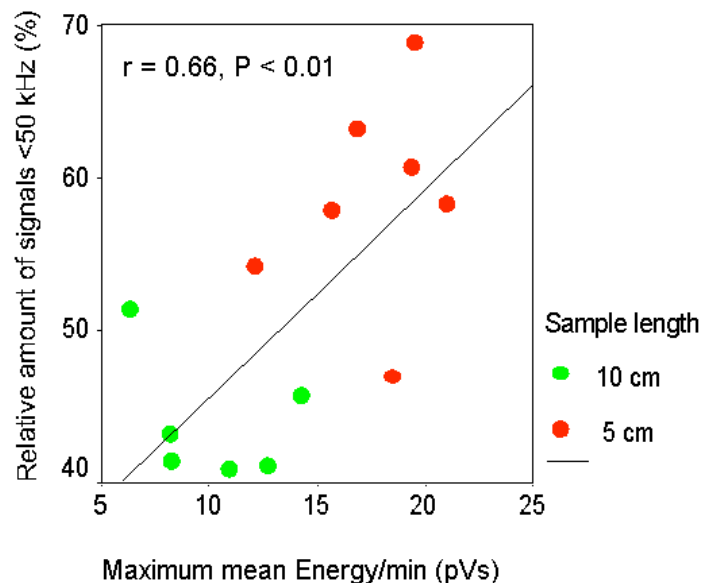


Fig. 5 Relationship between the relative amount of signals <50 kHz related to the total AE rate and the maximum mean AE Energy/min during the tension shrinkage period detected at the same time by R6 transducers.

Acknowledgements

This study was financed by the Austrian Science Fund FWF (Project T304-B16). Raphael Klumpp and Peter Kritsch are thanked for providing Norway spruce sample material.

References

1. C. Skaar, *Wood-Water Relations*, Springer-Verlag, 1988, 283 p.
2. T. Hölttä, T. Vesala, E. Nikinmaa, M. Perämäki, E. Siivola, M. Mencuccini, *Tree Physiology* **25**, 2005, 237-243.
3. I. Offenthaler, P. Hietz, H. Richter, *Trees*, **15**, 2001, 215-221.
4. M. Grabner, P. Cherubini, P. Rozenberg, B. Hannrup, *Scandinavian Journal of Forest Research*, **21**, 2006, 151-157.

5. M.T. Tyree, M.H. Zimmermann, *Xylem structure and the ascent of sap*, Springer, 2002, 283 p.
6. F.C. Beall, *Wood Science and Technology* **36**, 2002, 197-212.
7. S. Kawamoto, R.S. Williams, *Acoustic emission and acousto-ultrasonic techniques for wood and wood-based composites A Review*, U.S. Department of Agriculture, Forest Service, Forest Products Laboratory, Gen. Techn. Rep. FPL-GTR-134, 2002, 16 p.
8. R.E. Booker, *Proceedings of the 4th IUFRO Wood Drying Conference: Improving Wood Drying Technology*, 1994, pp. 133-140.
9. S. Rosner and R. Wimmer. *14th International Symposium on Nondestructive Testing of Wood*, Shaker Verlag, 2005, pp. 123-134.
10. S. Rosner, A. Klein, R. Wimmer, B. Karlsson, *New Phytologist* **171**, 2006, 105-116.
11. S.L. Quarles, *Wood and Fiber Science* **24**, 1992, 2-12.
12. P. Niemz, R. Emmeler, E. Pridöhl, J. Fröhlich, A. Lühmann, *Holz als Roh- und Werkstoff*, **52**, 1994, 162-168.
13. I. Cunderlik, W. Molinski, J. Raczkowski, *Holzforschung* **50**, 1996, 258-262.

CHARACTERIZATION OF TITANIUM HYDRIDES USING A HYBRID TECHNIQUE OF AE AND FEM DURING INDENTATION TEST

YOSHIHIRO TANIYAMA, HIDEO CHO, MIKIO TAKEMOTO
and GEN NAKAYAMA*

Faculty of Science and Engineering, Aoyama Gakuin University, Fuchinobe, Sagamihara, Kanagawa 229-8558, Japan; *Research Laboratory, Ishikawajima Harima Heavy Industry, Shin-nakahara, Isogo, Yokohama, Kanagawa, 235-8501, Japan

Abstract

Pure titanium (Gr.1) and titanium-0.6 mass% palladium (Gr.17) are prone to produce brittle hydrides when they absorb hydrogen. This research studied structures and mechanical characteristics of two hydrides in Gr.1 and Gr.17. Fracture strength of thin hydrides was measured by a hybrid method of AE and FEM during micro-indentation. We determined the threshold indentation load to cause the Mode-I fracture during Vickers indentation by AE monitoring and then computed the critical strain to cause the Mode-I fracture by the FEM. Utilizing the stress and strain curves of base metals and hydrides obtained by a dual indentation method, the fracture strain of the Gr.17 hydride is calculated as half that of the Gr.1 hydride. X-ray diffraction revealed that the Gr.1 and Gr.17 hydrides are $\text{TiH}_{1.971}$ and TiH_2 , respectively. Palladium in Gr.17 contributes to produce hard and brittle hydride with higher hydrogen content.

Keywords: Titanium hydride, mechanical property, fracture strain and strength, indentation, critical indentation force, FEM, Mode-I crack

Introduction

Study is underway to assess the endurance capability of titanium-clad overpack of high-level radioactive waste in deep underground water. The overpack will be exposed to oxygen-free 3.5% NaCl solution. Thus, pure titanium (Gr.1) and titanium-palladium (Gr.17) are likely to produce brittle hydrides by the cathodic current density (proton reduction) corresponding to the passivation holding current density. We previously reported both the fracture behavior and fracture dynamics of Gr.1 hydride [1]. Measurement of mechanical properties of hydrides is, however, difficult since the hydrides are thinner than 100 μm . We used a hybrid technique of AE and FEM during Vickers indentation on the thin hydrides.

This study reports AE results on the progression of micro-cracks in growing hydrides in a simulated underground environment. Next we report the mechanical properties of Gr.1 and Gr.17 hydrides using an indentation technique. AE was successfully utilized to determine the critical indentation load to cause the Mode-I fracture in the hydrides. Mechanical properties of Gr.1 and Gr.17 hydrides were found to be much different, due to chemical compositions of the hydrides.

AE from Micro-fractures in Growing Titanium Hydrides

Experimental method

The amount of hydrogen charge to the overpack in underground environment is calculated to be 10 MC/m^2 for 60,000 years storage [2]. We supplied the specimens with hydrogen at cathode

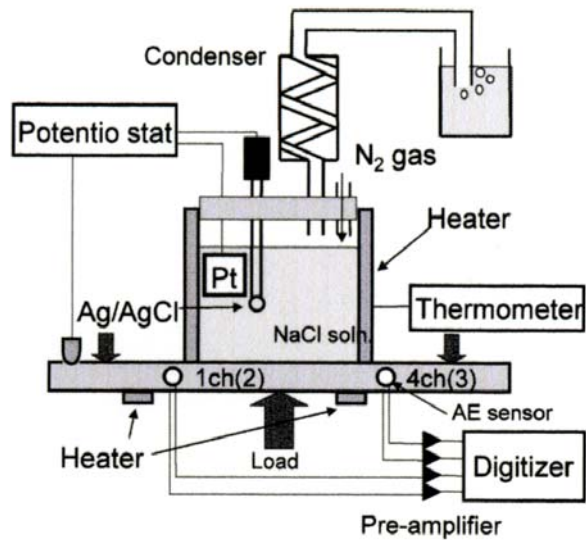


Fig. 1 Experimental setup for hydrogen charging and AE monitoring for Ti.

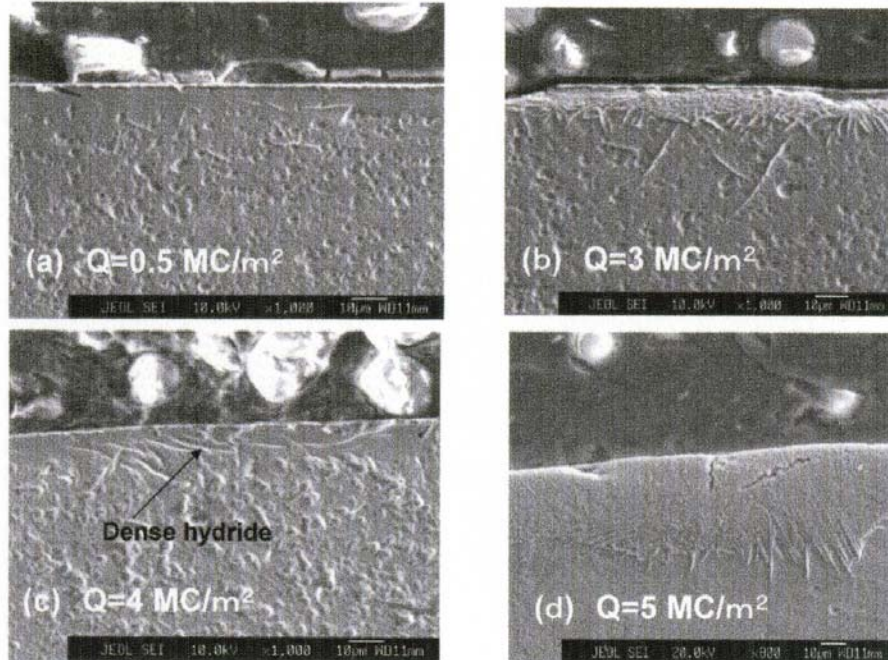


Fig. 2 Changes of the Gr.17 hydrides with hydrogen charge.

current density of 10 A/m^2 in a 0.6 mol/l NaCl solution purged by nitrogen gas at 70°C . The amount of hydrogen charging was 1, 3, 5, 6.5 and 10 MC/m^2 .

Figure 1 shows the hydrogen charging and AE monitoring method for plate-shaped Ti specimens of 11-mm thickness, 50-mm width and 145-mm length. The specimen was subjected to 3-point bending with surface tensile stress of 200 MPa. AE was monitored by four resonant-type small sensors (PAC: Type-PICO) mounted on the side surfaces of the specimen. Sensor outputs were amplified 40 dB by pre-amplifiers and fed to a personal computer.

Chemical composition of Gr.1 titanium is 0.01 mass% C-0.0007H-0.031O-0.0005N-0.032Fe and $<0.02\text{Pd}$. That of the Gr.17 is 0.014 mass% C-0.0007H-0.09O-0.003N-0.035Fe and 0.062Pd.

Growth behavior of hydrides

We studied growth behavior of Gr.17 hydride as seen in Fig. 2. Below 0.5 MC/cm^2 , we observed needle-shaped hydrides as shown in photo (a). Above 3 MC/m^2 , the needle shaped hydrides coalesce and forms colonies of dense layer of $10\text{-}\mu\text{m}$ thickness. Characteristic features of Gr.17 hydride are that these are non-uniform and irregular in shape. Above 4 MC/m^2 , plate-shaped hydride layer is produced. At 5 MC/m^2 , the hydride layer grows to thick plates of $20 \mu\text{m}$ as shown in (d). Thickness of Gr.17 hydride does not exceed $150 \mu\text{m}$ at 10 MC/m^2 , but the hydrides tend to crack on their own.

Figure 3 shows changes of cumulative AE counts with hydrogen charge for Gr.1 and Gr.17 Ti. In Gr.1 Ti, AE counts increased gradually till the charge amount of 6 MC/m^2 and rapidly increased above 6 MC/m^2 , while it increased rapidly above 4.5 MC/m^2 for Gr.17 Ti. Sources of AE were located using both the arrival-time difference of the So-wave and sheet velocity of 5990 m/s . All 33 events with strong So-wave were located in the corrosion cell. Figure 4 compares the transverse structure of two hydrides produced in Gr.1 and Gr.17 Ti at 10 MC/m^2 . Thickness of Gr.17 hydride layers reached approximately $120 \mu\text{m}$, while that of Gr.1 hydride is $10 \mu\text{m}$. For Gr.17 hydride, we observed dish-shaped shallow exfoliation. It is noted that crack morphology changes depending on the geometry and mechanical properties of the hydrides. We sometimes observed vertical and/or slant cracks.

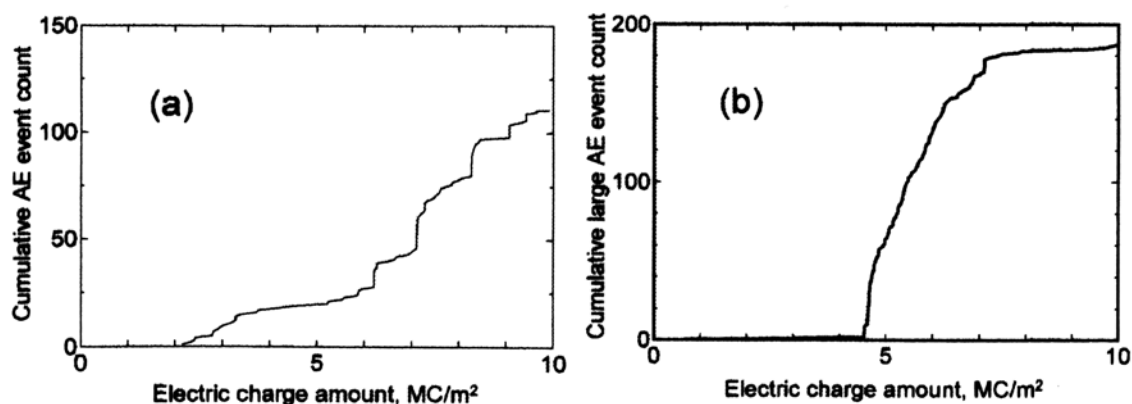


Fig. 3 Changes of cumulative AE counts with H charging to Gr.1 Ti (a) and Gr.17 Ti (b).

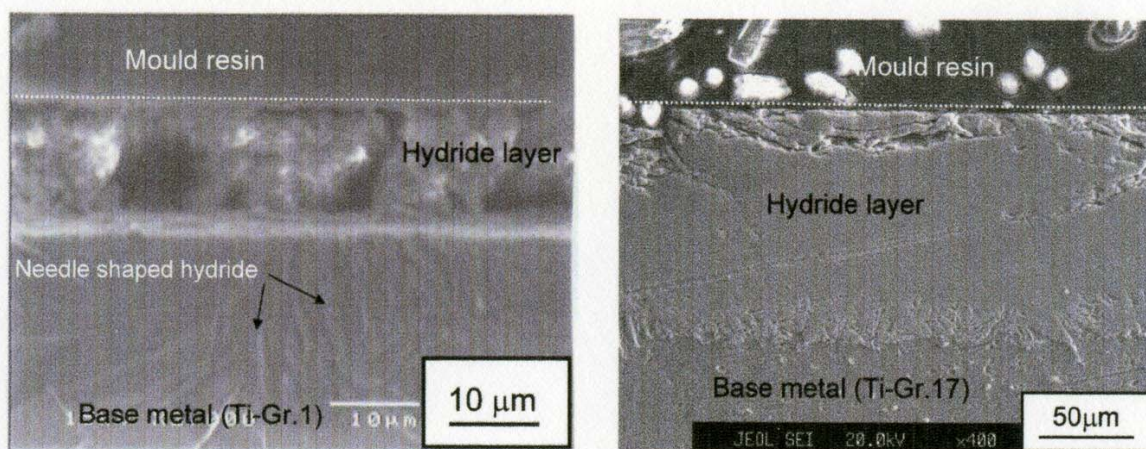


Fig. 4 Transverse SEM of Gr.1 (left) and Gr.17 hydrides after charging 10 MC/m^2 .

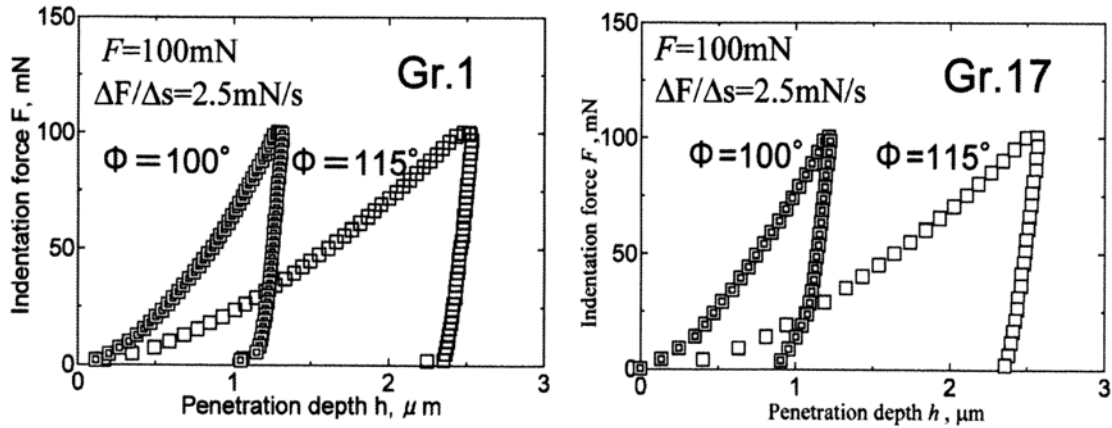


Fig. 5 Indentation force F vs. penetration depth h curves of Gr.1 and Gr.17 substrates by the dual indentation method.

Mechanical properties of Ti and hydrides

We first studied whether the Gr.17 hydride suffers median crack by micro-indentation. We observed no median crack, but slight extrusion around the periphery of the Vickers indentation, indicating that the hydride is not so brittle like ceramics, but possesses some extent of ductility.

Next, we measured the stress-strain curves of the substrates and hydrides using a dual indentation method. Indentation load: F vs. penetration depth: h curves were first obtained using a dynamic micro-indentation machine (Shimadzu, DUH-W201). Figure 5 compares the F vs. h curves of Gr.1 and Gr. 17 Ti, using two indenters with different tip-angle. Details of the dual indentation method can be found elsewhere [3, 4]. It estimates the Young's modulus: E , yield strength: σ_y , strength coefficient: R and work hardening coefficient: n of the stress-strain curves with $\sigma = R\epsilon^n$ in the plastic region.

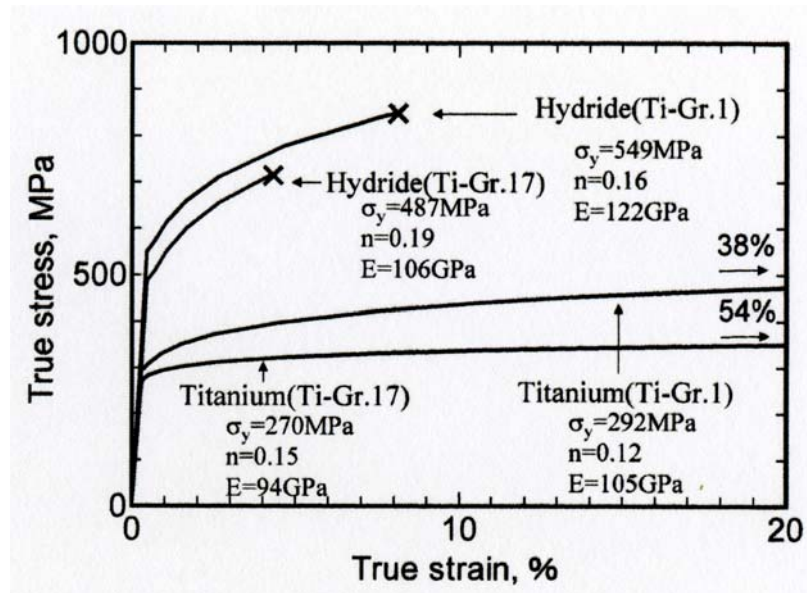


Fig. 6 σ - ϵ curves of substrates and hydrides by the dual indentation method.

Figure 6 compares the σ - ϵ curves of Gr.1 and Gr.17 Ti. Three parameters: E , R and n are shown in the figure. The fracture strains (38% for Gr. 1 and 54% for Gr.17) of the base metals

were determined by the tensile tests. Experimental σ - ϵ curves agreed quite well with those predicted by the dual indentation method.

Fracture strains of the hydrides

We determined the fracture strains by inducing a fine Mode-I crack using a new indentation machine. We studied whether the Mode-I crack can be induced by Vickers indentation, using a commercial indentation machine (HVM-2000). Figure 7 shows examples of cracks induced into thin hydride layer of Gr.1 Ti. The left figure shows the crack induced by loading up to 15 N, and the right figure by loading to 20 N. The vertical crack is produced by tensile stress induced by the indentation, and is the Mode-I crack. Large loading of 20 N produced both the partial exfoliation and subsequent Mode-II cracks as well the Mode-I crack. These data indicates that we can determine the critical strain to induce the Mode-I crack by FEM method, if we can correctly determine the critical load or the critical penetration depth.

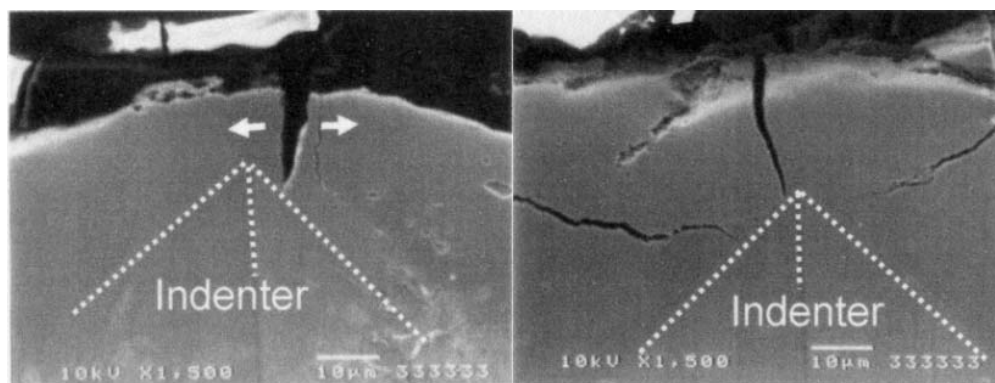


Fig. 7 Cracks induced in the hydride by Vickers indentation at 15 N (left) and 20 N (right).

The commercial indentation machine, however, does not measure the F vs. h curve. Thus, we developed a new indentation machine, which can measure the F vs. h curve and used AE system to monitor the critical load to cause the first Mode-I crack. The new indentation machine was constructed by modifying the micro-servo testing machine (Shimadzu, Microservo MNT-1000NB-10). We controlled the load using a feedback program developed in laboratory and monitored the penetration depth by an eddy-current displacement meter to the accuracy of 0.1 μm . Construction of sliding device of the sample from a microscope to the indentation machine was difficult. Positioning accuracy of this device is not so good as hoped for.

The critical load to cause the first Mode-I cracks was monitored by AE. We mounted two small sensors (PAC, Type-PICO) on the two counter surfaces. Output of the sensors were amplified by 60 dB and fed to a personal computer. AE from friction between the indenter and hydride were separated from AE by the Mode-I crack, using the polarization distribution of the first arriving So-mode waves [4]. The Lamb waves with the same So polarity was diagnosed as the AE from the Mode-I crack. Amplification of 60 dB is needed since the Mode-I crack is generally less than 5 μm and emitted weak Lamb waves.

Figure 8 compares the F vs. h curves for Gr.1 and Gr.17 hydrides. Vertical triangles near the curves indicate the first AE timing from the Mode-I cracks. The critical load to cause the first Mode-I crack is determined as 19.6 N for Gr.1 hydride and 7.4 N for Gr.17 hydride. We previously reported the critical load of 16 N for Gr.1 hydride [1]. Larger critical load and penetration depth for Gr.1 hydride than those for Gr.17 hydride indicates that Gr.1 hydride is less brittle.

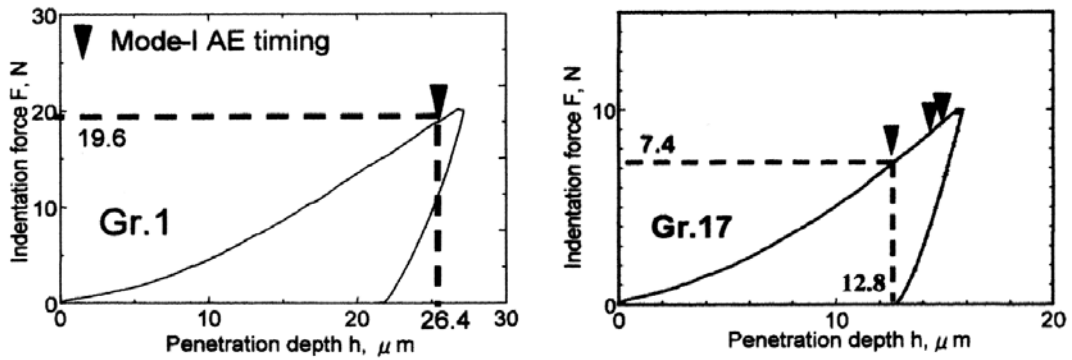


Fig. 8 F vs. h curves for Gr.1 and Gr.17 hydrides with timing of AE from the Mode-I crack.

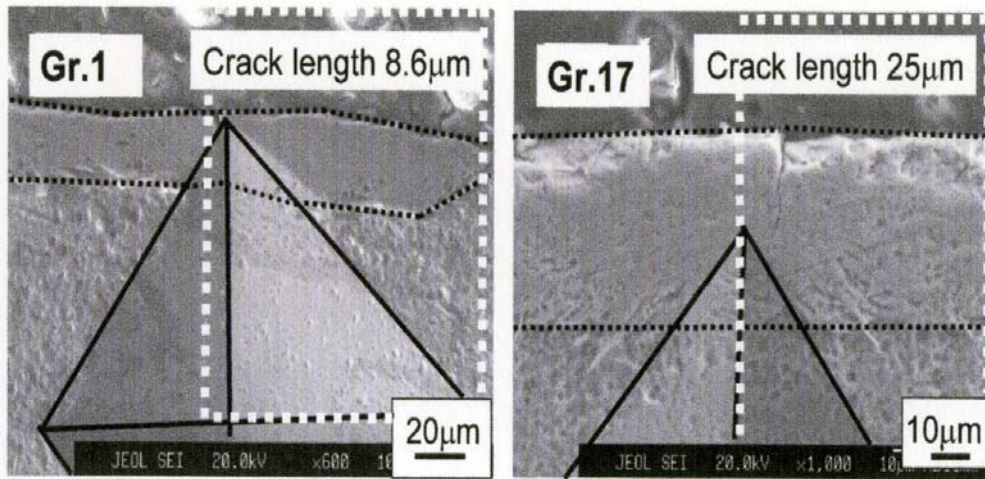


Fig. 9 SEM photos with the Mode-I cracks, indentations and region for FEM analysis.

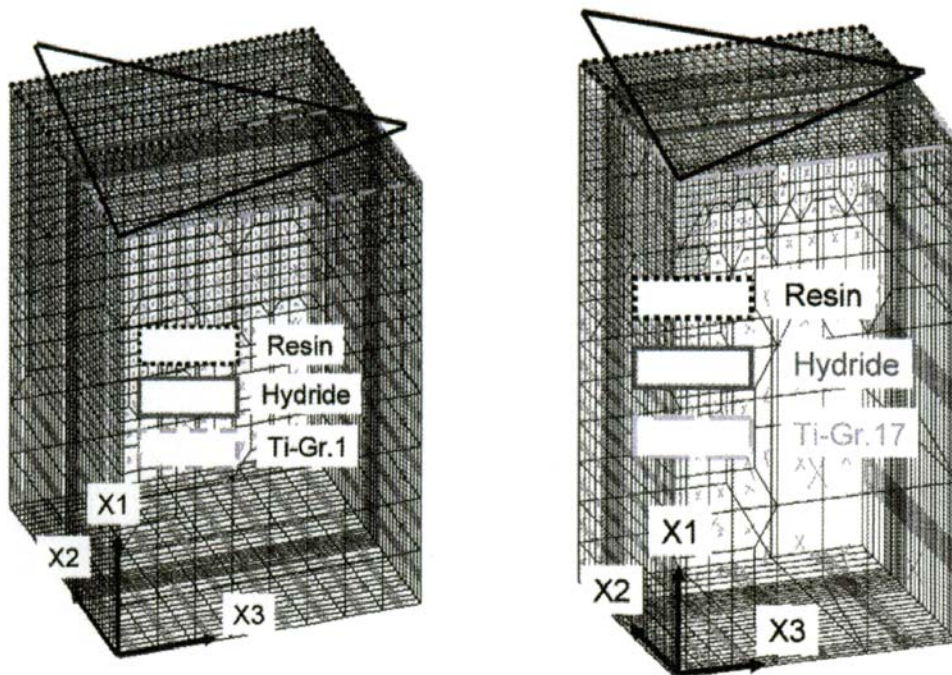


Fig. 10 Elements of quarter model for three dimensional FEM for strain computation during indentation.

Figure 9 shows the Mode-I cracks in two hydrides. Due to poor positioning capability of the sliding device developed, indentation location could not be accurately determined. Short crack of 8.6- μm length was induced in Gr.1 hydride when the indenter reached the hydride. FEM analysis was performed in the region surrounded by dashed line. Here, the triangle by solid line designates the ridge of the indenter. Center of the indentation was originally indented in the base metal. Figure 10 shows elements of a quarter model for 3-dimensional FEM. Lower left corner of the triangle corresponds the center of the tip of the indenter. We computed the strain ϵ_{33} in the direction of X_3 using the software package of MARC and MENTAT.

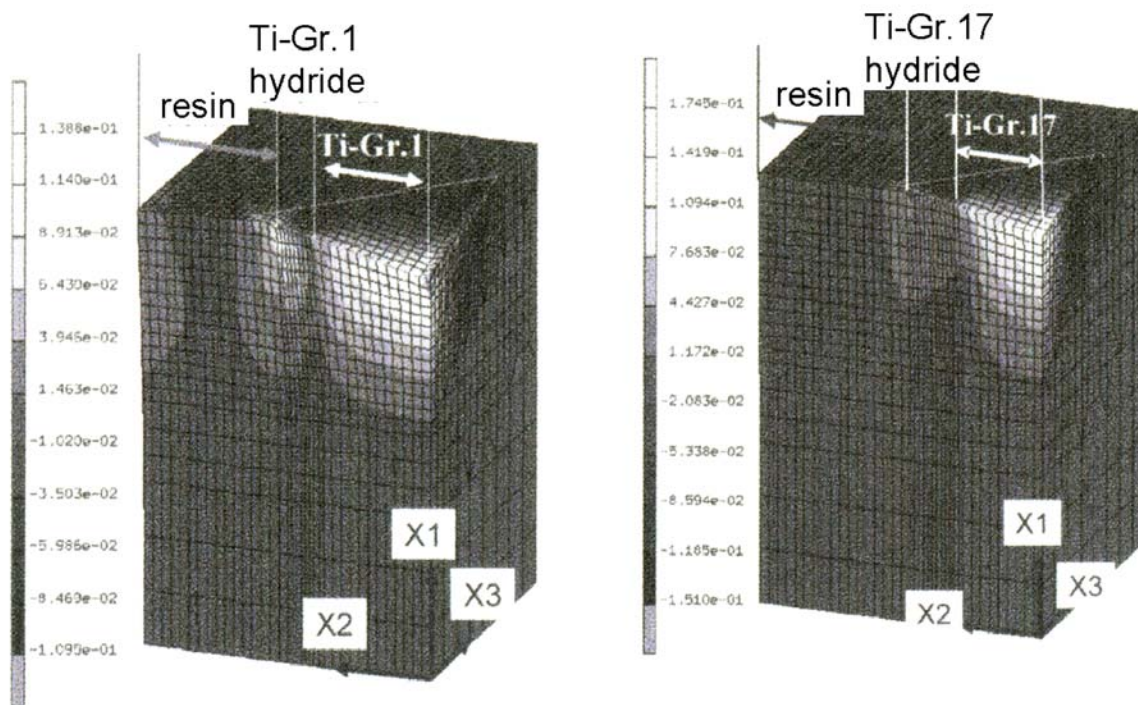


Fig. 11 Strain distribution around the Vickers indentation computed by 3-dimensional FEM.

The strains ϵ_{33} were computed using the F vs. h curves of both substrates and hydrides by changing the penetration depth (displacement controlling condition). Figure 11 shows the results. Detail strain distribution in the X_2 direction is shown in Fig. 12. The strain ϵ_{33} is lower at interface of the base metal/hydride, but increases toward the free surface. The critical strain is determined as 0.081 and 0.043 for Gr.1 hydride and Gr.17 hydride, respectively.

Deviation of the critical load to cause the Mode-I crack in Gr.1 hydride was studied by two graduate students (A and B) for three years. The student A reported the critical load of 16 N and 20. Student B reported, using another sample prepared by the same hydrogen charging condition, 19.6 N (this study). Average critical load for Gr.1 hydride is 18.5 N. Thus, the critical strain of 0.081 for Gr.1 hydride, obtained using 19.6 N, is supposed to be close to the critical strain computed using the average critical load of 18.5 N. Student B attempted to obtain more data for Gr.17 hydride, but could not, since the location accuracy of the sliding device was poor. He could not induce the Mode-I crack in the hydride. Thus we cannot discuss the correct critical load of Gr.17 hydride. We examined propriety of the FEM method. Figure 13 compares the experimental F vs. h curve with that by the FEM. Though the curve by the FEM is slightly lower than the experimental data, there observed a fairly good agreement, indicating a reliable simulation of experiment by FEM.

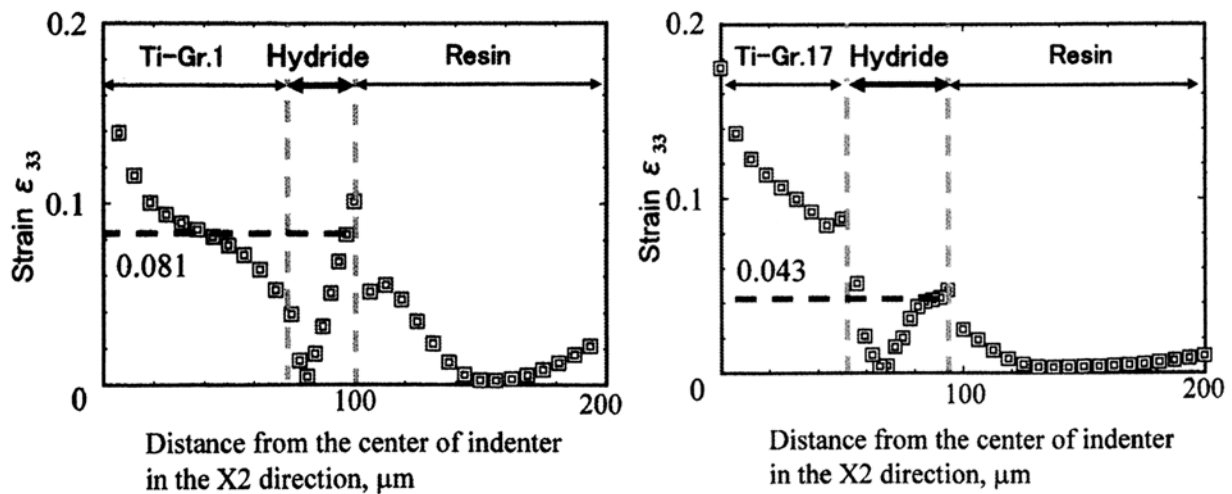


Fig. 12 Distribution of ϵ_{33} in the direction of X_2 .

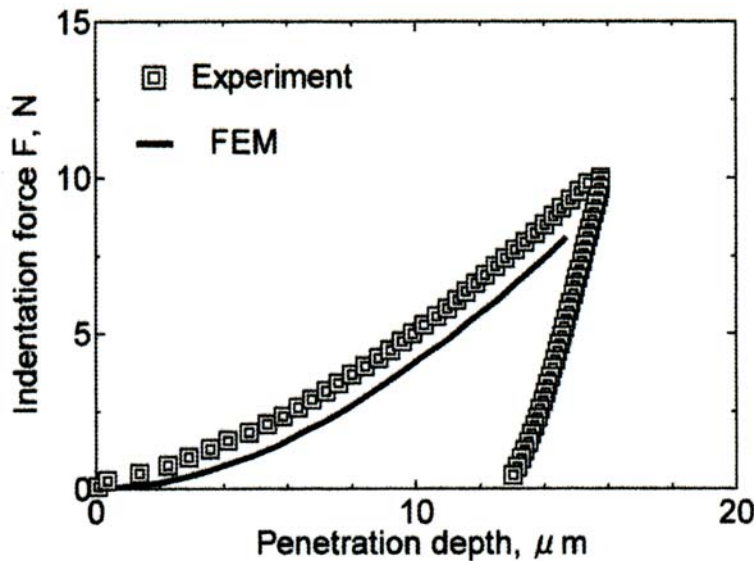


Fig. 13 Comparison of F vs. h curves measured and computed by FEM for the Gr.17 hydride.

The stress-strain curves in the final form were already presented in Fig. 7. Both the fracture strength and strain of Gr.17 hydride are smaller than those of Gr.1 hydride. This difference was thought to be due to chemical composition of the hydrides. We studied chemical composition of the hydrides by X-ray diffraction method and observed a broad diffraction peaks at around 98.6° for Gr.1 hydride and that at around 62.8° for Gr.17 hydride. According to the ASTM code 07-0370, Gr.1 hydride was determined as $TiH_{1.971}$ and Gr.17 hydride as TiH_2 . Brittleness of Gr.17 hydride appears to be due to its higher hydrogen concentration. From Fig. 8, we note three AE signals from the Mode-I cracks for Gr.17 hydride. This suggests that surface layer of the brittle Gr.17 hydride suffers small exfoliations following the first Mode-I crack. Another example is in the Fig. 5. We observed small multi-layer exfoliations in thin surface layer of the Gr.17 hydride.

Conclusion

In order to study the mechanical properties of hydrides produced in pure titanium (Gr.1) and titanium-0.06 mass% zirconium alloys (Gr.17), a hybrid method of AE and FEM was utilized for indentation test.

Results obtained are summarized as below.

- 1) Gr.1 titanium emitted AEs by cracking at charges of more than 6 MC/m^2 , while Gr.17 Ti emitted abrupt AE at 4.5 MC/m^2 . Thickness of the hydride layer of Gr.17 at 10 MC/m^2 reached approximately $120 \mu\text{m}$, while that of Gr.1 is $10 \mu\text{m}$.
- 2) Stress-strain curves of Gr. 1 and Gr.17 Ti and hydrides were estimated by dual indentation method. There observed a good agreement between the estimated and measured for the substrates.
- 3) Fracture strain of the hydrides were estimated using a new indnetation machine and FEM. Critical indentation load to cause the Mode-I crack was correctly determeind by AE monitoring. Fracture strain of Gr.1 hydride was calculated as 8.1%, while that of Gr.17 hydride as 4.3%. The Gr.17 hydride is more brittle than the Gr.1 hydride. Chemical composition of the Gr.17 hydride was measured as TiH_2 , and that of the Gr.1 hydride as $\text{TiH}_{1.971}$ by the X-ray diffraction method.

References

- [1] Y. Taniyama, T. Matsuo, H. Cho, M. Takemoto and G. Nakayama, *Progress of Acoustic Emission XIII*, 2007, pp. 295-302.
- [2] G. Nakayama, N. Nakamura, Y. Fukaya, M. Akashi, H. Ueda, *European Federation of Corrosion Publications*, Number 36, pp. 373-394, NANEY (2003)
- [3] M. Dao, N. Chollacoop, K.J. Van Vliet, T.A. Venkatesh and S. Suresh, *Acta Materialia*, **49**, (2002) 3899.
- [4] Ayman A. Salem, Surya R. Kalidindi, Roger D. Doherty: *Acta Materialia*, **51**, (2003) 4225-4237.

ANALYSIS OF THE HYDROGEN DEGRADATION OF LOW-ALLOY STEEL BY ACOUSTIC EMISSION

KRYSTIAN PARADOWSKI, WOJCIECH SPYCHALSKI,
KRYSTYNA LUBLINSKA and KRZYSZTOF J. KURZYDŁOWSKI

Faculty of Materials Science and Engineering, Warsaw University of Technology,
02-507 Warsaw, Poland

Abstract

The hydrogen effect of low-alloy steels applied to the petrochemical, chemical and energy industry is the phenomenon, which significantly influences the integrity and safety of industrial installations. Hydrogen degradation with other operating conditions, the elevated temperature, pressure and stress, produced many material defects in micro- and macro-scale. It is critical to determine the influence of degradation factors on mechanical properties of structural materials to assure safe operation. For the precise assessment by the AE, it is necessary to perform AE study in laboratory conditions and collect experimental data, which will provide information for analysis of AE measurements in the service conditions.

The study was performed on a 13CrMo4-5 steel with or without hydrogen charging. The AE signals were measured during loading applied by a testing machine. The AE study was compared to the investigation carried out by scanning electron microscopy, which showed many changes in the microstructure of material after hydrogen charging. The hydrogen charging was realized by cathode polarization. This presentation shows the results of laboratory study on the application of the AE testing during modified mechanical tests to evaluate the material degradation under the hydrogen influence and operating conditions.

Keywords: Low-alloy steel, degradation, hydrogen

Hydrogen Degradation

Systematic rise of interest in the use of hydrogen in different branches of the industry may be seen in recent years. Hydrogen is used for energetic purposes (as fuel, in synthetic fuel production processes involving coal liquefaction method, in refinery hydrogen processes) and non-energetic (as a raw material in chemical industry, as reducing gas in metallurgy). In the case of the oil refining industry, the desire of stepping up production of engine fuels is related to the inevitability of intensification of crude oil processing. It calls for starting new hydro-cracking or hydro-desulfurizing installations, and for launching new hydrogen generating plant. The material applied must show high resistance to the destructive influence of hydrogen. The degree of hydrogen degradation varies and depends on many factors (e.g., structural, mechanical). In the case of steel, hydrogen damage may reveal itself as delayed hydrogen cracking, degradation of mechanical properties, especially ductility, and can change microstructures and create bubbles filled with molecular hydrogen, methane or hydrogen sulfide. Intensity of the material degradation caused by hydrogen saturation, depends considerably on the speed of diffusion of hydrogen in the given type of steel, as well as on the metal's ability to dissolve hydrogen. Hydrogen penetration through the low-alloy steels is very high because of high coefficient of hydrogen diffusion through the crystal lattice of iron. Hydrogen can also be transported through the core of dislocation or grain boundaries, which greatly increases its penetration [1, 2]. The

process of hydrogen destruction of metals and its alloys is complex and therefore it is not possible to determine one form of hydrogen degradation. Predicting the form of hydrogen destruction or the degree of its intensity, and suggesting universal parameters allowing for prediction of deterioration of any material, without detailed experiments that match each case, is not possible. Aggressive thermo-mechanical conditions, to which materials are subjected under real operating conditions and the presence of hydrogen, create real danger of hydrogen degradation taking place. Those materials may undergo high temperature hydrogen attack, but their hydrogenation may take place at ambient temperature as well, e.g., in petrochemical installations where in real corrosive conditions, we also deal with hydrogen penetration.

Experimental Procedures and Results

The study was performed on a low-alloy steel 13CrMo4-5 (1Cr-1/2Mo). Results of experiments performed on the steel in the initial state, after cathodic hydrogen charging and after exposure to operating conditions were compared in this study. The hydrogen charging was by cathode polarization in a 0.5M-H₂SO₄ solution with the addition of 5 mg/dm³ As₂O₃, to promote hydrogen penetration at ambient temperature. The current density used was 20 mA/cm² for an exposure time of 3 hrs. The samples in the exposed state were taken from cut-outs of an industrial pipe, used for 10 years. This pipe was selected by performing non-destructive testing (NDT) that detected the reasonable hydrogen degradation. The substance transported through the pipe contained hydrocarbons, hydrogen, water and sulfur-containing fuel and had higher concentrations of H₂S. The maximum operating temperature of the pipe reached 60°C.

In order to show the effect of hydrogen on the microstructure, microscopic observations were carried out by using a scanning electron microscope (SEM). Samples selected for examination were chemically etched with 4% Nital. In order to determine the degree of material degradation, hardness tests, tensile tests and fracture toughness tests were performed. Hardness tests were conducted with Rockwell (A scale) and Vickers (HV5) methods. Tensile tests were performed at ambient temperature, with a strain rate of 4.17×10^{-4} [s⁻¹]. Fracture toughness tests were performed at ambient temperature with compact-type samples.

Acoustic emission (AE) examinations were performed during two different, modified mechanical tests, which were carried out with the help of the static loading machine of 5 kN maximum force. The first of them consisted in loading of the tested surface of the material with 5–mm diameter ball indenter. In order to perform this test specially designed test set-up was employed, which allowed for attaching AE sensor on the ball indenter. The maximum force during test was 0.6 kN. The second test was performed on compact-type samples for plane strain fracture toughness test with pre-cracks made before tests. Pre-cracks were made with the varying load method at 20-Hz frequency. The lowering of the force amplitude below 3 kN was the criterion for the pre-crack test end. The length of the pre-crack in the samples for AE tests was about 5 mm. During AE measurements, two AE sensors (150-kHz resonant frequency) were employed, mounted opposite on the sample surfaces parallel to the pre-crack plane. The maximum force during tests equaled 5 kN. Schematics of the AE tests together with the results are given later. Analysis of the registered AE signals is given as the diagrams of amplitude [dB] vs. time, which were correlated with the force graph. Those results were related to force vs. cumulative number of events (AE hits) graph, in order to show Kaiser and Felicity effect.

Mechanical Tests

Hardness tests did not reveal differences between materials in the initial state and after cathodic hydrogen charging and after exposure to operating conditions. Tensile test results demonstrated slight decrease of plasticity of material after exposure to the operating conditions of 5~10% in relation to the starting material. Yet all determined strength parameters of tested materials fulfilled all standard guidelines for steel types tested. In the case of fracture toughness tests, the sample size did not meet the criterion of plane strain state [3, 4]. For all cases, the plastic zone size at the crack tip was greater than 5% of the specimen thickness and crack surface morphologies indicated significant ductility. Additionally, the material subjected to operating conditions developed macroscopic structural defects, making further test impossible (Fig. 1). Microstructural defects under the cyclic loads increased to the critical size and stopped the crack propagation. Microstructure examination performed revealed numerous micro-structural changes in the degraded materials. The microphotograph showing changes in hydrogen charged material is displayed in Fig. 2.

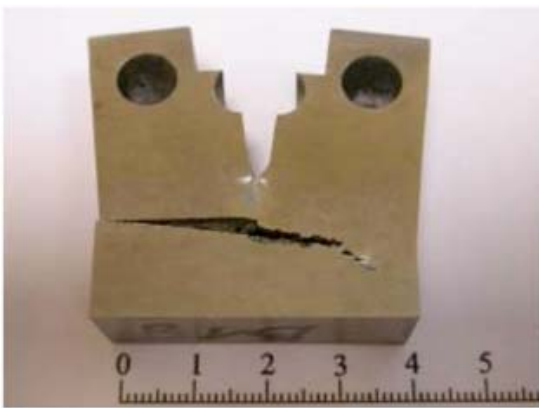


Fig. 1. Sample after fracture toughness test, material taken from a pipe.

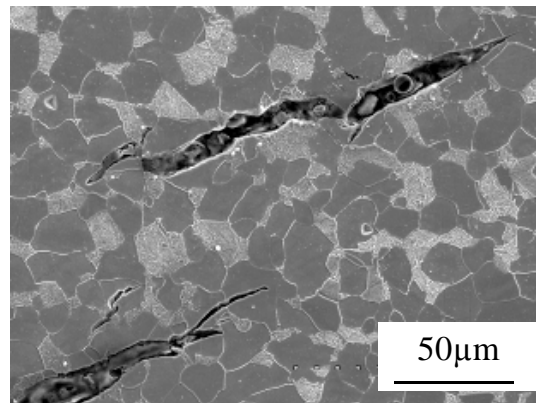


Fig. 2. Microstructural changes in hydrogen charged material.

In connection with problems described above, it was stated that quantitative determination of the degree of degradation of studied materials with the help of the mechanical tests performed is not possible.

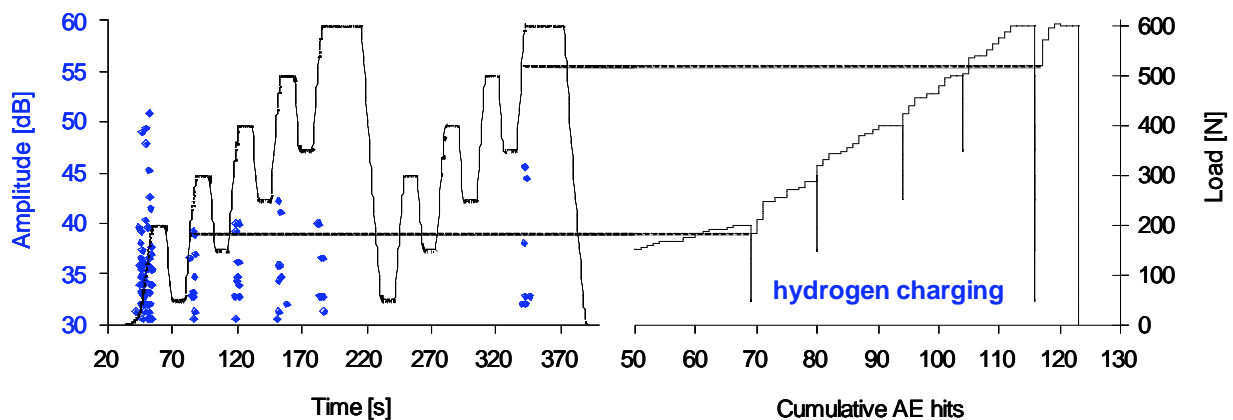


Fig. 3 AE measurement results of hydrogen charged material during indenter loading.

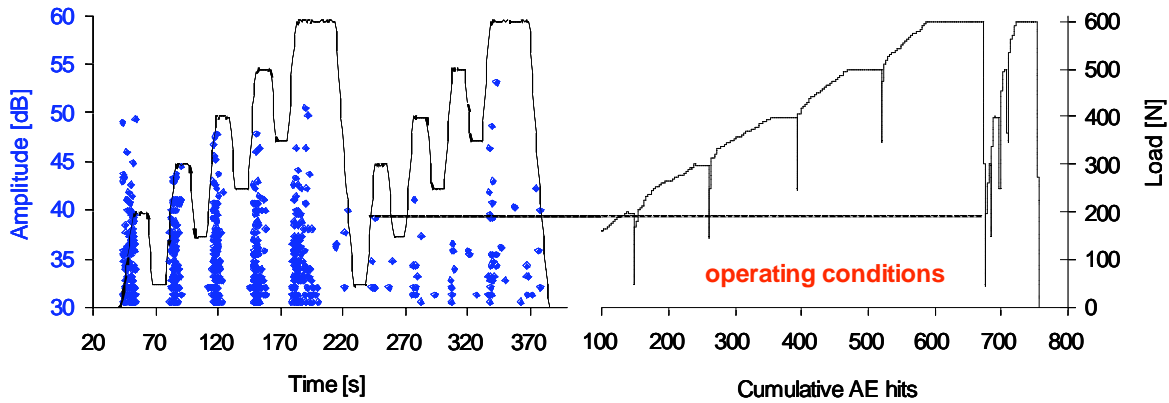


Fig. 4. AE measurement results of material after exploitation during indenter loading.

Acoustic Emission Study

AE study, using indenter, was performed during cyclic material loading in two measurement sequences shown in Figs. 3 and 4. In the case of the hydrogen charged material (under laboratory conditions), the number of accumulated AE hits was 123 (Fig. 3). The cumulative AE hits vs. force curve (Fig. 3) shows the presence of the Felicity effect during repeated loading of the material between 320 s and 370 s of the test with Felicity ratio of 0.87. In the case of the material after exposure, a higher acoustic activity was registered with clear Felicity effect (Fig. 4) during second measurement sequence. Cumulative AE hits reached 758, and Felicity ratio equaled 0.35. Material after exploitation characterized itself with higher acoustic activity during loading. In the case of the material, in the initial state, the number of cumulative AE hits was 101 and the Felicity effect was not detected.

In order to compare the results obtained for all three materials, relationship between severity and historic index is shown in Fig. 5. This clearly reveals the difference between AE recorded for degraded materials and material in the initial state.

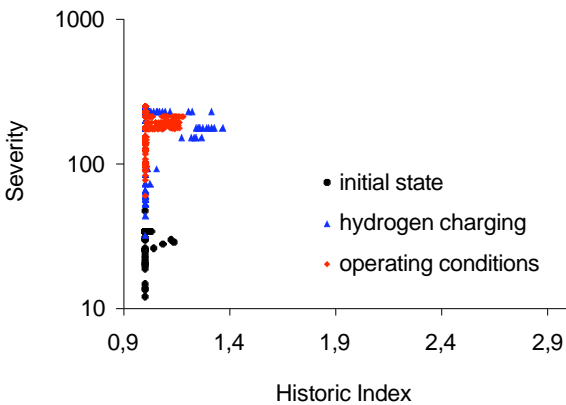


Fig. 5. Dependence of historic index on severity for materials loaded with indenter.

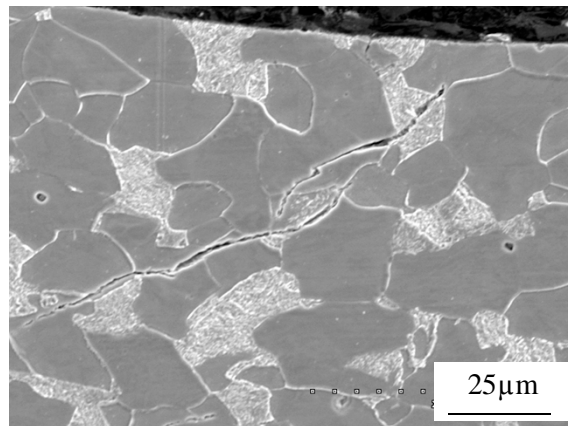


Fig. 6. SEM examination test of the hydrogen charged material, area under indentation with visible crack.

Though comparable number of signals recorded in the case of the hydrogen charged material and material in the initial state, severity values show, that these signals are of higher energy than those registered in the material in the initial state. SEM inspections performed on the material cross section under indentation surface revealed the presence of the cracks in the degraded

materials (Fig. 6). Cracks recorded may be the potential reason of increased AE activity during indentation tests.

AE tests of the compact samples with pre-cracks were performed during loading of the material according to the schematic shown in Figs. 7 and 8. One should note that the samples were subjected to hydrogen charging after pre-cracks were made. It could intensified the hydrogen-induced degradation at the pre-crack tip as comparing to specimens cut from the material after operating conditions. The atomic hydrogen during cathodic charging derived from metal-environment surface reaction diffuses to microstructural heterogeneities at the crack-tip such as voids and microcracks, recombines to the molecular form, and builds up a very high internal pressure [5]. Felicity ratio of the hydrogen charged samples prepared for fracture toughness test equaled 0.27.

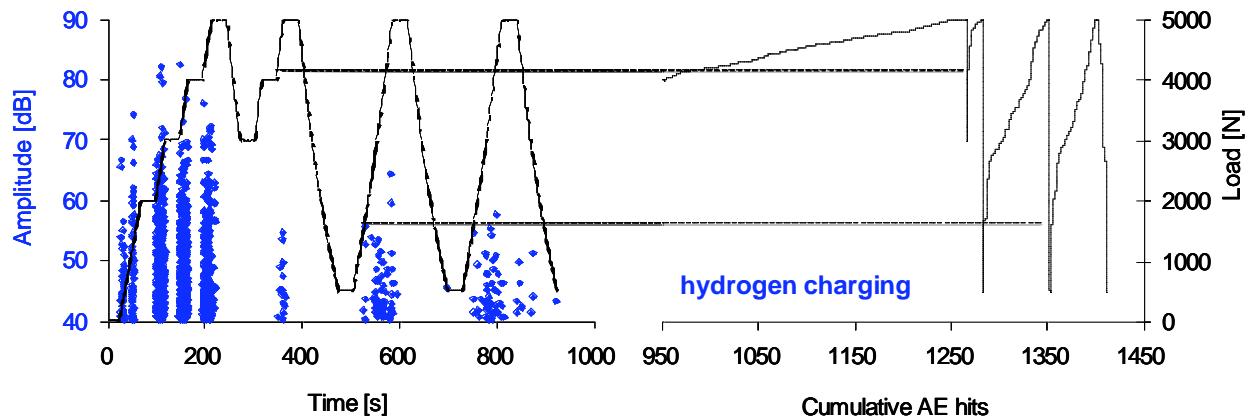


Fig. 7. AE measurement results of the hydrogen charged samples for fracture toughness test.

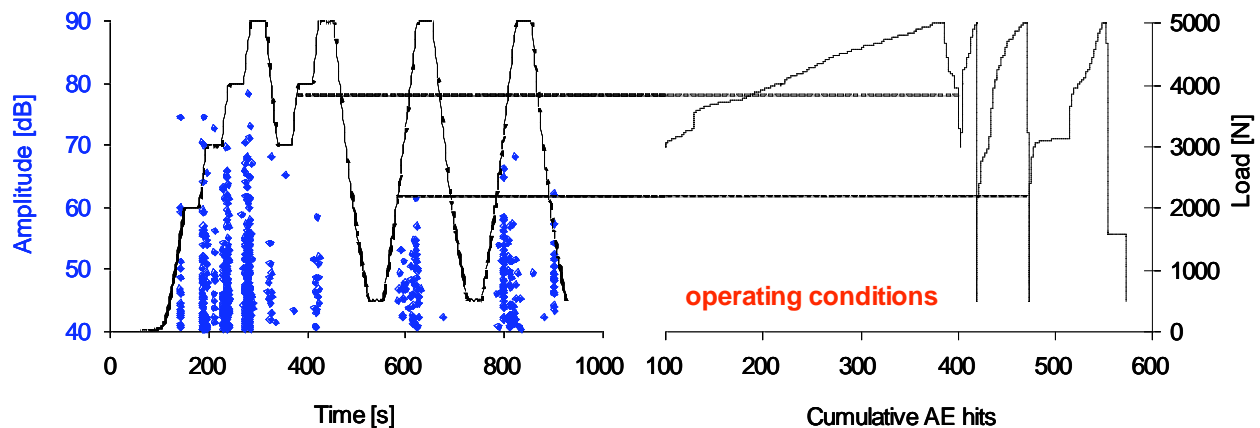


Fig. 8. AE measurement, during loading, results of the samples for fracture toughness test from the material after exposure to operating conditions.

Characteristic of the material after exposure to operating conditions, as compared to other materials is the presence of AE during load decreases in the first and last cycles. Felicity ratio of the material after exposure amounted to 0.43. In the case of the material in the initial state number of AE hits recorded amounted to 83, and Kaiser effect was observed. Material after hydrogen charging produced more AE signals in the first part of the test, than the material after exposure. The different extent of the material degradation at the crack-tip could influence AE activity during the first loading to the maximum. Higher number of cumulated AE hits 1412

(Fig. 7) relative to the material after exposure to operating conditions confirms this fact. This number for the material after exposure was 573 (Fig. 8).

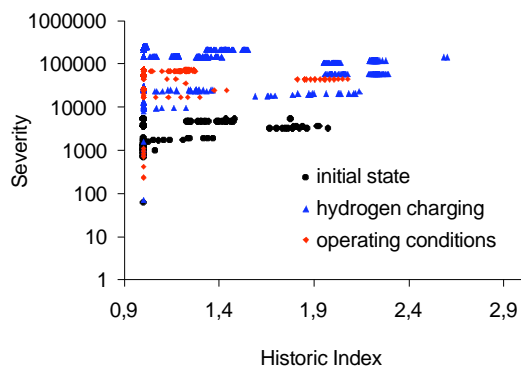


Fig. 9. Dependence of historic index on severity recorded on samples prepared for fracture toughness tests.

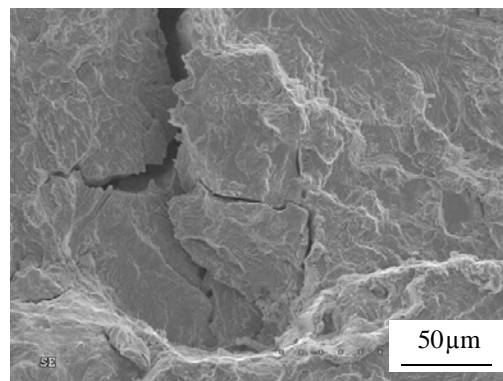


Fig. 10. Fracture of the sample prepared for fracture toughness test from the material after exposure.

Comparison of the test results performed on the compact samples is shown in Fig. 9, which illustrates meaningful rise of severity value for material in the degraded state. In Fig. 10, one can see fracture of the sample made of the material after exposure, with visible micro-cracks characteristic of degraded material. Microscopic examination revealed change of the fracture character from ductile for samples in the initial state, to locally brittle and mixed brittle – ductile (partly brittle for samples exposed to degradation).

Summary

Standard mechanical tests do not always allow the estimation of the degradation of the material exposed to operating conditions with hydrogen environment. The use of acoustic emission in connection with modified mechanical examinations showed significant differences in AE signals recorded. Suggested method of examination was devised on the basis of numerous tests conducted on the material charged with hydrogen under laboratory conditions. On this basis a series of tests were performed on the material taken from cut-out of the pipe operated under real life conditions. This clearly revealed the differences in AE signals recorded in relation to material in the initial state.

Acknowledgement

This work was supported by the Polish Committee for Scientific Research as research project N507/033 31/0813.

References

1. P. Timmins, *Solutions to Hydrogen Attack in Steels*, ASM, Mat. Park, OH USA, 1997.
2. J.P. Hirth, in *Hydrogen Degradation of Ferrous Alloys*, ed. R.A. Oriani, J.P. Hirth, M. Smialowski, Noyes Pub. 1985, p. 131.
3. S.D. Antolovich, *An Introduction to Fracture Mechanics*, ASM Metals Handbook, Vol. 19, 1997, p. 375.
4. J.D. Landes, *Fracture Toughness Testing*, ASM Metals Handbook, Vol. 19, 1997, p. 402.
5. P.S. Pao, *Mechanisms of Corrosion Fatigue*, ASM Metals Handbook, Vol. 19, 1997, p. 186.

HYDROGEN RELATED BRITTLE CRACKING OF METASTABLE TYPE-304 STAINLESS STEEL

HIDEO CHO and MIKIO TAKEMOTO

Faculty of Science and Engineering, Aoyama Gakuin University,
5-10-1 Fuchinobe, Sagamihara, Kanagawa 229-8558, Japan

Abstract

Among stainless steels, Type-316 steel is stable and shows high resistance to hydrogen-induced brittle cracking, but the meta-stable Type-304 steel shows a high susceptibility to the hydrogen-induced embrittlement and cracking. Mechanism of hydrogen-induced brittle cracking of the Type-304 steel was studied by AE monitoring under various combination of static and dynamic elastic and plastic deformations in a charging solution at room temperature and 80°C. Here, the hydrogen was supplied before and during tensile testing. We detected a number of AE signals from the Type-304 steel with hydrogen charging during dynamic plastic deformation at room temperature and observed hydrogen-induced cracks, while no AE for the Type-304 charged by hydrogen and deformed at 80°C. Maximum load of the Type-304 steel with hydrogen charging decreased to 30% that of the steel without charging. Type-304 steel, hydrogen charged after being quenched in liquid nitrogen, produced few AE during tensile loading at room temperature. We detected no AE from Type-316 steel during plastic deformation in charging solution at both temperatures. Hydrogen-induced brittle fracture of Type-304 steel was confirmed to be induced by both gliding dislocations and deformation-induced lath martensite. Hydrogen is supposed to be transferred to the martensite by gliding dislocations accompanying protons.

Keywords: Meta-stable austenitic stainless steel, hydrogen induced brittle fracture, strain induced martensite, gliding dislocation

Introduction

Meta-stable austenitic stainless steels are known to be susceptible to hydrogen embrittlement. Many researchers reported that strain-induced martensite suffered hydrogen embrittlement [1, 2]. Fracture type was intergranular (IG). Carpenter et al. reported that AE signals from sensitized Type-304 steel, during tensile loading in a charging solution, were produced by the IG-cracks caused by the grain boundary separation. Here the IG-cracking occurred when hydrogen charging was continued till the maximum load. They proposed a transport model by moving dislocations [3, 4]. Direct demonstration of this model is impossible at present, even if we use any kind of advanced analysis equipments. Collection of reliable data, which can or cannot support this model, is needed.

In this report, we studied the hydrogen embrittlement of Type-304 and -316 steels by monitoring AE during quasi-static loading in a charging solution at 25°C and 80°C.

Experimental procedure

We used commercially available Type-304 and -316 stainless steels. Chemical composition

is shown in Table 1. Test specimens of Fig. 1 were prepared by an electro-discharge machine to produce identical specimens. Width in gage section was controlled to 15 mm. A notch with the tip radius of 0.2 mm was induced on one side. These samples were abraded by silicon carbide abrasive papers of 150, 300, 400, 600, 800, 1000 and 1500 mesh, and mirror polished by aluminum oxide powder. The specimen was sensitized at 650°C for 24 hours in low-pressure furnace after solution treatment at 1050°C for 1 hour, and quenched in water. The specimen was sealed by rubber-based coating material, except for the exposure area of 15 mm x 10 mm. Hydrogen was charged in an H₂SO₄ solution of pH:2, at cathodic current density of 1 mA/cm² using a potentio-galvanostat.

Table 1 Chemical composition of austenitic stainless steel used (mass %).

	C	Si	Mn	P	S	Ni	Cr	Fe
Type 304	0.05	0.61	1.56	0.04	0.024	8.55	18.2	balanced
Type 316	0.05	0.57	0.82	0.02	0.0006	11.3	17.5	balanced

We monitored AE using four small AE sensors (PAC, Type- PICO), which were mounted on the sample as they make a line. Outputs of two sensors (channels 2 and 3 in the gage section) were amplified by a pre-amplifier (Gain: 40 dB) and fed to a personal computer. Two more sensors (channels 1 and 4 on the shoulder) were used to discriminate the friction noise from the signals. We monitored the crack propagation by a CCD camera.

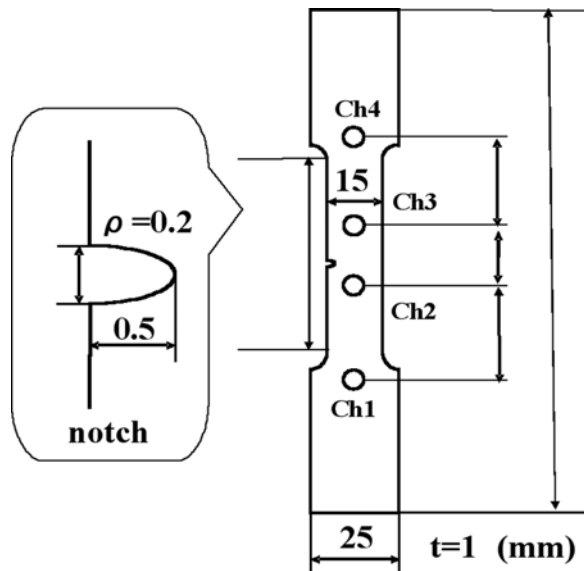


Fig. 1 Schematic of specimen and sensor location.

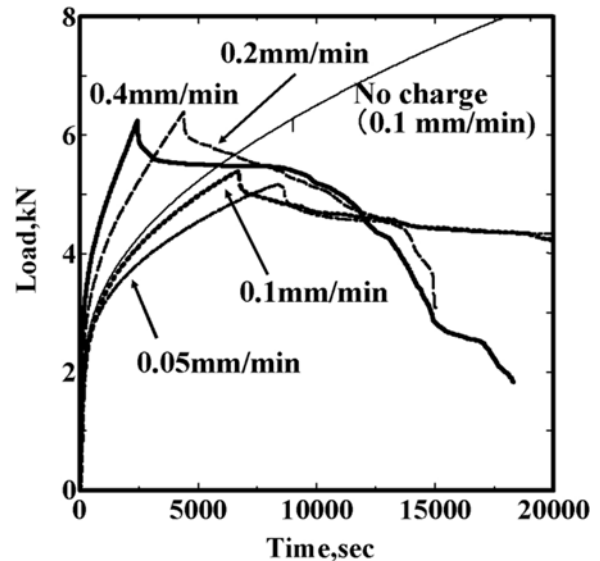


Fig. 2 Load - time diagram for the sensitized Type-304 specimens with various crosshead speeds in a charging solution.

Experimental results

Tensile loading in charging solution

Tensile load was applied to Type-304 specimen in a charging solution using crosshead control method, in the following sequence: (1) Increase the load at constant crosshead speed. (2) When a small load drop (~0.1 kN, probably from the start of cracking) was detected, crosshead

was stopped and held. (3) Then, monitor the load decrease for 3 hour.

In these tests, hydrogen charging was started with the loading. The crosshead speed was varied between 0.05 mm/min to 0.4 mm/min. Figure 2 shows the load-time diagram at crosshead speeds of 0.4, 0.2, 0.1 and 0.05 mm/min for the sensitized Type-304 specimen at 25°C. A fine smooth line indicates that of a non-charged specimen at crosshead speed of 0.1 mm/min. Five specimens show different behavior in the plastic range. The specimens hydrogen-charged during loading showed extensive load decay. Initial decay and the total load decay were larger at higher loading rates. The curve of the charged specimen at crosshead speed of 0.1 mm/min agrees fairly well that of the non-charged specimen, but deviates slightly at large loads. The maximum load reached was 5 to 6.5 kN. The maximum load increased with an increase of crosshead speeds.

Figure 3 shows changes of cumulative AE counts with time. Detected AE signals were classified by their frequency characteristics into two types (Type-A and -B) as shown in Fig. 4. Type-A was detected after the maximum load and showed broad frequency components. In contrast, Type-B was detected throughout loading. Frequency spectrum of the Type-B showed a limited frequency component and resembles the noise from hydrogen gas evolution in SCC [5]. We selected Type-A as the crack signal. We detected many signals during load increasing period, but few signals during the initial portion of the load decay. For two samples with crosshead speeds of 0.2 and 0.4 mm/min, we again detected signals during rapid load decay period after incubation times. However, we did not detect AE during load decay for two specimens with lower crosshead speeds of 0.05 and 0.1 mm/min. Detail mechanism of AE generation rate and its dependency on the crosshead speed is a future problem.

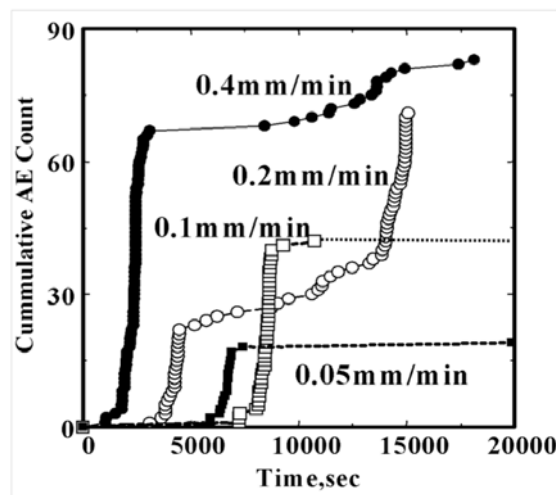


Fig. 3 Cumulative AE counts for the sensitized Type-304 specimens with various crosshead speeds in a charging solution.

Figure 5 shows CDD images of crack progression. White spots in the image are hydrogen gas bubbles. Timing of crack progression from the notch bottom agreed roughly with the first AE timing at 1,100 s, as shown by the photo (a) at 1,800 s. We observed a crack with large opening at the maximum load (photo (c)), but after that, a fine crack during load decay (photo (d)).

Figure 6 shows post-test SEM of the sample with the crosshead speed of 0.1 mm/min. We observed a number of IG-cracks and falling-off of grains around the notch. Here the falling-off of grains was caused by the grain boundary separation. As these cracks were considered to be

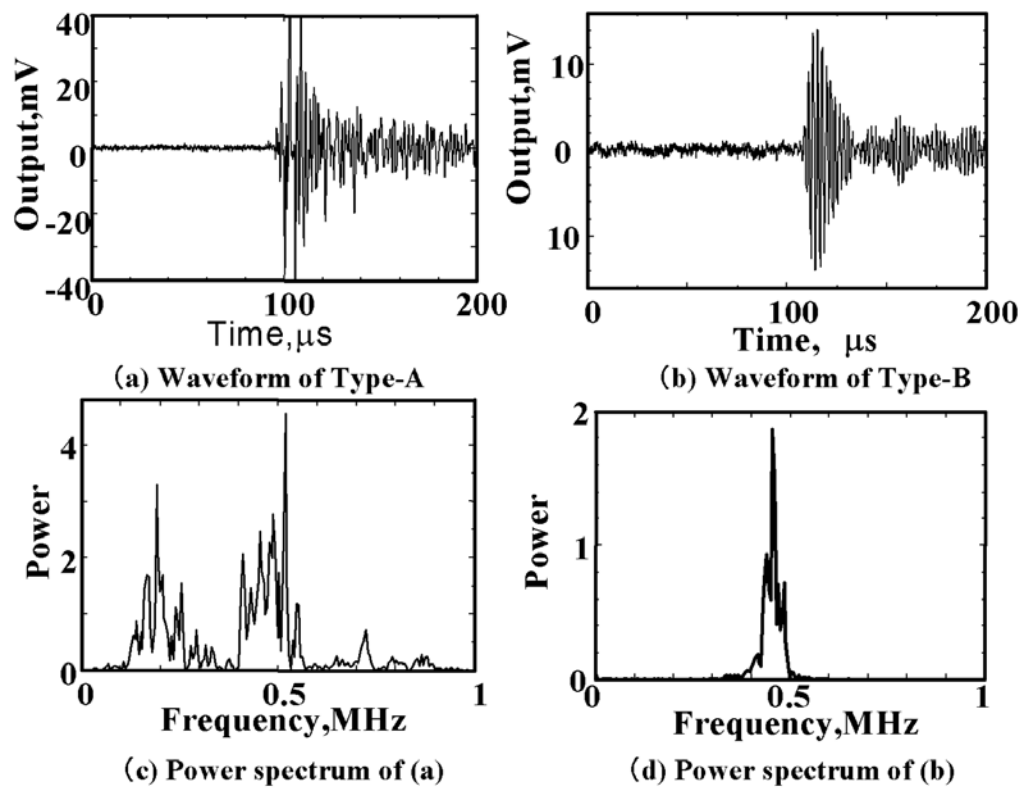


Fig. 4 Two types of AE signals detected and their power spectra.

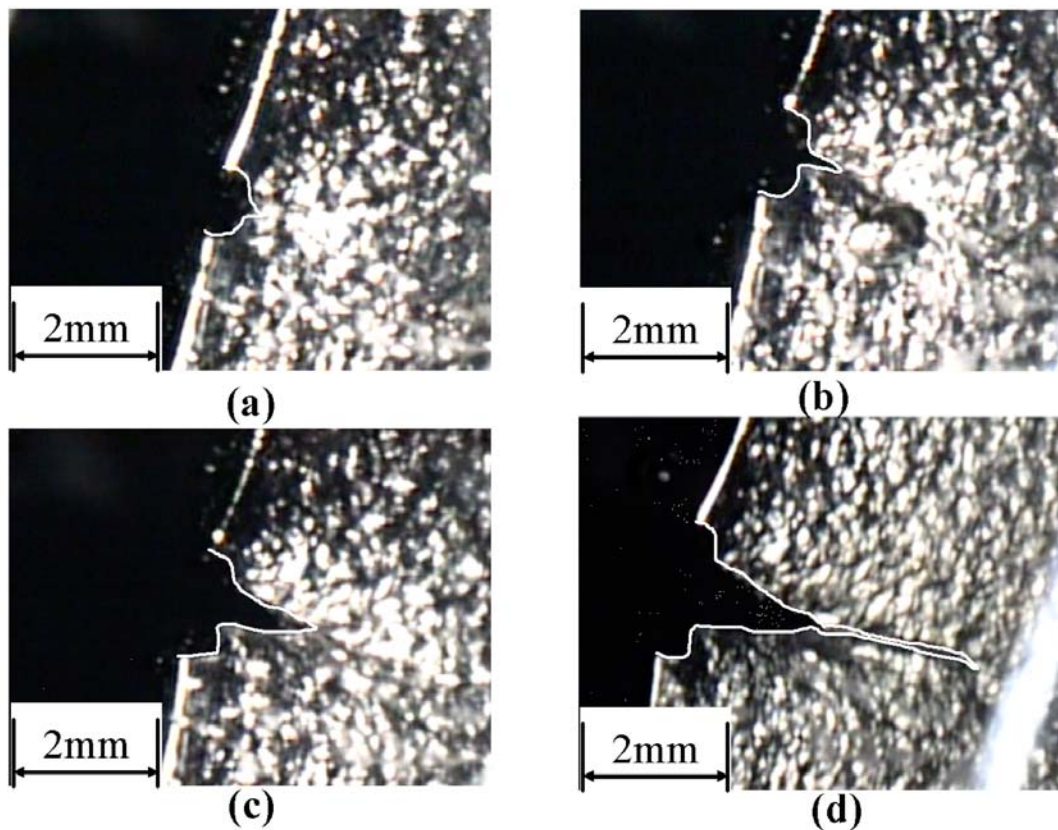


Fig. 5 CCD images of crack propagation of the sensitized Type-304 specimen with crosshead speed of 0.4 mm/min in charging solution. (a) 1800 s (after detection of first AE) (b) 2300 s (c) 2440 s (at max load) (d) 13200 s.

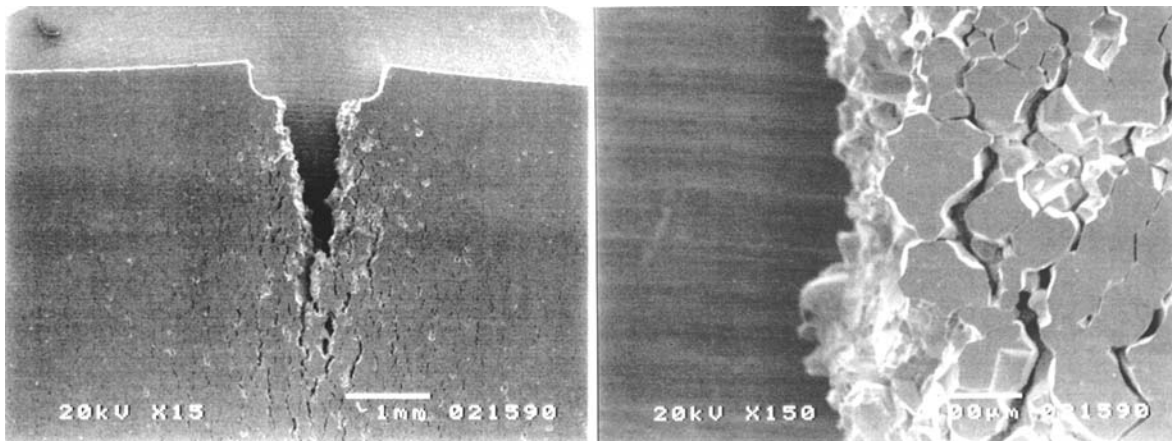


Fig. 6 SEM images of the sensitized type-304 specimen surface around the notch with crosshead speed of 0.1 mm/min at 25°C in charging solution.

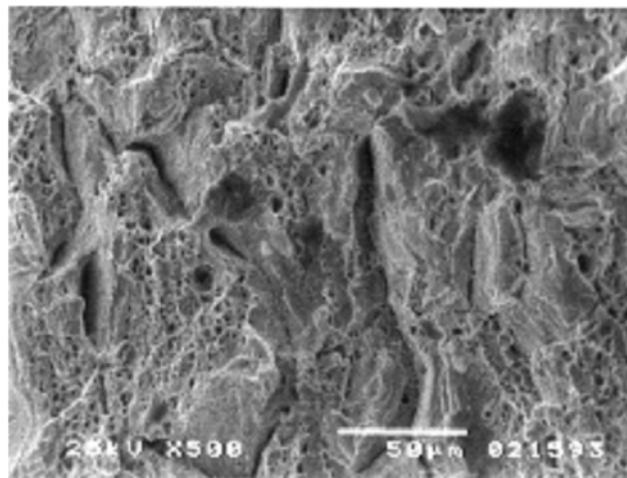


Fig. 7 Fracture surface of the sensitized sample with crosshead speed of 0.1 mm/min at 25°C in charging solution. Both dimple and cleavage fracture surfaces are shown.

caused by strain-induced martensite, we measured ferrite amount near the main crack using a ferrite meter. It was measured as 7%. Figure 7 shows fracture surface of another sample loaded to final fracture in the same charging condition. We observed both dimple and cleavage fracture surfaces, and deep grooves along the elongated grains.

Effect of strain-induced martensite on hydrogen induced cracking

We studied effect of strain induced martensite on the hydrogen-induced cracking using Type-304 and -316 steels. Transition temperature (M_d) of austenite to martensite of the Type-304 steel is 30°C, so we then compared the crack susceptibilities of the Type-304 steel at 25 and 80°C. We deformed the sensitized Type-304 sample, with charging at 80°C (0.1 mm/min) and detected no AE. The maximum load was not reached in loading up to 6 kN, while we observed high AE activity and the maximum load of 5.3 kN for the loading at 25°C (Fig. 3). Martensite amount was measured as below 1.0%. This result implies that the martensite is a necessary factor to cause the hydrogen-induced cracking.

The M_d temperature of the Type-316 steel is -28°C, and this steel produces no strain-induced martensite at 25°C. In order to confirm this, the sensitized Type-316 steel was tensile tested in

the charging solution at 25°C, by the same method as in the previous section. This steel produced three AE during the loading to 6 kN, indicating no susceptibility to hydrogen-induced cracking, as shown in Fig. 8.

Effect of Hydrogen charging and thermal martensite

Experimental data of previous sections suggested an importance of both the martensite and gliding dislocations during plastic deformation. The test in this section intends to confirm these. We attempted AE monitoring from the sensitized, and then nitrogen quenched and pre-charged Type-304 steel during tensile loading in air. Hydrogen was charged for 144 hr at current density of 10 mA/cm² (charge amount of 5184 C/cm²) prior to the loading. This specimen possesses thermally-induced martensite of approximately 15% near the notch bottom.

Figure 9 shows load-time curves of the quenched and pre-charged specimens in air. We detected no AE and no crack. Thermally-induced martensite increased the yield load by approximately 14% over that of the sensitized Type-304 steel without hydrogen charge, but is immune from the hydrogen-induced cracking. This implies that simultaneous supply of protons and generation of dislocation are needed for hydrogen-assisted cracking.

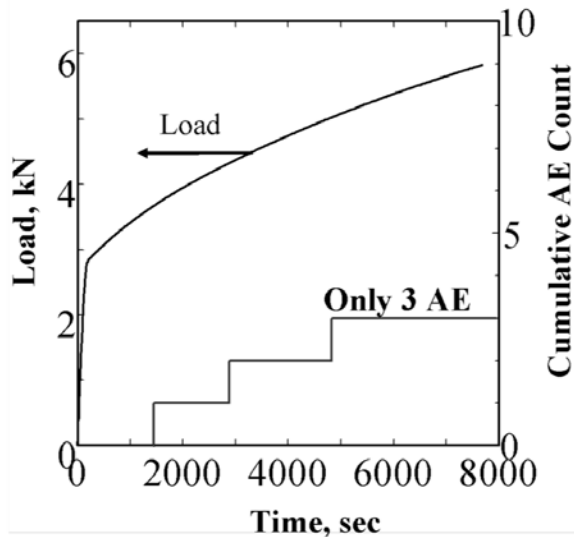


Fig. 8 Load-time diagram and cumulative AE count for sensitized 316 specimens with charging at 25°C.

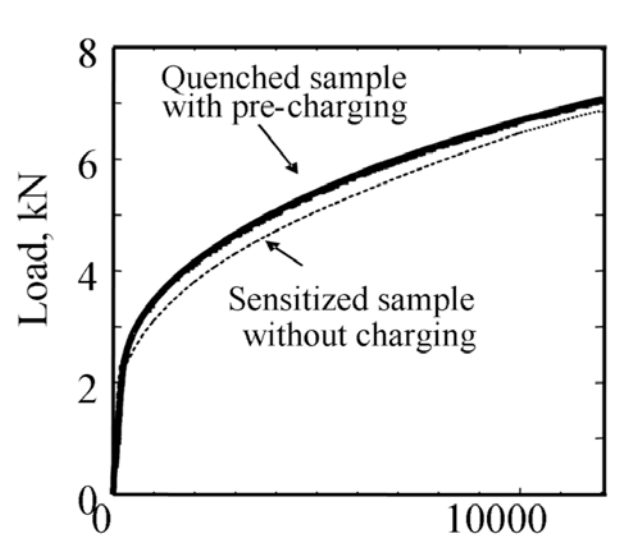


Fig. 9 Load-time diagram for the pre-charged sample quenched in liquid nitrogen in air. For comparison, sensitized sample without charging was shown.

Discussion

The martensite is a necessary condition for hydrogen-induced cracking but not the sufficient condition, as demonstrated by the last section’s experiment using quenched samples. Figures 2 and 3 imply that both the gliding dislocation by dynamic plastic deformation and the strain-induced martensite, and of course the diffusible protons, are necessary for hydrogen embrittlement. The grain boundary separation occurs when these three condition were simultaneously satisfied. These results agree with the results by Carpenter et al. [4]. We, however, could not explain the complicated AE behavior during load decay in Fig. 3. These must be explained based on the rate process of proton diffusion and martensite formation. Unsolved problems are

- 1) How the protons are transferred to the martensite at the tip of notch and growing crack, and
- 2) How the martensite distributes in the austenitic grains.

Diffusion coefficient of proton in the austenitic phase is as low as 10^{-12} cm²/s, million times smaller than (10^{-6} cm²/s) in the ferritic phase. Thus the proton can not quickly diffuse through the austenitic grains. Fast and sufficient supplement of protons to the martensite will be possible by gliding dislocation accompanying the protons or self-diffusion through the martensite. No advanced analysis equipment at present can differentiate them, but we can compare the crack velocity and proton diffusion rate under controlled stress intensity. The second problem includes a contentious martensite path for proton diffusion and the grain boundary separation. The grain boundary separation can be explained by the martensite formation along the chromium depleted zone. Distribution of the martensite, and possibly the initiation of crack, will be revealed by the advance analysis equipment.

We recently observed frequent grain boundary separations in polythionic APC-SCC of sensitized Type-304 steel [5]. AE were detected when the steel suffered the grain boundary separation. Detailed mechanism is not well understood. There is a possibility of hydrogen-induced grain boundary separation in the APC-SCC.

Conclusion

In order to study the mechanism of hydrogen embrittlement of austenitic stainless steel, we monitored AE. Results are summarized below:

- 1) We detected AE and crack for the sensitized type 304 when it is exposed to both the dynamic plastic deformation and hydrogen charging simultaneously. Much AE were continuously emitted during plastic loading at higher cross head speeds.
- 2) Experiment suggests that hydrogen assisted cracking occurs when sufficient protons were transferred to the strain induced martensite. Diffusion path and trap site of protons have to be studied in future.

References

- [1] M. L. Holzworth, *Corrosion*, **25**, 1968, 107.
- [2] N. Otani, S. Asano, Y. Fujishima and Y Yamamasu, *J. Japan Inst. Metals*, **37**, 1972, 746.
- [3] S.H. Carpenter and D. R. Smith, *Metallurgical transaction A*, **21A**, 1990, 1933.
- [4] S.H. Carpenter, K. Ono and D. Armentrout, *Progress in Acoustic Emission XIII*, 2006, p. 55.
- [5] A. Yonezu, H. Cho and M. Takemoto, *Progress in Acoustic Emission XIII*, 2006, p. 489.

ANALYSIS OF ACOUSTIC EMISSION FROM IMPACT AND FRACTURE OF CFRP LAMINATES

KANJI ONO, YOSHIHIRO MIZUTANI¹ and MIKIO TAKEMOTO²

Department of Materials Science and Engineering, UCLA, Los Angeles, CA 90095-1595, USA;

¹Tokyo Institute of Technology, Ookayama, Meguro, Tokyo 152-8552, Japan; ²Faculty of Science and Engineering, Aoyama Gakuin University, Sagamihara, Kanagawa 229-8558, Japan

Abstract

The impact damage of CFRP plates under impact load was evaluated using recording of AE, load and strain history. The threshold or critical impact force to cause internal damage in cross-ply CFRP laminates was determined using dynamic surface strain and Lamb-wave AE along with the impact force history. Loading was conducted in SACMA-type impact tests at 0.8 and 1-m/s velocity. Four types of cross-ply CFRP plates ($[0_n^o/90_n^o]_s$, $n = 4-10$) are impacted with a spherical steel-tup. Lamb-wave AE signals were detected by small AE sensors on both surfaces. Polarity of AE signals detected by both sensors are used in studying the progression of fracture. Only impact-induced AE (or Impact-AE) is obtained when the impact tup contacts the specimen at a lower speed. When internal fracture occurs, both Impact-AE and fracture-induced AE (Fracture-AE) were detected. The nature of Fracture-AE is examined in this study in conjunction with ultrasonic C-scan and surface evaluation. AE monitoring on both surfaces enabled us to clearly separate the S_0 and A_0 modes of Lamb-wave AE signals. Most of strong AE signals correlated with matrix fracture source, while other damages had no associated distinctive events.

Keywords: Impact-AE, fracture-AE, CFRP laminates, impact damage threshold

Introduction

Carbon-fiber reinforced plastics (CFRPs) are useful in a wide range of applications due to their high specific strength and stiffness. However, they are prone to impact damage even under modest hits. SACMA-type impact test is often used for investigating impact fracture of CFRPs [1]. Only load history and tup velocity are taken during the test, after which samples are subjected to compression testing. We added AE monitoring and strain sensing to the SACMA tests and obtained the impact damage threshold for CFRP plates [2]. In so doing, in lieu of limited data, i.e., maximum impact load, impact duration and energy, we found details of the dynamic fracture processes in the form of Lamb-wave AE signals as well as displacement and surface strain history. Two types of AE signals were identified; Impact-AE and Fracture-AE. Only a limited number of previous studies have been reported on impact damages with little materials analysis [3-6], despite abundant CFRP studies of compression after impact are known.

In this study, waveforms of Lamb-wave AE signals due to internal damage in cross-ply CFRP laminates are examined, in conjunction with dynamic surface strain and the impact force history measured during SACMA-type impact tests. In particular, two-surface sensing [7-9] allowed us to evaluate mode types of detected signals. Additionally, failure modes were examined using microscopic studies to determine crack length and types and using ultrasonic C-scan to reveal the extent of delamination. Results are compared to the observations during quasi-static tests of the same CFRP.

Specimen and Experimental Setup

A large-size plate of $([0_n^{\circ}/90_n^{\circ}]_s, n = 4, 6, 8, 10)$ was prepared by laminating pre-pregs. Carbon fibers were pitch-based XN-50 from Nippon Graphite Fiber with the nominal modulus of 490 GPa. Rectangular specimens with $150 \text{ mm}^L \times 100 \text{ mm}^W$ were cut with the fiber directions (0°) on the top surface along the longitudinal (or X-) direction. Impact tests used Dynatup 8250 from Instron Corp., which satisfied SACMA SRM 2R-94 standard. Impact load was applied at the center of a specimen via a hemispherical steel tup of 16-mm diameter, weighing 3.61 kg [2]. The edges of the specimen were clamped all around by steel flanges. Four small AE sensors (Physical Acoustic Corp.: Type Pico) were mounted on both surfaces at 32-mm from the impact point in the X-direction. Polarity of AE signals detected by both sensors are compared for investigating the progression of fracture. A top AE sensor was used for determining the damage initiation. Outputs of two of the AE sensors were amplified 40 dB and filtered by a band-pass filter of 200 kHz to 1.2 MHz for eliminating large-amplitude low-frequency AE due to impact. The other two outputs were recorded directly at 10-1200 kHz bandwidth. As signal saturation occurred with amplification, all the analysis here used only direct-recording data. These signals were digitized by 2 PAC MISTRAS boards at the sampling interval of 500 ns over 10.2 ms, and stored in computers. The strain gage was attached on the top surface at the 32-mm from the impact point. Outputs of the strain gage and the load cell on the impact tup were digitized at the sampling interval of $1 \mu\text{s}$ over 60-ms period. The strain gage data was used for deciding impact damage threshold and timing. See [2] for other information. The tup displacement was dynamically recorded with a strain-gaged leaf-spring and used for velocity measurement.

Impact tests for four types of cross-ply CFRP plates ($[0_n^{\circ}/90_n^{\circ}]_s$) were conducted at two impact velocities (nominally 0.8 and 1 m/s) by controlling the height of the tup. Impact test for the 40-ply plate at 0.8 m/s was omitted, because no damage was observed at 1.0-m/s impact test. Details of quasi-static tests of similar CFRP plates were reported earlier and most fracture mechanisms are expected to operate under dynamic conditions as well.

Two-surface Sensing

In thin plates, Lamb waves are usually detected as AE signals. Figure 1 gives examples of 20- μs -long waveforms from in-plane (IP) and out-of-plane (OP) pencil-lead breaks. Two Pico sensors were placed on opposite faces of a 3.2-mm thick stainless steel plate, 50 mm from an edge. For comparison, the left figure is for an IP source with two sensors on the same side.

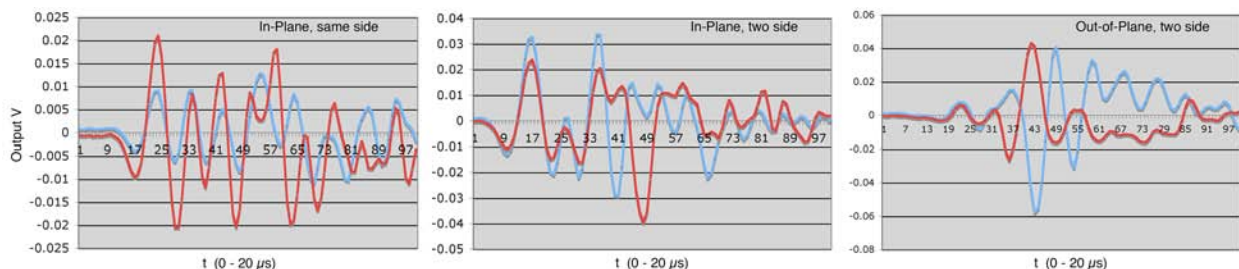


Fig. 1 Lamb waves from IP/OP pencil-lead break sources. Two Pico receivers were used.

Two Pico sensors on the same side showed similar wave character for the first 7 peaks, but differences became prominent after $\sim 8 \mu\text{s}$. The first $3.6\text{-}\mu\text{s}$ portion is S_0 mode, but the arrival of A_0 mode cannot be discerned from these waveforms. IP source detected on two sides produced

nearly same waveforms for the first 6 peaks ($\sim 8 \mu\text{s}$), indicating this part is S_0 mode. OP source (1 mm from the edge) showed the initial 4 peaks at the same phase, followed by 5 peaks at the opposite phases. The opposite phase waves are A_0 mode, while the initial part is S_0 mode. Such OP sources are often considered to generate primarily flexural modes, but this source was close to the edge and reflection contributed to the symmetric mode, albeit weaker.

It is clear that, with the two-side monitoring, we can distinguish symmetric (typically S_0) mode for the in-phase waves, while out-of-phase waves are asymmetric, flexural (typically A_0) mode. In CFRP plates used here, the calculated wave speed of S_0 mode varies widely; it is only about 15% faster than that of A_0 mode moving over the entire thickness at 500 kHz, and here the temporal separation of the two modes from a single source is not readily visible. However, faster propagating S_0 mode along the 0° -fibers exists with the measured velocity of 8-10 mm/ μs without much dispersion. When S_0 mode or A_0 mode is found by itself, a distinct source is expected to have been active. See [7, 8] for more discussion on two-surface sensing.

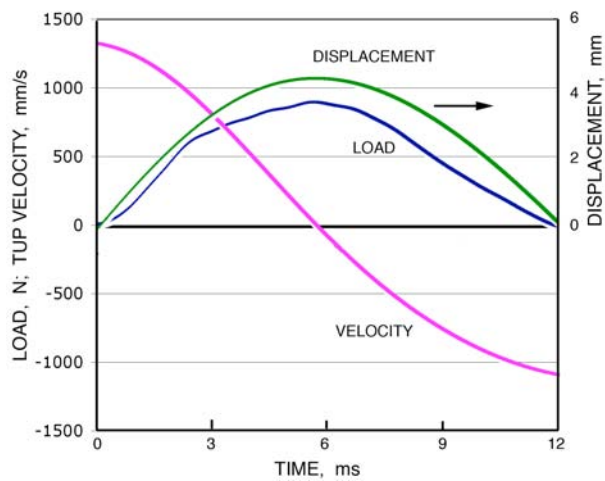


Fig. 2 Impact force-displacement-velocity vs. t for 16-ply CFRP at 1 m/s nominal velocity.

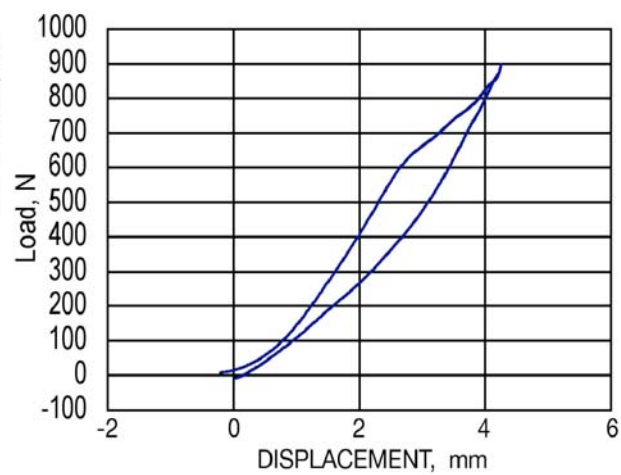


Fig. 3 Impact force vs. displacement plot of 16-ply CFRP at 1 m/s nom. impact velocity.

Impact History and Impact Damage

Measured impact force-displacement-velocity values are plotted against time in Fig. 2 for a 16-ply sample, hit at a nominal velocity of 1 m/s. The velocity at contact was 1.3 m/s, decreasing to zero at the peak load, from which point the tup reversed the direction as the load was reduced. The load vs. displacement plot is given in Fig. 3, which indicates the elastic loading and a sudden slope decrease (-45%) at 600 N, where damage initiated. A corresponding loading rate reduction is seen in Fig. 2. Most of bending displacement recovered upon unloading and the initial unload slope was unchanged from the load slope, implying minimal damage to the elastic stiffness of the plate. Directly recorded AE signals from Pico sensors are shown in Fig. 4. Early signals at 0.4 to 2.4 ms are Impact-AE (IAE) signals and have the flexural wave character. Fracture-AE (FAE) signals start at ~ 2.5 ms with 14 major events.

The first F-AE event coincides with the slope change of the load-time and load-displacement curves (cf. Figs. 2 and 3). This signal consists of a pair of S_0 and A_0 packets at 2.54 ms (Fig. 5a). The S_0 packet was 20- μs long, indicating the presence of fast through-fiber mode. This signal has a strong A_0 component, which is six times stronger than the S_0 packet preceding it (in p-to-p

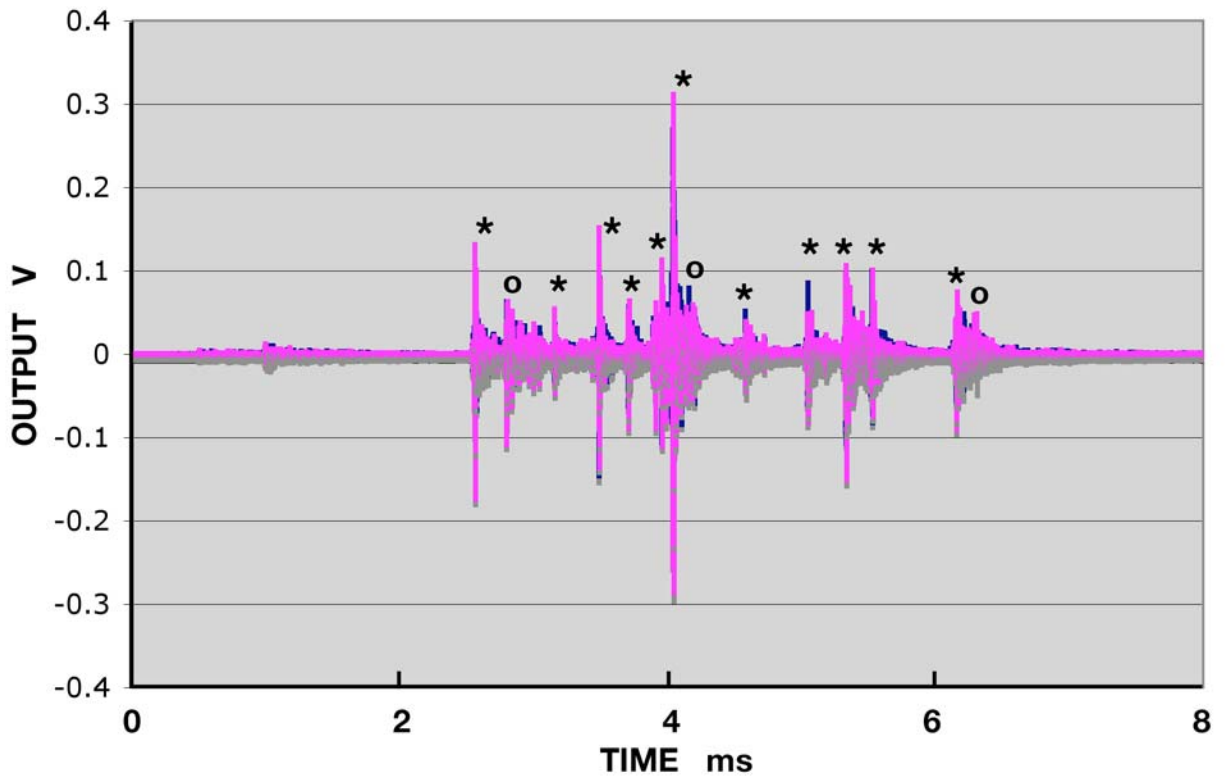


Fig. 4 Direct recording of AE signals from bottom sensor. 16-ply sample hit nominally at 1 m/s. Most of top sensor signals are hidden.

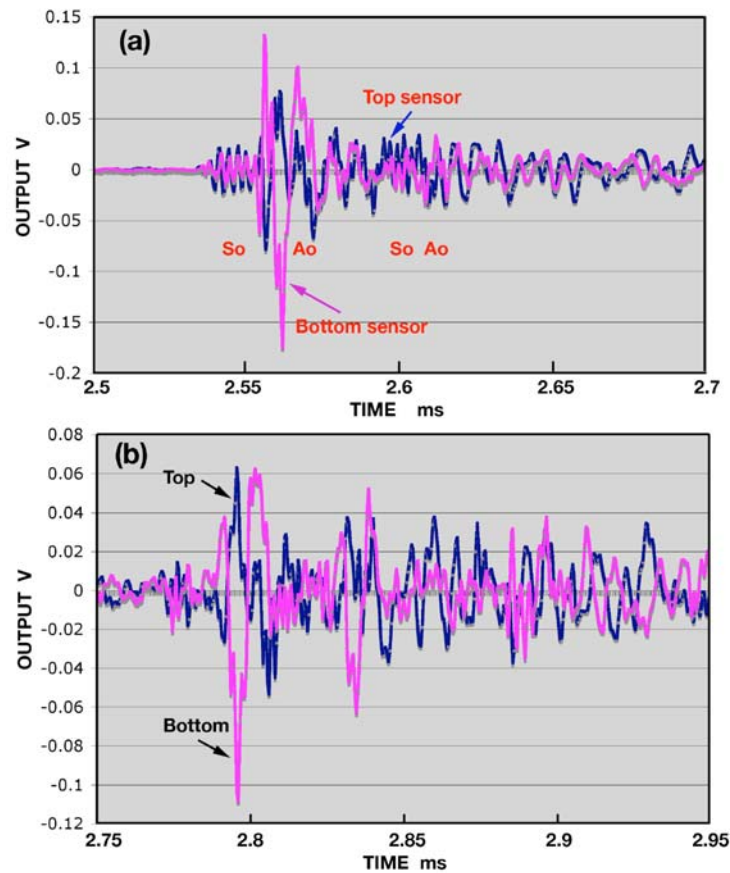


Fig. 5 The first two major events in Fig. 4, each shown in 200- μ s long segment for 2 sensors.

values). Most (11 of 14) of the recognizable AE events seen in Fig. 4 are of the type with both S_0 and A_0 components (Fig. 5a) and are marked with an asterisk. This signal type is almost identical to Type-D signal detected in the static tests of the same CFRP reported earlier [6, 7]. It was attributed to matrix fracture, found on the bottom surface under the impact point, splitting 0° -fibers. This signal type (-D) was weaker, but similar in appearance to Type-A signal in the static testing, which was very strong ($>2.5 V_{pp}$) and was attributed to fiber fracture, which was observed on the top surface in real time using a video camera.

The second event starting at 2.77 ms (Fig. 5b) is mostly comprised of A_0 packets when top and bottom sensor signals have reasonable similarity (with inverting). We found three such signals, marked with an “o” in this test and referred to as Type-D’. Overall, these two events (Fig. 5a and b) resemble each other. The second type appears to be of the same origin as the first except the weaker S_0 portion was disturbed by interference from the remnants of prior waves.

In this sample, a large matrix crack (53-mm long) was found on the bottom surface. The cross-sectional view of the plate (Fig. 6) shows this crack at the top. Delamination and fiber fracture are also observed in the middle layer. Delamination was extensive according to the observation by an air-coupled ultrasonic C-scan image (Fig. 7). The extent of damage spreads to as large as 42 x 15 mm double-tree shape area.

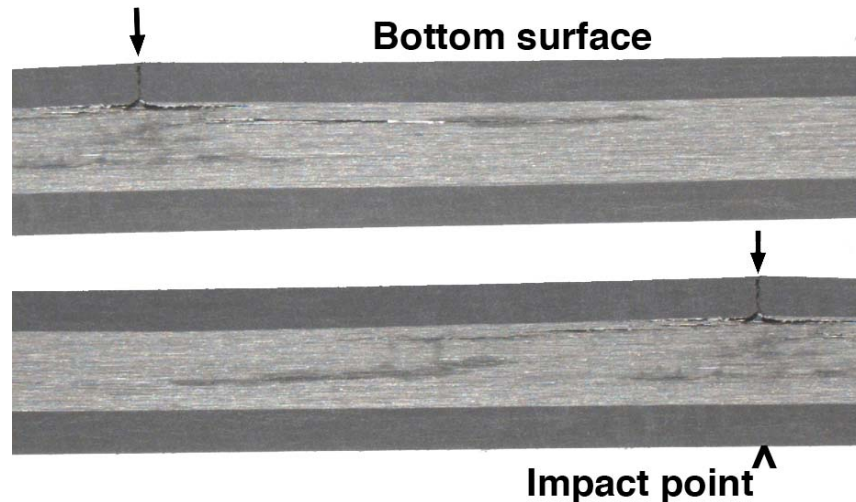


Fig. 6 Cross-section of the 16-ply sample with arrow pointing to the matrix crack.

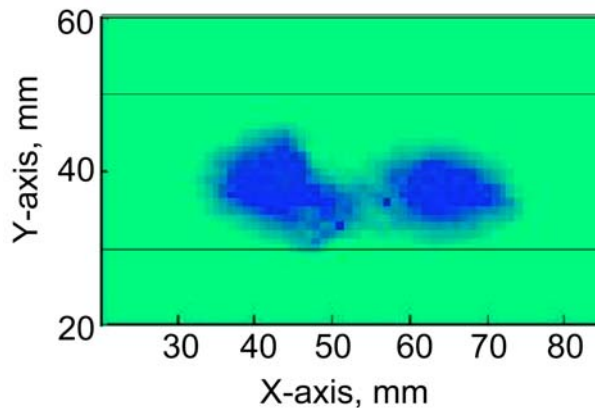


Fig. 7 Ultrasonic C-scan image of damaged area.

It is significant to note that, in dynamic tests, Type-D (and -D') signals were prevalent, but not so strong ($0.6 V_{pp}$ maximum). This implies that the matrix crack proceeded stepwise under dynamic loading, although this is counter-intuitive. Stepwise development of the matrix crack is likely to be induced by the underlying fibers, which may have to be fractured to allow matrix crack propagation. In other test samples, delamination occurred between bottom- 0° and 90° plies, and stepwise matrix crack growth was implied from AE findings. This point needs more study.

Another notable fact is the lack of AE signals that can be traced to the large delamination observed. All the major events are associated with the matrix crack and only the trailing parts of signals can explain delamination. It is feasible to recognize another signal type at 2.6 ms in Fig. 5a is, where a pair of S_0 and A_0 packets of similar amplitude are observed. This is characteristic of Type-C AE signals reported earlier for delamination between CFRP plies. This type is difficult to discern on waveform plots as many signals of various origins overlap as a rule. As the remaining waveform plots were surveyed, apparent S_0 and A_0 packets are also seen continually. However, distinct patterns fail to emerge. Despite extensive delamination observed, we found no distinctive AE type. It is likely that delamination developed continually without any sudden displacement jump. Under static loading, in contrast, nearly 20% of identified signals were Type-C, attributed to delamination. Also missing are signals (Type-B) previously assigned to transverse cracks (37% in the static test). These appear to constitute mostly A_0 -mode signals that followed strong Type-D signals. These differences between static and dynamic tests are expected due to visco-elastic nature of polymeric fracture processes, which require further examination.

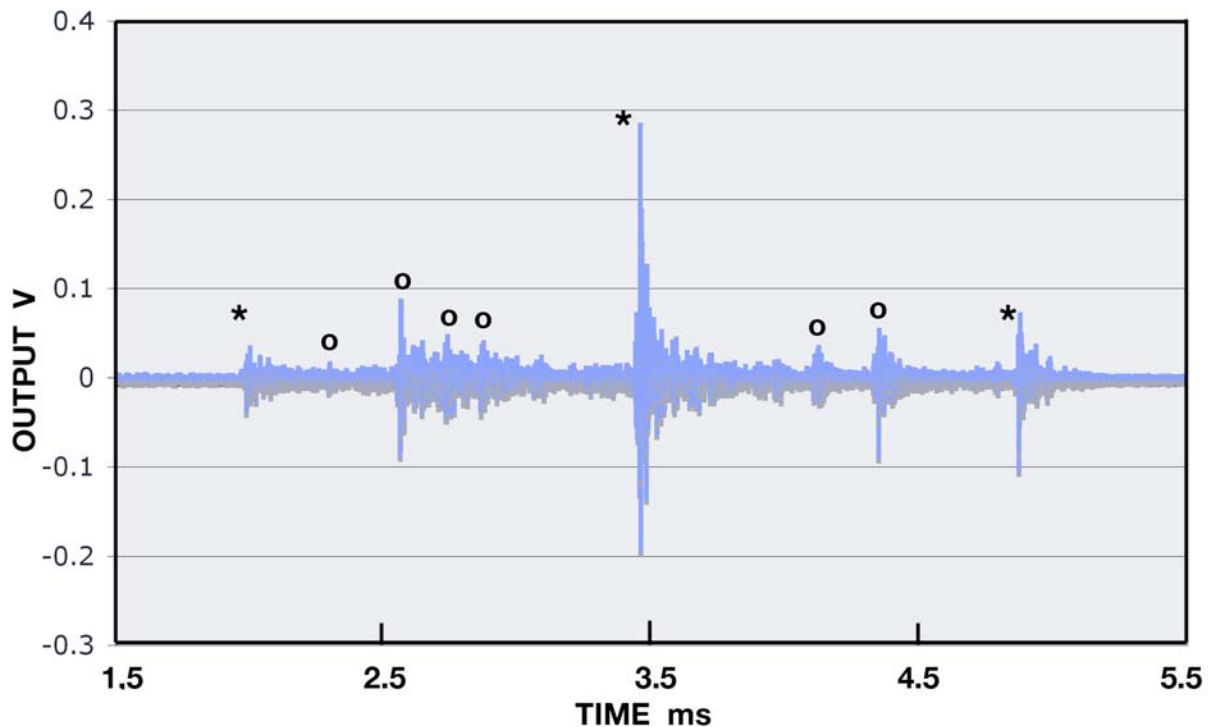


Fig. 8 F-AE signals of a 24-ply plate sample impacted at 1 m/s.

Three of six samples impacted at 1 m/s showed similar AE behavior described above. That is, over 60% of events were of Type-D and most of the remainder were Type-D'. The AE behavior of two other samples (24-ply and 32-ply plates, also impacted at 1 m/s) was slightly different as shown in Fig. 8. (Last one, 40-ply plate did not produce F-AE.) The first F-AE signal was detected at 2 ms and was of Type D (denoted with *) as before and the strongest signal was also of

Type-D (at 3.45 ms). In this sample, more A_0 -only Type-D' signals were observed as marked by an "o". In the 32-ply sample, the ratio of D' to D was the same; i.e., 2 : 1. In both cases, duration of F-AE observation was shorter (3 or 2 ms) than the 16-ply samples (~4 ms) due to higher stiffness of thicker plates. Thus, there are more overlaps of signals between strong events, probably converting Type-D into Type-D'.

Waveform of Type-D signal was previously simulated using the same CFRP and a line-focused laser pulse [6, 7]. Results are shown in Fig. 9, where the setup is at left, the waveform at center and its wavelet transform at right. The similarity of this waveform with that of Type-D is evident, including the period of the S_0 packet preceding the A_0 packet (20 μ s) and the ratio of A_0 to S_0 amplitude (5.4 : 1). The frequency of the S_0 packet was higher in the simulation, reflecting the nature of the fast rise laser source. In the simulated waves, it is 500-600 kHz, whereas the S_0 frequency in Fig. 5 was 250-400 kHz. Observed A_0 frequency of ~140 kHz was comparable to the simulated A_0 packet frequency. It is noted here that the frequency of A_0 waves due to I-AE was much lower at 20-40 kHz.

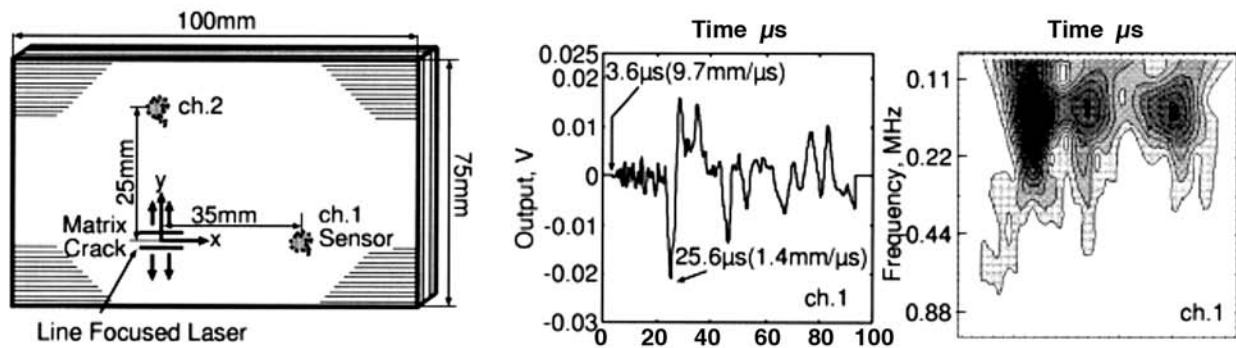


Fig. 9 Laser simulation of matrix cracking on the bottom surface using focused laser beam parallel to the 0° fibers. Pico sensor was 35 mm away (3 mm further than the present experiment).

Conclusions

This study reports on the utility of two-surface sensing in differentiating symmetric and asymmetric Lamb-wave modes. The method was applied to the monitoring of AE during the impact of CFRP plates of four different thicknesses. Different failure modes were seen under dynamic loading in comparison to quasi-static loading. A large matrix crack on the back surface and extensive delamination were the main features. AE signals attributable to matrix crack propagation were predominantly detected, while those due to delamination could not be discerned clearly. This was in marked contrast with the static case, where 4 separate failure mechanisms were correlated to 4 AE-signal types.

References

- 1) SRM 2R-94, SACMA Recommended Test Method for Compression After Impact, SACMA.
- 2) Y. Mizutani, K. Ono and M. Takemoto, Impact damage threshold of CFRP laminates and acoustic emission from impact and fracture”, *Progress in AE XI*, 2002, JSNDI, Tokyo, pp. 23-30.
- 3) S.I. Ochiai, K.Q. Lew and J.E. Green, Instrumented impact testing of structural fiber-reinforced plastic sheet materials and the simultaneous AE measurements, *J. of Acoustic Emission*, 1 (3), (1982), pp. 191-192.

- 4) N. Liu, Q.M. Zhu, C.Y. Wei, N.D. Dykes, P.E. Irving, Impact damage detection in carbon fiber composites using neural networks and acoustic emission, *Key Engineering Materials*, **167-168** (1999), pp. 43-54.
- 5) W.H. Prosser, M.R. Gorman and D.H. Humes, Acoustic emission signals in thin plates produced by impact damage, *J. of Acoustic Emission*, **17**, (1999), pp. 29-36.
- 6) A. K. Mal, F. Shih, and S. Banerjee, Acoustic emission waveforms in composite laminates under low velocity impact, *Proceedings of SPIE - Smart Nondestructive Evaluation and Health Monitoring of Structural and Biological Systems II*, Vol. 5047, 2003, pp. 1-12.
- 7) Y. Mizutani, K. Nagashima, M. Takemoto, K. Ono, Fracture mode classification in locally loaded cross-ply CFRP coupons using wavelet transform, *Proc. of AECM-6*, ASNT, Texas, pp.114-123.
- 8) Y. Mizutani, K. Nagashima, M. Takemoto and K. Ono, Fracture mechanism characterization of cross-ply carbon-fiber composites using acoustic emission analysis, *NDT & E. Intl.*, **33-2** (2000), pp. 101-110.
- 9) Y. Mizutani, Quantitative evaluation of impact force and damage of locally impacted fiber reinforced plastics, Doctoral Dissertation, Aoyama Gakuin Univ., 2000. 137 p.

NEURAL NETWORK BURST PRESSURE PREDICTION IN COMPOSITE OVERWRAPPED PRESSURE VESSELS

ERIC v. K. HILL, SETH-ANDREW T. DION, JUSTIN O. KARL,
NICHOLAS S. SPIVEY and JAMES L. WALKER II*

Aerospace Engineering Department, Embry-Riddle Aeronautical University, Daytona Beach, FL 32114 USA; *Non-Destructive Evaluation Branch, NASA Marshall Space Flight Center, AL 35812 USA

Abstract

Acoustic emission data were collected during the hydro-burst testing of eleven 380-mm (15")-diameter filament-wound composite over-wrapped pressure vessels. A neural-network burst pressure prediction was generated from the resulting AE amplitude data. The bottles shared commonality of graphite fiber, epoxy resin, and cure time. Individual bottles varied by cure mode (rotisserie versus static oven curing), types of inflicted damage, temperature of the pressurizing medium, and pressurization scheme. Three categorical variables were selected to represent undamaged bottles, impact damaged bottles, and bottles with lacerated hoop fibers. This categorization along with the removal of the AE data from the disbonding noise between the aluminum liner and the composite over-wrap allowed the prediction of burst pressures in all three sets of bottles using a single back-propagation neural network. Here, the worst-case error was 3.38%.

Keywords: Amplitude distribution, back-propagation, burst pressure prediction, composites, filament-wound, graphite/epoxy, neural networks, nondestructive evaluation, pressure vessel.

Introduction

Acoustic Emission

Acoustic emission (AE) is a nondestructive evaluation method that involves instrumenting a specimen with piezoelectric transducers and recording parametric representations of the waveform data from flaw growth activity in order to perform a structural integrity analysis. Analysis of the AE data allows for the determination of failure mechanisms that are active in the specimen. Consequently, it also contains information concerning the structural integrity.

Burst Pressure Prediction

The prediction of burst pressures in both damaged and undamaged filament wound composite pressure vessels has been previously accomplished using linear multivariate statistical analysis and back-propagation neural networks [1-3]. The goal of this research was to utilize a back-propagation neural network to make burst pressure predictions on 380-mm-diameter graphite/epoxy filament-wound composite over-wrapped pressure vessels (COPVs, otherwise known as bottles) that were varied in the method of cure, type of damage, temperature, and pressurization scheme. What made this research different from its predecessors was that the disbonding of the composite over-wrap from the aluminum liner generated multiple-hit AE data (noise), which had nothing to do with the structural integrity of the vessels. This precluded a straightforward solution similar to those obtained previously until the noise data were eliminated.

Neural Networks

Artificial neural networks are a diverse set of robust mathematical tools used to classify data into clusters, recognize patterns, process signals, and do predictive modeling and forecasting. Here, an unsupervised SOM neural network was used to classify the composite failure mechanisms that occur during pressurization. The back-propagation architecture is a feed-forward design that was subsequently employed for making supervised burst pressure predictions.

Kohonen Self Organizing Map (SOM)

In composite structures, the amplitude frequencies [of occurrence] generated during damage progression can be grouped and classified into failure mechanisms. For small data sets, these mechanisms can be seen as “humps” in the AE amplitude distributions. Figure 1 shows the amplitude distribution for bottle SN002, an impact damaged graphite/epoxy COPV used for training the back-propagation network, which appears to have four humps. This number of failure mechanisms (four) was confirmed by classifying the AE amplitude data with a Kohonen self-organizing map (SOM) neural network.

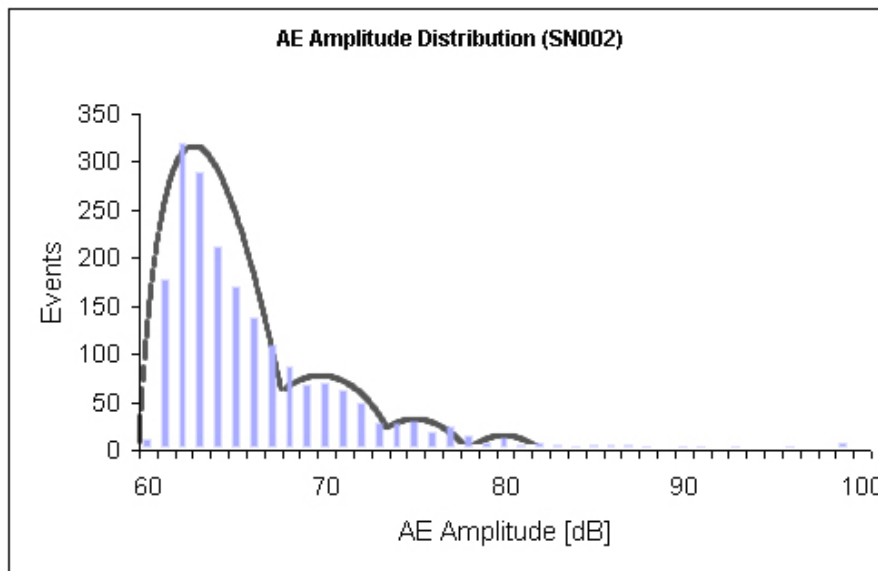


Fig. 1 AE amplitude distribution for COPV SN002.

Back-propagation

The back-propagation neural network is a feed-forward, supervised neural network, that is to say, it does not return a feedback signal to itself during each training pass, and it is necessary to train the network on a known solution before applying it to a new case. This is called supervised learning. A back-propagation neural network is typically constructed with an input layer, one or more hidden layers (each composed of multiple neurons) for mapping, and an output layer.

Experimental Procedure

Pressure Vessels

Eleven 380-mm-diameter filament-wound COPVs were wet-wound on a filament winder. The bottles were thin-walled aluminum cylinders over-wrapped with graphite fibers and epoxy resin. The winding sequence was 3 inner-hoop plies, followed by 2 helical layers, and then 2 outer-hoop plies. Eight of the bottles were rotated at slow speeds (rotisserie style) during oven curing; three were oven cured without rotation. Four of the COPVs were tested at ambient

temperature, while the remaining seven experienced cryogenic temperatures. Due to the nature of piezoelectric materials, it was thought that the large variation in temperatures would have a significant effect on transducer output voltage, as well as adding to the brittle nature of the composite material.

Varying amounts of artificial damage were inflicted on the bottles in the form of impacts from both blunt and sharp tups, as well as with the cutting of hoop fibers: five tows were cut in the mid-hoop ply and five in the first outer-hoop ply. The strain rate was also varied non-systematically in that the pressurization scheme used on each bottle test varied in both duration and number of pressurization ramps/holds; thus, no two bottles were pressurized alike.

The amount of diversity in some of these variables and the small number of bottles would not allow for statistical analysis of the effects of each variable. Therefore, neural networks were employed as the primary method of data analysis. Table 1 summarizes the test variables along with the failure or burst pressures.

Table 1 Summary of graphite/epoxy COPV variables and burst pressures.

S/N	Damage	Cure Type	Test Temperature	Burst Pressure [psig]
002	Impacted	Static	Cryogenic	1880
003	Impacted	Rotisserie	Cryogenic	2004
005	None	Rotisserie	Ambient	2960
009	None	Static	Cryogenic	2544
010	None	Static	Cryogenic	2460
013	None	Rotisserie	Ambient	2874
014	None	Rotisserie	Cryogenic	2390
018	Lacerated	Rotisserie	Ambient	2864
020	Impacted	Rotisserie	Cryogenic	1967
025	Lacerated	Rotisserie	Cryogenic	2393
026	Lacerated	Rotisserie	Ambient	2675

AE Data Collection

Acoustic emission data were successfully collected from all seven of the bottles in the test set. A multi-channel Physical Acoustics Corporation (PAC) AE analyzer was used to record the AE flaw growth data from seven AE channels, each representing a transducer at a unique location on the test bottles. This data acquisition unit also allowed for a separate parametric input, which was used to record a voltage signal representative of the pressure in the test specimen. Figure 2 shows a schematic diagram of the test setup.

Six PAC-R15 AE transducers were mounted equidistant around the circumference of the top and bottom hoop windings on each bottle. The seventh transducer was mounted near the upper polar boss on the helically wound portion of the bottles. In the ambient temperature tests, hot-melt glue was used to bond each transducer and provide acoustical coupling between the transducer and the specimen. For the cryogenic tests, high-aqueous vacuum grease and a mechanical housing were used to couple the transducers to the bottles. The data sampling threshold was set to record all AE hits that had an amplitude of 60 dB or greater.

AE Data Filtering

Even though constraints such as amplitude threshold, peak definition time (PDT=100 μ s), hit definition time (HDT=500 μ s), and hit lockout time (HLT=500 μ s) were applied to the AE

sampling, considerable noise and multiple-hit data were still present in the raw data sets. HDT is the minimum time that an AE event must have to be recorded, and the combination of HDT and HLT determines the maximum time for an event before it is considered to be a multiple-hit event [4]. These settings work in real-time as data are recorded.

Multiple-hit data occur when many AE waveforms reach the transducer closely spaced in time, one after another (in a condition of buffer overrun or in the cases where HDT and HLT are

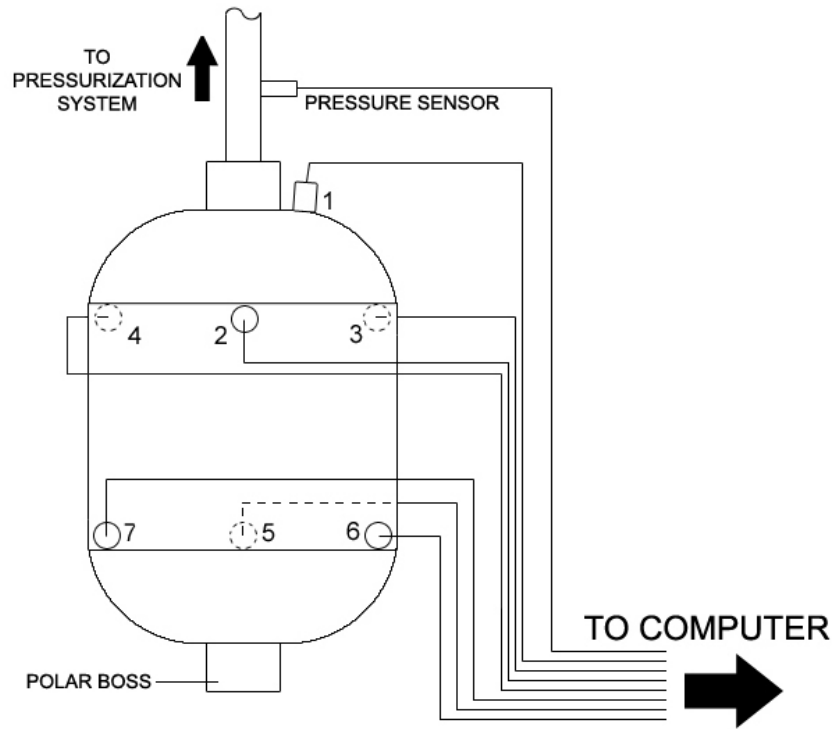


Fig. 2 Sensor positioning and test setup.

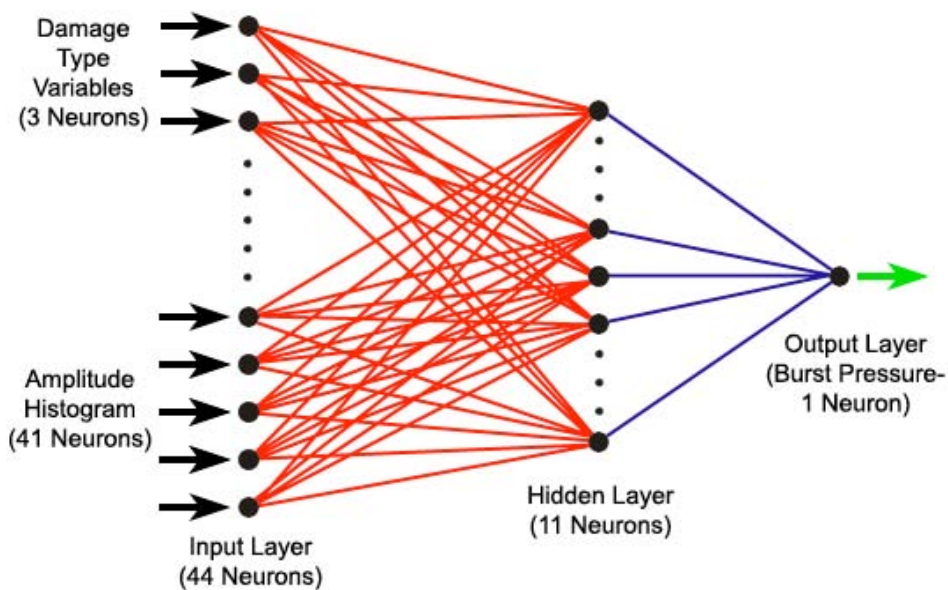


Fig. 3 Network architecture.

not properly set). This results in a long artificial waveform that is actually comprised of several shorter waveforms, which will have vastly different AE parameters than single-hit data. In this case, the multiple-hit data are probably the result of composite disbonding from the aluminum liner, a failure mechanism which should not affect the burst pressure.

In order to remove these multiple hits from the recorded data set, it was determined that any AE hits having durations longer than 100 ms were to be removed. Rise time, the waveform parameter that represents the time-to-peak of the waveform, was used to further remove suspected multiple hit data. Long rise times typically indicate multiple hits logged together. Thus, any hit with a rise time of greater than 25 ms was also removed from the data set. The AE energy parameter is a measure of the area under the rectified waveform envelope. In the case of these data, many hits were reported by the data acquisition system to have zero energy. These hits were also discarded under the assumption that they were noise.

The final filter applied to the data was to select those data points to be used in the actual burst pressure prediction. After removing all of the data prior to the start of pressurization (the acquisition hardware recorded AE parameter data before pressurization commenced), it was decided that the first 2000 data points would provide a sufficient sample size for the neural network to train on while still taking only those data that were acquired at or below 20% of the anticipated burst pressure. In general, damage is inflicted on composite bottles during any pressurization cycle; therefore, the goal was to predict on data taken at low proof pressures.

Using the final edited data set from each bottle, a frequency distribution of the amplitudes was extracted for training and testing of the back-propagation neural network. The histogram representation of an amplitude distribution for bottle S/N 002 can be seen in Fig. 1, and the amplitude distributions from the edited data for all eleven bottles are summarized in Table 2. The neural network was trained to analyze the subtle differences in the distributions from each bottle and match them to the damage type and burst pressures provided in the training set.

Table 2 Finalized amplitude distribution frequencies (with **categorical variables** in **bold**).

S/N	Amplitude Distribution Frequency Data	Burst Pressure [psig]
002	010 2 11 177 319 289 212 171 139 109 87 69 70 63 50 29 29 30 19 24 16 7 13 68 6 3 6 5 5 3 1 4 3 1 3 1 0 3 2 0 7 0	1880
003	010 2 66 452 461 268 171 130 89 76 44 37 40 25 35 20 13 17 11 4 10 7 2 4 1 2 4 2 0 0 0 1 0 2 0 0 0 0 0 0 1 4 1	2004
005	001 1 169 148 121 115 95 123 88 81 78 62 59 74 53 53 58 61 47 46 52 58 38 48 43 34 29 31 28 21 21 21 10 7 7 4 6 7 0 3 1 0 0	2960
009	001 1 39 360 452 285 177 119 88 82 70 46 42 31 40 28 32 20 13 9 8 8 6 4 6 7 7 3 1 4 3 3 0 2 0 0 0 1 0 0 0 4 0	2544
010	001 1 47 337 400 298 194 114 112 75 58 58 55 34 44 32 29 20 19 10 8 8 5 10 8 4 1 1 2 6 2 1 1 0 1 1 0 1 1 1 1 1 1 0	2460
013	001 1 71 401 380 254 169 96 76 67 61 42 44 49 42 29 23 33 16 16 16 21 15 15 12 9 7 4 10 8 7 3 0 3 0 0 1 0 0 0 0 0 0	2874
014	001 1 67 477 475 309 193 98 66 54 29 47 22 25 24 13 2 10 9 10 7 4 9 4 4 1 2 3 1 3 4 0 5 3 1 1 1 0 1 0 2 1 3	2390
018	100 3 225 222 211 176 160 136 137 99 98 80 85 67 54 2 44 40 23 19 21 15 15 5 2 6 4 2 0 0 0 1 0 0 0 0 0 1 0 0 0 0 0	2864
020	010 16 212 369 301 230 179 147 99 95 65 47 42 30 35 25 12 12 8 13 7 10 5 4 0 5 1 7 4 2 3 1 2 0 1 2 0 0 0 0 5 4	1967
025	100 3 30 224 309 294 216 176 132 102 99 76 63 39 48 36 26 19 18 15 12 10 13 8 6 5 0 3 0 0 1 0 2 5 0 1 1 1 1 0 0 7 2	2393
026	100 3 13 108 166 199 199 205 173 167 135 103 107 86 66 58 47 29 29 35 15 16 5 8 8 5 1 3 2 3 3 1 0 1 1 1 0 1 0 0 0 1 0	2675

Results

Network Architecture

The back-propagation neural network used herein [4] had the architecture shown in Fig. 3. The input for each bottle consisted of a 1 x 44 dimensional vector with 3 entries representing the damage categories (001 undamaged; 010 impacted; and 100 lacerated) plus 41 integers representing the frequency distribution of amplitudes from 60 to 100 dB (Table 2). The actual burst pressure was also supplied as an input for error calculation at the output.

Each neuron in the hidden layer contains a hyperbolic-tangent activation or transfer function that can be used to approximate the shape of the amplitude distributions. A large number of neurons can be used together to approximate compound and/or discontinuous curves that will fit the training data well, but if trained too closely, the back-propagation neural network may not predict accurately on the test data. Too few neurons in the hidden layer will result in loosely fit curves that will not correspond well to the training or test data. Using this approach, it was found that 11 neurons in the hidden layer offered the network that would best fit both the training and the test data.

Training the Network

The back-propagation neural network, generated using Neuralware's NeuralWorks Professional II Plus software package, was trained on a total of seven COPVs, including bottles from each of the three damage categories (Table 3). The training set was chosen so that a high and low burst pressure COPV from each damage category was included. The undamaged category also included a midrange burst pressure bottle. Thus, the epoch size was seven or the total number of bottles in the training set.

After numerous experimental iterations, the optimum network architecture and input parameters were determined [4]. The learning rule was the normalized cumulative delta, and the optimal learning coefficient for the network was found to be 0.30 with a momentum of 0.40. This relatively large learning coefficient allowed the network to train very quickly and to learn in only 71 cycles. Because the network trained so quickly, bias neurons were not employed to speed up the training process. Transition points and learning coefficient ratios were not important either because the default transition point of 5000 cycles was never reached, while the F' offset was set at 0.10.

A root-mean-square (RMS) error value on the seven COPVs in the training set is computed by the software after every training cycle to determine how well the network has trained. Here the RMS error convergence was set at 7%. This means that training was considered complete when the network-training curve was within an RMS error of 7% of the training data. It was found that a higher convergence criterion left the network too loosely fit to the training data, and a lower convergence criterion forced tighter fitting of the training data but poorer fitting of the test data.

Burst Pressure Predictions

Finally, the trained network was used to predict burst pressures for both the training and test sets. Table 3 shows a summary of the prediction results on all the COPVs. The maximum prediction error in the seven bottle training set was -2.78%, and the maximum error in the four bottle test set was 3.38%. All of these values were well within the goal of predicting the burst pressures to within a $\pm 5\%$ error.

Table 3 Summary of training and test results

S/N	Damage	Purpose	Burst Pressure [psig]	Predicted Burst Pressure [psig]	Error [%]
002	Impacted	Train	1880	1827.597	-2.78
003	Impacted	Train	2004	1964.115	-1.99
005	None	Test	2760	2853.188	3.38
009	None	Train	2544	2584.266	1.58
010	None	Test	2460	2432.273	-1.12
013	None	Train	2874	2791.009	-2.88
014	None	Train	2390	2358.271	-1.32
018	Lacerated	Train	2864	2869.181	0.18
020	Impacted	Test	1967	1999.875	1.67
025	Lacerated	Train	2393	2369.740	-0.97
026	Lacerated	Test	2675	2643.174	-1.19

Conclusions

The worst-case prediction error of 3.38% was low, and the network trained quickly in spite of the many test variables involved. If there were any variations in the amplitude distribution data due to cure mode, temperature, and pressurization scheme, they were automatically taken into account by the back-propagation neural network. The fact that network training was accomplished in only 71 cycles attests to the effectiveness of preprocessing or editing the AE data to remove the multiple-hit data and other noise.

References

1. E.v.K. Hill, J.L. Walker II, and G.H. Rowell, *Materials Evaluation*, **54**, 1996, 744-748.
2. J.L. Walker, S.S. Russell, G.L. Workman, and E.v.K. Hill, *Materials Evaluation*, **55**, 1997, 903-907.
3. M.E. Fisher and E.v.K. Hill, *Materials Evaluation*, **56**, 1998, 1395-1401.
4. S.-A. T. Dion, MSAE Thesis, Embry-Riddle Aeronautical U., Daytona Beach, 2006.

ACOUSTIC EMISSION SOURCE LOCATION IN A THICK STEEL PLATE BY LAMB MODES

M. A. HAMSTAD

National Institute of Standards and Technology, Materials Reliability Division (853), 325 Broadway, Boulder, CO 80305-3328 and University of Denver, School of Engineering and Computer Science, Department of Mechanical and Materials Engineering, Denver, CO 80208

Abstract

Through use of a validated finite-element modeling code, buried out-of-plane (two-dimensional code (2D)) and in-plane (three-dimensional code (3D)) acoustic emission (AE) dipole-point-sources were operated at different depths below the top surface of a 25.4-mm (1") thick steel plate with large transverse dimensions. The depths ranged from a source centered at 1.25 mm below the top surface to a source centered at the mid-plane. Most of the cases were run with a source rise time of 2.3 μ s. For each depth, the out-of-plane displacements were obtained as a function of time at a series of propagation distances up to 1016 mm (40") from the epicenter position for the out-of-plane sources and up to 381 mm (15") for the in-plane sources. The total time for each signal was from the initiation of the source up to 580 μ s (2D) and 200 μ s (3D). Since the displacements were obtained on both the top and bottom surfaces, results representing sources at various depths over the whole plate thickness were available. The modeled signals were examined with no filtering as well as with a 40-kHz high-pass filter or a bandpass filter of 100 kHz to 300 kHz. In order to correlate the AE displacement signals with Lamb modes, the relevant group-velocity curves were superimposed on wavelet transforms of the signals. Modal regions that carried a significant portion of the AE energy were identified by mode, frequency range and source depth. For sources located near the plate top surface, a Rayleigh wave was observed in the top-surface displacement signals. This wave was not present in the signals obtained from the bottom surface or from sources not located near the top surface. Signal arrival times at different propagation distances were obtained from the maximum wavelet transform (WT) coefficients at key frequencies of certain modes. Plots of propagation distance versus arrival times were used to find group velocities for a key frequency/mode combination (102 kHz for either the A_0 or S_0 Lamb modes). These velocities were found to be very close to those obtained from Lamb-wave theory. A method to identify the mode that led to the WT peak at the key frequency was demonstrated for AE events that were detected at four sensors in an array. This method could be automated to process digitized signals to significantly improve accuracy of source location in thick plates when nonresonant AE sensors are used.

Keywords: Acoustic emission arrival times, AE dipoles, finite element modeling, Lamb waves, source location, wavelet transform.

Introduction

The author and his co-workers have published a number of papers on the analysis of finite-element-modeled (FEM) acoustic emission (AE) signals in a 4.7-mm thick aluminum plate [1 - 4]. In this thin plate, only the two fundamental modes (A_0 and S_0) were significantly excited over the range of typical frequencies used in AE. One focus of this prior work was the use of a wavelet transform (WT) to obtain accurate arrival times of certain frequencies of the two fundamental modes. Since these arrival times were all associated with specific known group velocities,

accurate source locations could be calculated from the dispersive AE signals even in the presence of significant electronic preamplifier noise [3].

Over the last several years we have been creating an FEM database of AE signals for a 25.4-mm thick steel plate. The purpose of the research reported here was to apply a WT to identify certain important Lamb-wave modal regions and to extract accurate signal arrival times from these regions for the purpose of the calculation of source locations. A recent publication [5] considered the question of the extraction of arrival times in nominal 15-mm thick steel determined by use of the maximum magnitude of WT coefficients at certain frequencies. “Mathematically calculated” [5] waveforms that had been filtered to simulate a 150-kHz resonant sensor were studied. Experimental results also were obtained from a cylindrical steel pressure vessel with an outer diameter of 800 mm and a wall thickness of 15.5 mm. Experimental waveforms from both pressurization-activated sources and pencil-lead breaks were obtained with resonant (frequency of 150 kHz) AE sensors. The results indicated some success and some difficulties for maximum propagation distances of up to 360 mm.

Finite-Element Modeled AE Signal Database

To create the finite-element database used in this research, an axially symmetric (2D) code was primarily used. This choice allowed propagation distances up to 1016 mm (40 in) without extremely long parallel-processor computer runs. The domain size was large enough that reflections from the edges of the flat plate did not occur during the duration of the direct-path signal. For particular comparisons, some results with a 3D code (with an appropriate large domain size) were also used. The validations of the explicit finite-element codes can be found in published literature [6, 7].

The entire FEM signals were either left unfiltered or numerically processed with a 40-kHz (four-pole Butterworth) high-pass filter or a similar bandpass filter of 100 kHz to 300 kHz. Subsequently, all the signals were resampled from the original time step (see Table 1) to 0.1 μ s per point. This rate corresponds to typical sampling rates used to capture waveforms in AE experiments. The AE signals were examined out to 580 μ s after the source initiation time for the 2D code and 200 μ s for the 3D code. The sources in the continuous mesh domain were dipoles (self-equilibrating forces from two single-cell body-force monopoles each acting on one cell, with one cell between them) using the “equivalent body force” concept for displacement discontinuities [8]. The forces were applied with a “cosine bell” temporal dependence $T(t)$ given by

$$T(t) = \begin{cases} 0 & \text{for } t < 0, \\ (0.5 - 0.5 \cos [\pi t / \tau]) & \text{for } 0 \leq t \leq \tau, \text{ and} \\ 1 & \text{for } t > \tau, \end{cases} \quad (1)$$

where $\tau = 2.3 \mu$ s was the source rise time for most of the cases. One run was made with a 1.5- μ s rise time to check for significant changes in the higher signal frequencies with a shorter source rise time. No significant changes were observed. The finite-element calculations were made based on bulk velocities and density values for steel (longitudinal velocity = 5940 m/s, shear velocity = 3220 m/s and density = 7.8 kg/m³) [9]. Based on our previous experience, the uniform cell size was smaller for sources that were nearer to the plate surface for the 2D runs that were primarily used in this research. This change was made due to the presence of Rayleigh waves in those cases. Table 1 shows the source orientations, propagation distances, source depths (depth of center of source below the top surface of the plate), uniform cell sizes, and time steps of the finite-element calculations. The AE signals from single nodes provided the out-of-plane top-surface and bottom-surface displacement versus time corresponding to a perfect point-contact

sensor (pseudo-sensor) at a series of propagation distances. The use of bottom surface nodes extended the source depths shown in Table 1 without materially changing the code run times. For example, the source at a depth of 1.25 mm below the top surface corresponds to a source at a depth of 24.15 mm above the bottom surface when the bottom surface displacement signal was used. In essence, one computer run provided two depths. In the case of the 3D runs, the pseudo-sensors were located in the zero-degree propagation direction (the in-plane x-axis direction at several propagation distances up to 381 mm (15'') from the source epicenter. The in-plane dipole forces were also aligned in this direction.

Table 1 Description of finite-element database used in this study.

Source type	Depth of source below top surface (mm)	FEM: Cell size (mm) / time step (ns)
Out-of-plane dipole with propagation distances (in mm) of 127, 254, 381, 508, 635, 762, 1016 (2D code)	1.25	0.125 / 18.9
	4.73	0.249 / 37.7
	7.72	0.498 / 75.5
	10.71	0.498 / 75.5
	12.7	0.498 / 75.5
In-plane and out-of-plane dipoles with propagation distance of 381 mm (3D code)	1.25	0.498 / 75.5
	7.72	0.498 / 75.5
	12.7	0.498 / 75.5

Wavelet Transform Information

Wavelet transform results were used to enhance the identification of the AE signal Lamb modes and to obtain from WT coefficient peaks the different mode arrival times at key frequencies. The WT results were obtained using the AGU-Vallen Wavelet freeware [10] with the key parameter settings being: maximum frequency = 500 kHz, frequency resolution = 2 kHz and wavelet size = 600 samples. The Wavelet Time range settings for the number of samples (i.e., points) were up to about 5800 points, allowing the full-direct-arrival signal to be transformed for the out-of-plane source runs. For the in-plane sources a total of about 2500 points was used so as to fully correspond to the group velocity curves at the maximum propagation distance. In the color WT figures, the red color (surrounded by yellow) indicates the highest intensity region of the WT coefficients. In a black-and-white print out of the color results, the darkest region inside a lighter region indicates the high intensity region.

Group Velocity Curves for Thick Steel Plate

Using the bulk velocities and density provided above, the group velocity curves were calculated [11, 12]. The results are shown in Fig. 1 for the first five symmetric and anti-symmetric modes. Due to the many potential modes that are present in the typical frequency range of AE interest, this figure shows that there may be potential difficulties in mode identification in frequency regions where the group velocities are similar. This situation will be particularly true when the propagation distances are not large, since for many frequencies the arrival times of the various modes will not be widely separated in time. Thus, it was initially desirable to study signals for propagation distances that were fairly large in order to more easily distinguish different modes. Due to limitations on availability of computing resources for long runs, it was decided to use signals obtained from the 2D code for propagation distances up to 1016 mm (40''). The 2D code can be used to calculate cases only for axisymmetric out-of-plane sources in plates, whereas many real AE sources in metals can be primarily represented by in-plane dipoles. To establish

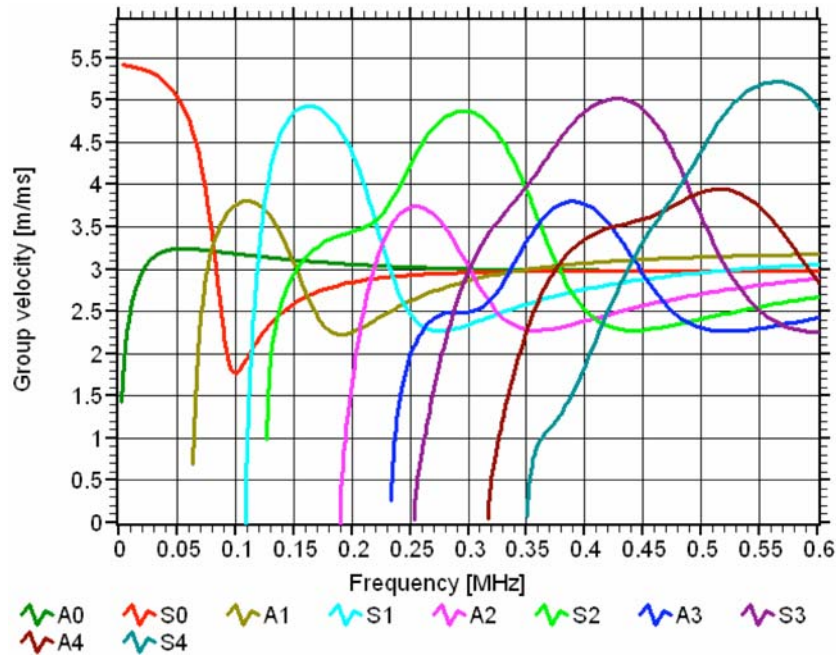


Fig. 1 Group velocities versus frequency for a steel plate of 25.4-mm thickness; first five symmetric and anti-symmetric modes shown.

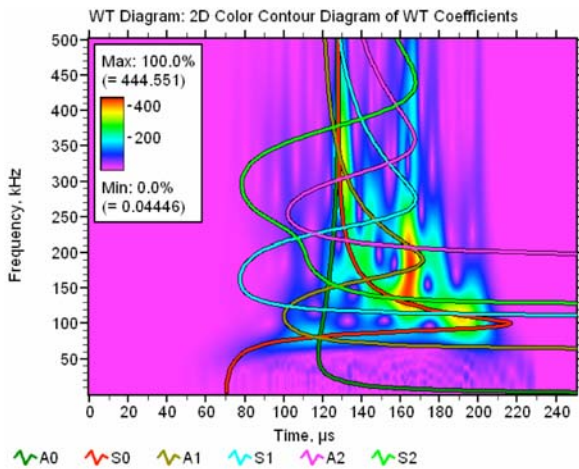


Fig. 2 WT for out-of-plane dipole at a depth of 7.72 mm below the surface, 40-kHz high-pass, 3D code.

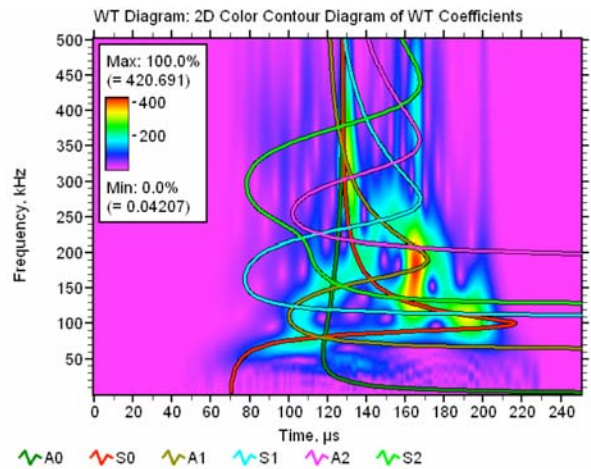


Fig. 3 WT for in-plane dipole at a depth of 7.72 mm below the surface, 40-kHz high-pass, 3D code.

whether the analysis results with the 2D code signals could be extended to in-plane source signals, we considered some comparisons of the displacement signals from out-of-plane dipole sources with in-plane dipole sources at a propagation distance of 381 mm in the next section.

Modes Excited by Out-of-Plane versus In-Plane Buried Dipoles

Figures 2 and 3 respectively show WTs of the displacement signals (top surface) from out-of-plane and in-plane (both 3D code) buried dipoles at a depth of 7.72 mm below the top surface of the plate. The out-of-plane displacements were obtained at a propagation distance of 381 mm. The WT results were obtained from the signals after applying a 40-kHz high-pass filter. The WT results have been superimposed with the first three symmetric and anti-symmetric Lamb modes.

Examination of these two figures shows that the modal intensity distribution is quite similar, particularly for the three regions with the highest WT intensity. Thus, we can expect that certain results determined from the analysis of the signals with out-of-plane dipole sources can be transferred to the signals from in-plane dipole sources.

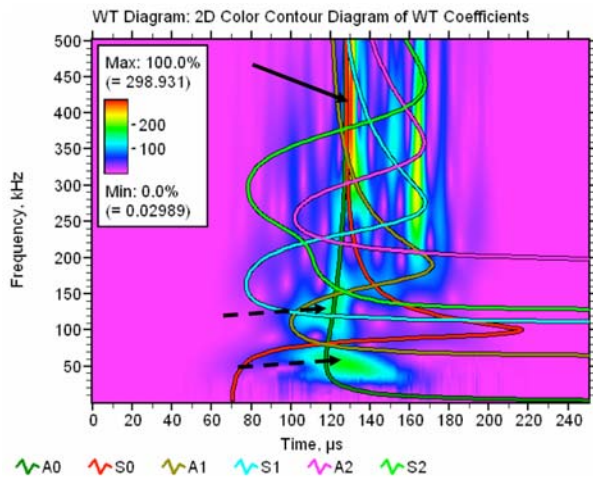


Fig. 4 WT for out-of-plane dipole at a depth of 1.25 mm below the surface, 40-kHz high-pass, 3D code.

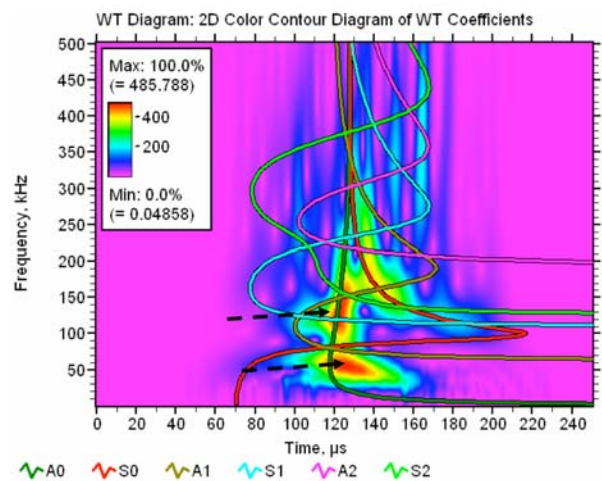


Fig. 5 WT for in-plane dipole at a depth of 1.25 mm below the surface, 40-kHz high-pass, 3D code.

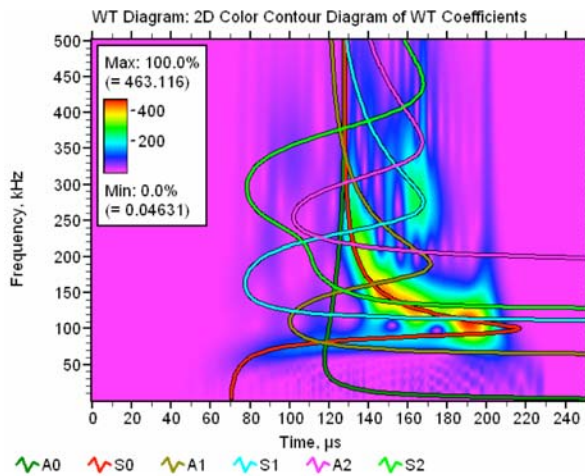


Fig. 6 WT for out-of-plane dipole at a depth of 12.7 mm below the surface, 40-kHz high-pass, 3D code.

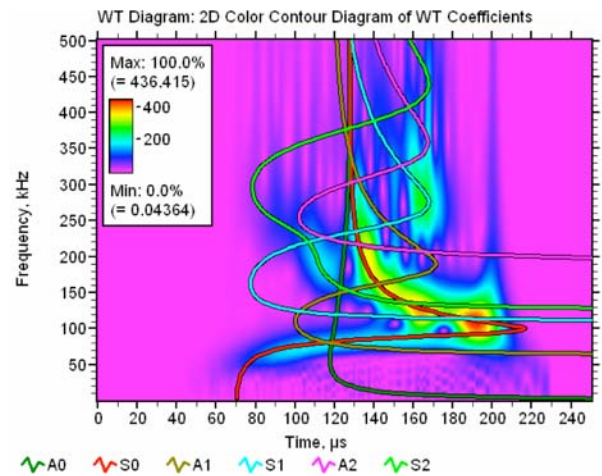


Fig. 7 WT for in-plane dipole at a depth of 12.7 mm below the surface, 40-kHz high-pass, 3D code.

The comparison of the out-of-plane and in-plane source-generated signals at the same propagation distance for depths nearer the surface (1.25 mm) and at the mid-plane (12.7 mm) demonstrate some similarities and some differences. Figures 4 and 5 (both 3D code) show the signals from the two orientations at a depth of 1.25 mm, and Figs. 6 and 7 (both 3D code) illustrate the displacement signals at a depth of 12.7 mm. At the 12.7-mm depth, the WT results are nearly identical for the two source orientations. The main differences between the two source orientations appear for a source at a depth of 1.25 mm. Figure 4 (out-of-plane) shows a high-frequency Rayleigh wave (see solid arrow) with the highest intensity at frequencies above about 340 kHz. Also in Fig. 4, there is a region of lesser intensity associated with the A_2 and S_1 modes at frequencies above about 250 kHz. These two regions do not appear with high intensity for the in-

plane source orientation. But the lower frequency regions of highest intensity for the in-plane case (see dashed arrows in Fig. 5) do have similar regions for the out-of-plane case (see dashed arrows in Fig. 4). In Fig. 5, these lower frequency regions do not stand out, due to the higher intensity of the high frequency regions. Thus, if only the lower-frequency regions are considered, we can expect that most of the analysis results for out-of-plane source-based signals can be extended to in-plane source-based signals. In the later sections of this paper, the emphasis will be on lower frequency regions; thus the differences noted here will not be important factors in extending the results from out-of-plane sources to in-plane ones.

Displacement Signals and WT Results at 1016 mm Propagation Distance for Out-of-Plane Dipoles

Figures 8, 9 and 10 respectively show at a propagation distance of 1016 mm the out-of-plane displacement versus time (as a function of the out-of-plane source depth below the surface of the pseudo-sensor) for the conditions of no filtering, 40-kHz high-pass and 100-kHz to 300-kHz bandpass (note that the fastest part of the S_0 mode requires about 180 μ s to reach the 1016-mm propagation distance). The corresponding WT results are shown in Figs. 11, 12 and 13 (for convenience in making comparisons arranged in the figures so that depths at symmetric distances from the midplane are next to each other). Some general observations based on these figures follow. First, as can be seen in Figs. 8 and 11 for sources nearer either surface (depths (in mm) of 1.25, 4.73, 20.67 and 24.15), considerable energy was present in the lowest frequency portion of the A_0 mode (see circled regions in Fig. 11) when no filter was applied. This result is similar to what we found in the 4.7 mm aluminum plate studies [13]. But there is an important difference. The frequencies with significant energy in this portion of the A_0 mode are less than 40 kHz in the 25.4-mm thick plate. These frequencies are below the frequencies normally used in AE monitoring. Thus, only in the case of a test environment that is free of significant low-frequency extraneous noise (coupled with the use of AE sensors with good sensitivity in the 10-kHz to 40-kHz frequency range) could this portion of the A_0 mode be exploited for AE monitoring.

Second, the signal displacements in Figs. 8, 9 and 10 show that the signal amplitudes increase gradually (from about 180 μ s) with increasing time, and they reach their highest amplitudes later in the signals. Thus, AE approaches that depend on threshold penetration for the determination of arrival times are likely to provide a set of arrival times that correspond to a wide variety of propagation velocities as a function of different propagation distances and/or source intensities. This result will be particularly true for larger propagation distances.

Third, even at the fairly large propagation distance of 1016 mm, there likely will still be difficulties in the determination of the mode that corresponds to a WT magnitude peak at frequencies above about 120 kHz due to multiple regions with intensities that change with different source depths as shown in WTs of Figs. 11, 12 and 13. Thus, for a source location calculation, it may not be clear as to which group velocity should be used for a certain set of WT-determined arrival times at frequencies above 120 kHz.

Fourth, as indicated by the solid arrows in Figs. 8 and 9 (see also Figs. 11 and 12), the Rayleigh wave (with frequencies above about 340 kHz) clearly appears in the displacement signals from sensors on a surface, only when the source is close to that surface (1.25 mm below the top surface, in this case). In the WT results for a source depth of 4.73 mm, the Rayleigh wave can still be observed (see solid arrows in Figs. 11 and 12), but it is not as easily observed in the displacement signals from the source at this depth.

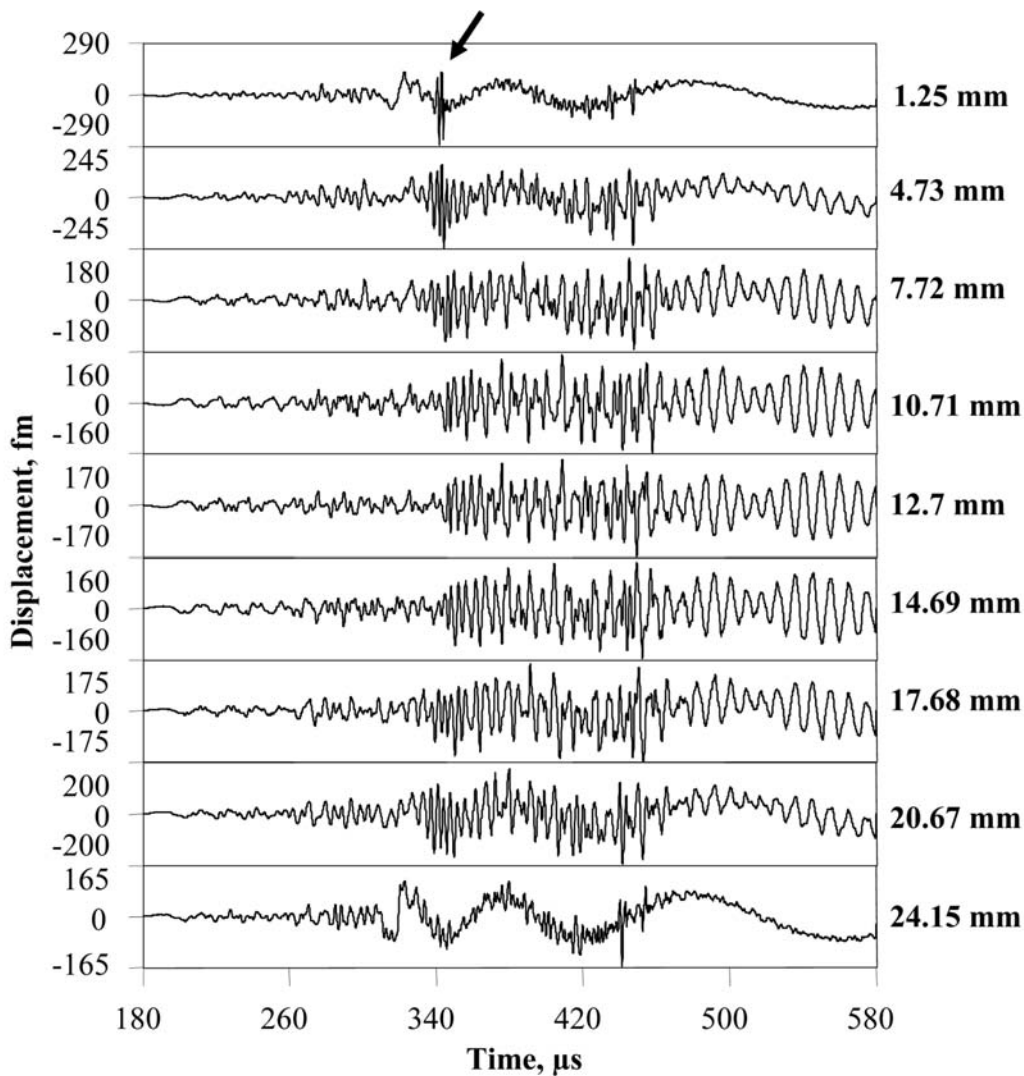


Fig. 8 Out-of-plane displacement vs. time at 1016 mm, out-of-plane source at depths shown below the top surface (location of pseudo-sensor), no filter.

Fifth, sources near the midplane of the plate had a WT maximum at about 100 kHz for the S_0 mode, as can be seen in the WT Figs. 11, 12 and 13 at the source depths of 4.73 mm through 20.63 mm (see dashed arrows). The relative intensity of this region becomes more dominant at source depths nearer the plate midplane. Since a WT maximum in this frequency range occurs for many depths and all three filter ranges, this frequency may be useful for the determination of arrival times. Sixth, for some source depths nearer the midplane, the AE displacement signals and their WTs become more similar for depths symmetric about the midplane of the plate.

The WT results shown in Figs. 11, 12 and 13 were examined to identify potential higher intensity mode and frequency regions that might be used to determine arrival times that could be associated with particular group velocities. Table 2 summarizes this information with the highest intensities listed first for each source depth. The table does not include high intensity regions where the mode could not be clearly distinguished. This situation occurred most often at higher frequencies for some source depths. Since a key goal of this research was to determine key frequencies associated with specific modes that could be used to determine accurate arrival times corresponding to a known group velocity, the next section attempts to identify useful frequency/mode combinations for this purpose.

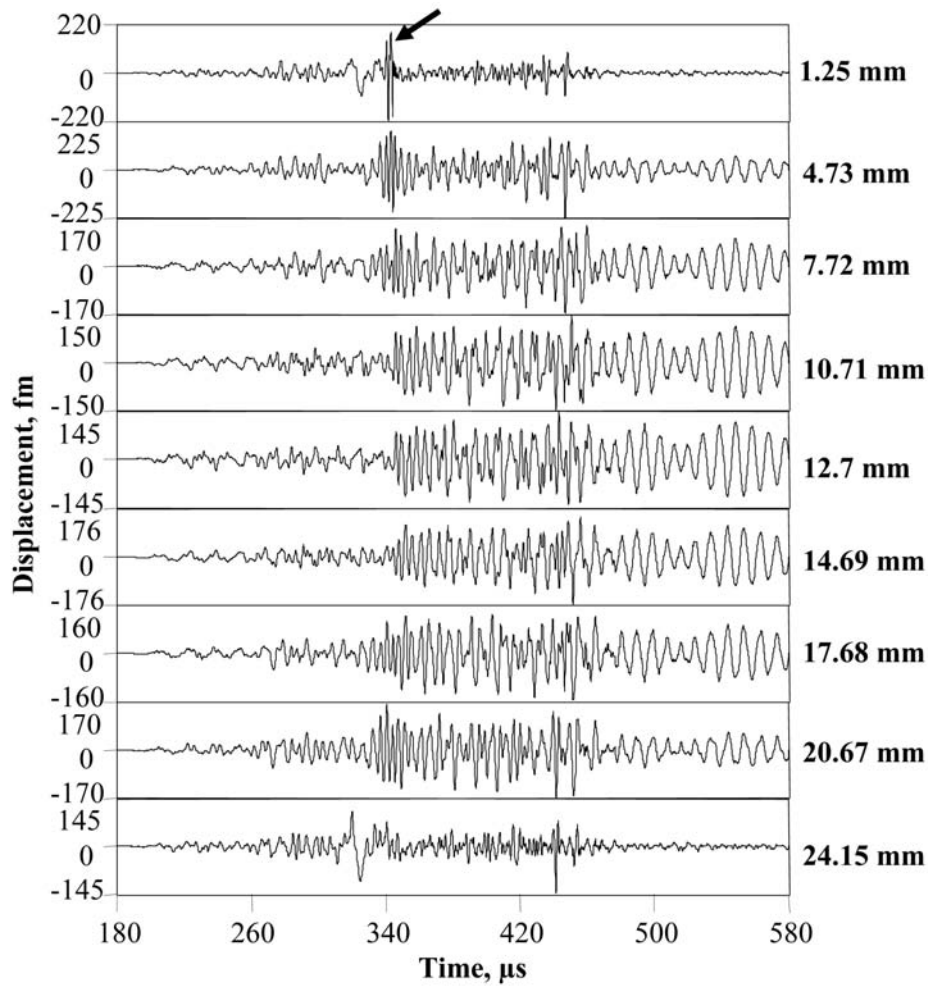


Fig. 9 Out-of-plane displacement vs. time at 1016 mm, out-of-plane source at depths shown below the top surface (location of pseudo-sensor), 40-kHz high-pass filter.

Table 2 Modes and frequency with larger WT magnitudes after 1016 mm of propagation.

Source depth (mm)	Anti-symmetric modes: mode/frequency (kHz)			Symmetric modes: mode/frequency (kHz)		
	No filter	40 kHz high-pass	100 to 300 kHz	No filter	40 kHz high-pass	100 to 300 kHz
1.25	A ₀ /20; A ₀ /420	A ₀ /420; A ₀ /52	A ₀ /318; A ₀ /352	—	—	—
4.73	A ₀ /374; A ₀ /14	A ₀ /374	A ₁ /192	S ₀ /102	S ₀ /102	S ₀ /102
7.72	A ₁ /186	A ₁ /186	A ₁ /186	S ₀ /102	S ₀ /102	S ₀ /102
10.71	—	—	—	S ₀ /102	S ₀ /102	S ₀ /102
12.7 mid-plane	—	—	—	S ₀ /102; S ₁ /276	S ₀ /102; S ₁ /276	S ₀ /102; S ₁ /272
14.69	—	—	—	S ₀ /102	S ₀ /102	S ₀ /102
17.68	A ₁ /182	A ₁ /182	A ₁ /184	S ₀ /102	S ₀ /102	S ₀ /102
20.67	A ₀ /278	A ₀ /186; A ₁ /278	A ₀ /266; A ₁ /186	S ₀ /102	S ₀ /102; S ₀ /268	S ₀ /102; S ₀ /256
24.15	A ₀ /20	A ₀ /54	A ₀ /138	—	—	—

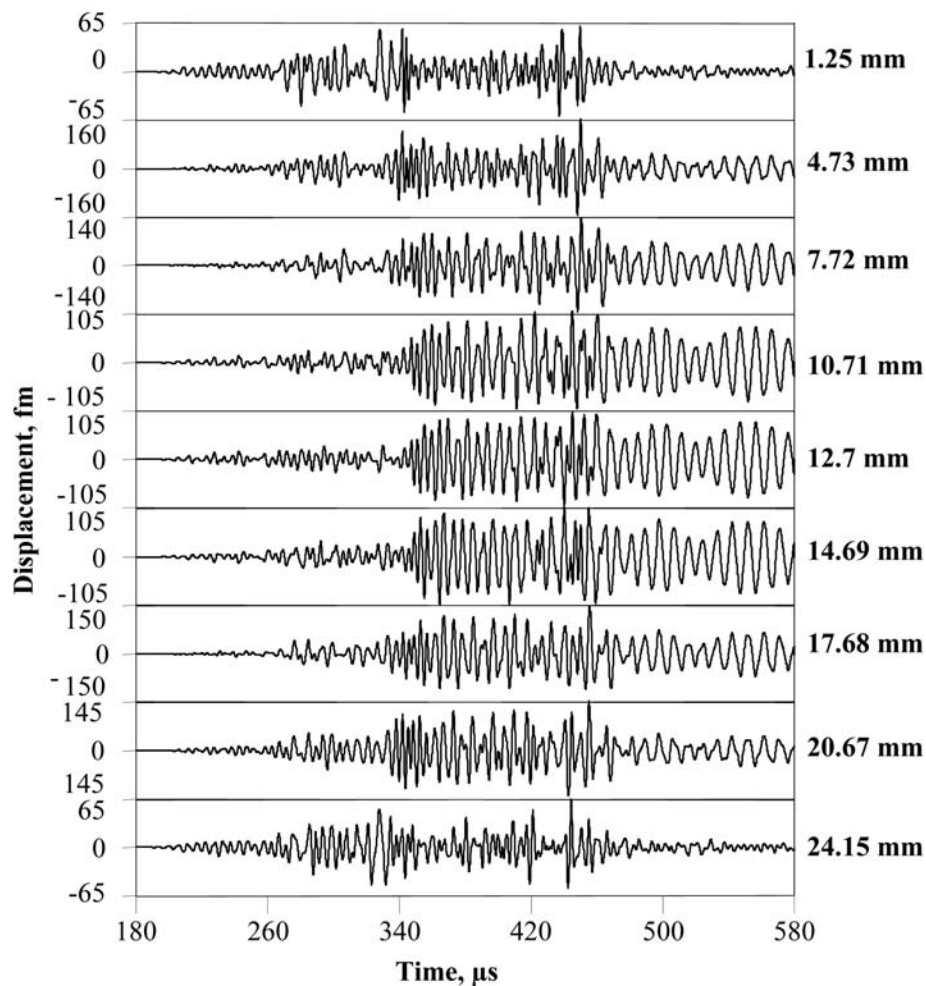


Fig. 10 Out-of-plane displacement vs. time at 1016 mm, out-of-plane source at depths shown below the top surface (location of pseudo-sensor), 100 to 300 kHz filter.

Useful Frequency/Mode Combinations to Determine Arrival /Times

Examination of the information in Table 2 demonstrates that the highest intensity (largest WT coefficients) mode/frequency combinations change as a function of source depth. There are four conditions that might be used to guide the selection of frequency/mode combinations that could be most useful to determine arrival times. First is the selection of frequencies that would be applicable for all three frequency ranges considered here. Second, frequency/mode combinations that cover a wide range of source depths for each combination are desirable. Third, the mode corresponding to each of the selected frequencies should be separated from any alternate mode(s) with intensity at these frequencies by a considerable amount of propagation time (or equivalently have group velocities that are significantly different). Finally, as is obvious, the WT maximum(s) at the frequencies selected should correspond to the mode arrivals.

To best meet the conditions listed above, the frequency selected was 102 kHz. This frequency can be associated only with the A_0 , A_1 or the S_0 modes, and it is possible to use this choice for all three of the frequency ranges. Further, as will be seen below, the A_1 mode did not provide a peak of the WT coefficients at this frequency, and the group velocities associated with the A_0 and S_0 mode peaks are very different at 102 kHz. It should be noted that the combination of $A_0/102$ kHz is not among the most intense modal regions at the 1.25 mm and 24.15 mm

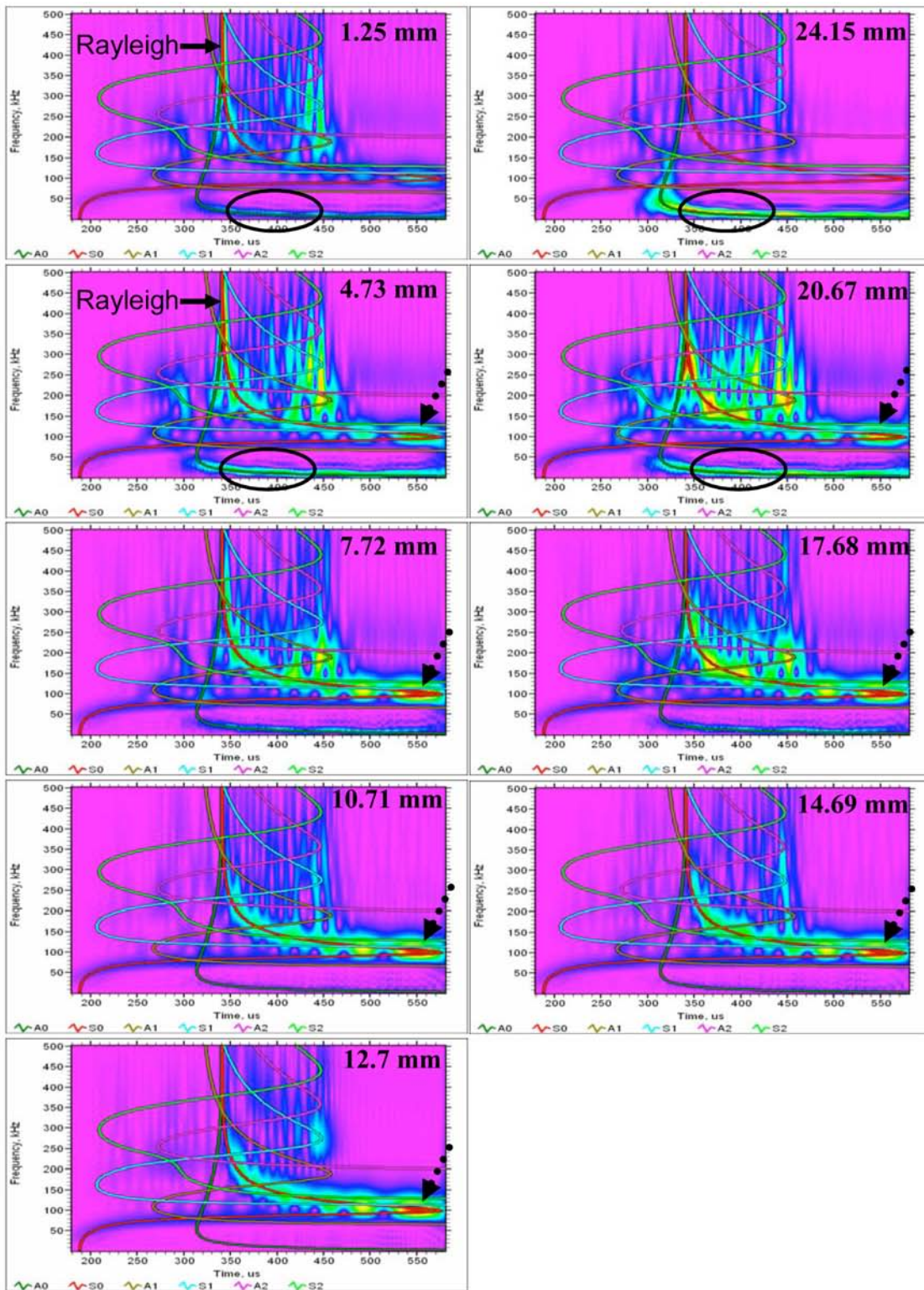


Fig. 11 WTs of Fig. 8 with superimposed group velocities, at indicated depths, 180 μ s to 570 μ s horizontal scale, 0 kHz to 500 kHz vertical scale.

depths. But, since earlier work [3] demonstrated that accurate arrival times could be determined at low signal-to-noise ratios, the lower intensity of this combination at these depths is not expected to be detrimental to its use.

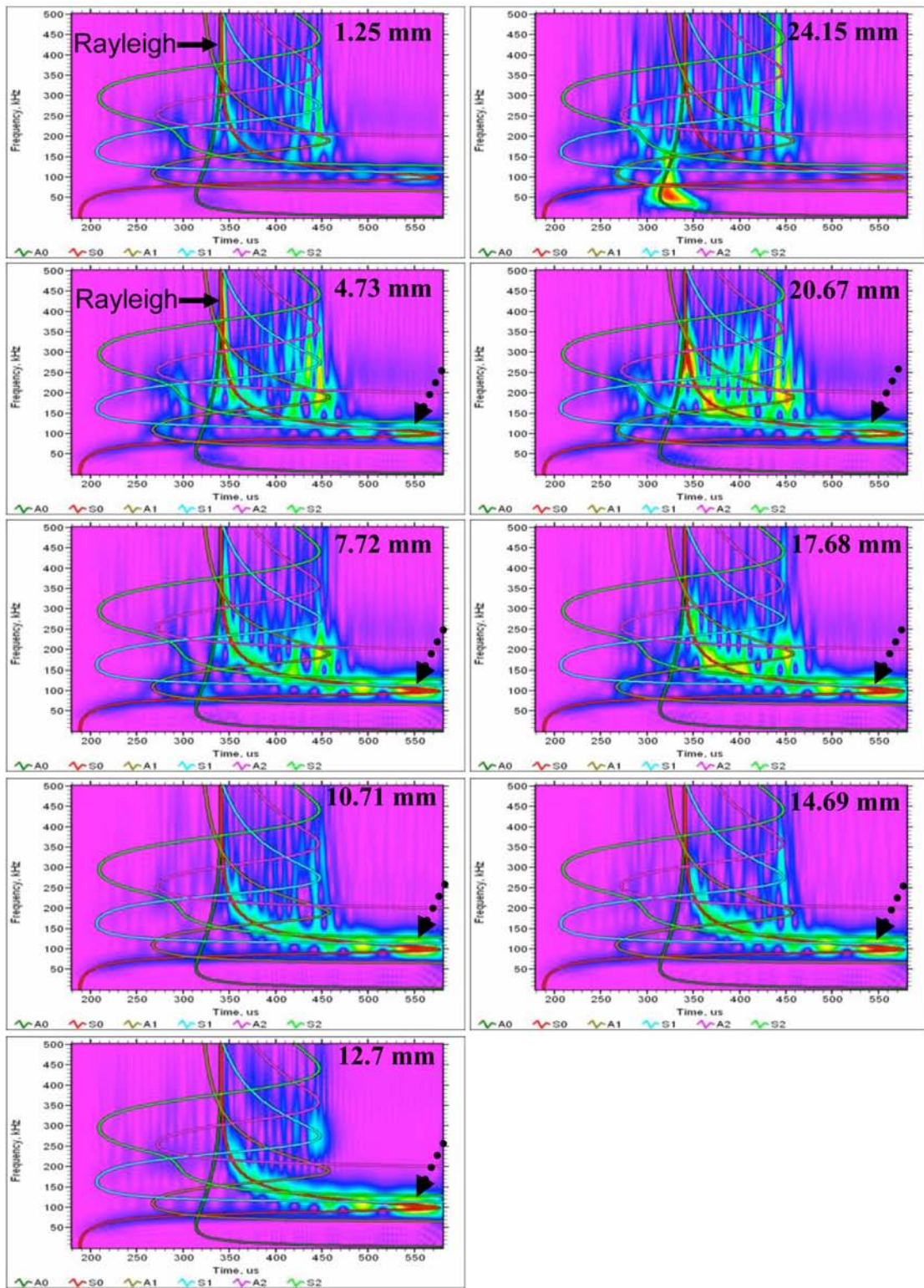


Fig. 12 WTs of Fig. 9 with superimposed group velocities, at indicated depths, 40-kHz high-pass, 180 μ s to 570 μ s horizontal scale, 0 kHz to 500 kHz vertical scale.

For all the source depths and propagation distances the arrival times, Table 3 provides the mode and the WT peak magnitude percentage (relative to the signal overall peak WT magnitude) at a frequency of 102 kHz for the 40 kHz high-pass data. Figure 14 shows (from top to bottom) a

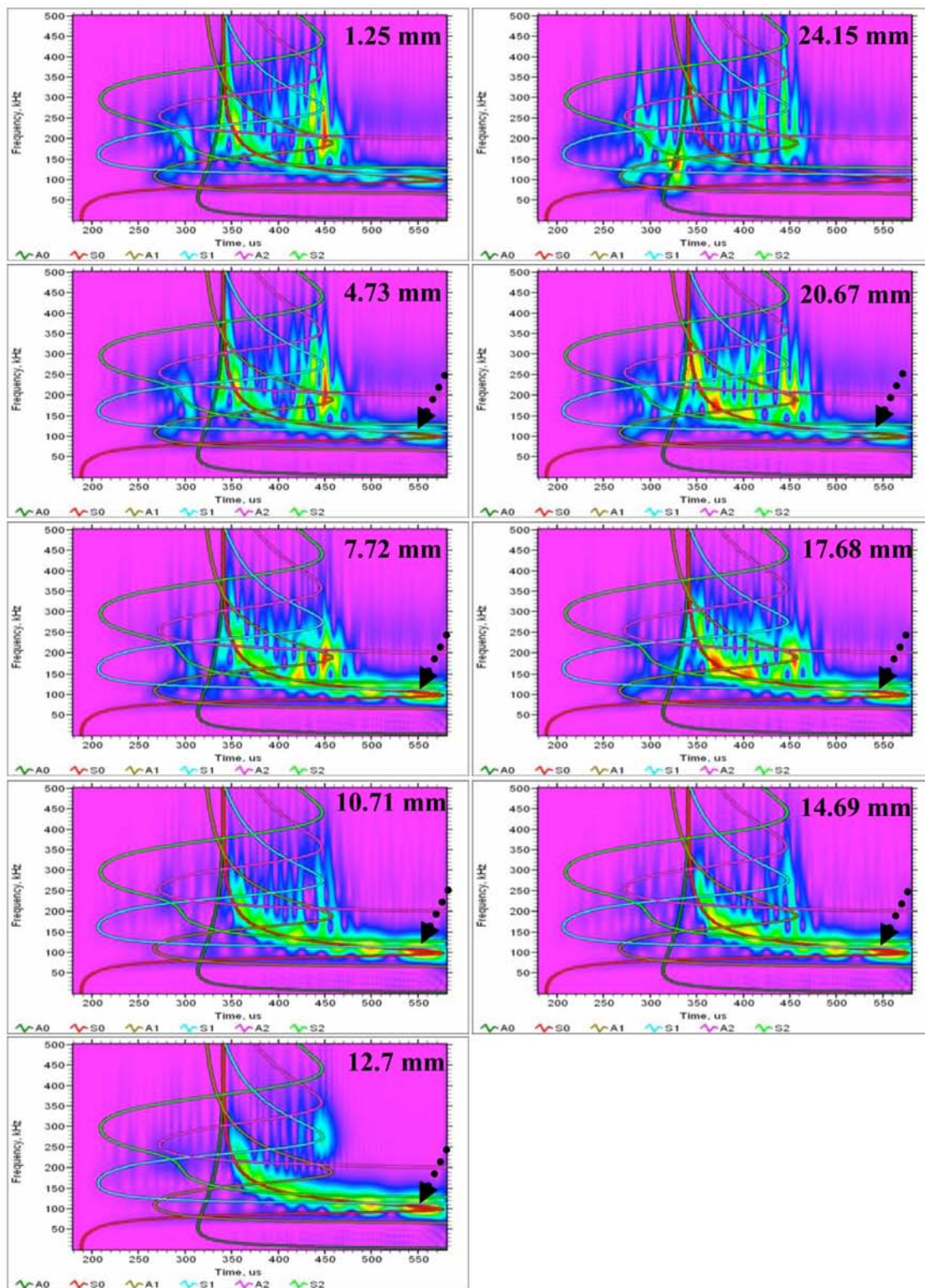


Fig. 13 WTs of Fig. 10 with superimposed group velocities, at indicated depths, 100 kHz to 300 kHz, 180 μ s to 570 μ s horizontal scale, 0 kHz to 500 kHz vertical scale.

typical AE displacement signal, a plot of the WT coefficients at 102 kHz versus time that lead to the maximum and associated arrival time (in this case from the S_0 mode), and the corresponding WT. The data in this figure are from a source depth of 7.72 mm and a propagation distance of

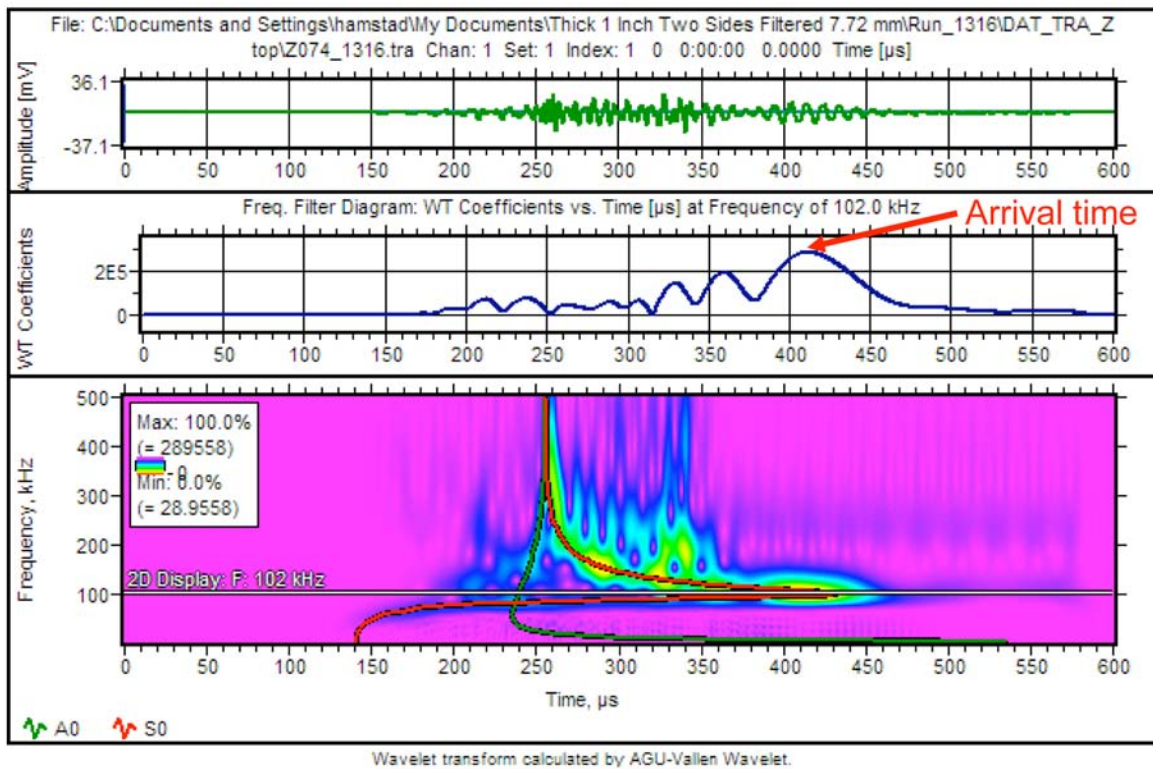


Fig. 14 Example from top to bottom of the signal, plot of the WT coefficients that lead to the peak arrival time (see arrow) at 102 kHz and the wavelet transform with group velocity curves at a propagation distance of 762 mm and a source depth of 7.72 mm.

762 mm. In addition, Table 3 lists the group velocities as directly determined from the slope of a plot of propagation distance versus the arrival times in the table. Finally, these group velocities can be compared in the table to the velocities (last column) determined from the group velocity curves (theory) for the relevant modes. The results in Table 3 show that group velocities very close to the theoretical values can be determined for the only two modes, A_0 and S_0 that produced the peak in the WT magnitude at 102 kHz. Results similar to those in Table 3 were obtained for the other two frequency ranges. The group velocity results for these two frequency ranges are summarized in Table 4 along with the “theory” velocities from the group velocity curves. The results show that the plots of propagation distance versus the arrival times again provide group velocities close to the theoretical values for these two frequency ranges. The maximum difference from the group velocity as determined by the group velocity curves and that from the slope of plots of distance versus arrival time was less than 3% for all three frequency ranges. These results imply that arrival times determined by the peak of the WT at 102 kHz accurately correspond to the relevant mode arrivals.

Of special interest was the fact that the data points for 127-mm propagation distance arrival time fit directly on the linear line that defined the group velocity obtained from the FEM data. Figures 15 (a) and (b) show typical plots (no filter data) for the propagation distance versus the arrival time for both the relevant mode cases, and they include the straight-line least-squares fit. It is worth noting that, at the 127-mm propagation distance, the ratio of distance over the plate thickness is only 5. It often has been assumed that a ratio of at least 10 could be required to fully develop Lamb waves [14].

Table 3 At 102 kHz, WT peak arrival times (μs), mode and percentage of peak WT magnitude for 40 kHz high-pass data.

Source depth (mm)	Propagation distance (mm)							Group velocity (mm/ μs) from slope	Group velocity (mm/ μs) from theory
	127	254	381	508	635	762	1016		
1.25	41.9, A ₀ , 81	78.5, A ₀ , 98	123., A ₀ , 42	162.5, A ₀ , 55	200.8, A ₀ , 52	243.2, A ₀ , 55	321.3, A ₀ , 48	3.16	3.18
4.73	64.7, S ₀ , 54	131.2, S ₀ , 74	198.9, S ₀ , 55	269.2, S ₀ , 88	339.6, S ₀ , 68	410.2, S ₀ , 61	549.3, S ₀ , 65	1.83	1.78
7.72	64.7, S ₀ , 95	131.0, S ₀ , 97	198.8, S ₀ ,100	269.9, S ₀ , 96	341.4, S ₀ ,100	411.2, S ₀ ,100	549.5, S ₀ ,100	1.83	1.78
10.71	64.7, S ₀ , 95	130.9, S ₀ , 99	198.8, S ₀ ,100	270.2, S ₀ ,100	342.2, S ₀ ,100	411.7, S ₀ ,100	548.8, S ₀ ,100	1.83	1.78
12.7	64.7, S ₀ , 95	130.9, S ₀ , 99	198.8, S ₀ ,100	270.2, S ₀ ,100	342.4, S ₀ ,100	411.8, S ₀ ,100	548.7, S ₀ ,100	1.83	1.78
14.69	64.7, S ₀ , 95	130.9, S ₀ , 99	198.9, S ₀ ,100	270.1, S ₀ ,100	342.3, S ₀ ,100	411.7, S ₀ ,100	548.8, S ₀ ,100	1.83	1.78
17.68	64.8, S ₀ , 81	130.9, S ₀ ,100	199.0, S ₀ , 87	269.6, S ₀ ,100	341.6, S ₀ ,100	411.1, S ₀ ,100	548.9, S ₀ ,100	1.83	1.78
20.67	65.0, S ₀ , 57	131.2, S ₀ , 63	199.1, S ₀ , 62	268.8, S ₀ , 60	340.1, S ₀ , 60	409.9, S ₀ , 67	549.5, S ₀ , 76	1.83	1.78
24.15	37.5, A ₀ , 50	81.6, A ₀ , 67	122.3, A ₀ , 76	163.6, A ₀ , 59	203.2, A ₀ , 80	242.8, A ₀ , 74	323.1, A ₀ , 76	3.13	3.18

Table 4 Summary of slope-determined group velocity results for no-filter and 100 kHz to 300 kHz data.

Source depth (mm) and mode of WT peak at 102 kHz	Group velocity (mm/ μs) from slope for no-filter data	Group velocity (mm/ μs) from slope for 100 kHz to 300 kHz filter data	Group velocity (mm/ μs) from group velocity curves ("theory")
1.25, A ₀	3.16	3.15	3.18
4.73, S ₀	1.83	1.83	1.78
7.72, S ₀	1.83	1.83	1.78
10.71, S ₀	1.83	1.83	1.78
12.7, S ₀	1.83	1.83	1.78
14.69, S ₀	1.83	1.83	1.78
17.68, S ₀	1.83	1.83	1.78
20.67, S ₀	1.83	1.83	1.78
24.15, A ₀	3.13	3.10	3.18

Further, Fig. 16 shows the wide variation in the signal durations for the different propagation distances. The primary part of the signals varied in duration from about 50 μs to about 400 μs as the propagation distance increased from 127 mm to 1016 mm. Further, over this range of distances The primary part of the signals varied in duration from about 50 μs to about 400 μs as the

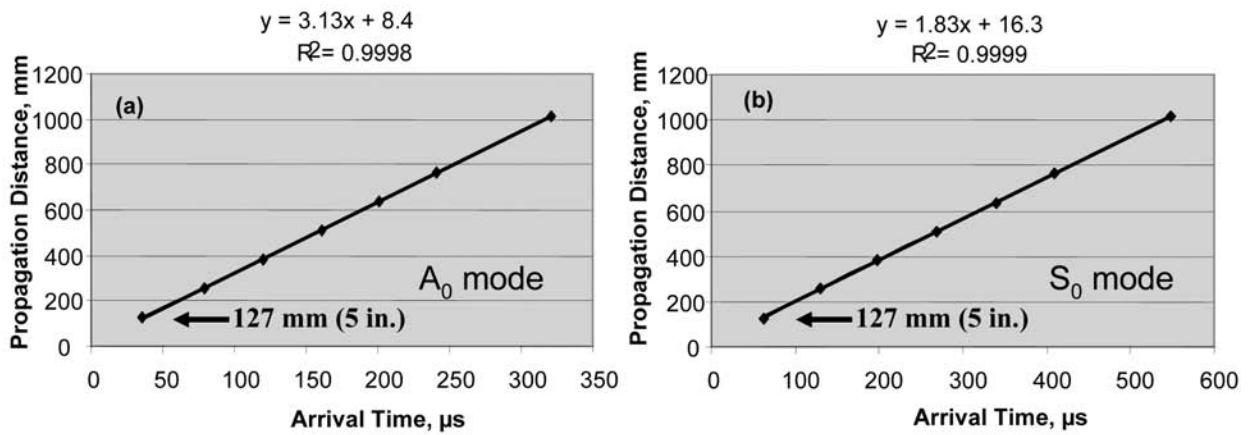


Fig. 15 Plot of propagation distance versus arrival time determined by WT maximum at 102 kHz; no filter data for an out-of-plane source depth of (a) 24.15 mm and A_0 mode and (b) 7.72 mm and S_0 mode; and equation of “fit” with correlation coefficient.

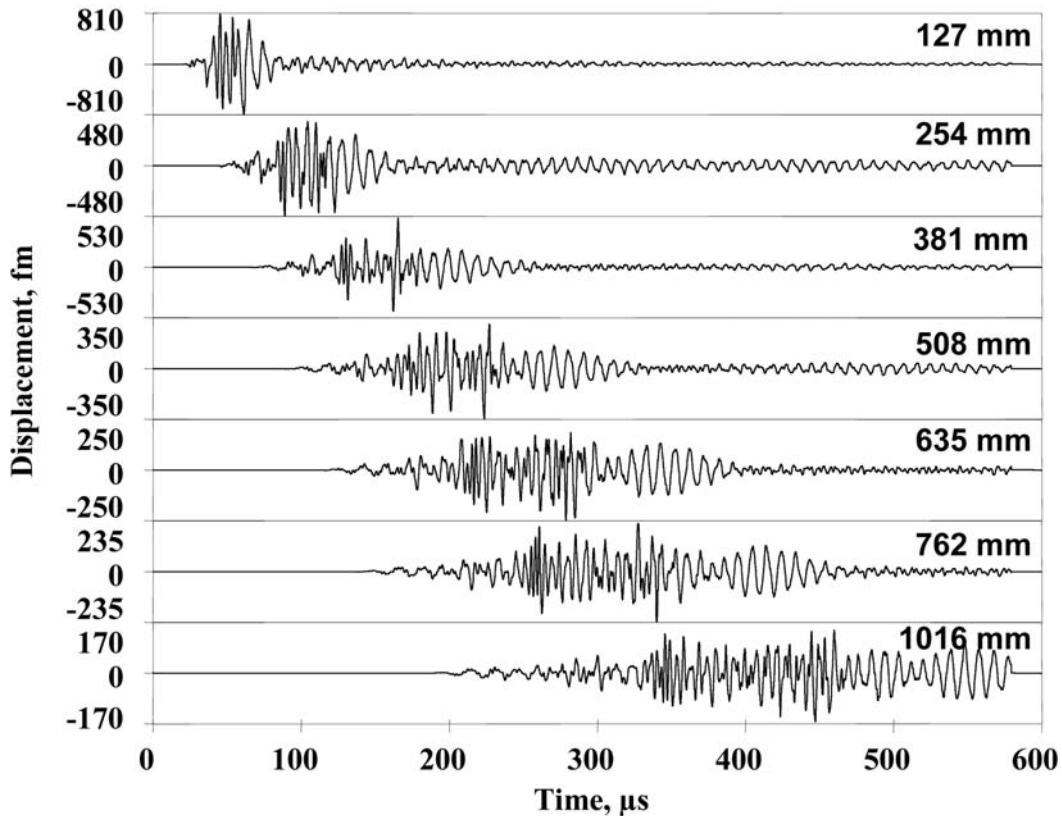


Fig. 16 Dispersion of AE signals at propagation distances shown for source depth of 7.72 mm; 40-kHz high-pass data.

propagation distance increased from 127 mm to 1016 mm. Further, over this range of distances the signal peak amplitudes decreased by 12 dB to 19 dB from the first distance to the last for the different depths and filter ranges. These large changes in durations and signal peak amplitudes did not affect the determination of accurate mode arrival times.

Two additional frequencies were examined (190 kHz and 50 kHz). In both cases, the mode that led to the WT peak magnitude was not constant at all the propagation distances for some source depths. Thus these frequencies were not pursued in detail.

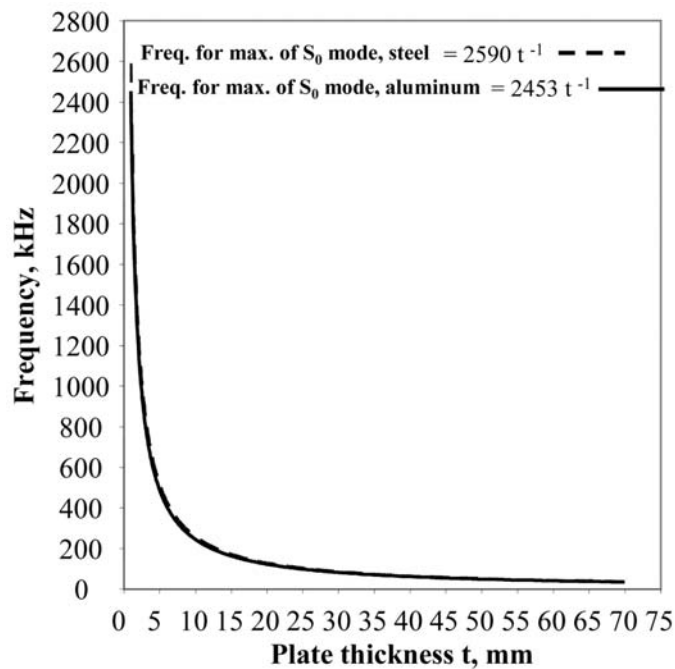


Fig. 17 Frequency of maximum WT intensity of the S_0 mode as a function of plate thickness for aluminum and steel plates.

Since the region of the S_0 group velocity curve that gave rise to the WT peak at 102 kHz is the same region that provided accurate arrival times for this mode at 522 kHz in the 4.7-mm thick aluminum plate [1], Fig. 17 was created to show how this frequency changes with plate thickness for both steel and aluminum. Potentially this figure could be used to select appropriate frequencies for plates of steel or aluminum of other thicknesses. These frequencies could be used to determine accurate arrival times for the S_0 mode (and at depths near a plate surface the A_0 mode, as demonstrated in this paper) by a WT or other equivalent approaches.

Application to Source Location and Related Mode Identification of the Single Frequency (102 kHz) Determined Arrival Times

Because in an actual experimental AE application the source depth for each AE event is unknown, a WT peak-determined arrival time at 102 kHz could be associated with either the A_0 or the S_0 mode (Note as pointed out before, no WT peaks at 102 kHz were observed with the other possible mode, A_1). Thus, we examined a possible approach that would allow determination of the mode that resulted in the WT-determined peak arrival time for a particular experimental AE event. It was assumed that the signals from the event were recorded at four different sensors in a location array. Using the available different propagation distances, a series of cases was examined with different placements of the sensors around a fixed source location. Figure 18 shows a particular case of the arrangement of the sensors around a source location (indicated by **X** in the figure). The arrival time information in Table 3 (40-kHz high-pass data) was used to calculate relative arrival times for the appropriate propagation distances. For each sensor array case, the arrival times selected corresponded to those for two different source depths that provided data for the two possible modes (A_0 and S_0). Planar source location software [15] was used to calculate the location by using each of the two possible group velocities (those found from the slope plots referred to earlier). Thus, for each case, a total of four locations were calculated with the 102 kHz data. These calculations were: (i) A_0 mode arrival times and A_0 mode velocity, (ii) A_0 mode arrival times and S_0 mode velocity, (iii) S_0 mode arrival times and A_0 mode velocity, and (iv) S_0

mode arrival times and S_0 mode velocity. From the results for each location calculation, the radius error from the actual known location to the calculated one was determined. It was found that the mode velocity that gave the least radius error corresponded to the known actual mode that corresponded to the set of WT peak determined arrival times for that mode.

Table 5 Sensor coordinates, arrival times, radius errors and uncertainty (“Lucy”)*.

Case no.	Array of sensor coordinates x/y (mm)				Relative arrival times at each sensor for the modes, A_0/S_0 (μ s)				Radius error at specified mode velocity (mm)		“Lucy” values at specified mode velocity (mm)	
	#1	#2	#3	#4	#1	#2	#3	#4	A_0	S_0	A_0	S_0
1	1410	1011.1	1697	906.8	0	44.5	122.3	164.7	9.62 ^{\$}	115 [#]	2.2	17.6
	1356.4	1204.8	1942.3	2219	0	67.7	208.4	279	241 ^{\$\$}	2 ^{##}	15	1.6
2	1117.6	1327.7	1443.7	737.4	0	36.6	158.9	201.3	8.65	145	0.30	55.3
	1447.7	1294.4	2118	2114.5	0	66.5	274.9	345.5	—	4.2	—	1.01
3	1121.9	1326.1	1595	886.6	0	36.6	81.1	120.6	4.6	105	5.4	33.6
	1442.4	1293.6	1586.9	1908	0	66.5	134.2	204.5	166	5.6	103	1.5
4	1190.6	1385.2	719.4	2234.1	0	36.6	120.6	279.4	5.2	190	1.7	152
	1647.7	1331.7	1433.2	1570.1	0	66.5	204.5	484.6	—	4.9	—	0.83
5	1436.6	1092.9	1840.3	586.7	0	39.5	77.8	198.3	5.8	143	2.2	20.4
	1211.1	1032	1656	2319.1	0	70.3	140.7	350.4	234	3.1	8.9	0.78
6	1175.6	1144.1	1585.4	1585.9	0	36.6	81.1	120.6	7.1	90	2.7	41.7
	1643.3	1281.4	1419	1875.6	0	66.5	134.2	204.5	—	5.6	—	0.93
7	1306.3	609.1	1759	823.8	0	158.9	201.3	279.4	4.7	178	0.7	181
	1616.4	1347.9	986.1	2459.9	0	274.9	345.5	484.6	—	3.2	—	0.73
8	1117.1	1467.1	913.3	1622.7	0	44.5	122.3	242.8	8	232	0.3	145
	1756.6	1234.8	967.5	2456.4	0	67.7	208.4	418.1	—	0.9	—	1.9
9	1444.1	1070.7	623.6	1983.7	0	84	122.3	242.8	5.2	210	4.7	95.4
	1405.9	1038.2	1744.3	2193.2	0	138	208.4	418.1	68.3	2	326	0.2
10	1085	937.4	1702.6	1839.9	0	44.5	84	122.3	9.1	73	0.55	31.1
	1739.6	1267.6	1367.9	1658.2	0	67.7	138	208.4	142	2.2	49.4	0.22

* Actual source coordinates for all cases $x = 1219.2$ mm and $y = 1524.0$ mm

— ... No result

^{\$} With velocity 3160 m/s for A_0 mode and arrival times for A_0 mode

^{\$\$} With velocity 3160 m/s for A_0 mode and arrival times for S_0 mode

^{##} With velocity 1828 m/s for S_0 mode and arrival times for S_0 mode

[#] With velocity 1828 m/s for S_0 mode and arrival times for A_0 mode

Table 5 provides a summary from a series of ten cases. The table shows the coordinates of the four sensors in each array along with the relative arrival times for each mode. The table also shows the radius errors for each of the two possible group velocities. Due to the nature of the database used for these calculations, the source location ($x = 1219.2$ mm, $y = 1524$ mm) was always the same for each case.

The results summarized in Table 5 indicate that accurate source locations (smaller radius of location errors, bold values) were consistent with the correct choice of the mode and associated group velocity. In some cases in this table, when the incorrect group velocity was used, the

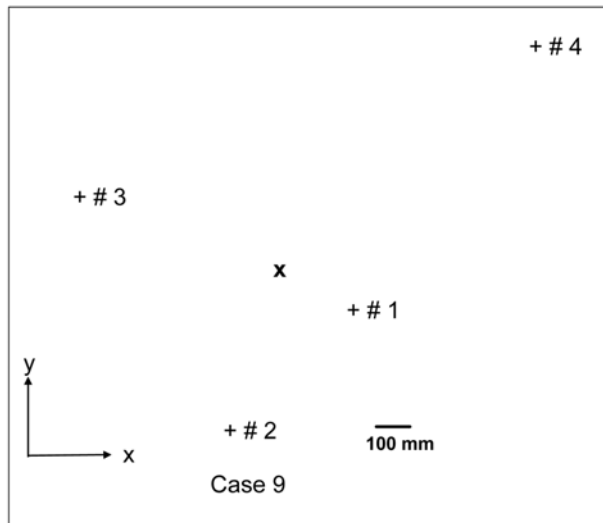


Fig. 18 Arrangement of sensors (#1, #2, #3, #4) around source location X ($x = 1219.2$ mm, $y = 1524$ mm). Scale shown as well as the directions of the x and y axis (origin not shown).

source-location software did not generate a result. Examination of the input data for those cases showed that the equation of the hyperbola that should locate the locus of possible locations of the source between each two-sensor set had a negative sign for the distance from the closest sensor to the hyperbola. This situation typically occurred when the higher A_0 -mode velocity was used with the slower velocity S_0 -mode arrival times. In addition, significant errors in the calculated source locations were the result of the use of the wrong mode and its associated group velocity. These facts indicated that a measurement of the “uncertainty” level of the iterative source location calculation might be used to determine the correct mode and associated velocity for a particular set of arrival times from an experimental source at an unknown depth. The source-location software [15] automatically provided an “uncertainty” value for each location calculation. Table 5 also shows this “uncertainty” parameter (called “Lucy” [for location uncertainty] by the software developer) for the two possible group velocities in each case. According to the software designer [15] “Lucy describes how well a calculated source position fits with the measured arrival time differences.” The value for “Lucy” is calculated from

$$\text{Lucy} = \left\{ \frac{1}{[n-1]} * [\sum (D_i - P_i)^2] \right\}^{1/2}. \quad (2)$$

In this equation, the sum is from $i = 2$ to n , where n is the number of sensors hit by the signals from each source event. The values of D_i are calculated from

$$D_i = dt_i * v, \quad (3)$$

where dt_i is the signal arrival time difference relative to the first hit sensor ($n = 1$), and v is the group velocity. The values of P_i are calculated from

$$P_i = R_i - R_1, \quad (4)$$

where R_i is the distance from the calculated source location to each of the sensors. “Lucy” can be determined as part of the result of a location calculation only if an event consists of at least one more hit than the minimum required to determine a location (in the cases considered here, three hits are the minimum for planar location). Clearly the table shows the “Lucy” value is the smallest (bold values) for the velocity that resulted in the least radius error. Thus, either the smallest “Lucy” value (directly identifies the correct mode) or no result (identifies the alternate mode velocity is correct) for the location calculation identified the correct mode and associated group velocity for the wide variety of sensor arrays examined.

Results equivalent to those in Table 5 were obtained for the other two frequency ranges (no filter and 100 kHz to 300 kHz). These results (not included in this paper) were similar to those shown in Table 5, and the conclusions relative to the relation between the smallest “Lucy” values, smallest radius error and correct group velocity were similar. In addition for all three frequency ranges, the average radius errors for the slower velocity mode were only about one half the average radius errors for the faster velocity mode. For example, the average radius errors respectively for the slow versus fast velocities were respectively 3.6 mm (standard deviation of ± 1.7 mm) and 7.1 mm (standard deviation of ± 1.7 mm) for the 100-kHz to 300-kHz bandpass data.

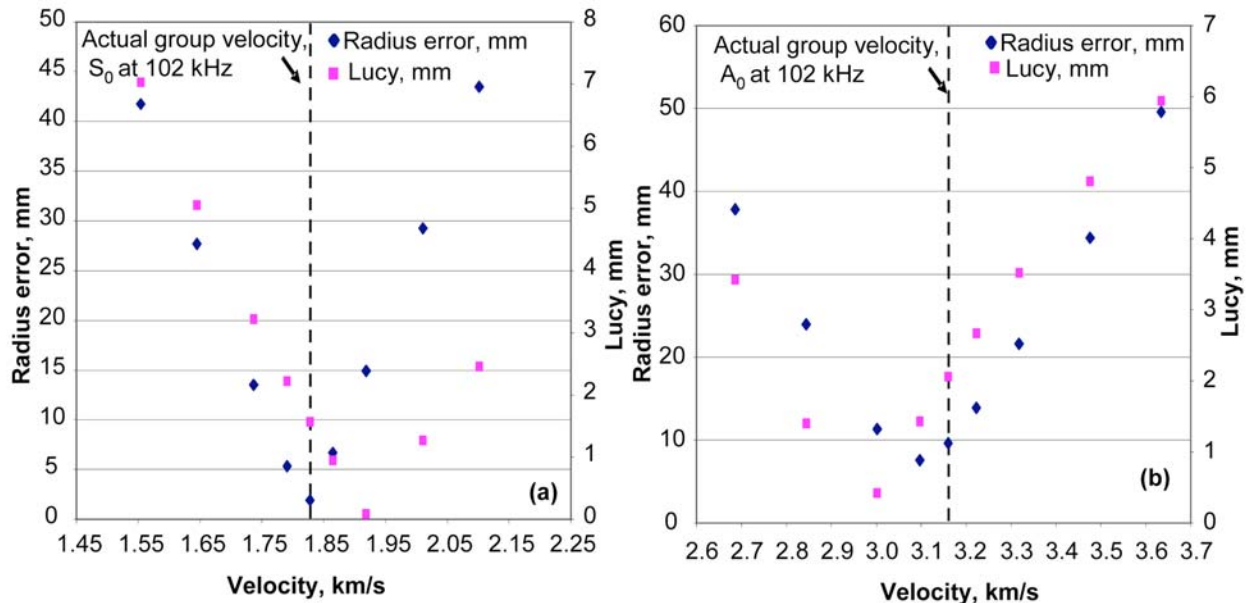


Fig. 19 Radius error and “Lucy” value versus group velocity in the vicinity of the correct velocity. Results for case 1 in table 5 with (a) for the S_0 mode and (b) for the A_0 mode.

The sensitivity to small errors in the velocity used in the approach (described above) to determine the correct mode and group velocity (for a set of arrival time differences) was studied. Calculations of the radius errors and “Lucy” values were made when the velocity was in error relative to the correct value for the mode. The velocity errors examined were $\pm 2\%$, 5% , 10% , and 15% from the correct mode velocities. Figure 19 shows a typical result of how the radius error and the “Lucy” values varied as a function of the group velocity used in the location calculation. Figure 19(a) shows the results for the slow velocity mode (S_0), and Fig. 19(b) shows the results for the fast velocity mode (A_0). These results for case 1 in Table 5 (using the 40 kHz high-pass data) show that the radius error and the “Lucy” values have minima near the correct velocity. It is worth noting that the minima of both parameters are not at exactly the same velocity. The fact that the radius error and “Lucy” values have minimum values near the correct velocity indicates that in experimental situations where there may be small errors in the mode velocities used, the technique proposed here could be expected to continue to result in correct identification of the mode that resulted in the set of arrival times for a particular AE event.

The method described in this section of the paper could be automated in software. Arrival times at an appropriate frequency could be determined by advanced signal processing of the digitized signals from each sensor in a location array for each event. Then location calculations could be made by using the two possible group velocities at the appropriate frequency. The

location calculation result that yielded the lowest “uncertainty” or the calculation that produced a location (no location result for one velocity) could then be selected. Thus the use of nonresonant sensors could improve the accuracy of source location even in thick plates, as has been shown in thin plates [16].

Conclusions

- The wavelet transforms of signals from in-plane and out-of-plane dipoles at the same depth demonstrates mostly similar regions of signal intensity.
- For sources near the top or bottom surface of the thick plate, the most intense portion of the A_0 mode is at frequencies below those normally used in AE monitoring.
- For sources near a surface, the signal from a sensor on that surface exhibits a Rayleigh wave at frequencies above about 340 kHz
- The signals from the 25.4-mm thick plate have multiple intense regions (combinations of mode and frequency) as the depth of the source varies.
- The choice of a frequency of 102 kHz provides wavelet transform peak determined arrival times for mostly the S_0 mode as the depth of the source varies. For sources near a plate surface, the wavelet transform peak at this frequency corresponds to the A_0 mode. No maximum peaks were observed for the A_1 mode at this frequency.
- Over a wide range of propagation distances (127 mm to 1016 mm) and source depths, the wavelet transform peak at 102-kHz frequency provided accurate arrival times, since the slope of plots of the propagation distance versus these arrival times provided group velocities very close to the theoretical values.
- For sources at an unknown depth recorded with at least a four-sensor array, the calculation of the planar location of the source from the WT peak arrival times at 102 kHz using the two possible group velocities yields two different locations or in some cases only a location with one of the two group velocities. The lowest value of the “uncertainty” or the only velocity that produced a location result from the two source location calculations corresponds to the correct location and the correct mode (and associated group velocity) of the arrival times.
- This method for the determination of the correct mode of the arrival times and associated group velocity could be automated to process digitized signals to significantly improve accuracy of source location even in thick plates when non-resonant AE sensors are used.
- This method is not dependent on the use of exactly the correct group velocity for the two modes at 102 kHz.

Acknowledgements

The development of the finite element code and case runs by Dr. John Gary (NIST retired) are acknowledged. Filtering of the FEM results by Ms. Abbie O’Gallagher, NIST Boulder, CO is appreciated. Also the analysis efforts of Mr. Matthew Papa (University of Denver, Mechanical Engineering undergraduate) are appreciated. Finally, the private communications listed in the references are highly appreciated.

Copyright Notice

This paper is a contribution of the U.S. National Institute of Standards and Technology; not subject to copyright in the United States. Trade and company names are included only for complete scientific/technical description; endorsement is neither intended nor implied.

References

1. Hamstad, M.A., K.S. Downs and A. O’Gallagher, “Practical aspects of acoustic emission source location by a wavelet transform,” *J. of Acoustic Emission*, **21** (2003), 70-94 and A1-A7.
2. Downs, K.S., M.A. Hamstad and A. O’Gallagher, “Wavelet transform signal processing to distinguish different acoustic emission sources,” *J. of Acoustic Emission*, **21** (2003), 52-69.
3. Hamstad, M.A. and A. O’Gallagher, “Effects of noise on Lamb-mode acoustic-emission arrival times determined by wavelet transform,” *J. of Acoustic Emission*, **23** (2005), 1- 24.
4. Hamstad, M.A. and A. O’Gallagher, “Modal-based identification of acoustic emission sources in the presence of electronic noise,” *J. of Acoustic Emission*, **22** (2004), 1-21, A1-A7.
5. Bayray, Mulu and Franz Rauscheer, "Wavelet transformation analysis for experimental AE waveforms on steel pressure vessel," *J. of Acoustic Emission*, **22** (2006), 22-43.
6. Hamstad, M. A., J. Gary and A. O’Gallagher, "Far-field acoustic emission waves by three-dimensional finite element modeling of pencil breaks on a thick plate," *J. of Acoustic Emission*, **14**(2) (1996), 103-114.
7. Hamstad, M.A., A. O’Gallagher and J. Gary, "Modeling of buried acoustic emission monopole and dipole sources with a finite element technique," *J. of Acoustic Emission*, **17**(3-4), (1999), 97-110.
8. Burridge, R. and L. Knopoff, “Body force equivalents for seismic dislocations,” *Bulletin Seismic Society of America*, **54** (1964), 1875-1914.
9. Kolsky, H., “*Stress Waves in Solids*,” Dover Publications, New York (1963).
10. Vallen, J., AGU-Vallen Wavelet transform software, version R2007.0309, Vallen-Systeme GmbH, Icking, Germany (2007). Available at <http://www.vallen.de/wavelet/index.html>
11. Cho, Hideo, Private communication, Aoyama Gakuin University, Sagamihara, Japan (2006).
12. Vallen, Jochen and Gabriel Corneanu, Private communication, Vallen-Systeme GmbH, Icking, Germany (2006).
13. Hamstad, M.A., A. O’Gallagher and J. Gary, "Examination of the Application of a Wavelet Transform to Acoustic Emission Signals: Part 1. Source Identification," *J. of Acoustic Emission*, **20** (2002), 39-61.
14. Sachse, Wolfgang and Yih-Hsing Pao, “Signals in the far-field of an AE source,” *Ultrasonics International 1981: Conference Proceedings*, IPC Science and Technology Press, Guildford, Surrey, UK, 1981, pp. 116-122.
15. Vallen, Jochen, Private communication, Vallen-Systeme GmbH, Icking, Germany (2001).
16. Ziola, Steven M., "Source location in thin plates using crosscorrelation," Ph.D. Thesis, Naval Postgraduate School, Monterey, CA., (1991).

NOVEL ACOUSTIC EMISSION SOURCE LOCATION

**RHYS PULLIN, MATTHEW BAXTER, MARK EATON, KAREN HOLFORD
and SAM EVANS**

Cardiff School of Engineering, The Parade, Newport Road, Cardiff, CF24 3AA, UK

Abstract

Source location is the most attractive aspect of acoustic emission (AE) monitoring. Source location relies on the ability of several sensors to detect an AE event and locate the event using simple triangulation methods based on the time of arrival of the fastest propagating wave mode. Two assumptions are made in any source location calculation; the wave speed remains constant and that there is a direct path between sensor and source. This is rarely the case with many structures containing change in thicknesses, resulting in changes in propagation velocity and discontinuities, such as lugs, that alter propagation paths.

A novel technique, Delta-T mapping, that overcomes the problems of thickness changes and discontinuities has been developed. An outline of the novel technique and the results of an artificial source investigation and two fatigue investigations one with a complex propagation path and a further specimen with varying thickness changes are presented. All investigations demonstrated that the Delta-T mapping has a great improvement over the current TOA technique.

Keywords: Source location, composites, aerospace materials, complex geometries.

Introduction

Source location is possibly the most attractive aspect of acoustic emission monitoring. If the location of an event is known, the number of possible source mechanisms is reduced as only certain mechanisms are associated with particular geometric features and conditions. In addition identifying the location of an AE event can allow other non-destructive evaluation (NDE) techniques, such as dye penetrant or ultrasound, to be utilised.

Current source location techniques rely on the ability of several sensors to detect an AE event and locate the event using simple triangulation methods based on time-of-arrival (TOA) of the fastest propagating wave mode [1,2]. However these source location methods are based on two assumptions; that wavespeed remains constant from source to sensor and that there is a direct wavepath between source and sensor.

When considering plate waves, invariably the case in bridges, pipes, pressure vessels and aerospace landing-gear modules, the velocity is dependant on thickness of the plate it is travelling in, demonstrating that wavespeed throughout a structure will rarely be uniform. Furthermore, in composite structures wave velocity varies with the angle of propagation depending on the direction of travel when compared with composite lay-up. In addition geometric features such as holes, lugs and structural discontinuities, often seen in real structures, can dramatically alter the wavepath. Indirect paths may include reflection, refraction, diffraction and paths depending on the geometry of the component again.

These assumptions introduce errors in a source location measurement. In simple cases, these problems can be overcome with expert knowledge, assessment of wavepaths and intelligent sensor locations. However, these are estimations and cannot provide accurate results.

Recent methods aimed at improving the accuracy of the source location technique by alleviating the problems inherent in selection of a single wave velocity include modal analysis, a method based on energy attenuation and acoustic tomography.

Single sensor source location [3,4] relies on the measurement of the time difference between the arrivals of the two primary modes, however it requires a detailed understanding of the dispersive nature of AE signals, which can be open to user interpretation and the arrival of the faster propagating S_0 mode needs to be captured and visible when compared with background noise.

Nivesrangsan et al. [5] have investigated the use of energy attenuation. The methodology follows TOA, location replacing time difference with energy difference and wave velocity with an attenuation coefficient. However, as this method is based on the same principals as TOA source location, similar error sources apply.

A further method based on computerised tomography (CT) that was developed for medical applications has been presented by Schubert [6] and utilised algebraic reconstruction techniques (ART). The method is as follows

- Set-up an array of sensors around an area of interest
- Divided the area into a grid, with each grid square assigned an initial wave velocity.
- Conduct a series of simulated events, either by pulsing each of the sensors or by generating events within the grids.
- Use the known wavepath and elapsed time from source to sensor to re-evaluate the wave velocity assigned to each of the grid squares that the wavepath intersects using algorithms such as ART.
- Repeat the previous step until the wave velocity in each grid space has suitably converged. It is possible to use the wave velocity map to accurately locate and future events.

Any geometric features, such as holes, will cause an altered wave velocity to take account of the change in wavepath. However, in a further paper [7], results using this technique from an aluminium plate with a saw cut were presented. The array used was unable to detect the cut until it intersects at least one of the wavepaths between sensors, a disadvantage of this method.

In this paper, a novel method of source location where an AE location array is mapped with an Hsu-Nielsen (H-N) source at known positions is presented. A more detailed description of the Delta-T technique can be found in [8]; however, a summary of the technique is provided below in five steps:

- *Determine area of interest.* Though Delta-T source location can provide complete coverage of a part or structure, it is best employed as a tool to improve source location around specific areas of expected fracture, which could be identified via finite element modelling.
- *Construct map system.* A grid is placed on the component over the area of interest and within which AE events will be located; the higher the resolution of the grid the greater the accuracy. It is possible to increase the resolution of the grid around features of interest, however it should not be smaller than one wavelength, as this is the minimum loca-

tion resolution. It should be noted that sources are located with reference to the grid and not the sensors.

- *Apply artificial source event to obtain time-of arrival data.* Artificial sources [9,10] conducted at the nodes in the grid provide AE data for each sensor. Several sources at each node are required to provide an average result and to eliminate erroneous data. It is not essential to have AE data from every node in the grid because missing data points can be interpolated from surrounding nodes.
- *Calculate Delta-T Map.* From each artificial source, a difference in time of arrival or Delta-T is calculated for each sensor pair (an array of four sensors has six sensor pairs). The average Delta T for each sensor pair at each node is stored in a map. These maps can be displayed as contour plots of equal Delta-T.
- *Compare Actual Data.* To locate an actual AE event, the Delta-T for each pair is calculated. A line or contour on each map corresponding to the calculated Delta-T can be identified. By overlaying results from each of the sensor pairs, a convergence point can be identified; the source location. As with time of arrival, a minimum of three sensors is required to provide a point location and more sensors will improve the location. In theory all lines will intersect at one location, however, in reality this is not the case. Therefore to estimate the source location, all of the convergence points can be calculated and a cluster analysis can be conducted on the points to determine the final location.

This paper presents three case studies demonstrating the developed novel source detection method.

Experimental Procedure

An artificial source investigation was completed on a 1-m² steel plate with a 250-mm ‘rough cut’ hole in the centre. Eight sensors were mounted on the plate, four in a regular square array and four in a random irregular array (Fig. 1). These two arrays allow comparison between a regular and irregular sensor groups. A 400-mm² grid with a 50-mm grid density centred on the cut-out was used (Fig. 1). Ten artificial sources were conducted at each node within the grid. Ten test locations were randomly selected within the grid and five artificial sources conducted at each location (Table 1).

Table 1: Artificial source coordinates and source location errors.

Location	Source Position [mm]		Delta-T Error [mm]			TOA Error [mm]			Error [%]		
	X	Y	All	Reg	Irreg	All	Reg	Irreg	All	Reg	Irreg
1	20	100	6	8	14	20	385	6	70	98	-133
2	70	230	38	52	24	55	113	62	30	54	61
3	100	300	4	3	5	108	36	16	96	91	68
4	130	90	21	22	25	51	103	63	59	78	60
5	200	330	10	12	25	117	52	530	92	76	95
6	260	90	24	38	70	47	73	103	48	48	32
7	300	300	1	13	23	92	120	217	99	89	89
8	320	160	35	53	24	44	42	33	20	-26	29
9	350	50	31	26	38	69	74	108	56	65	65
10	330	390	5	2	14	4	72	n/a	-7	97	n/a
Average	n/a	n/a	18	24	28	62	107	129	71	77	78

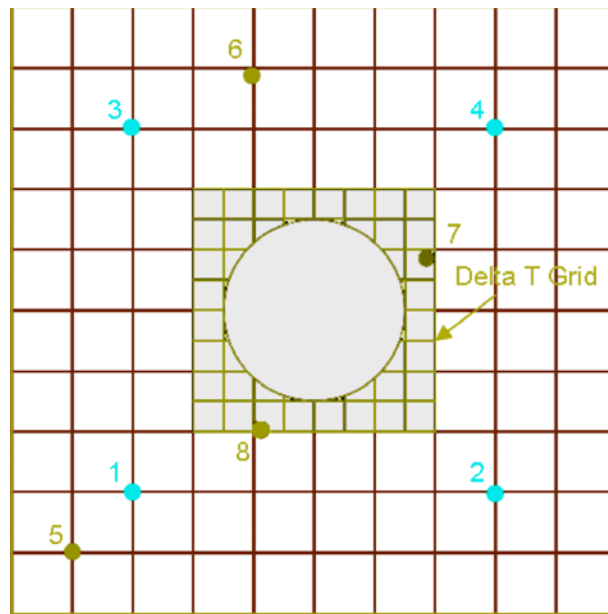


Fig. 1. Artificial source investigation showing regular and irregular array.

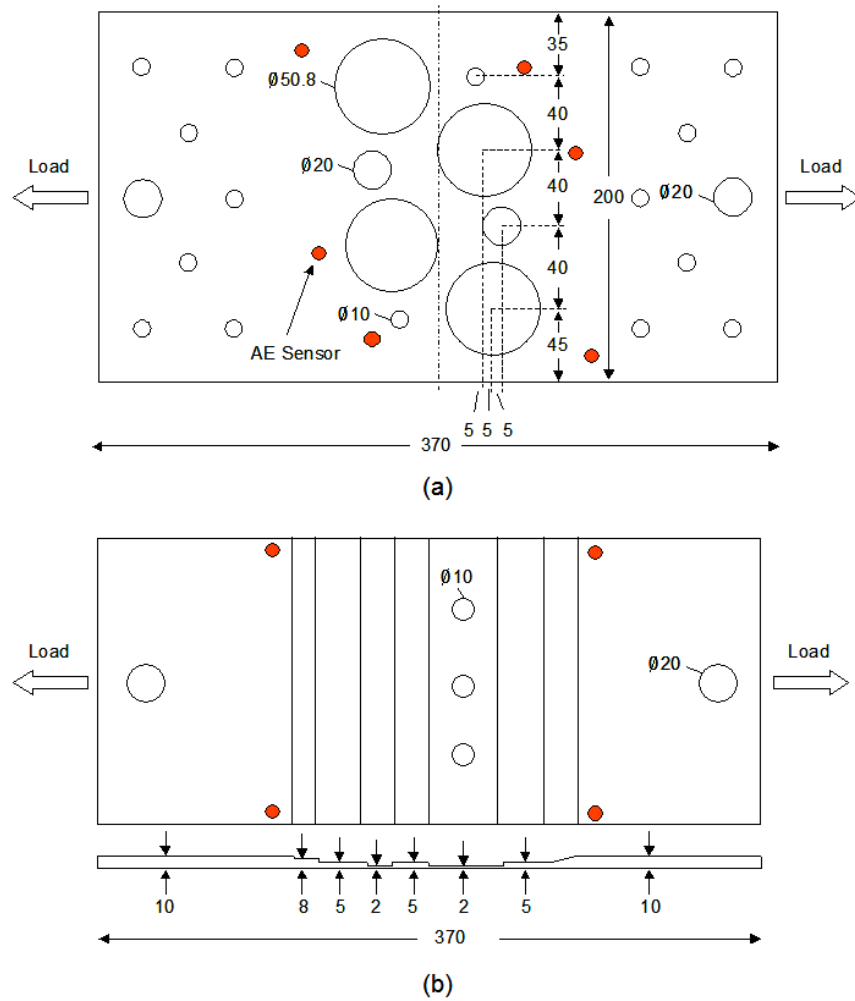


Fig 2. Specimens for validation of developed source location technique (a) disruption of source to sensor propagation path, (b) thickness change resulting in changes in propagation velocity (all dimensions in mm).

The specimen with numerous holes was made from 3-mm mild steel plate, but plate thicknesses were increased to 9 mm at the loading pins by the addition of two extra plates bolted to either side of the plate, to avoid failure at the loading pins. Physical Acoustics Limited (PAL) resonant sensors were mounted to the plates (as shown in Fig. 1 by filled circles), grease was used as an acoustic couplant and the sensors were held in position with magnetic clamps. The sensitivity of the mounted sensors was evaluated using the H-N source technique.

A 180 x 130-mm grid with a grid density of 10 mm and a 140 x 160-mm grid with a grid density of 20 mm were selected for the hole and step specimens, respectively. Five H-N sources were conducted at each available node to form the Delta-T grids. The specimens were fatigued under a load of 3.5 to 35 kN until failure. All AE feature data was recorded using a PAL MIS-TRAS system.

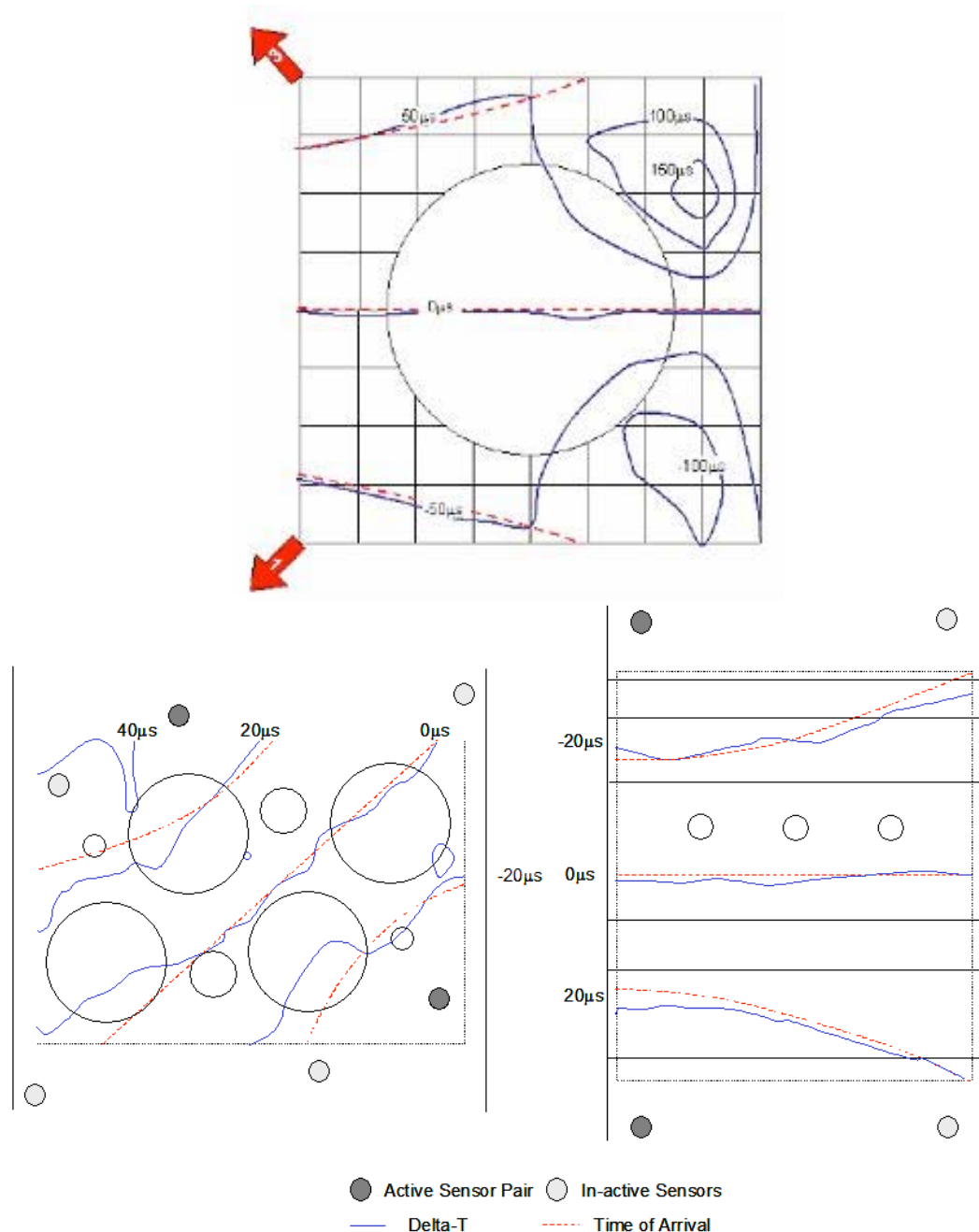


Fig. 3. Example of Delta-T source location maps for both specimens.

Results and Discussion

Response of all sensors to the H-N source in all investigations was above 98 dB, demonstrating that all sensors were mounted correctly. A wave velocity for the first threshold crossing was determined and used for all TOA source location calculations. The data from the H-N source events was used to create the Delta-T contour maps, as discussed previously. It is possible to create similar, theoretical maps for TOA using the above first threshold crossing wavespeed. Figure 3 displays a comparison between the Delta-T and TOA source location maps, for one sensor pair, for the three specimens. By examining the Delta-T map it is evident that the wavepaths are interrupted by the holes in the plates, which will cause errors in any source location calculation.

Figures 4 to 6 and Table 1 display the results from the artificial source investigation. Figure 4 shows the results from using all eight sensors. This array produced the most accurate results for both the TOA and Delta-T location methods. This is expected as the use of eight sensors produces 28 sensor pairs and increases the likelihood of direct wavepaths between source and sensor, thus reducing the effect of the 250-mm cut-out. Delta-T had an average error of 18 mm (38 mm maximum, 1 mm minimum) compared with 62 mm using TOA (117 mm maximum, 5 mm minimum), a 71 % reduction.

Figure 5 and 6 and Table 1 presents the results from the regular and irregular arrays respectively. Both location methods show an increase in error associated with the reduction in number of sensors. There is little difference between the regular and irregular arrays when locating with Delta-T. A difference in the two arrays is apparent in the TOA location methods, with an average error 107 mm for the regular array and 129 mm for the irregular array. It was not possible to locate source 10 (Table 1) using TOA for the irregular sensor array, however the Delta-T method located this source to within 14 mm. The Delta-T technique improved the location in both these arrays by 71-78%. The results show that it was more accurate (> 54 % reduction in error) to use a four sensor array with Delta-T location than to use TOA location with an eight sensor array when locating artificial sources in this plate.

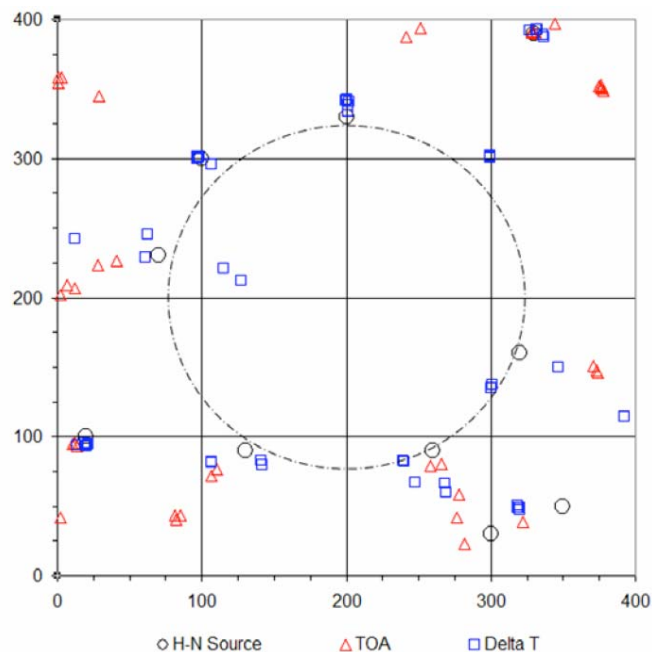


Fig. 4. Comparison of location methods of artificial sources using all 8 sensors.

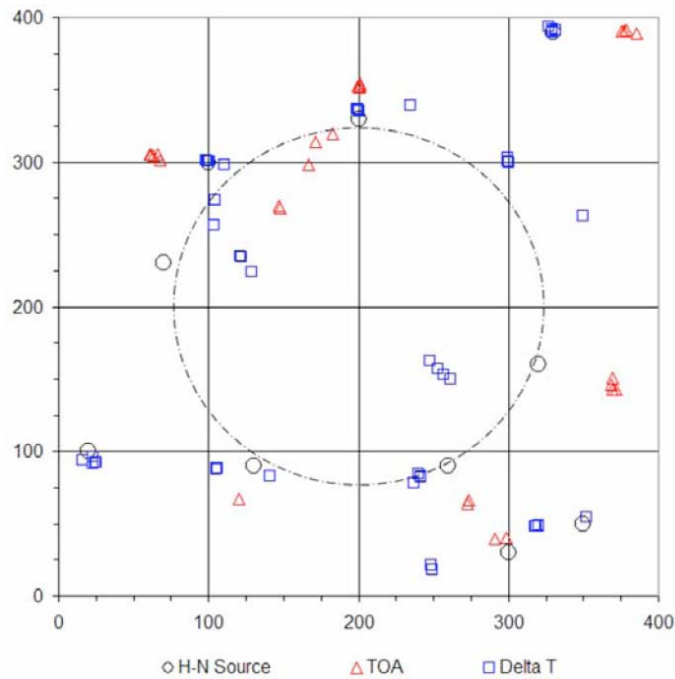


Fig. 5. Comparison of location methods of artificial sources using regular array.

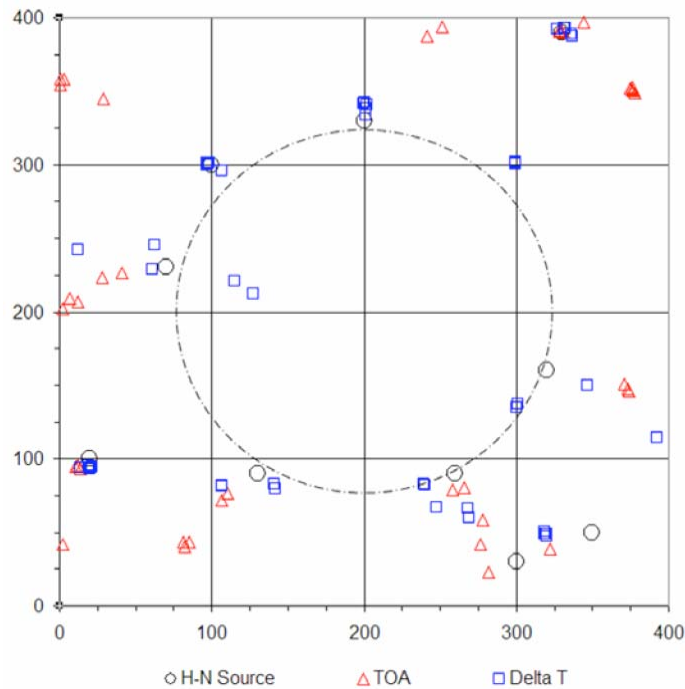


Fig. 6. Comparison of location methods of artificial sources using irregular array.

Figure 7 shows a comparison of the TOA with the Delta-T location techniques of the detected signals for both fatigue specimens. The specimen geometry and the site of fracture initiation have been superimposed. The plots demonstrate how the Delta-T technique shows significant improvement. In the hole specimen, the TOA results (Fig. 7a) show four peaks of activity of above 70 events, whilst the Delta-T results (Fig. 7b) have only one such peak. Furthermore, the location of the signals is more compact, demonstrating that a source cluster analysis of the source

would be achieved earlier using the Delta-T technique. The position of the peak cluster is also much closer to the position of fracture. Figure 7c shows the TOA plot for the change in thickness plates, and it can be seen that there is no single peak in close proximity to the fracture region. In Fig. 7d, the Delta-T technique clearly identifies the fracture position, although it is not the peak of events.

Based on the location of the initiation of fracture and the closest peak cluster, the TOA and Delta-T techniques show errors of 15.5 and 8.0 mm, respectively, for the plate with holes, demonstrating a reduction in error of 48%. It is not possible to determine an error for the step plate as there is no cluster in reasonable proximity that could be defined as coming from the fracture.

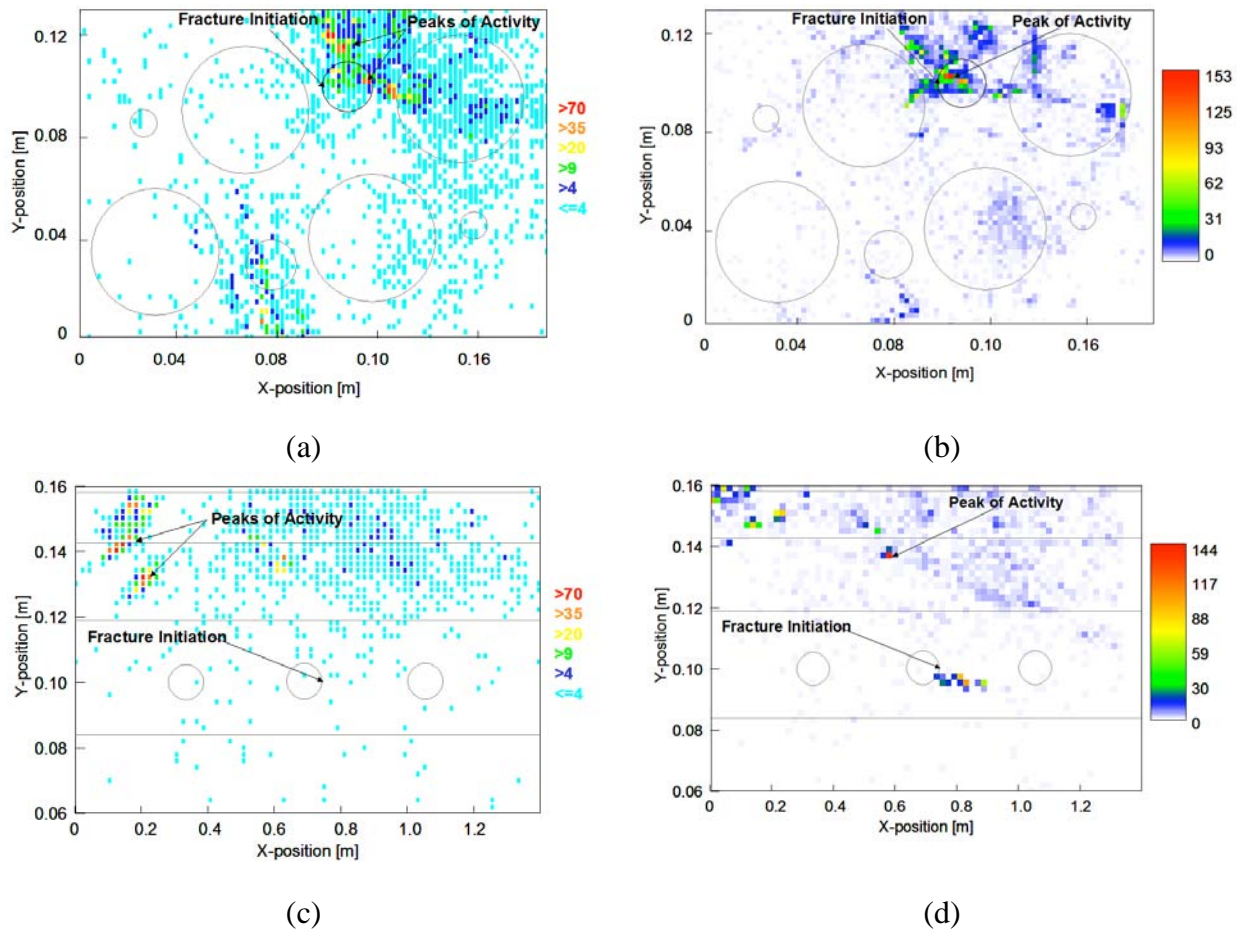


Fig. 7. Comparison of source location results from specimen with disruption of source to sensor propagation path (a) Hole: Time of arrival, (b) Hole: Delta-T technique, (c) Step: Time of arrival, (d) Step: Delta-T technique.

A further advantage of the Delta-T technique is that it has a tighter source clusters, as this can be seen when comparing the cluster sizes in Fig. 7a and b. Using the TOA technique (Fig. 7a) there are three clusters of >70 events whilst the Delta-T technique (Fig. 7b) has only one cluster of >140 events. This suggests that if a spatial cluster were to be used as an indication of developing damage, the Delta-T method would identify it earlier.

Conclusions

Delta-T source location provides a novel approach for overcoming particular problems associated with source location in complex structures with some current techniques (TOA and modal analysis). All investigations have demonstrated that the Delta-T mapping technique is superior to the current TOA technique.

Acknowledgements

The authors wish to acknowledge the funding of this work by Messier-Dowty the leading manufacturer of landing gears and landing gear components and EPSRC. In addition the technical support of Physical Acoustics Limited is acknowledged.

References

- [1] Miller, R. K. and McIntire, P. *Acoustic Emission Testing NDT Handbook*, Volume 5, American Society for Non-destructive Testing: p. 652, (1987).
- [2] Rindorf, H. J. "Acoustic Emission Source Location in Theory and in Practice", *Bruel and Kjaer Technical Review*. **2**, 3-44 (1981).
- [3] Pullin, R., Holford, K. M. and Baxter, M. G. "Modal Analysis of Acoustic Emission Signals from Artificial and Fatigue Crack Sources in Aerospace Grade Steel", *Key Engineering Materials*, **293-294**, 217-224 (2005).
- [4] Holford, K. M. and Carter, D. C. "Acoustic Emission Source Location" *Key Engineering Materials*, **167-168**, 162-171 (1999).
- [5] Nivesangsan, P., Steel, J. A. and Reuben, R. L. "AE Mapping of Engines for Spatially-Located Time Series", *Mechanical Systems and Signal Processing*, **19**(5), 1034-1054 (2005).
- [6] Schubert, F. (2004) "Basic Principles of Acoustic Emission Tomography" *26th European Conference on Acoustic Emission Testing*, Berlin, Germany, pp. 693-708.
- [7] Schubert, F. (2006). "Tomography Techniques for Acoustic Emission Monitoring" *European Conference on Non-destructive Testing*, Berlin Germany.
- [8] Baxter, M. G., Pullin, R., Holford, K. M. and Evans, S. L., "Delta T Source Location for Acoustic Emission" *Mechanical Systems and Signal Processing*, **21**(3), 1512-1520 (2007).
- [9] ASTM, Standard guide for determining the reproducibility of acoustic emission sensor response, American Society for Testing and Materials, E 976 (1994).
- [10] N.N. Hsu and F.R. Breckenridge, Characterization and Calibration of Acoustic Emission Sensors, *Materials Evaluation*, **39**, 60-68 (1979).

ACOUSTIC EMISSION SOURCE LOCATION ON AN ARBITRARY SURFACE BY GEODESIC CURVE EVOLUTION

G. PRASANNA, M. R. BHAT and C. R. L. MURTHY

Department of Aerospace Engineering, Indian Institute of Science, Bangalore 560 012, India

Abstract

Location of an acoustic emission (AE) source is generally obtained by assuming simplified velocity models on surfaces and solids, for which a definite parametric representation exists. These attempts employ triangulation to form distance equations using time-differences obtained from experimental data, which are solved analytically or numerically to get to the location of source. This approach may not be suitable for complex geometry components. Also, the problem gets compounded if the material of the structure is anisotropic warranting complex analytical velocity models. Hence, there has been a need to obtain a practicable source location solution in a more general setup on any arbitrary surface containing finite discontinuities. The approach suggested here is based on the fact that the wave takes minimum energy path to travel from a source to any other point in the connected domain. An AE signal takes this path from the source to an AE sensor array. By propagating the waves in reverse virtually from these sensors along the minimum energy path and by locating the first intersection point of these waves, one can get the source location.

Keywords: Source location, geodesics, geodesic evolution

Introduction

One of the major advantages of AE technique as an on-line monitoring tool is its capability to locate active defects in larger structural components without having to physically scan them. Different methods used for source location include zonal location, computed location, and continuous location. These approaches are affected by the signal attenuation and dispersion due to inhomogeneity and geometry of the material [1]. An alternative location technique uses the concept of 'the first sensor hit by an AE event' to identify a more generalized region around each sensor, from which the AE signal likely originated. In this case, one can determine which one of the several sensor regions on the test specimen has more concentrated AE activity [2]. Some AE systems determine signal arrival times using fixed threshold techniques [3] and because of the aforementioned complications, such AE systems measure arrival times for signals using various portions of the AE signal, which travel at different velocities.

The approach suggested here is based on the fact that the wave takes minimum energy path to travel from a source to any other point in the connected domain. In isotropic media, minimum energy path gets reduced to shortest distance path, which can be seen mathematically as shortest geodesics. Hence, by allowing geodesic waves to propagate from multiple sensors and identifying their point of meet, one can obtain the source location. In an object with complex geometry, a graph-theory based concept can be employed to determine the shortest path using Dijkstra's algorithm [4] for finding discrete geodesics, which are propagated from each sensor location till the source is reached.

Our approach

This conceptual view can be visualized as in Fig. 1, which shows waves propagating in all possible directions from a defect location, along the minimum energy path. With imposed material limitations, this path is generated by geodesics. Once the geodesic paths are extracted in a given geometry, the defect location is reached by back-propagating along those paths, from the sensor locations, as shown in Fig. 2. To start with, it can be assumed that AE sensors detect only Rayleigh waves, which in turn means that the study is restricted to 2-D surfaces.

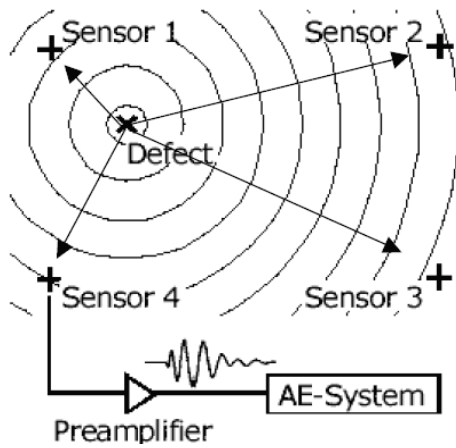


Fig. 1: Wave front propagation – from defect location.

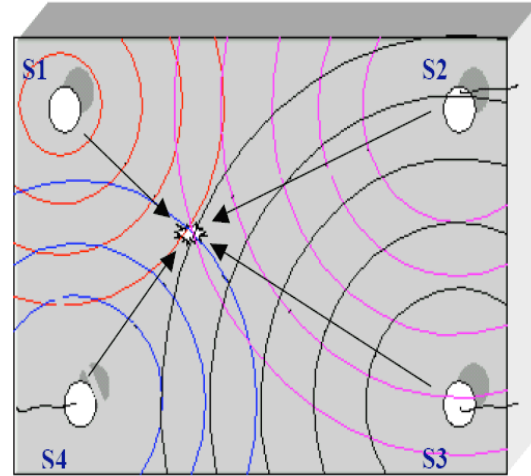


Fig. 2: Conceptual view – back-propagation to defect location.

It is to be noted that even the triangulation method utilizes the same approach, only that it has an inherent assumption that the geometry is a 3-D continuum resulting in simple distance equation based on Pythagorean theorem, which is solved analytically or numerically.

Since our approach builds on the fact that a wave takes minimum energy path, when the assumption of isotropy in the media is imposed, the shortest energy path reduces to shortest distance path, which is provided by the evaluating the geodesics. Mathematically, the energy along a path is seen as weighing function defined along the path. Hence, the minimum energy path is given by

$$\text{Energy along path, } L = \int w(x) dx,$$

$$\text{Min. Energy, } \min(L) = \min\left(\int w(x) dx\right)$$

$$\text{If isotropic, Min Energy path, } \min(L) = w \cdot \min\left(\int dx\right)$$

where, $\min(\int dx)$ is the required geodesic.

So, the minimum-energy-path problem is equivalent to shortest-distance-path problem. The intersection of geodesic wave fronts from multiple sources gives the location of the source.

Formulation - Wave Propagation Approach:

This approach involves discretizing the domain as curved or planar simplicial-complex chains, followed by finding local geodesics in each of the simplex and finally gluing them together to get the required global geodesic. There are many suggested methods to calculate

discrete geodesics and it is still an active area of research investigation [5-7]. Dijkstra [4] proposed an algorithm for the same and most of the present techniques is built over it.

The source location formulation proceeds as follows:

$$D(S1-S) - D(S2-S) = V.dt$$

which is recast into the implicit form,

$$\Phi(D, V, dt) = 0$$

The geodesics ‘D’ in above formulation is arrived from ‘wave-propagation’ perspective using graph-theory based Dijkstra algorithm.

The governing equation is subsequently further recast as

$$D(S1-S) \pm V.dt = D(S2-S)$$

This leads to the view that the solution lies in the boundary of the Voronoi diagram and the exact location is the intersection of two or more boundaries.

With above observation and understanding, the algorithm was implemented and tested for shortest path extraction over some simple cases and also over Stanford Bunny (Fig. 3), proving convincingly the wave-propagation based construction.

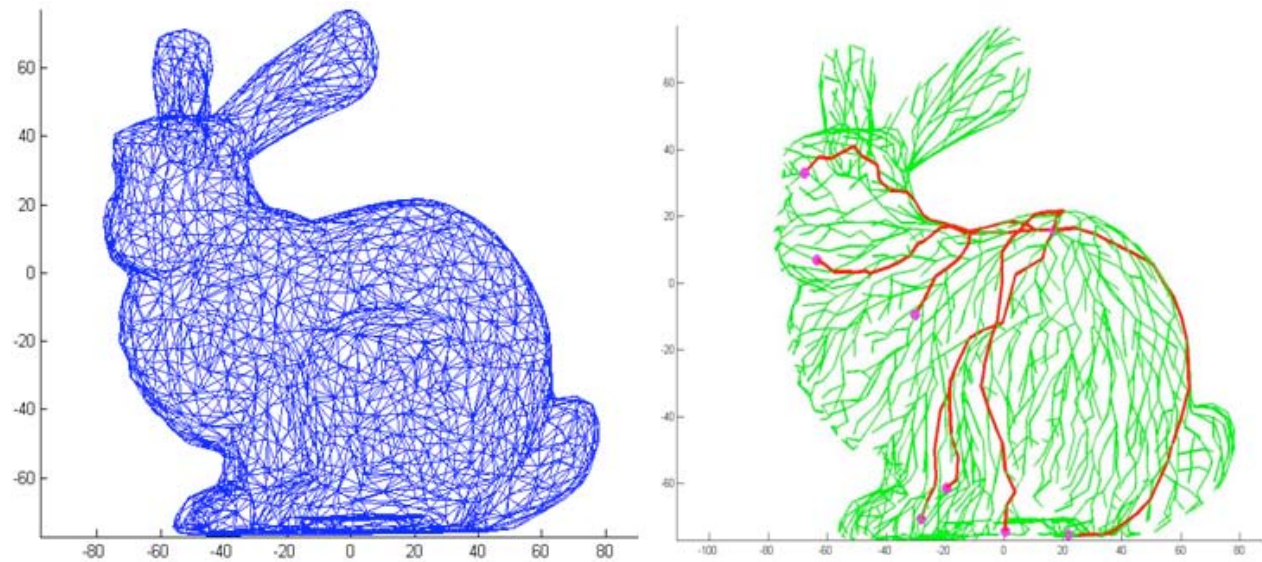


Fig. 3: (a) Surface model.

(b) Generated by geodesic propagation.

The bunny in Fig. 3(b) was generated by flow of wave along the shortest cost path from an arbitrary vertex in the mesh. The thick lines in the figure are samples of shortest paths between two points on the bunny surface (which are the required ‘geodesics’).

This proves the ability to extract discrete geodesics on arbitrary surface, which is the first part of geodesic evolution approach. The second part of solution is the construction of Voronoi-like diagram to locate the intersection of wavefronts, which is discussed in the following section.

Voronoi Construction:

Taking a case of 3-sensor setup provides 3 sets of time-difference equations. Using the recast formulation, all the points that are equidistant from sensor locations are found (using distance map calculated based on Dijkstra algorithm along with V.dt corrections).

When information from only two sensors is available, then only one equation is formulated and hence there exist multiple solutions meeting the distance criteria. This is depicted in Fig. 4(a) with the jagged thick blue line passing between sensors S1 and S2 indicating all points that are equidistant (which is the Voronoi diagram). An important observation is that this line passes through the defect location (AE source) and hence we need to search only along this line for getting to the source.

When information from one more sensor (S3) is considered, then 3 equations are formulated, from which the other lines in Voronoi diagram are constructed. All these lines intersect exactly at the AE source, as in Fig. 4(b). The geodesic lines joining the 3 sensors give the Delaunay triangle, which is the dual of conventional Voronoi diagram.

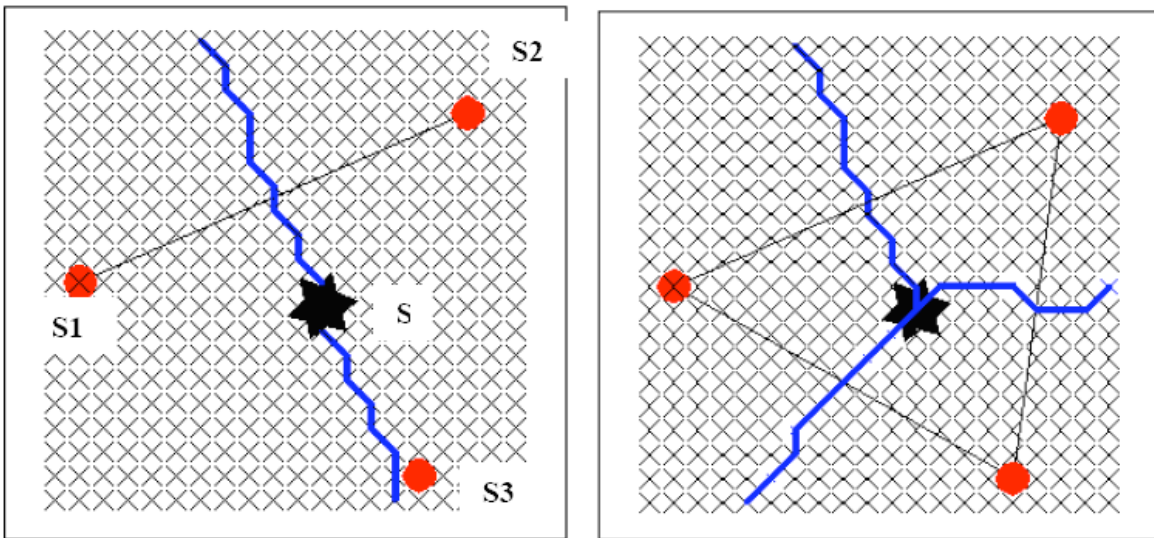


Fig. 4: Voronoi diagram considering (a) 2 sensors; (b) 3 sensors.

Above construction is trivial to implement in form of set operations. For a given mesh,

- Let nk be the k th node in the mesh and
- $D(nkS_i)$ be the distance between k th node and i th sensor and
- $Dk(S_{ij})$ be the difference in distances of a node k from sensors S_i and S_j , i.e.,

$$Dk(S_{ij}) = D(nkS_i) - D(nkS_j), \text{ then}$$

- the Voronoi line between any two sensors S_i and S_j is formed by nodes which satisfy the condition that $Dk(S_{ij}) = Vdt_{ij}$

where, dt_{ij} is the hit arrival-time difference between the sensor S_i and S_j and D 's are geodesic distances and the corresponding line can be seen as set of these nodes which is given by

$$L_{ij} = \{ nk \mid Dk(S_{ij}) = Vdt_{ij} \}$$

- Hence for 3 sensors we get, L_{12} , L_{13} & L_{23} as shown in Fig. 4. The intersection point is the intersection node in the set L_{ij} given by

$$\text{Source, } S = \{ n \mid (L_{12} \cap L_{23} \cap L_{13}) \}$$

- For surfaces, which are intrinsically 2-dimensional in parametric space, only two of the above sets are to be included for getting the source node.

Experimental Evaluation

The trial is initially made for a curved planar structure. Source location was attempted using both numerical-continuous and numerical-discrete (wave-propagation approach). It was followed by experimentation on an odd geometry component containing sharp changes and discontinuities. The AE setup that is used (MISTRAS) has an auto-sensor-test (AST) mode where each sensor acts as source and emits an AE pulse, which is received by other sensors. With known sensor locations, time-difference equations are formed and solved to get the velocity of the AE in the test component. AE sources were also simulated by pencil-lead breaks at known locations and the AE data was continuously recorded. The extracted data is sent to source location algorithm (coded in MATLAB) for evaluation.

Cylindrical Geometry:

The setup is shown in Fig. 5(a). Based on the dimensions, a sector of the object was meshed using ANSYS (Fig. 5b) and mesh information was imported to MATLAB. Wave propagation algorithm was applied over the mesh to find the location of artificially created sources. The program output shows a deviation of approximately 7.5% from the actual, as shown in Table I.

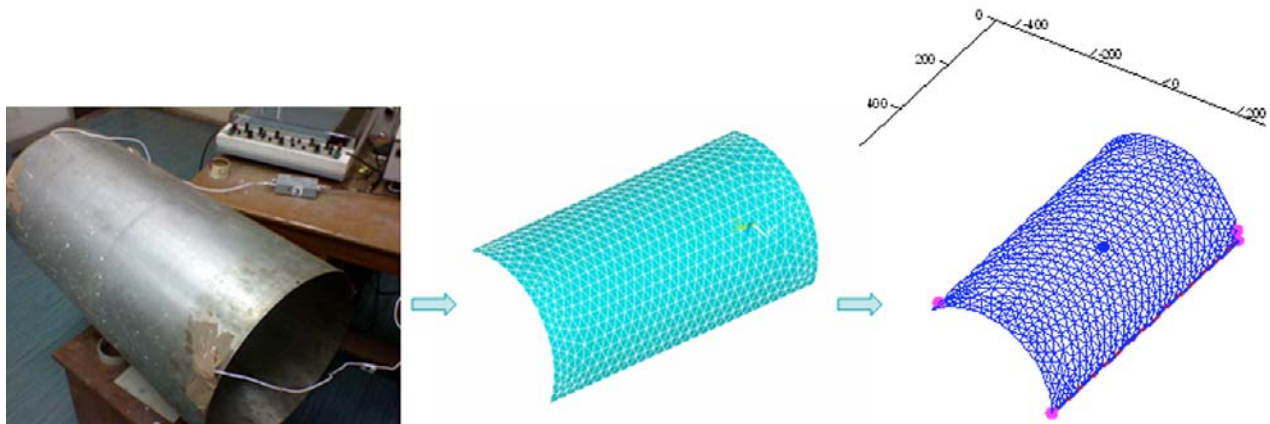


Fig 5 (a) Cylinder - AE setup (b) ANSYS mesh of a sector.

Table I: Source location in cylindrical geometry.

Sensor Location	Measured Value			Program output		
	X	Y	Z	X	Y	Z
S-1	105	0	0	105	0	0
S-2	-80.43	0	-67.49	-80.43	27.69	-67.49
S-3	-80.43	360	-67.49	-80.43	332.31	-67.49

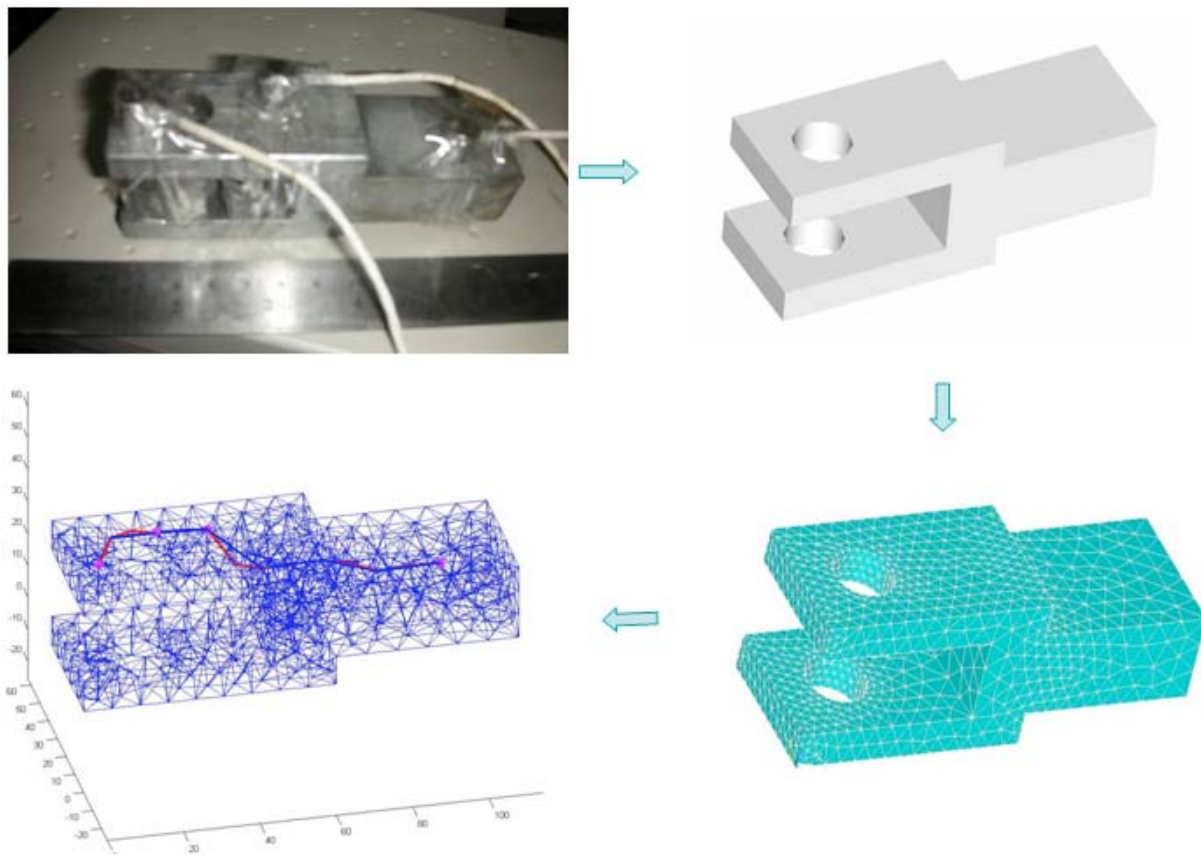


Fig. 6: Source location on a clamp with holes and sharp discontinuities.

Figure 6 shows the geometry as 3D model, the test setup, the ANSYS mesh and the MATLAB output (with a thick line showing the path from sensor location to the source). See Table II for the results. Error in this case is less than 10%.

Table II: Source location in clamp.

Location	Measured Value			Program output			% Error (Euclidean)
	X	Y	Z	X	Y	Z	
L-1	31	25	39	24.5	24.5	39.0	6.4
L-2	45	8	39	50	14.8	39.0	8.4
L-3	73	33	31.5	66	34	30.5	6.8
L-4	114	30	28	106	37	30.5	4.0
L-5	55	0	30	50	0	30	6.9

Conclusion

The approach presented in the study used a property of wave by which it tends to take minimum-energy path to travel between points on domain. This minimum-energy path was proved to be equivalent to shortest-distance path marking the birth of geodesics. The relation of geodesics to source location problem was established by proving that location of source is the first intersection point of multiple geodesics. This was implemented and proved by using Voronoi like diagram construction. The approach was experimentally validated on curved planar and odd geometry component. The solution based on two methods – conventional Numerical method and

Geodesic Evolution method was presented. It can be asserted that the geodesic curve-evolution method hold great promise for versatile implementation catering to non-conventional geometries. By the very nature of approach, extension of it to inhomogeneous and anisotropic geometry appears feasible.

References

1. M. Ohtsu. AE Theory for Moment Tensor Analysis, *Res. Nondestructive Evaluation*, vol. 6: 1995. pp. 169-184.
2. M.A. Hamstad and K.S. Downs, On Characterization and Location of AE Sources in Real Size Composite Structures - A Waveform Study, *J of Acoustic Emission*, **13** (1-2), 1995, 31-41.
3. Bernard Castagnede et al., Location of Pointlike AE Sources in Anisotropic Plates, *J. Acoust. Soc. Am.*, **86** (3), 1989, 1161-1171.
4. E. Dijkstra, A note on two problems in connection with graphs. *Numerical Math.* **1**, 1959. 269-271.
5. K. Polthier et al., Straightest Geodesics on Polyhedral Surfaces, *International Conference on Computer Graphics and Interactive Techniques, ACM-SIGGRAPH courses*, pp. 30-38, 2006.
6. G.V.V. RaviKumar et al., Geodesic Curve Computations on Surfaces. *Computer Aided Graphics Design*, Elsevier, 2003, pp. 119-133.
7. Vitaly Surazhsky et al., Fast Exact and Approximate Geodesics on Meshes, *Proceedings of International Conference on Computer Graphics and Interactive Techniques, ACM SIGGRAPH 2005 Papers*, pp. 553-560, 2005.

PROBABILITY OF DETECTION FOR ACOUSTIC EMISSION

ADRIAN POLLOCK

Physical Acoustics Corporation, 195 Clarksville Road, Princeton Junction, NJ 08550

Abstract

Probability of detection (POD) is a discipline within the field of nondestructive testing, that bears on the reliability of the inspection and has been of great value for selecting and validating NDT procedures, qualifying NDT personnel, and even establishing the acceptability of structural designs. This paper shows a way to bring the POD concept to AE technology. It reports the development of a model, which quantifies each step in the classic AE process – stress stimulus, flaw growth, wave release, wave propagation, sensing and detection. In its first implementation, the model treats fatigue crack growth in pressurized cylinders. A small percentage of the fracture surface is assumed to be formed by cleavage, the source of the AE. With the help of the Paris law for fatigue crack growth, the source theory of Wadley and Scruby, the power-law amplitude distribution and other relevant theory, it is possible to determine the probability of detecting AE from a flaw of given initial size, in a given vessel subjected to a given pressurization schedule. Because of attenuation the POD depends on the source position, so the findings are presented with POD encoded as color on a map of the vessel. Use of this POD concept will open the way to engineered AE inspections, better quality AE tests, and better integration of AE with other NDT methods to meet industrial needs for structural integrity.

Keywords: Probability of detection

Introduction: Probability of Detection (POD) in the NDT Industry

"Probability of detection" (POD) is a quantitative discipline with the field on nondestructive testing, addressing the topic of inspection reliability. In the late 1960's and early 1970's, it was common knowledge in the NDT industry that many inspections were producing incorrect results and that some inspection teams were more reliable than others. POD methodology was developed to address these facts and to furnish tools for securing adequate reliability of NDT on high-visibility, high-cost structures, such as the space shuttle [1]. Continuing to develop during the last 30 years, the POD discipline has delivered value in many activities especially selecting and validating NDT procedures, qualifying NDT personnel, and even establishing the acceptability of structural designs.

POD is the probability of actually detecting a given flaw that is assumed to be present in a given nondestructive inspection. POD is of obvious significance to structural integrity and safety. POD is a statistical quantity. The probability of detecting a given flaw depends on many factors including flaw characteristics (e.g. type, size, shape and orientation), test method and procedure, and personnel proficiency. In the early years of POD development, the approach was to collect together a large number of test objects with flaws and a substantial number of inspectors (sometimes teams of inspectors); to have the inspectors perform NDT; and to analyze the results in terms of how many flaws were detected. The outcome of this kind of analysis is conventionally presented as a graph showing POD as a function of flaw size. Work of this kind has provided valuable support to many programs, especially in the aerospace industry where the POD concept has been a good partner to the concepts of damage tolerance that were being

developed at the same time. The main setback to the empirical approach to POD (multiple test specimens, multiple inspection teams) is that it is laborious and costly. As the use of POD increased, techniques for modeling the NDT processes were brought in to supplement the empirical approach. By using models to handle some of the variables, the numbers of test specimens and inspectors needed to estimate POD could be reduced, resulting in a less costly and more efficient analysis.

Model Developed for Estimating POD for AE

A model for the probability of detecting flaws by means of AE was developed in the context of a project for monitoring a set of high-pressure gas cylinders during a planned 30-year service life. AE was under consideration both for the pre-service hydrotest and for in-service monitoring of these vessels. Availability of POD numbers for AE would support the project through the design approval process and lead to a more economical design. The model was developed first for the in-service monitoring scenario. The POD model is essentially a quantification of the classic path from AE source to processed data. All the variables along the path are quantified – stress stimulus, source behavior, wave propagation, sensor sensitivity, instrumentation gain and detection threshold. Figure 1 is a block diagram of the model, in which the variables are arranged in a way that facilitates the desired calculation.

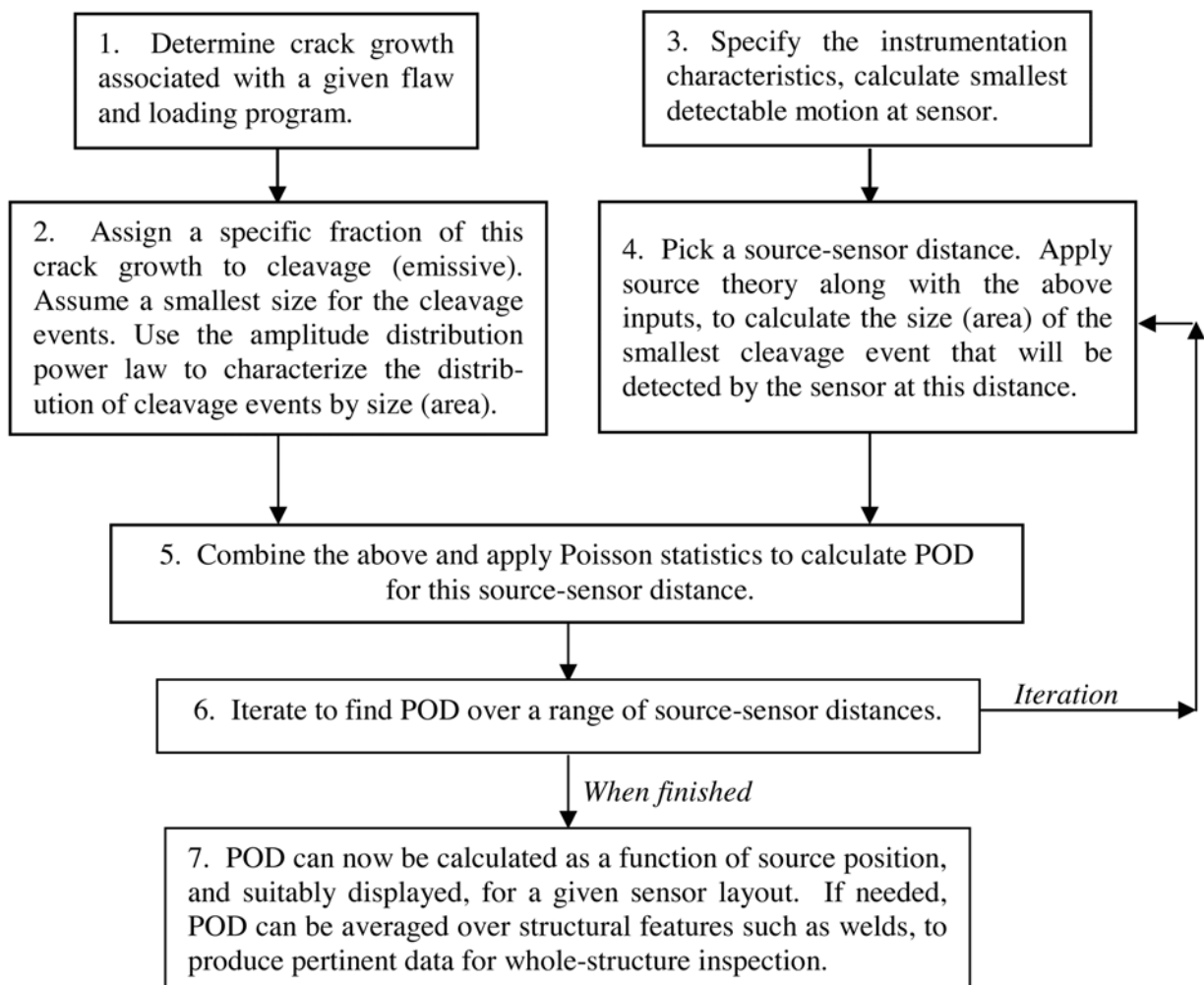


Fig. 1 Method for determining the probability of detecting a flaw with AE.

POD is determined at the convergence of two lines of inquiry, related to AE generation and AE propagation/detection respectively. The operative questions are:

1. *"How many cleavage-crack events will take place at the specified flaw under the loading program under consideration, and what is their size distribution?"*
2. *"How big is the smallest cleavage-crack event that will be detected by the AE equipment, at the distance under consideration?"*

Given the answers to these two lines of inquiry, it is not hard to find the probability of detecting the flaw during execution of the specified loading program, using the specified equipment setup. Because of attenuation, the probability of detection is naturally a function of source position. It is assumed that the AE is produced by "cleavage-crack events" that form a definite percentage of the fracture surface area. This assumption is a key feature of this particular case; i.e., fatigue crack growth in these metal cylinders. However, it is not essential to this POD methodology in general. Other cases could be based on different assumptions about AE source mechanisms. Indeed, this is a major area for the future growth of this POD methodology. To show how the process works, the less obvious steps of Fig. 1 will be discussed in turn.

1. *Determine crack growth associated with a given flaw and loading program.*

The loading program is a key part of any AE test [2]. For the case of fatigue crack growth in the high-pressure gas cylinder, the assumption was made that a flaw was growing according to the Paris law. A computer program and graphic user interface were developed to calculate the amount of flaw growth with user-entered initial flaw sizes and loading programs. The graphic user interface is shown in Fig. 2. The upper part shows the vessel dimensions, the pressures applied and the cycling process to be monitored. From the dimensions and pressures, the hoop and axial stresses and stress intensity factors are calculated by conventional techniques. Then, the program calculates the flaw growth cycle by cycle, finally arriving at the total new crack area opened up during the entire specified loading program.

2. *Characterize the cleavage increments (AE events) that will make up this crack growth.*

The model used here for fatigue crack growth is a synthesis of insights from several sources. The pioneering work of Pelloux [3] showed that in Stage II fatigue, the new surface is created mainly by slip-like dislocation movements; but, occasionally, this process is punctuated by abrupt transgranular cleavage events that can even be seen on fractographs. The studies of Wadley and Scruby on emission amplitudes from various source mechanisms, summarized in [4], indicate that such cleavage events would give useful AE signals while the dislocation movement would not. The early observation of Harris and Dunegan [5], that peak load emission does not occur on every cycle until the crack is growing relatively fast towards the end of its life, also fits our story that just a certain fraction or percentage of the fracture surface area is formed by cleavage, and that this is the source of the AE. This fraction or percentage is an input parameter to the POD model.

This gives us a total cleavage area resulting from the loading program under consideration. The next step is to break up this total area into discrete increments – AE events. This is done with the help of the amplitude distribution power law [6], whose exponent b is an input parameter to the POD model. It is assumed that the smallest event is single-grain cleavage, while large events correspond to cleavage extending over multiple grains simultaneously. Using the power law, the number of AE events $F(A)$ is calculated as a function of A , the cleavage area of the individual event. This completes the first line of inquiry, *Steps 1 and 2* in Fig. 1.

It is generally agreed that different flaw types have different AE characteristics. Therefore, the above argument is only a specific, limited prototype of this generic step in the POD model. Fresh thought will be needed when the scope of the methodology is extended to cover flaw types other than cracks, and/or loading regimes other than Stage II fatigue.

3. Specify instrumentation characteristics, sensor layout, attenuation.

The specified instrumentation characteristics include the sensitivity of sensor and preamplifier, the preamplifier gain and the detection threshold. These obviously influence whether a wave of given strength will be detected by the instrument. Another instrumentation characteristic that comes into the model is a characteristic frequency of the sensor. This is used to convert the stated sensor sensitivity from $V/(m/s)$ to V/m . This approach does not consider the full complexity of sensor spectral responses or directional effects, but it does allow a calculation of the smallest displacement at the sensor that will be detected at the characteristic frequency.

4. Source theory and wave attenuation.

The focus of this step is to determine the smallest cleavage increment detectable by the sensor. First, this requires some source theory, which is drawn from reference [2]. This source theory relates the cleavage event area to the resulting AE motion (displacement) as a function of distance in an infinite medium. We apply this source theory at a reference distance of one plate thickness from the source. Then, the measured attenuation from that distance outwards is used to infer the smallest detectable cleavage event area at any arbitrary distance.

5. Apply Poisson statistics to calculate POD for a given source-sensor distance.

This is an interesting step in the model. Here the stochastic nature of the AE phenomenon leads naturally to a stochastic (probabilistic) outcome for the detection process. Here also, evaluation criteria are considered. For now, detecting a single AE event is considered equivalent to detecting the flaw. Other evaluation criteria can be found in industrial practice. In tube trailer testing, for example, the evaluation criterion is framed in terms of a cluster of several events, located close together. The POD concept described here can be readily extended to such cases.

To conclude the present analysis: we have a probability distribution of cleavage event areas and we know the smallest cleavage event area that will be detected. The expected number of detectable events λ is immediately found. Then, this expected number λ can be used as the "rate" parameter of the Poisson distribution. This distribution (a function of λ) tells about the probability of actually detecting 0, 1, 2, ... events in a given test when the expectation number is λ . The probability of detecting no (zero) AE events is $e^{-\lambda}$. So the probability of detecting at least one AE event, is $(1 - e^{-\lambda})$. This is the probability of detecting the flaw; a good simple result to close out the POD model calculations.

Illustrative Results

Figure 2 shows input data used to generate the POD results in a typical run of the POD software. The structure being modeled is a cylindrical pressure vessel being subjected to 2000 pressure cycles. The flaw being modeled is a crack, initially 1.0-mm deep. AE is monitored using a 50-dB threshold setting. There are many adjustable parameters but to illustrate the functioning of the model, just these three will be varied while the others are held constant.

Figure 3 is map of calculated POD for the test setup detailed in Fig. 2. Six sensors are placed on the vessel, two rings of three sensors each. The POD values are encoded in color as shown in

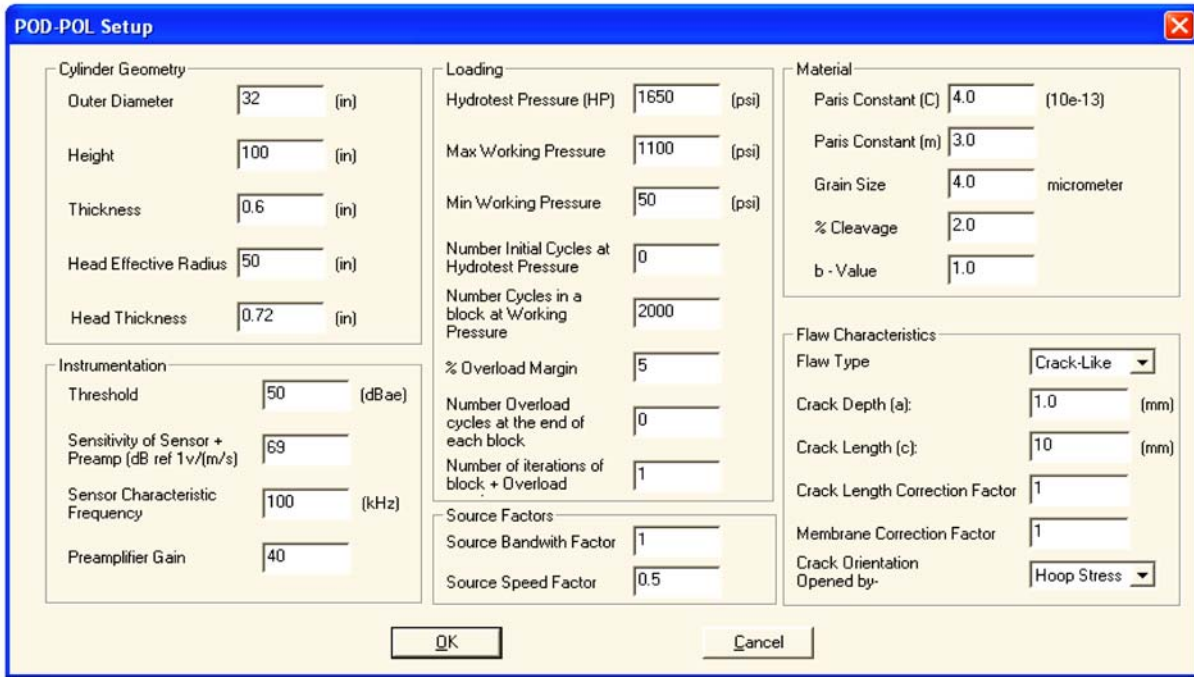


Fig. 2: Setup for illustrative runs of the POD-POL software.

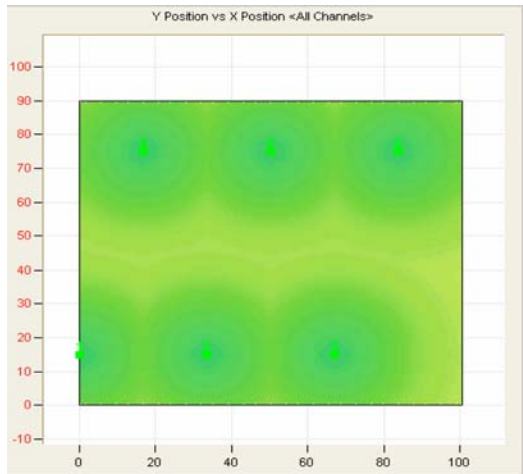


Fig. 3: 1-mm flaw, 2000 cycles, 50-dB threshold.

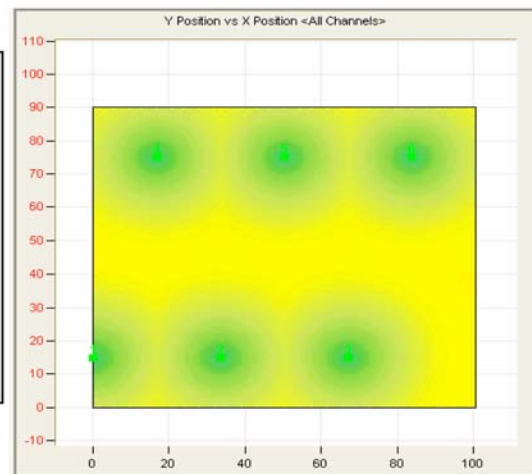


Fig. 4: 1-mm flaw, 1000 cycles, 50-dB threshold.

the key beside the map. The color is mostly green, indicating high POD (80-100%) for flaws almost anywhere on the vessel surface. Midway between the sensor rows, the POD is lower (60-80%). The model also displays some statistics of the flaw growth - the number of AE events occurring at the crack, the total area of cleavage, and the number of grains cleaved – but these cannot be shown here for the lack of space.

Figure 4 shows the result of only monitoring 1000 cycles instead of 2000, with the same initial flaw size. The POD drops to 40-60% over most of the vessel surface. The POD is only high if the flaw is close to a sensor. This kind of result can be useful in engineering an AE test, because it shows how the reliability of the test will depend on the duration of the monitoring.

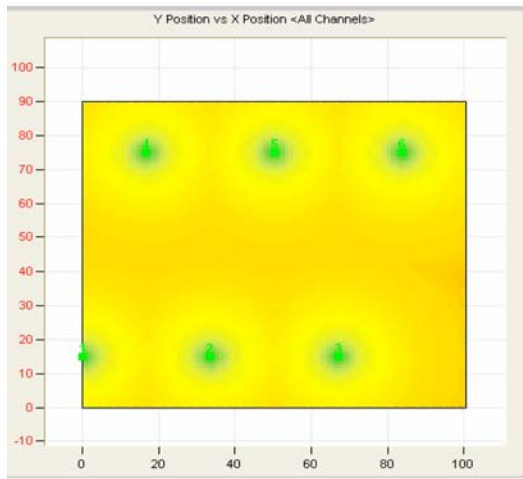


Fig. 5: 0.4-mm flaw, 2000 cycles, 50-dB threshold.

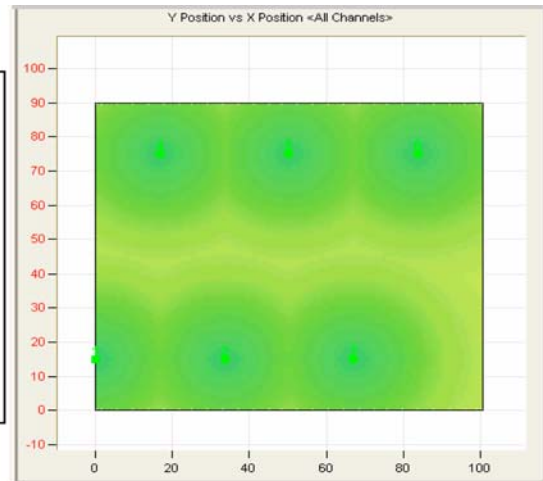


Fig. 6: 0.4-mm flaw, 2000 cycles, 40-dB threshold.

Figure 5 reverts to 2000 cycles of loading, but the initial flaw is only 0.4-mm deep instead of 1.0-mm. Now, the POD is only 30-55%, over most of the surface area. The flaw has to be very close to a sensor if it is to be detected with high reliability. This kind of result is useful because it shows how the AE test results will depend on the initial flaw size.

In Fig. 6, the detection threshold is lowered to 40 dB. This renders the 0.4-mm flaw detectable with much higher probability, 70-80% and better, over most of the vessel surface. In a real test, of course, lowering the threshold would also increase the likelihood of picking up noise sources.

Finally, Fig. 7 shows a logical extension of the POD concept: Probability of location (POL). This is readily incorporated in the model. Figure 6 shows how the POL is greatest when the source is in the open space surrounded by sensors. POD, in contrast, is greatest when the source is close to the sensors. POD and POL can both be considered when planning the strategy for an AE test or test series.

Discussion and Conclusions

These results illustrate how POD depends on the many variable parameters involved in the AE test. With this model, the effects of changing sensor layouts, sensitivities and test parameters in general can be assessed quickly, easily and quantitatively. AE test planning often involves tradeoffs around cost, technical difficulty and so forth. With this model, quantitative expectations about test results can now be included in this planning process. This quantitative planning capability will also make AE more viable in the eyes of reliability engineers, who are considering its use in their structural integrity assurance programs.

References

1. W.D. Rummel, Probability of Detection as a Quantitative Measure of Nondestructive Testing End-to-End Process Capabilities, *Materials Evaluation*, **56**, 1, 1998, 29-35.
2. A.A. Pollock, Loading and Stress in Acoustic Emission Testing, *Materials Evaluation*, **62**, 3, 2004, 326-333.

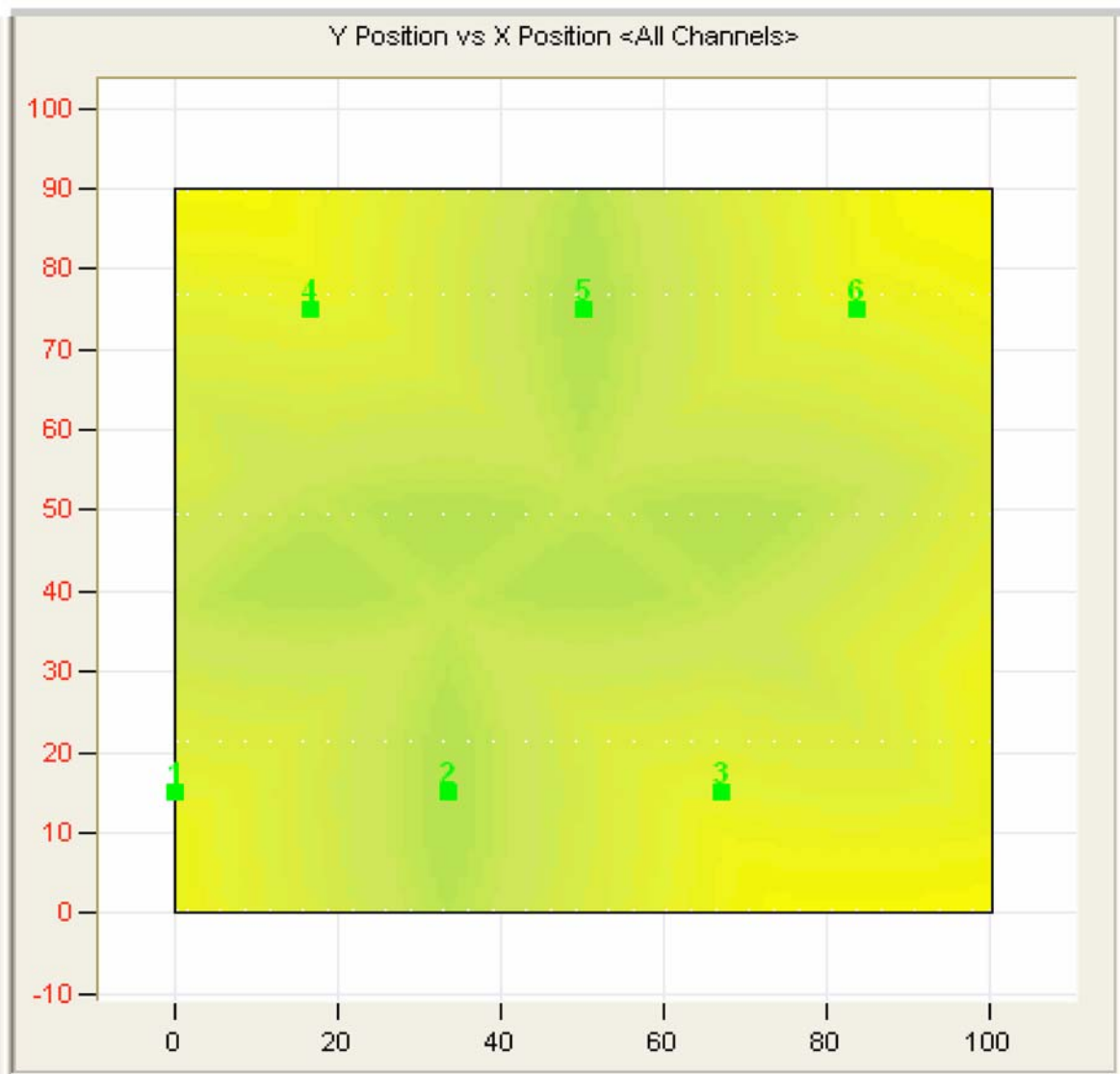


Fig. 7: Probability of location (POL).

3. R.M.D. Pelloux, *The Analysis of Fracture Surfaces by Electron Microscopy*, Boeing Scientific Research Laboratories, Report Z254824 (available from Storming Reports), 1963.
4. R.K. Miller and P. McIntire (eds.), *Acoustic Emission Testing, Nondestructive Testing Handbook*, 2nd ed., Vol. 5, American Society for Nondestructive Testing, 1987, pp. 77-78.
5. D.O. Harris and H.L. Dunegan, Continuous Monitoring of Fatigue Crack Growth by Acoustic Emission Techniques, *Experimental Mechanics, EXMCA*, **14**, 2, 1974, 71-81.
6. A.A. Pollock, Acoustic Emission Amplitude Distributions, *International Advances in Nondestructive Testing* (ed.: Warren J. McGonnagle), Vol. 7, 1981, pp. 215-240.

PLASTIC-REGION TIGHTENING OF BOLTS CONTROLLED BY ACOUSTIC EMISSION METHOD

YOSHIHIRO MIZUTANI, TADASHI ONISHI and MASAMI MAYUZUMI
Dept. of Mech. Sci. & Eng., Tokyo Institute of Tech., Meguro, Tokyo 152-8552, Japan

Abstract

We have proposed a control method for plastic-region tightening of bolts using AE method. In this paper, in order to investigate the validity of the tightening control by AE method, the tightening test in simulated factory environment was conducted and both tightening accuracy and variations were compared with those by conventional control methods. The results show that AE method is more effective for plastic-region bolt tightening control than the conventional methods. Finally, a new system using a Maharanobis distance for controlling plastic-region bolt tightening by AE method was developed.

Keywords: Plastic-region bolt tightening, tightening control, Maharanobis distance

Introduction

A plastic-region tightening method used in the automotive industries is known as a good method for preventing fatigue of bolts. However, the most common tightening-control method by using a torque wrench (called torque-control bolt tightening method) cannot apply to a plastic-region tightening [1]. Both an angle control method and a torque-gradient control method are regulated in JIS (Japanese Industrial Standards) [2] for a plastic-region tightening control, although the method requires a special torque wrench and complicated procedures. We have proposed a new control scheme using AE method, but the accuracy and validity were not examined. In this paper, in order to investigate the accuracy and validity of the tightening-control in field, the tightening test was conducted. The tightening-accuracy and variation by AE method were found superior to those controlled by conventional methods.

Experimental Setup and Method

When a tightening is performed in field, noise due to friction on bearing surfaces was monitored with AE. In order to confirm whether AE method can be utilized in an industrial condition, tightening test in simulated factory environment was performed. Moreover, accuracy and variation of the tightening control by AE method were compared to those by conventional methods (angle control method and torque-gradient control method). Figure 1 shows photograph and schematic illustration of experimental setup used for the test. The axial load of a bolt was measured by a load cell (TEAC, TU-NR-C50kN), which was placed between two steel plates (SKS93, thickness: 10 mm). We prepared two sets of steel plates, of which surface roughness (arithmetical mean surface roughness) were less than 3.1 μm (plate 1) and 25 μm (plate 2). A torque was measured with a digital torque wrench (Nakamura, DTC-N1000EX). A potentiometer (Nidec Copal Electronics Corp., M-22E10-050 1k) was used for measuring the rotation angle. A socket of a torque wrench was equipped with a timing pulley, rotation angle of a bolt was transmitted to the potentiometer with the timing belt, and the rotation angle was measured. An AE sensor (PAC, Type: PICO) was attached to a bolt head.

AE signals were filtered by high-pass filter of 100 kHz and amplified 66 dB by AE analyzer (NF Electronic instruments, Type: 9501). By using this experimental setup, a torque, an axial load, a rotation angle and AE can be measured simultaneously during bolt tightening.

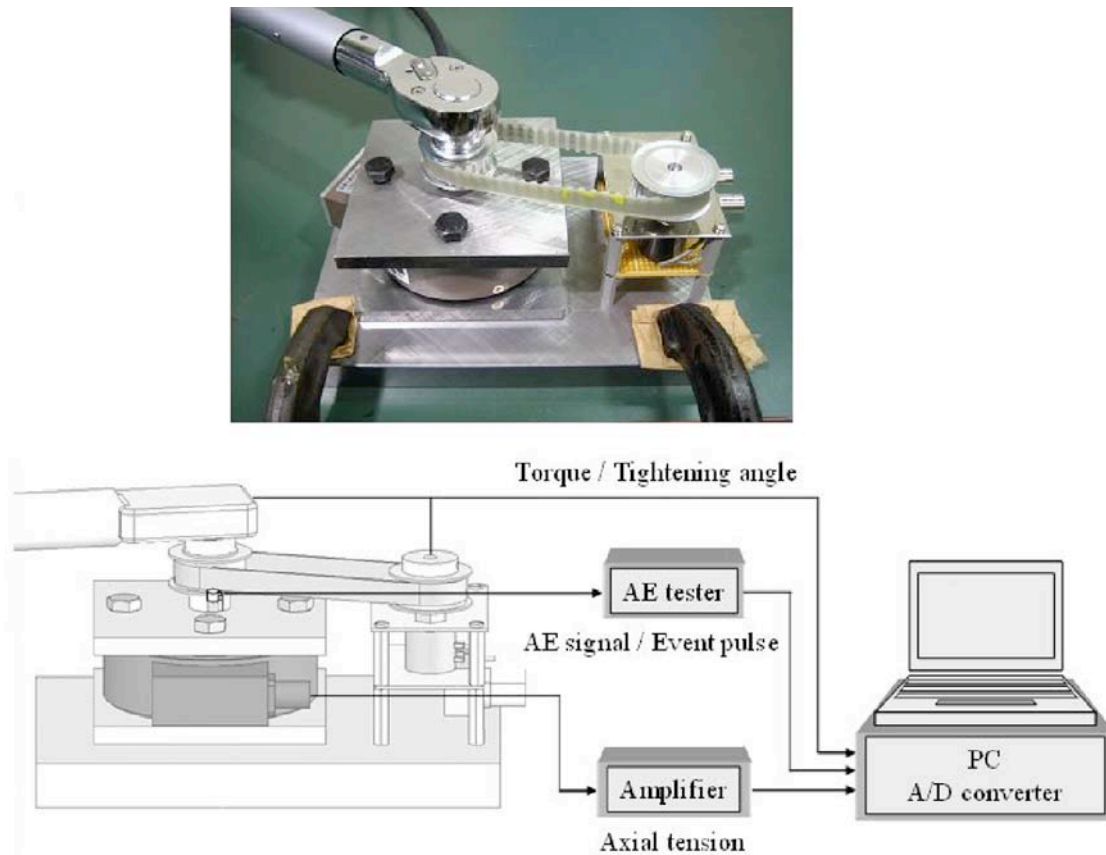


Fig. 1 Photograph and schematic illustration of tightening test.

Conventional Control Methods

We first investigated tightening accuracy and variation of conventional methods. One of the plastic-region tightening control methods regulated in JIS B 1083 is an angle control method. According to the JIS, desired angle (θ_{fA}) for a plastic-region tightening is determined by a following equation.

$$\theta_{fy} \leq \theta_{fA} \leq \frac{1}{2}(\theta_{fy} + \theta_{fu}) \quad (1)$$

Here, θ_{fy} is rotation angle corresponding to the yield point of bolts, and θ_{fu} is that of the ultimate point. Angles of θ_{fy} and θ_{fu} are determined by load-rotation angle diagram as shown in Fig. 2. Desired angle-range for plastic-region tightening (Eq. (1)) and axial-load-range controlled by the method are shown in the figure as $\Delta\theta_f$ and ΔF_f , respectively.

Next, we conducted several experiments and the accuracy and variation of tightening control were examined. Since the axial loads of yield point and ultimate point varied with torque applied to bolts and the applied torque is changed by tightening conditions (even if bolts with same lot are used), it is needed to normalize axial load when the data of different experiments are compared. The following normalized axial-load F^* is introduced for this purpose:

$$F^*_{\min} = \frac{F_{fA\min} - F_{fy}}{F_{fu} - F_{fy}} \quad F^*_{\max} = \frac{F_{fA\max} - F_{fy}}{F_{fu} - F_{fy}} \quad (2)$$

Here, F_{famin} and F_{famax} are axial loads correspond to minimum and maximum of desired angles by Eq. (1). F_{fu} and F_{fy} are the yield load and ultimate load determined by θ_f - F_f diagram for every experiment. Therefore, when a symbol F^* becomes 0, axial load of bolt reaches the yield point, and when a symbol F^* becomes 1, axial load reaches the ultimate point. Results of 8 experiments (1-5th experiments used plate 1, 6-8th experiments used plate 2) are shown in Fig. 3. When a desired tightening angle is set to a minimum in the range defined by the Eq. (1), the variation of axial loads for every examination becomes large, although, while a desired angle is set to a maximum, the variation becomes small and axial-loads are controlled at near the ultimate load. Axial tensions of each examination are always set in the range of 0 to 1, and it can be said that the angle control method is an accurate control method for plastic-region tightening. The other plastic-region tightening control method regulated in JIS B 1083 is a torque gradient control method. According to the JIS, desired torque gradient ($dT_f/d\theta_f$) for a plastic-region tightening is determined by the following equation:

$$\frac{1}{3} \left(\frac{dT_f}{d\theta_f} \right)_{\max} \leq \left(\frac{dT_f}{d\theta_f} \right) \leq \frac{1}{2} \left(\frac{dT_f}{d\theta_f} \right)_{\max} \quad (3)$$

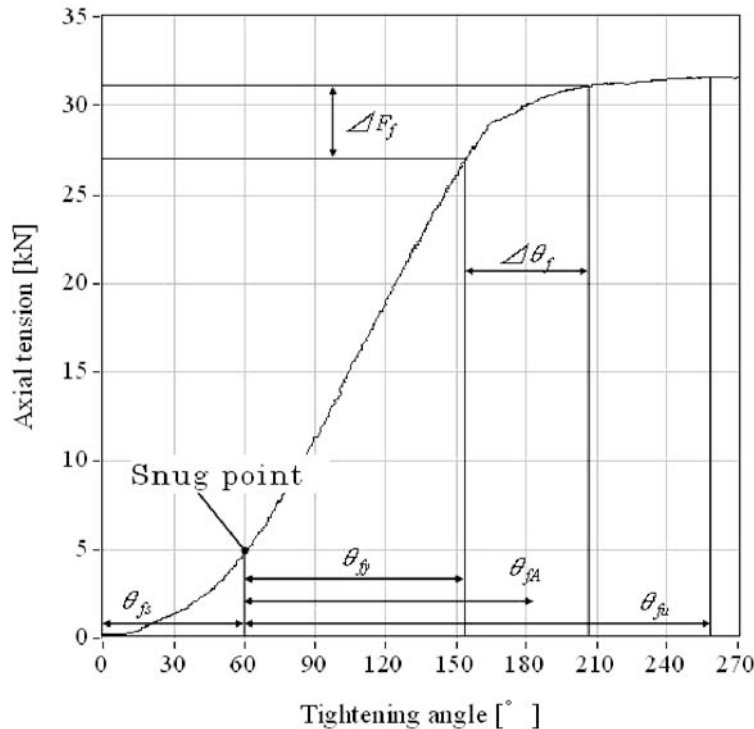


Fig. 2 Axial tension vs. tightening angle.

Torque, torque gradient and axial tension with tightening angle monitored during 1st experiment are shown in Fig. 4. Desired range for plastic-region tightening (Eq. (3)) and axial-load range controlled by the method are also shown. In order to discuss tightening control accuracy for each experiment and variation for every experiment, the normalized axial load of eight experiments are investigated (see Fig. 5). Tightening variations were large compared to

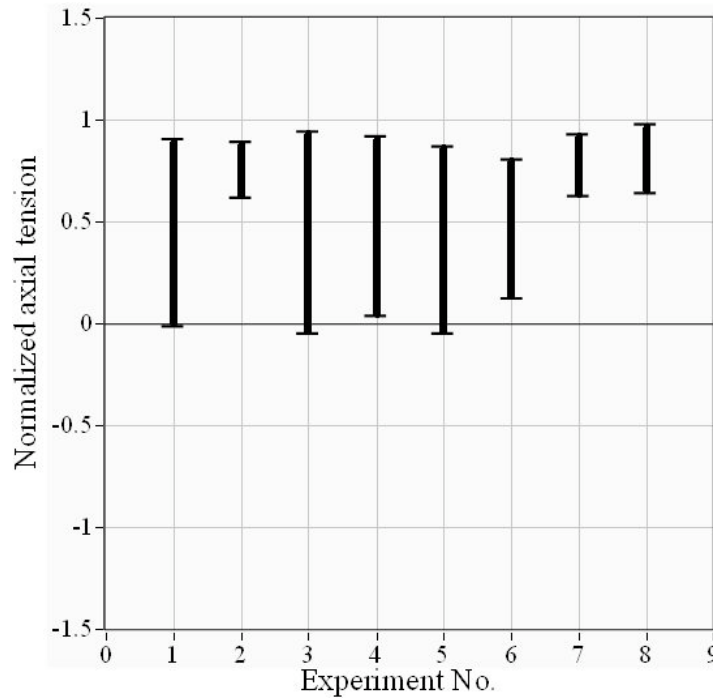


Fig. 3 Accuracy and variations of axial load.

those by angle-control method (Fig. 3). Furthermore, the result shows that there is a possibility that the axial load will not be managed in a plastic region in some cases. Therefore, this control method is inaccurate.

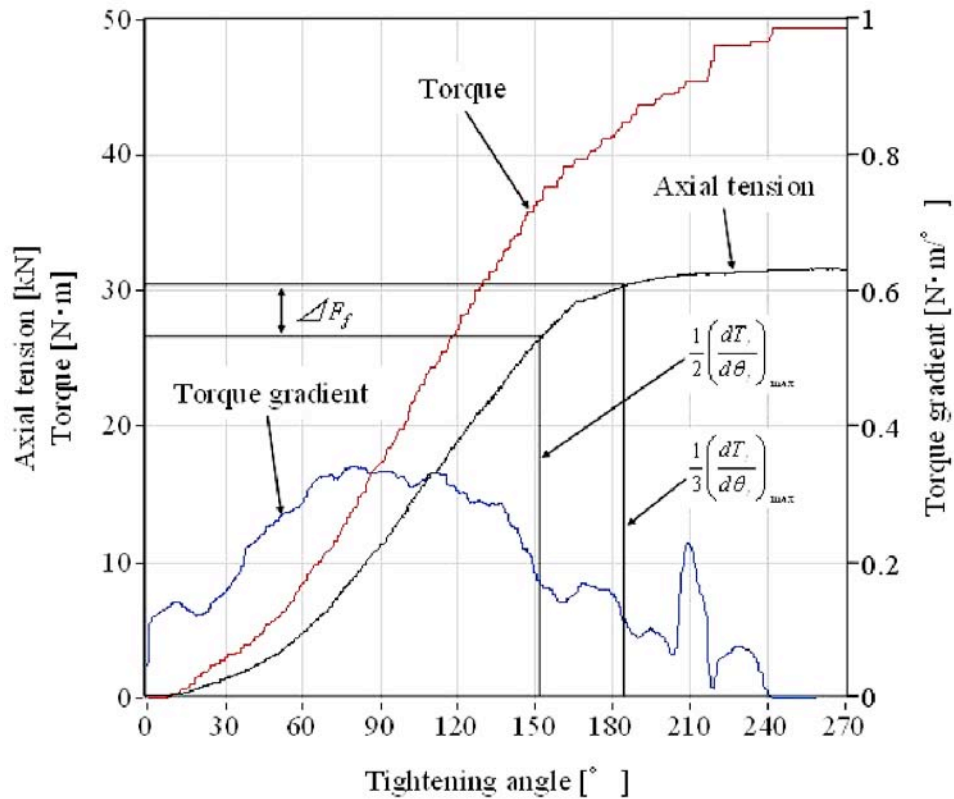


Fig. 4 Tightening range of torque-gradient method.

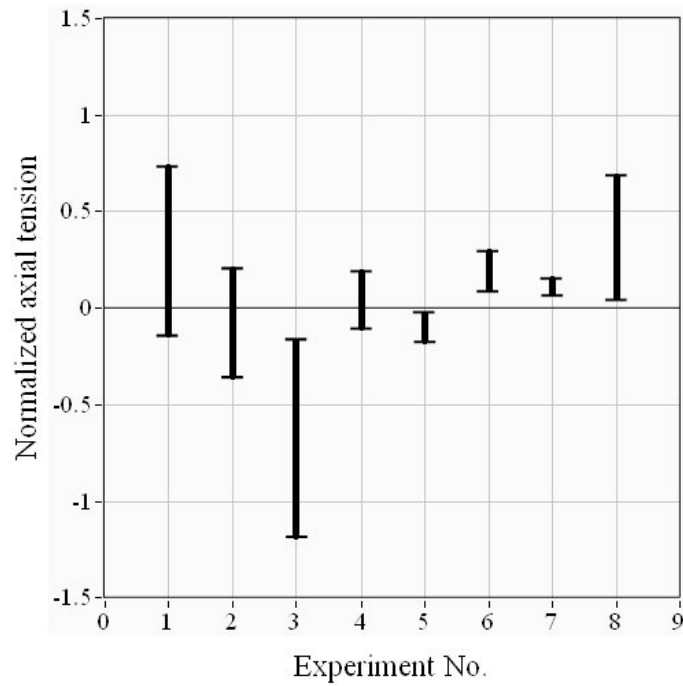


Fig. 5 Accuracy and variations of axial load.

Acoustic Emission Method

Variations of AE event count rates and Ib-values with tightening angle during tightening is shown in Fig. 6. Axial tension vs. tightening angle diagram is also shown.

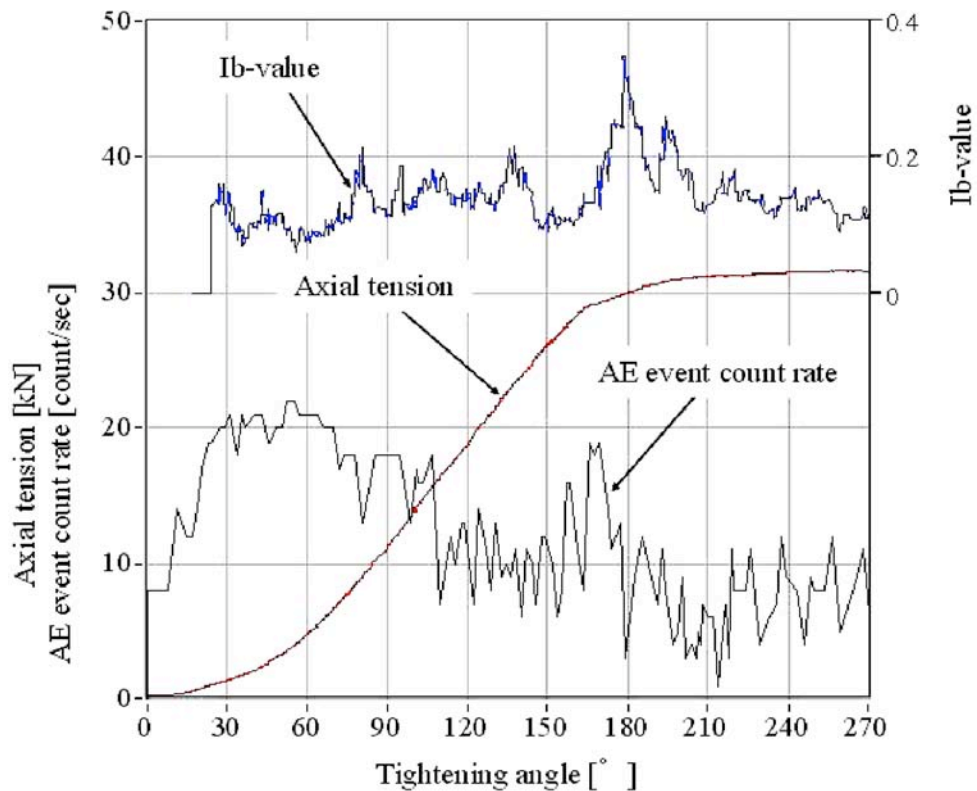


Fig. 6 AE activities during bolt tightening.

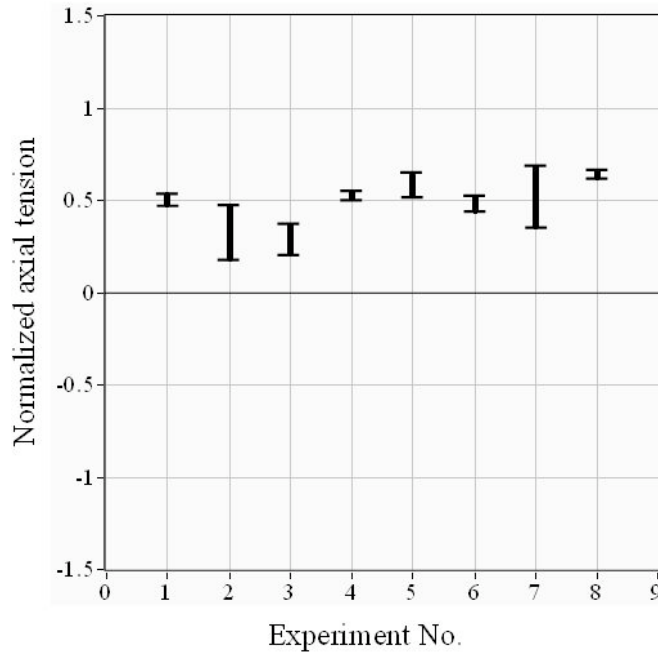


Fig. 7 Accuracy and variations of axial load.

We observed a large number of AE events in the initial stage of the test. These AE signals are noise due to friction on the bearing surfaces. In spite of having measured many noise events, this result clearly shows that AE event count rates have a peak near the yield point and I_b -values reach the peak just beyond the yield point. Therefore, AE signals due to plastic deformation can be monitored even in real tightening conditions as the indicator of yielding. Both AE event count rates and I_b -values will be useful parameters for controlling plastic-region tightening. Figure 7 shows normalized axial load controlled by AE method for eight experiments. Maximum position in each experiment is determined by the peak in I_b -values, and the minimum position by the AE event count rate peak. Variations for the experiments are similar to that of angle control method (when desired angle is set to the maximum value in Eq. (1)). The axial loads of experiments were controlled in the range of 0.2 to 0.7, and the average variation was ± 0.11 . This compares favorably with ± 0.16 and ± 0.30 for angle control and torque-gradient control methods, respectively. This demonstrates that AE method is the most accurate control method for plastic-region tightening among the three examined here. Although roughness of the bearing surfaces differs between the 1st-5th experiments and the 6th-8th experiments, AE method has controlled the axial load appropriately. The experimental results show that AE method is more effective in plastic-region bolt tightening control than the conventional methods.

Development of Plastic-region Bolt Tightening Control System

In the previous section, we showed a feasibility of controlling plastic-region tightening by AE method. However, it is difficult to judge the peak of AE parameters due to plastic deformation automatically by a computer system. Thus, we developed a method in lieu of the peak detection of AE event count rates and I_b -values. The new method relies on the Maharanobis distance and a new index for judgment is defined; i.e., the inverse of Maharanobis distance.

Here, Maharanobis distance of AE signals detected is defined as follows [3, 4]:

$$D = \sqrt{\frac{((x - \bar{x})/\sigma)^T \cdot R^{-1} \cdot ((x - \bar{x})/\sigma)}{p}} \quad (4)$$

Here, $x = [x_{rate}, x_{Ib}]$ is a two-dimensional vector consisting of the AE event count rate and the Ib value of the comparison data. $\bar{x} = [\bar{x}_{rate}, \bar{x}_{Ib}]$ is a two-dimensional vector, consisting of the averages of the reference AE parameters. We used the event count rate and the Ib-value that were detected at a yielding range of $\theta = 164^\circ$ - 180° in the 1st experiment for the angle-control method as the reference AE parameters. p is the number of the dimension and is two for this study. R^{-1} is an inverse matrix of a sample correlation matrix.

The inverse of Maharanobis distance during 4th and 6th experiment is shown in Fig. 8. The axial load-tightening angle diagram is also shown. The inverse of Maharanobis distance became large when the axial load reaches the yield point. This can be used to judge the yield point during tightening. Note that the conditions for 6th experiment tightening are not the same as those for the reference data (plate No. 2 was used); thus the absolute value of the inverse of the Mahalanobis distance is smaller than that of 4th experiment.

Based on the experimental results, the judging criteria of the plastic-region tightening was determined as follows;

- 1) The torque become larger than 20 [N·m].
- 2) Inverse of Maharanobis distance become larger than 5.

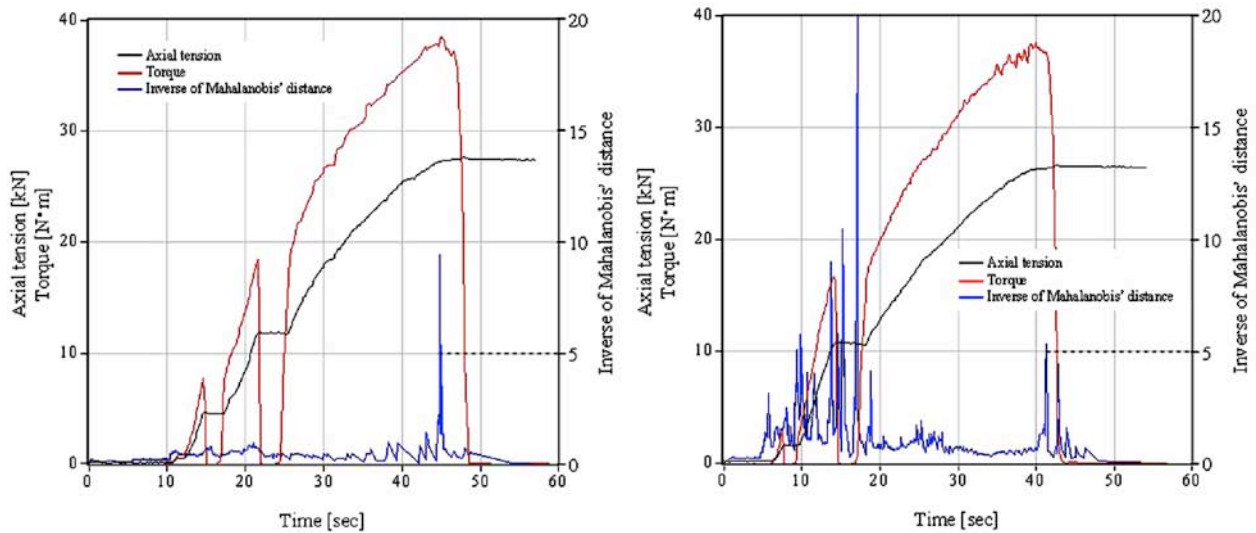


Fig. 8 Inverse of Maharanobis distance during the test (left: 4th experiment, right: 6th experiment).

We developed a control system for plastic-region tightening as shown in Fig. 9. The equipment consists of a digital torque wrench, an AE monitoring device, and an analysis system. AE sensor was attached to the head of a bolt. AE parameters and torque were monitored and analyzed by the developed software. When correct tightening conditions are reached, the LED in the software-screen is turn on. Figure 10 shows the axial load, torque and inverse of Maharanobis distance when tightening is conducted by the developed system. As we used plates in which the surface roughness was not regulated, tightening conditions differed from those of the

reference data. The absolute values of the inverse of the Mahalanobis distances were smaller than those of Fig. 8. Although ratchet mechanism of wrench was used during tightening, appropriate judging was performed by the developed system.

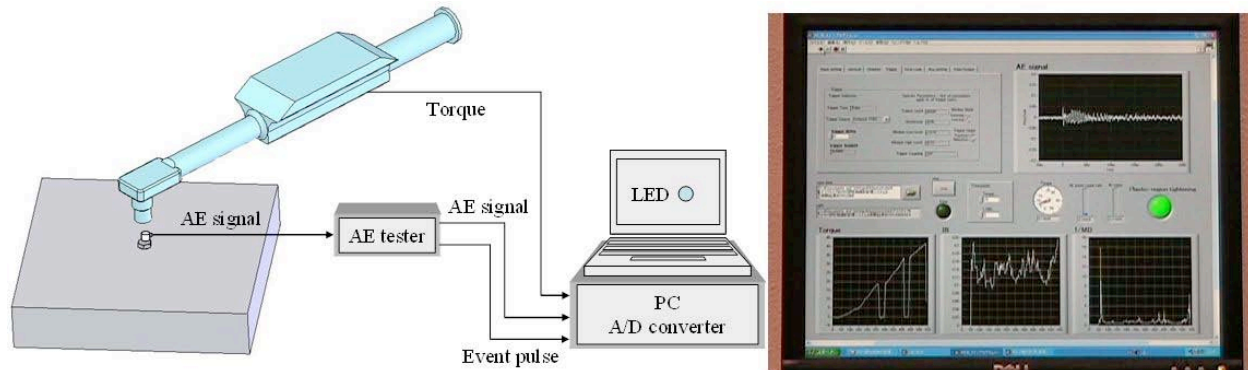


Fig. 9 Developed control system for plastic-region tightening.

Conclusion

Fundamental study of plastic-region bolt-tightening control by AE method was conducted. Results are summarized as follow:

- 1) Tightening test in simulated factory environment was conducted and both the accuracy and variations of tightening were compared with those by conventional control methods. It was found that AE method is superior to conventional methods for plastic-region bolt-tightening control.
- 2) A new control system for plastic-region bolt tightening was developed. A new index for judging the yield point was implemented in the analysis system. The utility of the developed system was demonstrated by conducting tightening tests successfully.

References

1. T. Hattori, Failure analysis and prevention of mechanical, adhesive and welded joints, paper delivered at study group on the accident/failure analysis method of JSME (2002).
2. JIS B 1083-1990 General rules for tightening of threaded fastener.
3. Y. Tanaka and K. Wakimoto, *Methods of Multivariate Statistical Analysis*, 14th ed., Gendai-Sugakusha, (2004).
4. http://en.wikipedia.org/wiki/Mahalanobis_distance

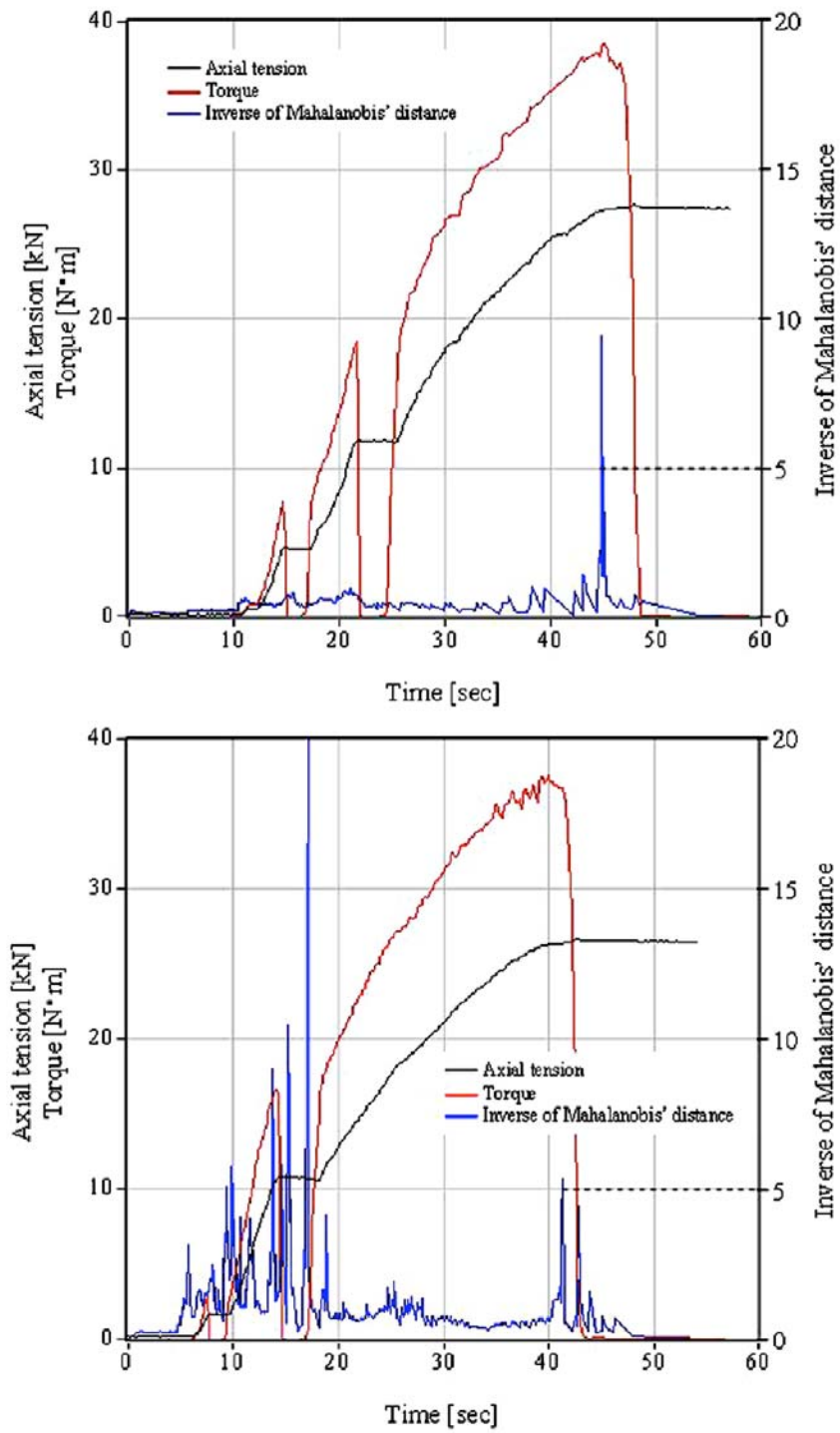


Fig. 10 Axial tension, torque and inverse of Maharanobis distance during the test.

REAL-TIME DENOISING OF AE SIGNALS BY SHORT TIME FOURIER TRANSFORM AND WAVELET TRANSFORM

KAITA ITO and MANABU ENOKI

Department of Materials Engineering, The University of Tokyo,
7-3-1 Hongo, Bunkyo, Tokyo 113-8656, Japan

Abstract

Laser AE method is a non-contact AE detection technique, which utilizes laser interferometer as sensor. This method is less subjected to environmental difficulties and can be adaptive for wider target than conventional PZT sensors. However, laser AE method has to improve its sensitivity because the noise level of laser interferometer is higher than PZT sensors. In this study, a method to reduce the noise component of output signal of laser interferometer is investigated. Output signals from laser interferometer were recorded continuously with 10-MHz sampling frequency and transformed into spectrogram (time-frequency-magnitude data) by time-frequency analysis method. After noise component in this spectrogram is cut, inverse transform is applied to obtain clear AE signals in time domain. Whole signal processing can be done in real time. Simulated AE detection test was conducted to confirm the effectiveness of this noise reduction scheme. In the result, weak AE signals buried in noise could be recovered and the improvement of sensitivity of laser AE system was demonstrated. Current real-time processing can extract about 100 events/s.

Keywords: Noise reduction, continuous waveform recording, short-time Fourier transform, wavelet transform

Introduction

Conventional PZT AE sensors are difficult to use under some of severe environments. For example, conventional AE sensor needs waveguide or some of heat avoidance mechanism if the testing temperature is higher than the Curie temperature of PZT. In another case, PZT sensors often cannot be attached to the target material during manufacturing process. Therefore, laser AE method [1] has been developed to realize a direct AE measurement under such severe environments by non-contact detection of AE with laser interferometer [2, 3]. However, laser AE method has to improve the sensitivity because the noise component of output signals from a laser interferometer is larger than the conventional PZT sensors. Frequency filtering is one of the most important techniques to improve the sensitivity. However, conventional analog filter is not so effective for the output waveform of laser interferometer because the noise component is closed to the frequency range of effective signal component. Digital signal processing (DSP) system can do more powerful and flexible noise reduction than analog system. In this study, a high performance method for noise reduction of the output signal from laser interferometer was investigated. The waveform from laser interferometer was continuously sampled and once transformed into spectrogram by time-frequency analysis methods. Effective noise reduction process was examined using this spectrogram.

Analytical Method

Time-Frequency Analysis

Time-frequency analysis is a method to convert a waveform (time-voltage data) into a spectrogram (time-frequency-magnitude data). In this study, short time Fourier transform (STFT) and wavelet transform (WT) were used as time-frequency analysis techniques. In STFT method, a long waveform is split into short sections and each section is processed by Fourier transform using the following formula:

$$F(\tau, f) = \int_{-\infty}^{+\infty} s(t)w(t - \tau)e^{-2\pi if} dt, \quad (1)$$

where $s(t)$ is the sectioned waveform, $w(t - \tau)$ is window function, f is frequency and $F(\tau, f)$ is the result of STFT. Meanwhile, in wavelet transform method, the original signal is expressed as summation of scaling and shift of certain short waveform called “mother wavelet” as

$$W(a, b) = \int_{-\infty}^{+\infty} s(t)h_{a,b}^*(t)dt, \quad (2)$$

where $h(t)$ is mother wavelet, a is the scaling factor, b is the shifting factor and $W(a, b)$ is the result of WT. Fourier transform loses the time information in the transform section because it supposes ordinary wave. Then, if the section length becomes shorter, the time resolution of STFT improves, but the frequency resolution degrades. Thus, the overall resolution of STFT cannot be so high by this trade-off relationship. Meanwhile, wavelet transform can get high resolution, but the calculation amount is larger than STFT, so wavelet transform of very long continuous waveform is not realistic. Thus, less-intensive calculation and low-resolution STFT is better for rough estimation of long waveform, and intensive calculation and high-resolution wavelet transform is better for strict estimation of short waveform. Tactful use of both methods is important.

Noise reduction

Figure 1 shows a spectrogram of output waveform of laser interferometer and contains two main components as discrete AE signal component and continuous noise component. The noise appeared in a broad frequency range between about 200 kHz and 500 kHz, and this range partially overlaps with the effective signal component. Furthermore, often the noise component is larger than the effective signal component in laser AE methods. In such a waveform, conventional frequency filter which utilizes moving average or pulse reaction is ineffective. In this study, pruning method and soft-thresholding methods are adopted as noise reduction process. This combination of the two processes was already reported in voice processing and ultrasonic testing area [4]. At first the spectrogram of recorded waveform is filtered by pruning method:

$$W_2(f, t) = \begin{cases} 0 & \text{for } f < f_1, f > f_2, \\ W_1(f, t) & \text{for } f_1 < f < f_2 \end{cases}, \quad (3)$$

where W_1 is waveform before processing, W_2 is waveform after the processing, f is frequency, t is time, f_1 and f_2 is cut-off frequency. Pruning method works as frequency filter and cuts off sharply. After that, remained white noise component was cut by soft-thresholding method:

$$W_2(f, t) = \begin{cases} 0 & \text{for } |W_1(f, t)| < \lambda \\ |W_1(f, t) - \lambda| & \text{for } |W_1(f, t)| \geq \lambda \end{cases}, \quad (4)$$

where λ is the threshold of noise and signal. Originally, these methods are used for wavelet transform result; however, it can be used for STFT result too. After these noise reduction

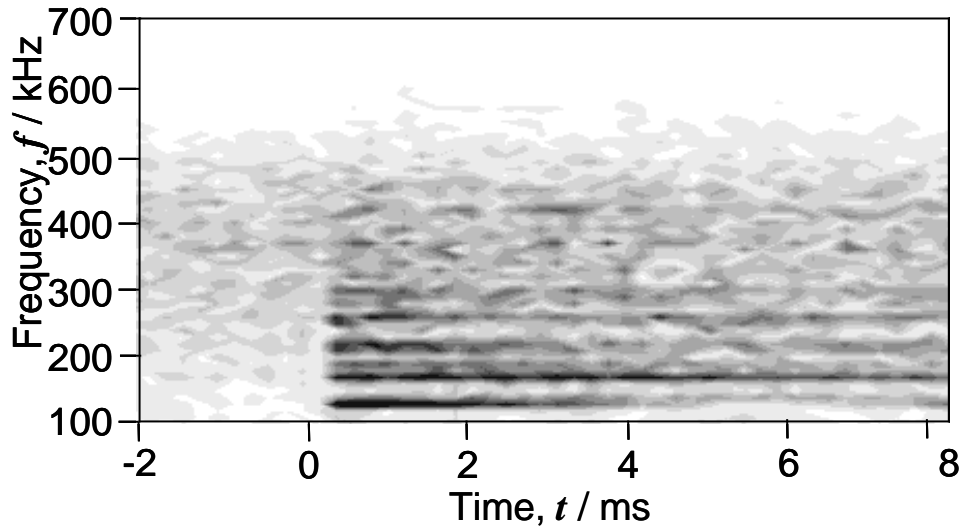


Fig. 1 Sample spectrogram of output signal of laser interferometer. processes, the spectrogram was reconverted into waveform by inverse STFT or inverse WT.

Real time signal processing

The CWM system basically can do a real-time noise reduction process based on the above theories by a combination of high-speed STFT and high-resolution WT. At first, the whole recorded waveform is converted into spectrogram by STFT. The noise component in the spectrogram is reduced by pruning method and soft-thresholding method. Then, the processed spectrogram is reverted by inverse-STFT with Hanning window function to connect smoothly at the connection points of inverse-STFT period. After that, AE events are extracted from the noise reduced time domain data. However, the time resolution of this waveform may not be enough because this waveform is processed by STFT-based method. Therefore, a waveform with a few milliseconds length is clipped out from as-recorded waveform around AE event and processed again by WT-based method to get precise time information. The WT-based method is the same manner as the STFT-based method.

In particular, the current CWM system with two 2.2 GHz processor (Athlon64 X2 Processor, AMD Inc.) can process 2-channel AE waveforms of 10-MHz sampling in real time by STFT-based method and can extract about 100 events/s by WT-based method.

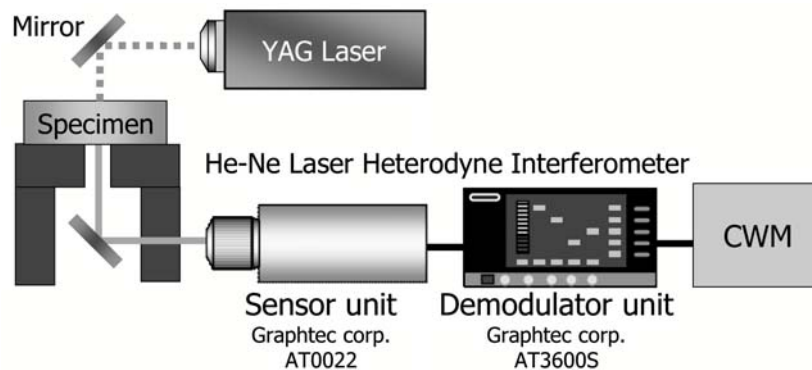


Fig. 2 Experimental equipments of simulated AE signal detection.

Experimental Procedures

Simulated AE detection test was conducted to confirm the above noise reduction method. Figure 2 shows the experimental equipment. Specimen was SUS304 disk of 30 mm in diameter and 5 mm in thickness. Simulated AE was generated by thermal stress of pulse YAG laser system (Tempest-20, New Wave Research, Inc.), measured by He-Ne laser heterodyne interferometer (AT3600S and AT0022, Graphtec Corp.) and analyzed by our CWM system [5]. The output power of YAG laser was 40 mJ/pulse or 20 mJ/pulse and pulse length was about 4 ns. The maximum detectable frequency of the laser interferometer was about 400 kHz. CWM sampled the output signal of AT3600S continuously during the whole test with 10-MHz frequency and 12-bit resolution. The noise level was about 30 mV in RMS.

Results and Discussion

Figure 3 shows the result of 40-mJ pulse. The pulse was strong enough to register as an AE event from as-recorded waveform (Fig. 3(a)). The spectrogram (Fig. 3(c)) of this waveform also contained strong signal component and weak noise component between 200 kHz and 500 kHz. In order to reduce this noise component, only a frequency range between 100 kHz and 250 kHz remained after applying pruning method. The white noise was reduced by soft-thresholding method with 6% of maximum magnitude as the threshold value (Fig. 3(d)). A clear waveform (Fig. 3(b)) was obtained by inverse STFT in comparison to the original waveform.

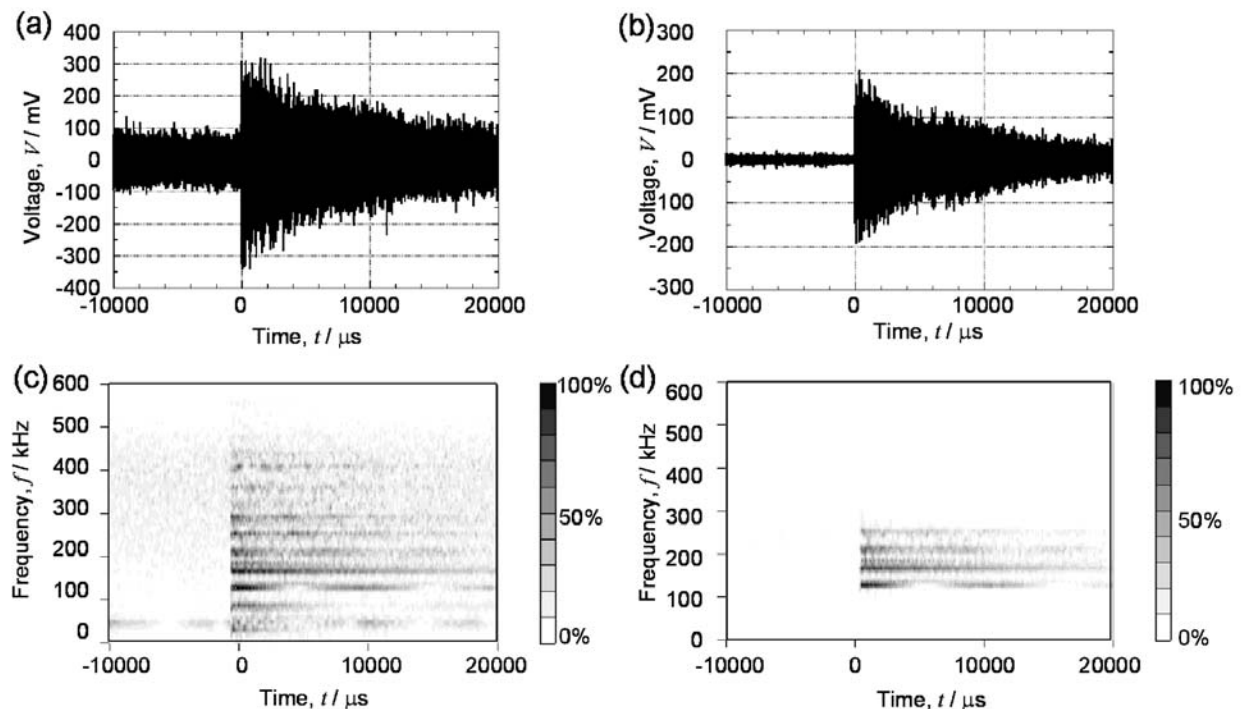


Fig. 3 Noise reduction of simulated AE signal by 40-mJ pulse; (a) recorded waveform, (b) processed waveform, (c) STFT result of recorded waveform, (d) spectrogram after noise reduction.

Figure 4 shows the result of 20-mJ pulse. Pulse was very weak and AE event was not visible in as-recorded waveform (Fig. 4(a)). However, a weak signal component was discernible in

the STFT result (Fig. 4(b)). Therefore, only a frequency range between 75 kHz and 175 kHz was remained by pruning method, and the white noise was reduced by soft-thresholding method with 6% of maximum magnitude as the threshold value. The processed waveform (Fig. 4(c)) could be detected as AE event.

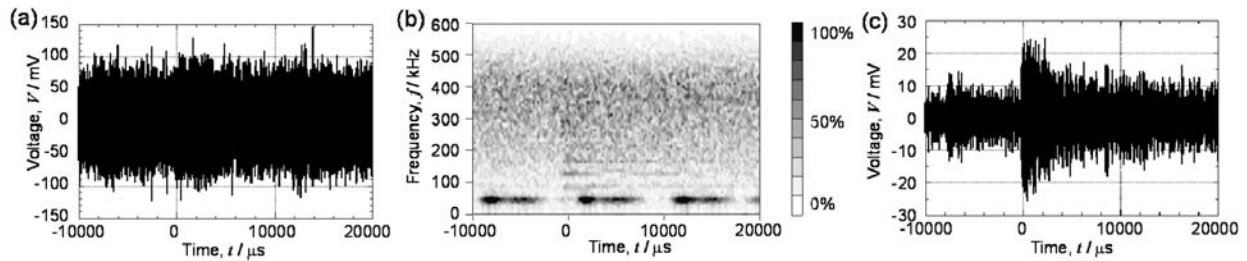


Fig. 4 Noise reduction of simulated AE signal by 20mJ pulse; (a) recorded waveform, (b) STFT result of recorded waveform, (c) noise reduced waveform.

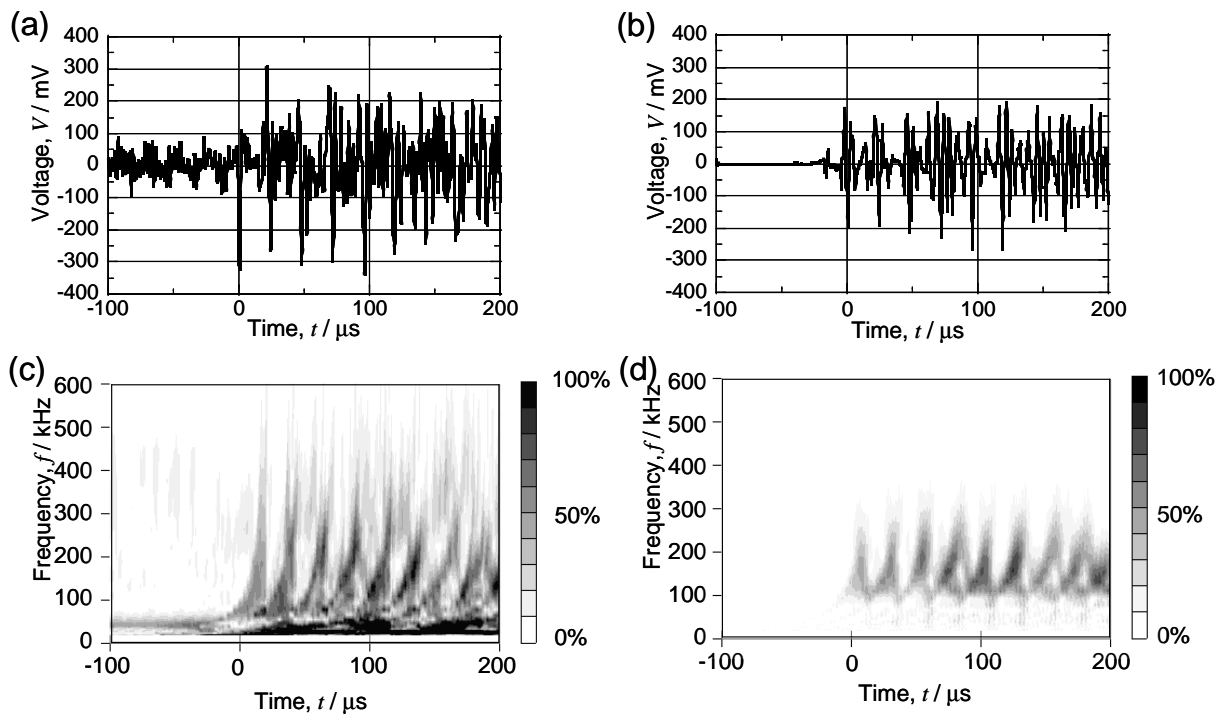


Fig. 5 Noise reduction of simulated AE signal by 40-mJ pulse; (a) recorded waveform, (b) noise reduced waveform, (c) WT result of recorded waveform, (d) spectrogram after noise reduction.

The noise-reduction processing was also conducted with WT. Figures 5 and 6 show the waveform and spectrogram of the same AE event in Fig. 3. The noise component below 100 kHz was relatively strong in the spectrogram of the as-recorded waveform, but this noise can be cut by pruning method (Fig. 5(d)). The noise-reduced waveform (Fig. 5(b)) is clear in the time domain and the major characteristics of waveform are kept as the original waveform. Figure 6 shows the comparison of a rising waveform by the STFT-based and WT-based noise-reduction processes. WT shows sharper rising waveform than STFT. This good time resolution of WT is effective for the location of AE events.

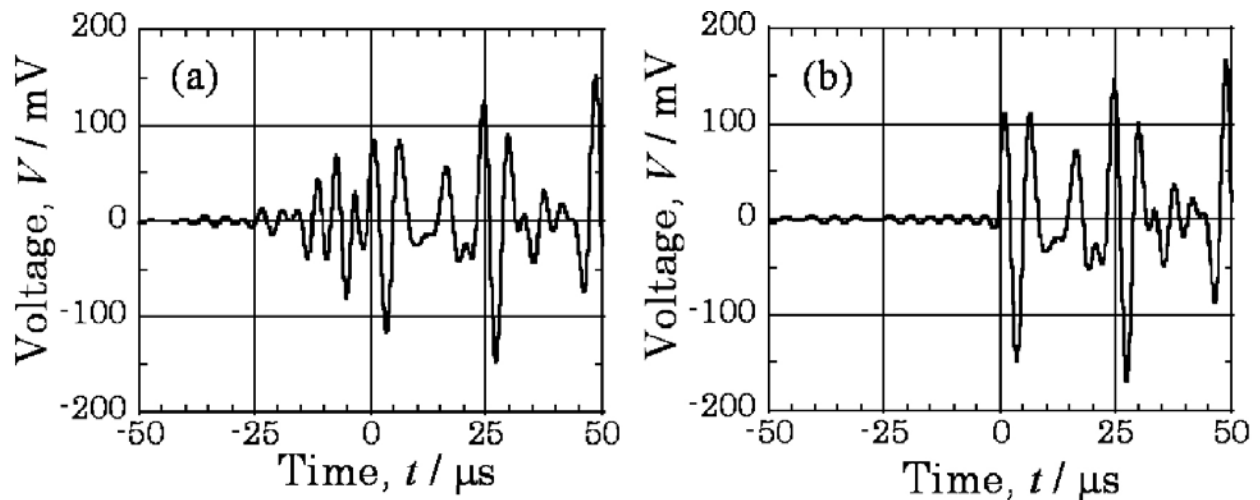


Fig. 6 Results of (a) STFT-based and (b) WT-based noise reduction process.

Conclusion

A noise-reduction process to improve the sensitivity of laser AE method was investigated. The output signal of laser interferometer was continuously recorded and the recorded waveform was processed to reduce noise component by time-frequency analysis and combination of pruning method and soft-thresholding method. Simulated AE detection test was conducted to confirm the effectiveness of the noise reduction process. Weak AE signals buried in noise can be recovered and the improvement of sensitivity of laser AE system was demonstrated. Current CWM system can process 2-channel AE waveforms of 10-MHz sampling in real time, extracting about 100 events/s.

References

1. M. Enoki, M. Watanabe, P. Chivavibul and T. Kishi, *Sci. Technol. Adv. Mater.*, **1**, 2000, 157-165.
2. M. Watanabe, M. Enoki and T. Kishi, *Mater. Sci. Eng. A*, **359**, 2003, 368-374.
3. S. Nishinoiri, M. Enoki, T. Mochizuki and H. Asanuma, *Mater. Trans.*, **45**, 2004, 257-263.
4. A. Abbate, S. C. Schroeder and P. Das, *IEEE Trans. on Ultrasonics, Ferroelectrics, and Frequency Control*, **44**, 1997, 14-26.
5. K. Ito and M. Enoki, *Mater. Trans.*, **48**, 2007, 1221-1226.

MONITORING THE EVOLUTION OF INDIVIDUAL AE SOURCES IN CYCLICALLY LOADED FRP COMPOSITES

RUNAR UNNTHORSSON, THOMAS P. RUNARSSON and MAGNUS T. JONSSON

Department of Mechanical & Industrial Engineering, University of Iceland, Reykjavik, Iceland

Abstract

An experimental methodology for tracking the locations of multiple individual sources of acoustic emission (AE), in cyclically loaded fiber reinforced polymers (FRP), is presented. The approach is developed, discussed, and demonstrated using AE data measured during the fatigue testing of an assembled CFRP prosthetic foot. The results are presented as 2D images where paths show evolution of AE sources. From these paths, the locations of the AE sources in each fatigue cycle can be tracked. Hence, this methodology makes it possible to monitor damage growth and to identify AE sources. The technique forms the basis for further study which otherwise would be difficult to accomplish due to the overwhelming number of sources with similar characteristics. As a result a useful tool for monitoring and evaluating the health of a composite is developed.

Keywords: Source tracking, carbon fiber, composites, fatigue

Introduction

Carbon Fiber Reinforced Polymer (CFRP) composites have many interesting properties such as high strength-to-weight ratio and excellent corrosion and fatigue tolerance. Despite this, damage in composites develops early in service [1-4] and continues to accumulate throughout the service life. The fatigue tolerance can be attributed to resistance to inhomogeneous damage growth, which is a property of highly inhomogeneous materials [3]. The high damage tolerance of composites means that composites are able to meet their in-service requirements for prolonged period of time while damage accumulates and grows. Consequently, there is a definite need to detect, monitor and evaluate individual damages. A system, which enables successful diagnosis and prognosis, can possibly be used to extend the service life and to prevent catastrophic failure.

The type and the location of damages are random and the fatigue behavior changes with different lamina sequences, geometry and loading conditions. For these reasons, and the fact that testing of composites shows a high experimental scatter [3, 5], fatigue modeling of composites is generally a formidable task. Existing fatigue models are based on certain materials, laminate sequences and loading conditions [1, 6, 7]. Due to these restrictions, the models cannot generally be extended to composites, which have different lay-up or are used under different loading conditions. Under repetitive or cyclic loading conditions, AE is emitted from both damage progression and from cumulated damage; i.e., rubbing of delaminated surfaces. As a result, multiple AE transients with varying amplitude, duration, and frequency are emitted in each cycle and many are emitted simultaneously. Furthermore, the values of the AE signal features from cumulated damage usually fall in the same range as the ones from damage growth [4, 8]. Waveform based parameters such as ring down count, amplitude, and energy have been used for the detection of damage; i.e., delamination, matrix cracking, debonding, fiber cracking, and fiber pull-out [8-12]. For this reason, an intuitive approach to monitoring is to keep track of one or more waveform parameters, which characterize the AE from the source of interest. Each parameter will follow a

probability distribution, which changes when the source (damage) changes. Because of the parameter fluctuations and the high rate of AE with similar parameter values, waveform parameters alone are not sufficient for distinguishing between sources. Additional indication is therefore needed. If each source emits an AE at the same load level in each cycle, then the load level of AE occurrence is sufficient to distinguish between the sources. However, as the delamination cracks grow, the load level of occurrence changes.

The methodology presented in this paper uses both the time of occurrence and the AE amplitude in each cycle for monitoring the evolution of many individual AE sources simultaneously. From the resulting images, one can locate interesting AE sources for further study, or for tracking, which otherwise would be difficult to accomplish due to the overwhelming number of sources with similar characteristics.

The remainder of the paper is organized as follows. In section 2 the proposed methodology is developed and in section 3, it is demonstrated and discussed by applying it to AE data, which has been studied before by the authors in [13]. Finally, a conclusion of the work is presented.

Methodology

This section describes the proposed experimental methodology, which is a graphical tool developed for tracking the locations of individual AE sources. It was designed for monitoring objects subjected to repetitive loading conditions. By using the images generated by the methodology, one can monitor the evolution of individual AE sources and locate interesting AE signals for further study. Figure 1 shows a schematic overview of the methodology.

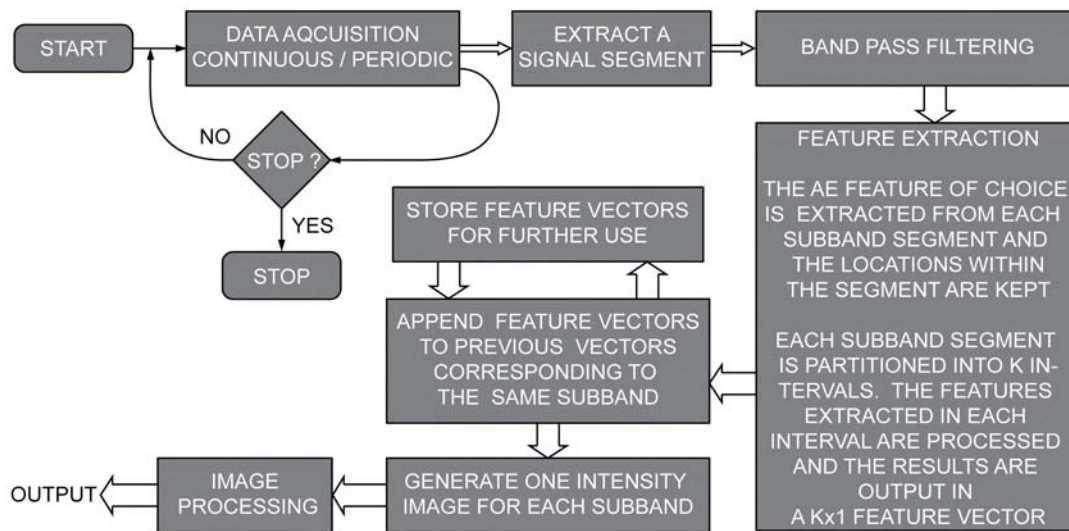


Fig. 1. Schematic overview of the proposed experimental methodology.

The first step of the approach is to split the AE signal into segments of length equal to the period of one cycle. If the AE signal is not continuously acquired, i.e., measured periodically, then care must be taken to ensure that the segments all start at the same phase of each cycle. A reference signal, such as displacement or load, can be measured simultaneously and used for segmenting. In the next step, each segment is bandpass filtered into N subbands. The user selects

the type of filtering, number of subbands (N), and the individual subband bandwidths. Figure 2 illustrates these two steps.

In the third step, a feature vector is generated from each subband segment. Each feature vector is generated in two stages. In the first stage, the AE feature of interest is extracted from the segment. Both the positions within the segment and the feature values are logged.

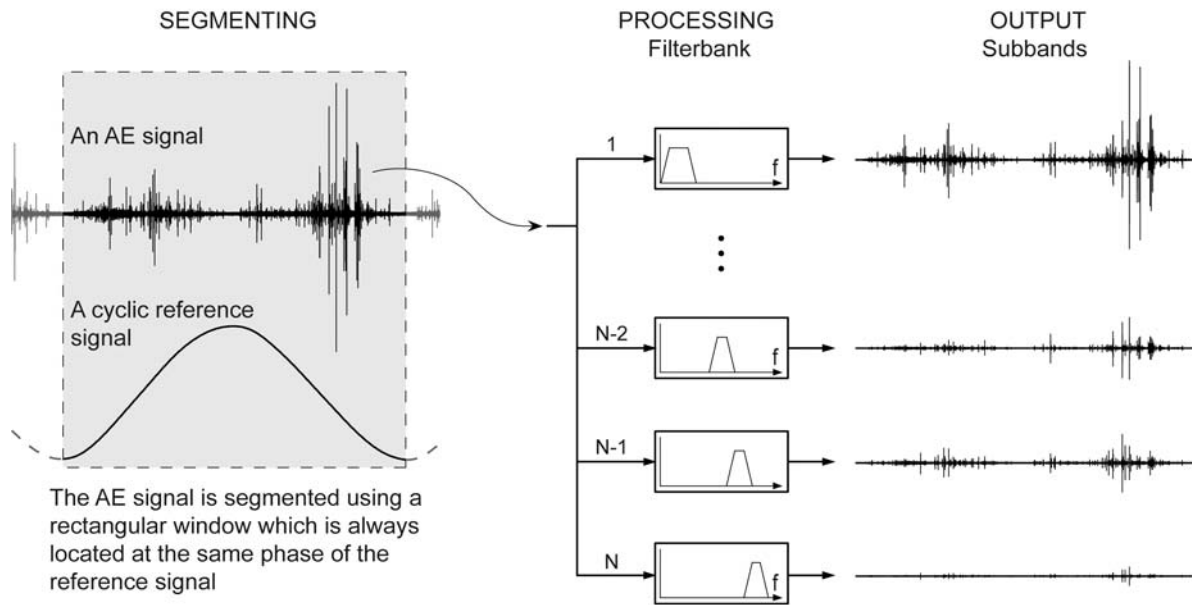


Fig. 2. The AE signal is segmented and each segment is split into N subbands.

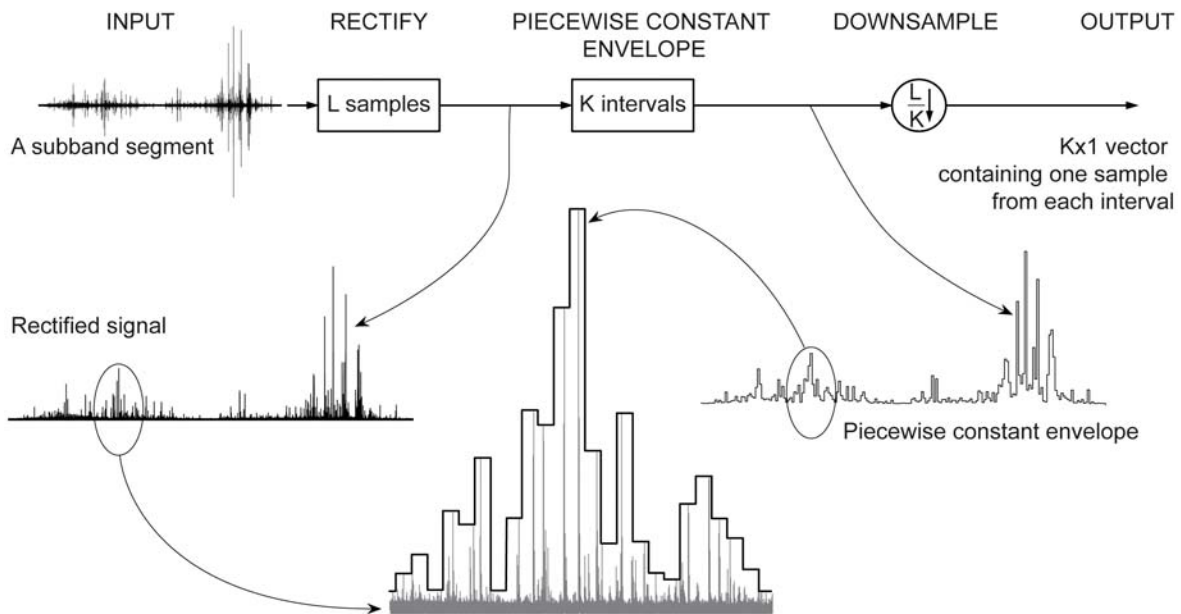


Fig. 3. For each subband segment, new feature vector is computed by first rectifying the signal, then computing a piecewise constant envelope, and finally down sampling the envelope.

In the second stage, the segment is partitioned into K intervals and the features extracted within each interval are processed. The user selects the number of intervals, K . The results from the processing are output as a feature vector ($K \times 1$). Depending on the processing in the second stage, the first stage can in some cases be omitted; i.e., when the energy in each interval is computed, or the maximum amplitude. In order to illustrate how a feature vector is generated, the maximum amplitude in each interval was chosen. Figure 3 explains the procedure. Each subband segment is first rectified and partitioned into K intervals and then the maximum amplitude within the interval is found; i.e., a piecewise constant envelope is generated. The envelope is then down-sampled by a factor L/K , where L is the length of the subband segment. The resulting feature vector contains one sample from each interval of the envelope. The amplitude filtering and down-sampling process extracts the amplitude of the strongest transient in each interval. Hence, the tracking capability is limited by this filtering. However, since the filtering is performed in all the subbands the tracking ability is improved because the AE energy from different sources often resides in different subbands. The down sampling also helps keep the data manageable since the number of samples acquired during one fatigue cycle can be high.

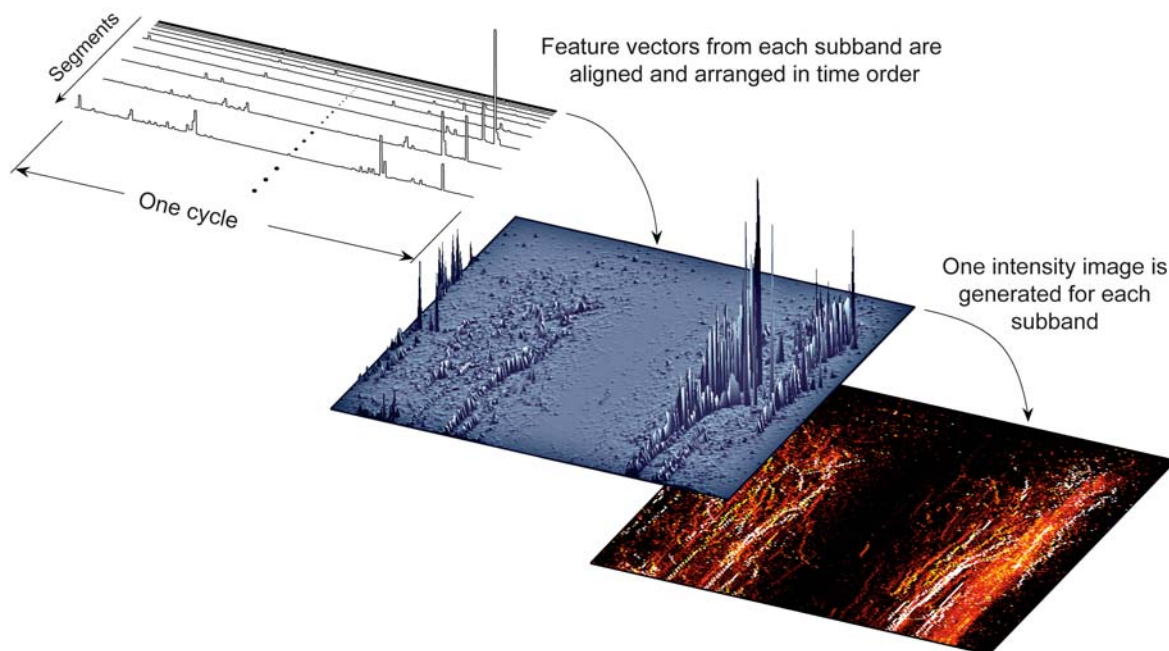


Fig. 4. For each subband, new feature vectors are appended to previous vectors and an intensity image is generated.

In the fourth step, each new feature vector is appended to previous vectors from the same subband and an intensity image is generated. Figure 4 illustrates this procedure. In the fifth and the last step, image processing is performed in order to enhance the images and to make the paths more prominent.

Experimental Procedures and Results

In order to demonstrate the methodology outlined above, it was applied to an experimental data measured during fatigue testing of an assembled CFRP prosthetic foot made by Össur hf. The foot was placed in the test machine and two actuators were used to apply amplitude controlled cyclic loading at 1 Hz. One actuator applied load to the forefoot and the other to the heel. The foot was cyclically tested until a 10% change in displacement, with respect to initial value,

was observed for either actuator. Figure 5 shows a schematic representation of the experimental setup.

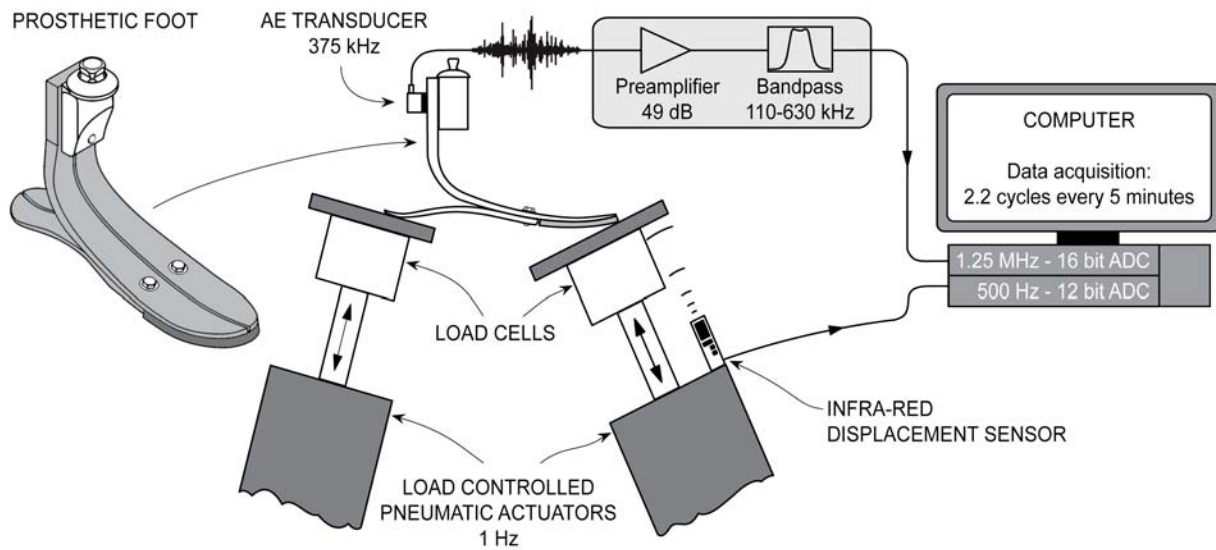


Fig. 5. A schematic representation of the experimental setup.

The AE signal and the position of the forefoot's actuator were measured simultaneously for 2.2 seconds every 5 minutes throughout the test. The sampling rates were set to 1.25 MHz and 500 Hz, respectively, for the AE and the position measurements. The L-Gage Q50 infra-red displacement sensor from Banner Engineering was used for the position measurements of the actuator loading the forefoot. For measuring the AE signals, the VS375-M AE transducer and the AEP3 preamplifier from Vallen Systeme GmbH were used. The preamplifier was equipped with 110-kHz high-pass and 630-kHz low-pass filters. The gain was set to 49 dB. The output from the preamplifier was fed to a 16-bit A/D converter for a full waveform digitization. For further information about the experimental setup the reader is referred to [13]. The position measurements were used for reference when the AE signal was segmented. Each AE measurement was trimmed so that it represented exactly one fatigue cycle, starting at the lowest position of the forefoot's actuator. Elliptical bandpass filters, each with 33-kHz bandwidth, were used to decompose the AE signal above 100 kHz into subbands. The bandpass filtering was performed using a phaseless filtering in order to avoid phase delay [14].

Each subband segment was divided into $K = 200$ intervals before computing the piecewise constant envelope. Figure 6 shows the resulting intensity image for the 133-166 kHz subband and also the evolution of the AE energy and the AE hit count from each segment. Intensity images are a convenient way to visualize the range of data; i.e., the higher the amplitude, the brighter the image pixels. The energy and the hit counts were computed from the unfiltered AE signal. The AE energy is the sum of the signal's values squared. The AE hits were determined using a short-term Fourier transform-based approach [13]. By comparing the evolution of the energy, and the AE hit count, to the subband images, one can gain better understanding of the changes, which are occurring in the material. An example is the energy spike, which occurred at segment no. 130. This spike was due to the formation of a new damage. After this spike, the signal's energy provided no further information about the damage evolution. However, from the subband images, the beginning of two new paths can be observed at segment 130 and their

evolution can be monitored up to segment no. 239 where an apparent increase in AE amplitude can be seen. At segment 239, a half of the foot delaminated but the 10% displacement failure criterion was not met.

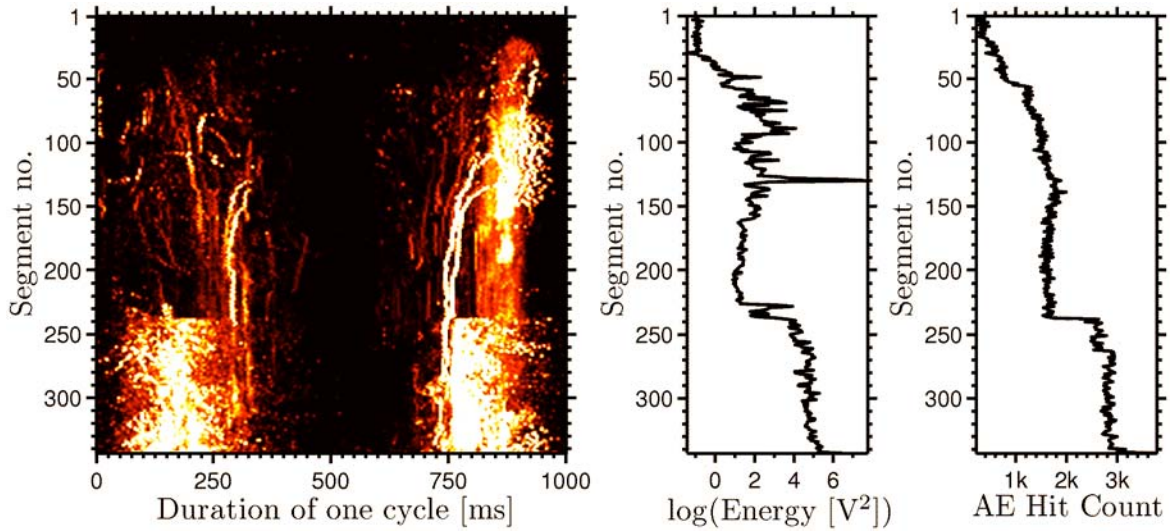


Fig. 6. The resulting images for the 133-166 kHz subband.

Figure 7 shows the resulting images for the 266-300 kHz (left) and 366-400 kHz (right) subbands. The evolution of some of the sources is present in both images; i.e., these sources emit AE signals, which lie in both subbands. The evolution of other sources is present in either image and not matched in the other. By studying different subbands, one can possibly detect band-limited AE and distinguish between two damages that emit AE signals at the same time but are evolving in different directions, as can be seen by comparing the circled paths in the left and right images of Fig. 7.

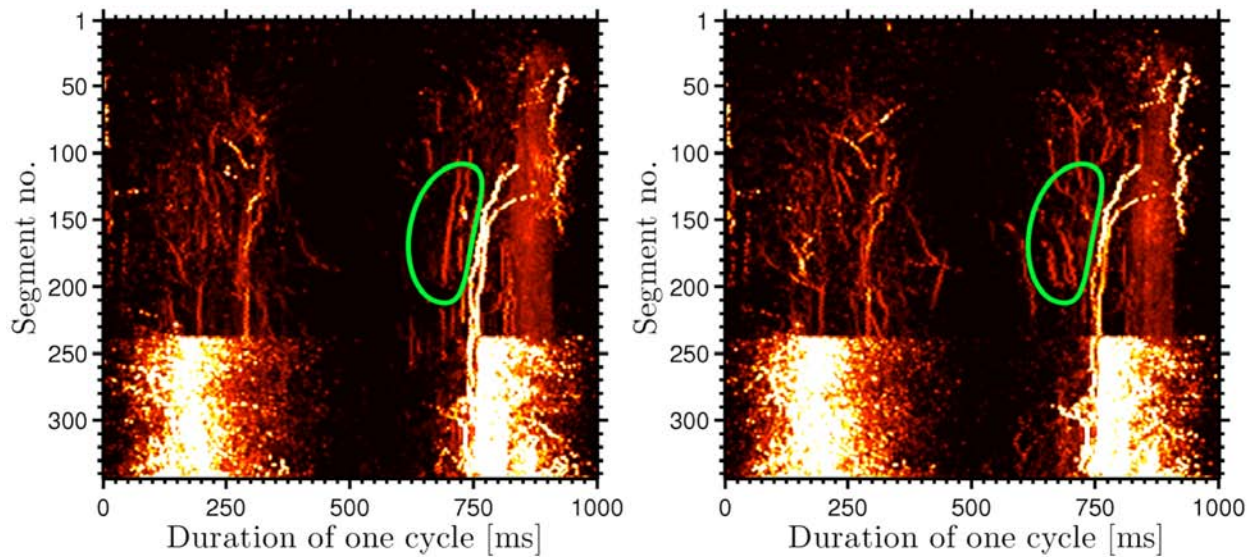


Fig. 7. The resulting images for the 266-300 kHz (left) and 366-400 kHz (right) subbands.

Conclusions

An experimental methodology for tracking the evolution of individual AE sources while monitoring cyclically loaded objects was presented. The decomposition of the AE signal into subbands enables the detection of band limited sources which otherwise would possibly go undetected. The methodology is a graphical tool, which aids with the monitoring and interpretation of AE data and should be a welcome addition to the toolbox of any engineer involved in AE monitoring of cyclically loaded objects.

Acknowledgements

The authors gratefully acknowledge Össur hf. for providing samples and access to their testing facilities. The work of the first author was supported by grants from: The RANNIS Research Fund, and the University of Iceland Research Fund.

References

1. J. Degrieck and W.V. Paepegem, *Applied Mechanics Reviews*, **54**, 2001, 279-300.
2. W. Van Paepegem and J. Degrieck, *International Journal of Fatigue*, **24**, 2002, 747-762.
3. H.G. Halverson, W.A. Curtin, and K.L. Reifsnider, *International Journal of Fatigue*, **19**, 1997, 369-377.
4. Y.A. Dzenis and J. Qian, *International Journal of Solids and Structures*, **38**, 2001, 1831-1854.
5. J. Baram, *Experimental Mechanics*, **33**, 1993, 189-194.
6. K.P. Dyer and D.H. Isaac, *Composites Part B: Engineering*, **29**, 1998, 725-733.
7. M. Knops and C. Bogle, *Composites Science and Technology*, **66**, 2006, 616-625.
8. D. Tsamtsakis, M. Wevers, and P. De Meester, *Journal of Reinforced Plastics and Composites*, **17**, 1998, 1185-1201.
9. M. Giordano, A. Calabro, C. Esposito, A. D'Amore, and L. Nicolais, *Composites Science and Technology*, **58**, 1998, 1923-1928.
10. M. Wevers, *NDT and E International*, **30**, 1997, 99-106.
11. H. Nayeb-Hashemi, P. Kasomino, and N. Saniei, *Journal of Nondestructive Evaluation*, **18**, 1999, 127-137.
12. E.R. Green, *Journal of Nondestructive Evaluation*, **17**, 1998, 117-127.
13. R. Unnthorsson, T.P. Runarsson, and M.T. Jonsson, *International Journal of Fatigue*, doi:10.1016/j.ijfatigue.2007.02.024, 2007.
14. C.A. Mercer. Prosig Inc., 2001.

ON USING AE-HIT PATTERNS FOR MONITORING CYCLICALLY LOADED CFRP

RUNAR UNNTHORSSON, THOMAS P. RUNARSSON and MAGNUS T. JONSSON
Department of Mechanical & Industrial Engineering, University of Iceland, Reykjavik, Iceland

Abstract

This paper presents the results of a study where AE-hit patterns are used for monitoring the location of AE sources. The AE-hit patterns contain information about the spacing between hits and other additional information about the hits, e.g., the amplitude. A methodology for detecting AE hits and coding the information is developed. A procedure for searching for AE-hit patterns in the coded representation and for processing the search results is also presented. The approach is demonstrated using experimental AE data acquired during fatigue cyclic testing of an assembled CFRP prosthetic foot. The results of this study show that the AE-hit patterns can be used to track the evolution of AE sources. Additionally, the results show that by adding the peak amplitude of AE hits to the hit patterns, the tracking of AE sources is improved significantly.

Keywords: Source tracking, hit patterns, carbon fiber, composites, fatigue

Introduction

The research idea behind this study is to investigate whether damages in carbon fiber-reinforced polymers (CFRP) generate characteristic sequences of AE hits, which could be used to monitor damage progression. In [1] the authors used the peak hit amplitude for tracking the locations of evolving AE sources within fatigue cycles. The purpose of this study was to evaluate whether better results could be obtained by monitoring the temporal AE-hit patterns.

One of the fundamental elements of music is rhythm. Rhythm can be determined by the relation between note accents (attack) and the rests between notes [2]. The term can be used to refer to either a repetitive pulse, or a beat, which is repeated throughout the music or a temporal pattern of pulses. The modeling and the interpretation of temporal patterns are of interest to people working in different disciplines. In the field of music information retrieval rhythm-based features have been extracted from audio and used for classifying music styles [3], i.e., blues, disco, polka, etc. In the field of computational neuroscience, patterns in spike trains are studied in order to understand the “language of the brain”[4].

The first step of working with temporal patterns is to determine the pulses. Once they have been determined, the rest, or duration, between them can also be determined and the results can be coded into features and processed. The detection of pulses starts usually with the processing of the signal in order to make the detection more accurate. The resulting signal is called a detection function and it can be in any domain of interest, e.g., time domain, frequency domain, and time-scale/time-frequency domain. An example of a detection function is one made using a model called a *rhythm track* [5]. The rhythm-track model is based on the assumption that the audio can be considered to be a random signal and the signal’s energy increases significantly when a pulse occurs. The rhythm track can be created using several methods; e.g., by using the signal’s instantaneous energy in the time- and the frequency domains [5, 6]. The pulses are detected from the detection function. The peaks in the detection function do not all correspond to

the onset of pulses, consequently, several approaches have been used to identify those that do; e.g., by using fixed threshold and peak-picking [6]. The approach taken here uses the signal's envelope as the detection function and hits are determined by peak-picking.

Interpreting hit patterns is a non-trivial task. Similar patterns can be generated differently, e.g., closely spaced hits can either be due to rapid AE release or due to multiple AE simultaneously emitted from the numerous AE sources in the material. In addition, the signal can be affected by processes, such as reflection and attenuation. The attenuation can be caused by geometric spreading, dispersion, internal friction, and scattering [7]. During the progressive degradation process of a cyclically loaded CFRP composite material, the damage mechanisms in the material grow and some evolve into different mechanisms [8]; i.e., delamination as a result of the coalescence of matrix cracks. By monitoring the evolution of hit patterns, and detecting changes, the inception of critical damage mechanisms can possibly be detected before the onset of catastrophic failure.

Methodology

This section describes and discusses the methodology used for locating the AE hits and the procedure for coding the results into a compact form. The procedure for searching and locating hit patterns in the coded representation is also described and discussed.

The aim is to monitor the location of evolving AE sources within fatigue cycles. Hence, the first step is to split the AE signal into segments of length equal to the period of one fatigue cycle. The AE hits are then determined from a detection function. The detection function is generated by converting the AE signal into decibels (dB). The logarithm transformation changes the dynamic range of the signal by enhancing low values, while compressing high values. The transformation is useful when the transducer cannot be placed at the location of damage and the AE signal suffers from high attenuation. Furthermore, the transformation makes it possible to use one setting for detecting both high and low amplitude hits.

The hits are detected and located by peak picking of the detection function. The peak picking is performed by an algorithm, which incrementally removes peaks and valleys that have peak-to-peak values below a threshold, T_{pp} , starting with the smallest ones [9]. The threshold controls the sensitivity of the approach. If the sensitivity is increased then smaller pulsations in the AE signal will be detected as hits.

Once the hits have been located, the results are coded into a coding vector. The structure of the coding vector can be accomplished in many different ways. Figure 1 outlines one possible structure of the coding vector, in which the coded inter-spike intervals (ISI) can be used with additional information. The information is coded and put in a vector, which is placed in between each coded ISI. Hence, each hit is represented by a substring in the coding vector.

In this study, two different coding approaches are investigated. The first uses only ISI coding and the second combines the ISI coding with a coded representation of the peak amplitude. The coding of the ISI is made by first logarithmically transforming (Log_{10}) the time between the peak amplitudes of successive hits, measured in milliseconds. The results are then shifted, scaled, and rounded so that each interval is represented by integers between $-N_{\text{ISI}}$ and -1 . The coding of the peak amplitudes is performed similarly. The amplitudes are logarithmically

transformed (Log_{10}), shifted, scaled, and rounded so they are represented by integers ranging from 1 to N_{AMP} .

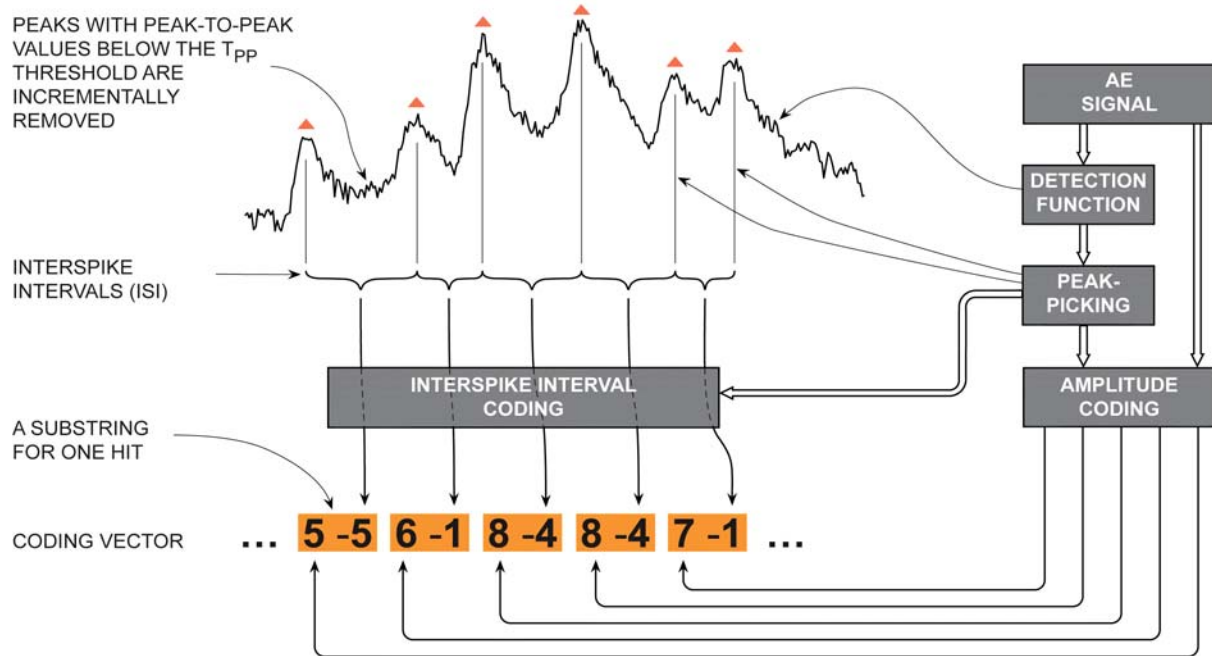


Fig. 1. The generation of the coding vector illustrated using substrings with coded amplitude and coded ISI.

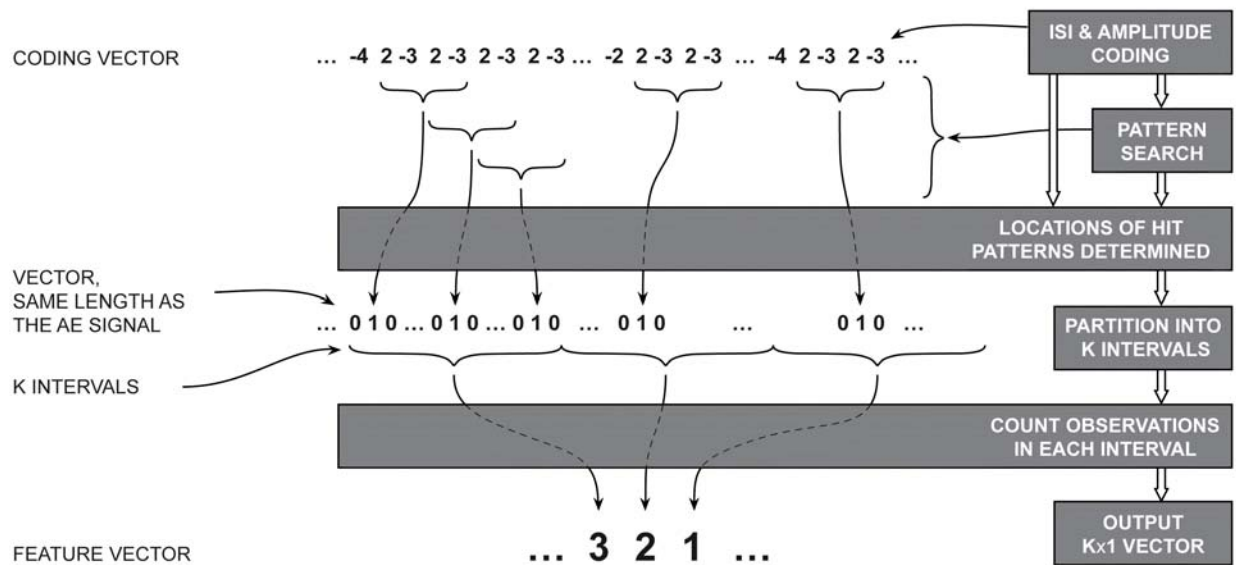


Fig. 2. The procedure for finding hit patterns and processing the results into a feature vector.

The procedure for searching for hit patterns in the coding vector is illustrated in Fig. 2. Before starting the search, the user must choose the lengths of the hit patterns. The lengths must be integer multiples of the substring length. The locations where a pattern, H_p , is observed are stored in an observations vector, O_p , where $P = 1 \dots N_p$ and N_p is the number of hit patterns. The observation vector is of same length as the original AE signal segment and initially contains only

zeros. The locations where a pattern, H_P , is observed within the AE signal are indicated by ones (1) in the observation vector. The vector is then partitioned into K intervals and the number of observations in each interval is counted. The results are put into a feature vector which has K entries.

Results.

The test specimen, the test setup, and the experimental procedure used in this study, were described in references [1] and [9]. The experimental data and the graphical tool presented in [1] were used for studying the evolution of AE hit patterns. The same settings were used for the subband filtering. The peak-to-peak threshold, T_{pp} , was adjusted for each subband, so the average number of amplitude pulses in the first 5 measurements was around 10.000; i.e., average pulse duration was 0.1 ms. The values of N_{ISI} and N_{AMP} were both set to 10 and $K = 200$ intervals were used when computing the feature vectors. Two different coding representations were studied: one using only ISI information and another using both ISI and the peak amplitude of the hits.

ISI coding

Approximately 60 patterns were obtained for each subband using ISI coding. However, only a handful of the patterns provided images which could be used to track the locations of the AE sources within the fatigue cycles. The two intensity images in Fig. 3 show the results obtained by logging the locations where two different patterns were observed. The prominent paths observed in both images show that the ISI is a characteristic feature of certain AE sources and it can be used to locate interesting AE sources for further study, or for tracking. Half of the foot delaminated at segment no. 239, but the displacement failure criterion was not met [6]. Due to the rubbing of the delaminated surfaces high number of AE hits with similar ISI were emitted. As a consequence, only few paths can be identified from the remaining segments.

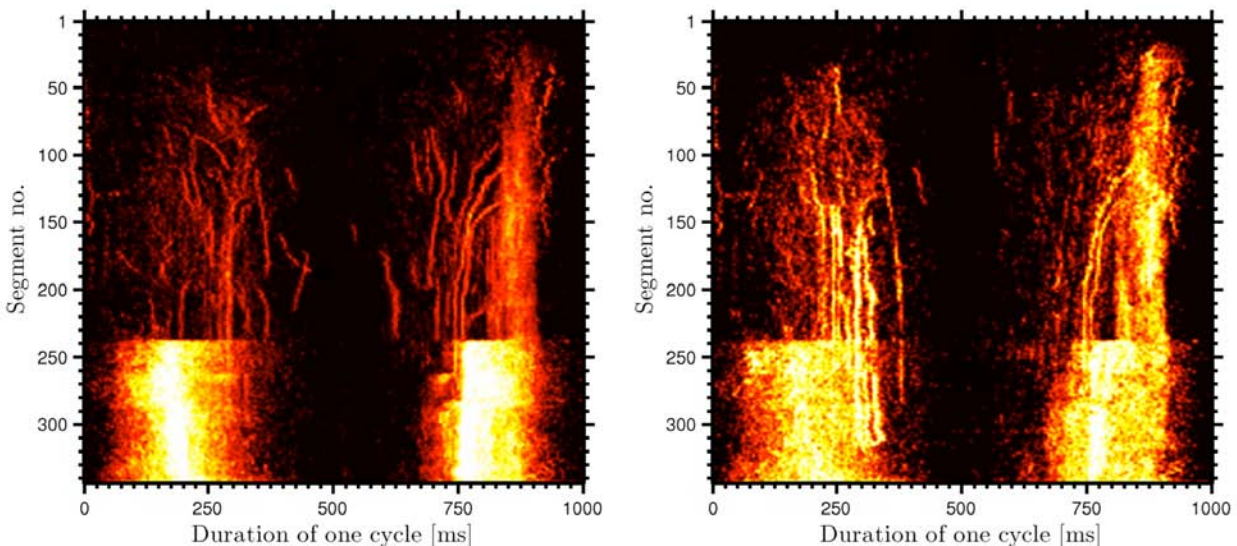


Fig. 3. The resulting images for two patterns using only ISI coding. The image on the left shows the results for the 333-366 kHz subband and the one on the right shows the results for the 133-166 kHz subband.

ISI/peak amplitude coding

By combining the ISI information with the peak amplitude of each hit, the total number of patterns increased up to approximately 600 patterns for each subband. The increase is a function of the number of quantization levels used for the amplitude, N_{AMP} . By visually inspecting the evolution of patterns and selecting patterns that show evolving trends, a composite image can be made which enables better understanding of the evolving damages in the material.

Figure 4 shows such an image, made by picking out, overlaying, and enhancing paths from 28 patterns. The patterns were handpicked from all subbands. The image on the right side of Fig. 4 shows the evolution of the AE energy in each segment. The AE energy was computed from the unfiltered AE signal by summing up the signal's values squared.

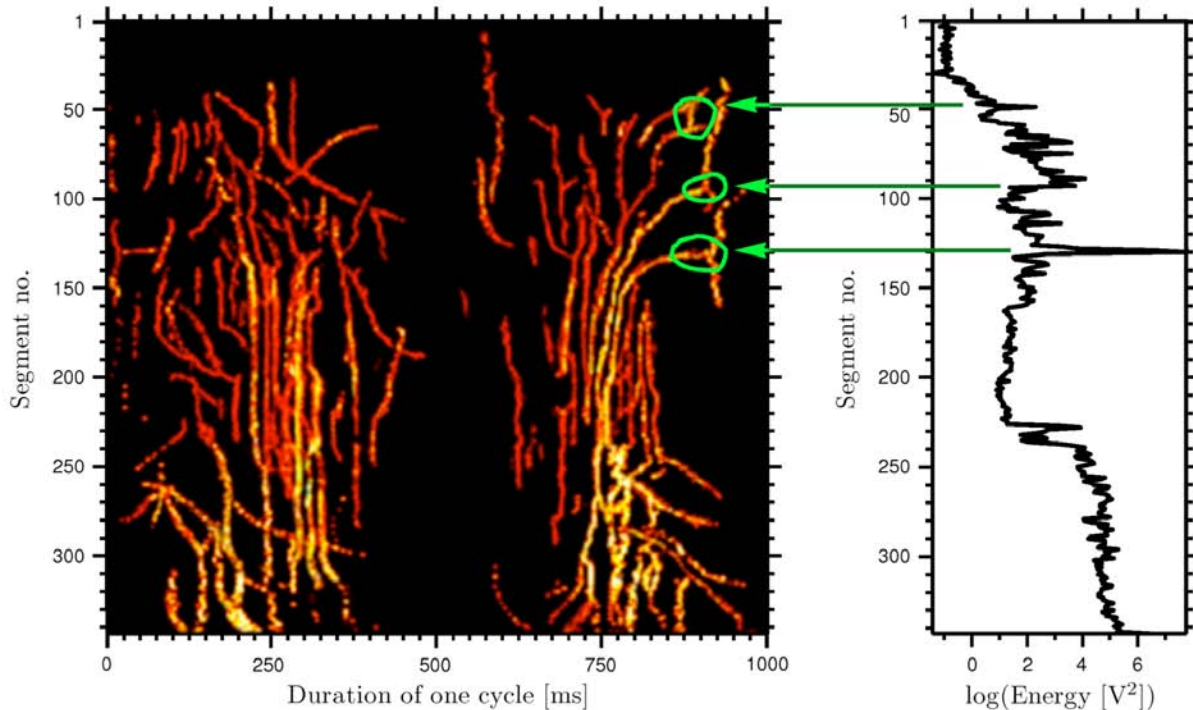


Fig. 4. A composite image made by overlaying and enhancing the results from 28 patterns (left) and the evolution of the signal's energy from each segment (right).

A comparison of the intensity images in Fig. 3 to the intensity image in Fig. 4 reveals that the addition of the peak amplitude makes it possible to track the evolution of several AE sources after segment no. 239. The tracking improvement can also be observed by comparing the 765-1000 ms region of the images. In this region of the fatigue cycle, the initiation of 3 paths can be observed (circled). These three paths can be monitored up to segment no. 239 where half of the foot delaminated.

In the 765-1000 ms interval strong AE signals were emitted from splinters [9]. Splinters, or tear outs, on the sides were commonly observed on the foot component in the area from the mid-foot to the ankle. The reason for the formation of splinters was the varying width of the foot components. The ends of the cut fibers were only held together by the matrix, which eventually failed due to repeated compression and tension loading. The splinter for this foot was located at the lower half of the foot component, i.e., below centre line. This caused the splinter to push out during upward movement of the toe's actuator (loading) and snap back during unloading, often producing an audible sound.

The reliability of the additional paths obtained by the combining the ISI and the peak amplitude in the pattern coding can be evaluated by comparing the paths, which can be obtained using both coding approaches. Based on this evaluation method, the additional paths must be considered to be significant.

Conclusions

In this paper, we developed a methodology for detecting AE hits and for coding information extracted from the detected hits, i.e., the duration between hit peaks. We also developed a procedure for searching for AE-hit patterns in the coded representation and for processing the search results. The approach was then demonstrated using experimental AE data acquired during the fatigue testing of an assembled CFRP prosthetic foot.

The results show that the information provided by the inter-spike intervals (ISI) of the AE hits alone can be used to track the locations of AE sources. This is especially interesting since the study of ISI as a feature to track AE sources has, to the best of our knowledge, not been studied previously. In [1] the authors proposed a graphical tool for tracking the locations of AE sources in cyclically loaded objects. The tool was demonstrated by using the maximum amplitude in each interval of the cycle as a feature to track. This tool was also used here for tracking AE sources. The results obtained by using only ISI information are similar to the results presented by the authors in [1].

A significant improvement in the source tracking was accomplished by combining the ISI information with the peak amplitude of each hit. The addition of the peak amplitude makes it possible to track sources when there is very high AE activity, for example once delamination has occurred. The reason for this is the additional information provided by the amplitude of the AE hits, which produces a higher number of AE-hit patterns. This increase in the number of patterns is because the observations of patterns with certain ISI coding were divided between several patterns; i.e., patterns with the same ISI coding but different amplitude coding. Hence, the amplitude addition worked like a filtering.

Currently, selecting useful hit patterns for AE tracking is done manually by visual inspection. It is unlikely that the same patterns will be useful for other test specimens. It would be, therefore, useful to develop a technique for the automatic selection of useful patterns.

Finally, the experimental data used for this study was obtained during multi-axial cyclic loading of an assembled (bolted) complex-shaped composite. Hence, it is concluded that the approach used here can be successfully applied in a real world setting.

Acknowledgements

The authors gratefully acknowledge Össur hf. for providing samples and access to their testing facilities. The work of the first author was supported by grants from: The RANNIS Research Fund, the Icelandic Research Fund for Graduate Students, and the University of Iceland Research Fund.

References

1. R. Unnthorsson, T. P. Runarsson, and M. T. Jonsson, in "*Proceedings of the Sixth International Conference on Acoustic Emission*" (Kanji Ono, ed.), AEWG, 2007, Lake Tahoe, Nevada, USA.
2. H. F. Olson, *Music, physics and engineering*, Dover Publications 1967, 460 p.
3. S. Dixon, E. Pampalk, and G. Widmer, in "*International Symposium on Music Information Retrieval*", ISMIR, 2003.
4. F. Rieke, D. Warland, R. de Ruyter van Steveninck, and W. Bialek, *Spikes: Exploring the Neural Code (Computational Neuroscience)*, The MIT Press, 1997, 395 p.
5. W. A. Sethares, R. D. Morris, and J. C. Sethares, *Speech and Audio Processing*, IEEE Transactions on **13**, 2005, 275-285.
6. J. P. Bello, L. Daudet, S. Abdallah, C. Duxbury, M. Davies, and M. B. Sandler, *Speech and Audio Processing*, IEEE Transactions on, **13**, 2005, 1035-1047.
7. W. H. Prosser, in "*Proceedings of the SPIE conference on Nondestructive Evaluation Techniques for Aging Infrastructure and Manufacturing: Materials and Composites*", December 2-5, 1996, Scottsdale, Arizona, pp. 146-153.
8. E. K. Gamstedt and B. A. Sjögren, *Composites Science and Technology*, **59**, 1999, 167-178.
9. R. Unnthorsson, T. P. Runarsson, and M. T. Jonsson, *International Journal of Fatigue*, doi:10.1016/j.ijfatigue.2007.02.024, 2007.

AE MONITORING OF SOIL CORROSION OF BURIED PIPE

HIDEO CHO and MIKIO TAKEMOTO

Faculty of Science and Engineering, Aoyama Gakuin University,
5-10-1, Fuchinobe, Sagamihara, Kanagawa 229-8558, Japan

Abstract

Most pipelines in Japan have been used for the past 30 years or more. AE method is expected to estimate the corrosion zone. We first studied AE activity of the rust produced by 10-week soil corrosion. Next, we studied attenuation of cylinder wave by the rust-prevention tape and wet soil. Finally, we report AE activity of the steel pipe subjected to soil corrosion for 20 years. For this pipe, AE signals were monitored for a short period using low-frequency AE sensors mounted close to the rust. We, however, cannot predict the active period of the rust. Thus, AE monitoring from the rust fractures of underground pipes is limited for short distances less than one meter. It takes a long time to monitor the AE signals from soil-produced rust.

Keywords: Underground pipe line, soil corrosion, cylinder wave, attenuation, rust fracture

Introduction

Underground pipelines in Japan were constructed during the time before Tokyo Olympics in 1964. Corrosion of the underground pipes is becoming serious problems both in chemical plants and public utilities. Japanese companies are recently inspecting the wall reduction of the underground pipelines using a guided-wave inspection system. This system generates strong F- or T-mode cylinder waves using piezoelectric or electromagnetic transducers and detects the waves reflected by wall reduction. The guided waves, however, cannot propagate more than 2 m for underground straight pipes due to large attenuation of the cylinder waves [1, 2].

Acoustic emission (AE) technology cannot monitor the wall reduction, but can estimate the corrosion zone, if we can detect AE signals from rust fracture. Strong requirement to the AE technique is the detection of localized corrosion of the pipelines, due to local damage to the rust prevention tape and asphalt cloth. AE activity of the rust produced by soil corrosion (soil-produced rust, hereafter) is considered to be different from the rust produced by atmospheric corrosion (atmosphere-produced rust). We first compared AE activities of the soil- and atmosphere-produced rust using steel plates exposed to weathering. AE activities of these plates under mechanical loading and thermal cycles were studied. Next, we studied attenuation of the cylinder waves by wet soil and new rust-prevention tape. Lastly, we monitored AE signals from a steel pipe with thick rust produced by underground corrosion for 20 year.

Structure of the Rust Produced by Soil and Atmospheric Corrosion

We prepared 250 steel plates (45-mm wide, 90-mm long and 2-mm thick), subjecting them to soil or atmospheric corrosion for 2, 5 and 10 weeks. The soil-produced rust was prepared by burying the plates in two types of soils. One is the so-called “red-soil” and another “black soil”. The former is pasty and the latter is muddy when they absorb water. These soils correspond to two layers of the four-layered loam of volcanic trass in Tokyo area [3]. The soil is slightly acidic.

The plates are coated by the rust-prevention adhesive tapes except the center portion of 20-mm square on one side, and buried in the soils.

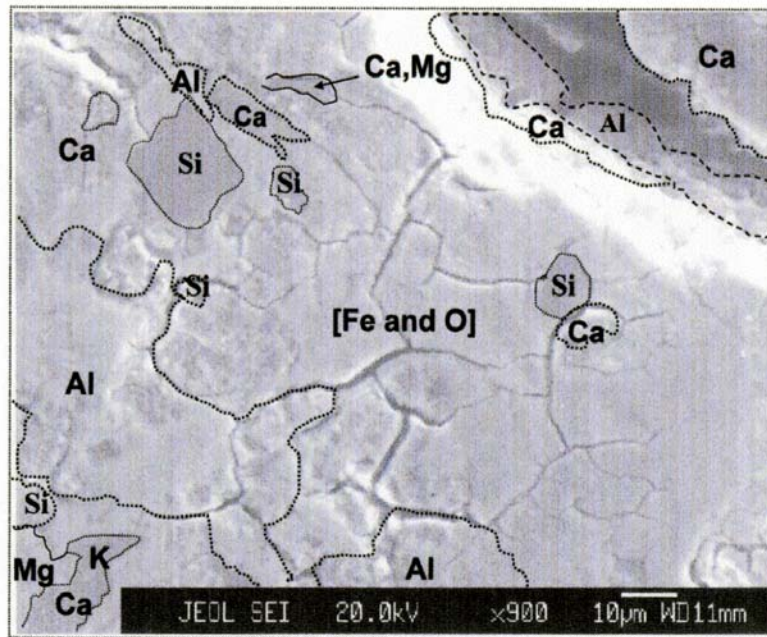


Fig. 1 Distribution map of elements in the soil-produced rust produced by soil corrosion.

The soil-produced rust was very hard and well adhered to the steel even after brushing by a fine brass wire brush. Thick rust of 1 mm or more were produced over 60% of the exposed area. In contrast, the plates exposed to the atmospheric corrosion produced thin rust, which were easily removed by brushing. Thick rust more than 0.5 mm were produced on only 5% of the exposed area.

As shown in Fig. 1 (transverse EPMA of the soil-produced rust), the rust contains a number of soil elements (SiO_2 , Al_2O_3 , Fe_2O_3 and less CaO , MgO , NaO and K_2O) in addition to the iron oxides (Fe_2O_3 and Fe_3O_4) shown as [Fe and O]. We observed a number of branched cracks in the soil-produced rust.

AE Activities of the Rust

AE activity by three-point bending

AE signals during three-point bending with the span distance of 30 mm were monitored by four small resonant sensors (PAC, Type-PICO) mounted on four corners of 30-mm square. Strain at loading point was measured by a strain gage mounted on the base metal, and is increased up to 0.2%. Sensor outputs were amplified 60 dB, and stored in a computer as digital data.

Figure 2 shows nine diagrams of cumulative AE event counts and strains for three rust produced by 2, 5 and 10 weeks of exposure. Average temperature of June was 22°C with 140 mm rain and that of July was 25°C with 170 mm rain. Average amplitude of the F-mode Lamb waves is also shown in the diagrams. The plates with atmospheric rust produced 100 events after 5-week exposure, while those buried in the red soil produced 600 events after 2-week exposure. Vertical arrows near the curves indicate the threshold strain, above which AE signals were

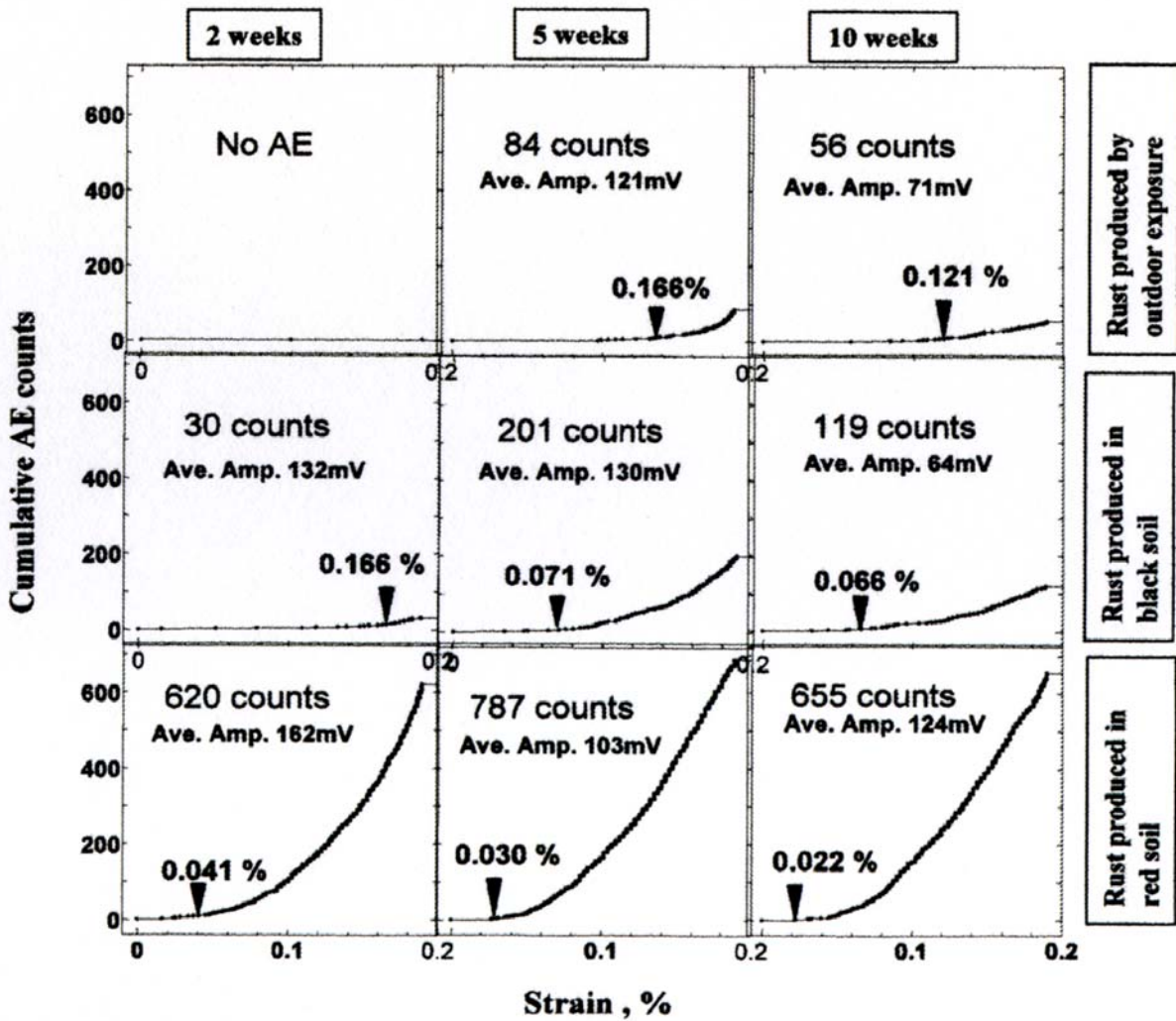


Fig. 2 Cumulative AE counts with applied strain for the steel plates exposed to soil and atmospheric corrosion.

continuously detected. The threshold strains are much smaller for the plates buried in the soils. This plate produced AE signals continuously at strains above 0.022%. It is noted, however, that the amplitude is almost identical for the atmosphere- and soil-produced rust. AE activities in term of the event counts are much higher for the soil-produced rust. This suggests that the external loading such as internal gas pressure to the underground gas pipelines is effective for monitoring the integrity loss.

AE activity the rusts by wet and dry cycles

Any steel plates, dried in a room after removal from exposure site, did not produce AE during thermal cycles between 25° to 40°C. These results suggest that drying of the rust must be avoided to measure the AE activity. Unfortunately, we dried all samples in room air and kept them in a desiccator, so we wondered what type of test methods we should use. After trials of many types of tests, we decided to measure the AE activity after immersing them in water for one day. We detected a few AE during the first heating, but no AE during second heating.

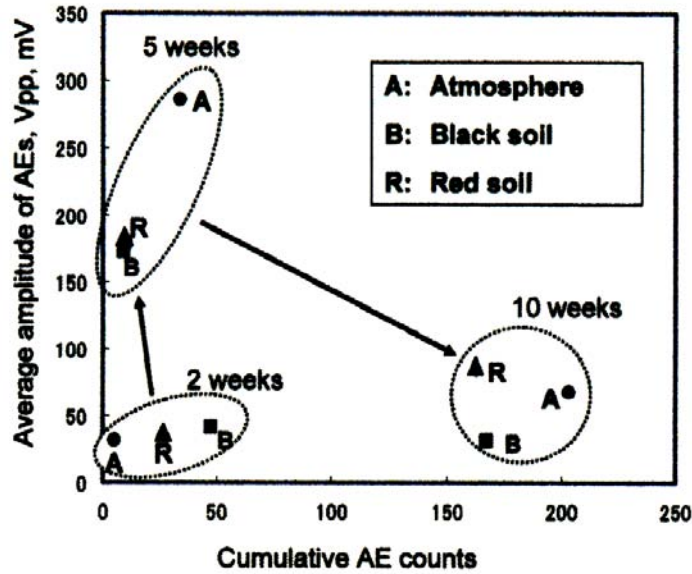


Fig. 3 Changes of event counts and average amplitude of AE signals from rusts.

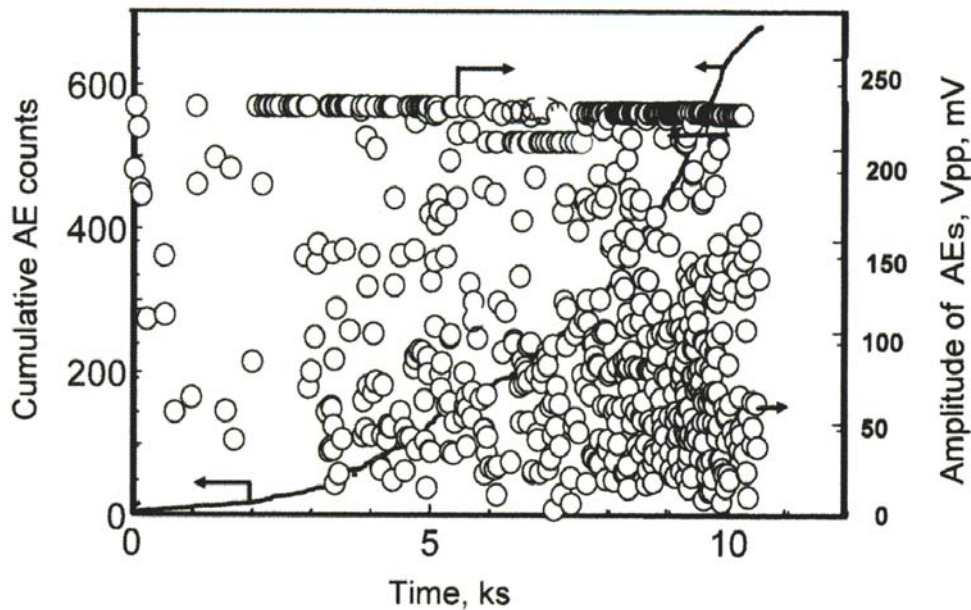


Fig. 4 Changes of cumulative event counts and amplitude during drying.

Figure 3 shows changes of the cumulative AE counts and average amplitude with exposure time. These show a strange change. Strong AE signals were produced after 5-week exposure, while the amplitude of AE signals decreased at 10-week exposure. There also observed no clear difference in both the amplitudes and event counts of the rust produced by atmospheric and soil corrosion. Atmosphere-produced rust produced strong AE, as seen in 5-week data. It is again noted that the result obtained by the proposed method does not necessary represent the AE activity of the rust as they are in natural weathering. AE activity must be measured at the site of a structure.

As the rust grows slowly and is generally brittle, large cracks rarely occur just after frequent large cracks. This is studied by another test and shown in Fig. 4. This figure shows change of

cumulative event counts and amplitude of Lamb waves during natural drying of the rust produced by black soil by 4-week exposure. Drying is done in air-conditioned room at 27°C. We observed vigorous AE signals with large amplitude during natural drying. This strongly indicates that AE must be monitored during the drying period of grown rust. It is, however, almost impossible to estimate the drying timing of the rust in the soil. Underground pipelines (1-m depth) are almost always in wet condition. If we dry the pipeline using inert hot gas, we can perhaps monitor the integrity loss of underground pipelines. This technique was once used for the field test of corroded pipes with cooperation with steel-making company. Result was inconclusive since the corroded pipes were once dried before being buried.

Attenuation of the Cylinder Waves by Rust Prevention Tape and Wet Soil

We measured the attenuation. Accurate attenuation measurement of the cylinder waves is difficult. We have to use an advanced method for calculating the energy of the separated mode [4]. We, thus, measured an apparent attenuation using the amplitudes of the L- and F-modes. Even in this method, a problem often arises for the F-mode wave, since the amplitude of the F-mode changes along the pipe circumference [5]. Figure 5 shows a method for measuring the attenuation. Method A is for measuring the attenuation by the rust-prevention tape (JIS Z1901, 0.4-mm thick polyvinyl chloride adhesive tape), and method B for that by the wet black soil with 40 mass% water. The cylinder wave was excited by a 100-kHz PZT transmitter of 80-mm diameter mounted to the right end surface and monitored by three AE sensors (PAC, Type-PICO) mounted at angle of 0°, 120° and 240°. Attenuation was measured by changing the width of the double wrapped tape and wet soil in the right portion.

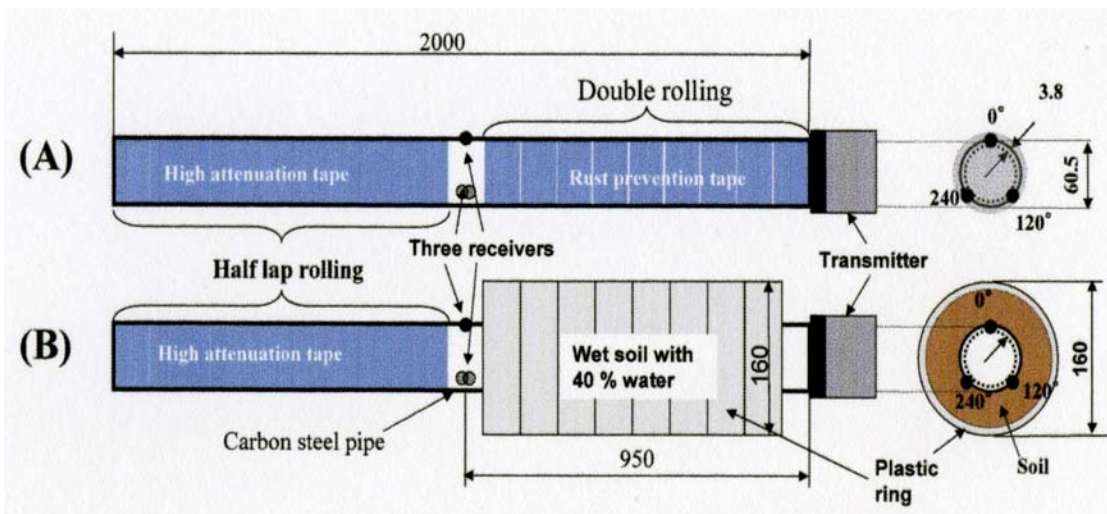


Fig. 5 Method for measuring the attenuation of cylinder wave due to the rust-prevention tape and wet soil.

The left of Fig. 6 shows changes of the amplitude of L- and F- modes with the length of the tape. Surprising is that the average attenuation (-12.7 dB/m) of the L-mode by the tape is larger than that (-6.8 dB/m) of the F-mode wave. The attenuation by the wet soil is much smaller than that by the rust-prevention tape. Another interesting finding, for the wet soil, is that the average attenuation (-3.8 dB/m) of the F-mode wave is larger than that (-0.8 dB/m) of the L-mode.

These data suggest that the attenuation by the new tape becomes hazard to AE monitoring. In another word, if AE is detected, it means the rust-prevention tape is aged. This timing may

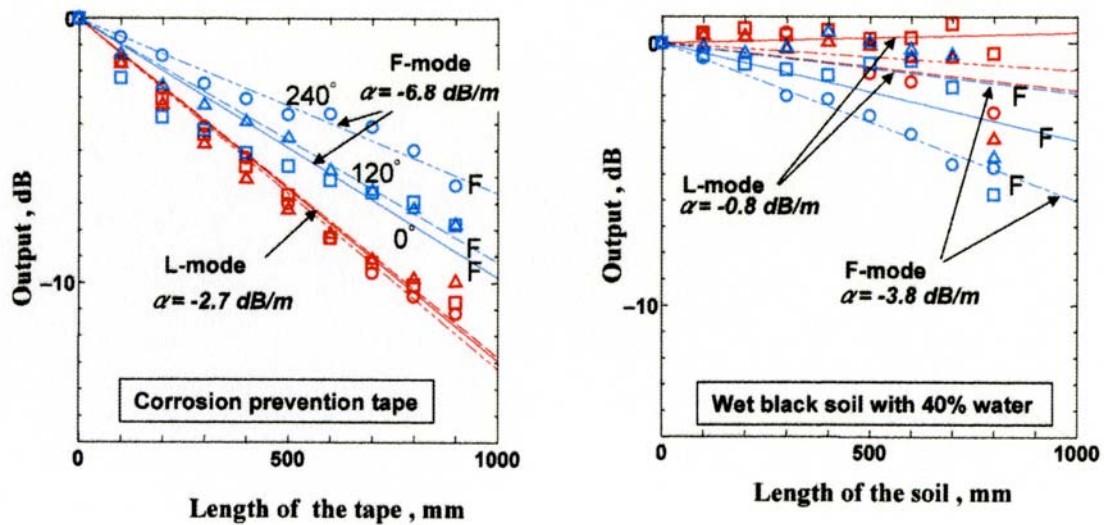


Fig. 6 Output of L- and F-mode cylinder waves vs. length of the attenuator. The left is by the corrosion-prevention tape and the right by the wet soil.

coincide with the timing of corrosion initiation of the coated pipeline. We also attempted to measure the attenuation with the asphalt cloth, but could not measure it due to too large attenuation.

AE Monitoring of the Steel Pipe Buried for 20 Years

This pipe was made of plain-carbon steel, 39-mm diameter, with polyethylene coating. The pipe was buried in soil for 20 years and some parts had through-wall corrosion. A 1-m section of the pipe with thick rust was tested. Figure 7 shows the steel pipe after removing the coating. It had ~2-mm thick rust over 100 mm long at the mid portion. The center 300 mm of this pipe was again buried in wet black soil for 4 months using a plastic box before AE monitoring. The soil was allowed to naturally dry, but was kept wet by supplying 1000 ml water every 2 weeks. This operation was meant to revive the rust activity.

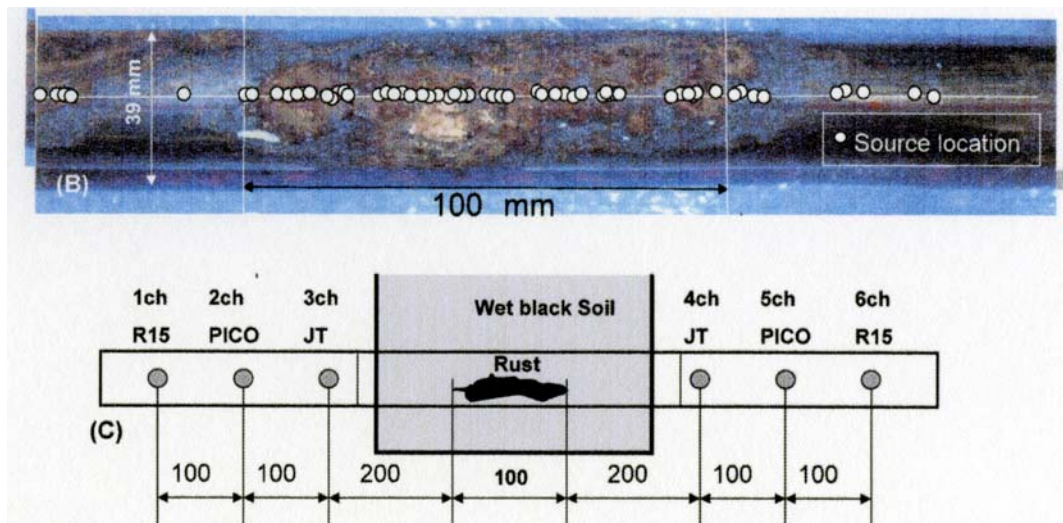


Fig. 7 A steel pipe buried for 20 years (the upper) and monitoring method of AE from the pipe in black soil. White dots indicate located AE.

AE was monitored using three types of sensors, i.e., PAC Type R15 (150 kHz resonant frequency, channels 1 and 6), PAC Type-PICO (450 kHz, channels 2 and 5) and JT (broadband sensor up to 1 MHz, channels 3 and 4). All sensors were located within 450 mm from the thick rust. Outputs of the JT sensor were amplified 60 dB, but those of other sensors were amplified 40 dB.

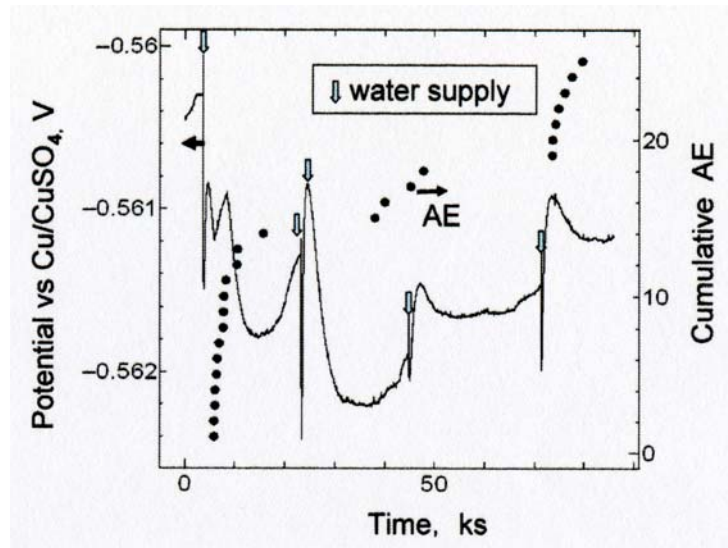


Fig. 8 Corrosion potential and AE of the rusted pipe from natural drying of wet soil.

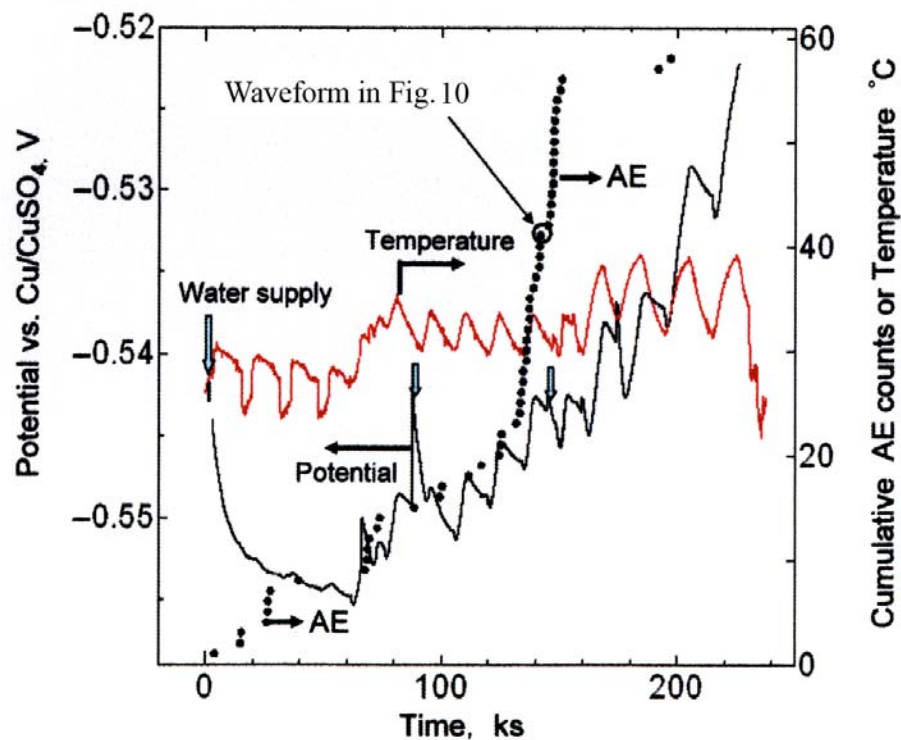


Fig. 9 Corrosion potential, temp. and AE from the rusted pipe during thermal cycles.

We monitored AE from the pipe wrapped by the rust-prevention tape for 2 days, but detected no AE. Then we monitored AE of bare pipe. Figure 8 shows change of cumulative event counts and corrosion potential with time over one day. Vertical open arrows indicate the timing of water supply of 300 ml. We detected few AE after water supply at 5-10, 40-50 and 75-80 ks. This suggested that we cannot monitor the integrity loss of the pipe by short-time AE monitoring.

Next we attempted another experiment 2 weeks later. We monitored AE during thermal cycles. The soil was 15 times heated and cooled by on-off operations of an infrared lamp during 2.5 days. Both the corrosion potential and AE were monitored simultaneously. Water (300 ml) was supplied 3 times (vertical open arrows). Figure 9 shows change of corrosion potential, temperature and cumulative event counts during thermal cycles. We detected an abrupt AE at around 140-160 ks, after 10 heat cycles, but no AE after this. This timing corresponds with shifting of corrosion potential to noble direction. However, we cannot predict this timing. Difficulty in damage monitoring of the underground structure is the estimation of such timing.

Source locations of AE, estimated using the arrival times of the F-mode waves, are shown in Fig. 7. 27 of 70 events were located in the zone with thick rust as shown by white circles in the upper photo. Waveforms of the AE detected at 122 ks are shown in Fig. 10. Amplifications are shown in each figure. Output amplitudes of the sensors (Ch. 1, 2 and 3) mounted on the left half of the pipe are higher than those on the right half (Ch. 4, 5 and 6), indicating the rust fractures occurred at the left portion of the 100-mm long rust. This gives us important information, i.e., large attenuation of the cylinder wave by wet soil. This attenuation appears to be much larger than that (-3.8 dB/m) in the Fig. 6. The reason is not well understood, but appears to be soil thickness. It was 50 mm in Fig. 5 and 300 mm in Fig. 7.

Other information on the resonance frequencies of the sensors is as follows. Amplitude of the two PICO sensor outputs is much weaker compared to those of the R15 sensors. Frequency components of the F-mode detected by the JT sensor are from 80 to 100 kHz. In order to monitor AE from underground pipes, we need to use sensors with resonance frequency lower than 80 kHz. Another important point is wrong sensor layout. We mounted all sensors on the upper line of the pipe where the rust is produced. This layout appears to be wrong. We have to determine the sensor position, at which we can monitor the strong AE in advance.

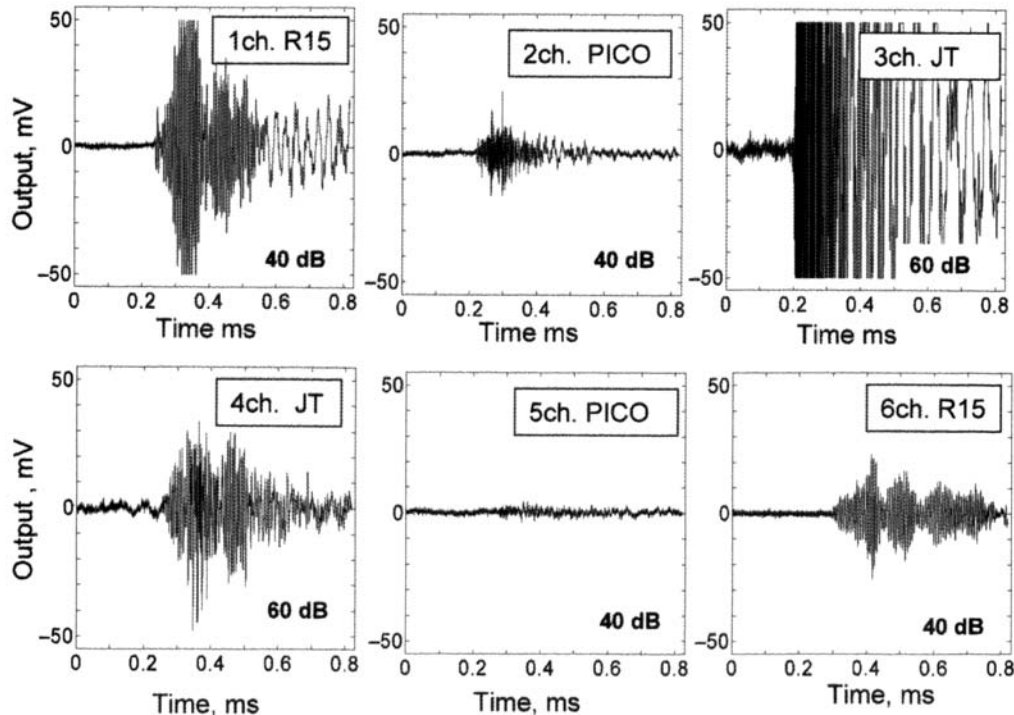


Fig. 10 Waveforms of cylinder wave signals detected at 122 ks by 6 sensors mounted at different locations near the rust.

Our conclusion from these tests is that AE monitoring of underground pipes over long distance is very difficult due to the large attenuation of the cylinder waves and the capricious nature of rusts. Monitoring distance of AE for the underground pipe may be limited to less than 1 m even if we use high amplification with resonant sensors at lower frequencies. When we detect AE from underground pipes, it means the pipes are under severe corrosion attack. Source location is not necessary since the sensors must be mounted close the corrosion zone.

Conclusion

We studied structure and AE activities of rust produced by soil corrosion and measured attenuation of the cylinder waves by wet soil and rust-prevention tape. Monitoring of AE from the corroded pipe with thick rust taught us important information on the integrity loss monitoring of underground pipe by AE. Results obtained are summarized below.

- 1) The rust produced by the soil corrosion grows thicker including soil elements and emits AE at being subjected to mechanical loading. The rust loses their AE activities once they were dried. AE activity of the survived rusts, however, changes in quite complicated manner, independent of the exposure period.
- 2) Attenuation of the cylinder waves by new rust-prevention tapes is larger than that by the wet soil. As the amplitude of the F-mode changes by sensor position on the pipe circumference, we have to determine the appropriate sensor position, which can measure the cylinder waves with higher sensitivity.
- 3) We monitored AE from the steel pipe with thick rust produced by the soil corrosion for 20 years. Few AE were detected in a limited period during thermal cycles. However, we cannot estimate the timing of rapid emissions of AE. Integrity loss monitoring of the underground pipe by conventional AE technique appears to be difficult due to large attenuation and capricious nature of the rust, and needs advanced inexpensive system, which makes a long-term monitoring possible. External loading may be effective for exciting the rust by fracturing.

References

- [1] Report by research committee on guided wave testing, J. Jpn. Soc. Nondestructive Inspection (in Japanese), **54**, 2005, 596-602.
- [2] T. Ikeda, R. Kinbara, M. Miyazawa, I. Matsuoka and M. Fujiwara, J. Jpn. Soc. Nondestructive Inspection (in Japanese), **54**, 2005, 595.
- [3] Earth Science Group, Cyclopedia of Earth Sciences. Heibon-sha (1996).
- [4] H. Kasama, M. Takemoto and K. Ono, J. Jpn. Soc. Nondestructive Inspection (in Japanese), **49**, 2000, 269.
- [5] H. Nishino, S. Takashina, F. Uchida and M. Takemoto, Jpn. J. Appl. Phys. **40**, 2001, 364.
- [6] D.C. Gazis, J. Acoust. Soc. Am. **31**, 1959, 568.

THIRTY YEARS EXPERIENCE OF INDUSTRIAL APPLICATIONS OF ACOUSTIC EMISSION TESTING AT TÜV AUSTRIA

PETER TSCHELIESNIG

Institute for Technical Physics, TÜV Austria Services, Deutschstr. 10, A-1230 Vienna, Austria

Abstract

Since 1977 the TÜV Austria (till 1990 TÜV Vienna) has tested different pressure equipment with acoustic emission. The aims for these tests have been different for various applications such as: first hydrotests, requalification tests of pressure containments, leak detection and the detection and evaluation of corrosion. The different equipment technologies shall be mentioned and their influence on the test results shall be pointed out. As examples for successful applications the following test objects shall be mentioned:

- Gas storage spheres,
- Flat bottomed storage tanks (leakage and/or corrosion testing),
- Steam drums (dryers) in paper mills,
- Leak detection with an acoustic pig,
- Automatic testing of receptacles during the filling procedure,
- Corrosion tests of oil tankers.

The importance of standardization beginning within the EWGAE, and now with CEN/TC138 WG7 "Non-destructive testing - Acoustic Emission Testing" as an accepted method in Europe will be pointed out. At the end the rules for the training and certification according to the EN473 and their implementation within the three NDT societies from Germany, Austria and Switzerland will be presented. The three societies give common training courses and certification examinations.

An outlook in the future of the on-coming application, based on EC funded project, shall be provided. This outlook will show that AE testing will become in the years ahead more and more important for the competitiveness of the European industry to make the inspection of pressure equipment cost-effective and safe.

Keywords: Pressure equipment, integrity test, leak detection, training and certification

Introduction

Since 1977 the TÜV Austria has tested different structures, especially pressure equipment, storage tanks and pipelines with acoustic emission. Till today more than 30.000 different structures were tested and although the methodology has changed tremendously over the time I will review some typical applications, which were performed in the last 30 years. During this survey, I will point out the different technology and equipment used. Especially the rapid development of the electronic data acquisition and treatment has changed the possibilities and application of AE testing tremendously.

Our first contacts with AE were in 1975, when TÜV was nominated from the Austrian government to supervise the AE testing of Exxon Nuclear (with Dwight Parry) of the pressure vessel of the Austrian nuclear power plant at Zwentendorf. Two years later, we started our first own

measurements with an Exxon Nuclear 2-channel equipment on different small structures even in the above-mentioned nuclear power plants. Our main tasks were pumps, penetrations through the pressure containment, valves and other installations. Although this equipment had no real-time data storage and mainly engaged to collect AE hits, it provided a Δt -measurement for linear location. With this tool, we were able to detect and also roughly locate different defects, leaks and non-reported repairs in the tested structures. Even then, perhaps more so, it was very important to combine the AE results with other information of materials science and conventional NDT applications. Based on the meaningful results, we decide to buy a 24-channel equipment from AE International (Richland, Washington, USA) in 1979. With this system, we were able to acquire and process data coming from 4-channel arrays. The analog information was stored on a multi-channel tape recorder with a dynamic range of 26 dB at 100 kHz, which was at that time remarkable [1], although this would for some of colleagues sound like a tale from the Stone Age. With this equipment we reached a complete new stage in the application of AE.



Fig. 1: Storage sphere (left) tested with acoustic emission; location map of acoustic emission test with active areas indicated by colored rectangles (right) at weld seams of the sphere.

Examples over the Years

Gas storage spheres

In 1979/80 the Viennese gas supplier built 2 natural gas storage spheres with a diameter of 32 m and a service pressure of 1 MPa [2]. The hydrotests before service were monitored with AE, where we found stress concentrations based on improper welding, because parts of the sphere with different wall thickness were not welded according the neutral phases. Both spheres have had small inside-surface cracks, mainly caused by the bending over the support during filling. Although all welds had to undergo an NDT before the hydrotest, one big slag-inclusion was detected and located and has to be repaired.

It was remarkable, that we found many problems in the spheres, although the contemporary AE equipment had only a few features. This shows, that the normal hydrotest with its binary information (pass or not) is not a sufficient acceptance test for pressure equipments. The repetition tests every 6 years with different AE technology verified the results.

We have monitored during pneumatic loading two gas storage spheres of 33-m diameter at West Berlin in 1982, and in 1991 a natural gas storage sphere with 39-m diameter at service pressure of 1.2 MPa (the biggest storage capacity for natural gas within Europe). The AE tests

were performed mainly for safety reasons (early alarm tool) as the structures were situated within a residential area, but also its NDT ability was used [3]. See e.g., Fig. 1.

Leakage testing of flat bottomed storage tanks

In 1981, we started, after laboratory tests and on-site trial tests, AE monitoring of the flat bottoms of storage tanks for leaks [4-6]. This testing method uses the turbulences of the fluid media in the gap and some secondary effects between the bottom and the basement. Over the time, we tested more than 300 tanks and were able to improve the method, especially for the discrimination between leak source and background noise and also developed special location software. In those days, every test was a combination (comparison) of a low-liquid level (1–2 m) and high-liquid level (nearly full) test.

A good example for the successful application of the method was the leak within the bottom of a product tank. This was not detected even by vacuum boxes and could only be verified by penetrant testing (PT) of the weld between the sump and the bottom. Further development of the method led to the application of the cross-correlation method, which also gave us the opportunity to use the continuous AE for the detection and location of leaks. Some changes in the Austrian legislation and the demands of the customer to get more information about the status of the bottom led to the development of the corrosion testing, within an European Commission (EC) funded project in the second half of the 1990's. See Fig. 2.

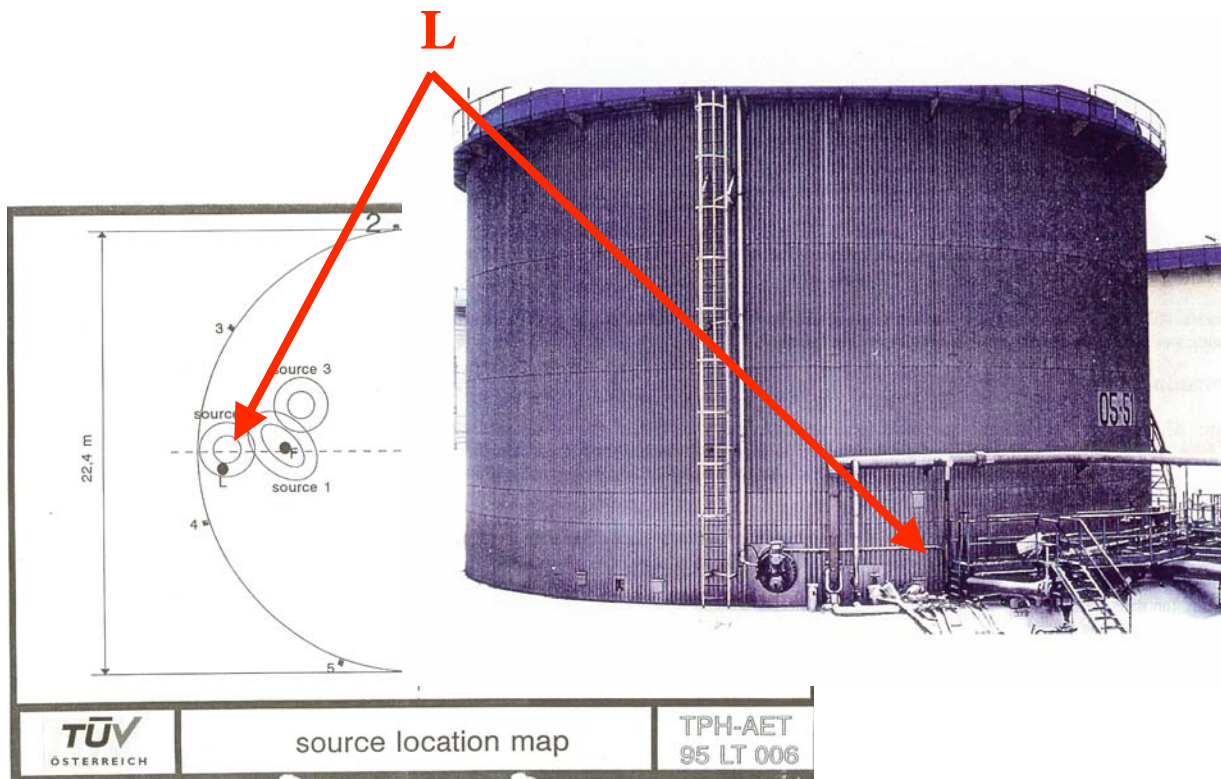


Fig. 2: Leakage testing of storage tanks; AE sources indicate position of leakage.

Corrosion testing of flat bottomed storage tanks

Beside the prevention of leaks, the corrosion problem was a pressing problem for the petroleum and petrochemical industry. Because it seems to be possible, but not proven, that corrosion can be detected with AE, the TÜV Austria together with a consortium of Vallen Systeme, (AE

equipment manufacturer), CISE (AE testing company) and Shell Global Solution and Dow Germany (Tank user) proposed in 1995 a research and development project to the EC, which was accepted in 1997.

By extensive research works during laboratory tests and real tank tests, the consortium was able to prove, that corrosion and leakage can be detected but it is also possible to distinguish both types of AE sources. To make the distinction, the normal AE parameters were inadequate. Therefore, we applied a frequency-domain pattern recognition system (VisualClass®) on the complete transient time signal. Based on the different physical events, the system was able to distinguish the different signals on a statistical basis. Of course, beside the pattern recognition additional filter criteria have to be applied on the whole data set. (Fig. 3)

Within the EC-funded project, which was completed in 2000, we could develop and validate this testing method. But the results showed that the AE testing has changed from a method, which was only counting hits, events or threshold crossings to a sophisticated method, where the data processing replaced more and more the experience and “feeling” of the test operator [7].

From now on, the flat-bottomed storage tanks in some refineries, tank farms and chemical plants will be tested regularly for corrosion and leaks. By testing several hundreds of tanks the necessary database will be enlarged permanently and testing method will be accepted by more and more authorities [8, 9].

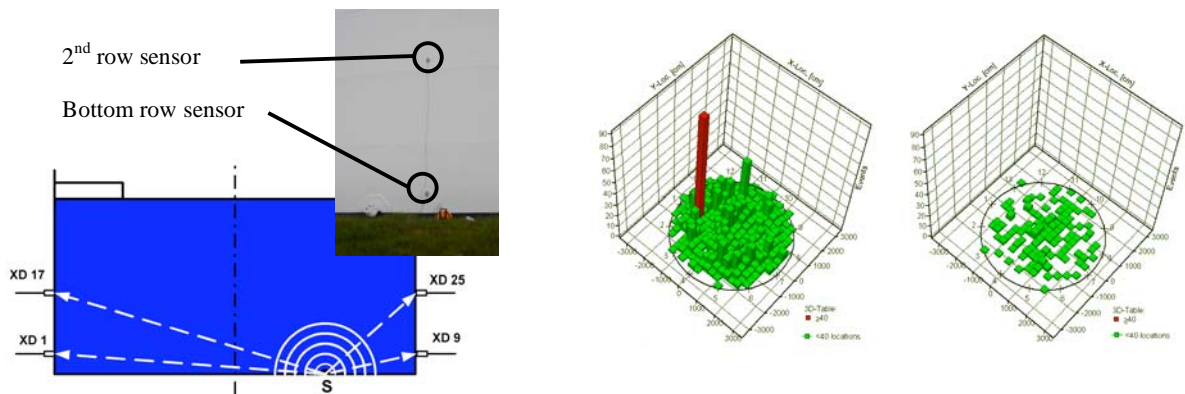


Fig. 3: Sensor layout for storage tank testing (left) and results obtained with only bottom row (red column, right) and with two rows of sensors (no indication, far right). With the arrangement in two rows it is possible to prevent the test result for the tank bottom from being flawed by corrosion of the floating roof.

AE testing of dryers (steam drums) in paper mills

For a long time, the paper mills have had the repetition of problems with their dryers tested by hydrotest and inside inspection. Problems increased more and more due to the enlarged production output. The higher rotation speed and higher temperature led also to a smaller wall thickness and resulted in damages to bearings, un-roundness and balance of the dryers during the hydrotests. If the cylinders have to be removed for the test, these resulted in shut-down periods of several weeks, which was unacceptable for the production. We started to develop a more sophisticated testing method than the hydrotest by the application of AE during a pneumatic loading of the drums in their normal service position [10, 11]. The AE testing was inserted as a pre-warning system for the pneumatic loading and also as a powerful NDT method, with a rough location based on a linear location. This became necessary due to the restricted accessibility of

the surface of the drums. During a shut-down period of 24 hours with AE testing, 6 to 8 cylinders can be tested. This brought not only big advantages for the performance of the paper industry, but a substantial gain for the safety was achieved. Defects, which were not detected during the conventional testing method, are now detected by the AE testing. (Fig. 4) Beside cracks, cavitations and corrosion attacks, we found also cracks in the balance weights. If these defects remain undetected during the shut-down period, these weights could destroy several cylinders during the subsequent service periods with further incalculable consequences.



Fig. 4: Testing of steam drum with AE sensor installation (left); Erosion found after entering into the steam drum due to indications obtained by AE measurement (right).

Leak detection Pig (ALARM)

In the early 1990's, we started with the OMV to develop a leak detection pig for diameters of 100 mm and up. This development was done for the connection lines between the refinery and tank farm of OMV. See Fig. 5. A pig has always the advantage, because it carries the sensor close to the AE source (leak) and gives the opportunity to check the pipeline in-service. After pre-tests in the laboratory and on a test rig, test runs on real pipelines with artificial leaks were done. The worst-case leak (drilled hole) sensitivity of the pig is 5 l/h at a minimum pressure of 300 kPa. Since 1994, the pigs (different modules for different diameters) run regularly on the OMV pipelines [12]. At a service for the Pinghu Oil & Gas field, near Shanghai (China), on a transmission line between on-shore and an off-shore loading platform over a length of 360 km, we detected 2 leaks and located them with an uncertainty of less than 1‰. This allowed the customer to repair these defects in welds.

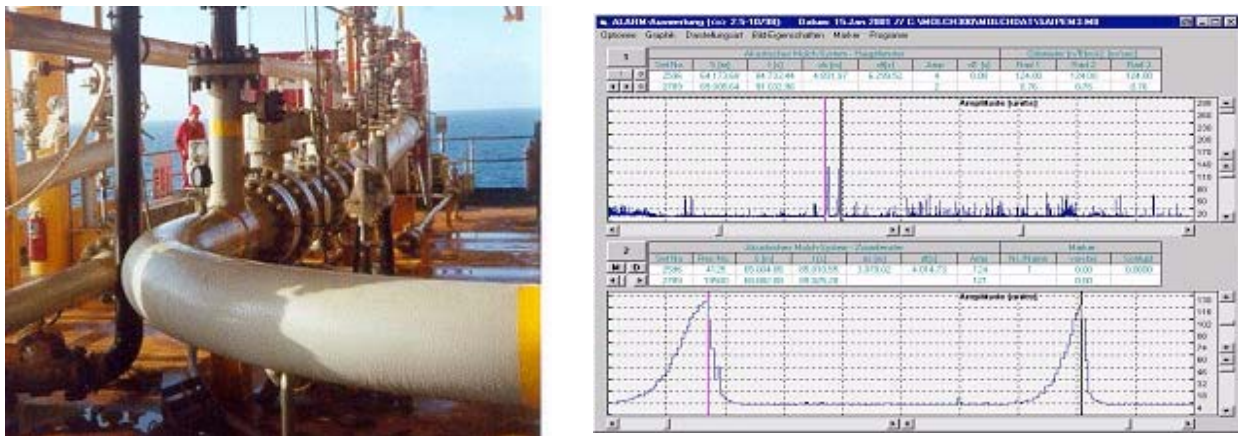


Fig. 5: Receiving pig trap off the coast of China (left) and indications of two leaks obtained by one pig run (right).

Automatic testing of receptacles during filling

Together with the gas distribution company Messer Austria, we developed a brand new test- and filling bench. Instead of testing the receptacles by a hydrotest, the tests will be performed automatically during the filling operation. The test rig allows overfilling the bottles up to 1.4 times of the service pressure. The whole period of this action will be monitored with 2 sensors each and the evaluation and stop criteria will be checked automatically from the computer according a pre-defined procedure (Fig. 6-right).. The criteria, which are established during lab-tests, are locked and can be changed only with our password. All rejected receptacles will be re-tested manually to identify the reason for the test-stop and undergoes a follow-up [13-15].



Fig. 6: AE testing on gas cylinders, 12 cylinders are tested simultaneously by pressurization with gaseous product (left), laboratory tests of fatigue cracks till burst with hydraulic pressurization for establishing a set of testing parameters (right top and bottom).

Detection and localization of corrosion attack on ship tankers

Based upon the application of AE testing for flat-bottomed storage tanks and horrible ship disasters in the last several years, e.g., Erika, Prestige, Napoli, which devastated hundreds of kilometers of the coast of Brittany, Galicia etc., we launched together with Vallen Systeme (Germany, equipment manufacturer) and four Polish companies, Gdansk University of Technology, Polish Registration society, Institute for Applied Sciences and Maritime Institute of Gdansk, an R&D project funded by the European Commission for detection and localization of corrosion attack on ship tankers.

The aims of the project were

- a permanent testing with an installed system, which will acquire the data during the shipping conditions and measure on-line the status of the structure and
- a spot-testing, which can be applied on ships in the harbor or on the anchor place before discharge.

Both systems have had to overcome the problems with the rough sea environment. Based on laboratory tests and background measurements on real ships (naval and commercial tankers), we found out that it is possible to distinguish the AE coming from corrosion and AE produced from shipping actions with different filter steps - frequency, localization and pattern recognition [16]. We demonstrated that we are able to detect “real corrosion sources” within ship tankers under normal shipping conditions (Fig. 7). For these measurements, it was necessary to develop intrinsically safe, explosion-proof sensors, which were certified for zone 0 according the European directive and approved from a shipping classification society [17].

The spot testing was solved with a new multi-element sensor (holder with 4 sensing elements; see Fig. 7-right), which was able to detect but also locate the direction from the incoming AE wave. This was a further advantage of this project and the application of this sensor type shall also be used for tank testing on-shore.

The project was finished in July 2006 [18]. Nevertheless, further investigations for ship corrosion become necessary, because the current technique acquires only those corrosion signals, which are in contact with liquid. A very important part for the integrity of a vessel is the deck, which at the moment cannot be checked.



Fig. 7: Oil tanker towed to the mooring buoy at an oil field off the coast of Poland (left), cargo tanks have been tested with a multi-element sensor (right) which was lowered down through deck opening and then immersed into the crude oil.

Standardization

Over the decades, the application of AE testing as an NDT method changed completely. At the beginning, it was an exotic method, which was applied only for very specific problems, and also the confidence on the results was limited, although AE testing has often demonstrated their ability and reliability. Now based on all further developments, AE testing became more and more an accepted and regular NDT method. But such a method needs beside the technical excellence:

- standardization of the method and their application and
- trained and certified personnel, which has to be demonstrated against a commonly accepted standard.

Based on these demands, the test method made a big step forward, when the CEN/TC 138 “Non-destructive Testing” established the Working Group 7 “Acoustic Emission” [19] for the development of basic standards for the method (terminology, control of the used equipments and general principles of the different possibilities of applications). Since then, the WG7 developed many standards, which sometimes are now under review.

The finalized standards are:

- EN 1330 – 9 “Terminology used in AE testing”,
 - EN 13477 -1/-2 “AE testing-equipment characterization and control of their abilities”,
 - EN 14584 “AE testing of metallic pressure equipment – planar location”,
 - EN 15495 “AE testing of metallic pressure equipment – zone location”
- and the following work items are under preparation;
- WI 00138140 “Corrosion detection on flat-bottomed storage tanks”
 - WG7 NWI 607 “AE testing of fiber-reinforced plastics”.

As important as these standards were, it was crucial that AE testing was included in the EN 473, which regulates the qualification and certification of the test personnel, and establish the abilities and allowances of the different 3 levels of AE testing personnel. The new EN 473:2007 or 2008 requires also a common training content all over Europe in TR 25107 “Guidelines for NDT training syllabi”. Although training and certification do not guarantee producing excellent AE testing personnel, it is an important basis for the further training on-the-job, which has to be performed in the respective testing organization [20].

Beside these bundle of standards of the methodology AE testing has been introduced to different product standards in normative and informative annexes, like

- EN 13445 – 5 “Unfired pressure vessels, Testing and Inspection”,
- EN 12817/18 “Inspection and re-qualification of LPG tanks up to 13 m³” and
- EN 14334 “LPG road tankers”.

All these standards give, beside the guidance for the application and the test performance, criteria and rules for evaluation, real-time control and source-severity grading. Nevertheless this is the weakest point of these standards, because the specific numbers and other qualitative threshold are based on the experience of the test organization and/or have to be defined in the product standards. It is obvious, that these test organization, which has a large database for many different test objects will not give them just for free to other competitors. This is a problem, which has to be solved hopefully in the years ahead.

Conclusions

The test history over the last 30 years showed, that acoustic emission was and is still a very prospective testing method. Although it is not a classical non-destructive test method, I think we shall require from it the same rules, which are taken into account for all other NDT methods.

- AE testing shall be only applied by qualified and certified test personnel, and has to be implemented in a test organization with a quality management system in accordance with EN/ISO 17025 and EN 473.
- AE testing shall be performed according to specific EN standards (process and/or product oriented), if available, or the method including the evaluation criteria have to be validated according to the specific EN or other international standards.
- AE testing has to be used only by well equipped and well experienced test organizations, which have available the specific database for the respective test object or has performed the necessary number of pre-tests on specific test samples. This is one very important requirement, because according to our experience every test object is unique in its AE behavior.

If these requirements are fulfilled AE testing will be and become much more in the future a real-time NDT, which will not only more time saving and cheaper than other testing method, but it will increase the safety of the structure and will be an excellent tool for the fitness for purpose for the structures.

References

1. Tscheliesnig P., Theiretzbacher H. (1981) "Praktische Erfahrungen mit Hilfe der Schallemissionsanalyse", 2nd ECNDT 1981, pp. 221-223.
2. Tscheliesnig P., Theiretzbacher H. (1982) "Practical experiences with Acoustic Emission on large storage pressure vessels", 10th WCNDT 1982.
3. Tscheliesnig P., Theiretzbacher H. (1984) "Schallemissionsprüfung bei Druckaufbringung mit gasförmigen im Vergleich mit flüssigen Medien", 3rd ECNDT 1984.
4. Tscheliesnig P., Theiretzbacher H. (1985) "Leakage test by Acoustic Emission Testing (AET) on flat bottom tanks", 11th WCNDT 1985 pp. 40-45.
5. Tscheliesnig P., Theiretzbacher H. (1989) "New results from the detection of micro-leakages in the petrochemical industry", 12th WCNDT 1989, pp. 905-911.
6. Tscheliesnig P., Krenn G., Schauritsch G. (1990) "Dichtheitsprüfung mittels akustischer Korrelationstechnik in der petrochemischen Industrie", ÖGfZP-Jahrestagung 1990, pp. 51-59.
7. TÜV Österreich, CESI Spa, Vallen System. Shell Global Solutions. DOW Deutschland (2000), /Inspection of Flat Bottomed Storage Tanks by Acoustical Methods", Synthesis report of SMT4-CT97-2177 (EC).
8. Marino A., Tscheliesnig P. (2002) "A comparison between AE and MFL for tank floor inspection", 8th ECNDT 2002, p. 116, CD.
9. Tscheliesnig P. (2002), "Acoustic Emission Testing (AE) of bulk liquid storage tanks – Basics, case studies and future perspectives", 8th ECNDT 2002, pp. 119, CD.
10. Strunz K., Heck G., Tscheliesnig P. (1995) "Moderne ZFP-Verfahren zur Prüfung von Trockenzylindern in Papiermaschinen", ÖGfZP-Jahrestagung 1995, pp. 65-73
11. Tscheliesnig P. (1998) "New inspection method of steam drums in paper mills", 7th ECNDT 1998, pp. 2288-2294.
12. Lackner G., Tscheliesnig P. (2004) "Field testing of flat bottomed storage tanks with acoustic emission – a review on the gained experience", 15th EUROCORR 2004, CD.
13. Tscheliesnig P., Krenn G., Schauritsch G., Edinger H. (1995) "An Acoustic Leak Detection Pig", 2nd International Pipeline Technology Conference 1995, pp. 205-210.

14. Tscheliesnig P., Lackner G., Hermeling W. "The automatic performance of the repetition tests of pressure bottles with AE" 15th WCNDT 2000, CD.
15. Lackner G., Tscheliesnig P. (2001) "Automatisierte Durchführung von Wiederholungsprüfungen an Gasflaschen mit Schallemission", 13. DGZfP-Kolloquium Schallemission 2001, pp. 193-201.
16. Tscheliesnig P. (2004) "Detection of Corrosion Attack on ships, especially oil tankers, with acoustic emission (AE)", 16th WCNDT 2004, CD.
17. Tscheliesnig P. (2005) "Entwicklung einer Schallemissionsprüftechnik zur Prüfung von Korrosionen an Öltankern", DGZfP Jahrestagung 2005, CD.
18. TÜV Austria et al., Final Report of the EC-funded project „Detection and Discrimination of corrosion attack on ships (crude oil tankers) with Acoustic Emission (AE)“ project No. EVG1-CT-2002-00067.
19. Tscheliesnig P., Fontana E. (1998) "European standardisation in CEN TC138 WG7", EWGAE 1998, pp. 287-290.
20. Tscheliesnig P. (2004) "Training and certification on field of acoustic emission testing (AT) according the European standardisation (EN 473)", EWGAE, pp. 235-237.

ACOUSTIC EMISSION TESTING OF SEAM-WELDED HIGH ENERGY PIPING SYSTEMS IN FOSSIL POWER PLANTS

JOHN M. RODGERS

Acoustic Emission Consulting, Inc., Fair Oaks, CA 95628

Abstract

The structural integrity of seam-welded fossil high-energy piping has remained a major safety and operations-maintenance issue for US utility companies. Several failures of seam-welded superheat and hot reheat piping segments have occurred since 1992, two of them catastrophic. Advanced methods of inspecting piping welds with ultrasonic testing (UT), such as time-of-flight diffraction and focused/phased arrays, are pushing back the envelope of detection to earlier stages of creep damage, but these are still very expensive, and involve considerable logistical planning and downtime to perform. The Electric Power Research Institute (EPRI) has sponsored development activities since 1986 to mature the utilization of a real-time online evaluation method for seam-welded piping: Acoustic emission (AE) testing guidelines were published by EPRI in 1995, and over 100 full-scale tests have been performed to develop a database and correlate results with other established evaluation methods. An effort was begun in 2002 to standardize the testing method within ASTM (AE Subcommittee of E07.04) utilizing the developed database. Tests to date have shown high sensitivity to early stage creep damage, which is evidenced by development of cavities around inclusions in the grain boundaries. Successful double-blind testing with advanced ultrasonic inspection methods has proven both the reliability and sensitivity of the AE technique. The economics of the method are highly favorable. Only small areas of insulation need to be removed every 4.6-6 m to weld waveguides to the piping surface. These form a linear location array along the length of piping, providing global coverage of the piping system. Testing is performed online with normal peak loading and load cycling. No outage schedule is required to perform the AE examination. Results will be presented showing that the AE method has become a reliable and economical field evaluation tool for seam-welded high energy piping.

Keywords: Seam-welded piping, fossil power plants, online monitoring, high temperature creep

Introduction

Ever since the catastrophic failures of seam-welded, hot reheat (HRH) piping at Southern California Edison's Mohave plant in 1985 and Detroit Edison's Monroe plant in 1986, utility companies have been carefully considering the need for periodic inspections of critical piping to guard against creep-induced failures. Figure 1 illustrates the creep-damage mechanisms associated with seam-welded, high-energy piping. A number of serious defects in seamed piping were removed after inspections in the late 1980's, and for a number of years there were no more catastrophic failures [3]. Beginning in 1992, however, there have been six known failures of seam-welded superheat (SH) link piping supplied with Combustion-Engineering boilers, as well as two failures in hot reheat long seamed bends. Two of these have been catastrophic: Virginia Power's Mt. Storm Unit 1 in June 1996, and Kansas City Power & Light's Hawthorne Unit 5 in August 1998. No loss of life occurred in either of those two failures, but the cost of repairs and loss of power generation is of critical concern to utility companies in this age of growing competition. All failures of SH link piping have occurred on units with accumulated service time of

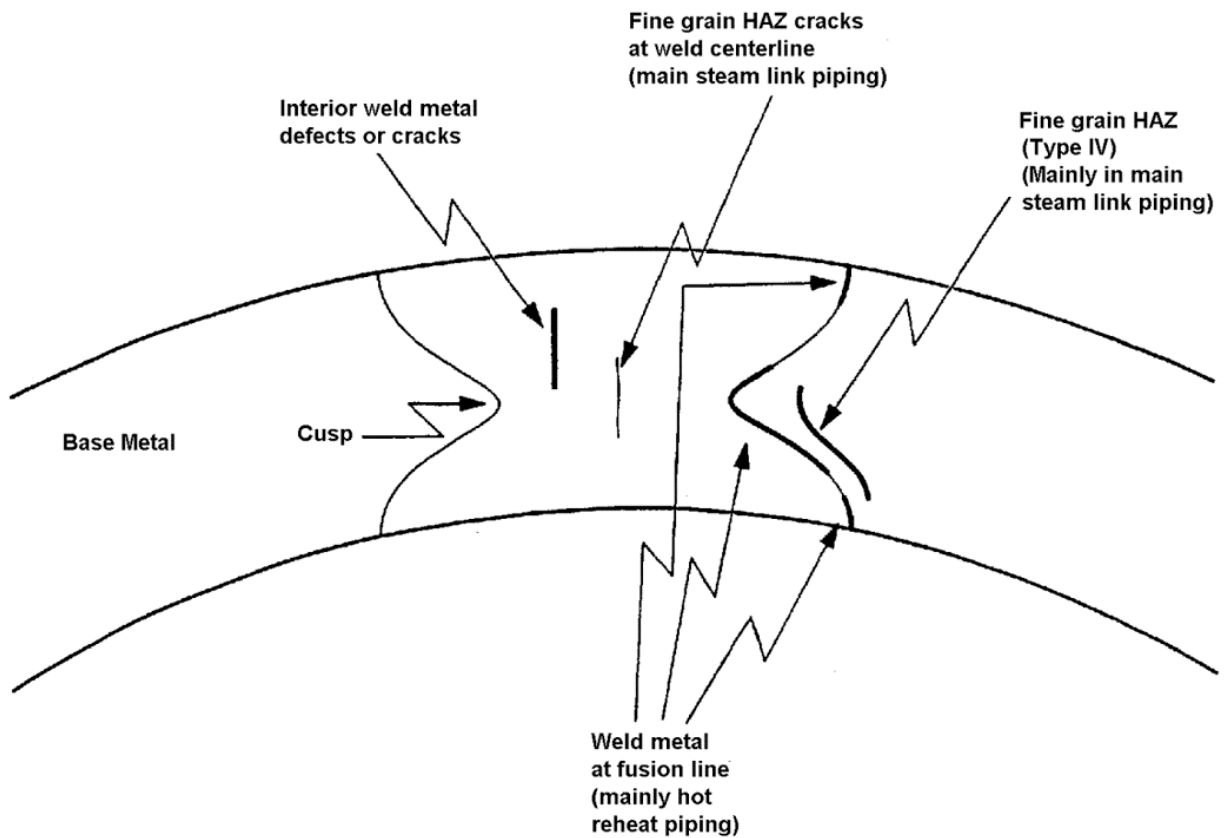


Fig. 1. Typical high-temperature creep damage occurring in seam-welded fossil piping systems constructed of P11 or P22 grade steels [3]. Type IV damage in the fine-grained HAZ typically occurs in subcritically annealed welds, which is more typical of thick-section SH link piping and some HRH piping.

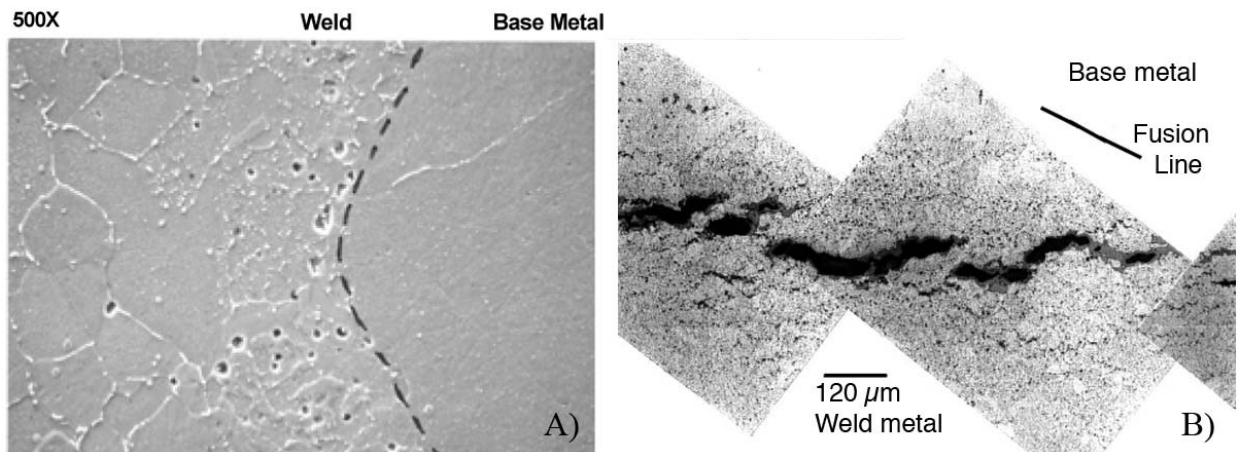


Fig. 2 a) Micrograph showing cavitation damage in the cusp region of an HRH double-V weld [4]. b) Micrograph showing advanced damage in the form of microcracks from a failed long seam bend [5].

125,000 to 225,000 hrs. Figure 2 shows micrographs of cavitation damage and advanced damage of microcracks from a failed long seam bend [4, 5]. These are truly microscopic defects. Compounding the problem of inspection is the inaccuracy of supplied documentation, which may not reflect the true alloy content and method of fabrication. The Hawthorne SH link piping

was not known to be seam-welded. The general aging of fossil plants will continue to raise concerns about the safety of operating seamed high-energy piping systems. Even seamless piping systems have had problems, including creep-related failures of circumferential welds, and the through-wall creep failure of a seamless SH bend that had been improperly fabricated. Current strategies for effectively managing the safety and life of seam-welded piping are based upon periodic inspection of the weld area for evidence of in service damage.

Equipment and AE Testing Set-up

The process of AE monitoring applied to piping systems starts with installation of AE transducers on welded waveguides (WG) along the length of the piping system. Spacing intervals for the WG are typically 4.6-6.1 m (15-20 ft), and installation of the sensors does not require full removal of piping insulation. There are several unique requirements for successful monitoring of high-energy piping with AE [1, 2]:

- The use of high-frequency sensors (300-400 kHz) and high frequency filtering (>200 kHz) to mitigate the effects of the steam-flow background noise. This noise is predominant below 300 kHz, and would obscure detection and accurate source location if lower-frequency, or broadband, sensors were used.
- The employment of a “floating” or automatic threshold that can control the sensitivity of detection by keeping the voltage threshold of detection above the average background noise.
- The use of active linear source location to determine the position of emitting sources on the line. The accuracy of location is dependent on the distance between sensor/waveguide positions, the pipe diameter, and the position of the emitting source. In the middle of the array between two sensors, accuracy has been demonstrated at ± 2.4 cm (± 0.6 ”). Near the sensors accuracy may degrade to ± 60 cm (± 24 ”). Still, this limits areas for follow-up inspection.
- The use of active AE-signal-feature filtering to further refine the data and eliminate obvious noise sources, such as flow turbulence. Rise time, duration, and average frequency have proven most valuable.
- Simultaneous recording of piping temperature and pressure are required to provide correlation between active AE sources and the likely source mechanisms.

Data Evaluation and Correlation

The primary characteristics of seam-weld creep-related sources are behavioral in nature—they respond to the pressure in the piping (hoop stress) and other mechanical sources of stress (geometry, hanger supports, etc.). During online conditions with normal peak load cycling, creep-related sources reveal themselves by repeated behavior with each peak load cycle [2]:

- The sources are sensitive to pressure, and may show a pronounced effect of emission rate with pressure (Figs. 3, 4).
- During load cycling, emission rates will typically peak near the start of the peak-load period.
- There is periodic emission activity during steady-state pressure and temperature conditions.
- The AE location profile is typically spread out over 1 m (40”) or more of piping length, and shows intermittent high-density locations of activity (Fig. 3).
- The amplitude range of emission sources broadens to higher values with higher activity rates (Fig. 2).

- Emission rates are much higher during startup conditions, even before substantial pressure loading. This demonstrates that the damaged area is responsive to stresses even when the piping is not in the creep regime ($>510^{\circ}\text{C}$, 950°F).

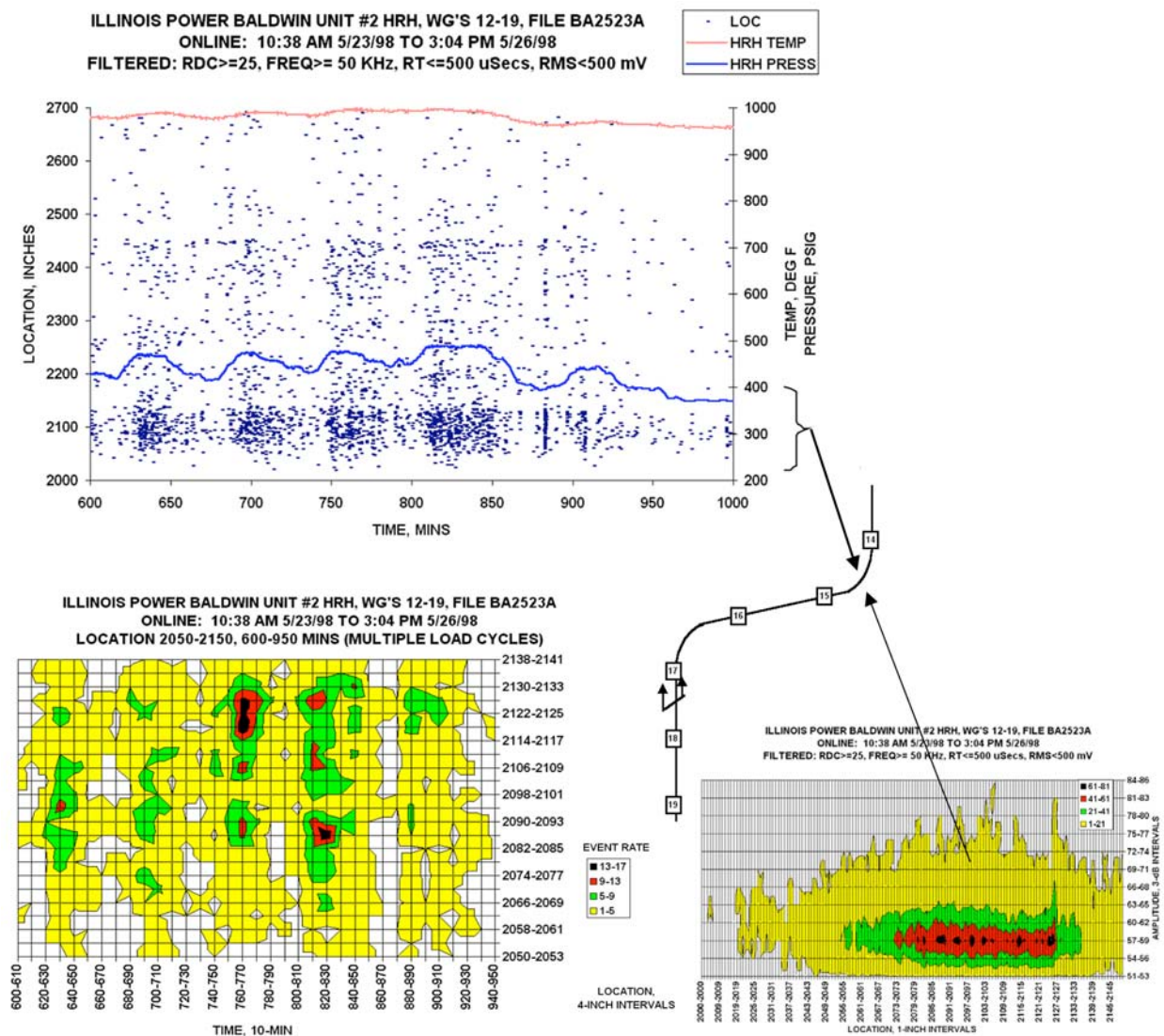


Fig. 3. A seam-welded clamshell elbow on Illinois Power’s Baldwin #2 HRH line shows typical creep-related AE behavior under cyclic pressure loading (upper left). The mechanism shows high sensitivity to load, and shows a distribution of activity along the elbow that varies with each load cycle (lower left). Bottom right shows the amplitude density feature map of this elbow location. Distributed higher activity sources are evident, and the amplitude dynamic range is larger in the high activity area. Defect growth at this early stage is probably related to decohesion of inclusions that are being affected by the creep process.

The amount of emission generated by the creep mechanism, the repetitive nature with each peak load cycle, and the extensive dynamic range (45-90 dB amplitude) of signals, is extraordinarily different from normal ductile fracture mechanisms, such as fatigue crack growth in mild steels. Many thousands of locatable signals are sometimes accumulated over 1 m or so of weld length and several cycles (days) of steam line operation at peak load. The sheer numbers of the sources is inconsistent with a ductile crack growth mechanism, which produces infrequent emission of more limited dynamic range with repeated load cycles. The acknowledged mechanism of

creep in seam welds is the development of cavities (cavitation) around nonmetallic inclusions and carbides on the grain boundaries in the fine-grained heat affected zone (HAZ) or fusion zone of the seam weld (Fig. 1). Isolated cavities soon give way to aligned cavitation along grain boundaries, then coalescing into scattered microcracks. Final consolidation and linking into macrocracks along the seam-weld direction occurs in the last stage of growth, which can be very rapid depending on a host of factors (wall thickness, annealing state, inclusion densities, thermal and localized mechanical stresses, etc).

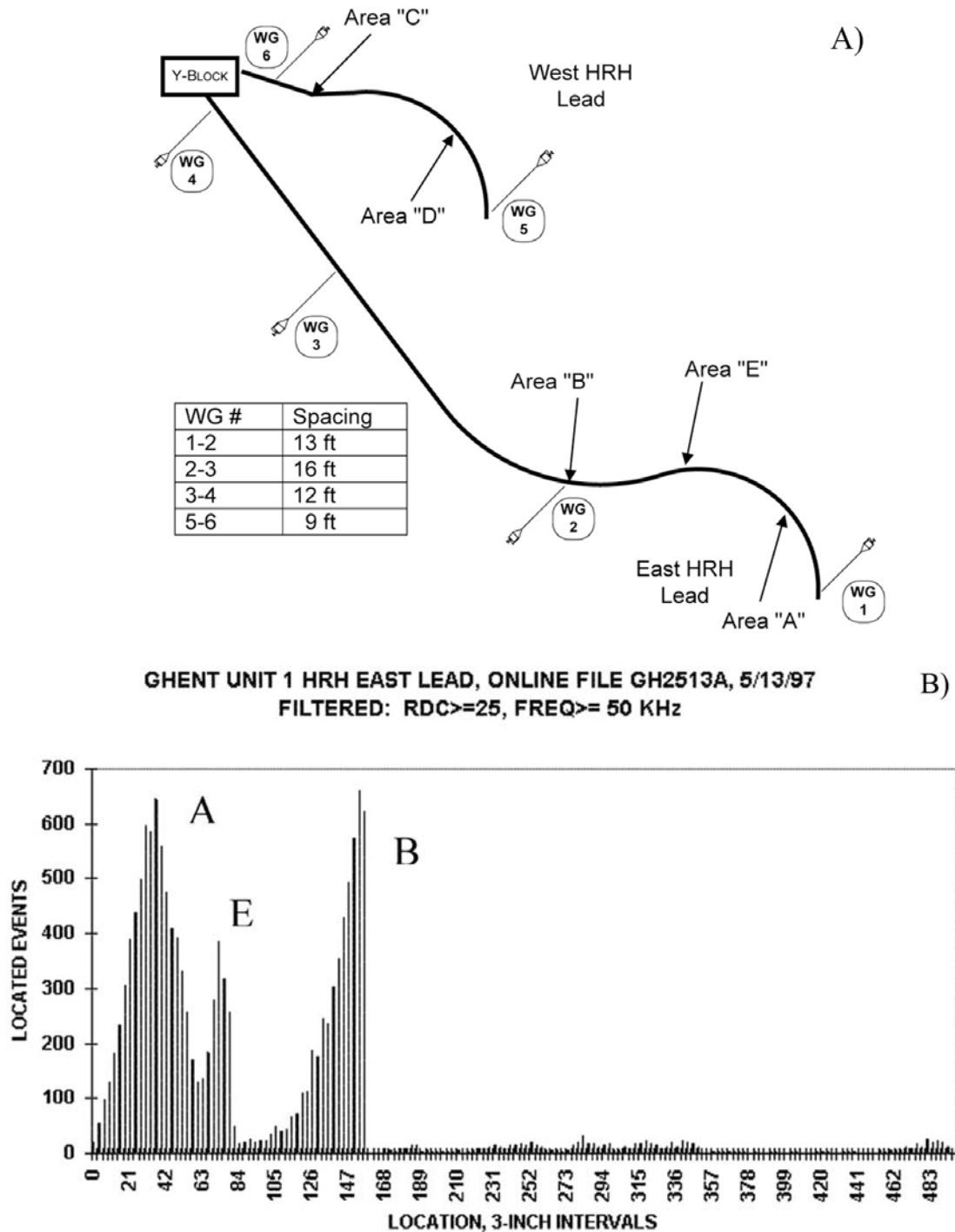


Fig. 4. Results of AE monitoring of the Ghent #1 East HRH link piping. a) Configuration. b) The linear source location plot shows three AE clusters detected (A, E, B).

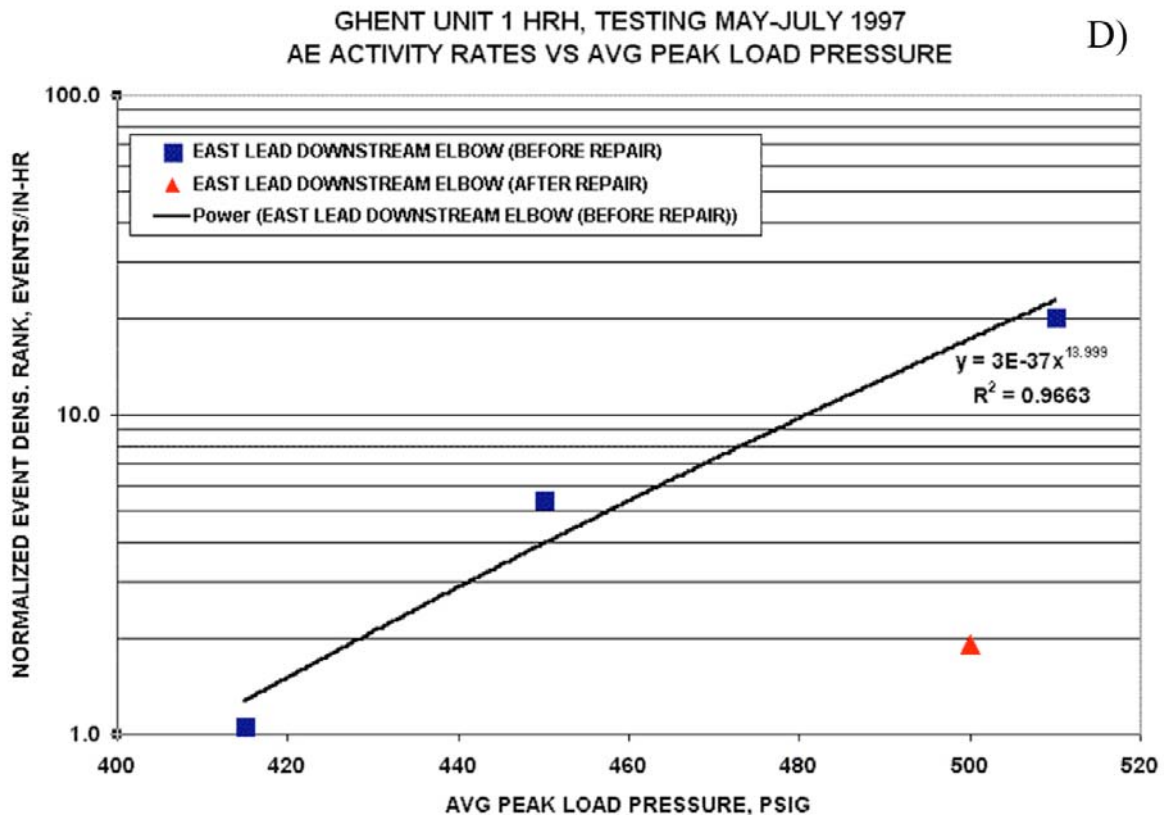
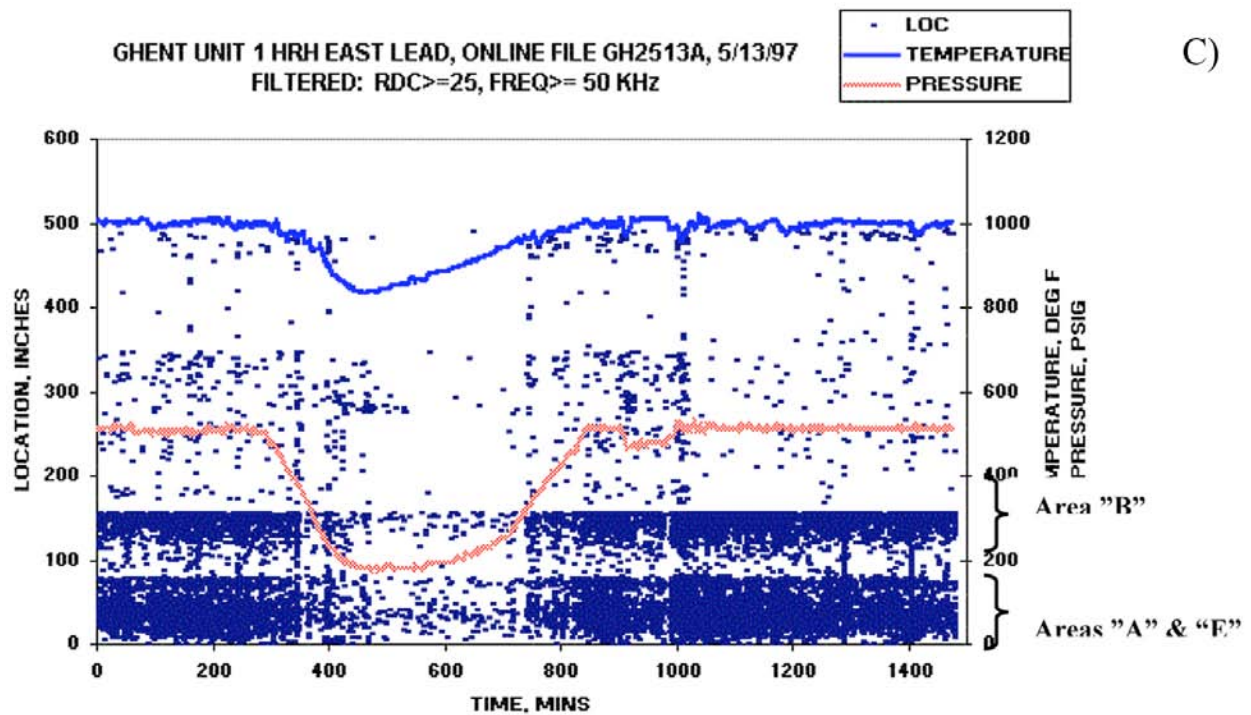


Fig. 4. Results of AE monitoring of the Ghent #1 East HRH link piping. c) A composite graph of plant parameters and AE source location vs. time for the three clusters detected. The pressure sensitivity of the sources is obvious, marking them as creep-related sources. d) The relative activity in events/inch-hr at different pressures for Cluster “A” in the original monitoring program. After through-weld repair of the piping, the activity drops by >90% for this area, indicating that the original sources of emission have been removed.

The early stage of this process involves the degradation of the bonding between particles and the metal matrix. These are load-carrying interfaces, and their eventual failure (decohesion) is the most plausible explanation for the amount and dynamic range of emission detected in the creep process. From the viewpoint of classifying AE behavior, this bears similarity to the experience of monitoring an organic-based composite material that has incurred extensive matrix damage. This also explains the emission that has been noted during the thermal excursion on startups, even without pressure in the system, when the piping is clearly not operating in the creep range. Damaged particle-to-matrix interfaces are prone to disbonding under high strain conditions, and startups are known to produce an even higher axial strain than at full load operation. Indeed, the results of the extensive EPRI field testing program to date has yielded detection of cavitation damaged seam welds that have not developed to the stage of micro- or macro-cracking.

A separate test program conducted in collaboration with a UK utility demonstrated that controlled creep-crack growth in small specimens produced increasing emission with increased crack growth rate. The emission rate was orders of magnitude higher for the increment of crack growth than would have been expected at lower temperatures and growth under fatigue conditions. The decohesion mechanism remains active throughout the creep regime, regardless of whether induced by directed stress at the tip of an active crack or in a volume of weld without visible cracking. This leads to high probability of detection of the creep-related failure process from very early stages, well before the damage represents a significant threat of structural failure.

Correlation of AE findings on seam-welded lines with other NDE methods and metallography were an important part of the EPRI studies and field tests from 1991 to 2001. Double blind testing was performed on Pacific Gas & Electric's Potrero #3 line in 1994, American Electric Power's Gavin #1 line in 1996, and Sierra Pacific Power's Valmy #2 line over 1997-1999. In these tests good correlation was established between conventional automated and manual multi-angle UT methods and AE cluster locations in seam and girth welds. But metallography was not used extensively in these tests to confirm the nature of the indications. Later testing would provide more extensive correlation between AE and advanced UT methods (TOFD, Phased Array, Focused Array), and more sensitive metallographic analysis (cryo-cracking with SEM examination). These included programs on Kentucky Utilities Ghent #1 HRH line and Brown #3 SH link piping (1997-98), Central Power & Light's Joslin #1 HRH line (1997), Illinois Power's Baldwin #1 HRH (1998), Salt River Project's Navajo #2 HRH line (1998), Southwestern Public Service Co's Harrington #2 HRH line (1999), and Portland General Electric's Boardman HRH line (2001).

By the late 1990's it was becoming better understood that creep damage in seam welds did not initiate as distinctive crack-like flaws, but rather as an accumulation of microstructural damage evidenced by "cavitation" development around inclusions and carbides along the grain boundaries in the heat affected zone or fusion zone of the seam weld (depending on whether the structure was normalized and tempered or subcritically annealed after welding). Several high-profile failures of seam-welded piping after missed or misinterpreted UT findings (Sabine #2 HRH bend in 1992, Mt. Storm #1 SH link piping in 1996, Gaston #4 HRH bend in 2001) led to a greater sense of urgency in the fossil utility industry to find earlier stage damage more reliably in seam welds. The AE studies mentioned provided proof of early stage detection of creep damage at the cavitation stage, often well before UT methods could reliably indicate a developing problem. Only the advanced metallographic method involving the use of cryo-cracking and SEM

examination at 2000-5000X was able to confirm this damage that AE was detecting at an early stage.

The standardization of the EPRI AE methodology for seam-welded piping began in earnest in January 2002 at the ASTM E07.04 acoustic emission subcommittee meeting. EPRI gave approval to the use of its documents and database as a necessary background for the development of the standard. The proposed standard WK 658 “Standard Test Method for Acoustic Emission Examination of Seam-Welded High Energy Piping” is nearing final balloting, and is expected to be approved in 2008. It is one of the most comprehensive and specific ever undertaken by an ASTM committee on an AE application.

Conclusions

Acoustic emission has proven its worth in online testing programs. Approximately 30% of lines tested have shown no significant findings of creep damage, and most others have shown only minor activity at suspect locations. The majority of seam-weld findings has been in elbows and bends, followed by hanger locations on horizontal line segments. These are known to be higher stressed areas, and offer further validation of the AE methodology. The correlation with follow-on nondestructive inspection has been very good, but the lesser sensitivity of UT inspection methods will generally not confirm early stage creep damage at the isolated cavitation stage. The economics of inspection and relative certainty of detection at an early stage of creep damage should be increasingly attractive to companies attempting to manage their piping systems in a climate of reduced capital and operations-maintenance spending.

References

1. B. Morgan, C. Foster, *Acoustic Emission Monitoring of High-Energy Piping, Volume 1: Acoustic Emission Monitoring Guidelines for Hot Reheat Piping*, Electric Power Research Institute, TR-105265-V1. 1995.
2. J. Rodgers, R. Tilley, *Standardization of Acoustic Emission Testing of Fossil Power Plant Seam-Welded High Energy Piping*, ASME Pressure Vessels & Piping Conference, San Diego, July 25-29, 2004, PVP-Vol. 471, pp. 113-131.
3. J. Foulds, R. Viswanathan, J. Landrum, “*Guidelines for the Evaluation of Seam-Welded High Energy Piping*”, Electric Power Research Institute, TR-104631, 1996.
4. R. Munson, J. Rodgers, R. Tilley, *The Utilization of Advanced Metallographic Techniques to Verify In-service Damage in Long-seam Welded, High Energy Piping*, EPRI Fossil Plant Inspection Conference, Atlanta, 1999.
5. J. Foulds, R. Carnahan, *Examination of Sabine 2 Hot Reheat Pipe Seam Weld Cracking*, Electric Power Research Institute, TR-107141, 1997.

ACOUSTIC EMISSION AND X-RAY TOMOGRAPHY IMAGING OF SHEAR FRACTURE FORMATION IN CONCRETE

TATYANA KATSAGA and R. PAUL YOUNG

Lassonde Institute and Department of Civil Engineering, University of Toronto, Canada

Abstract

This paper describes how different aspects of fracture formation in concrete can be investigated using a combination of acoustic emission (AE) techniques and high resolution computed tomography (CT). AE and elastic wave velocities were measured using the Hyperion GigaRAM AE Recorder, a device developed for the ultra-detailed investigation of brittle fracture and failure of rock and rock-like materials. AE analysis includes studying complex spatial and temporal fracture development during the slow quasi-static fracture process. Predominant microcrack mechanisms were analyzed at different stages of fracture formation. CT images were used to investigate the influence of concrete microstructure on fracture topography. Combined AE and CT images revealed different aspects of fracture development, thus expanding our understanding of AE events and their mechanisms. These images show how coarse aggregates influence fracture nucleation and development, as well as event sequences and mechanisms during aggregate fracturing.

Keywords: X-ray computed tomography (CT), concrete, aggregates, shear fracture.

Introduction

Fractures in concrete are directly influenced by the complexity of the concrete's microstructure, from nucleation and propagation to surface roughness formation. To study this influence, researchers used different techniques and approaches. One approach is to measure and analyze the fractal dimension of concrete fracture surfaces, depending on the kind of aggregate (Brandt et al., 1993) or the maximum aggregate size (Issa et al., 2003). A correlation has found between fractal dimension and fracture toughness. Another approach involves non-destructive 3D studies using AE techniques (Mihashi et al., 1991; Landis et al., 1995; Chen et al., 2004). These studies show how concrete microstructure influences the fracture process zone, fracture energy, and fracture toughness. In addition, advanced AE techniques can be used to define AE source mechanisms (Zang et al., 1998; Ohtsu et al., 1998; Grosse et al., 2003).

The detailed, nondestructive investigation of cracks inside materials has become possible with the development of X-ray Computed Tomography (CT) techniques. For example, Landis et al. (2000) calculated fracture energy using the actual surface area of internal cracks using CT data collected during loading. Chen et al. (2004) compared cracking paths, obtained by X-ray inspection, in concrete with different maximum aggregate sizes; Chen's study discovered a correlation between the width of the crack zone and the increasing of the maximum aggregate size. Young et al. (2007) combined CT and AE imagery to relate physical features within the sample to AE locations and phases of micro-scale damage.

In order to gain improved insight into the 3D micro-mechanics of failure in concrete, this study combined AE techniques with high-resolution X-ray CT techniques. The recorded AE event source locations were related to high resolution X-ray CT images obtained from core

samples extracted from the beam after testing. Furthermore, various aspects of failure were studied by analyzing the AE mechanisms associated with the different aspects of fracture propagation through the concrete components.

Experimental Procedure and Data Processing

This experiment has been a part of an extensive experimental program conducted at the University of Toronto (Sherwood et al., 2007; Katsaga et al., 2008). Using the Baldwin test frame, a large, lightly reinforced, normal-strength concrete beam with large coarse aggregates (maximum size = 55 mm) was loaded to shear failure in a three-point bending test. The specimen, designed to be shear-critical, was 9000-mm long, 1510-mm tall, 300-mm wide, and was supported on rollers spaced at 8100 mm apart.

AE setup

One half of the specimen was instrumented with AE sensors to record the acoustic emissions induced from microcracking during loading. The concentrated array of 24 sensors, 16 receivers (V103, Panametrics), and 8 pulsers (R15, PAC) was designed to investigate diagonal shear fracture development before failure and was installed on the surface of the beam using special holders screwed into the concrete (Fig. 1b). The monitoring parameters were selected based on the results of pencil-lead break or artificial shot (ultrasonic pulse) tests: 60 dB pre-amplification and 10 MHz sampling frequency.

Signals from the sensors were recorded using a sixteen-channel recording system called the Giga Recorder (Fig. 1a). Typically, AE systems experience downtime when they record discrete AE events because the transfer of events from their random access memory (RAM) results in recording blackouts. The Giga Recorder has the ability to acquire an ultrasonic waveform continuously at high sampling rates (up to 20 MHz) and at 14-bit resolution on a circular 40 GB RAM buffer; this buffer is then locked and downloaded to disk following the critical stage of an experiment (i.e. failure of a sample). Our experiment featured a sampling rate of 10 MHz, which translates into a 2-minute continuous waveform (Fig. 1c). In addition to the continuous waveform, the Giga Recorder also records discrete triggered AE signals (Fig. 1d) during the entirety of the experiment at a rate of 15 events per second. More detailed discussion of the Giga Recorder can be found in Thompson et al. (2006).

AE data processing

InSite (ASC, 2008) software was employed to analyze AE events, continuous waveforms and velocity data. Before AE data processing, P-wave velocities were defined, assuming straight ray-paths between pulsers and receivers. Wave velocities transmitted through the concrete beam before loading did not show any preferred direction in velocity variations; therefore, a homogeneous-isotropic velocity structure was assumed to exist throughout the concrete volume. A combination of Simplex and Geiger methods was used for locating AE events, a combination that provides faster solutions with improved error analysis.

One of the advantages of recording continuous waveforms, is the possibility of extracting discrete events by applying new settings. The program *SeisAcq* (ESG) was used to process the continuous records and to “re-harvest” triggered data from them. An AE event was triggered if signals on five channels exceeded the 80-mV threshold. By contrast, initial experimental settings used seven channels and a 100-mV threshold. None of the discrete events extracted from these

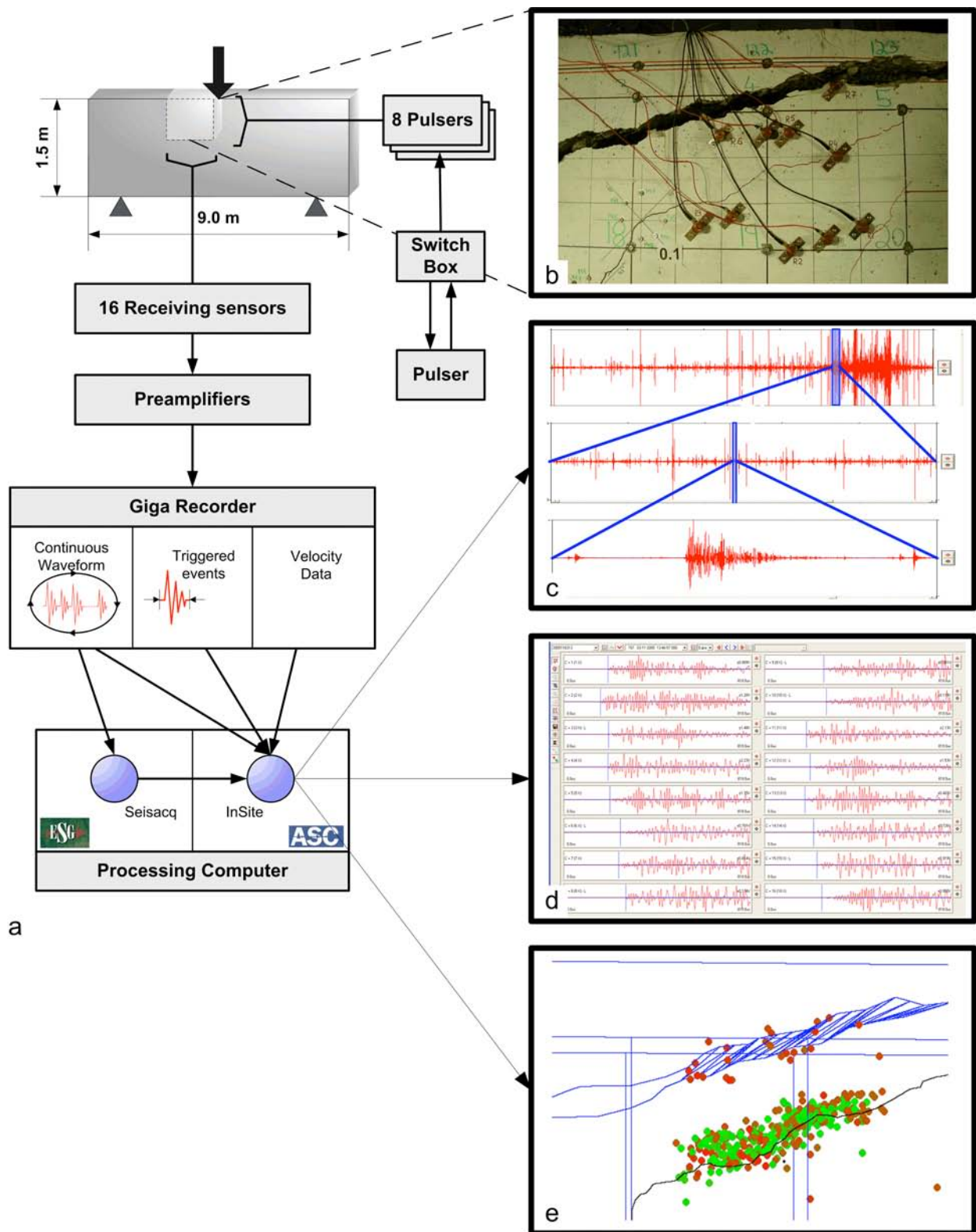


Fig. 1 a) Schematic diagram of acquisition system and processing software; b) Beam with array of sensors after testing (front view); c) continuous waveform; d) triggered event on 16 channels; e) AE source locations.

continuous waveforms were lost because the transfer of events from RAM involved no downtime. The detailed logic diagram of our equipment and software use is presented on Fig. 1.

The relative comparison of the size of AE events was done based on their instrument magnitude, which was calculated based on equation (1). An instrument magnitude is calculated for the event by averaging over the instruments used in the source location,

$$M = \log_{10}(r \cdot W_{RMS}) \quad (1)$$

where r is the source to receiver distance and W_{RMS} is the peak signal amplitude on the RMS waveform (ASC, 2008).

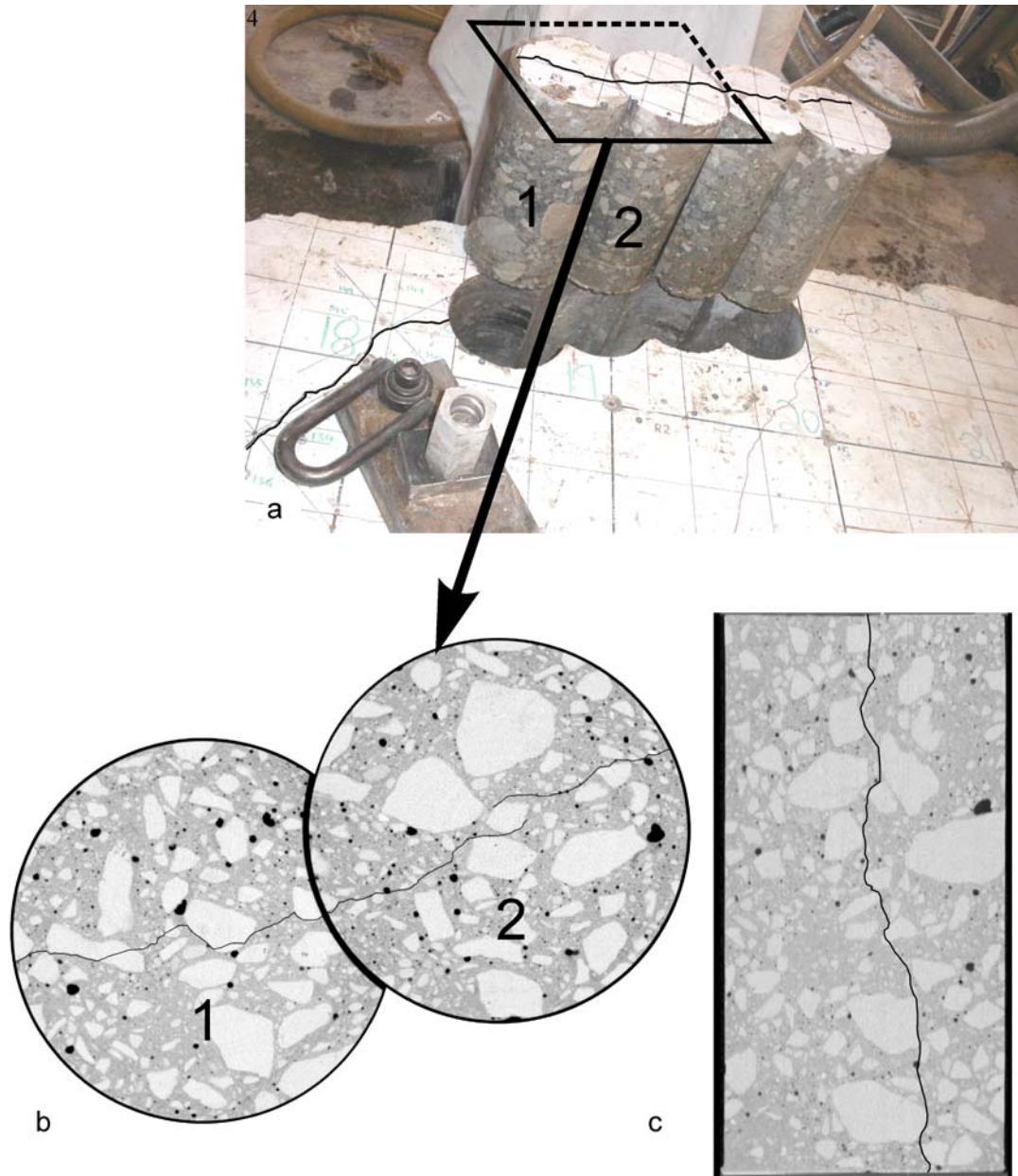


Fig. 2 a) 300-mm cores extracted from the beam: the jagged black line identifies fracturing that has occurred in the cores; b) CT images for two cores (section view); c) reconstructed image across the core length perpendicular the fracture.

To analyze the microcrack mechanisms and their evolution during shear fracture formation, P-wave first-motion polarities were defined and analyzed using a first-motion polarity method (Zang et al., 1998),

$$pol = \frac{1}{k} \sum_{i=1}^k sign(A^i) \quad (2)$$

where A is the first-motion amplitude and k is the number of sensors. In this study, positive polarity represents compressional pulses initiated by tensile fractures. Events are considered as tensile if pol is between 0.25 and 1, shear if pol is between -0.25 and 0.25, and crushing (implosion) if pol is between -0.25 and -1.

Computed tomography imaging

After the failure of the beam, four core samples containing the fracture that preceded the final failure were extracted from the beam (Fig. 2). The location of the coring was defined by studying AE event locations. Two samples were sent to the University of Texas for high-resolution X-ray Computed Tomography (Ketcham et al., 2001). The samples were imaged separately using a high energy scanning system designed for scanning large samples. Horizontal CT images were taken at 1 mm intervals across the sample diameter, with a resolution of 1024 x 1024 pixels (6.6 pixels per 1 mm) (Fig. 2b). These images were reconstructed to provide a view across the length perpendicular to the fracture plane (Fig. 2c).

Through the consequential CT sections, the 3D microstructure of the material can be non-destructively reconstructed. Different densities of concrete matrix and aggregates as well as strongly marked interface between them cause variation in X-ray attenuation, giving a clear picture of the microstructure. The density of fractures and air voids contrasts sharply with the rest of material, thus making them easily distinguishable on CT images. In this work, CT images were used for two purposes: to analyze the influence of the microstructure on fracture propagation and to reconstruct the temporal and spatial scenario of fracture formation using combined CT and AE data.

Combination of AE and CT data

The combination of CT and AE data is what the custom AutoCAD built-in dialog-based Visual Basic Application (VBA) was designed to do (Fig. 3). This application allows us to study the CT scan images in precise relation to the AE locations, using the advanced viewing and graphical tools of AutoCAD. VBA application loads data from an event parameter text file created by InSite and processes it in AutoCAD. The main features of this application are event filtering and drawing properties. Events can be differentiated by size, shape and color based on calculated instrument magnitude and time of occurrence.

CT images were imported in AutoCAD and placed in separate layers at their exact positions (Fig. 4a). Then fractures were traced and differentiated by color: black represented fractures that propagated through concrete matrix, blue through matrix-aggregate interface zones, and red through an aggregate (Fig. 4b). All of these traced cracks allowed us to reconstruct the complicated 3D topography of the fracture surface inside the material (Fig. 4c). As the next step, AE signals were imported (Fig. 4d) and filtered by ± 7 mm slices from the plane of the images and were superimposed onto these images (Fig. 4e).

Image analysis

After the cracks on the CT images were traced, they were separated into three different groups: matrix cracks, aggregate cracks, and interfacial cracks. The cracks were then converted into bitmap images and processed, using an automated image-processing program (Launeau et al., 1996) to investigate the influence of the concrete's microstructure on fracture propagation. This program is based on the intercept method, which involves scanning a drawing with a set of

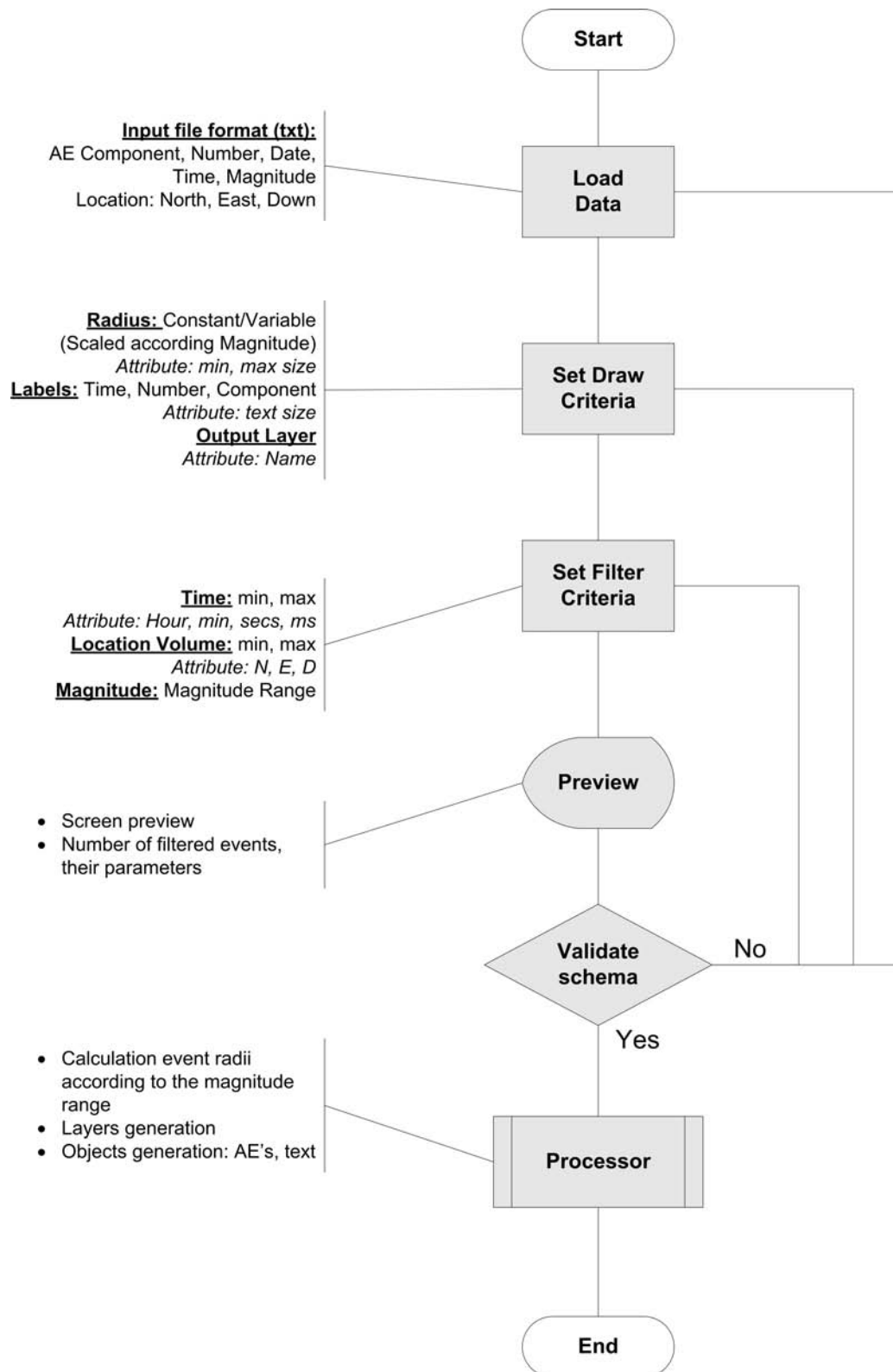


Fig. 3. Schema of VB Application for combining CT images and AE events in AutoCAD.

parallel lines at specified angular intervals and counting the number of intercepts with the crack lines. The results of the intercept counts were used to build a rose of directions for each group of cracks and to analyze statistical data.

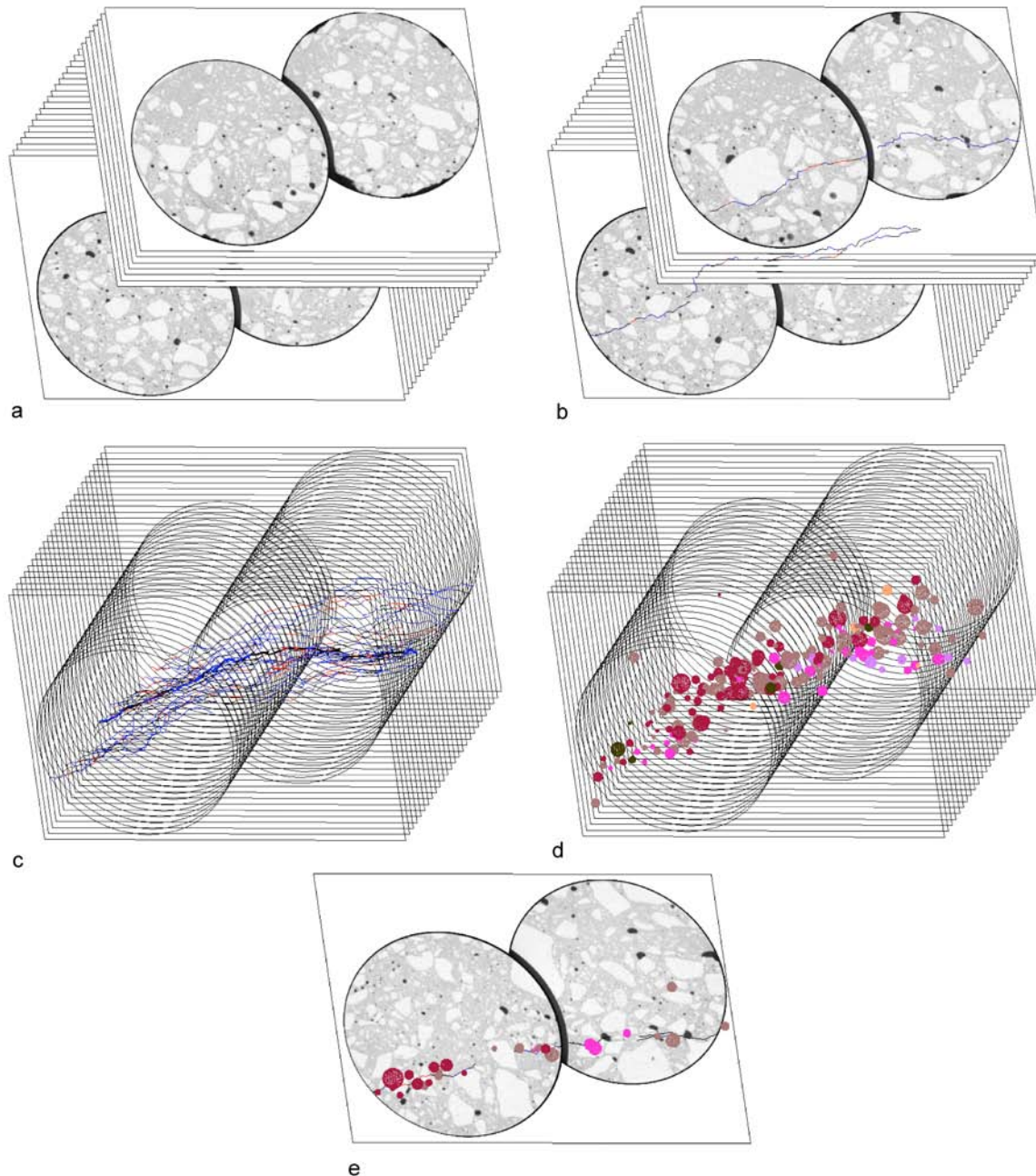


Fig. 4 Combination of AE and CT data in AutoCAD: a) loading images; b) crack tracing; c) 3D fracture surface topography; d) loading AE events; e) combined CT and AE image.

Results and Discussion

Crack topography

Images of three groups of cracks are presented in Fig. 5a. The results of intercept counting showed that, for this slow fracture propagation, interface cracks take 45.4% of the overall crack length, matrix cracks –43.6% and aggregate cracks –11 %. Direction Rose diagrams extracted from the analysis showed that aggregate cracks and matrix cracks have the same main crack direction (15° from 0) and almost the same maximum intercept directions (3.019 and 2.944). However, the situation is different for the interface crack: the direction of the main crack is almost the same (14°), but has a number of secondary intercept directions (Fig. 5b). These secondary

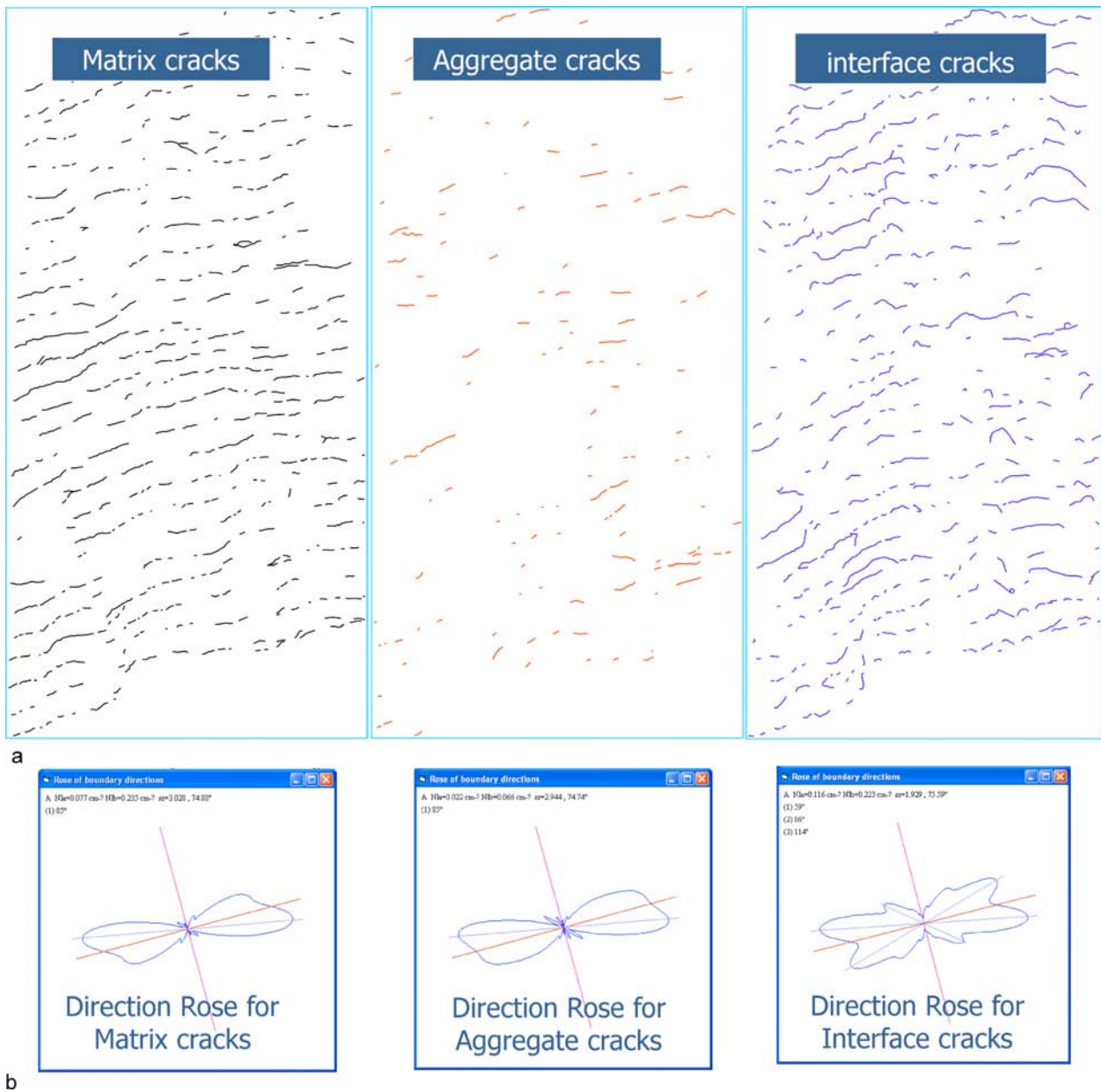


Fig. 5. Microstructural observations: a) crack path divided into matrix cracks, aggregate cracks and interfacial cracks; b) direction rose diagrams for each group.

directions show that interface cracks are responsible for the fracture surface's high degree of roughness.

Studying CT images revealed that large coarse aggregates have the largest impact on a fracture path. Figure 6a illustrates that large aggregates change the fracture direction locally and the fracture travels along one side of the aggregate. In this case, the fracture surface's roughness depends on the roughness of the aggregate. It was found that if a long aggregate crosses a fracture, the aggregate is more likely to be fractured (Fig. 6b). This phenomenon could be explained by the fact that in this case the fracture spends more energy traveling around the aggregate than fracturing it. Figure 6c shows the general cases of the fracture traveling around small and medium aggregates along aggregate-matrix interfaces. Aggregates of this size range thus control the fracture roughness in general. Therefore, by controlling the size and the shape of coarse

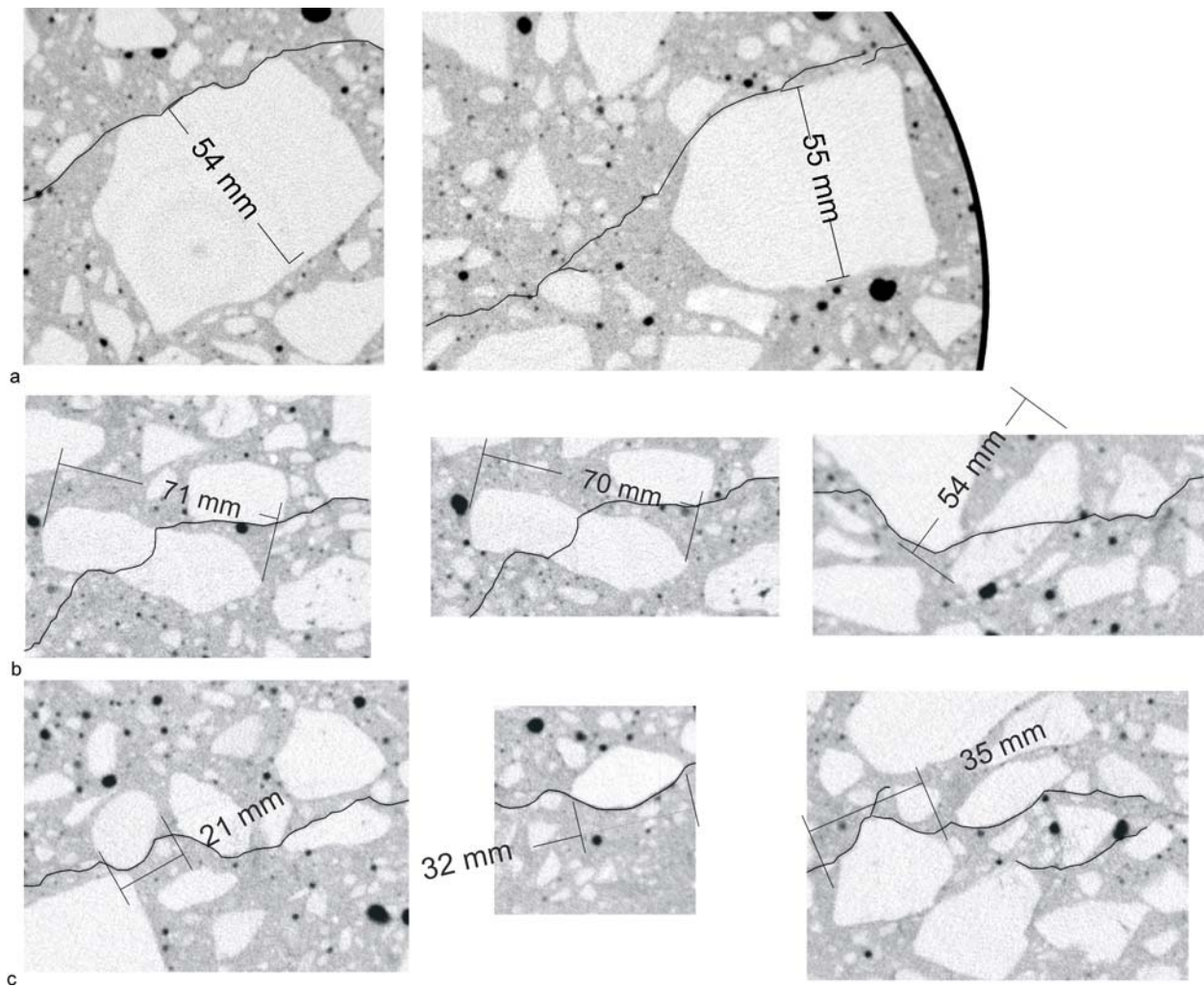


Fig. 6. Microstructural observations: a) large aggregates change fracture path; b) cleavage of the long aggregates; c) roughness formation through smaller aggregates.

aggregates, it is possible to create the rougher fracture surfaces necessary to improve aggregate interlock, an effect that plays an extremely important role in the transferring of shear stresses (Sherwood et al., 2007).

Acoustic Emissions

AE source locations, divided into time periods A to E, are presented from the top point of view in Fig. 7. Events for each time period are represented by different colors. Symbol sizes are scaled according to their event magnitude. Periods A, B, and 36 seconds of period C show triggered AE events, while the rest of periods C, D and E show AE events extracted from continuous waveforms. AE locations exhibited non-uniform event distribution along the fracture surface width. During period A, five isolated events occurred in the space ahead of the fracture front. During period B, several events nucleated near the front surface of the beam. Period C showed AE event development in two directions: forward and sideways, across the width of the beam in a narrow band leaving uncracked concrete between the band and the primary fracture front. During period D, the sideways fracture connected with the primary fracture front and propagated a few centimeters forward. Overall, 121 events were located. At the end of period D, microcracking was observed throughout the region of eventual fracture surface. Period E showed 120 events occurring, due to the shearing of the cracked surfaces at the fracture.

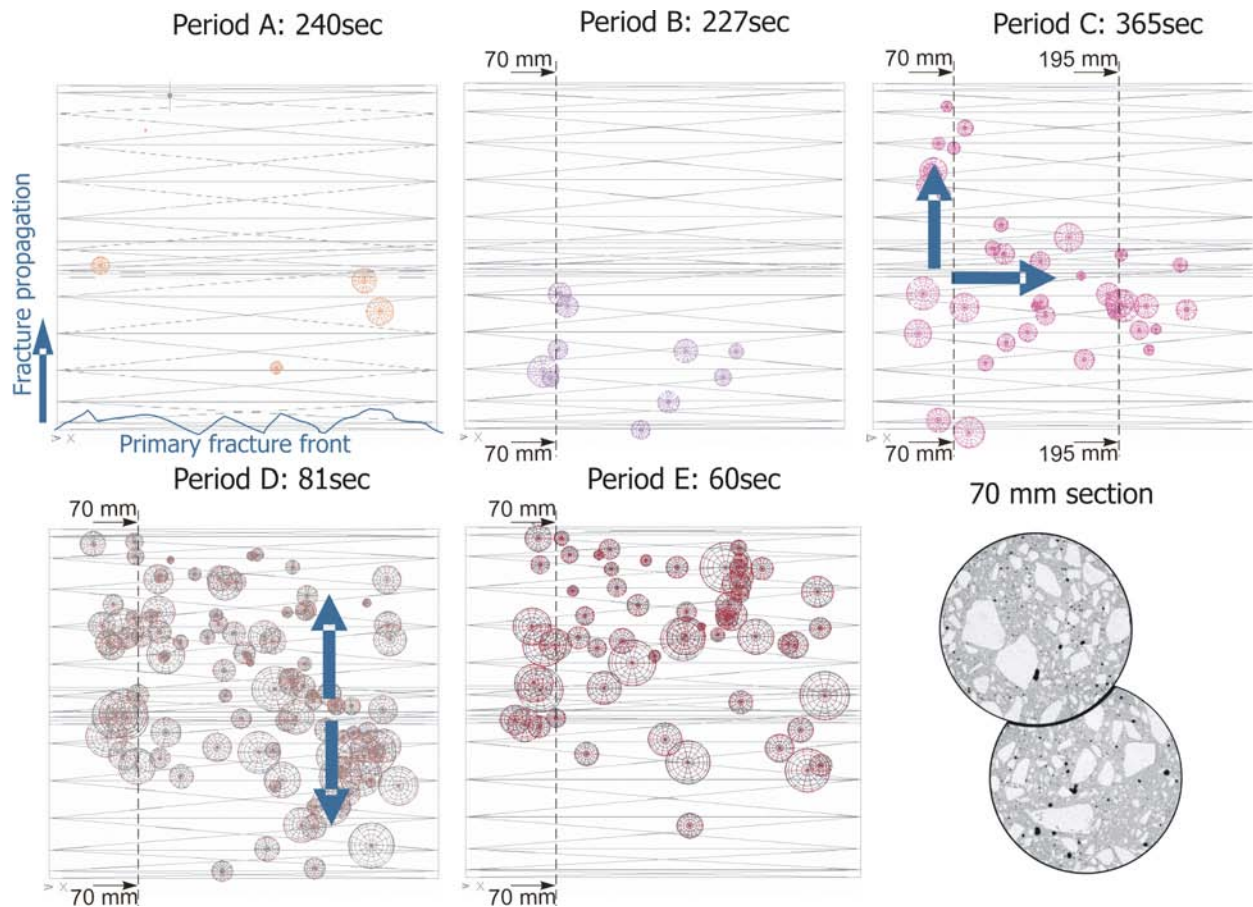


Fig. 7 AE source locations for different periods of fracture propagation and an example of a CT image that represent a section.

AE mechanisms, obtained using first-motion polarities, were investigated for each of the shown periods. The events during Period A, which signify fracture nucleation, are dominantly tensile (80 %). The number of tensile events decreases gradually with the fracture development (from 80 % to 25 %). The number of shear events stays almost the same for periods B, C and D (32-33 %) and increases dramatically during period E (66 %). It was also found that the shear events released large amount of energy and produced high magnitude events compared to tensile events. The implosion events were similar in magnitude to shear events. However, they were not presented in the first two periods and were rare during the final periods of the fracture formation (8-9 %), except for the period D (19 %). A close analysis of the implosion events is presented in the next section.

AE and Crack Topography

AE and CT techniques both carry significant amounts of information about different aspects of fracture in material. CT techniques show the connection between crack topography and material microstructure, whereas AE techniques reveal its spatial and temporal characteristics. Combining both of these techniques creates a unique opportunity to investigate the specifics of fracture formation and propagation. This investigation explained a number of important observations, including event sequences and the nature of the event mechanisms. Figure 8 shows a 70-mm section and corresponding AE events filtered by ± 7 mm from the plane of this section. This section was chosen because, at this level, the first event nucleation occurred during period B (Fig. 7). A combined AE and CT image (Fig. 8) shows that the first events during nucleation

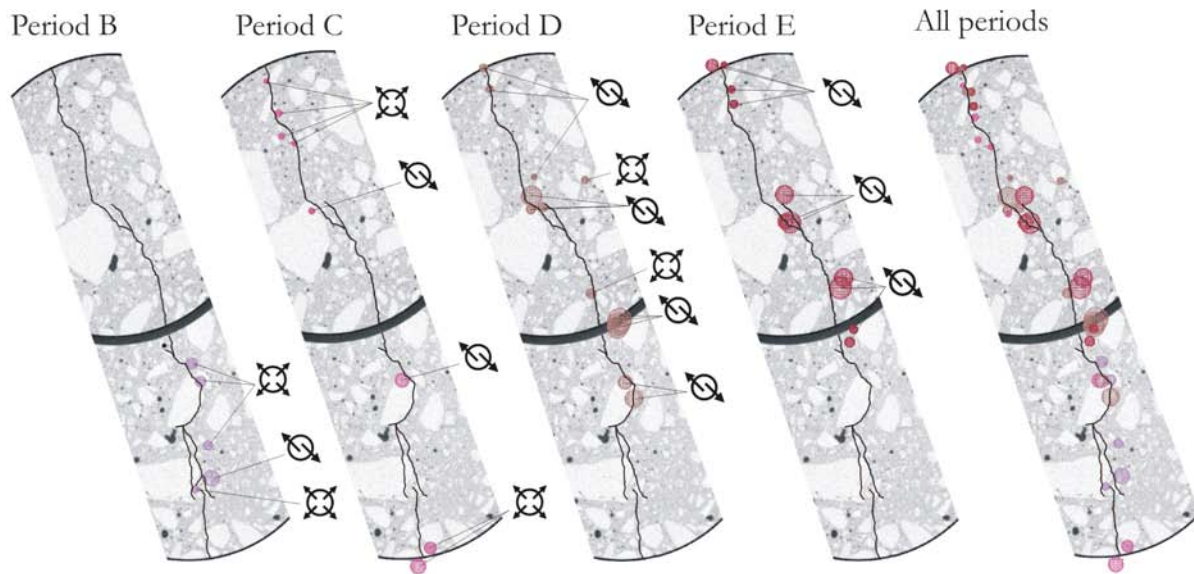


Fig. 8 CT image at 70-mm section (see its position on Fig. 7) and corresponding AE events and their mechanisms: \square - tensile events; \circ - shear events.

were initiated by fracturing at the edge of an aggregate. First motion polarity analysis showed that these events were actually a single tensile and shear event. At this level, the rest of the events during this period were tensile events that occurred at the interface of aggregates. During period C, a number of events the majority of which were also tensile events at the interface of large and small aggregates occurred along the fracture path. One large shear event appeared next to the tensile events from stage B. During period D, the character of events changed: most were large magnitude shear events which occurred at new positions and next to events from the previous period. Events from stage E were only shear events distributed along the fracture path. We can, therefore, assume that stage E shows the shearing of fracture surfaces that were formed before stage E.

The combination of CT images and AE events revealed why the spatial development of the fracture during period C was not uniform (Fig. 7). Large particles of coarse aggregate were found on both sides of the AE band. Because these large aggregates strengthened material locally, the fracture was forced to propagate only between aggregates.

In the section “Crack topography”, it was shown that 11% of the fracture path was through aggregates. It was also illustrated that some of these aggregates were elongated. However, analyzing CT images, we found a number of equiaxed aggregates fractured. Studying AE events related to these fractured aggregates showed that most of them were fractured during period D, which can be explained by the accumulation of higher stresses during this period. Figure 9a demonstrates a sequence of events and their mechanisms during the fracturing of an aggregate. A smaller tensile event (marked as 1) initiated the fracturing and three large magnitude shear events concluded the process. Only one normal-shaped aggregate was found fractured during Stage C (Fig. 9b). This aggregate was located at the level 195 mm (Fig. 7). As discussed above, during Stage C events were propagating non-uniformly in a narrow band between large aggregates. The presence of these aggregates caused a high local stress redistribution that forced the fracture to propagate through the aggregate located in middle. The sequence of events during the fracturing of this aggregate is similar to the previous case: a small tensile event (Fig. 9b, 1) is followed by a large shear event (Fig. 9b, 3). However, in this case, a large implosion event (Fig. 9b, 4) occurred

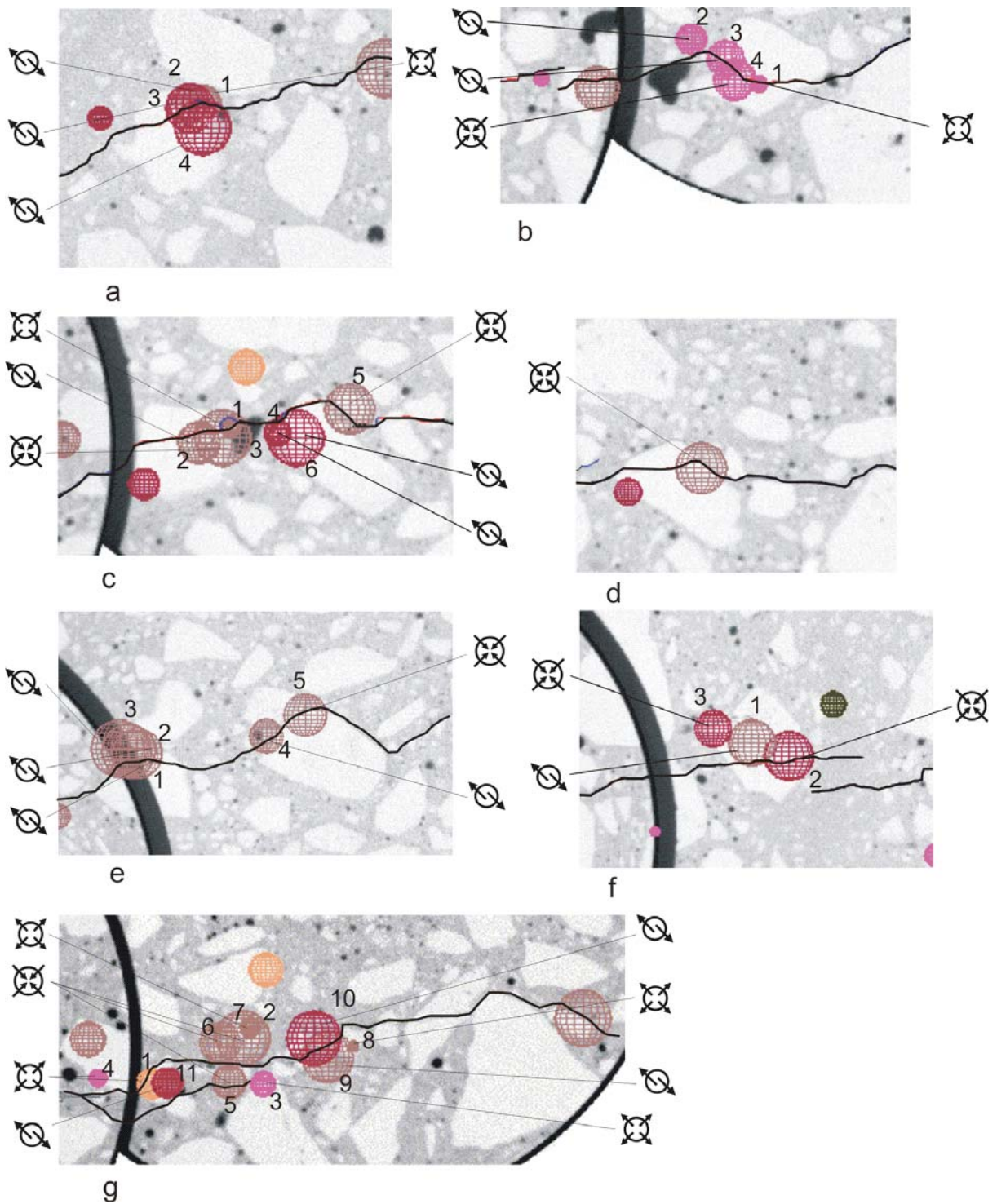


Fig. 9 CT images and corresponding AE events, their sequence and their mechanisms for different situations: - tensile events; - shear events; - implosion events.

between these two events. The analysis of further fractured aggregates and related AE events revealed more implosion events involved in aggregate fracturing (Figs. 9d, 9e, 9f). The fact that the most aggregate fracturing occurred during period D explains the large number of implosion events at this period, compared to the other periods. Some implosion events during period D were found in the concrete matrix. For example, in Fig. 9g, three large implosion events (Fig. 9g, 5-7) are shown in the space marked by the tensile events that occurred earlier (Fig. 9g, 1-3).

Conclusions

The combination of AE and CT imaging provides us with a unique opportunity to study AE events in relation to the microstructure of material.

High-resolution CT images in our study resulted in a detailed picture of the concrete microstructure, including the aggregates, cracks, and air voids. The influence of the concrete microstructure on the topography of the fracture surface was analyzed using these images. It was found that large aggregates can change the direction of a fracture path locally and that the fracture roughness is controlled by interface cracks. It is, therefore, possible to optimize aggregate interlock by controlling the size and shape of coarse aggregates.

The AE event locations revealed a complex, non-uniform spatial and temporal fracture development in the concrete with the large aggregates at the slow quasi-static stage of fracture propagation. The early stages of fracture formation were associated mainly with tensile events, the number of which decreased with fracture development. Finally, the number of shear events became dominant (66%) due to the shearing of the cracked surfaces. Therefore, studying the predominant mechanisms during monitoring or inspection can be helpful in defining the stage of fracture development.

As expected, the cracks on the CT images showed a close correlation with AE events. Analyzing the temporal and spatial evolution of AE events in relation to the CT images allows us to reconstruct the failure sequence precisely. Coarse aggregates are shown to play an important role in fracture nucleation and development: aggregate fracturing is found at the place of fracture nucleation and the non-uniform development of events is explained by the influence of large pieces of aggregates. A close analysis of combined AE and CT images showed that the events at the new location were mainly tensile events and subsequent events at the nearest position were shear events. A similar sequence of events is found when the fracture propagates through aggregates. Additionally, a number of implosion events were involved in the process of aggregate fracturing. It was revealed that aggregates were fractured mostly during the final period of fracture surface formation, which explained the large portion of implosion events compared to the other periods.

The overall results of the work show that the combination of AE and CT imaging provides an extremely effective tool for the investigation of the process of fracture formation in materials with complicated microstructure.

Acknowledgments

We are grateful to M.P. Collins and E.G. Sherwood for providing an experimental opportunity to apply AE techniques during their experimental program, in which the effectiveness of shear design methods was evaluated for large, lightly-reinforced concrete beams. We also would like to thank D. Collins, P. Benson, B. Thompson and F. Nasserri for helpful discussions and suggestions. This work was made possible through an Ontario Graduate Scholarship to Katsaga and Keck Chair research funds to Young.

References

Applied Seismology Consultants. <http://www.seismology.org/insite.aspx>. Cited Jan 14, 2008.

- A.M. Brandt, G. Prokopski, *J. Mater. Sci.*, **28**, 1993, 4762-4766.
- B. Chen and J. Liu, *Constr. Build. Mater.*, **18**:8, 2004, 585-590.
- C.U. Grosse, H.W. Reinhardt, F. Finck, *J. Mater. Civil Eng.*, **15**:3, 2003, 274-279.
- M.A. Issa, M.A. Issa, Md. S. Islam, A. Chudnovsky, *Eng. Fract. Mech.*, **70**, 2003, 125-137.
- T. Katsaga, R.P. Young, *Int. J. Fract.*, **148** (1), 2007, 29-45. See also *Int. J. Fract.* DOI 10.1007/s10704-008-9174-x, 2008.
- R.A. Ketcham and W.D. Carlson, *Computers & Geosciences*, **27**, 2001, 381-400.
- E.N. Landis and S.P. Shah, *Advn. Cem. Bas. Mat.*, **2**:3, 1995, 105-118.
- E.N. Landis and E.N. Nagy, *Engineering Fracture Mechanics*, **65**, 2000, 223-234.
- P. Launeau, and P.-Y.F. Robin, *Tectonophysics*, **267**, 1996, 91-119.
- H. Mihashi, N. Nomura, S. Niiseki, *Cement Concrete Res.*, **21**, 1991, 737-744.
- M. Ohtsu, T. Okamoto, S. Yuyama, *ACI Struct. J.*, **95**:2, 1998, 87-95.
- E.G. Sherwood, E.C. Bentz, M.P. Collins, *ACI Struct. J.*, **104**:2, 2007, 180-190.
- B.D. Thompson, R.P. Young, D.A. Lockner, *Pure Appl. Geophys.*, **163**:5-6, 2006, 995-1019.
- R.P. Young and B.D. Thompson, *Proc. 11th International Congress on Rock Mechanics*, Lisbon, 2007.
- A. Zang, F.C. Wagner, S. Stanchits, G. Dresen, R. Andresen, M.A. Haidekker, *Geophys. J. Int.*, **135**, 1998, 1113-1130.

GLOBAL MONITORING OF CONCRETE BRIDGE USING ACOUSTIC EMISSION

T. SHIOTANI, D. G. AGGELIS¹ and O. MAKISHIMA²

Department of Urban Management, Graduate School of Engineering, Kyoto University, C1-2-236, Kyoto-Daigaku-Katsura, Nishikyo, Kyoto 615-8540, Japan; ¹Research Institute of Technology, Tobishima Corporation, 5472 Kimagase, Noda, Chiba, 270-0222, Japan;

²Civil Engineering Headquarters, Tobishima Corporation, Sanbancho, Chiyoda, Tokyo, 102-8332, Japan

Abstract

Global monitoring of civil structures is a demanding challenge for engineers. Acoustic emission (AE) is one of the techniques that have the potential to inspect large volumes with transducers placed in strategic locations of the structure. In this paper, the AE technique is used to characterize the structural condition of a concrete bridge. The evaluation of AE activity leads to information about any specific part of the structure that requires attention. Consequently, more detailed examination can be conducted once the target area is selected. In this study, surface wave investigation was subsequently performed to detail the condition of the target area.

Keywords: Concrete structures, damage assessment, global monitoring, surface wave velocity.

Introduction

The deterioration of civil infrastructure worldwide calls for effective methods for damage evaluation. One of them, AE monitoring technique, uses signals generated within the structure, which are due to crack growth under stress, as well as secondary emissions due to friction of crack interfaces. This unique monitoring technique parameterizes the fracture/failure process, and distinguishes it from other nondestructive tests. This is the only one capable of real-time mapping of fracture processes. In addition to real-time source identification from the acquired AE signals, the energy level or “magnitude” of the detected signals can be evaluated, and provides immediate evidence of the degree of damage. A particular engineering advantage of the AE technique is its efficiency for global monitoring since a large and complex structure can be monitored with a limited number of sensors. Consequently, the most crucial part of the structure can be targeted with a more detailed AE monitoring for quantification of AE indices [1-4], or using other suitable techniques [5]. Results obtained from the AE testing depend highly on many external parameters such as the applied load and loading rate, the properties of the material and the type of structure. These factors restrict the development of comprehensively applicable tools. Additionally, due to the complex composition of most civil structures, AE waveforms depend on their propagation path from the source to the sensors [6]. However, in any case, valuable information can be extracted concerning which part of the structure has sustained the most severe deterioration.

In the specific case presented herein, a 45-m bridge span is under examination. Preliminary investigations of surface-crack observation and physical tests of excavated cores did not reveal any extensive damage. The cores can characterize only the area where they were extracted and the surface observation cannot reveal internal damage. Therefore, further monitoring was

conducted with AE technique. The AE testing was performed by moving a heavy vehicle over the bridge. Based on the AE activity the part of structure more likely to exhibit higher degree of damage than the other areas in the longitudinal direction was selected for the detailed investigation. A similar application on a much smaller scale was reported in [2]. A surface ultrasonic examination, which is indicative of the quality [7, 8], followed in order to investigate the pulse velocity of concrete at the area of interest.

Experimental Procedure

For the AE monitoring, 28 sensors were attached in all to the bottom surface of the bridge using a wax. They were placed on the longitudinal axis of the bridge with a separation of 1.4 m as shown in Fig. 1. Specifically, the sensitive AE sensors to concrete structures, R6 of PAC, were used. These sensors exhibit nominally the maximum sensitivity at 60 kHz and are widely used for concrete monitoring. The detected AE signals were pre-amplified by 40 dB and acquired by two synchronized data acquisition systems, namely a 16-channel DiSP and a 12-channel Mistras of PAC. Strain gauges were also placed in three locations on the top surface of the bridge, as shown in Fig. 1.

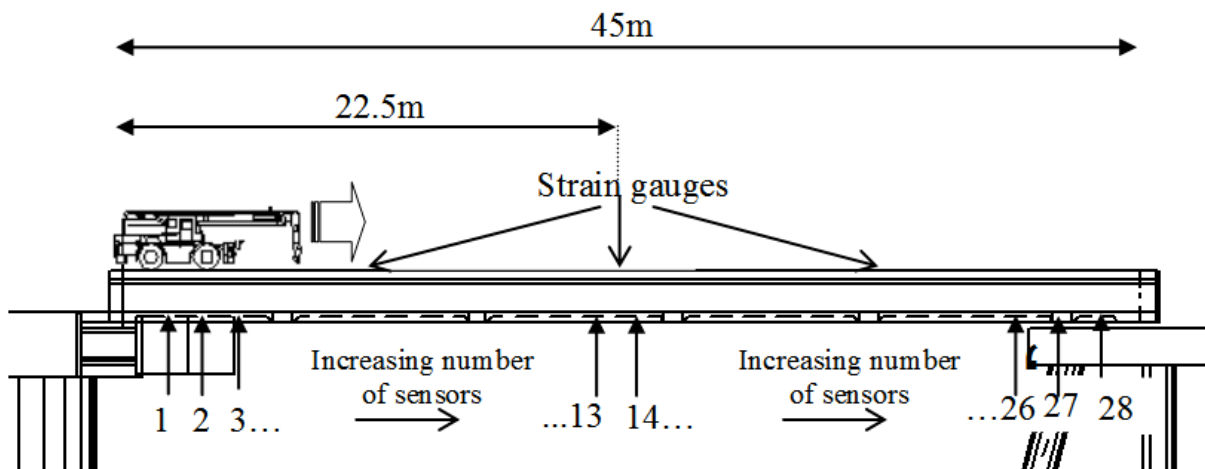


Fig. 1. Representation of the crane passing over the bridge and sensor location.

Acoustic Emission Activity

Damage indices

The interpretation of the detected AE activity is not always easy. This is the reason why different indices have been suggested and applied for the purpose of damage quantification. As stated earlier, when a material or structure is stressed, AE is produced. Additionally, the behavior during unloading is also crucial. In case the material is intact (or the applied load is low), the AE activity during unloading is of low intensity. For damaged material, the emission continues even during unloading. The number of AE hits during unloading divided by the number of hits during the whole cycle is defined as the Calm ratio and values near zero indicate intact material condition [2, 4, 9].

Another index comes from the analysis of the amplitude distribution of AE events, or so called the improved *b*-value analysis [1, 4]. Although a large-scale fracture in general corresponds to large AE peak amplitude, the use of the amplitude solely can be misleading. This is

because the accumulated damage increases the materials' attenuation rate due to scattering at the cracks. Therefore, even a high amplitude signal will be severely attenuated before being recorded by the sensors. In this respect, the amplitudes are studied through their cumulative distribution that uniquely changes as the damage is accumulated. Specifically, the gradient of the distribution is calculated. With the evolution of damage, this slope decreases, meaning simply that the ratio of the large energy AE events to that of the small relatively increases in the total population of AE events. It has been confirmed that at the moments of extensive cracking, the *I_b*-value exhibits severe drops [10-14].

AE monitoring results

The load for the AE monitoring was applied by a 20-ton crane vehicle, which passed three times over the bridge with a constant speed of approximately 0.5 m/s, as seen in Fig. 1. As the crane moved over the bridge, the strain and stress fields changed. The compressive strain measured on the top surface of the bridge at the mid-span can be seen in Fig. 2. The maximum strain was recorded at 88 s, when the vehicle was in the middle of the span, suggesting the highest tensile stress at the bottom layer of the structure. In the same figure, the cumulative number of AE hits recorded by all the sensors is depicted for one passage. It can be seen that the rate of AE hits was more intensive before the crane reached the center of the bridge at 88 s. Up to that moment, more than 70% of the total number of hits was recorded, implying that more active sources were located in the first half of the bridge.

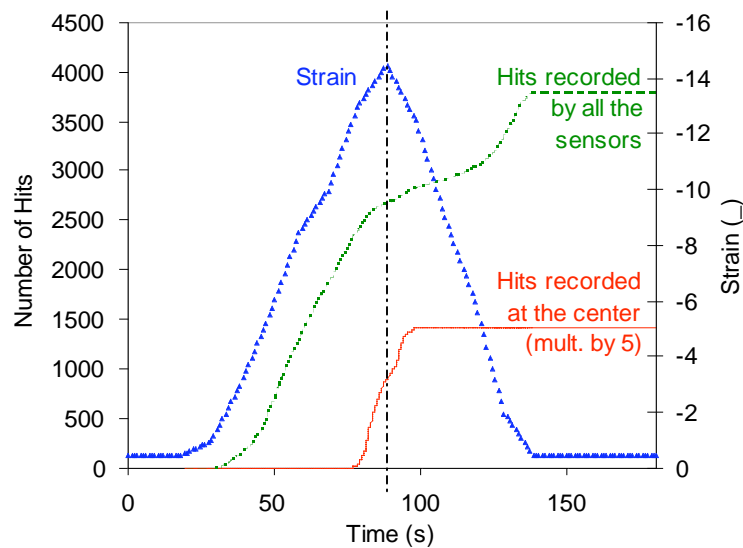


Fig. 2. Time history of strain at the center and cumulative AE hits during crane passage.

As stated, in order to calculate the Calm ratio, the AE activity should be correlated with a measured mechanical parameter. In this case, this was conducted using the measured strain at the middle point and the AE activity of the center part, recorded by the two sensors placed closest to the center (13 and 14 of Fig. 1). The activity of these sensors and AE hits of all sensors combined are plotted in Fig. 2. For clarity, the middle sensor hits are multiplied by a factor of 5. The hits of the middle sensors started at 74.5 s as the crane was approaching, and the last hit was recorded 10 s after the crane had passed over the bridge center, showing the intensive AE activity even during unloading. The number of hits for three different trips of the crane and the resulting Calm ratios are presented in Table 1. The Calm ratios concerning the center part of the bridge range from 0.3 to 0.45 for any individual passage of the crane, indicating serious damage according to past studies [2, 11, 12, 16, 17].

After location of the events, interesting conclusions can be drawn about the attenuation of the structure. In Fig. 3(a), the amplitude of the hits of all events is depicted vs. the distance from the source. The average first hit stands at amplitude of 54 dB. In Fig. 3(b), the linear fits to the amplitude of each individual event are plotted. Attenuation was calculated from the slope of each line. Averaging of the slopes of all the events results in -7.02 dB/m, which is representative for the attenuation of the whole structure. It is seen that hits of the weakest events still propagate 1.5 m before being reduced below the threshold level (40 dB). Therefore, they are recorded by at least 2 sensors. This shows that the separation of the sensors in this case allows source location. In general for the average amplitude of 54 dB at the source, 2 m for the sensor separation would provide a reasonable detection in this bridge. In any case, it is a crucial parameter that should be seriously taken into consideration since, in monitoring of most large structures, compromises must be made between the available number of sensors, time restrictions for measurement preparation and the desirable degree of detail of examination. Attenuation is a key parameter to make an adequate decision.

Concerning the Calm ratio, mentioned above, taking into account the measured attenuation and the fact that the Calm ratio is based on the results of two neighboring sensors (with separation of 1.5 m), the events should originate within a span of 4 to 5 m in the middle of the bridge. Thus, conclusions about material degradation based in this Calm ratio concern this zone.

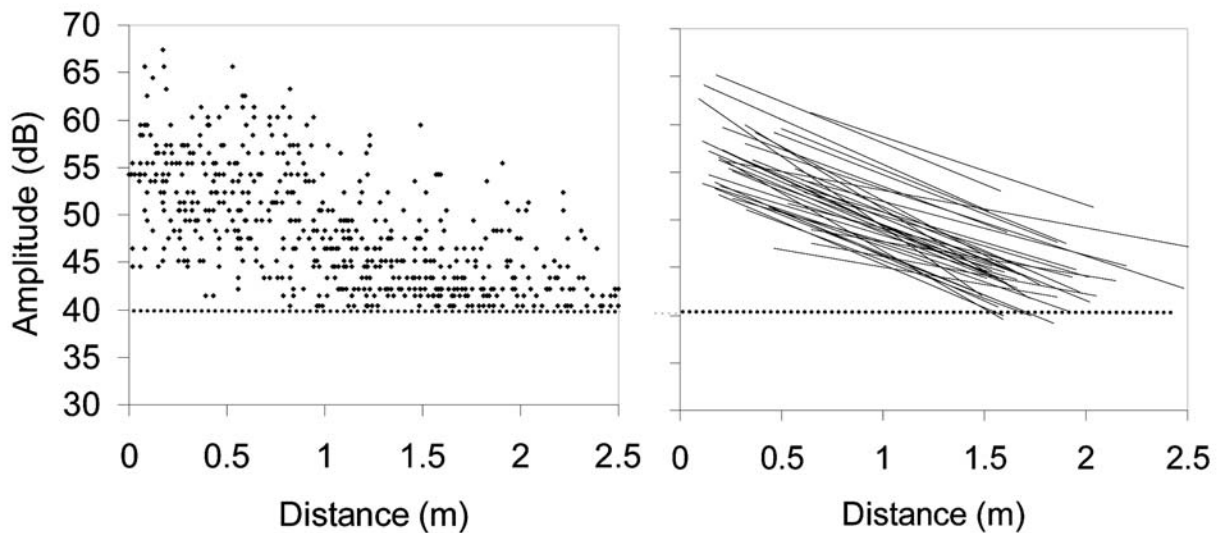


Fig. 3. (a) Hit amplitude vs. distance from event source, (b) individual attenuation slope for different events.

Table 1. Number of AE events for different stages of loading and Calm ratios.

Trip	Loading	Unloading	Calm ratio
1	175	146	0.455
3	409	179	0.304
5	295	208	0.414

Ib-value analysis

In Fig. 4, the *Ib*-values based on the AE events located at different zones of the bridge are plotted for the three different passages of the crane. The span was divided into 12 zones of 3 m

each, in order to allow the number of events for the Ib -value calculation. Specifically, the total number of events to be considered for the calculation of the Ib -value should be above 50 [1, 10-14]. The number of events for the same zones is also shown in the chart. It is evident that some areas of the structure exhibited larger number of events than others as seen in Fig. 4 and the Ib -value is calculated for the zones only exhibiting more than 50 events. Focusing on the Ib -values, it is seen that they vary between 0.05 and 0.13. According to established correlations, values above 0.2 imply the intact condition, between 0.1 and 0.2 suggests the moderate damage and it is becoming more intense as the Ib -value decreases below 0.1 [1, 2, 12]. This shows that a large part of the structure is deteriorated. While the limited AE activity of the rest does not allow the evaluation of this parameter, there were not many active sources in that area.

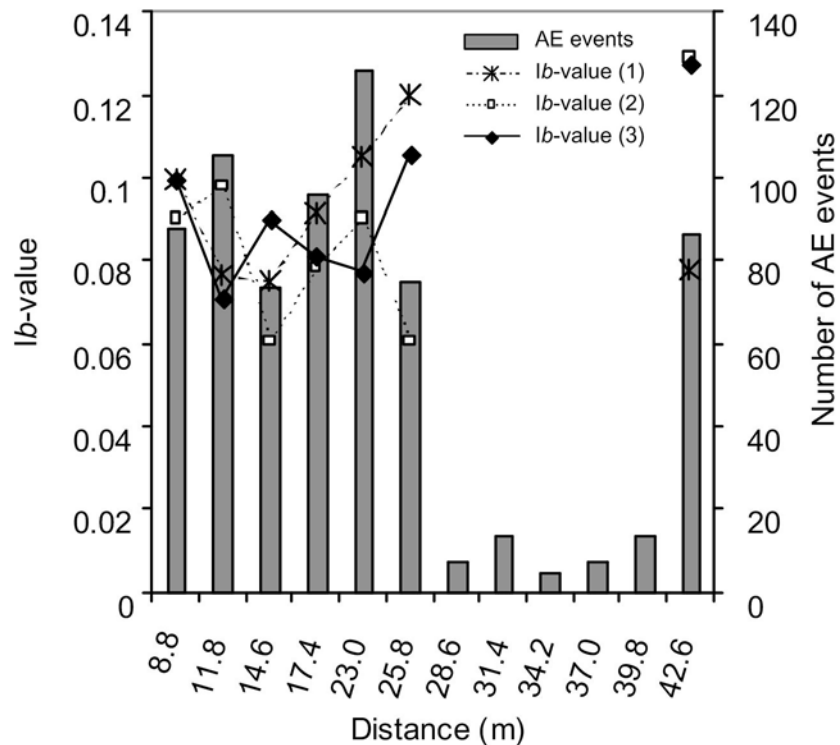


Fig. 4. Ib -values for three different trips of the crane and indicative AE events for the first trip.

Velocity measurements

In order to make a more detailed examination of the active area of AE activity, wave velocity measurements were made. Velocity has been established as an indicator of concrete quality for many decades and it is accepted that velocity above 4000 m/s indicates high quality, while below 3000 m/s suggests poor quality [7, 17].

For the velocity measurement, nine AE sensors were used in an arrangement of three parallel arrays of three. The separation distance was 1.5 m, resulting in an examined area of 3 m by 3 m, see Fig. 5. The excitation was conducted by pencil-lead break near the location of each transducer. Therefore, each time, one sensor was used as trigger for the acquisition and eight as receivers. In this way, a number of intersected paths were examined, and the results can be considered more representative of the area and more reliable than single measurement between two points. The velocity was measured by the time of the first detectable disturbance of each waveform, which corresponds to the onset of longitudinal waves.

The transit times of the individual paths, along with the sensor positions were supplied to a suitable tomography program [18]. This way the visualization of the velocity structure was obtained and the information of which parts of the surface area exhibit lower velocity than others was obtained as shown in Fig. 5. From this figure, considerable discrepancies of the wave velocity were found within the area of 9 m^2 . Specifically, a zone approximately in the center of the selected area exhibited velocities close 2500 m/s , while other areas had velocity higher than 4000 m/s .

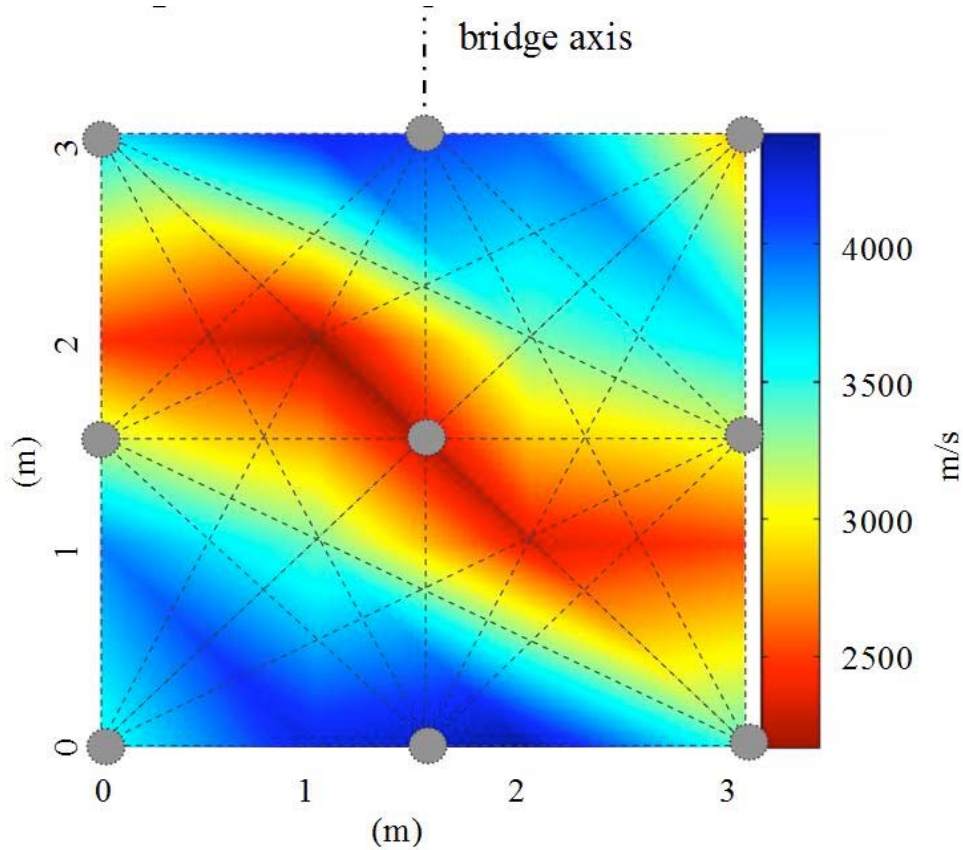


Fig. 5. Velocity structure of the bottom surface of the concrete bridge. The positions of the transducers are indicated by circle and the examined wave paths are drawn by dashed lines.

It is noted that no visual defect was observed on the surface. Therefore, the low velocity zone is attributed to a subsurface defect. The depth cannot be easily determined though. Concerning Rayleigh waves, it is accepted that the penetration depth is approximately similar to the wavelength [19]. In this case, however, the first arrival used to measure velocity corresponds to the longitudinal wave, which is in any case faster than Rayleigh or shear waves. Therefore, it is not straightforward how deep is the surface layer characterized by this velocity. Concerning Rayleigh propagation, typical velocities for the bottom part of Fig. 5 were around 2500 m/s , corresponding to the longitudinal velocity certainly higher than 4000 m/s . Although this implies good quality, the determination of Rayleigh velocity was not always possible due to severe attenuation and distortion of the waveform, especially for paths at the top of Fig. 5. This was because there was no characteristic point to use as reference for Rayleigh wave measurement [20]. This again shows that the continuous path was disrupted by a discontinuity. Using the Rayleigh velocity of 2500 m/s and the major frequency component of 150 kHz the wavelength is calculated to approximately 17 mm . Therefore, since the Rayleigh component was not visible at some areas, this should be due to a weak material zone (discontinuity) that extends very close to

the surface (even closer than 2 cm), because if it was deeper the Rayleigh would not be influenced. It is mentioned that the frequency of 150 kHz is measured by waveforms recorded 1.5 m away from the excitation. Close to the excitation the frequencies are higher, while for propagation of 3 m the major frequency component is just below 50 kHz. This complicates the quantification of the penetration depth, since the frequency content is not constant but is downshifted with propagation due to concrete damping. The characterization depth using surface wave examination (including Rayleigh and longitudinal components) needs further study, which is currently undertaken.

As to the AE events observed, concrete cracks, delaminations of different layers (e.g. asphalt on concrete) or friction between the tendon ducts and matrix concrete are possible origins. Follow-up investigations focusing on this weak area will clarify the source, while this sequential investigation, which started with AE activity and followed by detailed measurements of ultrasonic velocity is useful in characterizing the quality of large-scale concrete structures, leading to contribute to the rehabilitation program of aging infrastructures.

Conclusions

In this paper, the suitability of acoustic emission to monitor large concrete structures is presented. The AE technique was initially used to select the most deteriorated area based on the number of AE events and the values of quantification indices like the Calm ratio and Ib -value. The subsequently conducted ultrasonic examination exhibited very low velocities confirming that the area indicated by AE activity was actually deteriorated. This shows the potential of AE testing as a global monitoring for examination of large volumes using a limited number of sensors. Even if AE indices or parameters cannot be directly correlated with the degree of damage, they suggest which part of the structure needs further and detailed investigations. Subsequently, wave velocity measurements were conducted allowing a more general evaluation through the reported correlations between velocity and concrete quality. It is suggested that the combination of such stress wave techniques as AE and surface wave examination can assess the degree of damage of large civil structures that so far has been difficult to attain.

References

- 1) T. Shiotani, K. Fujii, T. Aoki, K. Amou, Evaluation of progressive failure using AE sources and improved b-value on slope model tests, *Prog. Acoust. Emiss VII*, (1994), JSNDI, Tokyo, pp. 529-534.
- 2) M. Ohtsu, M. Uchida, T. Okamoto, S. Yuyama, Damage assessment of reinforced concrete beams qualified by acoustic emission. *ACI Structural Journal*, **99**(4), (2002), 411-417.
- 3) C. Grosse, H. Reinhardt, T. Dahm. Localization and classification of fracture types in concrete with quantitative acoustic emission measurement techniques. *NDT&E Int*, **30**(4), (1997), 223–230.
- 4) T. Shiotani, Evaluation of long-term stability for rock slope by means of acoustic emission technique, *NDT&E Int*, **39**(3), (2006), 217-228.
- 5) V. M. Malhotra, N. J. Carino (Eds.), *CRC Handbook on Nondestructive Testing of Concrete*, (1991), CRC Press, Florida.

- 6) B. Schechinger, T. Vogel, Acoustic emission for monitoring a reinforced concrete beam subject to four-point-bending, *Construction and Building Materials*, **21**(3), (2007), 483-490.
- 7) T. R. Naik, V. M. Malhotra, The ultrasonic pulse velocity method, in: Malhotra, V. M., Carino N. J., (Eds.), *CRC Handbook on Nondestructive Testing of Concrete*, (1991), CRC Press, Florida.
- 8) T. Gudra, B. Stawinski, Non-destructive characterization of concrete using surface waves, *NDT&E Int*, **33**, (2000), 1-6.
- 9) S. Colombo, M. C. Forde, I. G. Main, M. Shigeishi, Predicting the ultimate bending capacity of concrete beams from the “relaxation ratio” analysis of AE signals, *Construction and Building Materials*, **19**, (2005), 746-754.
- 10) T. Shiotani, M. Ohtsu, K. Ikeda, Detection and evaluation of AE waves due to rock deformation, *Construction and Building Materials*, **15**(5-6), (2001), 235-246.
- 11) T. Shiotani, Y. Nakanishi, X. Luo, H. Haya, T. Inaba, Damage evaluation for railway structures by means of acoustic emission, *Key Engineering Materials*, **270-273**, (2004), 1622-1630.
- 12) T. Shiotani, Y. Nakanishi, X. Luo, H. Haya, Damage assessment in deteriorated railway sub-structures using AE technique, *Journal of Acoustic Emission*, **22**, (2004), 39-48.
- 13) J. H. Kurz, F. Finck, C. U. Grosse, H. W. Reinhardt, Stress drop and stress redistribution in concrete quantified over time by the *b*-value analysis, *Structural Health Monitoring*, **5**, (2006), 69-81.
- 14) S. Colombo, I. G. Main, M. C. Forde, Assessing Damage of Reinforced Concrete Beam Using “*b*-value” Analysis of Acoustic Emission Signals, *Journal of Materials in Civil Engineering-ASCE*, **15**(3), (2003), 280-286.
- 15) T. Shiotani, D. G. Aggelis, Damage quantification of aging concrete structures by means of NDT, *Proc. of Structural Faults and Repair-2006*, June 13-15, Edinburgh, (in CD).
- 16) T. Shiotani, X. Luo, H. Haya, Damage diagnosis of railway concrete structures by means of one-dimensional AE sources, *Journal of Acoustic Emission*, **24**, (2006), 205-214.
- 17) M. F. Kaplan, The effects of age and water/cement ratio upon the relation between ultrasonic pulse velocity and compressive strength. *Mag. Concr. Res.*, **11**(32), (1959) 85– 92.
- 18) Y. Kobayashi, H. Shiojiri, T. Shiotani, Damage identification using seismic travel time tomography on the basis of evolutionary wave velocity distribution model, *Proc. Structural Faults and Repair-2006*, June 13-15, Edinburgh. (in CD).
- 19) D. G. Aggelis, T. Shiotani, “Repair evaluation of concrete cracks using surface and through-transmission wave measurements”, *Cement and Concrete Composites*, **29**, (2007), 700-711.
- 20) L. Qixian, J.H. Bungey, “Using compression wave ultrasonic transducers to measure the velocity of surface waves and hence the dynamic modulus of elasticity of concrete”. *Construction and Building Materials*, **10**(4), (1996), 237-242.

DEMAND ON FLEXURAL TENSION STEEL REINFORCEMENT ANCHORAGE ZONES IN FULL-SCALE BRIDGE BENT CAPS QUANTIFIED BY MEANS OF ACOUSTIC EMISSION

THOMAS SCHUMACHER, CHRISTOPHER HIGGINS,
STEVEN GLASER* and CHRISTIAN GROSSE[†]

School of Civil and Construction Eng., Oregon State University, Portland, OR, USA;

*Dept. of Civil and Environmental Engineering, University of California, Berkeley, CA, USA;

[†]Non-Destructive Testing and Monitoring Techniques, Univ. of Stuttgart, Stuttgart, Germany

Abstract

This paper documents the development of an AE technique for monitoring and quantifying the demand on anchorage zones of the flexural-tension steel reinforcement in full-scale bridge bent caps. Bent caps are deep transverse bridge beams that support the longitudinal girders and transfer loads into the columns. The horizontal flexural-tension reinforcement at the bottom of the bent cap is anchored into the columns and acts as a crucial structural element. Pull-out or anchorage failure could lead to system collapse since this member is non-redundant. A new approach to monitor the column anchorage zone and to quantify the maximum demand of rebar pull-outs by means of quantitative AE is presented and applied to test data on full-size bent column anchorage sub-assemblages.

Keywords: Reinforced concrete, bridge bent caps, column anchorage zone, structural health monitoring

Introduction

Large numbers of conventionally reinforced concrete deck-girder (RCDG) bridges were constructed during the federal highway system expansion of the 1950s. During this time period, research developments on anchorage of reinforcing bars resulted in rapid changes to design specifications and practice. Specifically, the geometric standardization of deformed reinforcing bars in ASTM A305-50 resulted in higher allowable stresses with reduced detailing requirements. Failures later in the decade revealed that the contemporary design practice was inadequate. By the early 1960s, design specifications were amended and at the same time, pre-stressed concrete began to supersede conventionally reinforced concrete for bridge construction.

One concern of the design found in existing bent caps is the detailing of the anchorage zones in bent caps. The flexural-tension reinforcement at the bottom of a bent cap is anchored into the bent column. For many bridges, these rebars are straight (not hooked) and terminated so that minimum concrete cover (c_c) is provided at the tail. This is normally around $c_c = 38$ mm. The typical anchorage length provided in a 610-mm-square column is only around $l_d = 572$ mm. The development length (l_d) required by the current AASHTO-LRFD (2004) specification for a bar with a diameter of $d_b = 36$ mm (#11) is:

$$l_d = 1.25 \cdot A_b \cdot f_y / \sqrt{f_c'}, \text{ but not less than } 0.4 \cdot d_b \cdot f_y \quad (1)$$

which results in $l_d = 1490$ mm assuming Grade 60 ($f_y = 414$ MPa) rebar steel and concrete compressive strength of $f_c' = 28$ MPa. This required development length is more than 2.5 times

greater than the available anchorage length (although Grade 40 ($f_y = 276$ MPa) rebars were generally used in mid-20th century bridge construction).

Experimental Setup and Load Protocol

To better understand the behavior and structural mechanics during a rebar pull-out, reduced bent column sections were designed, constructed, and loaded until failure [1]. Figure 1 illustrates a test specimen with applied force P and the support reactions $P/2$. The force was applied with hydraulic cylinders supplied by a manually activated pump. Load cells measured the applied force.

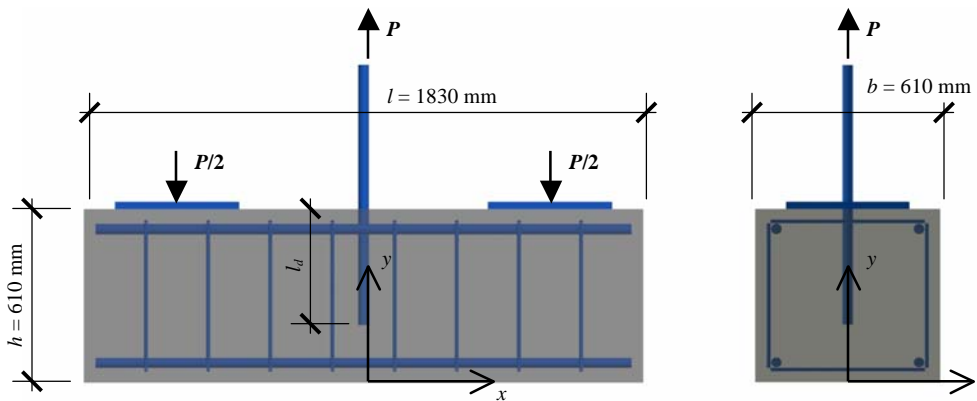


Fig. 1 Elevation and side view of a test specimen for rebar pull-out tests.

The overall dimensions of the tested bent column sub-assemblages were $l \times b \times h = 1830 \times 610 \times 610$ mm. Each specimen had four Grade 60 steel reinforcing bars with diameter $d_b = 36$ mm in the corners as well as one in the center for the actual pull-out. The embedment length for the pull-out rebars were chosen as $l_d = 533$ mm and $l_d = 305$ mm for specimen 1A and 1C, respectively. Ties were Grade 60 $d_b = 13$ mm (#4), spaced at $s = 203$ mm.

Both specimens were loaded using load steps (LS) with increasing amplitude followed by unloading until failure was reached. A Vallen AMSY-5 system with eight channels was used to monitor AE activity. For specimen 1A, eight broadband DECI SE1000-H sensors were used and for specimen 1C eight resonant Vallen SE150-M sensors. According to the calibration sheets, the variation of frequency response was 4 dB and 20 dB for the broadband and resonant sensors, respectively (for a frequency range between 40 and 250 kHz). For non-AE data acquisition, the software DASyLab 8 was utilized. The deformation of the pull-out rebar at the top and bottom ends was monitored during the experiment as well as support movements.

Figure 2 shows the applied force on the pull-out rebar and localized AE events for specimen 1A. Note that a filter (*LUCY*) was set to exclude inaccurate localization results (see next section for description). The experiment ended after reaching a force of $P_{max} = 492$ kN when the rebar started to enter strain hardening. Most of the AE events were produced in load step five (indicated by arrow) when the first visible surface crack formed on the specimen.

In Fig. 3, the applied force on the pull-out rebar and recorded AE events for specimen 1C are shown. The experiment was discontinued after reaching a force of $P_{max} = 382$ kN when the rebar pulled out of the concrete. In load steps five and six, the majority of AE events were generated

(indicated by arrows). Again, this corresponded well with the occurrence of major cracks on the specimen surface.

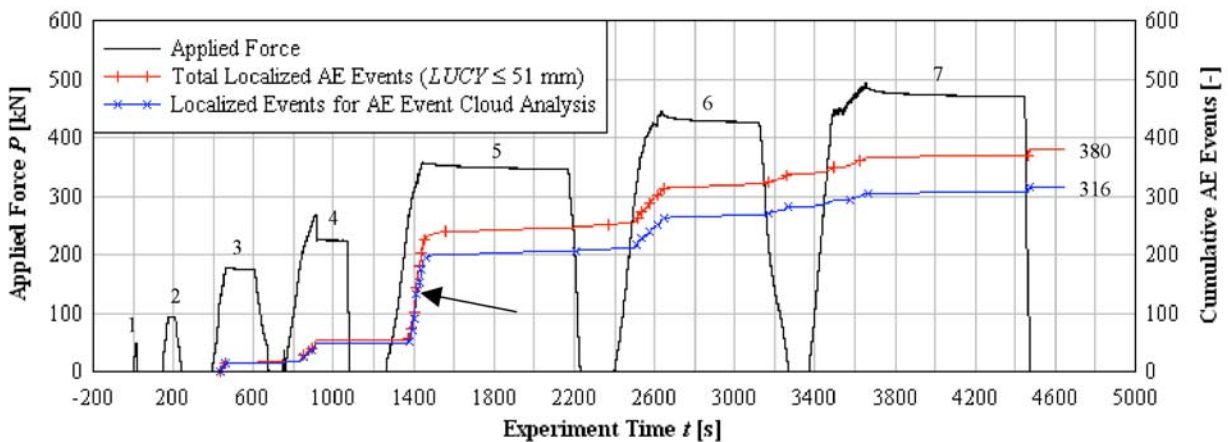


Fig. 2 Applied force vs. localized AE events for specimen 1A.

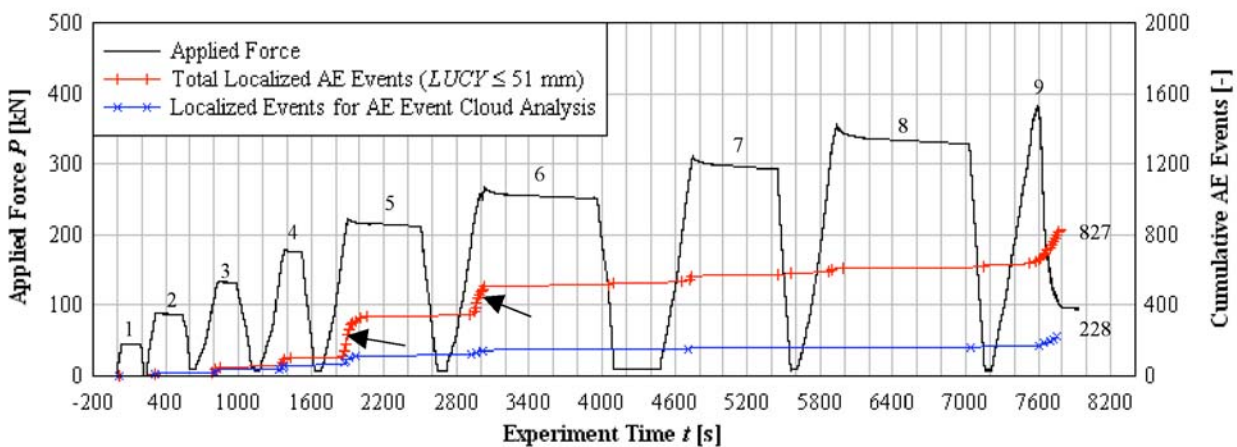


Fig. 3 Applied force vs. localized AE events for specimen 1C.

3-D AE Event Localization

In a first step, 3-D AE event localization was performed. The arrival-time picking was improved by introducing a floating threshold dependent on the recorded background noise. A factor, sometimes called crest factor, is multiplied by the background noise voltage to determine the threshold. This crest factor was set to 8.0 and 13.0 for the broadband and the resonant sensors, respectively. The threshold updating interval was set to 1.0 second. Pencil-lead breaks were performed on the surface of one of the specimens to quantify localization errors and variability in results. It was found that including five to seven signals in the computation leads to the most accurate localization results. For this study, only the first five arrival times within an AE event were included to maximize the number of localized AE events. This turned out to be helpful in later stages of the experiment where developed cracks distorted stress wave paths and increased localization errors. A comparison with 26 real AE events recorded from one load step was performed using PolarAE, a program developed at the University of Stuttgart, Germany. The average spatial difference of the results over all events was found to be $\Delta_{xyz} = 16$ mm between the two programs. It was concluded that the developed picking and localization options available with the commercial product used for this study was sufficiently accurate for this experiment and the specimen size. A filter setting to eliminate inaccurate localization results was set to $LUCY \leq 51$ mm. *LUCY* stands for

location uncertainty and is the root-mean-square of the difference between calculated and observed distances between source and sensor that is calculable when at least five arrival times are available. It describes how well a calculated source position explains the observed arrival time differences. Unfortunately, *LUCY* does not contain any directional information. A better representation of the uncertainty would be the principal standard deviations of the numerical least-squares solution.

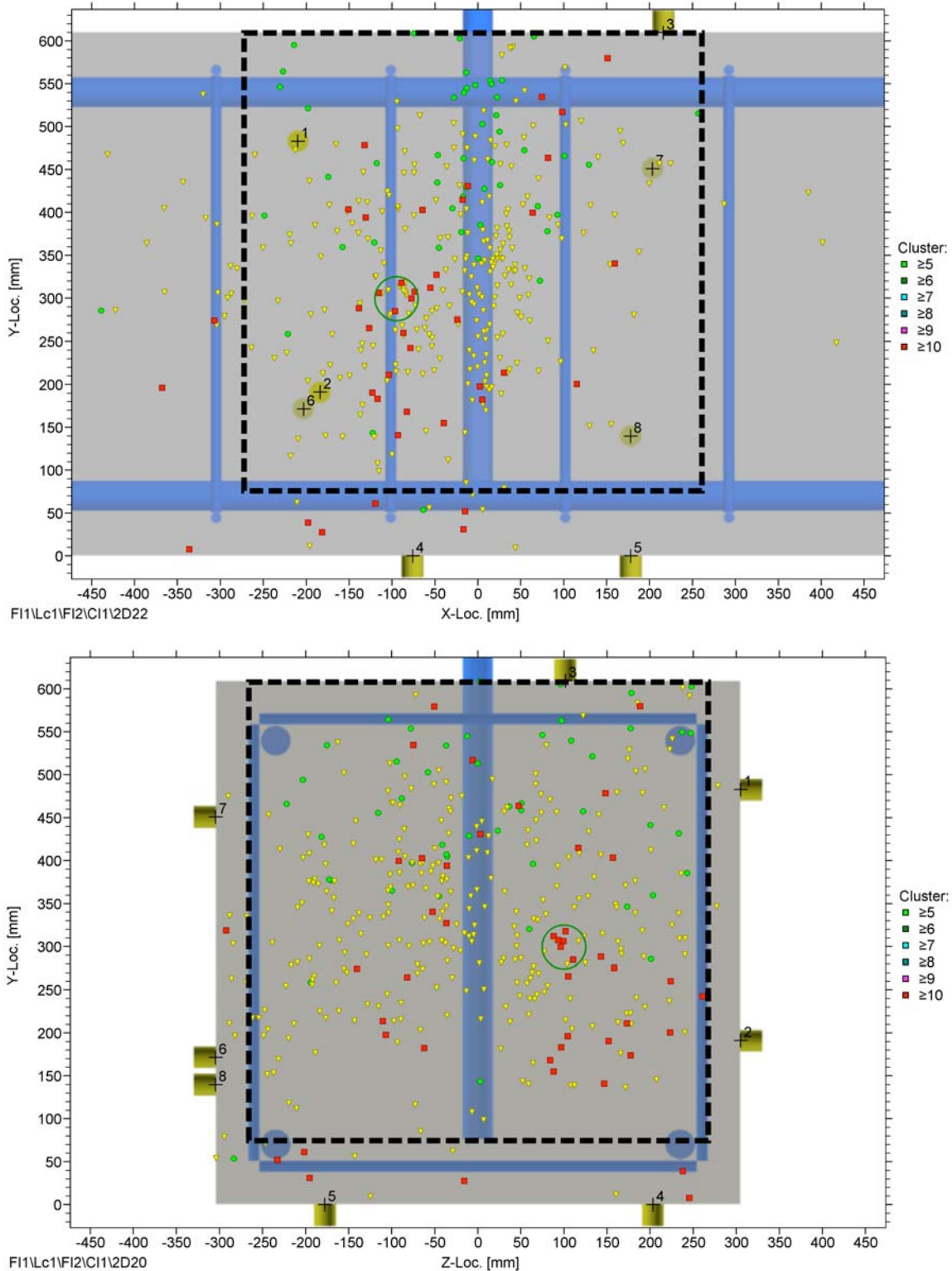


Fig. 4 AE event localization results for specimen 1A.

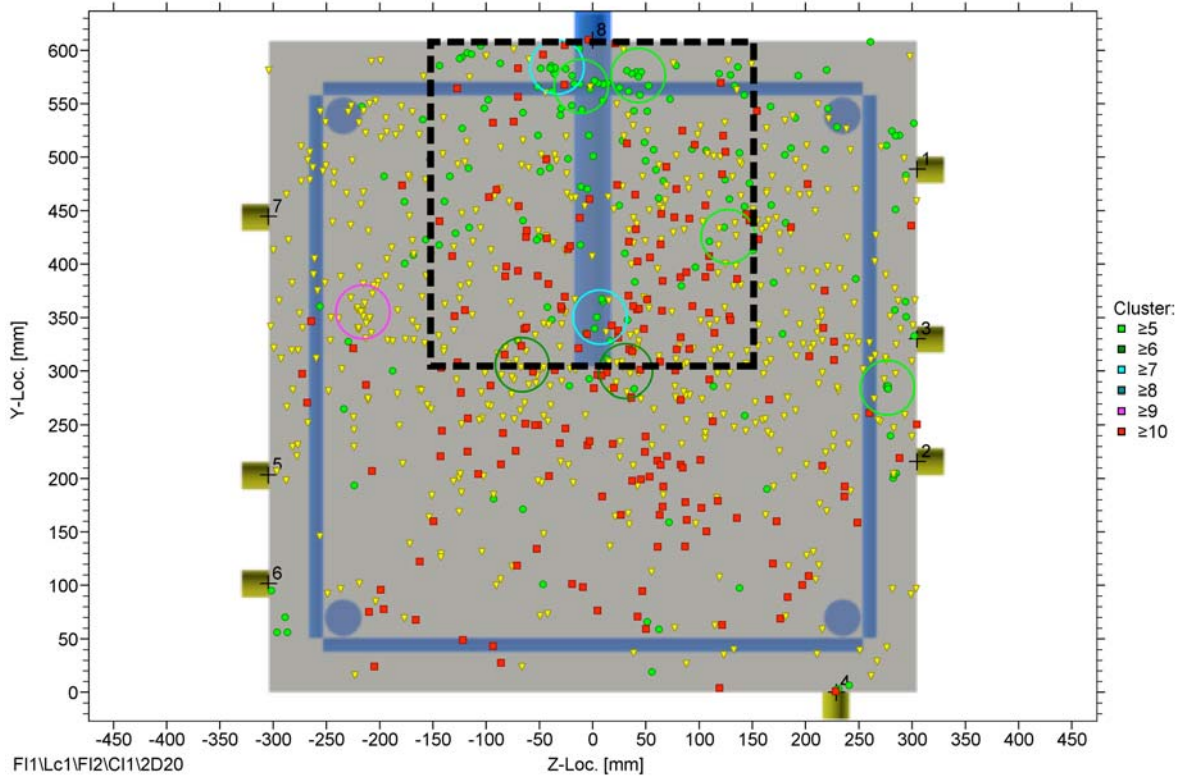
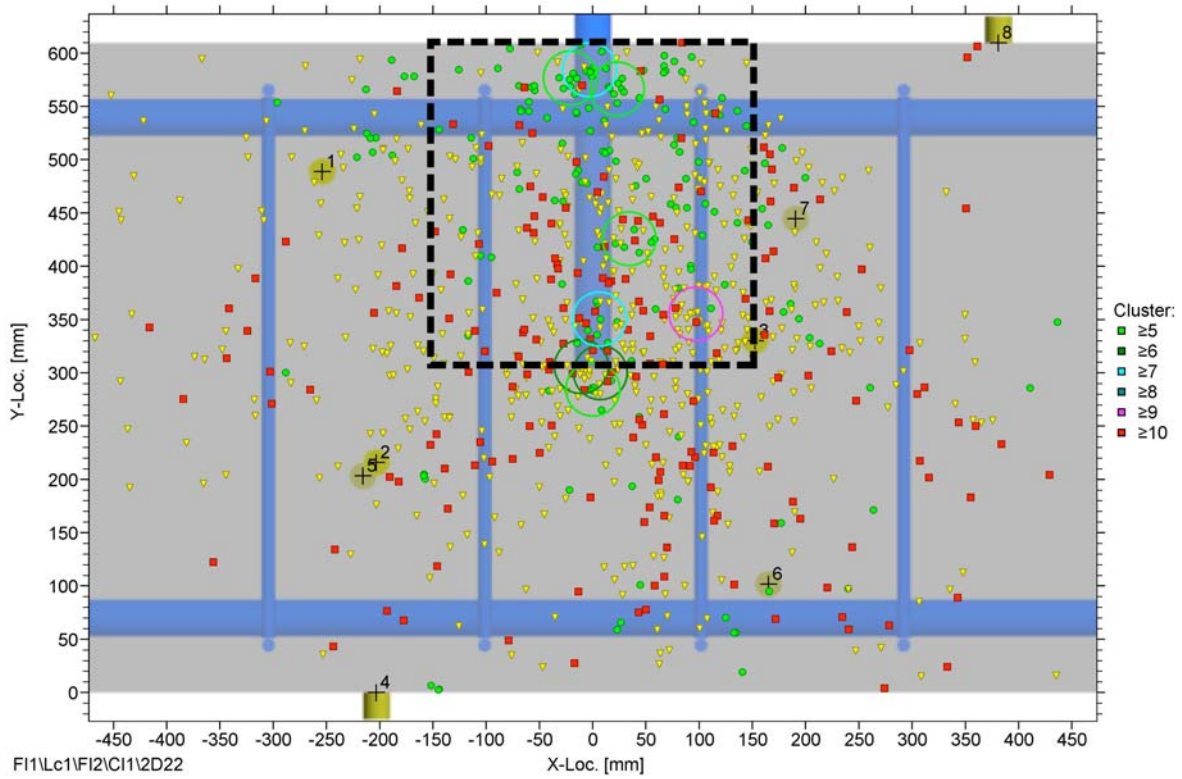


Fig. 5 AE event localization results for specimen 1C.

The first author of this paper has implemented a localization algorithm in MatLab based on Geiger's method that plots 3-D error ellipsoids with principal standard deviations as axes for each localization result. In future analyses, this algorithm will be used to enhance interpretation of localization results.

Figures 4 and 5 illustrate all localized AE events during the experiment. The green circles (●) represent AE events that occurred during the load steps before the major failure (macro-) crack formed, the yellow triangles (▼) the AE events between that observation and the failure load step, and the red squares (■) the AE events during the final load step when the experiment was terminated due to rebar strain hardening and pull-out for specimen 1A and 1C, respectively. The circles represent spatial clusters of AE events that occurred within a sphere with a diameter of 51 mm, which indicates localized activity in a certain area. The numbered yellow cylinders illustrate the AE sensors mounted on the surface of the specimen.

It can be observed that there were fewer localized AE events for specimen 1A than 1C. The reason was that one of the sensors for specimen 1A did not work properly and the utilized broadband sensors are less sensitive than the resonant ones.

Indicated with a dashed line in Figs. 4 and 5 are the spatial filter settings used for the analysis of AE event cloud front, to be described subsequently. Only AE events that were identified inside the cube were taken for further analysis. This volume was chosen as a cube with a side length equal to the embedment length of the pull-out rebar, i.e. $l_d = 533$ mm and $l_d = 305$ mm for specimen 1A and 1C, respectively and centered about the rebar.

AE Event Cloud Front Analysis

Many experiments on monitoring of AE activity during rebar pull-out experiments can be found in the literature [2-5] and both qualitative as well as quantitative AE evaluation methods have been applied to the test data. This study intends to use AE event localization as a quantitative means to describe the demand on the pull-out rebar during a load test. The central idea is that there should be an evolution of the location of the captured AE events while going to higher load levels.

Bond stresses are assumed as uniform and their integration leads to a linearly increasing rebar stress over the embedment length. Based on this idealized bond stress distribution, it was expected that AE events are created when a certain stress threshold is crossed along the embedment length (l_d). As higher forces are applied to the pull-out rebar, the higher the stress gradient becomes, and AE events should therefore progress along the embedment length away from the free surface of the specimen. The *AE event cloud front* was identified as the location of the upper quartile (75%) of all localized AE events within one complete load step. A normal distribution of AE events was assumed for statistical evaluation. The depth of progression for this cloud front was then expressed as a percentage of the embedment length and given the variable name q .

Figures 6 and 7 illustrate the progression of the *AE event cloud front* for all load steps of the two specimens. The y-coordinate corresponds with the longitudinal orientation of the pull-out rebar. Statistical values such as median and mean with 95 % confidence bands for localized AE events are given as well as the *AE event cloud front* (thick dashed line). Some of the first load steps were not included in the analysis because too few AE events occurred.

Conclusions and Future Work

A clear trend of progression of the *AE event cloud front* from one load step to the next can be found for specimen 1A, which supports the proposed hypothesis. For specimen 1C, the trend is less clear. This could be due to the fact that only few localized AE events were created. Generally, after

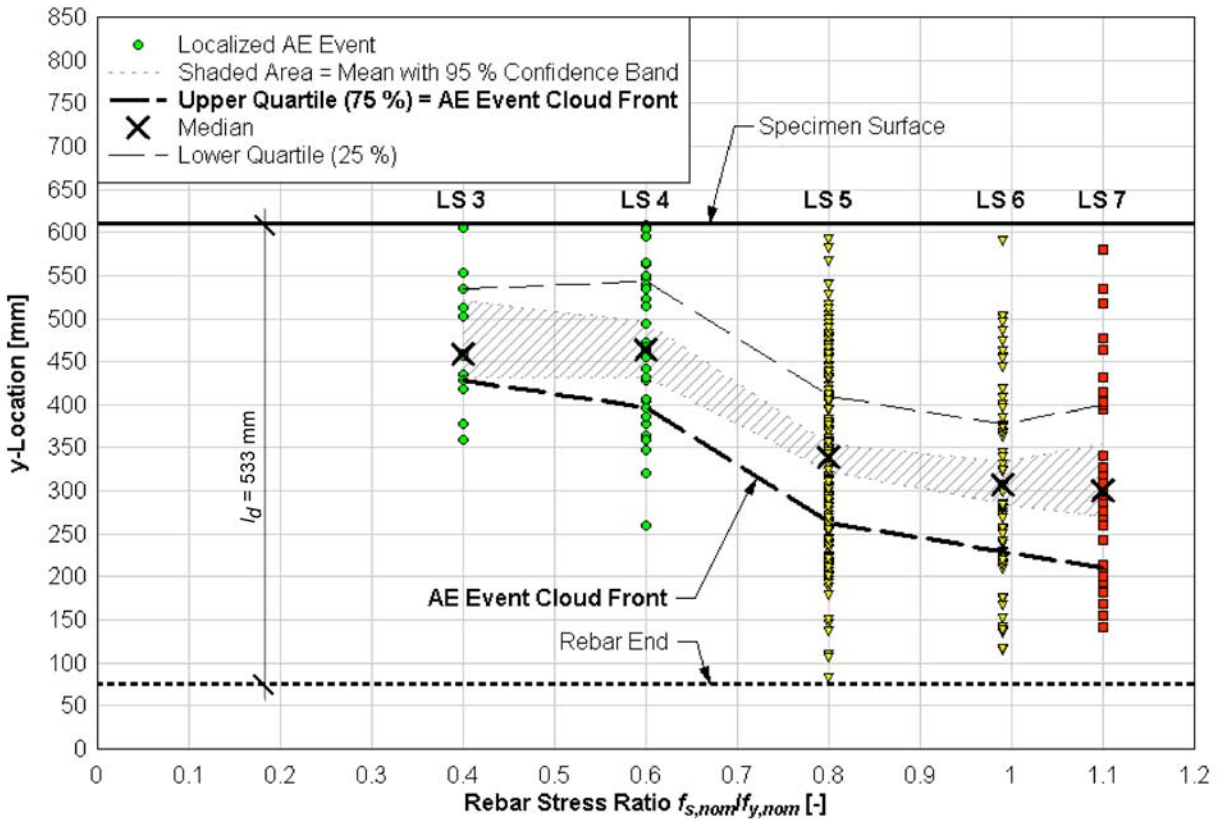


Fig. 6 AE event cloud analysis for load steps 3 through 7 of specimen 1A.

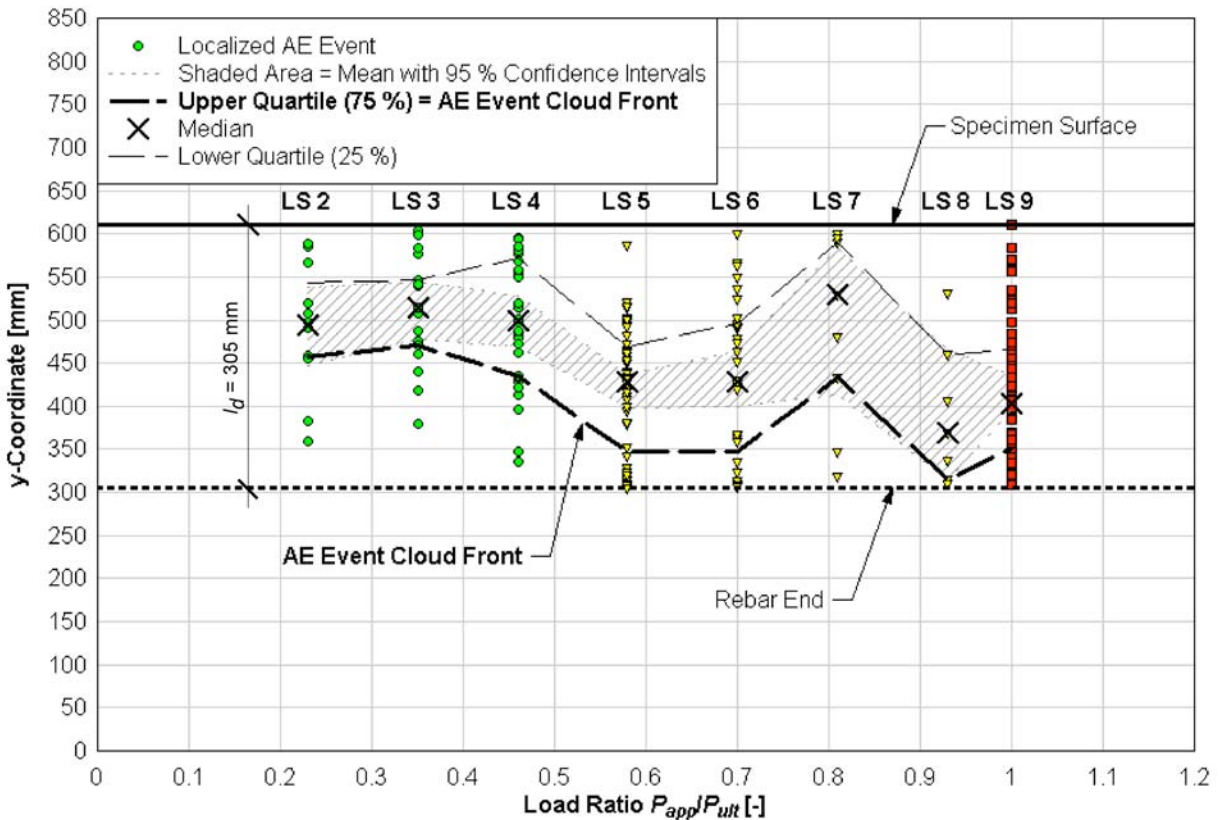


Fig. 7 AE event cloud analysis for load steps 2 through 9 of specimen 1C.

big cracks form, localization of AE events becomes more difficult due to distortion of the media. Stress waves travel longer and more convoluted paths, which lead to bigger errors in the computed source location. The maximum value for the progression of the AE cloud front was found to be $q = 75\%$ for specimen 1A where the rebar did not pull-out (experiment discontinued after rebar entered strain hardening) and $q = 96\%$ for specimen 1C where the rebar pulled out of the concrete. It appears that this maximum value could be taken as an indication of the maximum rebar demand.

In a next step, the behavior of other rebar configurations (two and four rebars) with applied normal forces (similar to a real bent cap) will be studied. The final goal will be to evaluate AE data collected from full-scale bent cap experiments and use AE event localization to quantify anchorage demands at overall member failure.

References

1. C. C. Koester, M.S. Thesis, Oregon State University, 2007.
2. G. L. Balazs et al., Magazine of Concrete Research, **177**, Dec. 1996, 311-320.
3. A. S. Kobayashi et al., Experimental Mechanics, **9**, Sept. 1980, 301-308.
4. St. Koepfel, Dissertation ETH Zurich, Technical Report Nr. 272, Feb. 2002.
5. S. Weihe et al., Characterization of damage and failure during the pull-out of a reinforcement bar by acoustic emission and numerical simulation, *1st International Conference on Damage and Failure of Interfaces*, Vienna 1997.

DAMAGE EVALUATION OF POST-TENSIONED CONCRETE VIADUCT BY AE DURING PROOF LOADING

EDOARDO PROVERBIO, GIUSEPPE CAMPANELLA and VINCENZO VENTURI*

Dept. Industrial Chemistry and Materials Engineering, University of Messina, 98166 Messina, Italy. *Sidercem srl, 95045 Misterbianco (CT), Italy.

Abstract

Recent collapses of civil structures (reinforced concrete, prestressed concrete or mixed steel structures, i.e. buildings, bridges, dams, and so on) have demonstrated once again the need for reliable tools for an early monitoring of damage progression. Damages due to deterioration processes, overload, bad design, poor material quality, can grow subcritically until final collapse. Acoustic emission has been successfully used for more than 20 years in industry for monitoring metal equipments (pipelines, pressure vessels, gas tanks, etc.) and the technology is quite mature. The application of the AE technique in the civil engineering requires however the overcoming of several problems related to structural complexity, material inhomogeneity and the high attenuation factor for high-frequency acoustic waves in concrete, and environmental noise. A great effort yet has to be done on data handling and data interpretation.

We have used AE technique for damage evaluation of two severely deteriorated viaducts during proof loading. The viaducts, made at the end of the 1950's along the national road 114 in Sicily (Italy), consist of several spans. Each span was built in a post-tensioned concrete girder configuration. The load test consisted basically of 5 loading steps and 5 unloading steps. For each load test step, it has been possible to evaluate the displacements in the middle, in the border and in the center of the span. It was observed that, during loading phase, the mean AE hits rate, corresponding to a minimum in the mean amplitude, reached a maximum at an intermediate load, while at higher loads a reduced number of AE hits characterized by high mean energy was recorded. AE behavior was asymmetric with respect to the loading sequence (relaxation dominant), indicating the advanced degradation status of the viaducts.

Keywords: Concrete structures, bridge, proof loading, corrosion

Introduction

Segmental cast-in-place post-tensioned structures were extensively used in Italy during the reconstruction processes soon after the Second World War, as innovative design solutions adopted for a rapid and economical building of bridges. After 50 years, most of those structures have formally concluded their design service life, but social and economic reasons frequently force their owners toward rehabilitative solutions instead of undertaking demolition and rebuilding. The rehabilitation project and the evaluation of the residual load-carrying capacity involves the solution of unusual problems arising during the degradation assessment step linked to the peculiar geometry and to the structural weakness of such constructions. For such structures, the main concern is the status of prestressing or post-tensioning cables.

The evaluation of corrosion of the post-tensioning cables (usually grouted in ducts placed in box girder walls) required the use of new, but not yet well established, techniques such as those

based on magnetic induction, while indirect techniques such as impact echo could locate grouting defects, but not give any information about cable conditions.

Since the difficulties in accessing to cable anchorage and the impossibilities to re-tensioning cables themselves the evaluation of mechanical characteristics and performance of the viaducts could be estimated on the basis of a dynamic behavior analysis, whose main limit is however the definition of the right theoretical model. AE technique seems to be very promising in this field since it is not invasive, allows a volume evaluation and at the same time has the possibility to locate discrete defects. AE was however introduced very recently in the field of health assessment of reinforced concrete structures notwithstanding some difficulties to be overcome in the field of data handling and analysis. Relationship between AE signal parameters and failure processes that produce these signals have in fact to be properly defined for example by means of the development of pattern recognition techniques. With the same aim, several health indices as well as “Load ratio”, “Calm ratio”, “Felicity ratio” or “Historical index” have been defined [1-2].

Experimental

The Agrò and Fiumedinisi viaducts, on the national road number 114 on the eastern coast of the Sicily Island were designed in 1954 by Riccardo Morandi and built during 1955-56. They are 13- and 8-spans viaducts, respectively, with the span length of ~22 m. The viaducts are segmental cast-in-place post-tensioned prestressed concrete box girder type, characterized by a five-cell longitudinal trapezoidal void section box girder. Four cast-in-place diaphragms were provided at each end and along each span of the bridge. An 11-cm-thick top concrete slab was monolithically cast-in-place. The post-tensioning ducts of 40-mm diameter were drilled in-place and the post-tensioning internal tendons consisted of 5-mm wires bundle. Following detailed visual and instrumental inspection, which showed a critical degradation status due to seaside vicinity and to the “advanced” age [3], it was decided to evaluate damage effects on structural behavior by means of proof-loading test and a simultaneous AE monitoring.

The set-up of the AE system involved a long series of calibration tests on concrete samples at rest, carrying out the scratching and breaking of pencil-leads of different hardness and dimensions on the surface of samples; these tests have been carried out in different environments to test the effectiveness of filter system and to calibrate the “trigger threshold” suitable to extract the significant components of AE signals.

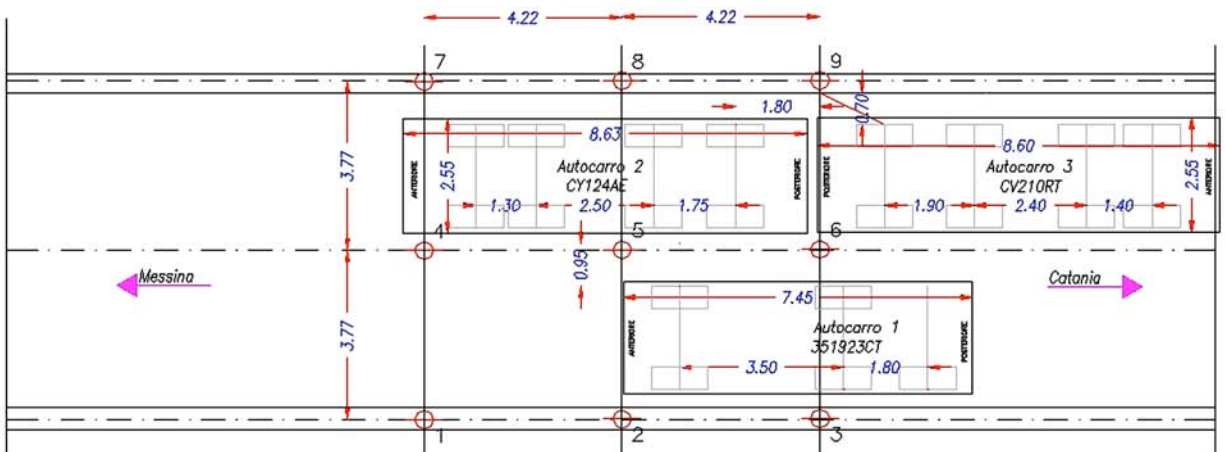


Fig. 1. Scheme of the static loading condition during the fourth loading step.

The proof loading test consisted basically of 5 load steps:

I° load test step: the load was produced by a 30-ton (0.3 MN) truck set in the mid-span;

II° load test step: the load is produced by a 30-ton truck set in the middle and by a 20-ton (0.2 MN) truck set on the parallel lane; Total = 0.5 MN

III° load test step: the load is produced by two 30-ton trucks set on the same lane; 0.6 MN

IV° load test step: the load is produced by two 30-ton trucks set on the same lane and a 20-ton truck set on the parallel lane; 0.8 MN

V° load test step: the load is produced by two 30 tons (0.3 MN) trucks set on the same lane and a 20-ton (0.2 MN) truck plus 30-ton (0.3 MN) truck set on the parallel lane; 1.1 MN.

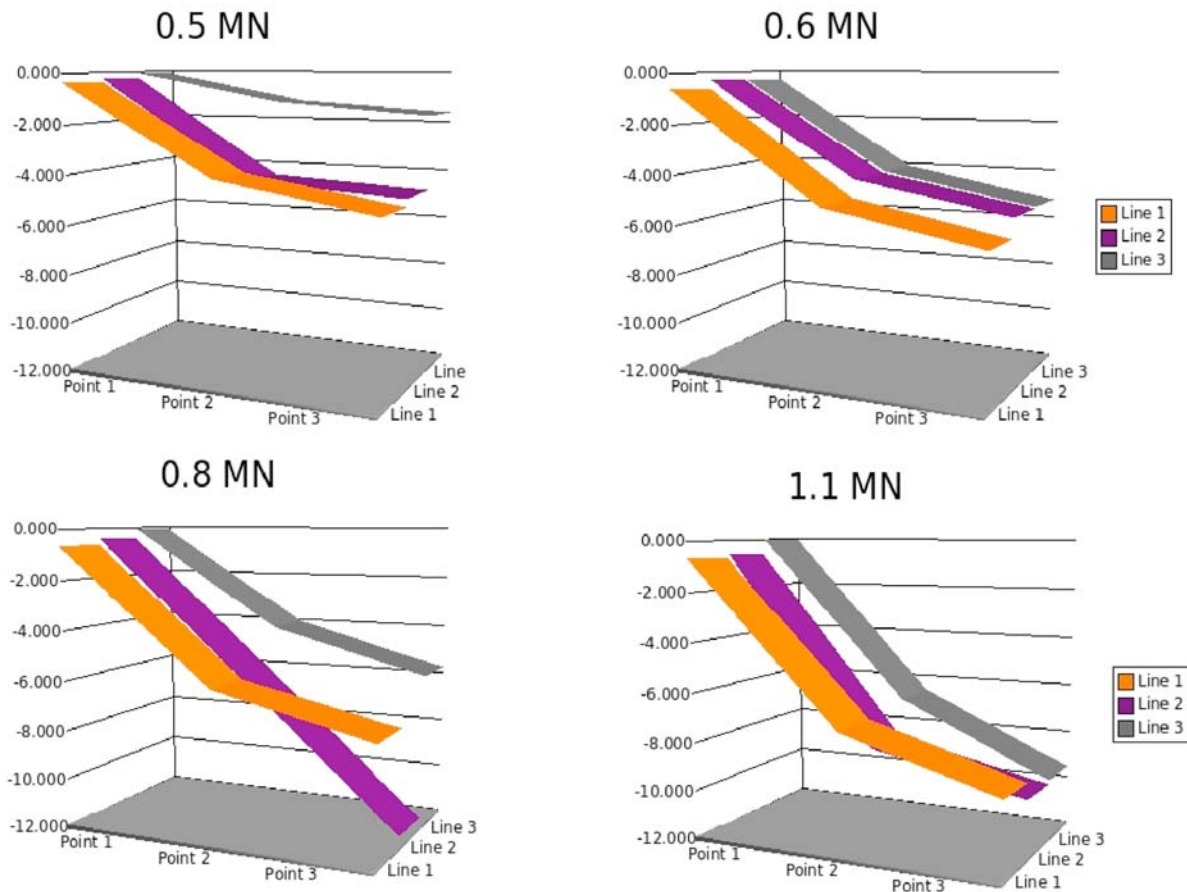


Fig. 2. Displacement of the measuring point (Fig. 1) on the viaduct span during proof loading.

A scheme of the 4th load test step with the indication of displacement measurement points is reported in Fig. 1. For each load test step, it has been possible to evaluate the displacements in the middle of the span in the border and in the center (Fig. 2). AE sensors adopted were VS30-V flat response type (23-80 kHz bandwidth, 140 pF capacitance), a total of ten sensors were used and positioned on the lateral side of different segments of box girders as shown in Fig. 3.

Results

The AE application has proven effective to detect vibration phenomena produced by trucks crossing on the structure, and the intense AE activity recorded was connected to the residual stress in the structure induced by the post-tensioning system, while the events recorded during the first phase seems to be connected with the phenomena of internal rearrangement of pre-existing defects.



Fig. 3. AE sensors positioning on box girders.

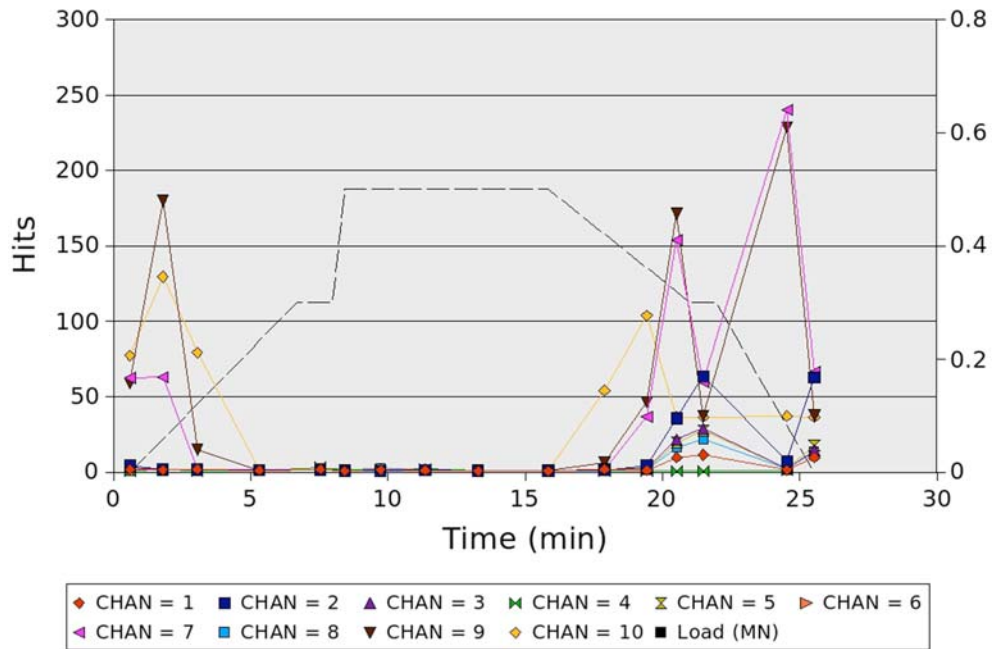


Fig. 4A. Mean numbers of hits for all channels vs. time for the second load step (load: dashed line; load scale on the right side in MN).

Considering the huge amount of data recorded, only a limited amount of available results are reported here and related to span No. 12 of the Agrò viaduct. Hits, energy and amplitude of AE events have been reported as mean values of the total amount of events recorded during a specific loading step (i.e., within a specific time interval).

An example is reported in Fig. 4 and refers to the second load step. One of the main aspect that must be highlighted is that the great amount of hits have been recorded during transient phases (loading and unloading), while, at the maximum load, the structures remained almost silent (Fig. 4A). On the contrary, the energy of the AE events reached the maximum value at the

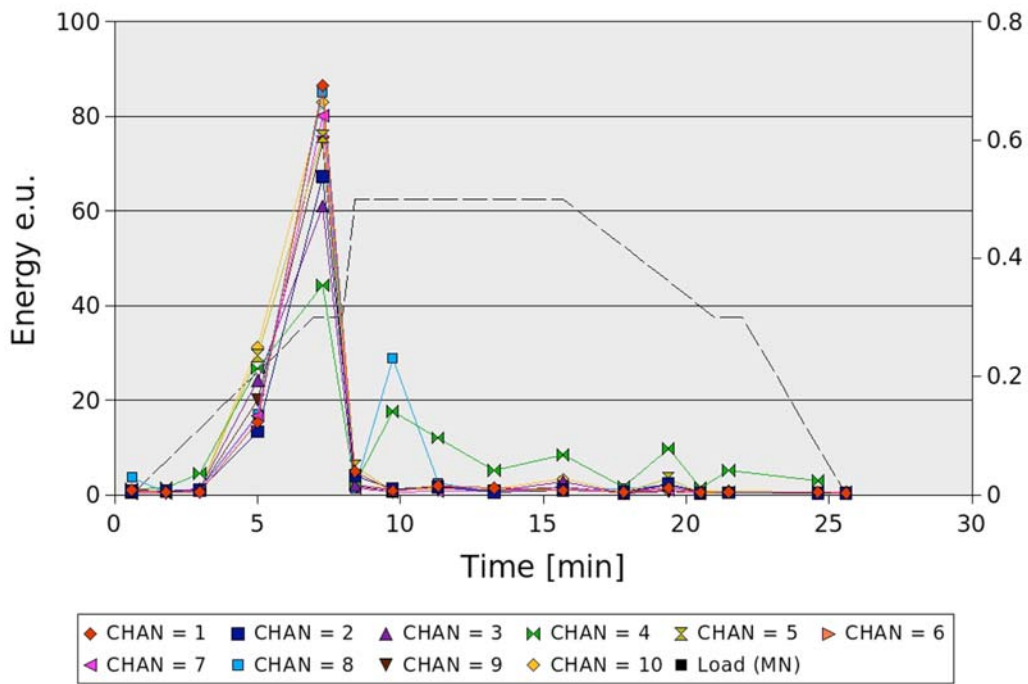


Fig. 4B. Mean energy for all channels vs. time for the second load step ($1 \text{ eu} = 10^{-14} \text{ V}^2 \text{ s}$; load: dashed line; load scale on the right side in MN).

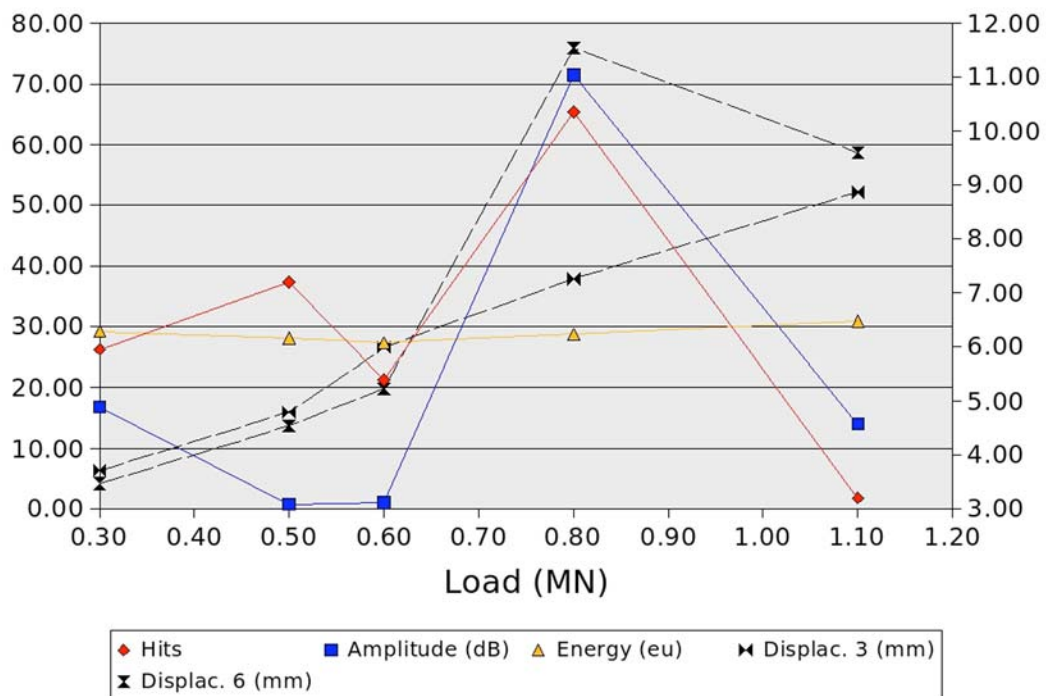


Fig. 5. Mean hits, amplitude and energy for channel 7 during loading steps matched with effective displacement measured at points 3 and 6 (Displacement scale on right side).

intermediate loading (0.3 MN) as reported in Fig. 4B. It is important to keep in mind that by considering the specific loading procedure, which considered the presence of asymmetric loads, the maximum displacements of all the measuring points of the side beams do not correspond to the maximum load applied (Fig. 2). In Fig. 5, relationship between AE parameters for sensors 7 and displacements measured at the nearest measurement points (3 and 6) are reported.

As a further evaluation of the degradation status of the viaduct, we carried out a relaxation ratio analysis [4]. Relaxation ratio is defined as the ratio of the average energy during unloading phase to the average energy during loading phase. Considering that AE activity during the unloading process is generally an indication of structural instability [5], a relaxation ratio greater than one (relaxation dominant) implies a defective structure.

In Fig. 6, results obtained on the second box girder are reported. A strong peak in the relaxation ratio during the third loading condition is evident for channels 3, 8 and 9 (on the same box girder side), while at higher load condition (0.8 MN) the peak was recorded on channel 4 (on the opposite side of the box girder).

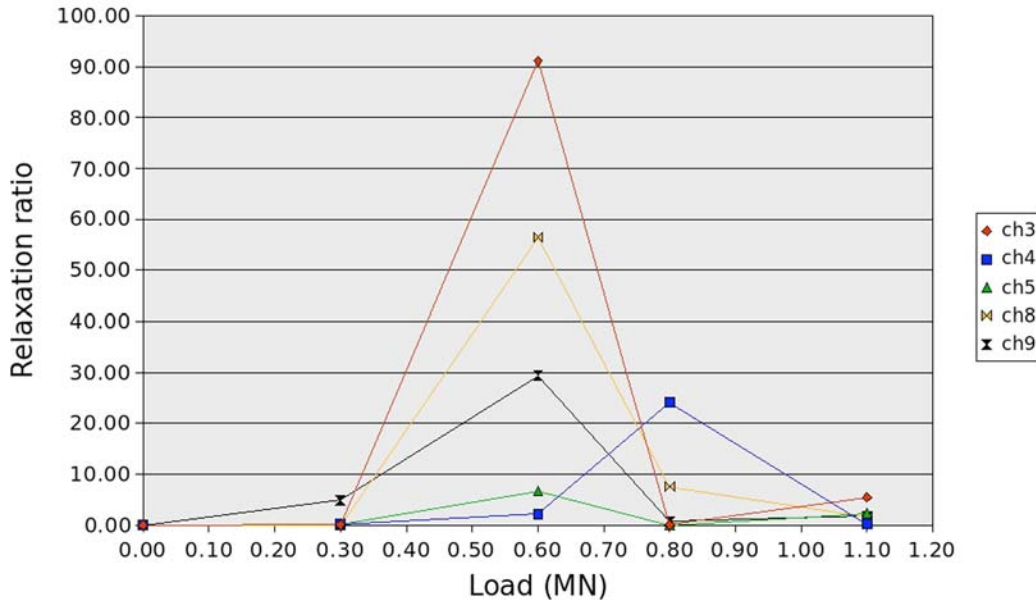


Fig. 6. Relaxation ratio for channels 3-4-5 and 8-9 on box girder No. 2.

Conclusions

We used AE technique for damage evaluation of two severely deteriorated viaducts during proof loading. The viaducts, made at the end of the 1950s along the national road 114 in Sicily (Italy), consist of several spans. Each span was built in a post-tensioned concrete girder configuration. It was observed that during loading phase, the maximum mean AE hits rate, corresponding to a minimum in the mean amplitude, was reached at an intermediate load, while at higher load a reduced number of AE hits characterized by high mean energy was recorded.

The application of the relaxation ratio analysis indicated the structural instability (relaxation dominant) of the two viaducts.

Acknowledgment: The present research was carried out with the financial support of the Ministry of University and Scientific Research in the frame of the research project n°12278 “New technologies for the evaluation of deterioration and the control of prestressed reinforced concrete structures”.

References

1. L. Golaski, P. Gebski and K. Ono, J. Acoustic Emission, **20**, 2002, 83-98.
2. Recommended Practice for In-Situ Monitoring of Concrete Structures by Acoustic Emission, NDIS 2421, Japanese Society for Non-Destructive Inspection, 2000.
3. E. Proverbio, G. Laganà, V. Venturi, *Integrated Lifetime Engineering of Buildings and Civil Infrastructures* Proc. 2nd Int. Symp. ILCDES 2003, pp.239-244
4. S. Colombo, M.C. Forde, I.G. Main, J. Halliday and M. Shigeishi, *Materials and Structures*, **38** (11), 2005, 851-856.
5. M. Ohtsu, M. Uchida, T. Okamoto and S. Yuyama, *ACI Structural Journal*, **99** (4), 2002, 411-417.

EARLY FAULT DETECTION AT GEAR UNITS BY ACOUSTIC EMISSION AND WAVELET ANALYSIS

CHRISTIAN SCHEER, WILFRIED REIMCHE and FRIEDRICH-WILHELM BACH

Institute of Materials Science, Department of Non-Destructive Testing,
Leibniz Universität Hannover, An der Universität 2, 30823 Garbsen, Germany

Abstract

To secure the availability of machines and facilities, the reaction to beginning damage must be as fast as possible. Thus, early detection of damage initiation is crucial to the quick planning and execution of reconditioning measures. This helps to minimize downtime and increase availability. Modern high performance transmissions in fabrication and energy industries more and more have to satisfy high requirements concerning their nominal load, running properties and operational stability. Helical cut gears with small modules are usually used to meet these demands. To assure an undisturbed operation, to avoid unplanned downtimes and consequential damages of high performance transmissions a condition monitoring and fault diagnosis is useful.

Vibration analysis is a good tool for detecting faults and unacceptable operating conditions of machines in an early stage, due to its large dynamic range when using spectral and correlation analysis. Detecting a defect in a machine by vibration analysis is however not possible before the degree of damage is already affecting its vibration characteristics. Using classical vibration analysis, especially the detection of cracks and their propagation in rotating shafts and gear wheels, is possible only with relatively short forecasting times before failure. Early detection of cracks in shafts and gear wheels is possible by acquisition and analysis of acoustic emissions (AE). Unlike accelerometers that capture the physical behavior of the component, like low- or high-frequency vibrations up to 200 kHz with a linear frequency response, an AE sensor is very sensitive in its resonances at higher frequencies in order to detect ultrasonic impulses caused by changes within the material's structure like crack formation and crack propagation [1, 2].

For the detection of gear defects in transmissions by AE analysis, the signal path should be as short as possible. This minimizes interferences, like the influences of ball bearings and other machine parts and emphasizes on useful information about faults. At a gear wheel test bench, acoustic emission sensors were placed on the gearbox casing and additionally on the ends of the rotating shafts in order to detect defects at an early stage as well as enabling their location and the determination of the affected component. Because of the superimposed emissions of the rolling element bearings and other components it is not sufficient to regard only the number and intensity of the emissions. Therefore an additional evaluation of the short-time excitations in frequency domain is necessary using wavelet analysis. Compared with an FFT, wavelet analysis offers a higher resolution in time domain especially for high frequent events. The crack initiation and crack propagation at the root of a tooth shows early changes in the wavelet plot, which are periodic with rotational speed. Propagating pitting shows a different behavior. Both different faults show a characteristic development during the lifetime of a gear wheel.

Keywords: Wavelet analysis, condition monitoring, gear faults, rotating machinery, rotating sensors

Introduction

Due to increasing competition, companies are forced to introduce innovative production technologies rather than only relying on the evolution of established processes. The striving for economic production methods with short processing times as well as the more stringent requirements for properties of today's high performance components brings near-net-shape forming methods into the centre of attention. The goal of the Collaborative Research Centre 489 (SFB 489) is to develop new technological and logistical innovative as well as economic process chains, based on precision forging technology for the mass production of high performance components. One main target is to realize a considerable reduction of the entire process chain, which is founded on the integration of manufacturing steps as well as the substitution of metal cutting sequences by the employment of the precision forging technique. Thus, it is necessary to convert smooth metal cutting sequences for the precision forging process together with an integrated heat treatment [3].

Dynamic load test of components in the process chain "Precision Forging"

The high demands on technological properties of the precision forged components like gear wheels require tests at realistic operating conditions. Hence one central point of the project is fixed by the diagnosis of components where the precision forged gear wheels are tested in the gear test bench to analyze the running behavior and the development of damages. In addition to the running and sound behavior the rate of wear and the development of damages have to be acquired and described by adapted measurements of acceleration and improved analysis techniques.

Another point is the out-of-phase determination of quality features dependent on the loading state, like the tooth flank strength and the tooth root strength of precision forged gears, which is essential for the optimization of the component's properties and the manufacturing steps in the processing line. Other factors of influence given by the manufacturing process are the surface finish, deviation of tolerances, the reshaped material itself, and the hardening process. The precision forged components are compared with conventional machined components to characterize the influences of the heat treatment and the hard finishing on the qualities and the properties. This enables the other sectional projects to optimize the component and the individual process steps [3].

Wavelet-analysis

Wavelet analysis provides a method of decomposing a recorded signal into a family of component parts. It is therefore a suitable new analysis technique to determine fault patterns. For general signal analysis, the objective is usually to extract frequency data from the signal and learn how its frequency composition changes with time. Besides the short-time-Fourier transform (SFFT), the wavelet transform is a method for the visualization of the time-frequency-intensity behavior. But in this case the wavelet transformation allows a higher resolution in time domain than the SFFT. Using the wavelet transform a so-called mother-wavelet has to be chosen, which is continuous in time and frequency and has an average value of zero. The wavelet transform scales this mother-wavelet for each section of the signal to allow the best fit in frequency and amplitude. The two scaling factors plotted in time domain are the frequency and amplitude coefficients of the wavelet plot. The wavelet transform has the advantage of showing low-frequency signal components as well as high frequency components with a high resolution in time domain, even if they only arise for a short time [4, 5].

Acoustic Emission Analysis at Rotating Machinery

In addition to the instrumentation with accelerometers one of the gearboxes was equipped with AE sensors at different measurement positions. At first gear wheels were tested as can be seen in the right part of Fig. 1. For these tests two AE sensors were placed on the two bearing housings, fixed bearing and loose bearing. One was placed on the lubrication conduit and another one right in the oil beam of the oil conduit in order to obtain AE signals, which may cause a feedback via the oil beam. Last but not least a rotating AE sensor was placed at the end of the shaft with the test gear. The sensor itself is positioned at the rotating end of the shaft, containing a sender, which is facing a receiver and sending the AE information via induction [6].

Further tests were performed using pinion shafts as displayed in the left part of Fig. 1. Another arrangement of sensors was used to enable location of AE events. At the corners of the gearbox four sensors are placed in addition to two rotating ones at the ends of the shafts.

For data acquisition a multi-channel AE measurement system was used using statistical methods to investigate AE properties like amplitude, energy, hits and counts. Additionally, the sensor signals were periodically obtained by a high frequent transient measurement system to get transient data of several revolutions of the test shaft [7-9].

New sensor arrangement for pinion shaft

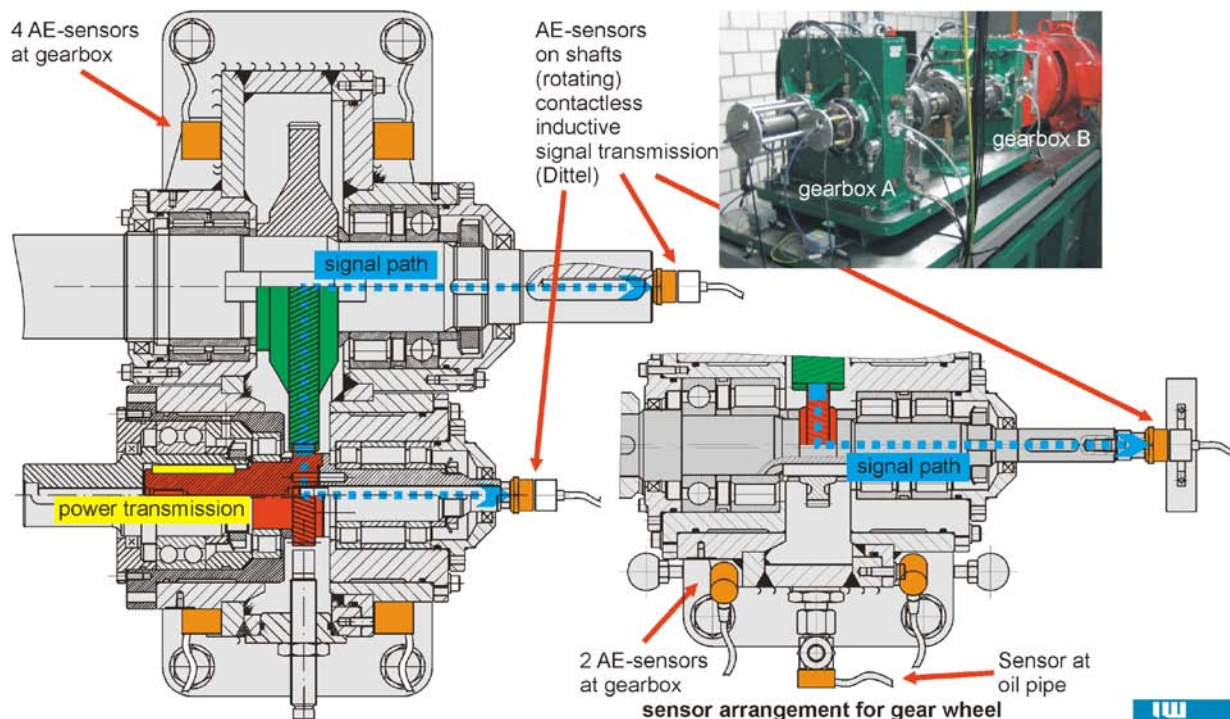


Fig. 1: Arrangement of AE-sensors at gearbox.

During the first test measurements with different speeds and different loads the influences of these parameters on the signal to noise ratio were identified and the thresholds for the AE amplitudes were set. Different loads ranging from 200 to 450 Nm showed no significant influences. For the following description of the fault initiation and propagation only the information of the rotating acoustic emission sensor at the end of the test shaft is used. The other sensors showed no significant information about the condition of the test wheel because of their complex signal path

and superimposed AE from other components of the test bench. Figure 1 shows the arrangement of the different sensors and the transmission path from the teeth to the sensor. The mounting of an AE sensor directly on the gearwheel was not possible because of the shape and size of the gear wheel and the dimensions of the gearbox. Additionally, the connection of signal cables to a sensor directly on the gear wheel via the rotating shaft is quite difficult.

After the mounting of a test wheel and start-up of the test bench during the first hours of operation a quite high amount of AE signals can be detected. Seizing of the keys and contact areas of the test gear and the shaft caused these AE signals. After a few hours, this run-in effect is over and the normal operation condition with only a small amount of events is reached. Additional disturbances may occur if there is too much slack between shaft and gear wheel. Therefore, seizing occurs between shaft and gear wheel, which causes a high amount of AE signals. Another event causing AE signals was the fracture of a key between shaft and gear wheel. The propagating fault caused AE signals over several hours. In this case the detection of faults at the gear wheel is possible only with a close fit between shaft and gear wheel. Additionally the test bench has to be run-in and has to be working at operating temperature.

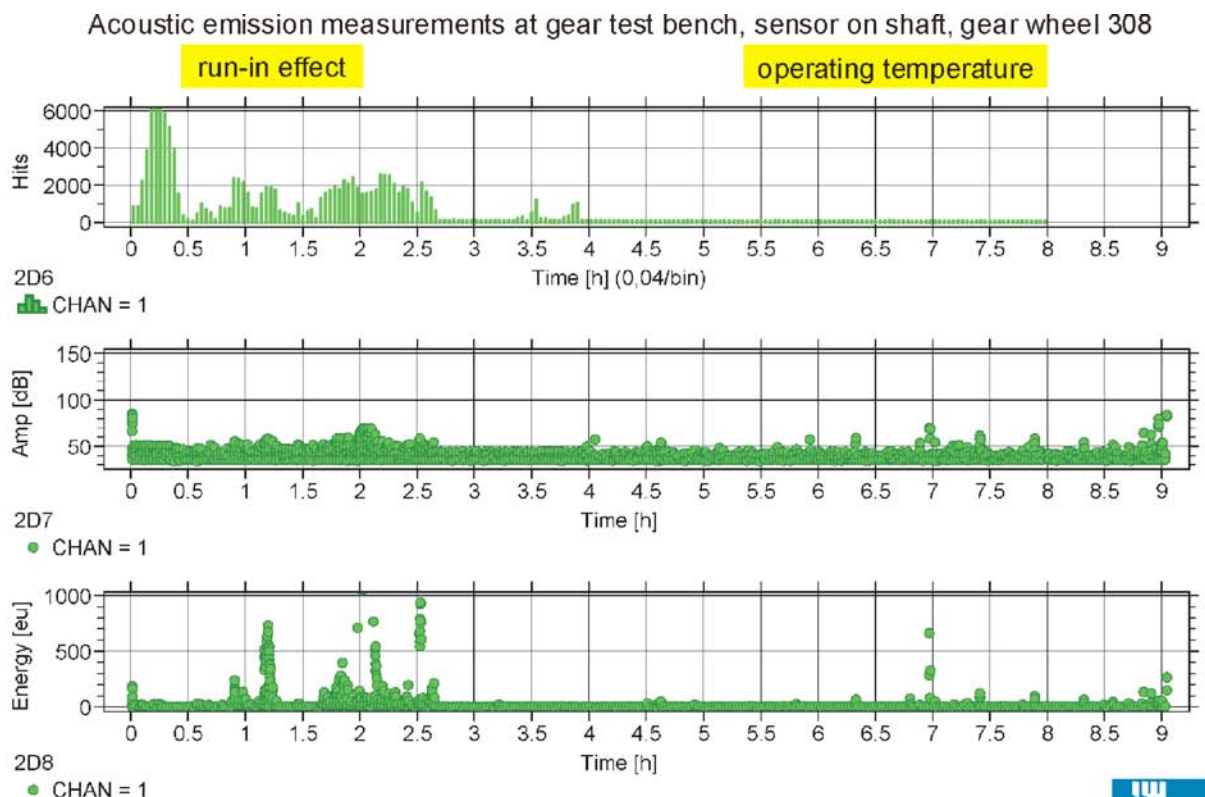


Fig. 2: Run-in behavior of gear wheel.

The start-up of the test bench with gear wheels and too much slack between shaft and gear wheel is shown in Fig. 2. The relation of the hit rate to the other properties of AE signals shows information about the source of the AE signals. A high hit rate with concurrent high amplitudes or energy assumes the source of AE signals to be close to the sensor and therefore in the area of the joint between shaft and gear wheel by the keys. Because of the long distance between sensor and teeth mesh AE signals from the teeth reach the sensor at the end of the shaft with low amplitudes only.

The fixed bearing at the beginning caused the high amount of AE signals with low amplitudes. Figure 3 shows AE signals at start-up, which occur with ball-spin frequency (BSF) at the fixed bearing. Intense heating of the shaft after start-up causes decrease in bearing gap. When the operating temperature is reached, the bearing gap is correct and there is a decrease in AE signals. Additionally there are increased relative motions between surfaces during start-up and run-in. After about three hours the run in effect is finished and there is normal operation with low hit rates only.

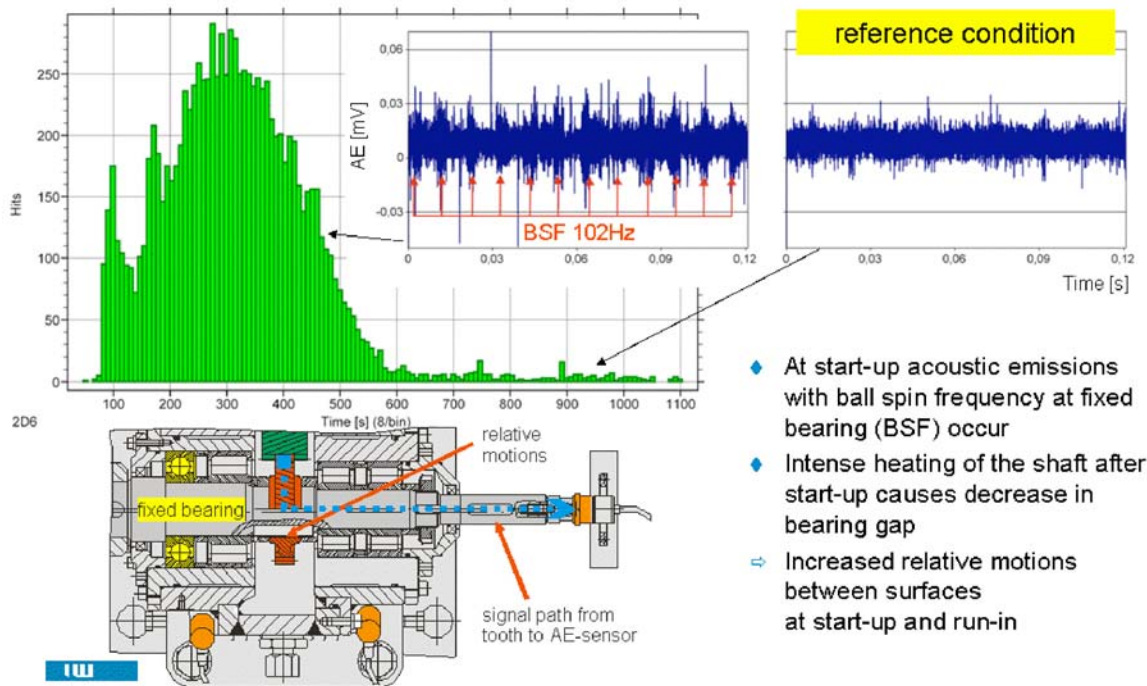


Fig. 3: Influence of fixed bearing at start-up.

Detection of Gear Faults by AE Analysis

The progression of the properties of an AE signal for the undisturbed reference condition after run-in and the crack initiation and propagation until the failure of the gear wheel and shut down of the test bench is displayed in Fig. 4. For the description of the AE signals, the number of hits and the energy of the signals are shown, which are usually used for failure detection.

In the upper part of the figure, the number of hits during the reference condition is very low, whereas in the lower diagram the crack initiation can be detected by an increasing hit rate caused by the opening and closing of the crack during one revolution of the test wheel. With an increase of load cycles the fracture of one half of the tooth occurs. Since the other half of the tooth is still carrying the load the test bench could be operated further. In this case, the energy of the AE-signals shows no significant changes regarding the fracture of a gear wheel tooth.

Another example of the detection of gear faults is presented in Fig. 5. Here, the beginning and propagation of pitting at the teeth flanks is shown. Compared to the reference condition, there is an increase in the hit rate, which is not as great as in the case of a crack. Also the hit rate may decrease again, when pitting has developed. There is a more fluctuating behavior of the hit rate. The propagation of pitting in the lower diagram of Fig. 5 shows this swelling progression to be more significant.

Acoustic emission testing, gear test bench, sensor at shaft, gear wheel 170

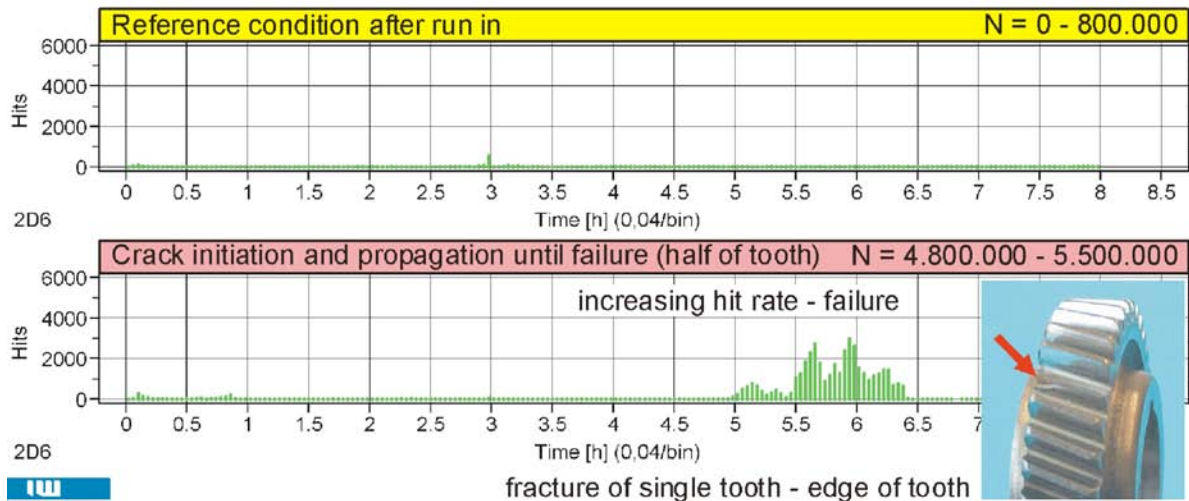


Fig. 4: AE data of reference and crack.

Acoustic emission testing, gear test bench, sensor at shaft, gear wheel 179

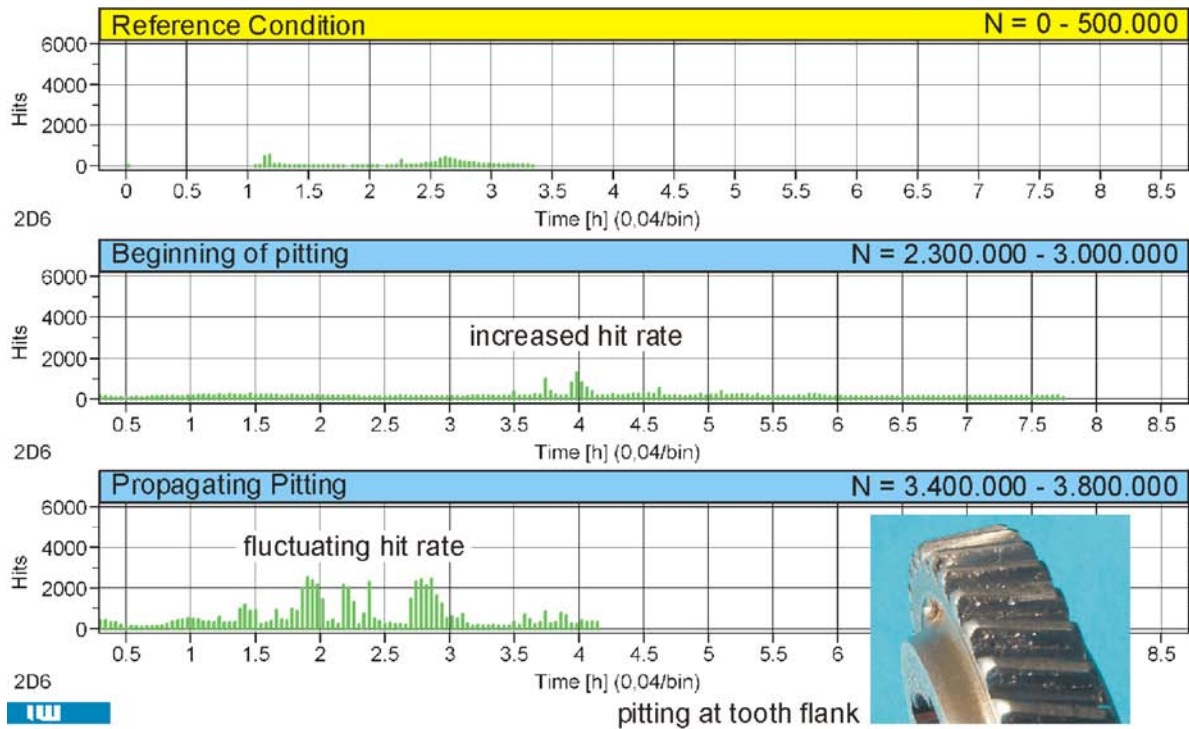


Fig. 5: AE data of reference and pitting.

More significant differences between crack development and pitting show transient signals of the shaft sensor, logged over several revolutions of the shaft. These were recorded using an additional high-speed data-acquisition card with 1-MHz acquisition rate through 250 ms. The amplitude of an AE sensor is influenced chiefly by its main resonance ranges because of its non-linear behavior. To evaluate signal components out of these ranges a transformation into frequency domain is necessary. Especially the wavelet transform is a good means for this kind of high frequency analysis with short-time events.

The time-frequency components of a crack development compared to the reference condition are displayed in Fig. 6. The wavelet transform is used here with the Morlet-wavelet as the mother-wavelet. The reference condition as well as the crack at a single tooth shows high amplitudes at about 100 kHz (resonance of the sensor, resp. the measurement chain). These low-frequency parts of the signals are not detected by the AE system because it uses a 120 kHz high-pass filter. The crack is clearly visible by short-time pulses in the frequency range of 200-250 kHz. They appear at ca. 0.04 s intervals, which equals the rotational speed of 25 Hz. Six revolutions are displayed in the diagram and during each revolution there is a short-time excitation at 200-250 kHz when the damaged tooth comes into mesh.

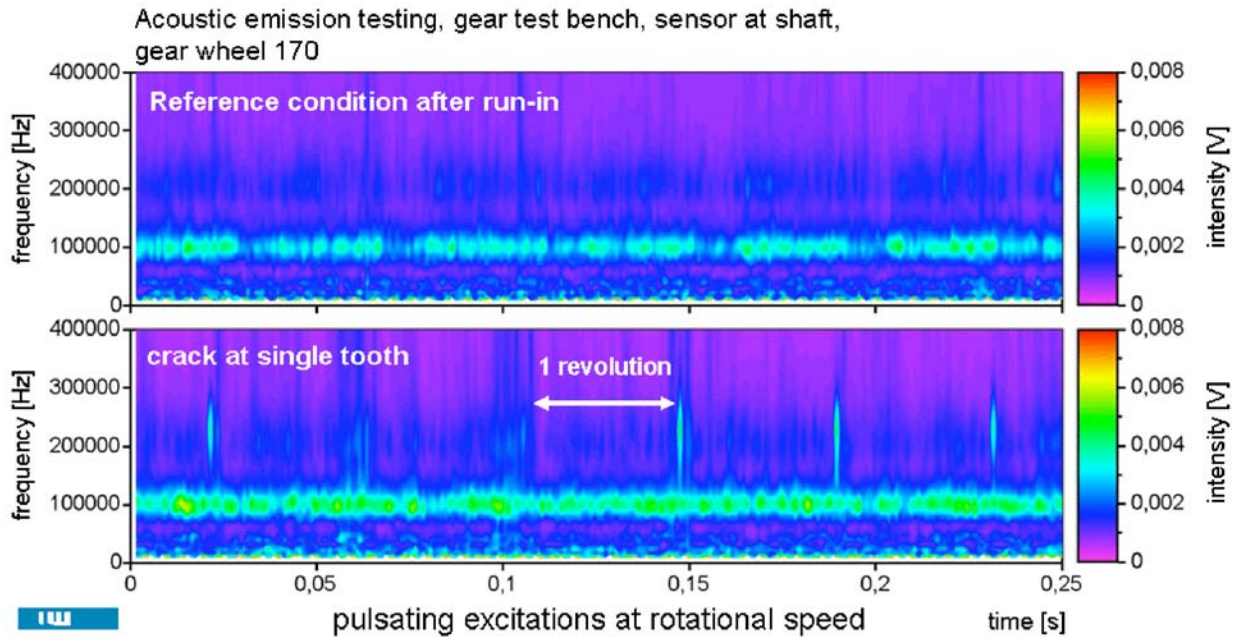


Fig. 6: Wavelets of reference and crack.

The behavior of pitting can be seen in Fig. 7 in contrast to the crack development in Fig. 6. The dominant signal component at 100 kHz is visible in this plot, too. There is a much more broad-banded signal component visible over the whole frequency range up to 400 kHz, which lasts much longer than the excitation of the crack development. It is excited more than once per revolution because of the pitting development at several teeth simultaneously. When these teeth are in mesh the pitting propagates and AE signals are generated.

Location of Fault-specific Events

Because of the very high acquisition rates of up to several MHz, the location of AE signals is possible using run-time analysis of several sensor data. The sound waves propagate in concentric circles, resp. spheres, from the point of origin and can be detected by AE sensors. Propagating through solid matter the waves are damped. The maximum range of the sound waves depends upon the material properties, the geometric and surrounding conditions of the object and the number of surface contacts between different objects. At metal parts these high frequency sound waves may be detected beyond a distance of several meters. The determination of the speed of sound, which is necessary for the location, is quite difficult at complex three-dimensional structures, because it varies dependent on different media and many contact surfaces. Performing this

location of AE events inside a gearbox an averaged speed of sound is used. Further analysis of the signal paths, the materials and contact surfaces will improve this method.

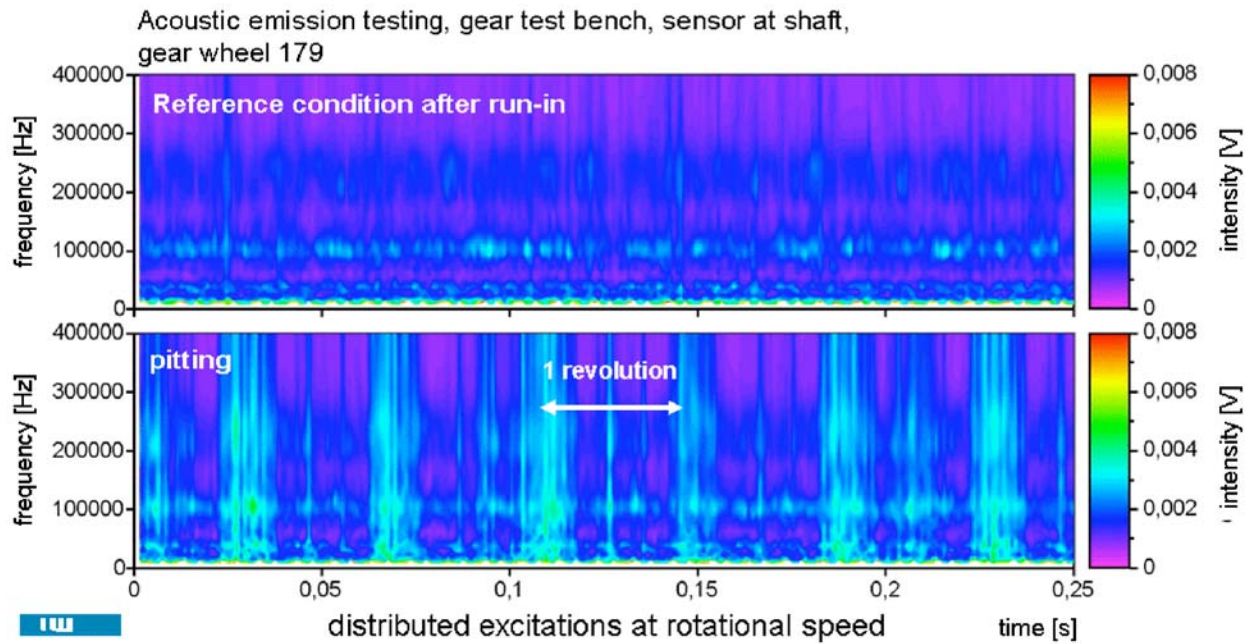


Fig. 7: Wavelets of reference and pitting.

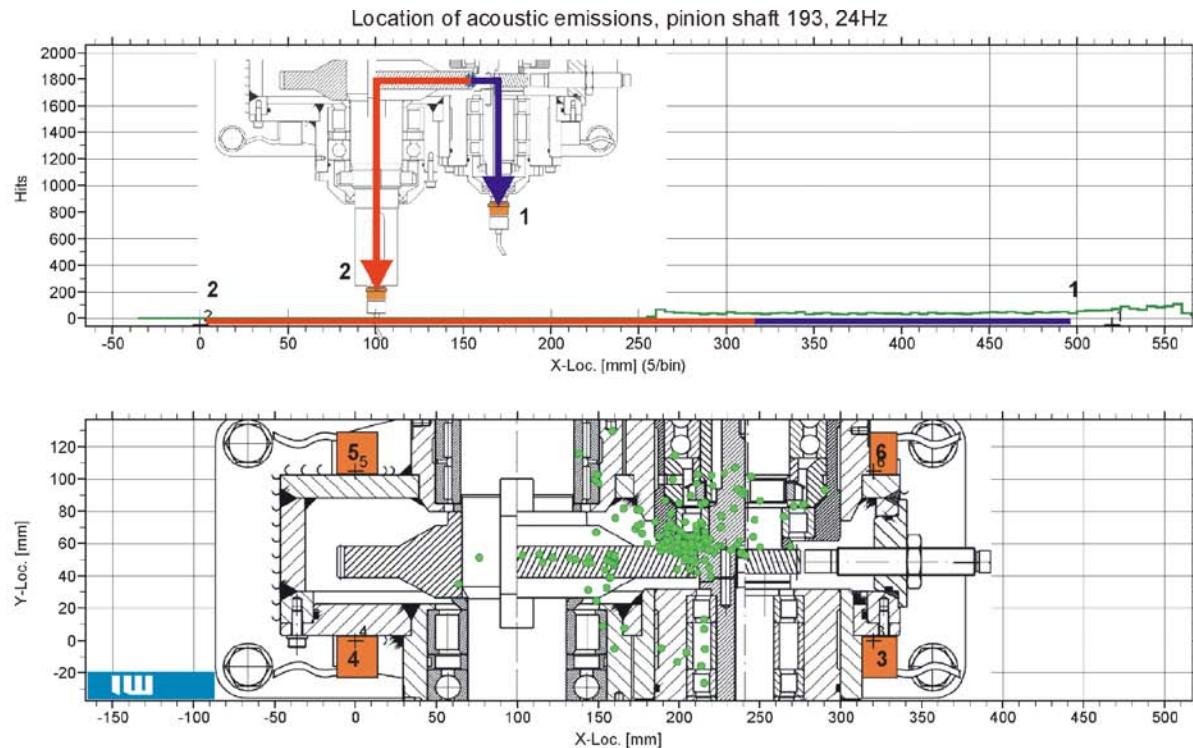


Fig. 8: Location of teeth mesh inside the gearbox.

Four sensors at the corners of the gearbox near the shafts are used to locate AE-events inside the gearbox (Fig. 1, Fig. 8). This enables a location on a sectional plane of the gearbox. Because of the very good results of the shaft sensor an additional rotating sensor was placed at the end of the second shaft to realize a linear location between these two sensors.

Additionally, the gear test bench has been modified for a pinion shaft as another test object. The advantage to the gear wheel is the difference between signal path for the sensor and transmission path of the load. The power transmission is not in the area of the signal path from teeth mesh to the rotating sensor at the end of the shaft (Fig. 1). This causes much less AE events by seizing in the fit and at the keys. Therefore, the run-in effect could be minimized and additionally a higher rotational speed of 45 Hz could be used.

The locations of the AE events inside the gearbox are presented in Fig. 8 and Fig. 9. The linear location between sensor 1 and sensor 2 is visualized in the upper part of the figures. In the lower part of the figures, the sectional plane of the gearbox is visible showing the location of AE events inside the gearbox. Figure 8 shows the reference condition with only few events located between the sensors 1 and 2 and in the area of the teeth mesh in the sectional plane located by the sensors 3 to 6.

The propagation of faults is shown in Fig. 9. Regarding the linear location a deviation of the hit maximum towards sensor 1 is clearly visible. The distances from the maximum to sensor 1 and sensor 2 identify the AE events as coming from the area of the teeth mesh. The location by the sensors at the gearbox shows a similar result. Using the sensors 3 to 6, there is an accumulation of AE events in the area of the teeth-mesh and at the roller bearing on the pinion shaft. The AE signals from the teeth mesh are generated by the teeth mesh itself as well as by the development of a crack, shown in green. The AE signals in the bearing area are caused by seizures in the close fits and a wrong fit of the bearing inner ring, shown in red (cp. Fig. 1). Additionally, there are several location results, which are not feasible, shown in light blue.

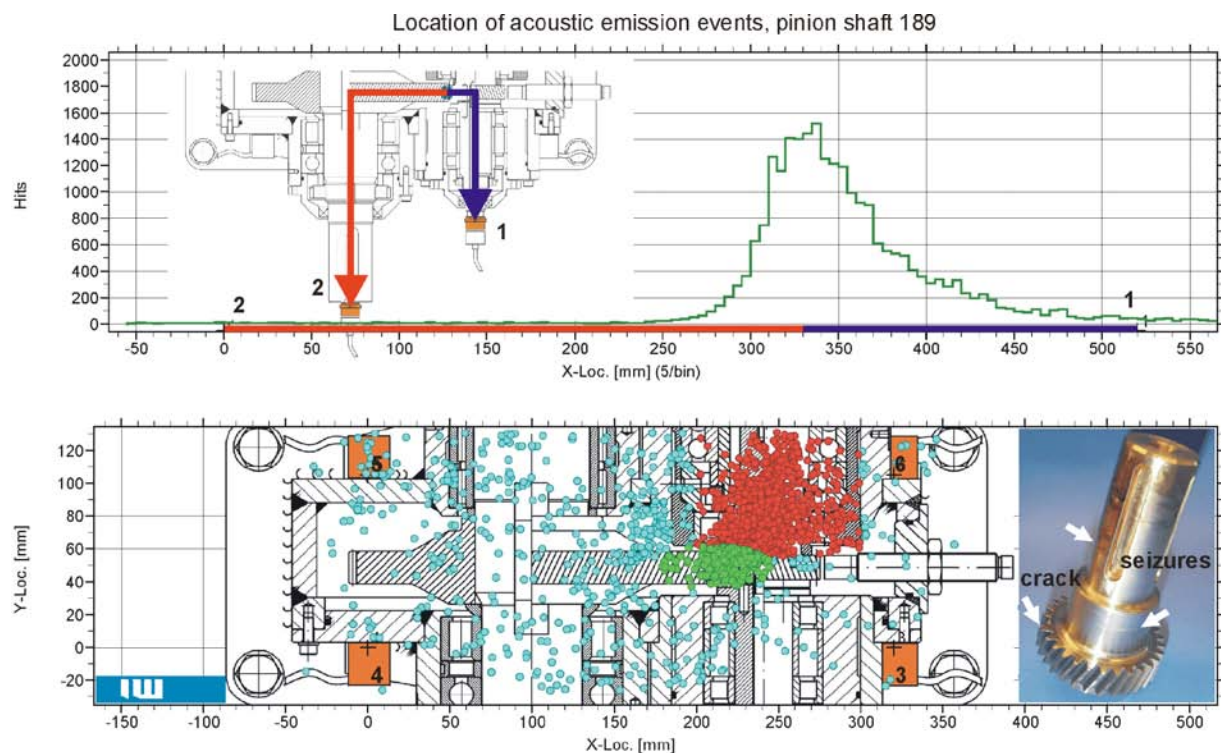


Fig. 9: Location of faults inside the gearbox.

Future work consists of filtering the AE data according to their location to improve the distinction between different gear faults, run-in effects, seizures and faults at other components like rolling element bearings.

Summary

Condition-based maintenance is a contribution to ensure the reliability of operation, high availability and efficiency of industrial machines and plants. This necessitates the acquisition of information about the condition of single components.

1. The condition monitoring of the gear test bench at the Institute of Materials Science (IW) is achieved by vibration measurements to describe the operating condition and detect the development of faults by analysis in both the time and frequency domains. Slow developing faults like pitting can be detected quite early by this method. The detection of cracks leading to tooth fractures is possible with a very short forecast time only.
2. The analysis of AE signals allows an early detection of cracks in the tooth root because of the crack propagation before the teeth mesh is disturbed and the vibration behavior changes.
3. The location of acoustic emission events enables the allocation to specific components inside the gearbox to improve the distinction between gear faults, run in effects, seizures, and rolling-element bearing faults.

Acknowledgements

We express our sincere thanks to the German Research Foundation for the promotion of this work within the Collaborative Research Centre 489 “Process Chain for the Production of Precision-forged High Performance Components”.

References

1. Toutountzakis, T., Mba, D.: Observations of Acoustic Emission Activity during Gear Defect Diagnosis, *NDT&E International*, 2003, **26**, 471-477.
2. Tan, C. K., Irving, P., Mba, D.: Prognostic Potential of the Acoustic Emission Technique for Spur Gears, *Essential Technologies for Successful Prognostics, 59th Meeting of the Society for Machinery failure Prevention Technology*, Virginia Beach, US, April 2005.
3. Bach, Fr.-W., Kerber, K.: Sonderforschungsbereich 489 „Prozesskette zur Herstellung präzisionsgeschmiedeter Hochleistungsbauteile“, www.sfb489.uni-hannover.de, 2006.
4. Misiti, M., Misiti, Y., Oppenheim, G., Poggi, J.-M.: *Wavelet Toolbox User's Guide*, Mathworks, 2000.
5. *AGU-Vallen Wavelet, wavelet transform tool*, Vallen-Systeme, Icking, 2005.
6. Sporer, A.: Hohe Sensibilität entwickeln, Acoustic-Emission-Systeme für die Schleifprozessüberwachung, Walter Dittel GmbH, Werkstatt und Betrieb 03/2006.
7. Vallen, H.: *Die Schallemissionsprüfung*, Castell-Verlag, 2003.
8. Vahaviolos, S.J.: *Acoustic Emission: Standards and Technology Update*, ASTM STP-1353, 1999.
9. AMSY-5 Users Manual, Vallen-Systeme GmbH, 2004.

APPLICATION OF ACOUSTIC EMISSION IN MONITORING OF FAILURE IN SLIDE BEARINGS

IRENEUSZ BARAN, MAREK NOWAK and WOJCIECH DARSKI*

Cracow University of Technology, Institute of Production Engineering M-6, Kraków, Poland;

*Gdańsk University of Technology, Ocean Eng. and Ship Technology, Gdańsk, Poland

Abstract

The article describes the laboratory tests, which make the first stage of the study concerning the use of the AE method to determine the technical state of the slide bearings in engines with self-ignition. The aim of the present tests was to compare the recorded signals in relation to the technical state of the material of the bearing bush and to check the possibility of using the AE method in determining the transition moment from the fluid friction into the semi-dry friction in the bearing and signaling the first micro-defects of the material of the bearing bush. The experiment has not solved the problem, but they are of a development character and will be continued in the nearest future.

Keywords: Frequency analysis, slide bearing, friction factor, bearing bush

Introduction

Ship combustion engines with self-ignition have fundamental influence on the profitability of ships and their safety at sea. Therefore, it is important to ensure the failure-free operation of these engines. In ship engines, the maintenance of the sliding abilities of the main bearings and connecting-rod bearings is of special importance because the failures of these bearings constitute almost 30% of the total number of failures in all parts of engines. Since the costs of failures of combustion engines caused by the failures of slide bearings are high, intensive theoretical and experimental tests of the slide bearings properties have been undertaken [1, 2].

The currently used methods of monitoring of the technical state of slide bearings indicate the state of failure only when a considerable degradation of the slide bearing material appears. In many cases, this is unsatisfactory in avoiding severe defects or failures. Testing by means of the AE method occurs in real time, and this method can be used as a system of the early warning to avoid damage in structural parts of combustion engines [3, 4].

The presented tests were carried out on the fully computer-controlled laboratory stand (PG-2 1Ł type) for the examination of slide bearings, as shown in Fig. 1. This stand enables one to simulate the real performance conditions of a bearing and to record all the essential parameters, such as: moment of friction, rotational speed, temperature of the bearing and of the lubricating oil. Technical data of PG-2 1Ł laboratory stand:

- Power of engine: 11 kW,
- Range of rotation of shaft: 1-4000 RPM,
- Maximum transversal load: 150 kN,
- Diameter of shaft: 76.18 or 80.25 mm,
- Length of bush: 36.75 or 40.00 mm.

The tested bearing bush of MB10-type (Fig 2) is used in C-330-type diesel engine. This engine is generally used for drive auxiliary assembly on ships.



Fig. 1. The laboratory stand PG-2 1L for examination of slide bearing.

Technical data of MB10-type bush:

- Catalogue No.: 1006022010
and 1006021010,
- Length: 40.00 mm,
- Outside diameter: 86.00 mm,
- Thickness of wall: 2.905 mm,
- Thickness of steel part:
2.600 mm,
- Diameter of seating of frame:
86 mm.

Tests were made under different conditions of slide bearings:

- Constant transversal load and constant rotation:
1 or 2 kN, 1700 RPM,
- Constant transversal load and cyclic variable rotation:
1 or 2 kN, 1-1700 RPM,
- Step changing transversal load and cyclic variable rotation:
1, 2, 4 and 8 kN, 1-1700 RPM.



Fig. 2. The bearing bush MB10-type after several cycles.

The trials by the AE method were carried out with the use of the Vallen AMSY5 system with different types of sensors (VS150RIC-Vallen, WD-PAC and others) in order to cover the widest band of frequency measurements. At the same time, the AE system enabled us to record the test parameters (moment of friction, rotational speed, loading force, temperature) in order to correlate them later with the recorded AE.

Measurements of the acoustic background

The first stage of the tests concerned both the measurement of the acoustic background and the noise generated by the operation of the installations on the testing stand. That is why the first tests were carried out on a new bearing in different loading variants and rotational speeds with the recording of signals in a widest band of frequency. The frequency analysis of the recorded signals allowed us to determine the main band of noise and the selection of frequency high-pass and low-pass filters for subsequent measurements in order to minimize noise coming from the operation of the testing stand.

An example of the recorded bands of frequency on two wide-band PAC-WD sensors with constant transversal load and constant rotation is presented in Fig. 3. Two examples are given for narrow-band filtered signals (a) and wide-band signals with strong low-frequency activity (b).

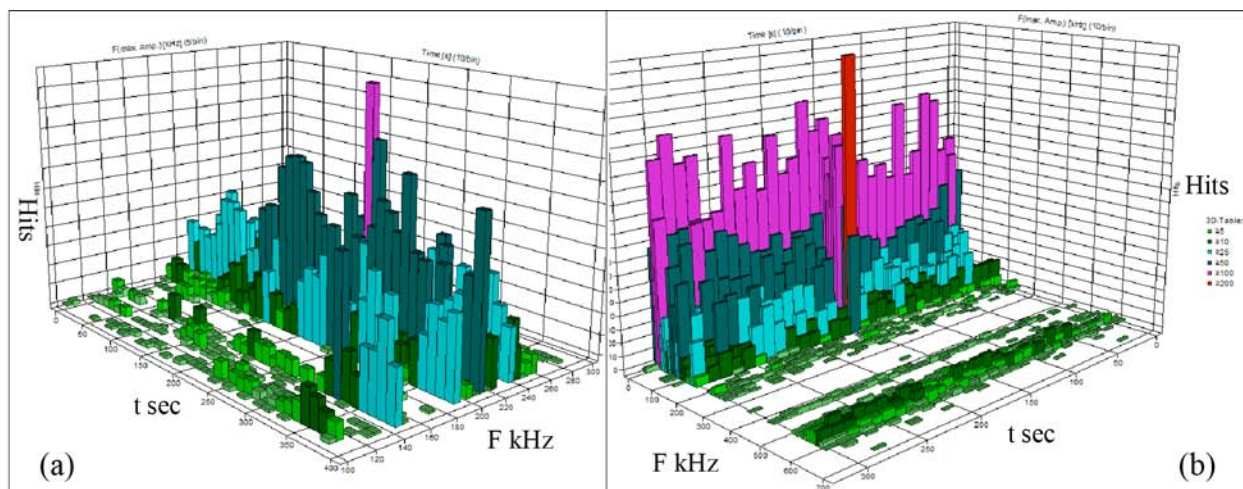


Fig. 3. The arrangement of the frequency bands of the signals recorded by 2 wide-band sensors. (a) narrow band, 100-300 kHz segment of 95-850 kHz filter output; (b) Wide band, 20-850 kHz.

Measurements of bearings in different technical state

The first stage of the tests using frequency filters was the measurement of a new bearing with the accepted conditions (loading and rotational speed) similar to the preliminary tests. We used the constant rotational speed of the shaft of 1700 RPM and two values of the bearing loadings, 1 and 2 kN. The AE parameters for these operating conditions for a new bearing established the basis of comparison in the remaining tests.

In order to compare the AE signals recorded during the testing of the new bearing with the signals coming from defected bearing, the measurements were taken of three sliding bearings made of the same material (simulated different bearing capability):

- The new bearing bush without defect – full bearing capability,
- The bearing bush with an opening, simulating a local defect in the material of the bush, which caused disturbances in the flow of lubricating oil – a small but apparent loss of bearing capability,
- The bearing bush with longitudinal and circumferential scratches simulating considerable wear of the bush material – large loss of bearing capability.

High activity of AE was recorded but clearly different for each kind of tested bearing bushes. General AE parameters such as: Hits, Counts, Duration, Energy and RMS showed differences between bushes. However, Amplitude of signals contained similar ranges for all the tested bearing bushes. To evaluate different activities of AE, uses of different threshold levels made comparison difficult with these parameters. At this time, the best parameters for comparison are RMS and frequency distribution of signals. Recorded RMS for the new bearing and the bearing simulating the local loss in the bearing bush material are presented in Figs. 4, 5 and 6. There are data of RMS from different channels with different frequency ranges. Two types each of low- and high-frequency data (with or without *) and medium frequency data are shown. Note RMS for High Frequency (red line) is off-scale because overloading occurred on this channel.

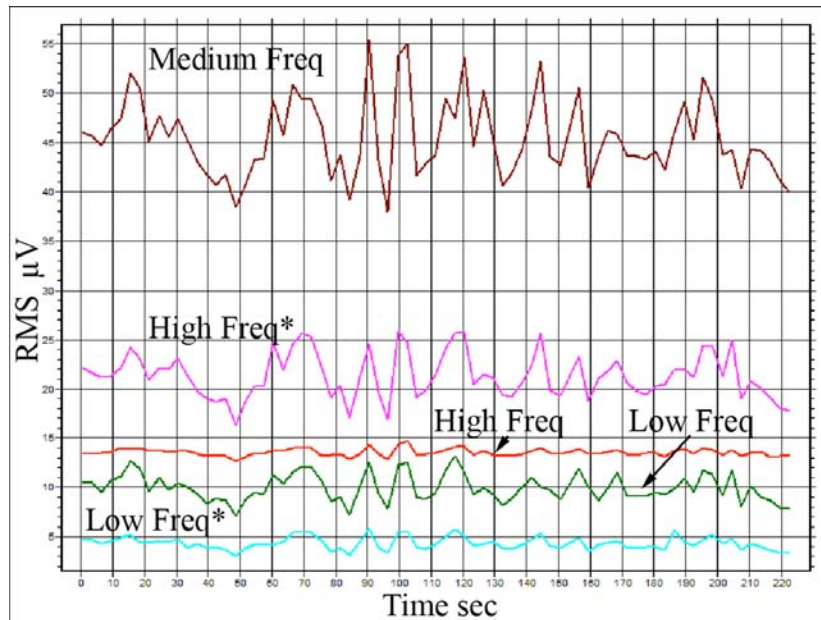


Fig. 4. RMS for different ranges of frequency filters – new bush with no defect.

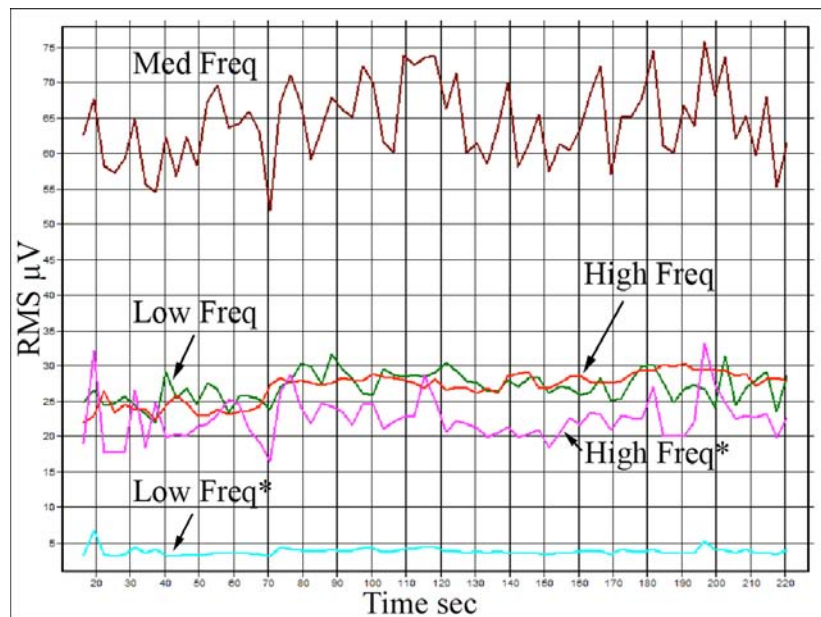


Fig. 5. RMS for different ranges of frequency filters – bush with an opening defect.

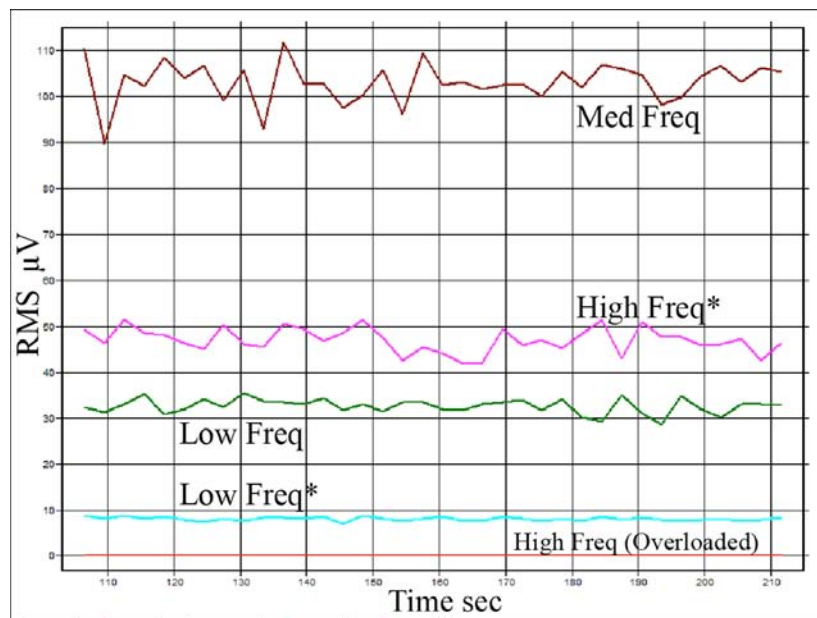


Fig. 6. RMS for different ranges of frequency filters – bush with scratches.

The observed data shows general increase of AE RMS levels (except Low* and High* channels between Figs. 4 and 5). Medium and High channels respond to bush damage states sensitively. The relative changes in the 5-channel data provide clear indication of the bush damage states.

The initial dimensions of the bearing and the bearing's fit are of vital importance on the parameters of the recorded AE. For the bearings of the same dimensional group, different level of the AE activity was recorded. It is especially visible in the first stage of the bearing operation, when the initial wear of bearing bush surfaces to the shaft neck takes place. Therefore, it is vital to enlarge the data library by taking a larger number of measurements for each of the accepted variant of the bearing states.

Considering the serious differences in the intensity of emission for the particular kinds of the state of bearings during the measurements, changes were being made in the arrangements of the acquisition parameters in order to record the measuring data, which could enable the subsequent analysis with the use of the waveform [5].

The measurement of the bearing with changeable parameters

During the testing of the new bearing, a measurement was also taken under the conditions of variable rotational speed and step changing of transverse load, which were to lead to a quicker wear of the bearing bush material. After the cyclic changes in rotational speed, the AE was recorded during the operation of the bearing under the established conditions. The recorded AE was to detect the appearance of the first damage in the material of the bearing. The sum of distribution of hits in frequency bands is presented in Fig. 7. The visible change in the activity of hits indicated a change in the operation of the bearing. The reason of the sudden increase in the AE activity was the wear of the surface layer of the bearing. These changes were invisible in the conventional bearing parameters (moment of friction, temperature, ...) recorded on the testing stand PG-2 1L. It was indicated that significantly changing inside slide bearing is detectable by AE. The example of one of the half bush after these tests is shown on Fig. 2, where surface wear

can be seen. It should be noted that this research requires a larger number of the trial tests in order to record AE in different states of wear of the bearing material.

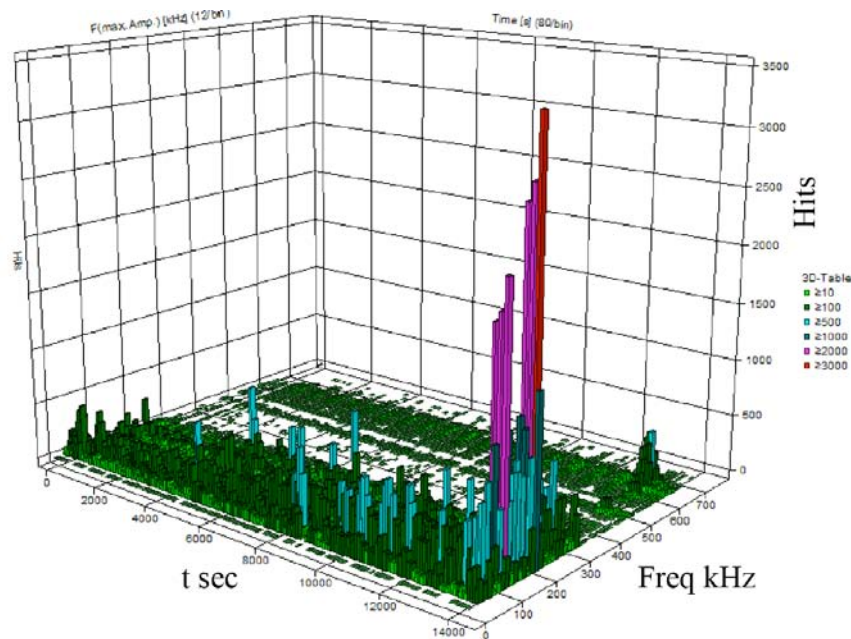


Fig. 7. The arrangement of the frequency bands of the signals during long-time tests with variable rotation and step changing of transverse load.

The measurement under the conditions of intermittent fluid friction

One of the essential aspects of the tests was the measurement of AE during the disappearance of the fluid friction and transition into the semi-dry friction; i.e., at the moment of the first contact of the pin with the bearing bush. To this end, the test methodology was modified and caused to decrease the friction factor till the start of the contact of the metal pin with the bearing bush. The AE recorded at this time signaled the decrease of the friction factor due to the disappearance of the activity of the AE signals. This was followed by the increase in the friction factor during the contact of the pin surface and the shaft, then a sudden increase in the activity of AE was observed. Figure 8 shows the changes of the bearing parameters, the moment of friction (left) and RPM (right) in the new bearing test. The changes in the AE hit activities in various frequency bands are also presented in Fig. 8. Here, actual RPM reached zero when the friction was high. No AE was emitted in this period and until ~700 RPM was reached.

In this connection one should suppose that carrying out of a larger number of tests will allow the unequivocal identification of the moment of transition from the fluid friction into the semi-dry friction. The presented tests were carried out on the testing stand under the laboratory conditions. In the future, measurements of the bearings installed in combustion engines are planned.

Conclusions

The application of the frequency filters allowed the reduction of the majority of noise for the testing stand, but in the future it will be necessary to determine noise on real engines. The presented examples illustrate that it is possible to apply the AE method in order to define the state of the bearing material. The sensitivity of the AE method allows one to record the signals,

which indicate the transition from the fluid friction into the mixed friction. In the future, it will be advisable to use a pattern-recognition analysis software to identify the recorded signals.

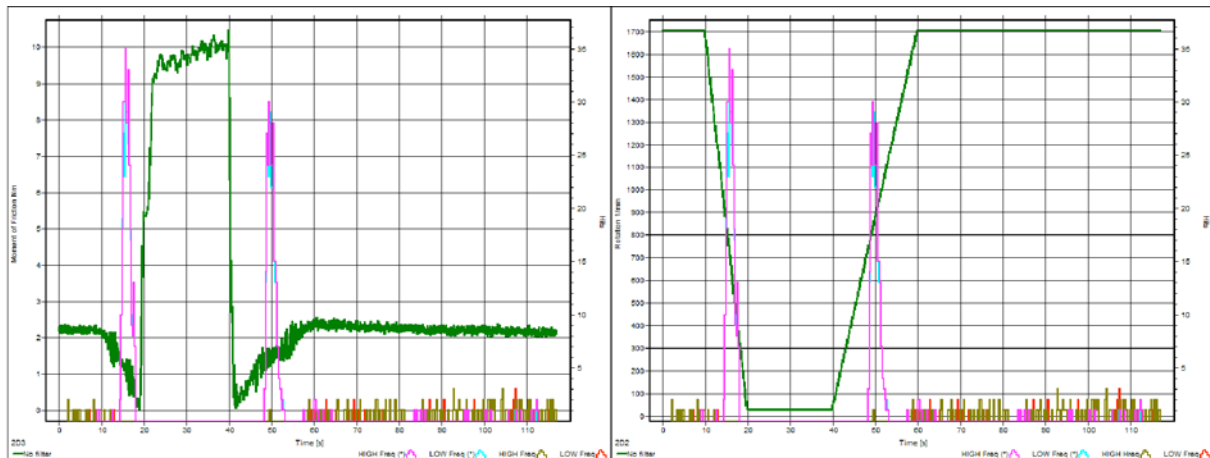


Fig. 8. The changes of the moment of friction (left) and RPM (right) parameters and the AE hit activities in the new bearing test.

References

- [1] Burger W. Albers A. Scavino R. Dickerhof M.: Proc. of WTC2005 World Tribology Congress III, Sept. 12–16, 2005, Washington DC, USA.
- [2] Scavino R., Burger W., Fritz M., Albers A.: Tribologie Fachtagung 2004, Hungary Academy of Sciences, Kozma: Veszprem.
- [3] Al-Ghambi, Zhechkov D., Mba D.: 26th European Conference on Acoustic Emission Testing, Berlin, 2004,
- [4] Yoshioka T., Fujiwara T.: Wear, **81** (1), 1994, 183-186.
- [5] Gołaski L., Gębski P., Baran I., Ono K.: J. of Acoustic Emission, **17** (3-4), 1999, S37.

MAPPING OF WHEEL FLANGE RUBBING ON RAIL USING AE: LABORATORY TEST

N. A. THAKKAR, R. L. REUBEN and J. A. STEEL

Mechanical Engineering, School of Engineering and Physical Sciences, Heriot-Watt University,
Riccarton, Edinburgh, Scotland EH14 4AS UK

Abstract

Abnormal contact stresses between wheels and rails can give rise to excessive rail wear and, in more extreme cases, to rolling contact fatigue (RCF) and gauge corner cracking (GCC). The independent investigation into the Hatfield train disaster in the UK, whose primary cause was a rail defect, highlighted the need for improved awareness of the condition of railway rails. This work is aimed, not specifically at detecting rail cracks, but at monitoring the intensity of contact between wheel and rail using acoustic emission with a view to making an in-service update of estimated remanent life.

A test-rig has been built in order to simulate rail-wheel contact, providing for variations in normal contact force and rolling speed, and allowing the simulation of a range of defects in a way that would not be possible at full scale. In this paper, wheel flange rubbing on the rail (a precursor to GCC) has been simulated and monitored using acoustic emission (AE). A simple analytical model for AE arising from normal wheel contact has been used to locate parts of the track where a wheel flange is rubbing on the rail. The method works by comparing AE peaks above normal with natural defects with and without the additional defect of flange rubbing, calculating a cross-correlation function, whose peakedness is an indication of how well correlated the defects are with the AE peaks. In all cases, cross-correlations were better when rubbing was present indicating that flange rubbing can be detected even in the face of natural defects.

Keywords: Rail/wheel interaction, structural integrity monitoring.

Introduction

Fracture of railway rails can have serious consequences [1], and some shallow angle defects cannot easily be identified even by the most advanced NDT defect detection techniques [2]. Contact stresses are responsible for rail defects and Miller [3] has identified the main factors affecting contact stresses as external load, traction force, and rail-wheel contact area. Contact area and hence the stress between rail and wheel had been measured as a function of load using ultrasonic NDT although this has not yet been used to establish the exposure to wear and surface fatigue under a range of conditions, such as load, speed and surface lubrication [4, 5]. More detailed mechanics analyses based on contact stresses (e.g., Ringsberg and Josefson [6]) have established the conditions for RCF initiation on rail heads.

Acoustic emission monitoring has been applied to a number of contact problems, such as bearings and defects, and has been found to be sensitive to bearing defects [7] and gear defects [8] in reciprocating and rotating machineries. Contacts involving curved surfaces lead to particular issues with durability and, given that contact between a ball bearing and race and between rails and wheel have some similarities [9], it is reasonable to suppose that AE monitoring can be used to examine the rail-wheel interaction and perhaps also be sensitive to surface and sub-

surface condition. It has already been claimed that fatigue initiation and propagation in rolling contact fatigue (RCF) can be detected using AE, Guo *et al.* [10]. Equally, it has been found that ultrasound is not useful for identifying gauge corner cracking in rails and even the eddy current technique is not able to find all individual rail surface defects [2].

The principle of this work is that AE can be used to determine whether the contact between a rail and wheel is “normal” or abnormal, abnormalities being defined as rough areas of the rail surface, out-of-round wheels, poor flange conformity or misshapen rails. Being able to do this would allow a rail-mounted sensor to be used to count the contact cycles in terms of intensity as well as number in a way that could not be derived from traffic figures alone, thus supplementing rail maintenance management systems. In earlier work, Thakkar *et al.* [11] devised an analytical model for the particular experimental set-up used, which describes the AE level from normal rolling using some simple AE propagation coefficients derived from pencil-lead break tests on the track. This model was used to identify areas on the track where natural surface defects cause additional AE in a similar way to defect identification in bearings and gear teeth. In this paper, a parallel set of experiments is reported, using the same track surface condition, but with an eccentricity of the wheel trajectory in relation to the track, so that flange rubbing takes place over a controlled length of the track.

Experimental Procedure

The test rig (Fig. 1b, c) consisted of a circular track round which a single wheel was driven using a motor at the centre of the track and a rigid arm, to which the wheel was attached. To obtain a rubbing effect of the wheel flange on the track, the motor shaft was displaced by about 2.4 mm (Fig. 1a) from the centre of the circular track. The variation of contact around the circumference was therefore mostly “normal” with an arc, within which the flange comes into contact with the rail, reaches a maximum contact load and then comes out of contact with the rail.

PAC Micro-80D AE sensors and PAC type 1220A preamplifiers (dual gain 40dB-60dB) were mounted on one side of the joint in the circular track (Fig. 1b) and connected to an NI 6115 data acquisition board used to collect raw AE data.

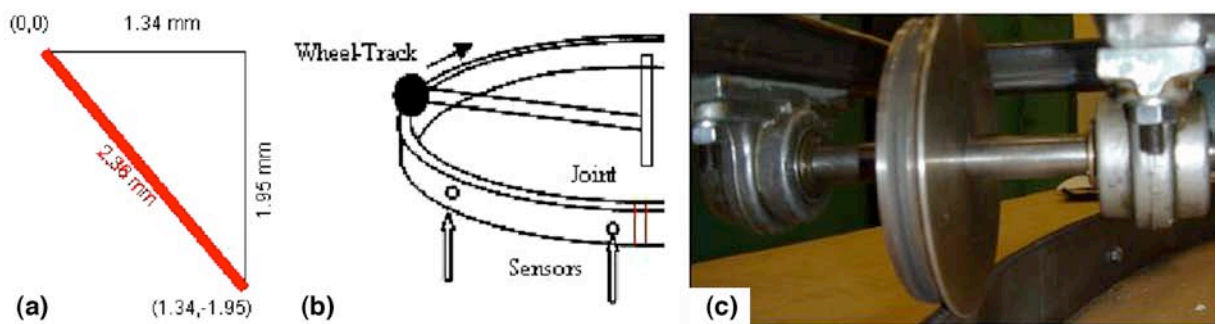


Fig. 1: (a) Motor shaft displacement, (b) sensor positions on rail, (c) wheel flange rubbing on rail.

The sensors were mounted on the web of the rail at 0.1 m and 1 m from the joint, the sensor nearest the joint being used as the trigger sensor and the other to collect the data for processing. The raw-data measuring sensor leaves 4.4-m distance on the other side of track, for wheel to travel before wheel arrives once again on top of the joint. The reason why raw-data measurement sensor was placed 1-m away from joint is to get adequate raw signal on both sides of placed sensor for the even minimum wheel speed (1 ms^{-1}). Four different wheel speeds (1 ms^{-1} ,

1.5 ms⁻¹, 3 ms⁻¹ and 3.5 ms⁻¹) were used and four different contact loads (4 kg, 5 kg, 6 kg and 6.5 kg) were applied and, corresponding to applied speed, wheel travelling distance increased (2-m, 3-m, 6-m and 7-m, respectively) as the data-storage time was constant, 2 sec. The mounting points were cleaned with sand paper and vacuum grease was used as a couplant with the sensors being held against the surface using magnetic clamps. Data was acquired at 2.5 MHz, for 5 Msamples corresponding to 2-sec recording time, in which the wheel moves, for a speed of 3.5 ms⁻¹, 7 m including the pre-trigger distance (0.14 m), completing more than a full revolution of the test rig (5.4-m circumference) for the condition discussed. Five records were taken for every wheel speed and load giving a total 80 records, under 16 different conditions. The track was made from 50 mm×6.25 mm profiled mild-steel bar, cold bent into the circular shape and joined by a simulated fish plate with a 3-mm gap. The wheel was of cylindrical shape of diameter 90 mm with a flange on the inner edge and was mounted on two rolling-element bearings (Fig. 1c).

A dial gauge was mounted on the supporting arm (Fig. 2a) to measure the position of the rail relative to the motor shaft after displacement (Fig. 1a) and measurements of the radial distance between the rail and the arm tip taken at regular intervals around the track circumference. The actual fitted (through measured points) and nominal circles are shown to scale in Fig. 2b, the nominal circle being the one, which assumes the design radius of 850 mm and a centre at (0,0). Figure 2c shows the same data with the radial coordinate amplified by subtracting 840 mm from each radial value, and shows the flange contact zone, which corresponds to distances of 1.4 to 2.4-m from the joint.

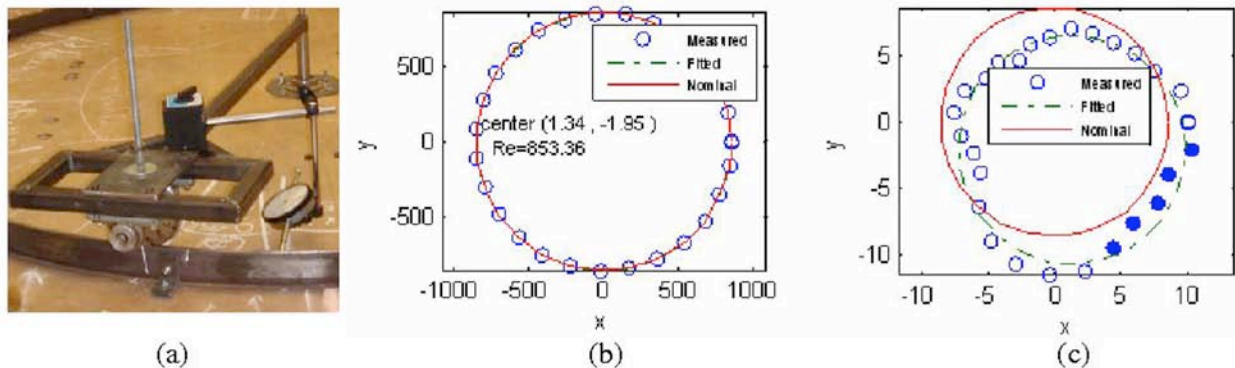


Fig. 2. (a) Dial gauge on supporting arm, and measured points and fitted and nominal circles, (b) at full scale and (c) with amplified radial scale.

Results and analysis

A simple attenuation model has been developed [11], which treats a wheel as continuously moving source that generates AE energy, E_0 , throughout its travelling. AE energy increases with increasing speeds, on the simulated track for the constant raw-data measurement time (2 sec). The total energy, E_t , is recorded at fixed sensor 1-m away from the joint. The circumferential position x_1 is the position of the wheel between joint to sensor when wheel approaches towards the sensor while circumferential position x_2 is the position of the wheel between sensor to joint when wheel travels away from the sensor. For both positions, we considered five different paths (direct wave travelling, reflected wave travelling once it hits the joint from both sides and transmitted wave travelling from both sides of joint) that change with respect to continuously changing wheel positions so that E_t can be calculated by equation 1 and 2 to discriminate the changes in the signal due to wheel position with respect to raw data measurement sensor.

$$E_t = E_0 e^{-kx_1} + RE_0 e^{-k((c_2-x_1)+c_2)} + RE_0 e^{-k(c_1-(c_2-x_1)+(c_1-c_2))} + TE_0 e^{-k(c_1-x_1)} + TE_0 e^{-k(c_1+x_1)} \quad (1)$$

$$E_t = E_0 e^{-kx_2} + RE_0 e^{-k(x_2+c_2+c_2)} + RE_0 e^{-k(c_1-(c_2+x_2)+(c_1-c_2))} + TE_0 e^{-k(c_1-x_2)} + TE_0 e^{-k(c_1+x_2)} \quad (2)$$

This model is fitted to RMS voltages of measured raw signals for explained condition and time steps used for both are 2.9 ms. During the described time step, waves are travelling 8.99-m (1.66 times the track circumference) as the wave velocity was found to be 3100 ms⁻¹ during calibration test by using pencil-lead break tests with four sensors in single array and similar three arrays used by keeping source sensor at constant distance and moving rest of the sensors 0.26-m away from source. The attenuation coefficient, $k = -0.57$ dB/m, was found using the same calibration set up while calibrating reflection coefficient ($R = 48\%$) and transmission coefficient ($T = 25\%$) from and through the joint, respectively.

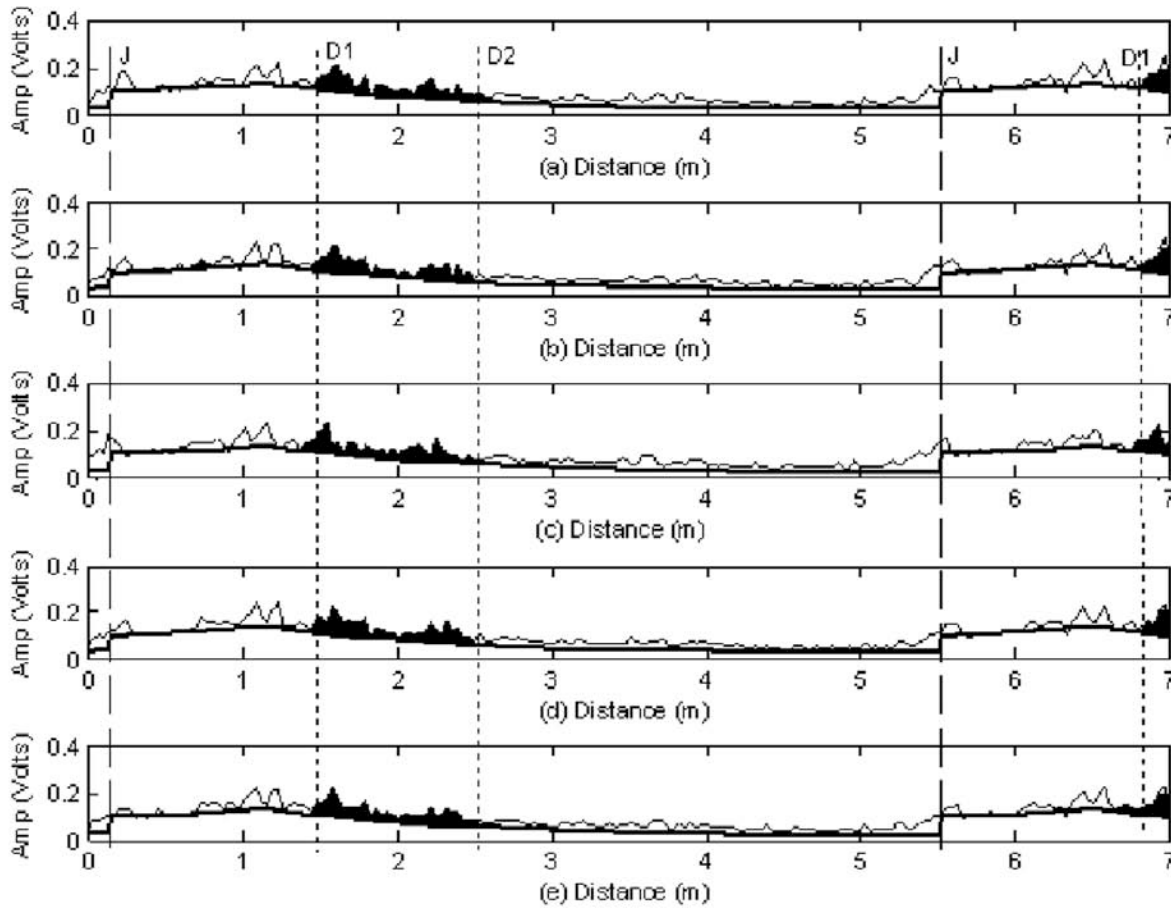


Fig. 3: Measured rms AE at a wheel speed of 3.5 m/s. — rms AE; - - - analytical model.

Only one unknown in Eqs. 1 and 2 is E_0 , as c_1 and c_2 are the track circumference and distance between joint and sensor, respectively. These are known and can be varied at not only every measurements but also for Eqs. 1 and 2, to produce a best-fit level of the model. It takes the average value of RMS signal until the wheel arrives on top of the sensor from joint for Eq. 1 and again takes average value of RMS but this time for Eq. 2 and distance of wheel from top of the sensor to wheel arrival on joint for the explained condition. Once the wheel arrives on top of the sensor again the cycle starts from the beginning.

Comparing the circumferential variation in AE with the best-fit model allows the identification of areas where there is an indication of abnormal contact. Figure 3 shows five independent measurements of the rms averaged AE (averaging time 0.01 s) along with the fitted normal contact curves for one example of a wheel velocity of 3.5 ms^{-1} and a preload of 4 kg. As can be seen, the signal is significantly and consistently above the model fit in the flange-rubbing zone, highlighted by black fill, between D1 and D2.

The dashed lines marked with “J” are the positions where the wheel passes over the joint and here spikes are evident due to wheel impact on the joint. The location of the joint in the AE record is an important part of the curve-fitting process as it allows the discontinuity between Eq. 1 and Eq. 2 to be identified. At the example wheel speed of 3.5 ms^{-1} , the wheel arrives twice at the sensor during each record.

In the earlier work [11], the natural defects on the surface of the rail were measured and Fig. 4 shows their intensity, measured as the total length of defect per 0.1-m length of track alongside the rms AE above background noise again averaged per 0.1-m length of track for each of the five records at the example condition of 3.5-ms^{-1} wheel speed and 4-kg load. Figure 5 shows the corresponding autocorrelation function for each of the five records with their corresponding kurtosis values, ranging from 1.9 to 2.07. Figure 6 shows the defect intensity distribution with flange rubbing added, along with the corresponding AE signal above normal rolling. Figure 7 shows the cross-correlations for the flange-rubbing case along with the corresponding values of kurtosis (1.66 to 1.88) for comparison with Fig. 5, again for the example condition. As can be seen, the kurtosis is improved over the case without flange rubbing.

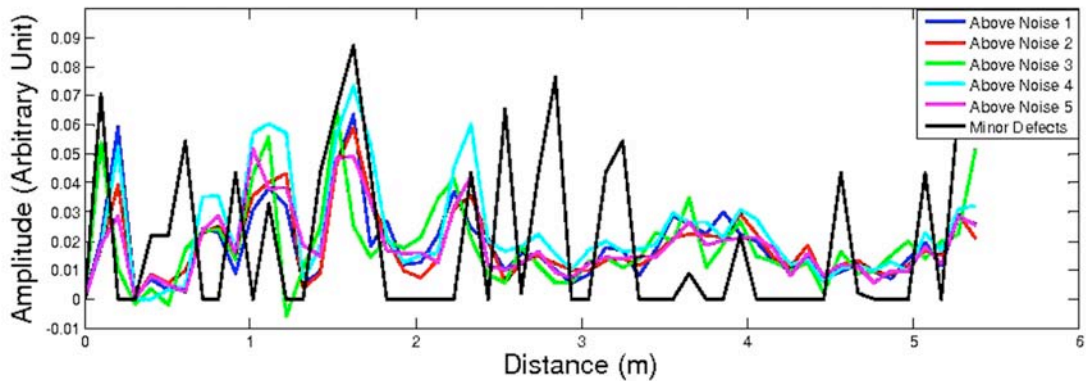


Fig. 4: Signal above normal and defect intensity without flange rubbing.

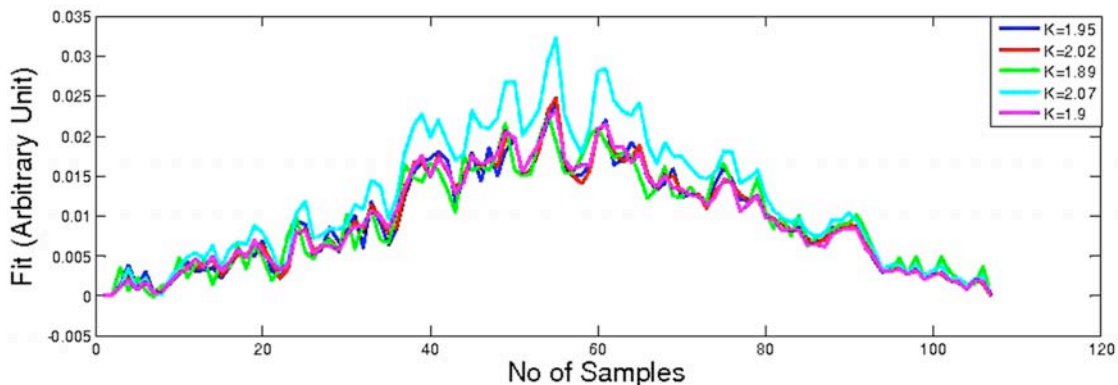


Fig. 5: Cross correlation between defect intensity and AE above normal without flange rubbing.

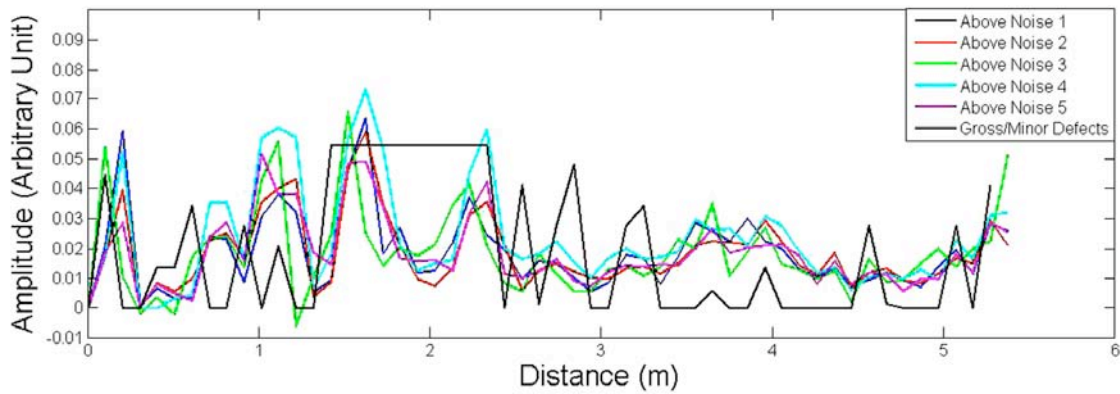


Fig. 6: Signal above normal and defect intensity with flange rubbing.

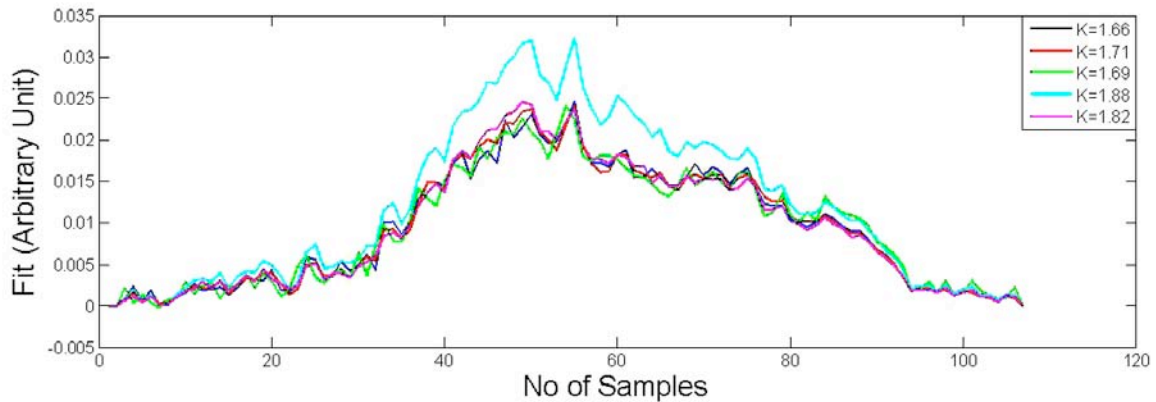


Fig. 7: Cross correlation between defect intensity and AE above normal with flange rubbing.

Applying the same approach to the remaining speeds at a 4-kg load yields similar results, and Fig. 8 shows the averaged value of kurtosis for the five records at each condition. It is clear that the average kurtosis is always smaller with flange rubbing, indicating a more peaked cross-correlation function, although the difference is more marked at the lowest speed, where the kurtosis is generally higher, indicating generally poorer cross-correlation. It is suspected that the poor correlation for low speeds is partly due to the fact that a complete revolution is not acquired in the low-speed records and, more importantly, to the fact that the sensitivity to natural defects is low at low speeds; this is also the case for low loads. Whereas the effect of speed and load on sensitivity to natural defects is a matter for future investigation, it appears at present that the sensitivity to flange rubbing is not affected as much by the experimental conditions.

Conclusions

Using a simple model of AE for normal rolling and correlating the AE signal above the model value with a measure of defect intensity per unit length of track, the following conclusions can be drawn.

1. The signal-above-normal-rolling can be correlated with the intensity of natural defects and flange rubbing can be treated as defect of unit intensity.
2. The correlation is improved when flange rubbing is present and the correlations persist for flange rubbing under conditions where it is poor for natural defects.
3. The effect of experimental conditions (speed and load) on defect sensitivity is matter for future investigation.

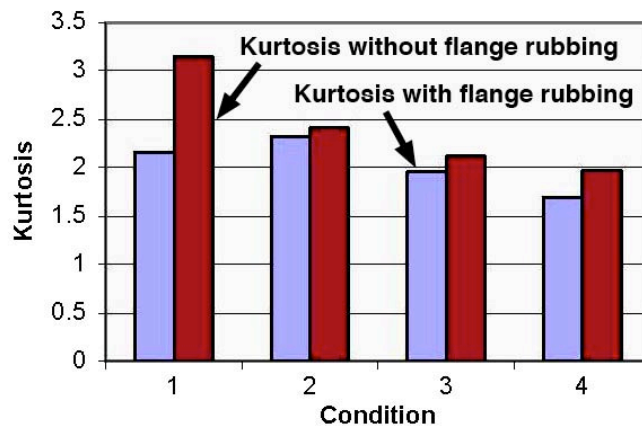


Fig. 8: Kurtosis with and without flange rubbing for all wheel speeds at 4-kg load. (Conditions 1-4; 1 ms^{-1} , 1.5 ms^{-1} , 3 ms^{-1} and 3.5 ms^{-1} , respectively)

References

1. Office of Rail Regulation (ORR). “Train derailment at Hatfield: A final report by the independent investigation board”, (UK) Health and Safety Executive, July 2006.
2. Bruzelius, K., Mba, D., “An initial investigation on the potential applicability of acoustic emission on rail track fault detection”, *NDT & E International*, **37**, 2004, 507-516.
3. Miller, K.J., “Structural integrity – whose responsibility?”, *Proceedings IMechE*, Part L, **217**(1), 2003, 1-22.
4. Pau, M., Aymerich, F. and Ginesu, F. “Ultrasonic measurements of nominal contact area and contact pressure in a wheel-rail system”, *Proceedings of IMechE*, Part F, **214**, 2000, 231-243.
5. Pau, M. “Ultrasonic waves for effective assessment of wheel-rail contact anomalies”, *Proceedings of IMechE*, **219**, 2005, 79-90.
6. Ringsberg, J.W. and Josefson, B.L. “Finite element analysis of rolling contact fatigue crack initiation in rails”, *Proceedings of IMechE*, Part F, **215**, 2001, 243-259.
7. Morhain, A. and Mba, D. “Bearing defect diagnosis and acoustic emission”, *Proceedings IMechE*, Part J, **217**(4), 2003, 257-272.
8. Toutountzakis, T. and Mba, D. “Observation of acoustic emission activity during gear defect diagnosis”, *NDT & E International*, **36**(7), 2003, 471-477.
9. Kalker, J.J. “Survey of wheel-rail rolling contact theory”, *Vehicle System Dynamics*, **8**(4), 1979, 317-358.
10. Guo, Y.B. and Schwach, D.W. “An experimental investigation of white layer on rolling contact fatigue using acoustic emission technique”, *International J. of Fatigue*, **27**(9), 2005, 1051-1061.
11. Thakkar N.A., Reuben, R.L., Steel, J.A. “Rail-wheel interaction and defect location using acoustic emission: a laboratory study”, *Mechanical Systems and Signal Processing*, submitted, 2007.

DAMAGE ASSESSMENT OF GEARBOX OPERATING IN HIGH NOISY ENVIRONMENT USING WAVEFORM STREAMING APPROACH

DIDEM OZEVIN, JASON DONG, VALERY GODINEZ and MARK CARLOS

Physical Acoustics Corporation, 195 Clarksville Road, Princeton Junction, NJ 08550

Abstract

Threshold and timing parameters are two fundamental factors that control arrival times and waveform signatures collected in an acoustic emission test. While this approach works successfully in many applications, recording the complete, continuous waveforms emitted from an AE test independently of threshold value is more appropriate for some specific applications. Applications such as those with high background noise or complex structures with numerous boundaries and interfaces are better served by continuously streaming with duration in the order of hundreds-of-ms instead of the traditional hundreds-of- μ s-long AE waveforms. State-of-the-art AE data-acquisition hardware enables this “AE Waveform Streaming” approach at high sampling rates throughout a traditional AE test. These waveforms can subsequently be analyzed in real time to extract traditional AE features in the time and frequency domain.

In this paper, the application of waveform streaming will be shown on detecting corrosion pitting on gear teeth under a high background noise environment. The tests were performed using an FZG machine to generate pitting corrosion on gear teeth under fatigue. In these tests, a recently designed “integrated” AE-vibration sensor was used for collecting high- and low-frequency data while monitoring the condition of the gears. Recording the complete, continuous waveforms provided flexibility during post-processed data analysis, which can be implemented in real time during consecutive tests. The paper also presents the impact of the waveform streaming approach in terms of understanding threshold effects on waveform signatures, in the ability to set and analyze different digital filters, and in the extraction of low frequency vibration information.

Keyword: Waveform streaming, threshold independent, gearbox, frequency analysis, real time analysis

Introduction

Threshold-based data acquisition has been used and operated successfully in many acoustic emission (AE) applications. Threshold is a key factor for AE technology as the technology is mostly based on arrival times for source location and time- and frequency-domain feature extraction for pattern recognition [1, 2]. However, the threshold-based approach creates a detection reliability problem for high noise, high hit-rate applications, such as monitoring of highly dynamic systems or process monitoring. Additionally, threshold and timing settings may perturb the direct AE wave signature, which is substantial for a quantitative analysis and source discrimination [3]. While this approach works successfully in many applications as presented in Table 1, recording the complete, continuous waveforms emitted from an AE test independently of threshold value is more appropriate for some specific applications. In this paper, we will present the use of waveform streaming in addition to threshold-based data acquisition. The advantages of streaming waveform approach are discussed using the gearbox-testing application.

Table 1. The comparison of threshold based and waveform streaming approaches.

Threshold Based Approach		Waveform Streaming Approach	
Capabilities	Limitations	Capabilities	Limitations
Very well applied for flaw detection, location and many other applications	In high noisy environments and high hit-rate applications, the system saturates and loses data	Complete waveforms with no distortion due to DAQ setting	Memory and fast computer need for very long duration waveforms
Not much memory needed, real time feature extraction and fast analysis		Extracting vibration information for rotating machinery	Time of arrival extraction can be cumbersome

Approach

The high sampling rate required and the high hit-rate of AE signals are two constraints for the continuous recording of waveforms. State-of-the-art data acquisition hardware allows recording waveforms continuously with high sampling rates throughout an AE test. The data acquisition system can record long-duration waveforms with high sampling rate continuously or at pre-defined time intervals. The waveform shown in Fig. 1 has 2-sec. duration sampled with 500-kHz rate at 5-sec. interval. The waveform presents several transient signals during the 2-sec. period as shown in the zoomed view. This transient signal is an indication of bearing damage. These transient signals have typical AE signal characteristics; i.e., short duration, rise time and decay time. The waveform streaming approach allows the identification of the transient signal characteristics without being affected by threshold and timing parameters.

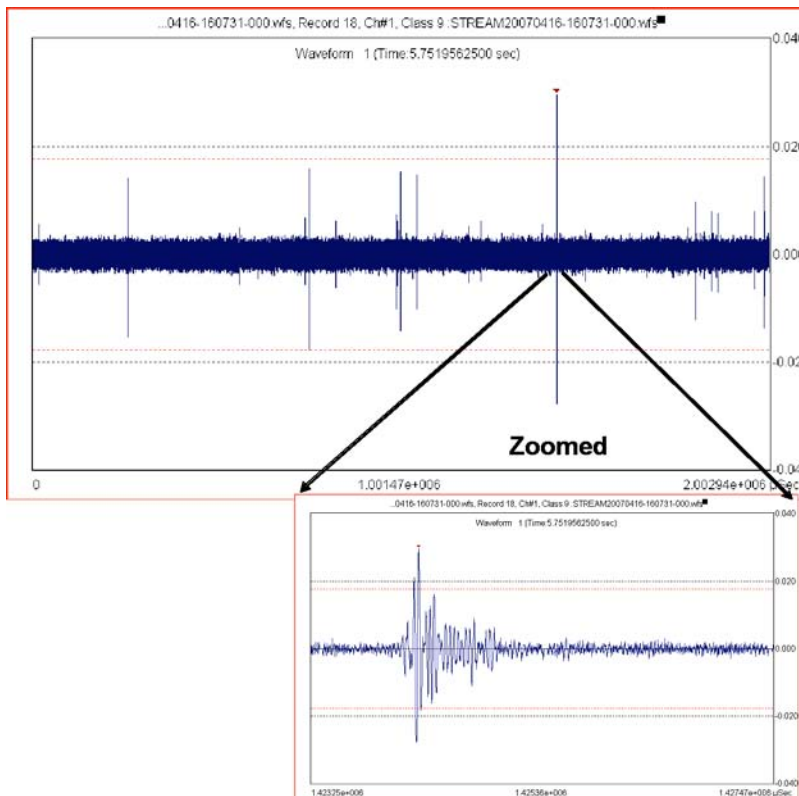


Fig. 1. An example of long-duration waveform (2 sec.) sampled with 500-kHz rate.

The waveform streaming can be triggered using four different modes:

- Hit-based trigger: When the data acquisition system detects a hit exceeding threshold, the system records a long duration waveform (longer than the hit duration defined by timing parameters).
- Time-based trigger: The system streams waveforms at each time interval. The time-based trigger is an efficient way to determine the condition of machinery that requires periodic measure of a machine's ability to perform efficiently.
- Manual trigger: Waveform streaming is activated manually during acquisition.
- External trigger: If there is a certain parametric input such as pressure, the waveform streaming is activated as a function of parametric input level.
- Continuous mode: Waveforms are streamed throughout an entire AE test.

Recording complete, continuous waveforms provides flexibility during post-processed data analysis, which can be implemented in real time in consecutive tests, for example:

- Understanding the effect of threshold and timing settings on waveform feature extraction that can be used to optimize the settings of threshold-based acquisition for consecutive tests.
- Extracting time-domain features using post-process digital filters and different threshold setting.
- Optimizing frequency segments for spectral feature configuration.
- Extracting low-frequency vibration information if AE waveform length is sufficiently long to capture multiple revolutions.

Additionally, although the arrival-time information of transient signals is not registered in real time, single or multiple AE hits in a streamed waveform can be separated with their actual arrival times using the NOESISTM software. The NOESISTM software has an option to extract features and arrival times of multiple transient signals in a streamed waveform, based on threshold or length. Furthermore, streamed waveforms of multiple channels can be synchronized so that the relative arrival times of transient signals of different channels can be extracted or waveforms of different channels can be cross-correlated in order to find arrival-time differences. The waveform streaming can be acquired using PCI-2 (2-channel) or PCI-8 (4-channel AE, 4-channel vibration) board developed by Physical Acoustics Corporation [PAC]. It is important to note that these boards have the capability to record threshold-based data and waveform streaming concurrently. A successful application of waveform streaming together with threshold-based approach was demonstrated on the condition monitoring of a rolling-element bearing [4]. In this paper, the application of the approach on the detection of pitting corrosion growing on gear teeth due to fatigue is demonstrated.

Gearbox Application

As an example of the flexibility offered by the waveform-streaming approach for practical AE monitoring, a series of tests were performed at the Ohio State University Gearbox Laboratory using an FZG machine to generate micro-pitting or spalling in spur gears at elevated temperatures. The temperature at steady state reached 90°C. The rotation speed of the input gear was 1440 RPM with 220 N·m torque. The input gear had 26 teeth; the output gear had 17 teeth. The first data set included a gear with no damage at the beginning and end of 1-hr duration testing. The second data set included a gear with damage at the beginning of the testing and the damage grew over the 1-hr test duration. The third data set included a gear with no damage at the beginning of the testing and the damage (pitting) formed and grew over a 6-hr test. In these tests, AE

and vibration data was collected continuously. The first and second tests were used to form a classifier for background noise and pitting emission; the third test was used to determine if the classifier could detect the pitting formation. Table 2 is a summary of the tests and the damage states of the specimens at the beginning and end of the tests.

Table 2. The initial and end conditions of the test specimens.

Test No	Duration (hr)	Initial State	End State
1	1	Undamaged	No visual damage
2	1	Damaged	Damage grew considerably
3	6	Undamaged	Small pitting initiated

The gear pitting formation under fatigue was monitored using two integrated AE-vibration [AE/VIB] sensors recently developed by PAC [5]. The sensors were mounted on the front and side panel of the FZG machine (shown in Fig. 2b). AE/VIB 1 was mounted below the lubricant level of the machine and AE/VIB 2 was mounted at the same level as the lubricant. A PCI-8 board was used to record the data from two AE/VIB sensors. The board has 16-bit A/D conversion capability and 1-MS/s waveform-streaming rate. The board was installed inside a PAC μ -Samos chassis, and this DAQ system was controlled by a laptop as shown in Fig. 2c.

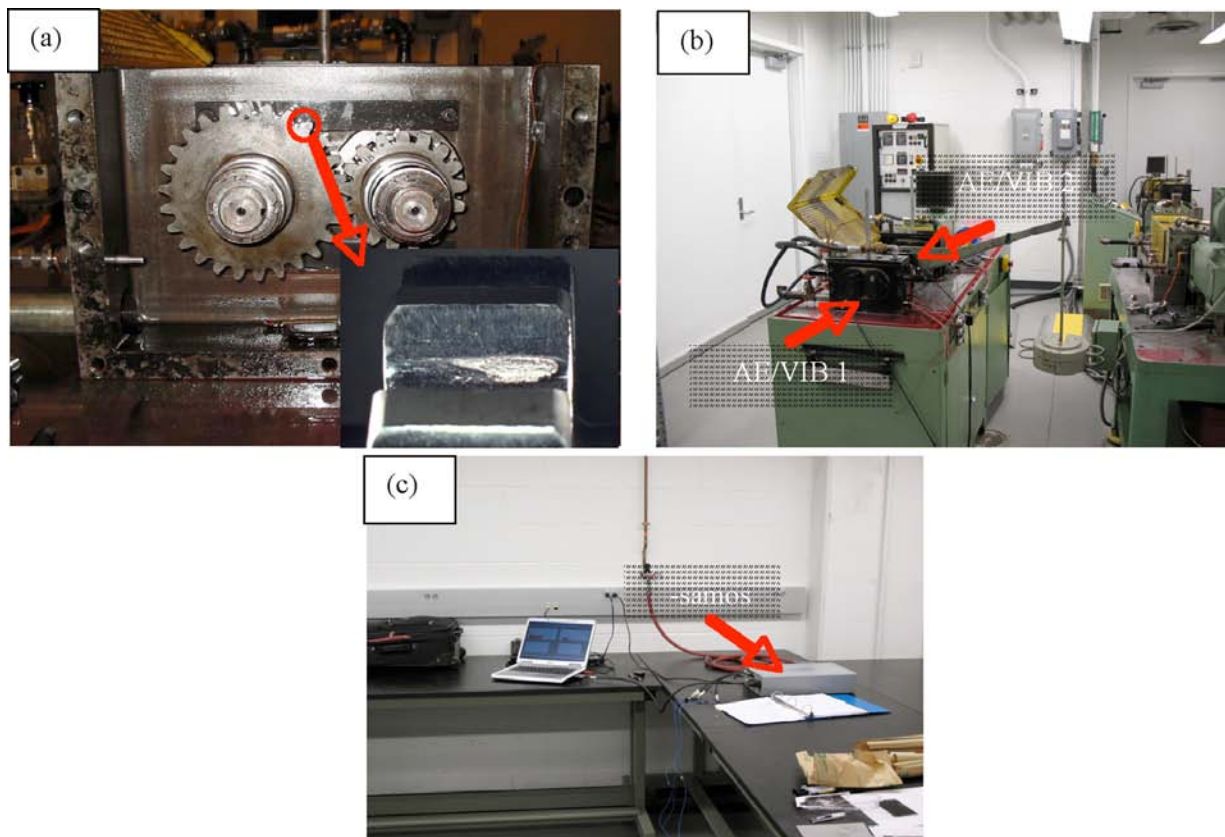


Fig. 2. Photographs of (a) input and output gears, (b) AE/VIB sensors, (c) DAQ system.

AE waveforms having 100-ms duration were collected every second. The sampling rate for AE waveforms was 1 MHz. The band-pass analog filter setting was 20 kHz to 400 kHz. The AE sensor gain was 40 dB.

Extracting features using different sets of digital filters and spectral divisions

Test 1 included a gear with no damage at the beginning and end of 1-hr test. Test 2 included a gear with a minor damage at the beginning of the testing and the damage grew over the 1-hr test. The same gear but opposite teeth was used at Test 1 and Test 2. Fig. 3 shows the energy trends of two tests recorded by the AE/VIB 1. The fluctuation was because of water pump operation to cool the lubricant inside the gearbox. While the same gear was used during the tests, the time-domain signal level changed because the gearbox was opened and the opposite side of the gear teeth, which had a minor damage tooth, was mounted. Variation of time-domain feature due to mechanical feature indicates the difficulty of comparing one test to another if the mechanical structure has any slight modification. Spectral features gain significance as descriptors to differentiate damage emissions and background noise emissions.

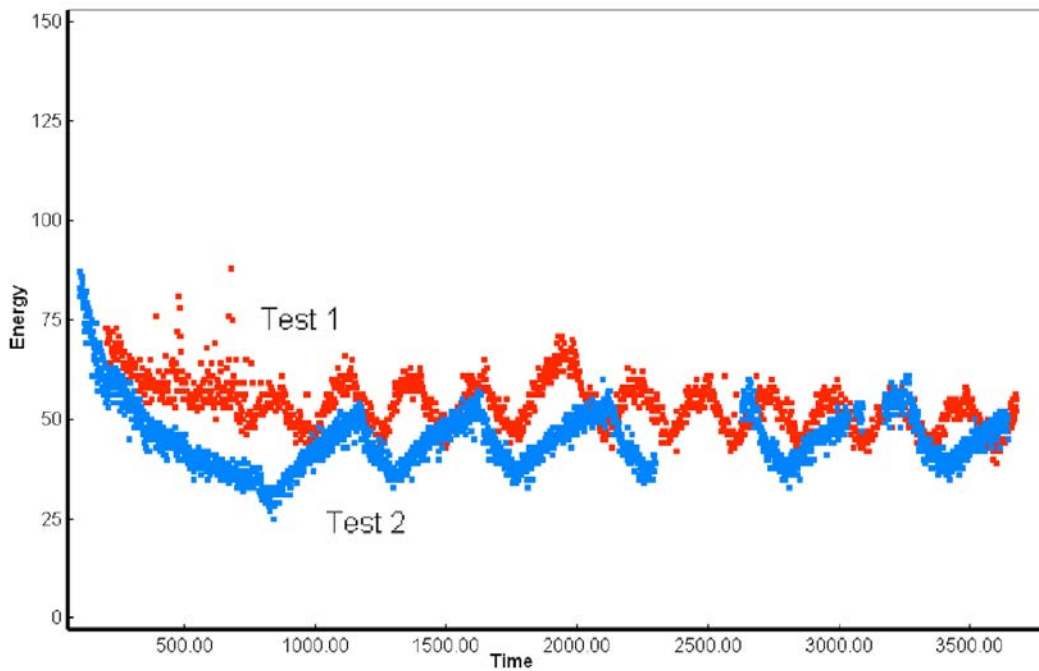


Fig. 3. Time-domain feature, energy (e.c.), trends for two tests recorded for ~3600 sec. The fluctuations were generated due to the operation of water pump inside the gearbox.

Figures 4a and 4b show examples of a raw, streamed waveform and its frequency spectrum. The frequency spectrum of the raw waveform, Fig. 4b, indicates the dominant frequency components to be due to mechanical noise at 22 kHz and 33 kHz. If frequency centroid or peak frequency were calculated directly using a raw waveform, the mechanical noise frequencies would mask the result. When a waveform is streamed from an AE sensor, it is expected that low-frequency mechanical noise and high-frequency damage growth emission would be summed. Extracting high-frequency, relatively low-amplitude (as compared to mechanical noise) damage-growth emissions, requires filtering background noise frequencies. Figure 4c shows the same waveform with 80-kHz high-pass filter using 10th-order Butterworth filter. Figure 4d shows the frequency spectrum of the segmented section between two green lines as shown in Fig. 4c. The peak frequency of complete waveform is dominated by low frequencies (<50 kHz). Digital filtering and segmented frequency spectrum provide information about the content and occurrence time of high-frequency transient signals. As shown in Fig. 4d, the segmented section of AE waveform has the frequency peak at 240 kHz together with 120 kHz and 300 kHz frequency components.

The software allows segmenting (green lines) the time-domain waveform for frequency spectrum calculation. Spectral features, such as peak frequency, partial powers (partial powers indicate how the energy distribution at defined frequency segments changes as compared to the full defined spectrum band) can be extracted using digital filters.

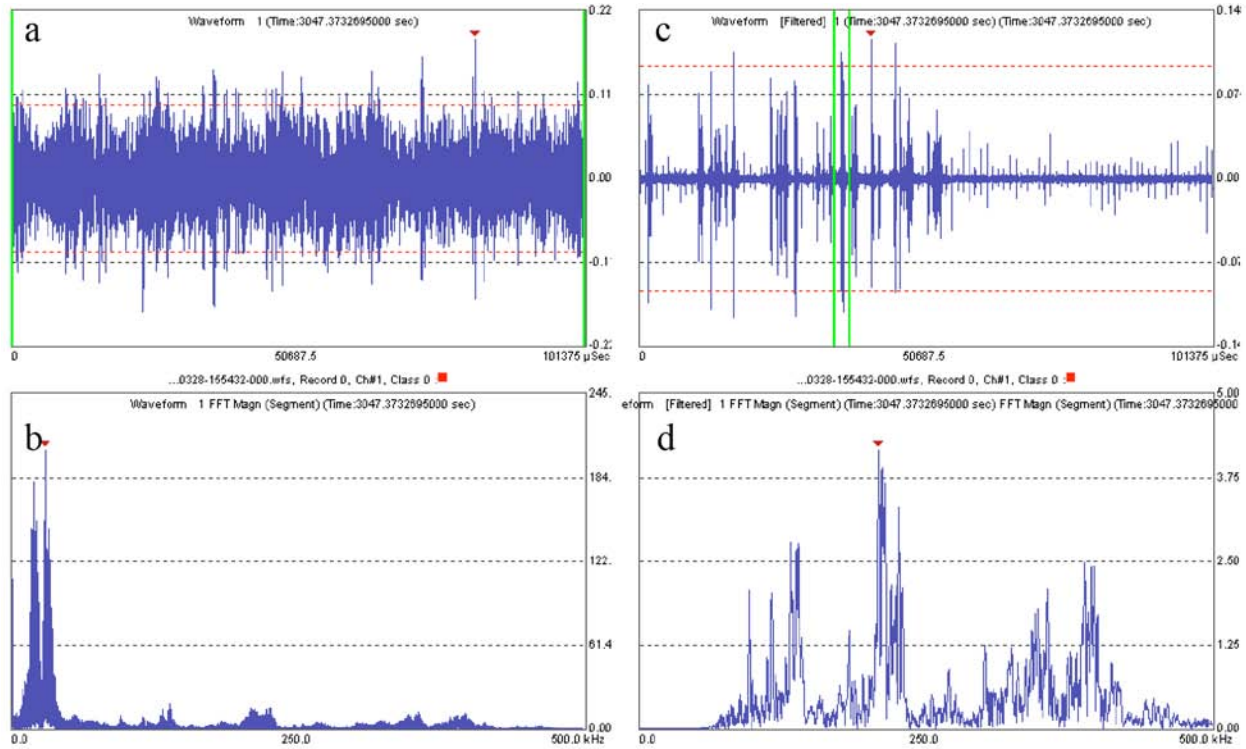


Fig. 4. A streamed waveform of Test 2 (a) raw waveform and (b) its frequency spectrum (0-500 kHz), (c) filtered waveform having 80 kHz high-pass and (d) its segmented (between green lines in c) frequency spectrum (0-500 kHz).

Applying pattern recognition to determine pitting corrosion emissions during Test 3

In this application, AE features were extracted from streamed waveforms using 35-dB threshold, complete waveform length and 80-kHz high-pass, 10th-order Butterworth filter. In the initial set, the features extracted from Test 1 and Test 2 waveforms were amplitude, absolute energy, frequency centroid, peak frequency and partial powers. Partial powers indicate how the energy distribution at defined frequency segments changes as compared to the entire spectrum band. Energy values at individual frequency segments are normalized to the entire spectrum band. In this application, the entire spectrum band was chosen as 80 to 400 kHz segmented into three parts, 80-100 kHz, 100-200 kHz and 200-400 kHz. In pre-processing, AE features were normalized using unit variance. Principal component analysis was performed. The max-min distance method with Euclidian distance and 0.8 distance threshold were the parameters of the unsupervised pattern recognition method. Different sets of AE features were used to optimize the clustering result using R and Tou criteria [6]. Peak frequency, PP1 and PP2 resulted in the most optimal set of AE features. As mentioned above, time-based features are sensitive to mechanical variation from one test to another while there is no damage growth. The unsupervised algorithm identified three clusters having one cluster further apart than two clusters. In our interpretation, we called the farthest cluster as “damage AE” (detected mostly during Test 2, in which pitting corrosion occurred), and the other two clusters as two distinct background noise sources.

The classifier was used to identify if pitting developed on the gear teeth used in Test 3. In Test 3, no tooth had pitting at the beginning of the test; however at the end of the fatigue test, some teeth show pitting as shown in Fig. 5. Therefore, the classifier would have been expected to find some data points corresponding to the “damage AE” cluster. The data points were pre-processed and classified. Figure 6 shows the result of the last 40 minutes of the data.

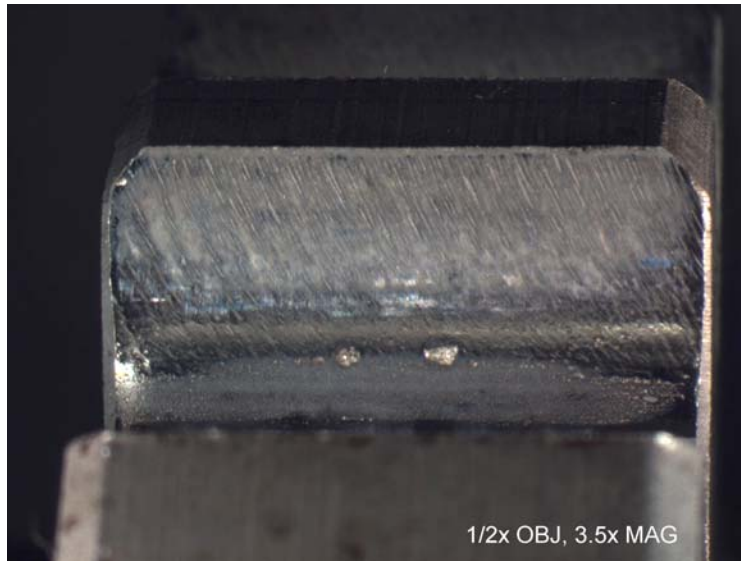


Fig. 5. The end state of the gear used in Test 3.

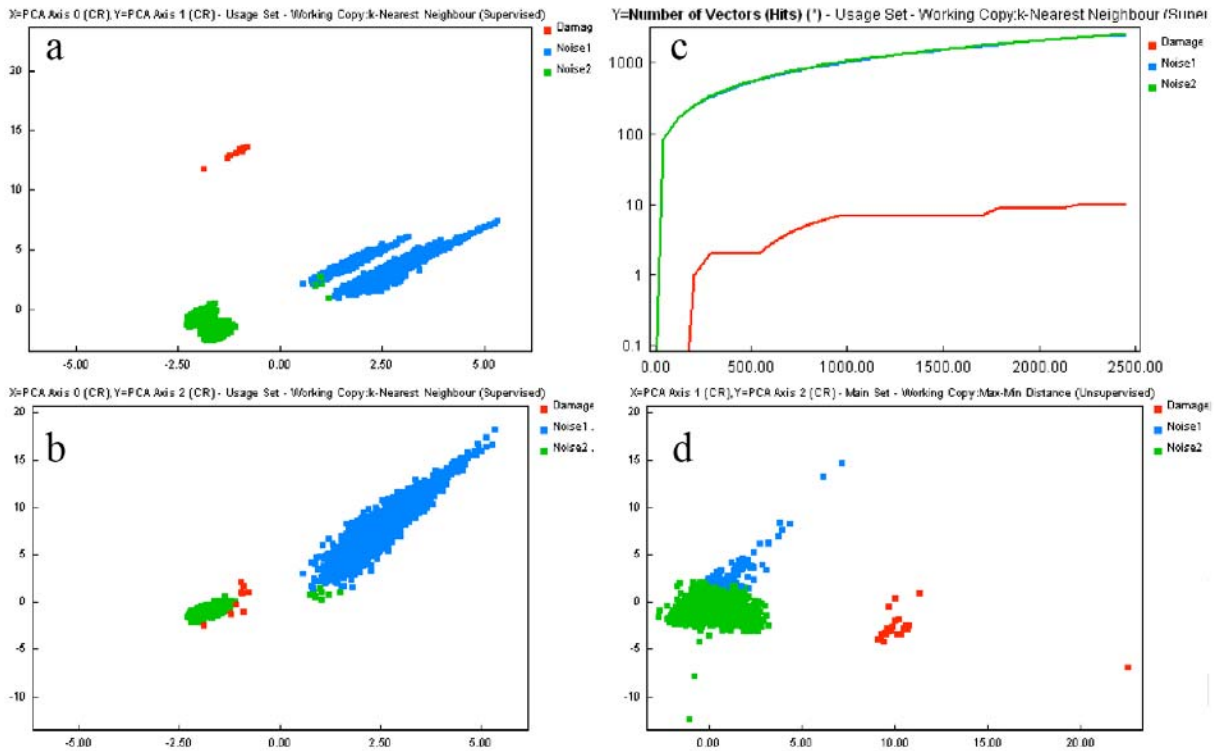


Fig. 6. The classification result of Test 3 using the classifier formed above. a) PCA analysis for axes 0 and 1; b) PCA analysis for axes 0 and 2; c) Classified hits vs. time for Damage (red), Noise 1 and 2 (blue and green); PCA analysis for axes 1 and 2.

As discussed above, principal component analysis (PCA) was conducted to minimize the number of AE features used for the classifier formation. Three PCA axes were selected to represent the data sets. Figure 6a shows the scatter plot of PCA 0 and PCA 1 axes after the classifier was applied to the usage set (Test 3 data). The 2-D distributions of PCA 0 versus PCA 1 (Fig. 6a) and PCA 1 versus PCA 2 (Fig. 6d) indicate distinctly the separation of “damage AE” class from background noise classes. The 2-D distribution of PCA 0 versus PCA 2 has significant overlap of “damage AE” and “noise 2” classes. However, the use of three principal component axes provides multidimensional analysis to discriminate class centers and classifies unknown hit class accurately. Figure 6c shows the AE accumulation of three classes. Two background noise classes were consistently detected during the testing. However, “damage AE” activities were detected at random time intervals as expected from a corrosion-pitting source, which grows throughout a fatigue loading test.

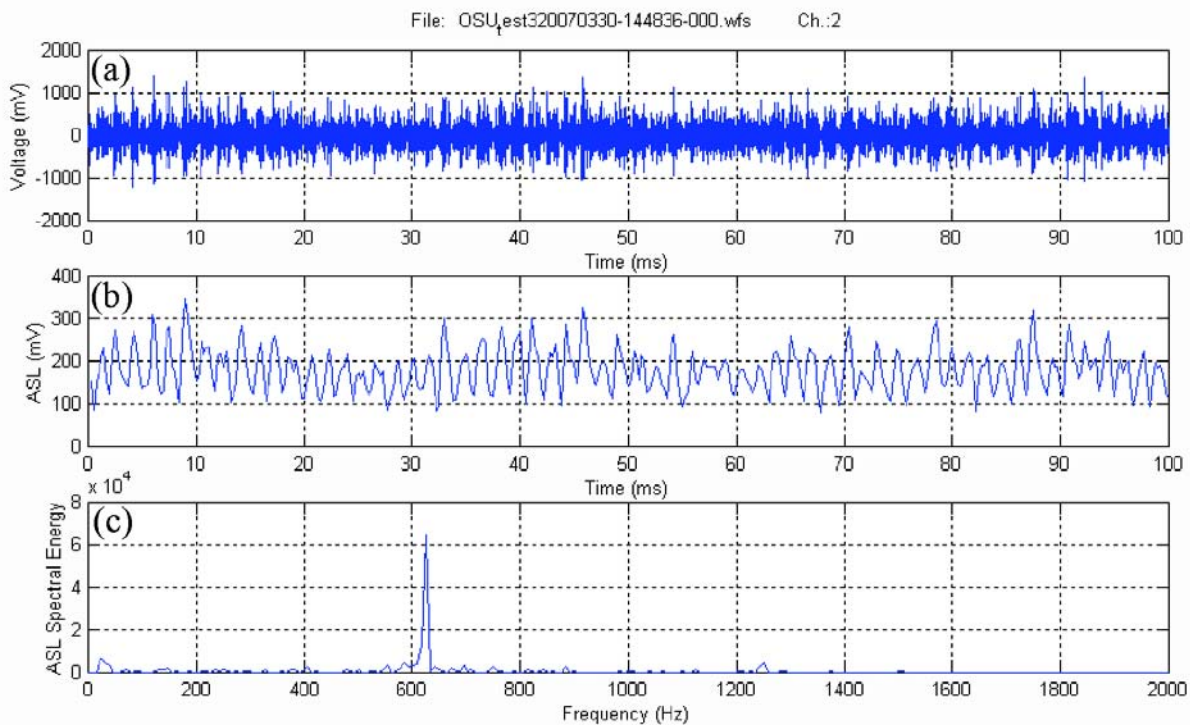


Fig. 7. Extracting gear-mesh frequency using a long duration AE waveform, (a) AE waveform, (b) Average Signal Level (ASL) trend, (c) ASL spectral energy.

Extracting gear-mesh frequency

Vibration monitoring detects coupling failure by comparing two different states (undamaged versus damaged) of structural components. The most fundamental challenge for detection of cracking is that it is typically a local phenomenon and may not significantly influence the lower-frequency global response of a structure that is typically measured during vibration tests [7]. However, vibration monitoring provides additional information to the findings of AE method. It is advantageous to extract vibration information using long-duration AE waveforms.

The gear-mesh frequency is the combined effect of all gear inertia. In these tests, the input gear rotation speed was 1440 RPM, which corresponds to 24-Hz frequency. The input gear has 26 teeth, which correspond to gear-mesh frequency of 624 Hz. Figure 7a shows a long-duration AE waveform acquired in Test 2. The time-variant Average Signal Level (ASL) is extracted from this streamed waveform so that high frequency noise is filtered out as shown in Fig. 7b.

ASL spectral energy is further calculated based on the time-variant ASL and its maximum spectral energy that just lies in the gear-mesh frequency as shown in Fig. 7c. ASL spectral energy plot indicates that the streamed AE waveform can be effectively used to extract a gear-mesh related feature that is not available with the conventional AE signal processing technique.

Summary

Waveform streaming, recording complete, continuous waveforms, provides flexibility during post-test data analysis, such as, understanding signal characteristics without being influenced by threshold and timing parameters, and identifying damage emission frequency information. Additionally, governing vibration frequencies can be extracted using AE sensor if AE waveform length is sufficiently long to capture multiple revolutions. Waveform streaming can also be used to optimize the settings of threshold-based data acquisition.

Acknowledgements

This study was performed as a part of SBIR Phase II program sponsored by NAVAIR under contract number N68335-04-C-0202. We would also like to thank Professor Ahmet Kahraman and his graduate student Jeremy Bluestein for their help during testing in the Ohio State University Gearbox Laboratory.

References

1. V.F. Godinez, F. Shu, R. Finlayson, B. O'Donnell, *Proceedings of SPIE, Health Monitoring and Smart Nondestructive Evaluation of Structural and Biological Systems III*, 2004, Vol. 5394, pp. 428-437.
2. V.F. Godinez, F. Shu, R. Finlayson, B. O'Donnell, Anastopoulos, A., and Tsimogiannis, A., *Canadian Institute for NDE (CINDE) Journal*, **25**, 2004, 8-16.
3. M. Ohtsu and K. Ono, *J. of Acoustic Emission*, **5**, 1986, 124-132.
4. S. Prieto, MSc Thesis, School of Engineering, Cranfield University, 2006.
5. V.F. Godínez-Azcuaga, D. Ozevin, A. Anastopoulos, A. Tsimogiannis, *Aging Aircraft Conference*, 2007, in publication.
6. Anastopoulos, A., Philippidis, T.P., "Clustering Methodology for the Evaluation of Acoustic Emission from Composites," *J. of Acoustic Emission*, **13**(1-2), 1995, 11-22.
7. C.R. Farrar, S.W. Doebling and D.A. Nix, *Philosophical Transactions of the Royal Society A: Mathematical, Physical and Engineering Sciences*, **359**, 2001, 131-149.

CLUSTERING ANALYSIS OF AE IN ROCK

N. IVERSON, C.-S. KAO and J. F. LABUZ

Department of Civil Engineering, University of Minnesota, Minneapolis, MN 55455

Abstract

Clustering analysis, through a fractal dimension, offers quantitative information with regard to the spatial distribution of AE events, which can be used to identify the characteristic of the failure process in quasi-brittle materials. For example, an inspection of AE locations from a mechanical test on rock can be interpreted using the fractal dimension: three represents random events occurring in a volume while a fractal dimension of two signifies that the events have localized on a plane. A clustering algorithm is used to analyze laboratory tests performed on specimens undergoing tensile or shear-type failure. Because failure of rock involves localization of deformation in the form of microcracks, the location of AE can be used to track the failure process, and the fractal dimension provides a basis for determining localization.

Keywords: Fractal dimension, clustering analysis, localization, strength testing

Introduction

A common feature of failure in a quasi-brittle material such as rock is the development of microcracking, which releases energy in the form of elastic waves called acoustic emission (AE). The AE technique can be used to monitor the evolution of damage, through the entire volume, at various stages of loading. The coordinates of an acoustic source can be obtained from the arrival times of the P-wave at the receivers. The locations of AE provide a picture that forms a basis for the justification of mechanical models of damage and failure (Shah and Labuz, 1995; Ono, 2005).

Specimens of rock were tested in a closed-loop, servo-hydraulic load frame and the data from LVDTs, strain gages, and load cells were stored on a computer and time stamped for synchronizing with AE events. Eight piezoceramic AE sensors, connected to preamplifiers with bandpass filters from 0.1 – 1.2 MHz, were bonded to a specimen using a modified alkyl cyanoacrylate adhesive. One sensor was used as a trigger, with a threshold of 7 mV after amplification at 40 dB gain. The AE signals were recorded using four, two-channel high-speed digitizers, at 20 Msamples per second with a 100- μ s recording window, and stored for later analysis. A pre-trigger region, set at 50 μ s, was included to ensure capture of the first arrival. Various algorithms for analysis of AE (e.g. first arrival detection, locations, source characterization) were developed and used to interpret failure of rock.

AE Locations

The unknowns for a three-dimensional location, assuming that the P-wave velocity is known, are the three AE source coordinates (x , y , z) and the time of source inception (t_o). However, the quadratic nature of the distance equation requires a minimum of five receivers to remove any ambiguity in optimizing the source location. The optimization is achieved by minimizing the residual ε in a least-squares sense using the Levenberg-Marquardt technique:

$$\varepsilon^2 = \sum_{i=1}^{\#_of_Sensors} \left(\left[\frac{\sqrt{(x_i - x)^2 + (y_i - y)^2 + (z_i - z)^2}}{c} + t_o - t_i \right]^2 \right) \quad (1)$$

where x_i , y_i , and z_i are the coordinates of the i^{th} sensor; c is the P-wave velocity; and t_i is the arrival time at the i^{th} sensor (e.g. Salamon and Wiebol, 1974).

To find the relative arrival time, the waveform was checked to see when the signal passed a designated threshold value, which was determined from the mean amplitude and standard deviation of the noise during the pre-trigger period. The threshold was set at three times the standard deviation from the mean. When the threshold value was exceeded, the point was stored as the trigger point. The data were scanned preceding the trigger point until the point in which the channel's mean value was obtained; this point was then used for the potential arrival of the event. The next 120 points were checked to see if the trigger threshold was crossed three more times during that interval. If the threshold had indeed been exceeded three subsequent times, the point was then stored as the arrival time. About 65% of the total events were located within 5 mm error. The error for each event was calculated as the average difference between the distances from the calculated location and the estimated arrival times.

Clustering Analysis

One way of describing a geometric figure is by its fractal dimension, which can be thought of as the number of variables required to describe a shape. For example, a line has a fractal dimension of one, a plane has a fractal dimension of two, and a volume has a fractal dimension of three (Mandelbrot, 1983). The use of fractal analysis to monitor the evolution of the failure process is reasonable because a fractal dimension of three represents random events occurring in a volume, and a fractal dimension of two signifies that the events have localized on a failure plane (Hirata et al., 1987; Smalley et al., 1987).

The process used to obtain the fractal dimension is the correlation integral, which compares the proximity of events to one another:

$$C(r) = \frac{2}{N(N-1)} N_R(R < r) \quad (2)$$

where $N_R(R < r)$ = the amount of pairs (p_i, p_j) with a distance smaller than r (e.g. Knox, 1963; Williams, 1983). The correlation integral can then be used to calculate the fractal dimension (FD):

$$C(r) = r^{FD} \quad (3)$$

By varying the value for r , a plot can be made to represent the changing value of the correlation integral versus the distance r . The fractal dimension is the slope of the function on a log-log plot, as shown in Fig. 1.

To demonstrate the clustering analysis, three sets of 100 data points, which can be thought of as AE locations, were placed randomly (i) in a volume (Fig. 1a), (ii) on the surface of a sphere (Fig. 1b), and (iii) along a line (Fig. 1c). The clustering analysis was performed, and the corresponding fractal dimensions were 3.0, 2.0, and 1.0, respectively. In laboratory tests associated with failure of rock, a common feature is a plane of fracture or shear band, so the fractal dimension offers the possibility to identify localization of deformation.

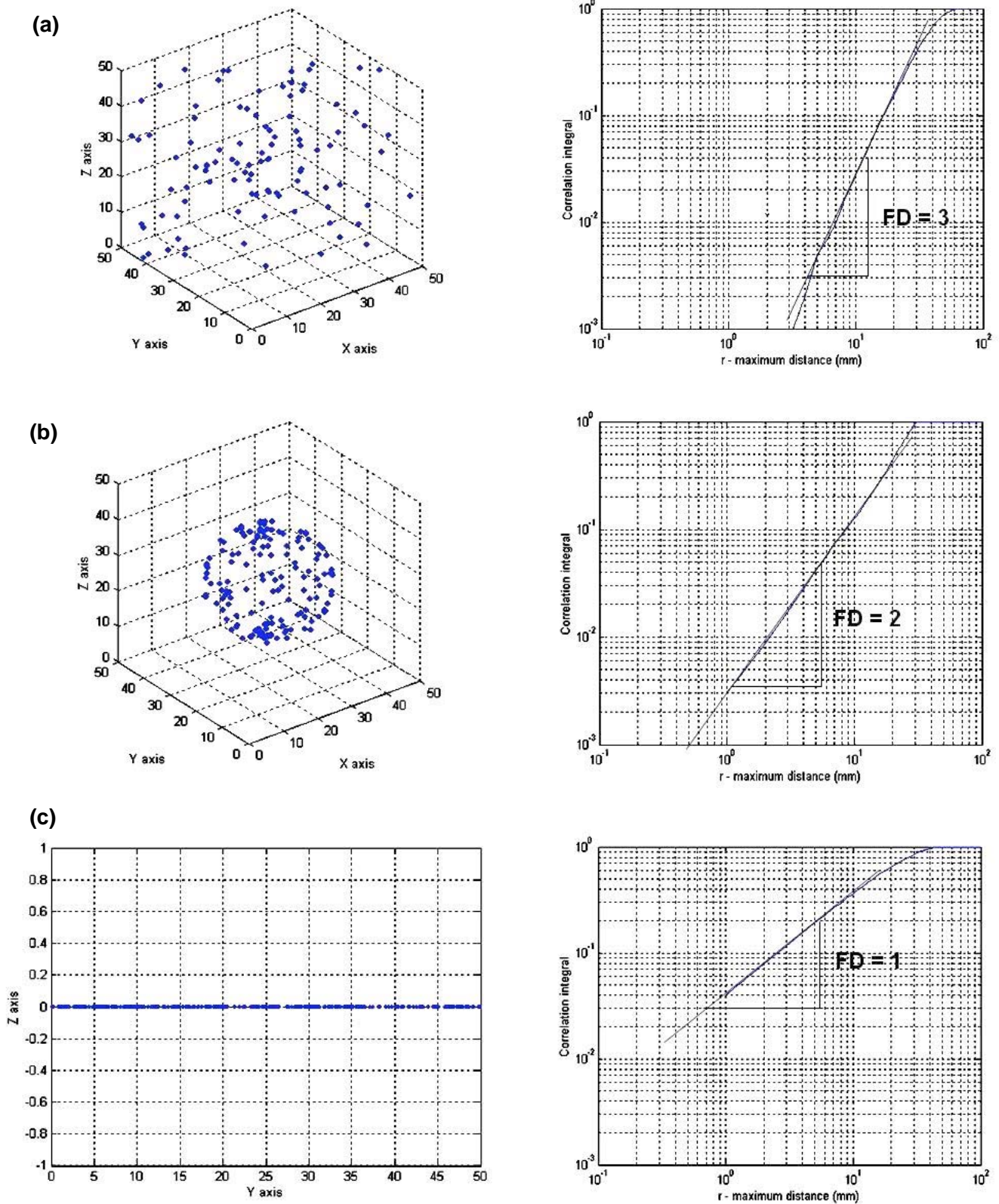


Fig. 1. Points randomly distributed (a) in a volume, (b) on a surface of a sphere, (c) along a line.

Simulated Failure Plane

One hundred events were spread randomly across a 50-mm plane (vertical range = 0) and the fractal dimension was calculated to be 2.0. This was then done again with a different vertical variance to simulate AE location error, the tortuosity of a crack, or the thickness of a shear band. This variance was created by assigning a random vertical component to each point, and calculating the fractal dimension. The vertical variance was increased in 5-mm increments until the vertical variance was equal to that of the width (50 mm) and a cube was formed. The results are shown in Fig. 2.

With the points in a plane, the fractal dimension was 2.0 (Fig. 2a). Figures 2b and 2c represent a vertical range of 5 and 20 mm, respectively, and the fractal dimensions were 2.15 and 2.70. Thus, for a location error of about 5 mm, a fractal dimension of 2.2 signifies that failure has localized along a planar feature. As the vertical range increased to the height of the specimen, 50 mm, the locations were spread throughout the volume and the fractal dimension was 3.0 (Fig. 2d). From 25 – 45 mm vertical range, the fractal dimension of 2.9 does not change appreciably (Fig. 3).

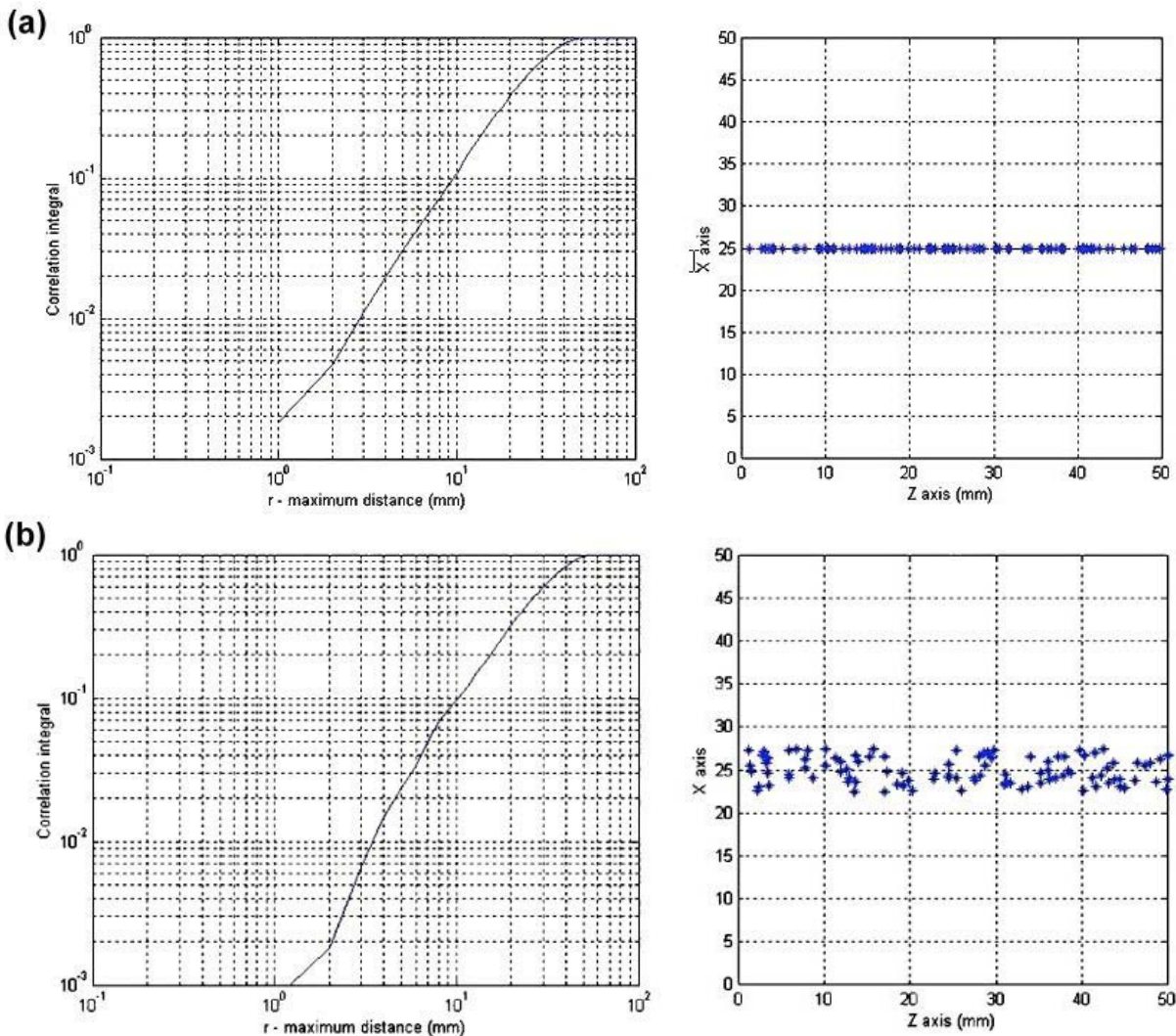


Fig. 2. Points randomly distributed across a plane.
(a) vertical range = 0. (b) vertical range = ± 2.5 mm.

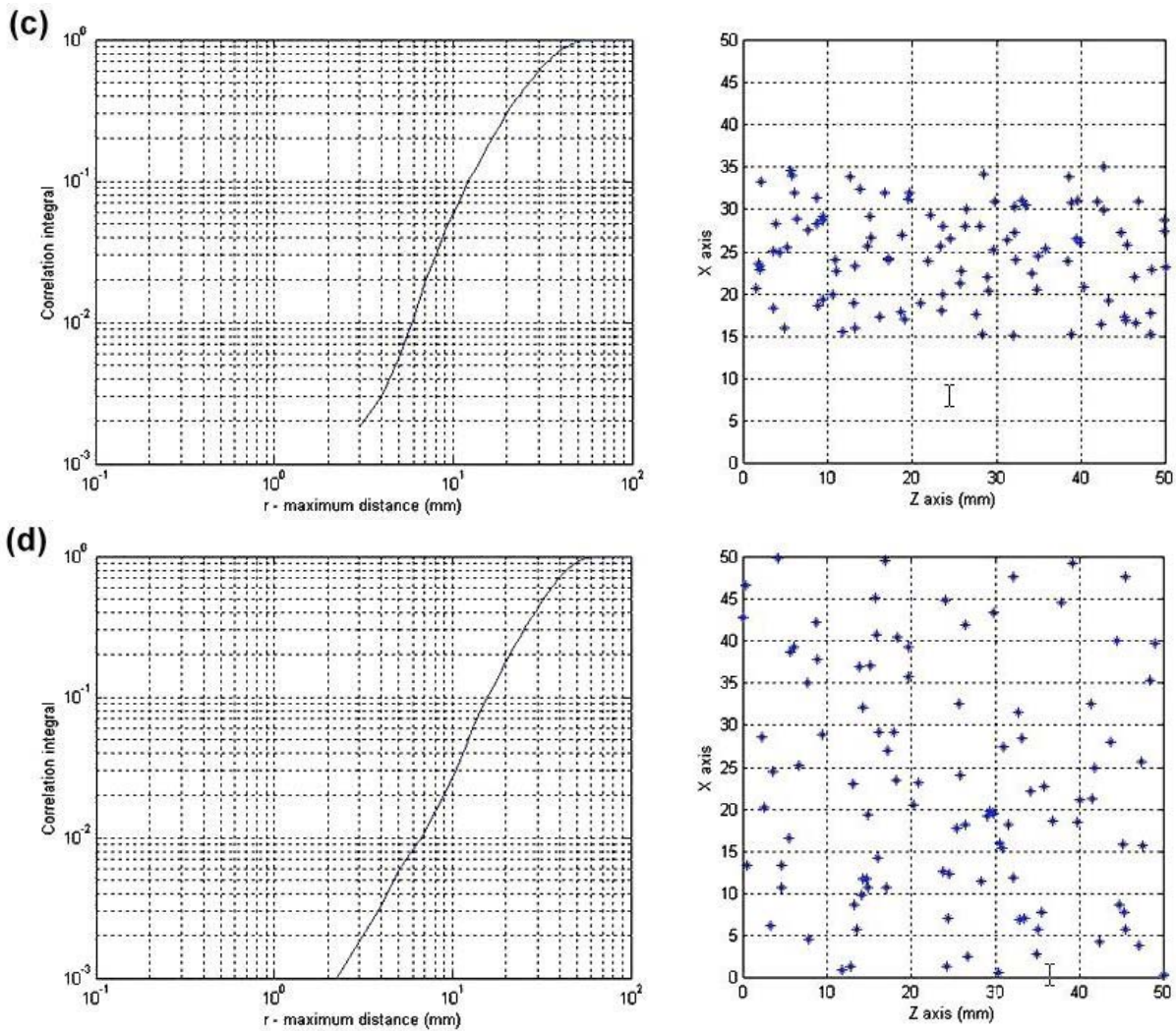


Fig. 2. Points randomly distributed across a plane.
 (c) vertical range = ± 10 mm. (d) vertical range = ± 25 mm.

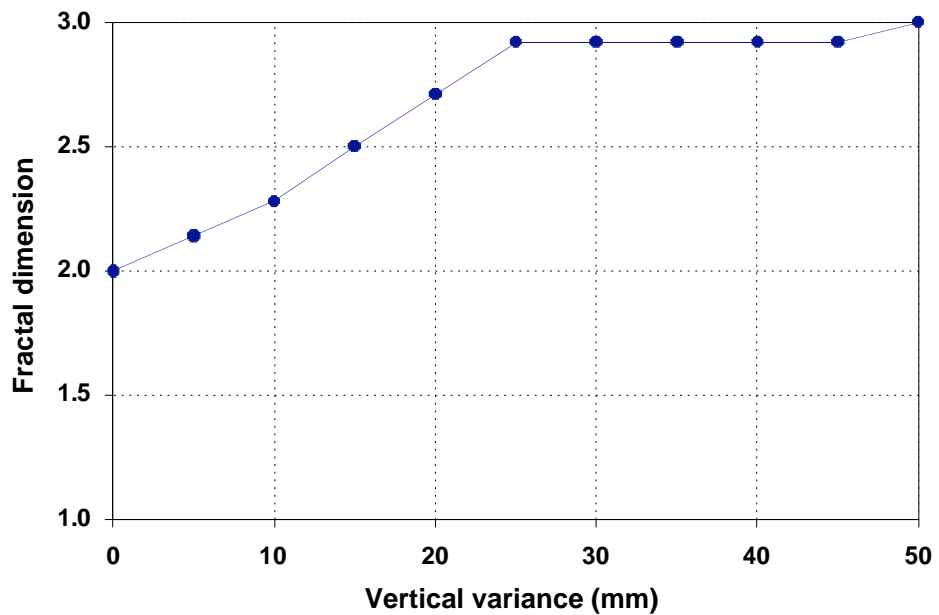


Fig. 3. Results of FD change with respect to variance of points on a plane.

It has been documented that the initiation of tensile failure is associated with a damage zone of concentrated microcracks, and an intrinsic zone of finite width is identified (Labuz and Biolzi, 1998); a distinct fracture does not form until further deformation into the post-peak regime. For shear failure in compression, a shear band is formed by a region of inelastic processes such as microcracking and porosity increase within a thickness of 5 – 10 grain diameters (Riedel and Labuz, 2007). Thus, for both tensile and shear type failure, a fractal dimension greater than 2.0 may be realized upon localization because of the failure processes.

Experimental Results

Three Point Bend Test

The first series of experiments involved initiation and propagation of tensile failure through mode I fracture. Smooth boundary (no notch) specimens of Serena sandstone were loaded in a three-point bend configuration. The beams were cut to a length of 310 mm, a width of 80 mm, and a thickness of 32 mm; the distance between supports was 300 mm. A strain-gage based displacement transducer with a gage length of 20 mm was placed at the center position to measure the crack mouth opening displacement (CMOD), which was used as the control signal within the closed-loop, servo-hydraulic load frame.

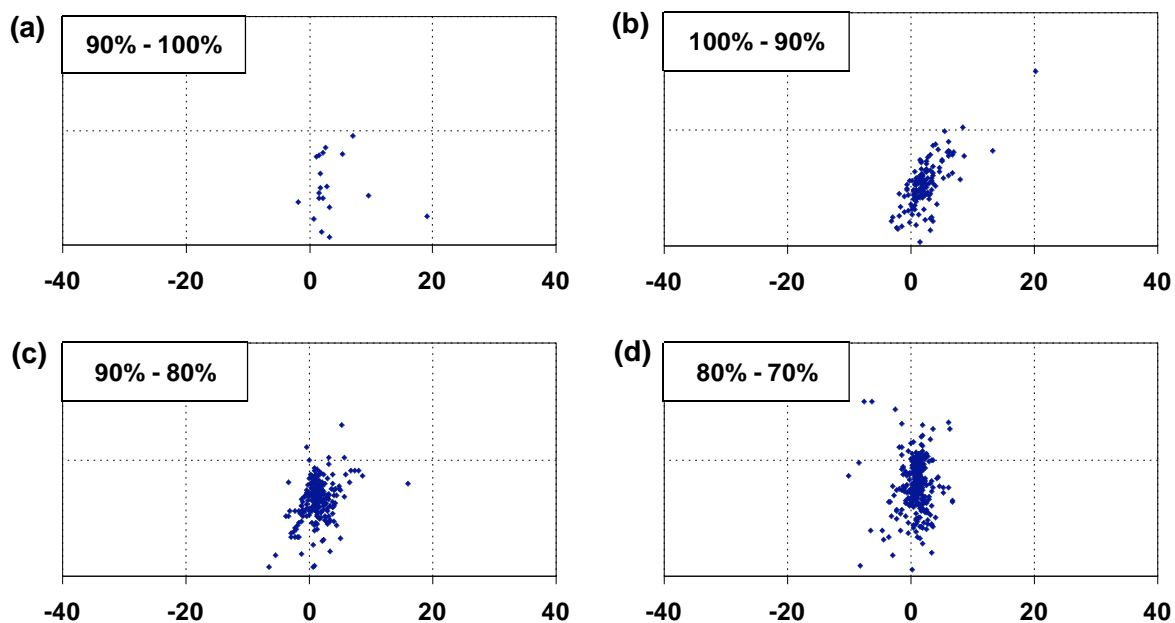


Fig. 4. AE events in beam with no notch at different load ratios: (a) pre-peak 90 – 100%; (b) 100 – 90% post-peak; (c) post-peak 90 – 80%; (d) post-peak 80 – 70%.

Figure 4 shows the located events with error <5 mm at different stages of loading, as indicated by the % of peak load called the load ratio. A migration of AE locations with loading was observed and the AE tracked the propagation of the fracture. Because of the absence of a stress concentrator—the boundary of the beam was smooth—only 18 events were located between the 90 – 100% load ratios (Fig. 4a). Nevertheless, a region of localization, which may be related to an intrinsic length of the rock, was evident (Labuz and Biozli, 1998). A fractal dimension of 2.3 was calculated (Fig. 5) for mode I fracture initiation. As CMOD was increased beyond peak load, 152 events were located between the 100 – 90% load ratios (Fig. 4b). The fractal dimension remained at 2.3, even though the post-peak regime is essentially controlled by crack propa-

gation. From the load ratios of 90 – 80%, the located AE events increased to 239 (Fig. 4c), and fractal dimension decreased to 2.2 (Fig. 5). The AE locations showed greater activity near the tip. Between the 80 – 70% load ratios, the located AE events numbered 329 and the length outlined by AE increased (Fig. 4d); the fractal dimension was slightly less than 2.0.

The clustering analysis showed that the fractal dimension started at about 2.3, certainly influenced by the gradient of axial stress due to bending, but localization was identified independently through a speckle interferometry technique. Crack propagation was responsible for the decrease in the fractal dimension in the post-peak regime.

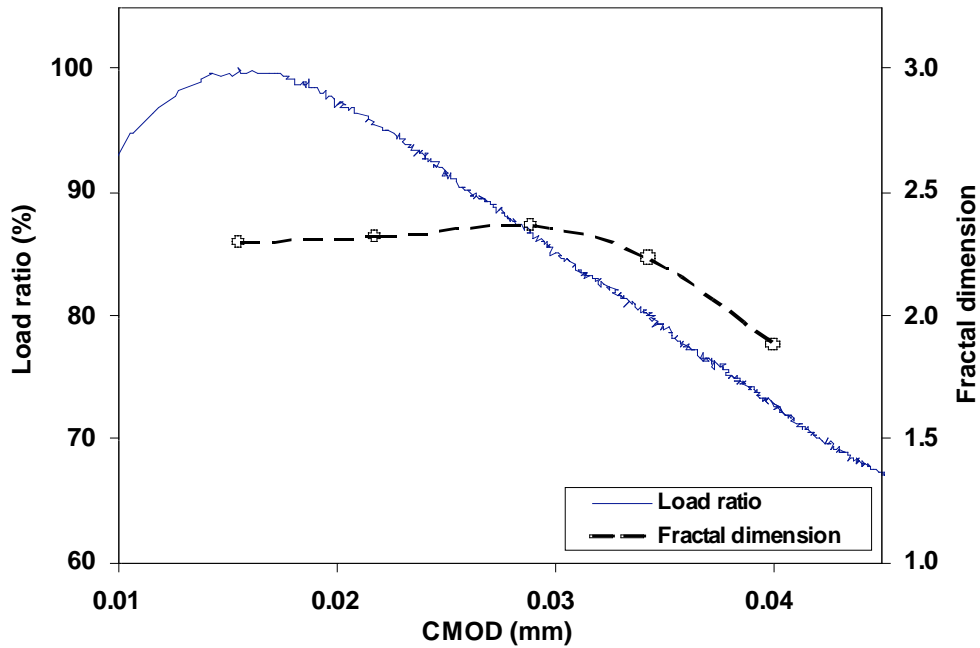


Fig. 5. Load history near peak and fractal dimension for beam with no notch.

Biaxial Test

A plane-strain (biaxial) compression apparatus (Drescher et al. 1990; Riedell and Labuz 2007) was used to examine shear banding in Berea sandstone. The apparatus allows the failure plane to develop and propagate in an unrestricted manner by attaching a low friction linear bearing to the upper platen. Plane-strain deformation is enforced by a thick-walled steel cylinder called the biaxial frame. A significant number of events (778) were located with < 5 mm error at various stages of loading (Fig. 6).

The clustering analysis was applied to the biaxial experiment by considering the AE locations in groups of 70 events (Fig. 7). From load ratios of 95 – 98% (lateral displacement of 0.085 – 0.093 mm), 219 events were located and the fractal dimensions were 2.64, 2.86, 2.59. The value of 2.6 was associated with inelastic deformation, but it is interesting to note a slight increase of the fractal dimension to 2.86 at a lateral displacement of 0.088 mm prior to peak load. From 98 – 100% peak load (lateral displacement of 0.093 – 0.101 mm), the fractal dimension dropped to 2.49 (Fig. 6b); a loss of homogeneous deformation was also recorded by the lateral LVDTs. In the post-peak region, the fractal dimension remained at 2.49 (Fig. 6c) and decreased to a value of 2.36 (Fig. 6d), before terminating the test. An examination of the specimen after the experiment showed a localization of deformation in the form of a shear band (Riedell and Labuz, 2007).

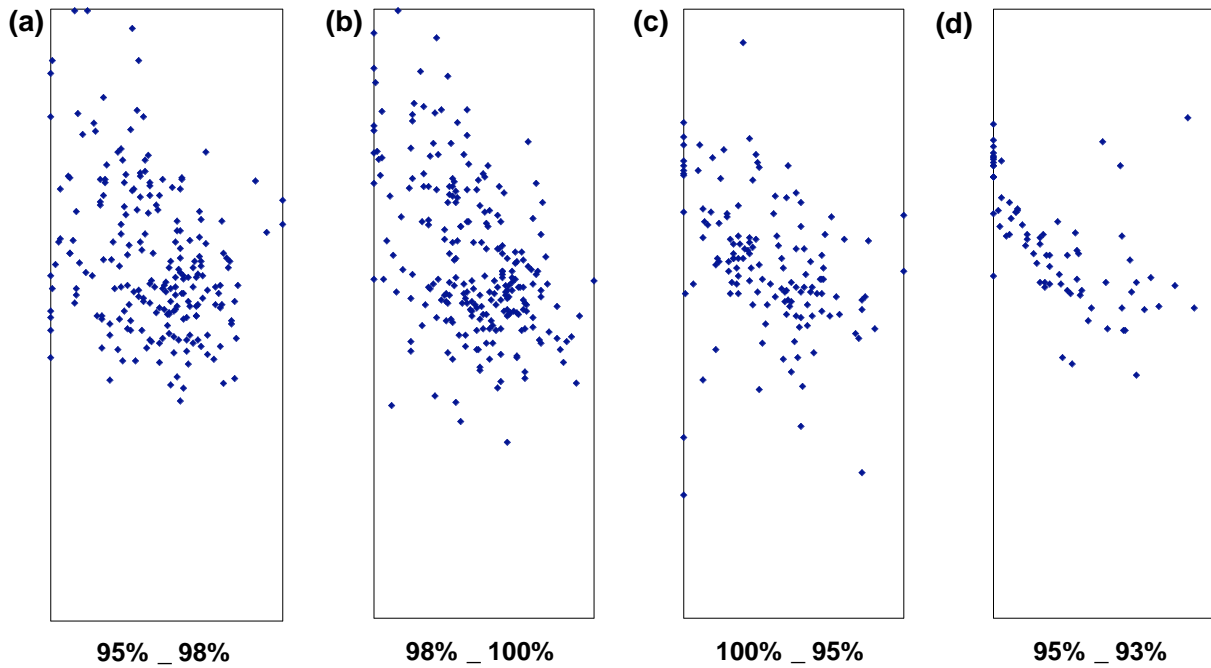


Fig. 6. AE events in a biaxial specimen at different load ratios: (a) pre-peak 95 – 98%; (b) pre-peak 98 – 100%; (c) post-peak 100 – 95%; (d) post-peak 95 – 93%.

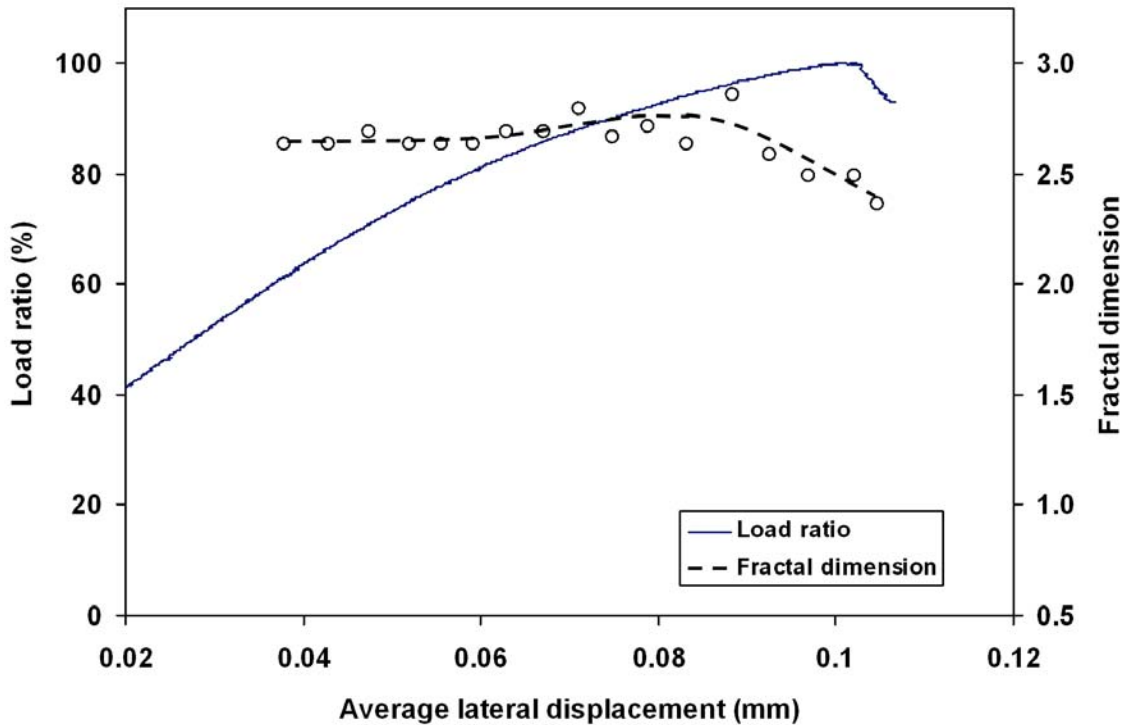


Fig. 7. Load history and fractal dimension for the biaxial test.

Conclusions

This research was focused on the development of numerical methods to analyze AE data. Specifically, a location algorithm for estimating the source hypocenter was used to map the failure process of rock under tensile and shear type loading. A clustering analysis based on fractal

theory provided a quantitative method for describing the transition from random microcracking to localized failure.

The distribution of events within an increment of load has a fractal structure that can be characterized by a fractal dimension, a reduction of which indicates clustering of hypocenters. A parametric study was used to provide a visual interpretation of a fractal dimension between three (random events) and two (localization of events on a plane), while a series of simulated failure planes with different vertical variance was used to test the sensitivity of the fractal dimension. The algorithms developed were used to interpret AE data from various experiments on rock. The results for the beams with a smooth boundary (no notch) showed that near peak load the fractal dimension was about 2.3, and approached 2.0 in the post-peak phase of loading as crack propagation occurred. Confined, plane strain compression tests involving shear-type failure showed that the fractal dimension was approximately 2.5 at peak load, and as the test progressed and shear banding developed, the fractal dimension decreased to around 2.4.

Acknowledgements

Partial support was provided by NSF Grant Number CMS-0070062 and the GAANN program of the Department of Education.

References

1. A. Drescher, I. Vardoulakis, and C. Han, *Geotech. Testing J. ASTM* **13**, 1990, 226-234.
2. T. Hirata, T. Satoh, and K. Ito, *Geophysical J. of Research, Astronomical Society*, **90**, 1987, 369-374.
3. G. Knox, *British J. of Preventive and Social Medicine*, **17**, 1963, 17-24.
4. J.F. Labuz and L. Biolzi, *Int. J. Solids Struct.*, **35**, 1998, 4191-4204.
5. B.B. Mandelbrot, *The fractal geometry of nature*, W.H. Freeman, 1983, 468 p.
6. K. Ono, *J. Strain Anal. Engng Design*, **40**(1), 2005, 1-15.
7. J.J. Riedel and J.F. Labuz, *Int. J. Num. Anal. Meth. Geomech.* **31**, 2007, 1281-1299.
8. M.D.G Salamon and G.A. Wiebol, *Rock Mech.*, **6**, 1974, 141-166.
9. K.R. Shah and J.F. Labuz, *J. Geophys. Res.*, **100** (B8)2/3, 1995, 15527-15539.
10. R.F. Smalley Jr., J.-L. Chatelain, D.L. Turcotte, and R. Prevot, *Bulletin of the Seismological Society of America*, **77**(4), 1987, 1368-1381.
11. G.W. Williams, Time-space clustering of disease, in *Statistical Methods for Cancer Studies*, R.G. Cornell, ed., New York, 1984. Marcel Dekker, Inc.

IMPACT IMAGING METHOD TO MAP DAMAGE IN CONCRETE BRIDGE DECK SLABS

STEPHEN D. BUTT, VIDYADHAR LIMAYE¹ and JOHN P. NEWHOOK²

Faculty of Engineering, Memorial University, St. John's, Newfoundland and Labrador, Canada;

¹MacDonnell Consulting Group Limited, Halifax, Nova Scotia, Canada;

²Dept. of Civil & Resource Engineering, Dalhousie University, Halifax, Nova Scotia, Canada

Abstract

An acoustic impact imaging method was developed to map damage in concrete bridge deck slabs and was evaluated by conducting a survey on a damaged full-scale bridge deck model. The imaging system consisted of a mechanical hammer source, two acoustic sensors and a digital waveform recorder. Imaging surveys were conducted along transverse lines that resulted in acoustic measurements on a 30-x-30-cm grid covering the entire upper surface of the slab. Acoustic measurements were processed to determine relative attenuation and then displayed using spatial imaging software. The resulting images showed increased levels of attenuation around punch-out failure zones and coinciding with many of the cracks mapped on the upper deck surface. Overall, the imaging technology showed good potential as a means of rapidly and nondestructively mapping damage in concrete bridge deck slabs.

Keywords: Impact imaging method, damage survey, concrete bridge deck inspection, structural health monitoring, acoustic transmission technique, acoustic attenuation.

Introduction

A simple and robust acoustic impact method was developed to identify damage in concrete bridge deck slabs by measuring the relative signal attenuation between two acoustic sensors [1]. This technique was applied to monitor progressive damage during fatigue testing of a full-sized model of a bridge deck slab at the Heavy Structures Laboratory at Dalhousie University, Halifax, Canada. Testing ended with punch-through failure of the deck and details of the pre-failure acoustic monitoring are presented in related publications [1-3]. This paper is focused on the related Impact Imaging Method (IIM), which was developed for post-failure mapping of damage in the bridge deck model. The IIM is an improvement over many existing acoustic impact methods, which have been used for several decades to map damage in engineering structures [e.g., 4], since it incorporates image generation to enhance damage resolution. The objective of this work was to evaluate the potential of the IIM to provide reliable mapping of bridge deck slab damage to aid inspection of bridges in-service.

The bridge deck slab model measured 12.2 m x 3.0 m on plan and was divided internally into four 3.05 m long panels along its length, each with varying internal reinforcement. Panel A was the control panel with no internal reinforcement while Panel B was similar to Panel A, but with a 75-mm high crack trainer midway along its length. Panel C had a bottom mesh of GFRP crack control reinforcement, and Panel D had a bottom mesh of steel crack control reinforcement. Each panel was tested under step-wise increasing fatigue loading to simulate wheel loading in-service until punch-through failure of the panel by the formation of a punch shear cone beneath the loading pad. Throughout testing, internal and external measurements of load, displacement and strain were made, and detailed mapping of visible cracks were made at regular intervals (Fig. 1). After

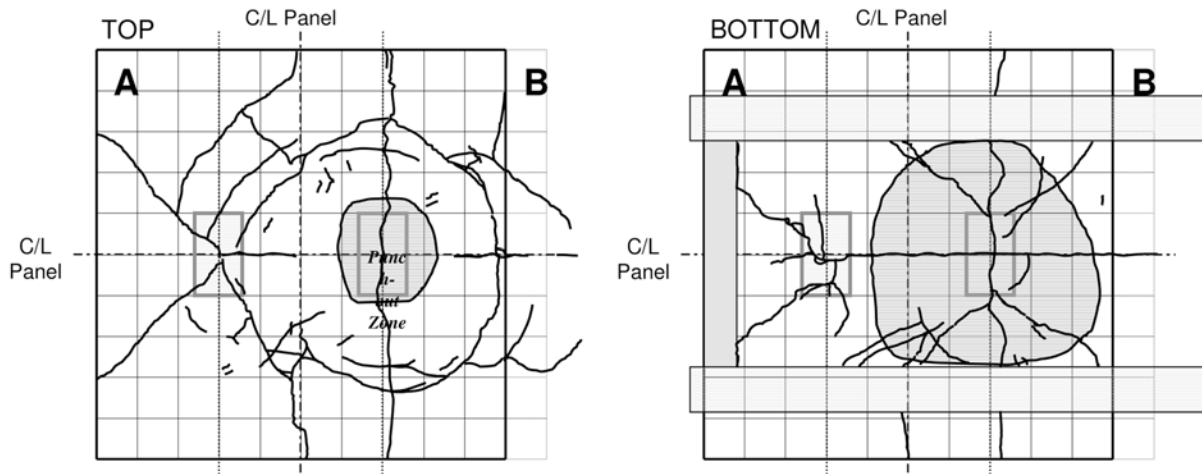


Fig. 1. Crack patterns mapped on the top and bottom surfaces of Panel A after punch-through failure. The punched-out conical slab is shaded in gray.

all 4 deck slab panels had failed, the IIM was used to map damage over the full area of the deck using the methodology described in the next section. Further details regarding the deck slab model fabrication, configuration, instrumentation and testing procedures are provided in related publications [5, 6].

Acoustic Survey Method

Acoustic System and Survey Procedure

The acoustic system consisted of a mechanical acoustic source, two acoustic sensors, a PC-based acoustic signal digitizing and recording system, and custom data processing software [1]. For the damage survey, the acoustic source was a ball-peen hammer that was struck onto thin steel plates, measuring approximately 7.5 x 7.5 cm, that were mounted on the side of the deck model at mid-height using quick-setting epoxy. The acoustic sensors were Physical Acoustics Corp. R6I acoustic transducers with a frequency range of 25 to 110 kHz, and were mounted on the upper deck utilizing vacuum grease as an acoustic couplant.

Survey Procedure

The acoustic survey was conducted over the top surface of the deck on survey lines oriented along the transverse direction, i.e., along the short dimension of the deck slab. The first survey line was situated 30 cm from the transverse edge of Panel D and adjacent lines were spaced at 30 cm along the longitudinal direction. Details of the survey procedures along each transverse line are given in Fig. 2. Along each survey line:

- a) One acoustic sensor (reference sensor) was fixed at a position 30 cm from the edge of the panel.
- b) The second sensor (active sensor) was positioned at a position 30 cm further along the survey line from the reference sensor.
- c) The hammer source was struck on the steel plate, resulting in the recording of the same waveform as it propagated past the reference and active sensors. Multiple hammer strikes were made and later averaged during data processing.
- d) The active sensor was moved to a new position 30 cm further along the survey line and Step c) was repeated.

e) Step d) was repeated until the active sensor was positioned in its final location at the longitudinal centerline of the deck slab.

Steps a) through e) were then repeated for the next transverse survey line. When the survey was completed along one side of the deck, the survey was repeated on the other side of the deck with the final active sensor positions also ending at the longitudinal centerline of the deck. At the completion of this procedure a reference or active sensor had been positioned at every point of a 30-x-30 cm grid pattern covering the entire upper surface of the deck.

Acoustic Data Processing

The acoustic waveform magnitude measured by each sensor for the hammer strikes was computed by summing the positive area under the recorded full waveform to get the integrated amplitude I_{Amp} . The normalized magnitude M of each recorded waveform was then determined by:

$$M = \frac{I_{Amp}_a}{I_{Amp}_r} \quad (1)$$

where the subscripts a and r denote the active and reference sensors, respectively. The dataset of M values was then analyzed to evaluate the standard fall-off of acoustic signal magnitude F_s during propagation from one sensor position to the next in undamaged regions of the deck:

$$F_s = \frac{M_{n+1}}{M_n} \quad (2)$$

where the M_n and M_{n+1} are the normalized waveform magnitudes at two sensor positions spaced 30 cm apart along the same transverse survey line with little or no damage between them. Figure 3 shows the standard fall-off values resulting from this analysis. Note the anomalous fall-off values from 0.6 m to 1.2 m are what are attributed to the focusing of the acoustic waveform when propagating from the thickened haunches to the thinner deck slab. The relative attenuation $Atten_{rel}$ of the waveform when propagating through the deck slab was then computed as:

$$Atten_{rel} = \frac{F_s - (M_{n+1}/M_n)}{F_s} \quad (3)$$

where the M_n and M_{n+1} are defined above and F_s given as Eq. (2). Thus, the relative attenuation represents the decimal percentage that the actual signal fall-off is less than the standard fall-off i.e. when there is no damage along the wave travel path.

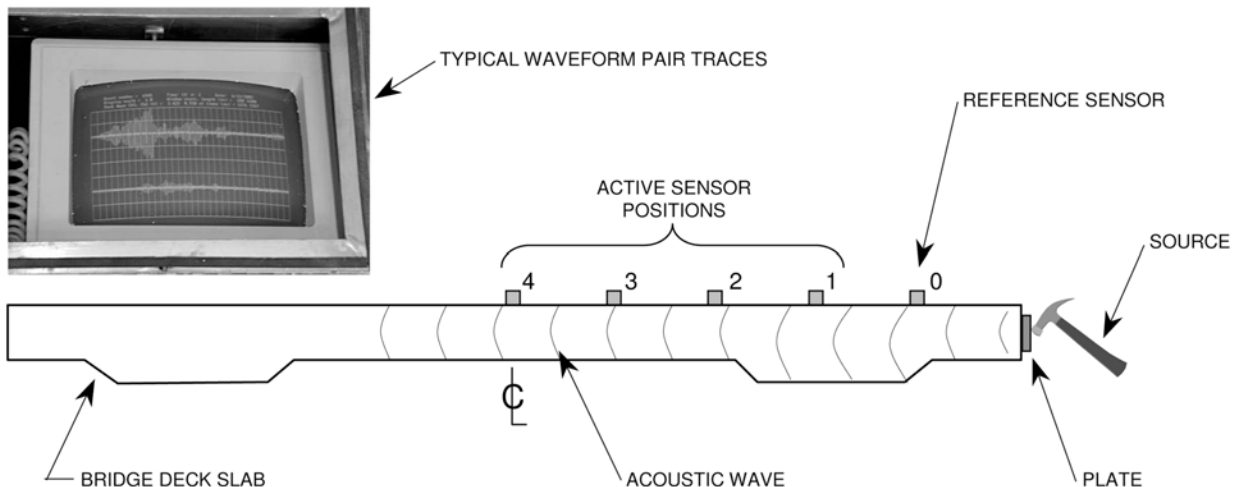


Fig. 2. Schematic of acoustic survey procedure along a single transverse survey line.

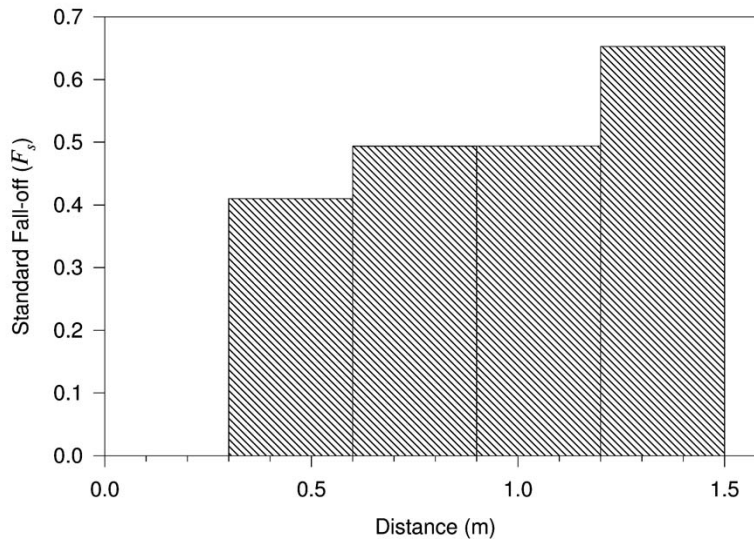


Fig. 3. Values of standard fall-off used to determine relative attenuation. The distance shown is with respect to the edge of the deck model.

Image Generation

Image generation was based on the presentation of the relative attenuation values as a 2-D plan image of the deck slab. The relative attenuation values were assigned 2-D coordinates, which were 15 cm from the active sensor position along the transverse survey line in the direction of the reference sensor. Global variogram analysis was conducted to generate a suitable semi-variogram model for the relative attenuation data and standard point estimation methods using ordinary kriging [7] were used to estimate the relative attenuation values on a 15-x-15 cm grid covering the full plan of the deck model. Industry-standard geostatistical modeling software was then used to generate the contoured relative attenuation images.

Figure 4 presents a plan composite photograph of the deck model showing the cracks mapped on the upper surface of the slab and the upper trace of the punch-through failure zone for each panel. For comparison, the relative attenuation image is given in Fig. 5. Note the good correlation between damaged and cracked regions of the deck and the regions of highest attenuation.

Discussion

As stated above, there is good correlation between the regions of highest acoustic attenuation shown in Fig. 5 and many of the cracked and damaged regions visible on the upper deck surface shown in Fig. 4. For example, each of the four punch-through failure zones is surrounded by a region of greater than 16% relative attenuation, which increases to up to 40% relative attenuation immediately adjacent to the failure zone. As well, most of the longitudinal cracks and other cracks oriented at less than 45° to the transverse survey direction are imaged as zones of greater than 16% relative attenuation. The cracks that are not imaged well include the discontinuous low-aperture longitudinal crack running from Panel A to Panel D on the upper side of Fig. 4 and most of the transverse oriented cracks. This makes sense since the transverse cracks are in a direction parallel to the survey direction and thus are not generally crossed by the acoustic wave raypath between the sensors during the survey.

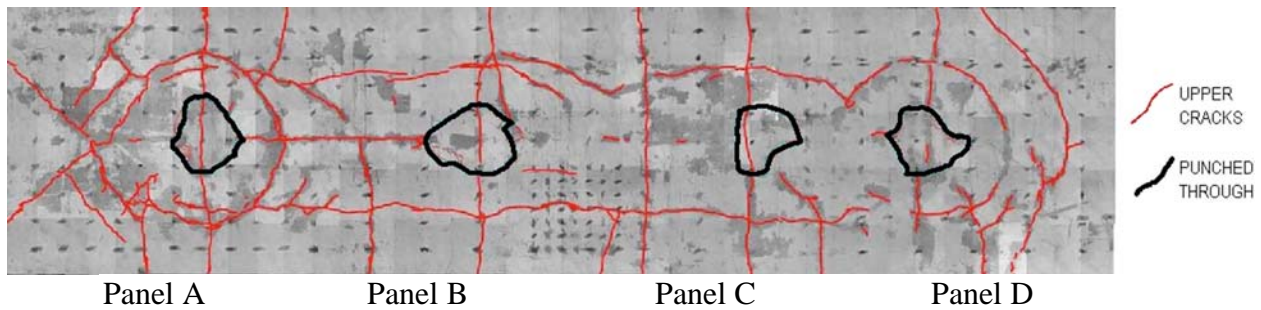


Fig. 4. Composite photograph looking down onto the upper surface of the deck model after punch-through failure of all four panels. The regular pattern of sensor positions can be partially seen as the regular grid pattern of dark spots. The legend is to the right.

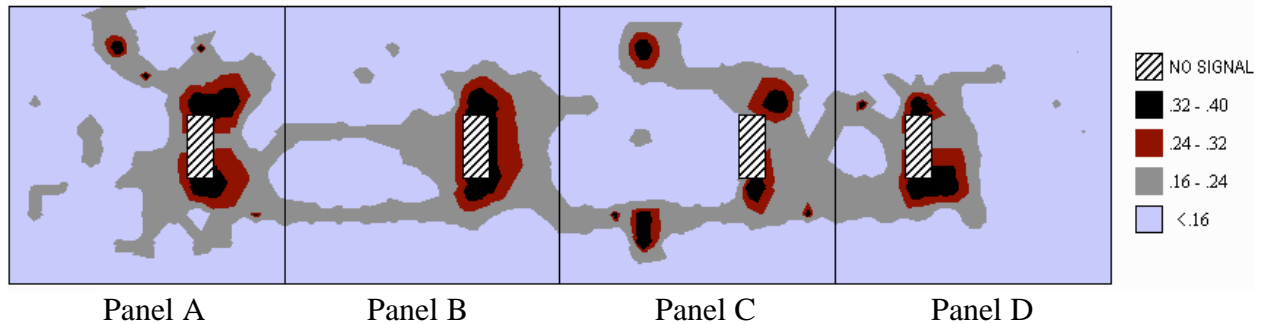


Fig. 5. Acoustic attenuation image of the bridge deck model. The image is oriented the same as Fig. 4 and the legend is to the right.

A final observation from these imaging results is that there are no regions with high levels of relative attenuation that do not have corresponding damage. In other words, the acoustic imaging technique does not generate false positives indicating damage where there is none. From a structural health point of view, this feature of the technique is as significant as its ability to correctly identify locations where damage is present.

Conclusions and Recommendations

Overall, the Impact Imaging Method has demonstrated good potential to image damage due to cracks in concrete bridge deck slabs. Cracks are imaged best when they are oriented perpendicular to the direction of the acoustic survey and worst when they are oriented parallel. Equally important, the imaging technique does not falsely identify damage when there is none. Both of these factors highlight the robustness of the imaging technique and its potential to contribute to the non-destructive evaluation and structural health monitoring of concrete bridge deck slabs. Based on these promising results, several recommendations can be made for further research and development with respect to this technology. From an operational point of view, recommendations for future work include:

- Acoustic surveys should be run in multiple directions to ensure that all cracks are imaged and, at a minimum, each area should be covered by two perpendicular survey orientations.
- Investigate the use of rolling acoustic sensors and sources to enable surveys to be done more rapidly than the method described in the paper.
- Investigate the impact of asphalt layers on imaging the underlying concrete slab.

Acknowledgements

This investigation was funded by Intelligent Sensing of Innovative Structures (ISIS) Canada and the National Science and Engineering Research Council (NSERC).

References

1. S.D. Butt, V. Limaye, A.A. Mufti and B. Bakht. Acoustic Transmission Technique for Evaluating Fatigue Damage in Concrete Bridge Deck Slabs, *ACI Structural Journal*. **101**, 1, 2004, 3-10.
2. S.D. Butt and V. Limaye. Damage Detection in Concrete Bridge Deck Slabs using Acoustic Attenuation, in *Proc. 1st Int. Conf. on Structural Health Monitoring of Innovative Civil Engineering Structures*, Winnipeg, Sept. 2002.
3. S.D. Butt, V. Limaye and D. Connors. Imaging damage in concrete bridge deck slabs using acoustic attenuation, in *Proc. 31st CSCE Conference*, ed. N.B. Moncton, June, 2003, 1406-1414.
4. R. Schroerer, Acoustic Impact Technique, *Non-destruct Test*, **3**(3), June, 1970, 194-6.
5. V. Limaye, A.A. Mufti, B. Bakht and S.D. Butt. Steel-free Deck Slabs under Cyclic Loading, in *Proc. 6th Int. Conf. on Short and Medium Span Bridges*, Vancouver, July/Aug, 2002.
6. V. Limaye, *Steel-free bridge decks under cyclic loading: a study of crack propagation and strength degradation*, Ph.D. dissertation, Dalhousie University, 2004, unpublished.
7. A.G. Journel and C.J. Huijbregts, *Mining Geostatistics*, Academic Press, New York, (1978).